

AKO 32 828.1-4H-CF

DIFFRACTIVE OPTICS: DESIGN, FABRICATION, AND APPLICATIONS

DTIC
ELECTE
FEB 07 1995
S G D

Sponsored by
Optical Society of America

19950203 174

1994 TECHNICAL DIGEST
SERIES VOLUME 11

JUNE 6-9, 1994
ROCHESTER, NEW YORK

DISTRIBUTION STATEMENT A

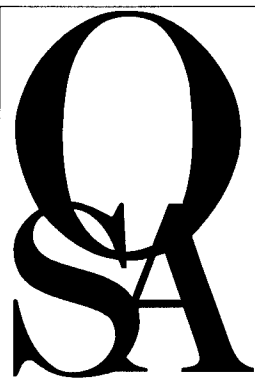
Approved for public release;
Distribution Unlimited

REPORT DOCUMENTATION PAGE

Form Approved
OMB No. 0704-0188

Public reporting burden for this collection of information is estimated to average 1 hour per response, including the time for reviewing instructions, searching existing data sources, gathering and maintaining the data needed, and completing and reviewing the collection of information. Send comments regarding this burden estimate or any other aspect of this collection of information, including suggestions for reducing this burden, to Washington Headquarters Services, Directorate for Information Operations and Reports, 1215 Jefferson Davis Highway, Suite 1204, Arlington, VA 22202-4302, and to the Office of Management and Budget, Paperwork Reduction Project (0704-0188), Washington, DC 20503.

1. AGENCY USE ONLY (Leave blank)		2. REPORT DATE December 1994	3. REPORT TYPE AND DATES COVERED Final	
4. TITLE AND SUBTITLE Diffraction Optics: Design, Fabrication, and Applications			5. FUNDING NUMBERS DAAH04-94-C-0080	
6. AUTHOR(S) David W. Hennage (Principal Investigator)				
7. PERFORMING ORGANIZATION NAME(S) AND ADDRESS(ES) Optical Society of America 2010 Massachusetts Avenue NW Washington, DC 20036-1023			8. PERFORMING ORGANIZATION REPORT NUMBER	
9. SPONSORING/MONITORING AGENCY NAME(S) AND ADDRESS(ES) U.S. Army Research Office P.O. Box 12211 Research Triangle Park, NC 27709-2211			10. SPONSORING/MONITORING AGENCY REPORT NUMBER ARO 32828.1-PH-CF	
11. SUPPLEMENTARY NOTES The views, opinions and/or findings contained in this report are those of the author(s) and should not be construed as an official Department of the Army position, policy, or decision, unless so designated by other documentation.				
12a. DISTRIBUTION/AVAILABILITY STATEMENT Approved for public release; distribution unlimited.			12b. DISTRIBUTION CODE	
13. ABSTRACT (Maximum 200 words) Summaries of papers presented at the Topical Meeting, Diffraction Optics: Design, Fabrication, and Applications, June 6-9, 1994, at Rochester, New York.				
14. SUBJECT TERMS Diffraction, Optical Gratings, Optical Interconnects, Fabrication, Light Transmission, Laser Systems, Microlenses, Optical Coatings			15. NUMBER OF PAGES 370	
			16. PRICE CODE	
17. SECURITY CLASSIFICATION OF REPORT UNCLASSIFIED	18. SECURITY CLASSIFICATION OF THIS PAGE UNCLASSIFIED	19. SECURITY CLASSIFICATION OF ABSTRACT UNCLASSIFIED	20. LIMITATION OF ABSTRACT UL	



Diffraction Optics: Design, Fabrication, and Applications

*Summaries of papers presented at the
Topical Meeting, Diffraction Optics:
Design, Fabrication, and Applications*

June 6-9, 1994
Rochester, New York

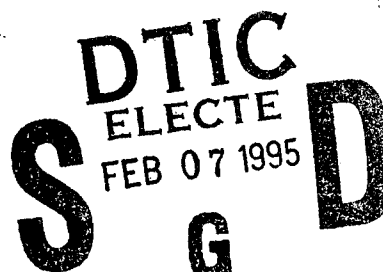
1994 Technical Digest Series
Volume 11

CONFERENCE EDITION

Sponsored by
Optical Society of America

Partial support from
The National Science Foundation
National Aeronautics and Space Administration
The Army Research Laboratory

Optical Society of America
2010 Massachusetts Avenue NW
Washington DC 20036-1023



Accession For	
NTIS	CRA&I <input checked="" type="checkbox"/>
DTIC	TAB <input type="checkbox"/>
Unannounced <input type="checkbox"/>	
Justification	
By	
Distribution /	
Availability Codes	
Dist	Avail and/or Special
A-1	

Articles in this publication may be cited in other publications. In order to facilitate access to the original publication source, the following form for the citation is suggested:

Name of author(s), title of paper, in Diffractive Optics, Vol. 11, 1994 OSA
Technical Digest Series (Optical Society of America, Washington, DC, 1994),
pp. xx-xx.

ISBN Number

Conference Edition	1-55752-348-7
Postconference Edition	1-55752-349-5
1994 Technical Digest Series	1-55752-321-5

Library of Congress Catalog Card Number

Conference Edition	93-65360
Postconference Edition	93-65361

Copyright © 1994, Optical Society of America

Individual readers of this digest and libraries acting for them are permitted to make fair use of the material in it as defined by Sections 107 and 108 of the U.S. Copyright Law, such as to copy an article for use in teaching or research, without payment of fee, provided that such copies are not sold. Copying for sale or copying for use that exceeds fair use as defined by the Copyright Law is subject to payment of copying fees. The code 1-55752-321-5/94/\$6.00 gives the per-article copying fee for each copy of the article made beyond the free copying permitted under Sections 107 and 108 of the U.S. Copyright Law. The fee should be paid through the Copyright Clearance Center, Inc., 21 Congress Street, Salem, MA 01970.

Permission is granted to quote excerpts from articles in this digest in scientific works with the customary acknowledgment of the source, including the author's name and the name of the digest, page, year, and name of the Society. Reproduction of figures and tables is likewise permitted in other articles and books provided that the same information is printed with them and notification is given to the Optical Society of America. Republication or systematic or multiple reproduction or of any material in this digest, including contents and abstracts, is permitted only under license from the Optical Society of America; in addition, the Optical Society may require that permission also be obtained from one of the authors. Electrocopying or electrostorage of any material in this digest is strictly prohibited. Address inquiries and notices to Director of Publications, Optical Society of America, 2010 Massachusetts Ave., NW, Washington, DC 20036. In the case of articles whose employees of the U.S. Government or its contractors or grantees, the Optical Society of America recognizes the right of the U.S. Government to retain a nonexclusive, royalty-free license to use the author's copyrighted article for U.S. Government purposes.

Printed in the U.S.A.

**DIFFRACTIVE OPTICS:
DESIGN, FABRICATION AND APPLICATIONS
TECHNICAL PROGRAM COMMITTEE**

J. Leger, *General Chair, University of Minnesota*

J. Jahns, *Program Co-chair, AT&T Bell Laboratories*

M. G. Moharam, *Program Co-chair, University of Central Florida*

R. Athale, *George Mason University*

D. Buralli, *Sinclair Optics*

J. A. Cox, *Honeywell*

N. Gallagher, *Purdue University*

T. Gaylord, *Georgia Institute of Technology*

M. Hayford, *Optical Research Associates*

H. P. Herzig, *University of Neuchatel, Switzerland*

S. Lee, *University of California, San Diego*

C. Londono, *Polaroid Corporation*

G. Michael Morris, *University of Rochester*

T. Shiono, *Matsushita Electrical Industries, Ltd., Japan*

G. Swanson, *MIT Lincoln Laboratory*

Contents

Agenda of Sessions	v
DMA Electromagnetic Theory of Gratings	1
DMB Novel Applications	21
JMC Joint Session on Diffractive Optics Design	43
DMD Optical Interconnects	63
DTuA Fabrication Methods	85
DTuB Poster Preview and Poster Session	107
DTuC Design I	185
DTuD Light Propagation and Diffraction	213
DWA Design II	233
DWB Subwavelength and Coated Structures	251
DWC Applications for Laser Systems	273
DWD Fabrication by /Direct-Write Techniques	299
DThA Microlens Fabrication and Applications	315
DThB Fabrication and Characterizations	333
Key to Authors and Presiders	353

AGENDA OF SESSIONS—Continued

TUESDAY, JUNE 7, 1994

Ballroom A	Ballroom B	Ballroom C	Ballroom D
8:30 am–10:00 am ITuA, Space Optics I—Hubble	8:30 am–10:00 am DTuA, Fabrication Methods	8:30 am–9:00 am GTuA, Opening Remarks	8:30 am–10:00 am OTuA, Finishing Technology
		9:00 am–10:00 am GTuB, GRIN Design, Raytracing and Aberration Theory	
10:00 am–10:30 am COFFEE BREAK, Exhibit Hall South			
10:30 am–12:30 pm ITuB, Lens Design Poster Paper Previews	10:30 am–11:15 am DTuB, Diffractive Optics Poster Paper Previews	10:30 am–12:00 m GTuC, GRIN Waveguide Fabrication, Characterization and Modelling I	10:30 am–12:00 m OTuB, Polishing Techniques
Diffractive Optics and Lens Design Poster Session, Exhibit Hall South			
12:00 m–1:30 pm LUNCH (on your own)			
1:30 pm–3:30 pm ITuC, Optimization	1:30 pm–3:30 pm DTuC, Design I	1:30 pm–3:15 pm GTuD, GRIN Waveguides Fabrication, Characterization and Modelling II	1:30 pm–3:30 pm OTuC, Science of Finishing
3:30 pm–4:00 pm COFFEE BREAK, Exhibit Hall South			
4:00 pm–5:30 pm ITuD, Design Examples II	4:00 pm–5:30 pm DTuD, Light Propagation and Diffraction	4:00 pm–5:30 pm GTuE, Ion Exchange Propagation	4:00 pm–5:30 pm OTuD, Specialized Fabrication Techniques
6:00 pm–7:30 pm CONFERENCE RECEPTION, Upper Lobby Foyer			

AGENDA OF SESSIONS

SUNDAY, JUNE 5, 1994

6:30 pm–8:30 pm REGISTRATION, Upper Level Lobby

MONDAY, JUNE 6, 1994

Ballroom A	Ballroom B	Ballroom C	Ballroom D
8:30 am–10:00 am IMA, Design Methods and Theory, I	8:30 am–10:00 am DMA, Electro-magnetic Theory of Gratings		8:30 am–10:00 am OMA, Optical Fabrication and Testing
10:00 am–10:30 am COFFEE BREAK, West Corridor			
10:30 am–12:30 pm IMB, Design Methods and Theory, II	10:30 am–12:00 m DMB, Novel Applications		10:30 am–12:00 m OMB, Matching Centers and Tooling
12:00 m–1:30 pm LUNCH (on your own)			
1:30 pm–3:30 pm JMC, Diffractive Optics Design (Joint Session with Diffractive Optics)			1:30 pm–3:30 pm OMC, Process Enhancements in Microgrinding
3:30 pm–4:00 pm COFFEE BREAK, Exhibit Hall South			
4:00 pm–5:30 pm IMD, Optical Design Examples, I	4:00 pm–5:30 pm DMD, Optical Interconnects		4:00 pm–5:30 pm OMD, Surface and Subsurface Characteristics
8:00 pm–10:00 pm IME, Optical Design Software Workshop			

AGENDA OF SESSIONS—Continued

THURSDAY, JUNE 9, 1994

Ballroom A	Ballroom B	Ballroom C	Ballroom D
8:30 am–10:00 am IThA, Engineering Analysis	8:30 am–10:00 am DThA, Microlens Fabrication and Applications		8:30 am–10:00 am OThA, Metrology
10:00 am–10:30 am COFFEE BREAK, West Corridor			
10:30 am–11:45 am IThB, Micro and Integrated Optics	10:30 am–12:00 m DThB, Fabrication and Characterization		10:30 am–12:00 m OThB, Ion Milling
12:00 m–1:15 pm IThC, Software Workshop—Wrap-Up			
12:00 m–1:30 pm LUNCH (on your own)			
1:30 pm–3:30 pm JThD, Design for Fabrication and Testing (Joint Session with Optical Fabrication and Testing)			
3:30 pm–4:00 pm COFFEE BREAK, West Corridor			
4:00 pm–5:30 pm IThE, Design Examples III			

AGENDA OF SESSIONS—Continued

WEDNESDAY, JUNE 8, 1994

Ballroom A	Ballroom B	Ballroom C	Ballroom D
8:30 am–10:00 am IWA, Asymmetric Optical System Design	8:30 am–10:00 am DWA, Design II	8:30 am–10:00 am GWA, Gradient Index Fabrication and Characterization I	8:30 am–10:00 am OWA, Instrumentation and Analysis
10:00 am–10:30 am COFFEE BREAK, Exhibit Hall South			
10:30 am–12:30 pm IWB, New Applications	10:30 am–12:00 m DWB, Subwavelength and Coated Structures	10:30 am–12:00 m GWB, Gradient Index Fabrication and Characterization II	10:30 am–12:00 m OWB, Interferometry
12:00 m–1:30 pm LUNCH (on your own)			
1:30 pm–3:30 pm IWC, Non-imaging and Illumination Systems	1:30 pm–3:30 pm DWC, Applications for Laser Systems	1:30 pm–3:30 pm GWC, Applications Engineering with GRIN	1:30 pm–3:30 pm OWC, Green Optics
3:30 pm–4:00 pm COFFEE BREAK, Exhibit Hall South			
4:00 pm–5:30 pm IWD, Space Optics II	4:00 pm–5:30 pm DWD, Fabrication by Direct-wire Techniques	4:00 pm–5:30 pm Postdeadline Paper Session	4:00 pm–5:30 pm OWD, Center for Optics Manufacturing

MONDAY, JUNE 6, 1994—Continued

ROOM B

4:00 pm–5:30 pm

DMD, OPTICAL INTERCONNECTS

Jurgen Jahns, *AT&T Bell Laboratories, Presider*

4:00 pm (Invited)

DMD1 Diffractive optic design for board-level free-space optical interconnects, Raymond K. Kostuk, *Univ. Arizona*. The three-dimensional nature of board-level interconnects suggests the use of free-space optics for the connection medium. Several diffractive optic designs for this application are presented. (p. 64)

4:30 pm

DMD2 Design of achromatic holographic grating couplers for backplane optical interconnects, Michael R. Wang, Freddie Lin, *Physical Optics Corp.* Laser wavelength shifts cause undesirable coupling alignment problems in multiboard systems using optical backplane interconnections. An achromatization technique based on a three-grating structure is introduced. (p. 68)

4:45 pm

DMD3 Design and fabrication error analysis of input couplers for integrated planar micro-optic systems by rigorous diffraction theory, Seung Gol Lee, Tae Wan Kim, *Inha Univ., South Korea*; Seok Ho Song, *Electronics and Telecommunications Res. Inst., South Korea*. Based on the rigorous diffraction theory, input couplers for integrated planar micro-optic systems are designed and their fabrication errors are analyzed numerically. (p. 72)

5:00 pm

DMD4 Selective cell-based algorithm for designing high-efficiency beam array generators, Rick L. Morrison, Mike J. Wojcik, *AT&T Bell Laboratories*. An iterative algorithm that investigates only cells along phase transition boundaries and is able to increase its spatial resolution as necessary is used to design large two dimensional Fourier-plane holograms generating arbitrary intensity spot arrays. (p. 76)

5:15 pm

DMD5 Coupled kinoforms for space variant optical interconnect systems, David Zaleta, Michael Larsson, Walter Daschner, Sing H. Lee, *UC-San Diego*. We present three design methods to maximize the propagation distance for space variant optical interconnect systems and compare it to a standard DOE design. (p. 80)

TUESDAY, JUNE 7, 1994

ROOM B

8:30 am–10:00 am

DTuA, FABRICATION METHODS

M. C. Hutley, *National Physical Laboratory, Presider*

8:30 am (Invited)

DTuA1 X-ray lithography: applications to fabrication of diffractive optics, F. Cerrina, *Univ. Wisconsin-Madison*. The high resolution, depth of focus, and process latitude make x-ray optics an ideal technique for the production of large-area and high-volume diffractive optics. We will review XRL and its status today, and present some demonstration of high-resolution and high-aspect ratio optics. (p. 86)

9:00 am

DTuA2 Fabrication of ultrahigh-resolution gratings for x-ray spectroscopy, Max Wei, Erik H. Anderson, David T. Attwood, *Lawrence Berkeley Laboratory*. Large area ($20\ \mu\text{m} \times 90\ \mu\text{m}$) gratings of 50 nm period have been recorded in PMMA using soft x-ray archromatic holographic lithography. (p. 91)

9:15 am

DTuA3 Interferometric and TIR holographic fabrication of high carrier-frequency surface-relief elements, P. Ehbets, H. P. Herzig, P. Blattner, P. Nussbaum, *Univ. Neuchâtel, Switzerland*; F. S. M. Clube, S. Gray, J. C. Tisserand, *Holtronic Technologies SA, Switzerland*. High carrier-frequency surface-relief elements for spot array generation have been fabricated by interferometric recording and by a holographic mask aligner. (p. 95)

9:30 am

DTuA4 Investigation of the defects introduced when diamond-tuning hybrid components for use in infrared optical systems, Andrew J. McDowell, Patrick B. Conway, Chris W. Slinger, *Defence Research Agency, England, U.K.*; Andrew C. Cox, Richard A. Parker, Andrew P. Wood, *Precision-Optical Engineering, England, U.K.* A practical and theoretical investigation of the effects of periodic and random defects introduced when diamond turning hybrid components for use in infrared optical systems. (p. 99)

9:45 am

DTuA5 Effects of fabrication errors on the performance of binary gratings, Drew A. Pommert, M. G. Moharam, Eric B. Grann, *Univ. Central Florida*. The effects of the errors in the depth, grating period, linewidth, and 'squareness' of the profile due to the fabrication process on the desired diffraction characteristics are investigated. (p. 103)

ROOM B

10:30 am–12:30 pm

DTuB, POSTER PREVIEW AND POSTER SESSION

G. Michael Morris, *University of Rochester, Presider*

10:30 am

DTuB1 New developments in the diffraction behavior of Echelle gratings, Erwin G. Loewen, *Milton Roy Co.*; Daniel Maystre, *Univ. d'Aix Marseille III, France*; Evgeny K. Popov, Lyubomir Tsonev, *Institute of Solid-State Physics, Bulgaria*. Diffraction efficiency of Echelle gratings has been carefully examined and found more complex than predicted by scalar theory. New rigorous theoretical calculations have confirmed the observations. (p. 108)

MONDAY, JUNE 6, 1994

ROOM B

8:30 am–10:00 am

DMA, ELECTROMAGNETIC THEORY OF GRATINGS

J. R. Leger, *University of Minnesota, Presider*

8:30 am (Invited)

DMA1 Fundamentals of grating diffraction, Thomas K. Gaylord, Elias N. Glytsis, David L. Brundrett, *Georgia Institute of Technology*. (Abstract not available.) (p. 2)

9:00 am

DMA2 Implementation of the rigorous coupled-wave technique: stability, efficiency, and convergence, M. G. Moharam, Drew A. Pommet, Eric B. Grann, *Univ. Central Florida*. Efficient and absolutely stable implementation of the rigorous coupled-wave technique is presented for the analysis of one-dimensional surface-relief gratings. (p. 4)

9:15 am

DMA3 Mathematic-issues in the electromagnetic theory of gratings, Gang Bao, *Univ. Minnesota*; David C. Dobson, *Texas A&M Univ.*; J. Allen Cox, *Honeywell Technology Center*. A variational approach is presented. Existence and uniqueness of solutions, convergence of the variational method, and sensitivity to TM polarization are discussed. (p. 8)

9:30 am

DMA4 Optimization techniques for the design of resonance domain diffractive optical elements, J. T. Sheridan, R. Ehrhardt, T. O. Körner, *Univ. Erlangen–Nürnberg, Germany*. Nonlinear optimization techniques, in particular genetic algorithms and simulated evolution, are applied in conjunction with the Legendre exact eigenfunction method to design surface relief gratings. (p. 12)

9:45 am

DMA5 Observation and numerical analysis of finite-beam Bragg diffraction by a phase grating, Michael R. Wang, *Physical Optics Corp.* A numerical impulse response technique and waveguide experiments are introduced to study the propagation and Bragg diffraction of a finite-width beam in a phase grating. (p. 16)

ROOM B

10:30 am–12:00m

DMB, NOVEL APPLICATIONS

Joseph N. Mait, *U.S. Army, Presider*

10:30 am (Invited)

DMB1 Diffractive micro-optics in Switzerland, H. P. Herzig, *Univ. Neuchâtel, Switzerland*. A review of the current activities in diffractive microoptics in Switzerland is presented. Of interest are phase elements with multilevel and continuous microreliefs. (p. 22)

11:00 am

DMB2 Single-element achromatic diffractive lens, Donald W. Sweeney, Gary Sommargren, *Lawrence Livermore National Laboratories*. A diffractive harmonic lens allows a continuous trade-off between lens thickness and achromatic performance. These single-element lenses are shown to produce excellent white-light images. (p. 26)

11:15 am

DMB3 Wavefront sensing applications of binary optics, D. R. Neal, M. E. Warren, J. K. Gruetzner, *Sandia National Laboratories*. Binary optics technology was used to build wavefront sensors for directly measuring Zernike modes. These sensors are useful for metrology, adaptive optics, and fluid dynamics measurements. (p. 30)

11:30 am

DMB4 New uses of computer-generated holograms for measuring astronomical optics, James H. Burge, *Univ. Arizona*. Two new applications of circular computer-generated holograms for certifying null correctors for primary mirrors and for measuring large convex secondary mirrors are described. (p. 34)

11:45 am

DMB5 Patterned Schottky barrier solar cells, H. Grebel, K. J. Fang, *New Jersey Institute of Technology*. In order to increase light collection efficiency in solar cells, patterned, Schottky barriers were investigated. In particular, the shapes, the patterning technique, and the electrical barrier height were studied. (p. 38)

DIFFRACTIVE OPTICS/ INTERNATIONAL OPTICAL DESIGN CONFERENCE

ROOM A

1:30 pm–3:30 pm

JMC, JOINT SESSION ON DIFFRACTIVE OPTICS DESIGN

William C. Sweatt, *Sandia National Laboratories, Presider*

1:30 pm (Invited)

JMC1 Using diffractive lenses in optical design, Dale A. Buralli, *Sinclair Optics, Inc.* The properties of diffractive optics are reviewed, with emphasis on those features most relevant to optical design. Examples and applications are given. (p. 44)

2:00 pm (Invited)

JMC2 Modeling of diffractive optics, Michael W. Farn, *MIT Lincoln Laboratory*. Methods used in analyzing surface-relief diffractive optics are described, both theoretically and by design example. Special emphasis is given to the issue of diffraction efficiency. (p. 48)

2:30 pm

JMC3 Optical systems employing refractive and diffractive optical elements to correct for chromatic aberration, C. William Chen, *Hughes Aircraft Co.* Diffractive optical elements can simplify the optical design form and improve the image quality of many refractive optical systems. The design principles are discussed and several examples are illustrated. (p. 52)

2:45 pm

JMC4 Achromatic and apochromatic diffractive singlets, G. Michael Morris, Dean Faklis, *Rochester Photonics Corp.* A multi-order diffractive (MOD) lens is used in conjunction with broadband illumination to bring two or more spectral components to a common focus in space with high efficiency. (p. 53)

3:00 pm

JMC5 Diffractive optics applied to eyepiece design, Michael D. Missig, G. Michael Morris, *Univ. Rochester*. Several features of diffractive optics are utilized in the eyepiece design problem to improve upon performance levels of all-refractive, conventional designs. Wide-field design examples and experimental results are presented. (p. 57)

3:15 pm

JMC6 Iterative methods for the kinoforms synthesis, S. N. Khonina, V. V. Kotlyar, I. V. Nikolsky, S. V. Philippov, V. A. Soifer, *Image Processing Institute, Russia*. (Abstract not available.) (p. 61)

TUESDAY, JUNE 7, 1994—Continued

11:06 am

DTuB19 High-efficiency, metallic diffraction gratings for laser applications, B. Boyd, J. Britten, D. Decker, B. W. Shore, B. Stuart, M. D. Perry, *Lawrence Livermore National Laboratory*; Lifeng Li, *Univ. Arizona*. We describe theory and experiment developing large-area gratings having high diffraction efficiency (>95% in order -1) and high threshold for laser damage. (p. 175)

11:08 am

DTuB20 Holographic couplers for optical fibers in on-axis off-Bragg and off-axis configurations, Pavel Cheben, Maria L. Calvo, *Complutense Univ., Spain*. Some fundamental aspects arising in the theoretical analysis of wavefront conversion process in holographic couplers is treated. The analytical integral solutions of wave equation for volume holographic diffraction grating is presented. The coupled-wave analysis approach is used. (p. 179)

11:10 am

DTuB21 Hybrid optics for deep UV, Hans-Jörg Heimbeck, *FISBA OPTIK AG, Switzerland*. UV-Optics for use below 200 nm should be color-corrected, but the only convenient material is fused silica. Hybrid solutions containing diffractive elements are discussed. (p. 183)

ROOM B

1:30 pm–3:30 pm

DTuC, DESIGN I

Dale A. Burall, *Sinclair Optics, Presider*

1:30 pm (Invited)

DTuC1 Diffractive optics beyond the paraxial domain, Jari Turunen, Eero Noponen, *Helsinki Univ. Technology, Finland*; Frank Wyrowski, *Berlin Institute of Optics, Germany*. We consider, by electromagnetic theory, the efficiency of diffractive elements with wavelength-scale transverse features for different values of the width of the signal window. (p. 186)

2:00 pm

DTuC2 Optical waveguide gratings having double-surface corrugation for highly efficient input coupling, John C. Brazas, Stephen Barry, Jeffrey Hirsh, *Eastman Kodak Cor.*; Lifeng Li, *Univ. Arizona*; Amanda L. McKeon, *Univ. Rochester*. Input-coupling efficiencies and branching ratios near the theoretical limit were obtained with a grating coupler having nearly identical gratings on the upper and lower surfaces of the waveguide. (p. 190)

2:15 pm

DTuC3 Design of nonperiodic diffractive elements with respect to illumination wave, Harald Aagedal, Thomas Beth, Stephan Teiwes, *Univ. Karlsruhe, Germany*; Frank Wyrowski, *Berliner Institut für Optik, Germany*. The influence of illumination waves on the diffraction pattern of non-periodic diffractive elements is analyzed for the coherent and incoherent case. (p. 194)

2:30 pm

DTuC4 Aperiodic gratings in waveguides, Tanveer Ul Haq, Kevin J. Webb, Neal C. Gallagher, *Purdue Univ.* A scattering optimization method is presented for designing highly efficient and compact aperiodic gratings for mode conversion applications in over-moded waveguides. (p. 198)

2:45 pm

DTuC5 Holographic optical interconnects, H. Grebel, Su Chiou Tsay, *New Jersey Institute of Technology*. We designed a new type of planar optical interconnects: the transverse holograms. The fanning in these holographic patterns is made along the direction of the optical wave propagation. (p. 202)

3:00 pm

DTuC6 Diffractive coupling lenses: design, calculation, and CAD-data generation, Helmut Zarschitzky, Albert Stemmer, *Siemens, Germany*; Alfons Daiderich, *Siemens-Nixdorf, Germany*. On-axis and off-axis diffractive lenses for laser-diode to fiber coupling are calculated with the extended CAD-program SIGGRAPH®-Optik. The construction of 2-D arrays consisting of individual single lenses is possible. (p. 205)

3:15 pm

DTuC7 Diffractive optical elements for laser and fiber mode selection, Victor A. Soifer, Mikhail A. Golub, Vladimir S. Pavelyev, *Image Processing Systems Institute, Russia*. New application of diffractive optics to the transverse mode selection is presented. Complex-to-phase coding methods based on special diffraction gratings are suggested. (p. 209)

ROOM B

4:00 pm–5:30 pm

DTuD, LIGHT PROPAGATION AND DIFFRACTION

Adolf W. Lohmann, *University Erlangen-Nürnberg, Germany, Presider*

4:00 pm (Invited)

DTuD1 Space-time duality: diffraction, dispersion, and temporal imaging, Brian H. Kolner, *UC-Los Angeles*. The mathematical duality between diffraction and dispersion suggests broader applicability in a system capable of imaging time waveforms. We analyze the dualities and discuss applications from communications to fundamental science. (p. 214)

4:30 pm

DTuD2 Effects of diffractive optical elements on ultrashort pulses analyzed using the finite-difference time-domain method, Diane H. Hochmuth, Alan D. Kathman, *Teledyne Brown Engineering*; Eric G. Johnson, *SY Technology, Inc.* In this paper, finite-difference time-domain techniques are used to analyze the behavior of ultrashort pulses in systems employing diffractive optics. (p. 218)

4:45 am

DTuD3 White-light optical information processing with achromatic processors, P. Andres, G. Saavedra, *Univ. Valencia, Spain*; J. Lancis, E. Tajahuerce, V. Climent, *Univ. Jaume I, Spain*. We present different white-light optical information processing techniques using achromatic Fourier, or Fresnel, transform systems constituted by diffractive optical elements. (p. 220)

5:00 pm

DTuD4 Partially coherently illuminated uniform-intensity holographic axicons, Ari T. Friberg, Sergei Yu. Popov, *Helsinki Univ. Technology, Finland*. Performance of apodized annular-aperture logarithmic axicons illuminated with spatially partially coherent light is assessed and interpreted by exact numerical calculations and asymptotic stationary-phase techniques. (p. 224)

5:15 pm

DTuD5 Polychromatic illumination of logarithmic annular-aperture diffractive axicon, Z. Jaroszewicz, Juan F. Roman Dopazo, *Univ. Santiago Compostela, Spain*. The uniformity of the on-axis intensity distribution of the diffractive annular-aperture logarithmic axicon is significantly improved when the illumination beam is polychromatic. (p. 228)

TUESDAY, JUNE 7, 1994—Continued

10:32 am

DTuB2 Edge diffraction theory for phase apertures, William H. Southwell, *Rockwell International Science Center*. Fields are propagated by summing simple diffraction functions from only the edges in the aperture. Edges are lines where any change occurs in transmittance or phase. (p. 112)

10:34 am

DTuB3 Fresnel interference observed by means of zone plates, Voldemar Petrovich Koronkevitch, Irina Georgievna Pal'chikova, *Institute of Automation & Electrometry, Russia*. Interference fields produced by the amplitude or phase zone plates illuminated by white or monochromatic light was studied. Multibeam interference pattern is interpreted as a set of two-beam patterns. (p. 116)

10:36 am

DTuB4 Gray-scale masks for diffractive optics: I. Spatially filtered halftone screens, Donald C. O'Shea, Patrick L. Thompson, Willie S. Rockward, *Georgia Institute of Technology*. Gray-scale masks for diffractive optical elements have been generated using standard halftone screens, desktop publishing techniques, and a simple spatial filtering geometry. (p. 119)

10:38 am

DTuB5 Gray-scale masks for diffractive optics: II. Commercial slide imagers, Donald C. O'Shea, Thomas J. Suleski, *Georgia Institute of Technology*. Gray-scale masks for fabrication of diffractive optical elements have been generated using standard desktop publishing programs and commercial slide imagers. (p. 123)

10:40 am

DTuB6 In-situ measurement of resist development process in electron beam lithography, E.-B. Kley, B. Schnabel, *Friedrich-Schiller-Univ. Jena, Germany*. An interferometric measuring procedure is applied to measure in-situ the resist development process in electron beam lithography. Results and applications are given. (p. 125)

10:42 am

DTuB7 Micromachining of diffractive optics with excimer lasers, Michael T. Duignan, *Potomac Photonics, Inc.* Using a tabletop ultraviolet waveguide excimer laser-based micromachining workstation, we etch diffractive structures directly into the substrate without masks or intermediate processing steps. (p. 129)

10:44 am

DTuB8 Rapid prototyping of multilevel diffractive optical elements, Peter Kung, Li Song, *QP Semiconductor Technology Inc., Canada*. A manufacturing procedure using HOLOCAD™ to generate GDSII data and focused ion beam (FIB) direct writing method to create multilevel DOE will be presented. (p. 133)

10:46 am

DTuB9 New techniques for genetic algorithm optimization of diffractive optical elements, Alan D. Kathman, David R. Brown, *Teledyne Brown Engineering*; Eric G. Johnson, *SY Technology, Inc.* This paper demonstrates new techniques for the use of genetic algorithms in the design of diffractive optical elements. These techniques are ideal for systems that require general, non-intuitive solutions. (p. 137)

10:48 am

DTuB10 Optimum quantization rules for computer generated holograms, U. Krackhardt, *Univ. Erlangen-Nürnberg, Germany*. From the requirement of optimum light efficiency analytic expressions for quantization rules of computer generated phase-only holograms are derived. Numerical and experimental results are shown. (p. 139)

10:50 am

DTuB11 Transition between diffractive and refractive micro-optical components, S. Sinzinger, M. Testorf, W. Singer, *Physikalisches Institut der Univ., Germany*. Most micro-optical components combine diffractive and refractive effects. We investigate how the properties of both effects work together in hybrid elements to achieve superior performance. (p. 143)

10:52 am

DTuB12 Exact surface relief profile of kinoform lenses from a given phase function, Y. Han, C. A. Delisle, *Univ. Laval, Canada*; L. N. Hazra, *Calcutta Univ., India*. A method for determining the exact surface relief profile of kinoform lenses from a given phase function is described. (p. 147)

10:54 am

DTuB13 Application of the Yang-Gu algorithm to the design of diffractive phase elements for achieving multiple optical functions, Benyuan Gu, Guozhen Yang, Bizhen Dong, *Institute of Physics, China*; Ming-Pin Chang, Okan K. Ersoy, *Purdue Univ.* We extend the original Yang-Gu algorithm to treat the optical system with the illumination of light beam consisting of several wavelength components. Numerical simulations are carried out for the design of diffractive phase element achieving both demultiplexing and focusing functions. (p. 151)

10:56 am

DTuB14 Interpolation approaches to computer-generated holograms, Nobukazu Yoshikawa, Toyohiko Yatagai, *Univ. Tsukuba, Japan*. An interpolation method of image points reconstructed by Fourier transform CGH is described, so that a sufficient large size hologram can be synthesized by a small size hologram. (p. 155)

10:58 am

DTuB15 Direct search method for the computer design of holograms for the production of arbitrary intensity distributions, Matthew S. Clark, *Imperial College, U.K.* A direct search algorithm for designing computer generated holograms and its controlling cost function structure are discussed. Optical and digital reconstructions are presented. (p. 159)

11:00 am

DTuB16 Diffractive zoom lens based on rotational moiré, U. Krackhardt, A. W. Lohmann, *Univ. Erlangen-Nürnberg, Germany*. Varifocal Fresnel zone patterns result from the superposition of twisted patterns. New methods are proposed to increase transmittivity and usable area portion of the pattern. (p. 163)

11:02 am

DTuB17 Superimposed grating for use with magneto-optical disk heads, Shigeru Aoyama, Tsukasa Yamashita, *Omron Corp., Japan*. A superimposed grating, which acts as a polarizing beam splitter and a cylindrical lens, has been developed for use with magneto-optical disk heads. (p. 167)

11:04 am

DTuB18 Application of diffractive optics to photonic integrated circuit packaging, M. E. Warren, S. H. Kravitz, G. R. Hadley, J. R. Wendt, G. A. Vawter, M. G. Armendariz, J. C. Word, R. F. Corless, R. F. Carson, B. E. Hammons, *Sandia National Laboratories*; R. E. Leibenguth, *AT&T Bell Laboratories*. Photonic packaging concepts using anamorphic microlenses and second-order grating couplers were demonstrated by coupling a ridge waveguide to an out-of-plane single-mode fiber. (p. 171)

WEDNESDAY, JUNE 8, 1994—Continued

3:00 pm

DWC6 Diffractive optics for CO₂ industrial lasers: reducing lens damage, Russell W. Gruhlke, *Auburn, California*. Conventional, refractive focusing lenses in CO₂ industrial lasers can be replaced with longer focal length diffractive focusing elements to reduce lens damage. (p. 291)

3:15 pm

DWC7 Serrated aperture and its applications in high-power lasers, Ximing Deng, Dianyuan Fan, Liejia Qian, *National Laboratory on High Power Laser and Physics, China*. The design procedure for serrated apertures has been presented. We have studied its applications in high-power lasers to provide uniform illumination of target. (p. 295)

ROOM B

4:00 pm–5:30 pm

DWD, FABRICATION BY DIRECT-WRITE TECHNIQUES
Jurgen Jahns, *AT&T Bell Laboratories, Presider*

4:00 pm (Invited)

DWD1 Fast and high quality surface profiling for microoptical applications, E. Bernhard Kley, *Friedrich-Schiller Univ., Germany*. Adaptations of lithographic technologies (variable shaped e-beam, variable dose and energy writing) for microoptical applications and new profitable lens profiles (> 10 lenses/s) were described. (p. 300)

4:30 pm

DWD2 Focusing DOE fabrication using variable shaped electron beam lithography, Sergey Babin, Victor Danilov, *Physics and Technology Institute, Russia*. (Abstract not available.) (p. 301)

4:45 pm

DWD3 Fabrication of multi-level phase gratings using focused ion beam milling and electron beam lithography, S. M. Shank, M. Skvarla, F. T. Chen, H. G. Craighead, *Cornell Univ.*; P. Cook, R. Bussjager, F. Haas, D. A. Honey, *USAF Rome Laboratory*. The fabrication and optical performances of continuously graded gratings using focused ion beam milling and 8-level gratings using electron beam lithography and reactive ion etching, are evaluated. (p. 302)

5:00 pm

DWD4 Laser writing and replication of continuous-relief Fresnel microlenses, M. T. Gale, M. Rossi, R. E. Kunz, *Paul Scherrer Institute, Switzerland*; G. L. Bona, *IBM Research Center, Switzerland*. Planar, continuous-relief Fresnel microlenses with high numerical apertures (>0.5) are fabricated by direct laser writing in photoresist and replicated by hot embossing and casting techniques. (p. 306)

5:15 pm

DWD5 Fabrication of diffractive optical elements by laser writing with circular scanning, V. P. Koronkevich, V. P. Kiryanov, V. P. Korol'kov, A. G. Poleshchuk, V. A. Cherkashin, A. A. Kharissov, *Institute of Automation and Electrometry, Russia*. New circular laser writing system for fabrication of diffractive optics is described. The results of synthesis of diffractive element masks without photoresists usage are presented. (p. 310)

THURSDAY, JUNE 9, 1994

ROOM B

8:30 am–10:00 am

DThA, MICROLENS FABRICATION AND APPLICATIONS
Margaret B. Stern, *MIT Lincoln Laboratory, Presider*

8:30 am (Invited)

DThA1 Manufacture of microlenses, Michael C. Hutley, *National Physical Laboratory, U.K.* The paper reviews a variety of techniques for the manufacture of microlenses and their diffracting equivalents (micro zone plates). The relative merits of refracting and diffracting components are considered from a practical point of view. (p. 316)

9:00 am

DThA2 Diffractive coupling lenses: fabrication and measurement of silicon elements, Albert Stemmer, Helmut Zarschizky, Franz Mayerhofer, Guy Lefranc, Wolfgang Gramann, *Siemens, Germany*. Binary and multilevel diffractive lenses for laser-diode to single-mode fiber coupling are fabricated in silicon. The production is based on E-beam lithography and ion etching. (p. 317)

9:15 am

DThA3 Phase-matched Fresnel elements for optical interconnects, M. Rossi, R. E. Kunz, *Paul Scherrer Institute, Switzerland*; G. L. Bona, *IBM Research Center, Switzerland*. Experimental and theoretical results are presented for novel, single planar element optical interconnects, namely focusing Nx1 fan-out elements and fast laser-diode/fiber-connecting lens arrays. (p. 321)

9:30 am

DThA4 Diffractive interconnecting device for fiber-to-chip coupling, Ph. Regnault, G. Voirin, *CSEM Centre Suisse d'Electronique et de Microtechnique SA, Switzerland*; H. Buczek, *Optique Consulting H. Buczek, Switzerland*; O. Anthamatten, *Ascom Tech., Switzerland*; Ch. Zimmer, H. Gilgen, *Swiss PTT Research and Development, Switzerland*. A pair of fibers is coupled to a double-channel GaAs modulator with a double-side diffractive optical device fabricated using a binary optics process. (p. 325)

9:45 am

DThA5 Diffractive optical elements with high efficiency fabricated by thin film deposition, E. Pawlowski, D. Berger, T. Hies, B. Kuhlow, *Heinrich-Hertz-Institut für Nachrichtentechnik Berlin GmbH, Germany*. We fabricated AR-coated multilevel diffractive optical elements with small f/numbers and high efficiency and investigated the effects of fabrication errors on the diffraction efficiency. (p. 329)

ROOM B

10:30 am–12:00 m

DThB, FABRICATION AND CHARACTERIZATION
Hans Peter Herzig, *Univ. Neuchatel, Switzerland, Presider*

10:30 am (Invited)

DThB1 Overview of binary optics fabrication technology, Margaret B. Stern, *MIT Lincoln Laboratory*. A review of binary optics processing technology is presented. Pattern replication techniques that have been optimized to generate high-quality efficient diffractive and refractive microoptics in visible and IR materials are described. (p. 334)

WEDNESDAY, JUNE 8, 1994

ROOM B

8:30 am–10:00 am

DWA, DESIGN II

J. R. Leger, *University of Minnesota, Presider*

8:30 am (Invited)

DWA1 Opportunities for diffractive optical systems, Adolf W. Lohmann, *Univ. Erlangen–Nurnberg, Germany*; Jorge Ojea-Castañeda, *Inade, Mexico*. Our aim is to propose the simplest system for a given job. For example, simple binary masks can perform complex operations if one dimension suffices. (p. 234)

9:00 am

DWA2 Fresnel lens array for optical fiber semiconductor laser coupling, P. McKee, J. Towers, A. Thurlow, D. Wood, *B. T. Laboratories, U.K.* The design and fabrication of a low F number lens in quartz is described. The device is characterized for semiconductor laser/optical fiber coupling. (p. 235)

9:15 am

DWA3 Design and fabrication of multilevel phase holograms for on-axis optical interconnects, Arthur F. Gmitro, Christopher Coleman, *Univ. Arizona*; Paul E. Keller, *Pacific Northwest Laboratory*; Paul D. Maker, *Jet Propulsion Laboratory*. An improved method for the design of multilevel phase holograms and a technique for direct fabrication by e-beam are presented. (p. 239)

9:30 am

DWA4 An algorithm for the generation of reduced e-beam fabrication data for general aspheric diffractive optical elements, Jiao Fan, David Zaleta, Sing H. Lee, *UC–San Diego*. A new CAD algorithm for e-beam fabrication of aspheric DOEs is presented. This algorithm is general, stable, and relatively efficient in terms of data size. (p. 243)

9:45 am

DWA5 Generation of binary, phase-only, holograms by on-line feedback of output plane intensity, E. G. S. Paige, R. H. Scarbrough, *Univ. Oxford, U.K.* Near-diffraction-limited performance is demonstrated for an optical system, including aberrator, using iterative optimization in feedback between a detector and SLM. (p. 247)

ROOM B

10:30 am–12:00 m

DWB, SUBWAVELENGTH AND COATED STRUCTURES

Thomas Keith Gaylord, *Georgia Institute of Technology, Presider*

10:30 am (Invited)

DWB1 Subwavelength structured surfaces: design and applications, Daniel H. Raguin, *Rochester Photonics Corp.*; G. Michael Morris, *Univ. Rochester*. Subwavelength structured surfaces can be used as antireflection coatings, polarization components, narrowband filters, and phase plates. These applications, as well as their design principles, are reviewed. (p. 252)

11:00 am

DWB2 Design of ideal reflection filters using resonant waveguide gratings, R. Magnusson, S. S. Wang, *Univ. Texas at Arlington*. It is shown that ideal reflection filter characteristics can be obtained by integrating planar waveguide gratings with half-wave and quarter-wave thin-film layers. (p. 256)

11:15 am

DWB3 2-D subwavelength gratings as artificial anisotropic media, Eric B. Grann, M. G. Moharam, Drew A. Pommé, *Univ. Central Florida*. 2-D symmetric and asymmetric subwavelength binary gratings are investigated. A method for determining the three effective indices of the equivalent anisotropic medium is presented. (p. 260)

11:30 am

DWB4 Numerical modeling of multilayer-coated gratings, Lifeng Li, *Univ. Arizona*. Significant improvements to the differential method of Chandezon et al. for multilayer-coated surface relief gratings in conical diffraction mountings are presented. (p. 264)

11:45 am

DWB5 Polarizing properties of dielectric layer with subwavelength structured surfaces, V. N. Bel'tyugov, S. G. Protsenko, A. V. Leis, *The Institute of Automation and Electrometry, Russia*. The polarizing properties of dielectric layer with structured surfaces are considered both theoretically and experimentally. The available applications of such elements are discussed. (p. 268)

ROOM B

1:30 pm–3:30 pm

DWC, APPLICATIONS FOR LASER SYSTEMS

J. Allen Cox, *Honeywell Inc., Presider*

1:30 pm (Invited)

DWC1 Applications of diffractive optic design to acousto-optic signal processing, Joseph N. Mait, *U.S. Army Research Laboratory*; Ravindra A. Athale, *George Mason Univ.* To the sequence algorithms, architectures, hardware that is necessary for the proper development of an optical processor, we add component design and show how techniques for the design of diffractive optical elements have been applied to the design of an acousto-optic-based incoherent image correlator. (p. 274)

2:00 pm

DWC2 Use of diffractive phase plates for high modal discrimination in short laser resonators, D. Chen, J. R. Leger, *Univ. Minnesota*. A diffractive phase plate is used in conjunction with a diffractive mode-selecting mirror to make a short laser resonator with high modal discrimination. (p. 278)

2:15 pm

DWC3 Apodized diffraction grating as outcoupling element for a 1.06 μm Nd-YAG laser, A. Mitreiter, J. Guhr, H.-J. Rostalski, *Berliner Institut für Optik GmbH, Germany*; G. Bostanjoglo, *Festkörper-Laser-Institut GmbH, Germany*. A new technique of fabrication and application for apodized diffraction grating as outcoupling element for a 1.06 μm Nd-YAG laser is presented. (p. 282)

2:30 pm

DWC4 Large aperture kinoform phase plates for beam smoothing, S. N. Dixit, M. Rushford, I. Thomas, R. Merrill, M. Perry, H. T. Powell, *Lawrence Livermore National Laboratory*; K. A. Nugent, *Univ. Melbourne, Australia*. We have designed and fabricated large aperture kinoform phase plates (KPPs) for tailoring the focal plane intensity distribution. Results of optical performance are presented. (p. 286)

2:45 pm

DWC5 Excimer laser machining with kinoforms, Anna-Karin Holmér, Fredrik Nikolajeff, Jörgen Bengtsson, Björn Löfving, Sverker Hard, *Chalmers Univ. Technology, Sweden*. A kinoform distributed the excimer laser power to a mask pattern in a laser machining study. A diffractive beam homogenizer of novel design was manufactured. (p. 289)

THURSDAY, JUNE 9, 1994—Continued

11:00 am

DThB2 Metrology of diffractive optics, Paul Caber, Don Cohen, John Podlesny, James C. Wyant, *WYKO Corp.* This paper describes the use of both optical profilers and scanning probe microscopes for measuring the micro-structure of diffractive optical elements. (p. 338)

11:15 am

DThB3 Phase shift mask metrology using scatterometry, Susan M. G. Wilson, S. Sohail H. Naqvi, B. K. Minhas, John R. McNeil, *Univ. New Mexico*; Herschel M. Marchman, *AT&T Bell Laboratories*. We present preliminary results on the use of scatterometry for the determination of critical parameters of a phase etched diffraction grating test structure. (p. 342)

11:30 am

DThB4 Image quality assessment of diffractive elements replicated in SURPHEX™, J. Allen Cox, *Honeywell Technology Center*; Felix P. Shvartsman, *Datacard Corp.* We show that diffractive elements can be replicated in DuPont's SURPHEX™ photopolymer with very high fidelity and with image quality limited only by the substrate planarity. (p. 346)

11:45 am

DThB5 CIM for fabricating HOE by embossing and injection method, Rong-Seng Chang, Chern Sheng Lin, Yun Long Lay, *National Central Univ., China*. We provide a computer integrated manufacturing (CIM) technique to obtain the large or small quantities and variable types of holographic optical element (HOE). (p. 350)

FUNDAMENTALS OF GRATING DIFFRACTION

Thomas K. Gaylord, Elias N. Glytsis, and David L. Brundrett
School of Electrical and Computer Engineering
Georgia Institute of Technology
Atlanta, GA 30332-0250

Diffraction optics is of increasing importance in a wide variety of application areas. Example present-day uses include diffractive optical elements, head-up displays, laser scanners, wavelength multiplexers/demultiplexers, optical interconnects, laser feedback devices, optical memories, spectrometers, and many more. Due to its significance, it is important to be able to introduce students and new workers in this field to the fundamentals of grating diffraction in an intuitive and visual manner and in a fashion that allows them to analyze basic grating structures without specialized mathematical tools and further gives them the directions to follow if they wish to pursue the analysis of more complex grating structures.

For overview purposes, the classification of gratings according to spatial frequency, modulation type, surface-relief types, orientation of plane of incidence, material, transmission/reflection, and diffraction regime are given. Plane wave interference is reviewed and used to motivate the Floquet condition and Floquet waves. Each i^{th} Floquet wave is phase matched to a propagating or evanescent wave in the forward and backward directions at the grating surfaces as indicated by the grating equation. The directions of all forward-diffracted and backward-diffracted propagating waves are determined in this manner. The m^{th} Bragg condition is satisfied when the wavelength of the $(i = m)^{\text{th}}$ Floquet wave inside the grating is equal to the wavelength that would exist in the bulk material with no grating modulation.

To determine the amplitudes of all of the diffracted waves, Maxwell's equations must be solved for this problem. This may be done in numerous ways. For instructional purposes, the case of a $\mathbf{E} \perp \mathbf{K}$ (TE) polarized wave incident on a planar dielectric grating with slanted fringes is treated. The Floquet fields are substituted into the wave equation formed from Maxwell's equations. From this the infinite set of second-order coupled differential equations are developed. These are the rigorous coupled-wave equations for this grating problem [1-2]. From linear systems theory a state variables solution is available

Monday, June 6, 1994

Electromagnetic Theory of Gratings

DMA 8:30am–10:00am
Room B

J.R. Leger, *Presider*
University of Minnesota

Implementation of the Rigorous Coupled-Wave Technique: Stability, Efficiency, and Convergence

M. G. Moharam, Drew A. Pommet, and Eric B. Grann

Center for Research and Education in Optics and Lasers, University of Central Florida
12424 Research Parkway, Suite #400 , Orlando, Florida 32826
Tel: (407) 658-6833, Fax: (407) 658-6880, e-mail: moharam@faculty.creol.ucf.edu

Introduction

Over the last ten years, the Rigorous Coupled-Wave Technique¹ (RCWT) has been the most widely used method for the accurate analysis of the diffraction of electromagnetic waves by periodic structures. It has been used successfully and accurately to analyze both holographic and surface-relief grating structures. It has been formulated to analyze transmission and reflection planar dielectric/absorption holographic gratings, arbitrary profiled dielectric/metallic surface-relief gratings, multiplexed holographic gratings, two-dimensional surface-relief gratings, and anisotropic gratings for both planar and conical diffraction¹⁻⁸.

The rigorous coupled-wave technique is a relatively simple method for the exact solution of the vector Maxwell's equations for the electromagnetic diffraction by grating structures. It is a non-iterative, deterministic technique utilizing a state variable method which will always converge to the exact solution without any inherent numerical instabilities. The accuracy of the obtained solution depends solely on the number of terms in the field space harmonic expansions and conservation of energy is always observed. However, recently numerical instabilities have been discussed⁹⁻¹¹. These numerical difficulties are not inherent in the technique, but are the result of the lack of incorporating the nature of the diffraction process in the implementation. Specifically, the implications of the non-propagating evanescent fields and the space harmonics in the grating region on the numerical implementation must be clearly understood.

In this work, an efficient and absolutely stable implementation for the coupled-wave technique are presented for arbitrary profile one-dimensional surface-relief gratings. An investigation of the dependence of the convergence rate on the number of terms in the field space harmonic expansion is presented for both TE and TM polarization.

Rigorous Coupled-Wave Technique

In the formulation of the rigorous coupled-wave technique, the arbitrary surface-relief periodic grating is viewed as stack of binary (lamellar) gratings. In each layer of the stack, the binary permittivity is decomposed into its Fourier harmonic components. The electromagnetic fields in

for the space harmonic (Floquet) fields inside the grating in terms of the eigenvalues and eigenvectors of the coefficient matrix of the coupled-wave equations. Using the boundary conditions that the tangential electric field and tangential magnetic field must be continuous across the front and back surfaces of the grating, allows the diffracted fields to be determined. Plotting the fields inside the grating is useful for visualizing the diffraction process.

In the important limiting cases of Raman-Nath regime diffraction [3] and Bragg regime diffraction (Kogelnik analysis [4]), the rigorous coupled-wave equations have analytic solutions. For the Raman-Nath case the diffracted amplitudes are given in terms of Bessel functions and for the Bragg regime case the amplitudes are given in terms of sines and cosines. Criteria for the use of these limiting cases are reviewed.

Extensions of the rigorous coupled-wave analysis beyond the TE polarization, planar dielectric grating to other cases such as arbitrary polarization and conical incidence and to gratings such as surface-relief gratings, metallic gratings, subwavelength gratings, anisotropic gratings, multiplexed gratings, and two-dimensional gratings are indicated.

This work was supported in part by grant no. DAAH-04-93-G-0027 from the Joint Services Electronics Program.

- [1] M. G. Moharam and T. K. Gaylord, "Rigorous coupled-wave analysis of planar-grating diffraction," *J. Opt. Soc. Amer.*, vol. 71, pp. 811-818, July 1981.
- [2] T. K. Gaylord and M. G. Moharam, "Analysis and applications of optical diffraction by gratings," *Proc. IEEE*, vol. 73, pp. 894-937, May 1985.
- [3] C. V. Raman and N. S. N. Nath, "The diffraction of light by high frequency sound waves: Part I," *Proc. Ind. Acad. Sci. A*, vol. 2, pp. 406-412, Oct. 1935.
- [4] H. Kogelnik, "Coupled wave theory for thick hologram gratings," *Bell Syst. Tech. J.*, vol. 48, pp. 2909-2947, Nov. 1969.

factor of four reduction in the memory requirement. In this work, we will present the formulation for the reduction of the coupled-wave equation for TE, TM, and conical diffraction for one-dimensional gratings.

Convergence

A stable, efficient implementation of the rigorous coupled-wave technique, as described above, will always converge to yield the exact diffracted field amplitude. The accuracy of the solution depends solely on the number of the terms of the space harmonic expansion of the field in the grating regions. A study of the dependence of the number of space harmonics required for convergence on the grating index, angle of incidence, and grating period/ wavelength ratio, and duty cycle for TE, and TM polarization is presented.

References

1. Moharam, M.G., and Gaylord, T.K., "Rigorous coupled-wave analysis of planar gratings," J. Opt. Soc. Am., **71**, 811- 818, (1981).
2. Moharam, M.G., and Gaylord, T.K., "Diffraction analysis of dielectric surface-relief gratings," J. Opt. Soc. Am., **72**, 1385-1392, (1982).
3. Moharam, M.G., and Gaylord, T.K., "Three-dimensional vector coupled-wave analysis of planar grating diffraction," J. Opt. Soc. Am., **73**, 1105-1112, (1983).
4. Baird, W.E., Moharam, M.G., and Gaylord, T.K., "Diffraction characteristics of planar absorption gratings," Applied Physics B, **32**, 15-20, (1983).
5. Moharam, M.G., and Gaylord, T.K., "Rigorous coupled-wave analysis of metallic surface-relief gratings," J. Opt. Soc. Am. A., **3**, 1780-1796, (1986).
6. Moharam, M.G., "Diffraction analysis of multiplexed holographic gratings," Proc. Spring '86 OSA Topical Meeting on Holography (March 1986), 100-103, (1986).
7. Moharam, M.G., "Coupled-wave analysis of two-dimensional gratings," Proc. S.P.I.E., **883**, 8-11, (1988).
8. E. N. Glytsis and T. K. Gaylord, "Rigorous three-dimensional coupled-wave diffraction analysis of single and cascaded anisotropic gratings," J. Opt. Soc. Am. A., **4** 2061-2080, (1987).
9. D. M. Pai and K. A. Awada, "Analysis of dielectric gratings of arbitrary profiles and thickness," J. Opt. Soc. A. **8**, 755-762, (1991).
10. M. Neviere and E. Popov, "Analysis of dielectric gratings of arbitrary profiles and thickness: comments," J. Opt. Soc. A. **9**, 2095-2096, (1992).
11. S. T. Han, Y-L Tsao, R. M. Walser, and Michael F. Becker, "Electromagnetic scattering of two-dimensional surface-relief dielectric gratings," Applied Optics, **31**, 2343-2352, (1992).

the layer are decomposed into space harmonics having the periodicity of the grating. These space harmonics are determined by solving a set of coupled-wave equations constructed for each layer. The electromagnetic fields within each layer, represented by the space harmonics, are matched to the electromagnetic fields in the two adjacent layers. The electromagnetic fields in the two end layers are also matched to the fields associated with the backward and forward propagating or an evanescent wave in the two exterior regions. Solving this very large system of equations yields the amplitudes of the diffracted fields. As described above, the brute force approach for coupled-wave technique is inherently stable with no numerical difficulties, but it is very inefficient. Typically, field matching between the layers is carried out using piece-wise approach. This is done using some form of matrix propagation or other algorithm. Poor implementation of such a technique is the cause of the reported numerical instabilities.

Stability

The main cause of reported numerical instabilities is the improper handling of the evanescent field components of the field space harmonics in the grating regions. The eigenvalues (propagation constants) associated with non-propagating fields have large positive and negative exponents resulting in numerical overflow and underflow. Numerical overflow can be handled by proper normalization of the eigenvector associated with the problem eigenvalue. However, this leaves a virtual zero column in the electromagnetic field matching matrix at any one interface (i.e. singular or ill-behaved matrix). Thus, matrix inversion, which is required in matrix propagation methods, results in numerical difficulties and instabilities. A stable matrix propagation method that utilizes the two matrices resulting from field matching at the two boundaries of the layer is presented and is shown to be inherently stable. Calculations are presented for any gratings groove depth for TE, TM, and conical diffraction. This technique has been found to be absolutely stable with no numerical difficulties whatsoever for all grating depths, and profiles. Figure 1. shows stable calculation of the diffraction efficiency for extremely deep (up to 100 wavelengths!) 8-level binary grating for both TE and TM polarizations. The diffraction efficiencies are calculated for several grating period to wavelength ratios, as suggested by Neviere and Popov¹⁰ to be one of the criteria for evaluating the stability of the differential type diffraction analysis techniques.

Efficient Implementation

Efficient implementation of the RCWT is obtained through two distinct processes. First, the symmetry in binary lamellar grating is utilized to reduce the matrix constructed for the coupled-wave equation from $2N \times 2N$ to $N \times N$ for TE and TM polarization and from $4N \times 4N$ to $2N \times 2N$ for conical diffraction. The reduction in the matrix size will result in almost a factor of eight reduction in the time required to determine the field space harmonics in each layer which is estimated to be 80% of the total execution time. In addition, this matrix size reduction results in a

Mathematical Issues in the Electromagnetic Theory of Gratings

Gang Bao

Institute for Mathematics and Its Applications
University of Minnesota
Minneapolis, MN 55455

David C. Dobson

Department of Mathematics
Texas A&M University
College Station, TX 77843-3368

J. Allen Cox

Honeywell Technology Center
10701 Lyndale Ave S
Bloomington, MN 55420

1. Introduction. The electromagnetic theory of gratings has been studied extensively since Rayleigh's time. The advent of computers thirty years ago greatly accelerated activity in the area and has given rise to several approaches and numerical methods to yield rigorous solutions to the problem, including differential methods (French, Gaylord,...), integral methods (French,...), analytical continuation (Bruno and Reitich), variational method (Dobson, Abboud) and others. In light of the essential mathematical nature of the problem, it is noteworthy that by far the largest number of papers in the literature have come from the engineering community and proportionately few from applied mathematicians. Evidence of this is found in Petit's and Cadilhac's remarks on the lack of existence and uniqueness theorems for the problem. Even more glaringly absent has been convergence analysis of the various numerical methods, although the more recent work by applied mathematicians in the analytic continuation method and the variational method have begun to rectify this.

Here we draw on work done in this area at the Institute for Mathematics and Its Applications since 1990 ([1]–[7]) and address specifically the issues of existence and uniqueness of solutions and convergence of the variational method implemented by us. In particular, optimal rates of convergence can be obtained for TE polarization. In the TM polarization case, however, the convergence analysis is much more difficult. In fact, everyone active in the field is well acquainted with the situations (usually involving a complex index of refraction) where solutions for TM polarization converge much more slowly than TE polarization. We provide some insight into the nature of this phenomenon.

2. The scattering problem. Figure 1 summarizes the geometry, equations, and assumptions for the grating problem. Notice that the geometry and material properties can be extremely general.

For simplicity, we restrict ourselves to the two dimensional setting, *i.e.*, we assume that the medium and grating surface are constant in the x_2 direction. The variational approach presented here can be generalized to study bi-periodic diffraction problems, see *e.g.* [6].

Suppose that the whole space is filled with material with index of refraction $k = \omega\sqrt{\epsilon}$ that satisfies

$$k = \begin{cases} k_1, & \text{in } \Omega_1^+ \cup \bar{\Omega}_1, \\ k_0(x), & \text{in } \Omega_0, \\ k_2, & \text{in } \Omega_2^+ \cup \bar{\Omega}_2, \end{cases}$$

where $k_0(x)$ is a bounded measurable function, k_1 and k_2 are constants, k_1 is real and positive, and $\operatorname{Re} k_2 > 0$, $\operatorname{Im} k_2 \geq 0$.

We want to demonstrate our variational approach by solving the diffraction problem with TE polarization. The Maxwell equation then becomes an Helmholtz equation. Therefore, we wish to solve the Helmholtz equation

$$(1) \quad (\Delta + k^2)u = 0, \quad \text{in } \mathbb{R}^2.$$

We assume an incoming plane wave $u_I = e^{i\alpha x_1 - i\beta_1 x_2}$ is incident on S from Ω_1 , where $\alpha = k_1 \sin \theta$, $\beta_1 = k_1 \cos \theta$, and $-\frac{\pi}{2} < \theta < \frac{\pi}{2}$ is the angle of incidence.

We are interested in "quasiperiodic" solutions u , that is, solutions u such that $ue^{-i\alpha x_1}$ are 2π -periodic.

8-Level Binary Grating

$n=1.5, \theta_i=10^\circ$

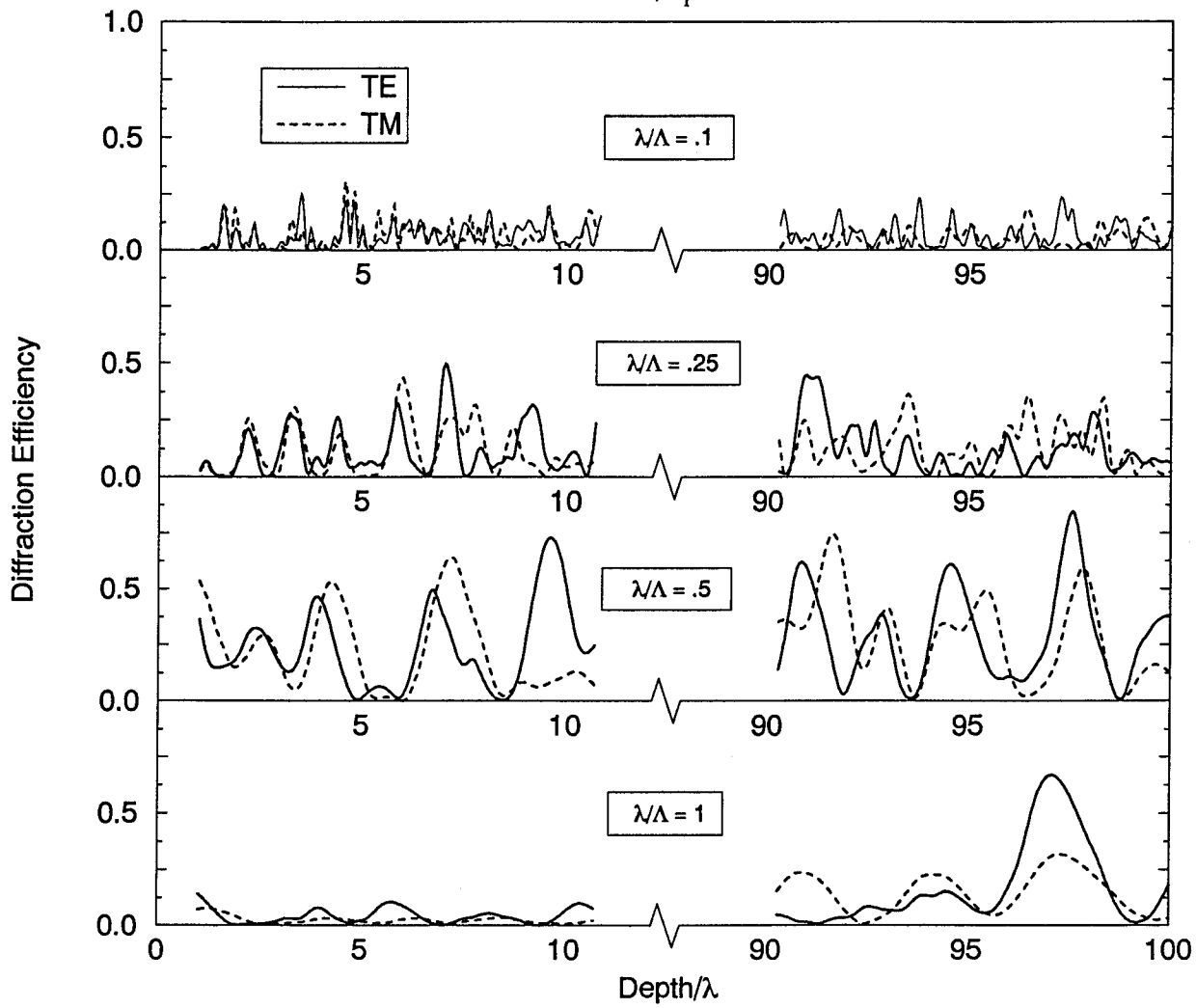


Fig 1. Stable diffraction efficiencies calculated for extremely deep 8-level binary gratings for both TE and TM polarizations.

The operator T_j is defined by

$$(5) \quad (T_j f)(x_1) = \sum_{n \in \mathbb{Z}} i\beta_j^n(\alpha) f^{(n)} e^{in x_1},$$

where $f^{(n)} = \frac{1}{2\pi} \int_0^{2\pi} f(x_1) e^{-in x_1} dx_1$.

The scattering problem can be formulated as follows: find $u_\alpha \in H^1(\Omega)$ that satisfies

$$(6) \quad (\Delta_\alpha + k^2)u_\alpha = 0, \quad \text{in } \Omega,$$

and (3-4). The function space $H^1(\Omega)$ is a standard Sobolev space. It contains complex valued functions g that satisfy $g \in L^2(\Omega)$ and $\partial_{x_1} g, \partial_{x_3} g \in L^2(\Omega)$ in the distribution sense. The space $L^2(\Omega)$ contains all the functions that are square integrable in Ω . Similarly, $H^2(\Omega)$ contains square integrable functions, whose first order and second order derivatives are also square integrable in Ω . It is obvious to see that $H^2(\Omega) \subset H^1(\Omega) \subset L^2(\Omega)$.

THEOREM 2.1. (*Existence and uniqueness*) Suppose that k is bounded measurable. Then for all but a discrete set of frequencies ω , there exists a unique solution $u_\alpha \in H^1(\Omega)$ to the variational problem (6), (3), and (4).

The proof of Theorem 2.1 may be found in [5] or [2].

3. Variational approach. The scattering problem has an equivalent variational form: find $u_\alpha \in H^1(\Omega)$ such that

$$(7) \quad a(u_\alpha, \phi) = (f, \phi), \quad \forall \phi \in H^1(\Omega),$$

here the sesquilinear form is defined by

$$\begin{aligned} a(w_1, w_2) = & \int_{\Omega} \nabla w_1 \cdot \nabla \overline{w_2} - \int_{\Omega} (k^2 - \alpha^2) w_1 \overline{w_2} - 2i\alpha \int_{\Omega} (\partial_{x_1} w_1) \overline{w_2} \\ & - \int_{\Gamma_1} (T_1 w_1) \overline{w_2} - \int_{\Gamma_2} (T_2 w_1) \overline{w_2}, \end{aligned}$$

and

$$(f, \phi) = - \int_{\Gamma_1} 2i\beta_1 e^{-i\beta_1 b} \overline{\phi}.$$

Let us now briefly describe the basic idea employed in the variational (or finite element) approach. Let $\{S^h : h \in (0, 1]\}$ denote a family of finite dimensional subspaces of H^1 , usually a space of piecewise polynomials, where h stands for the maximum mesh size after partitioning Ω into simple subdomains. Assume also that S^h satisfies some standard approximation assumptions. We define the finite element approximation u^h of the solution u_α of (7) by the following equation, for each $v^h \in S^h$,

$$(8) \quad a(u^h, v^h) = (f, v^h).$$

In fact, this provides the basic idea for solving our model equation, *i.e.* one first chooses a basis of S^h , $\{\phi_1, \phi_2, \dots, \phi_k\}$, which is a finite set according to the definition of S^h . Substituting the expression of

$$u^h = c_1 \phi_1 + c_2 \phi_2 + \dots + c_k \phi_k$$

into the equation (8), by choosing $v^h = \phi_i$, $i = 1, \dots, k$, one gets a system of linear equations. Solving this system for $\{c_j\}$ then leads to an approximation of u_α in S^h .

Next, we want to address the convergence properties of our method.

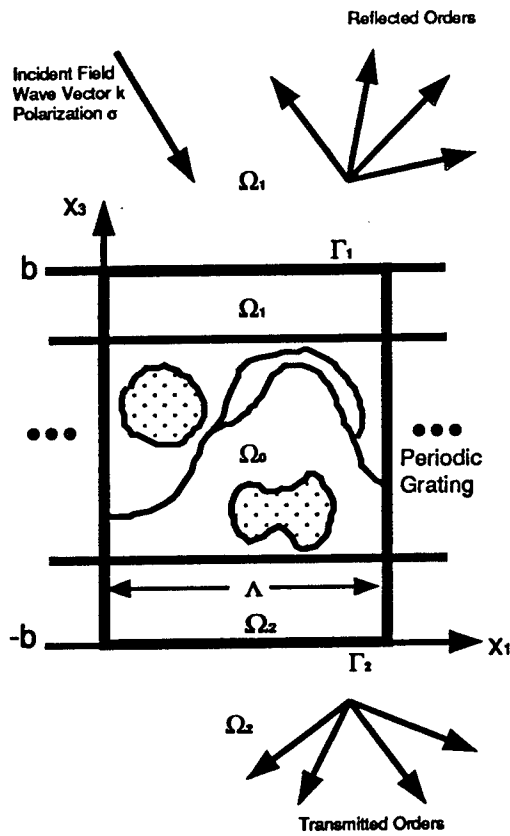


FIG. 1. Problem geometry.

Maxwell's Equations

- source free
- time harmonic $\rightarrow \exp(-i\omega t)$

$$\nabla \times \mathbf{E} - i\omega\mu\mathbf{H} = 0$$

$$\nabla \times \mathbf{H} + i\omega\epsilon\mathbf{E} = 0$$

Periodic Interface Separating Two Homogeneous Half-spaces

- $\mu = 1$ everywhere
- $\epsilon = \begin{cases} \epsilon_1 & \text{in } \Omega_1 \\ \epsilon_2 & \text{in } \Omega_2 \end{cases}$
- bounded measurable in Ω_0
- $\epsilon(x+\Lambda, x_3) = \epsilon(x, x_3)$

Incident Monochromatic Plane Wave

$$\mathbf{E}_I(x, x_3) = \exp[i(k \cdot \mathbf{x} + k_3 x_3)]$$

Seek Solutions

$$\mathbf{E} = \mathbf{E}_I + \mathbf{E}_R \quad \mathbf{H} = \mathbf{H}_I + \mathbf{H}_R$$

Satisfying:

- Quasiperiodic
 $\rightarrow \mathbf{E}(x+\Lambda, x_3) = \mathbf{E}(x, x_3)\exp(ik \cdot \Lambda)$
- $\mathbf{E}_R, \mathbf{H}_R$ are bounded at infinity (outgoing radiation condition)
- (• Usual jump conditions)

Define $u_\alpha = u e^{-i\alpha x_1}$. Then u_α satisfies

$$(2) \quad (\Delta_\alpha + k^2)u_\alpha = 0, \quad \text{in } \mathbb{R}^2,$$

where the operator Δ_α is defined by $\Delta_\alpha = \Delta + 2i\alpha\partial_{x_1} - |\alpha|^2$.

We next reduce the problem to the bounded domain $\Omega = \{(x_1, x_3) \in \mathbb{R}^2 : -b < x_3 < b\}$. This may be done by introducing a pair of "transparent" boundary conditions on Γ_1 and Γ_2 . Let us first impose a radiation condition for the scattering problem. We insist that u_α is composed of bounded outgoing plane waves in Ω_1 and Ω_2 , plus the incident wave u_I in Ω_1 . Since u_α is periodic in the x_1 direction, it has a Fourier series expansion. Moreover, in the regions Ω_1 and Ω_2 , the media are homogeneous. It follows that another expression of u_α based on the fundamental solutions, or Green's functions, are available. Thus by matching these two expansions on Γ_1 and Γ_2 and using the radiation condition, one can derive the following boundary conditions:

$$(3) \quad \left. \frac{\partial u_\alpha}{\partial \nu} \right|_{\Gamma_1} = \sum_{n \in \mathbb{Z}} i\beta_1^n(\alpha) u_\alpha^{(n)}(b) e^{inx_1} - 2i\beta_1 e^{-i\beta_1 b} = T_1(u_\alpha|_{\Gamma_1}) - 2i\beta_1 e^{-i\beta_1 b},$$

$$(4) \quad \left. \frac{\partial u_\alpha}{\partial \nu} \right|_{\Gamma_2} = \sum_{n \in \mathbb{Z}} i\beta_2^n(\alpha) u_\alpha^{(n)}(-b) e^{inx_1} = T_2(u_\alpha|_{\Gamma_2}),$$

where for $j = 1, 2$, the coefficients

$$\beta_j^n(\alpha) = \begin{cases} \sqrt{k_j^2 - (n + \alpha)^2}, & k_j^2 > (n + \alpha)^2, \\ i\sqrt{(n + \alpha)^2 - k_j^2}, & k_j^2 < (n + \alpha)^2. \end{cases}$$

We assume that $k_j^2 \neq (n + \alpha)^2$ for all $n \in \mathbb{Z}$, $j = 1, 2$. This condition excludes "resonance" and ensures the existence of the fundamental solution for (2) inside Ω_1 and Ω_2 .

Optimization Techniques for the Design of Resonance Domain Diffractive Optical Elements.

J. T. Sheridan, R. Ehrhardt, T. O. Körner

Physics Institute, University of Erlangen-Nurnberg, Germany.

1. Introduction

In this paper the implementation of a very stable rigorous electromagnetic numerical algorithm is discussed. Such an algorithm can be combined with an iterative non-linear optimization procedure to design surface relief gratings whose period are of the order of magnitude as the incident wavelength. Several types of optimization algorithm are presented and their general characteristics discussed.

2. The Legendre Exact Eigenfunction Method

Exact eigenfunction methods ¹² have been successfully applied to examine diffraction by surface relief gratings. Such methods offer some numerical advantages over methods which require the use of the Fourier expansion of cross-section permittivity profile ^{3,4}, since the Gibbs phenomena and related numerical problems can be avoided ⁵. Careful rewriting of the boundary conditions has allowed numerical difficulties, arising due to the exponentially increasing and decreasing evanescence at the boundaries and within the grating, to be eliminated in the case of dielectric gratings ⁶. The rewritten boundary conditions also allow the use of non-implicit power conservation to test the convergence of the results. Recently it has been suggested ⁷ to use a piecewise description of the field inside a lamellar grating in terms of Legendre polynomials. Within each region of constant refractive index along a period the eigenfunctions are expressed as sums of continuous Legendre polynomials. In this way the eigenvalues and eigenfunctions of the structure can be found using simple matrix operations, avoiding the use of root finding algorithms ^{8,9}. In this Legendre Exact Eigenfunction Method, LM, there is little difference in complexity between the calculations for the TE and TM polarisation cases. Using the LM in conjunction with rewritten boundary conditions, numerically stable calculations for lossless and metallic lamellar gratings have been carried out ¹⁰. In all cases non-implicit power conservation, reciprocity and examinations of the convergence of the individual diffraction

THEOREM 3.1. *The variational approach converges to the solution of the model problem. Moreover, the following estimates hold*

$$\begin{aligned} \|u_\alpha - u^h\|_{L^2(\Omega)} &\leq Ch^2, \\ \|u_\alpha - u^h\|_{H^1(\Omega)} &\leq Ch^1, \end{aligned}$$

where the constant C is independent of h .

Further, the error estimates are optimal. Next, since the boundary operators are nonlocal, it is essential to obtain error estimates when truncations of these operators take place. We showed that the estimates in Theorem 3.1 still hold, provided that sufficiently many (but finite) terms are taken in the expressions of T_j . The proofs may be found in [1].

4. The TM case. In the TM case, Maxwell's equations can be reduced to

$$(9) \quad \nabla \cdot \left(\frac{1}{\epsilon} \nabla u \right) + \omega^2 u = 0, \quad \text{in } \mathbb{R}^2,$$

where ϵ may vary in different parts of the medium. The variational approach can be carried out similarly in the TM case. Although the finite element method does converge in the TM case, the algorithm converges more slowly than TE case. However, in general it is very difficult to obtain any explicit convergence rate without making use of the special grating structures. The difficulties are largely due to the discontinuous coefficient presented in the second order operator of the model equation. This presents a clear contrast to the TE case, where discontinuous coefficients only occur in the lower order terms. Thus in the TM case, the singularities caused by the discontinuous coefficients can spread more destructively. As the result, the solution in general is only in H^1 , and can not be any more regular, while the solution in the TE case is in H^2 in general.

Finally, because of the mathematical nature of the model equations, for general structures the convergence difficulties will appear, perhaps in a different manner, in all other known methods for solving the grating problem.

REFERENCES

- [1] G. Bao, *Finite elements approximation of time harmonic waves in periodic structures*, IMA Preprint Series # 1156, submitted.
- [2] G. Bao and D. Dobson, *Diffractive optics in nonlinear media with periodic structure*, IMA Preprint Series # 1124, submitted.
- [3] O. P. Bruno and F. Reitich, *Numerical solution of diffraction problems: a method of variation of boundaries*, J. Opt. Soc. Amer. A., to appear.
- [4] X. Chen and A. Friedman, *Maxwell's equations in a periodic structure*, Trans. Amer. Math. Soc., **323** (1991), 465-507.
- [5] D. Dobson, *Optimal design of periodic antireflective structures for the Helmholtz equation*, Euro. J. Appl. Math., **4** (1993), to appear.
- [6] D. Dobson, *A variational method for electromagnetic diffraction in bi-periodic structures*, Modél. Math. Anal. Numér., to appear.
- [7] D. Dobson and A. Friedman, *The time-harmonic Maxwell equations in a doubly periodic structure*, J. Math. Anal. Appl., **166** (1992), 507-528.
- [8] T. K. Gaylord and M. G. Moharam, *Analysis and applications of optical diffraction by gratings*, IEEE Proceedings, Vol. 73 No. 5 (1985), 894-937.
- [9] R. Petit, *Electromagnetic Theory of Gratings*, Topics in Current Physics, Vol. 22, edited by R. Petit, Springer-Verlag, Heidelberg, 1980.

Both the SA and GM can converge to a solution rapidly given a good set of starting parameters, i.e. a good initial guess or approximate model ¹⁷. However, although SA may avoid local minima successfully, neither method is absolutely local minima proof. Two NLOTs which, although more numerically intensive than either the GM or SA, offer more protection against such problems are the Genetic Algorithm, GA, and Simulated Evolution, SE. The GA operates by starting with a large initial set of parameter values. Those with the highest fitness, i.e. the best CFs, are selected and used as the progenitors for the next generation. The next generation (which has fewer members) is chosen by combining the parameter characteristics of the previous with some crossover probability. Mutation or variations in parameter values, with some predined probability, ensures that a too early specialisation is avoided. GAs are in fact a type of search procedure used up to now mainly in the area of Artificial Intelligence ¹⁸. SE also starts from many initial sets and tries to find better solutions by random deviation from these. Each generation of parameter sets is produced by introducing Gaussian noise into the previous and selectively retaining a reduced number ¹⁹. A further advantage of both these techniques is that using the GA and SE manufacturing tolerances can be directly included in the design.

The choice of CF is an issue of great importance in the design of DOEs using. In most cases examined in the literature the CF is defined in a single objective sense, i.e. although many physical parameters may be varied during a search, only one DOE function, for example the efficiency of a single diffraction order is maximized ²⁰. Using Multiple Objective Decision Making ²¹ the CF allows several functions with different importance weightings to be optimised simultaneously to produce optimised multifunctional DOEs.

The advantages of such software techniques include time saving and flexibility during design, optimum DOE performance, low running and capital costs compared to techniques based on trial and error, and provide the possiblility for quality control and process calibration. The potential financial and practical advantages of the various NLOTs applied to the manufacture of DOEs can be shown to be quite considerable ²².

4. Conclusions

The Legendre Exact Eigenfuntion Method has been discussed. The ability to carry out calculations for a large range of lamellar grating parameters using this method in combination with rewritten boundary conditions has been indicated. Numerical results for a particularly extreme set of grating parameters have been presented. Various types of non-linear optimization techniques have been discussed and their general characteristics compared. In particular Genetic Algorithms and Simulated Evolutionary techniques have

orders have been used to test convergence. Calculations for a large range of grating parameters have been carried out using the LM and comparisons with numbers available from the literature show excellent agreement ^{11,12}. In order to further test the method several numerically difficult grating cases have been examined. Examples are presented in the following table. In this case the results for a lamellar metallic grating illuminated by a plane wave are examined. The grating has the following parameters. The period $\Lambda/\lambda = 4/3$, and height $h/\lambda = 5.0$. The refractive index of the step and substrate material is $n_s = 8.2 + j81$, (Au at $\lambda = 10.6\mu\text{m}$). there is air above and in the grooves of the grating, $n_a = 1.0$. Filling factor $t = (\text{width of the step}/\Lambda) = 0.9$. In all the calculations presented the number of Legendre orders in the step was $m_0 = 30$, and the number in the groove was $m_1 = 20$.

Diffraction Order	Efficiency, TE		Efficiency, TM	
	$\theta = 0.1 \text{ rad}$	$\theta = 0.2 \text{ rad}$	$\theta = 0.1 \text{ rad}$	$\theta = 0.2 \text{ rad}$
-1^{st} R	0.0661	0.3034	0.0161	0.0626
0^{th} R	0.8726	0.5460	0.9522	0.8971
$+1^{\text{st}}$ R	0.0503	0.1353	0.0072	0.0133
N	21	19	19	13
$\sum \eta$	0.99991	1.00072	0.99999	0.99978

Table 1: Angle of incidence θ , number of eigenfunctions included N in the calculation.

3. Non-linear Optimization Techniques

The use of Non-Linear Optimisation Techniques, NLOTs, to design Diffractive Optical Elements, DOEs, has received ever increasing attention in the last 10-20 years. This has occurred because of their proven record of success in producing high performance manufacturable DOE designs, and the availability of inexpensive high power computers. In the last 5-10 years NLOTs have also been applied to the generation of resonance domain surface relief structures ^{13,14}. In these cases it is necessary to calculate the scatter function of the grating using Rigorous Electromagnetic Theory, REMT, in order to formulate the design Cost Function, CF. Although a considerable number of different NLOTs exist, only two methods, the Gradient Method, GM ¹⁵, and Simulated Annealing, SA ¹⁶, have been widely applied to such problems. In both cases the numerically calculated derivative of the CF is used to iterate towards a minimum, thus locating the optimum set of DOE parameters.

Observation and Numerical Analysis of Finite Beam Bragg

Diffraction by a Phase Grating

Michael R. Wang
Physical Optics Corporation
20600 Gramercy Place
Torrance, CA 90501
Tel. (310) 320-3088
FAX (310) 320-4667

Bragg diffraction by a phase grating is recognized as an important scheme in the implementation of a variety of devices including filters, wavelength division (de)multiplexers, couplers, optical memories, and optical interconnects. Important considerations in the design of these devices are not only wavelength dispersion, efficiency, crosstalk, and fanout issues but also the effects of finite beam diffraction when the laser beam sizes are comparable to, or smaller than, the grating interaction length. Finite beam Bragg diffraction effects have been considered for thick planar gratings and for symmetrical diffraction geometries [1-4]. Solutions to asymmetry diffraction ($\alpha_d \neq -\alpha$) is, however, required in order to account for various device geometries and application requirements.

Here, we report on the results of a numerical study and experimental observation of the asymmetric finite Gaussian beam diffraction by a holographic phase grating. An impulse response technique is used, in conjunction with coupled wave theory, to study the dependence of diffraction efficiency and wavelength and angular selectivities on the incident beam and grating parameters. The grating length-to-beam width ratio ($q = d/\omega_0$) is found to be an important parameter in determining diffraction performance. In the regime $1 < q < 5$, with $d = 300 \mu\text{m}$, and a center wavelength $\lambda_0 = 632.8 \text{ nm}$, several basic results are predicted. These include a departure from the plane wave behavior of $(\text{sinc})^2$ dependence for diffraction efficiency η , with a corresponding modification in the side lobe features; beam profile distortion for given d/ω_0 ratios and diffraction angle α_d ; a decrease in η with increasing q and diffraction angle α_d ; and lastly, an increase in selectivity bandwidth at longer center wavelengths. The analysis presented here can also be used to predict finite beam contributions for other center wavelengths and grating interaction lengths.

The approach to analyzing the finite beam, Bragg diffraction problem, for a given d/ω_0 ratio, is a two fold process. First, the planar phase grating is partitioned into grating subsections, with each subsection length being much smaller than the incident beam size. the incident Gaussian beam is likewise partitioned into a series of delta function inputs, each having different amplitudes and spatial locations. Second, the results of plane wave theory are applied to each subsection by calculating a weighted diffraction efficiency, based upon the spatial location of the propagating diffracted and undiffracted beams, for each impulse optical input. Finally, all impulse responses are summed to yield the resulting output beam profiles as a function of grating length, incident beam size, incidence and diffracted angle orientation, and grating modulation index.

been presented. Diffractive optical elements designed using these techniques will be presented, and their characteristics discussed.

5. References

- ¹ L. C. Botten, M.S. Craig, R. C. McPhedran, J. L. Adams, J. R. Andrewartha, *The finitely conducting lamellar diffraction grating*, Opt. Acta **28**, 1087-1102, (1981).
- ² S.-E. Sandström, G. Tayeb, R. Petit, *Lossy multistep lamellar gratings in conical diffraction mountings: An exact eigenfunction solution*, J. Electromagnetic Waves and Applications **7**, 631-649, (1993).
- ³ K. Knop, *Rigorous diffraction theory for transmission phase gratings with deep rectangular grooves*, J. Opt. Soc. Am. **68**, 755-762, (1978).
- ⁴ T. K. Gaylord, M. G. Moharam, *Analysis and applications of optical diffraction by gratings*, Proc. IEEE **73**, 894-937, (1985).
- ⁵ L. Li, C. W. Haggan, *Convergence of the coupled-wave method for metallic lamellar diffraction gratings*, J. Opt. Soc. Am. A **10**, 1184-1189, (1993).
- ⁶ J.. Y. Surratteau, M. Cadillac, R. Petit, *Sur la determination numerique des efficacites de certains reseaux dielectriques profonds*, J. Opt. (Paris), **14**, 273-288, (1983).
- ⁷ H. P. Herzig, M. T. Gale, H. W. Lehmann, R. Morf, *Diffractive components: computer-generated elements*, Ch 5, Perspectives for Parallel Optical Interconnects, Ph. Lalanne, P. Chavel (Eds.), ESPRIT Basic Research Series, 71-108, Springer-Verlag, Berlin, (1991).
- ⁸ L. C. Botten, M. S. Craig, R. C. McPhedran, *Complex zeros of analytic functions*, Comput. Phys. Commun. **29**, 245-259, (1983).
- ⁹ G. Tayeb, R. Petit, *On the numerical study of deep conducting lamellar gratings*, Optica Acta **31**, 1361-1365, (1984).
- ¹⁰ T. O. Körner, J. T. Sheridan, J. Schwider, *Classical diffraction by deep rectangular gratings using the Legendre Method*, J. Opt. Soc. Am. A, submitted (1993).
- ¹¹ D. M. Pai, K. A. Awada, *Analysis of dielectric gratings of arbitrary profiles and thicknesses*, J. Opt. Soc. Am. A **8**, 755-762, (1991).
- ¹² L. Li, *A modal analysis of lamellar diffraction gratings in conical mountings*, J. Mod. Opt. **40**, 553-573, (1993).
- ¹³ E. Noponen, A. Vasara, J. Turunen, J.M. Miller, M. R. Taghizadeh, *Synthetic diffractive optics in the resonance domain*, J. Opt. Soc. Am A **9**, 1206-1213, (1992).
- ¹⁴ H. Haidner, J. T. Sheridan, N. Streibl, *Dielectric binary blazed gratings*, Appl. Opt. **32**, 4276-4278, (1993).
- ¹⁵ J. Abadie, Nonlinear Programming, North-Holland, Amsterdam, (1967).
- ¹⁶ E. Aarts, Simulated Annealing and Boltzmann Machines, John Wiley and Sons, New York, (1989).
- ¹⁷ H. Haidner, J. T. Sheridan, J. Schwider, N. Streibl, *Design of a blazed grating consisting of metallic subwavelength binary grooves*, Opt. Comm. **98**, 5-10, (1993).
- ¹⁸ D.E. Goldberg, Genetic Algorithms in Search Optimisation and Machine Learning, Addison-Wesley, Reading, Mass. (1989).
- ¹⁹ L. Fogel, Artificial Intelligence Through Simulated Evolution, Wiley, New York, (1966).
- ²⁰ H. Haidner, P. Kipfer, J. T. Sheridan, J. Schwider, N. Streibl, M. Collischon, J. Hutfless, M. März, *Diffraction gratings with rectangular grooves, exceeding 80% diffraction efficiency*, Infrared Physics **34**, 467-475, (1993).
- ²¹ T. Gal, J. Nedoma, Management Science **18**, 406-421, (1972).
- ²² R. Ehrhardt, J. T. Sheridan, *Low cost design and testing of optical devices using computer simulation and optimization*, Wirtschaftsinformatik, submitted (1993).

$$\eta = \frac{\sum_{n=-\infty}^{\infty} |h[n\Delta x']|^2}{\sum_{m=-\infty}^{\infty} |F[m\Delta x']|^2} \quad (4)$$

Fig. 2 shows diffraction efficiency η as a function of both q and diffraction angle α_d , for $q = 1, 3$, and 5 , respectively. Note that $q = 0$ corresponds to the plane wave diffraction case. An increase in q is seen to result in a significant decrease in overall diffraction efficiency and a shift in the maximum possible diffraction angle to smaller α_d . At the same time, each of the curves for q shows a turning point in the α_d dependence, a region which defines the transition from single to multiple diffraction peaks and, therefore, distortion of the original Gaussian beam profile. Single peak behavior is maintained for values of $\eta > 60\%$ in all cases. Angular selectivity behavior is shown in Fig. 3 for the same values of q under normal incidence conditions. For the case when the beam size is comparable to the grating interaction length ($q = 1$), the efficiency response is similar to that of the plane wave case, with nearly identical $(\text{sinc})^2$ dependence and peak efficiency which approaches 100%. As q increases, the peak efficiency decreases, while the sidelobe features decrease and eventually disappear, signifying a greater finite beam contribution to the diffraction process. This behavior is accompanied by a slight broadening of the curves, as measured from the full-width half-maxima. Wavelength selectivity is similar to angular selectivity.

The effect of finite beam Bragg diffraction, including the transition of diffracted beam profiles from a single peak to multiple peaks, departure from the $(\text{sinc})^2$ dependence for selectivity curves, and lowering of diffraction efficiency should be considered in optimizing device designs. Center wavelength and interaction length d dependent angular and wavelength selectivity bandwidths can be used to transfer the results and curves to other d and center wavelength conditions. These theoretical results have been verified by experimental observation in a planar waveguide geometry of diffracted beams that change from a single peak to multiple peaks as d increases.

References:

1. R. S. Chu and T. Tamir, "Bragg Diffraction of Gaussian Beams by Periodically Modulated Media," J. Opt. Soc. Am., 66, 220-226 (1976)
2. R. S. Chu and T. Tamir, "Diffraction of Gaussian Beams by Periodically Modulated Media for Incidence Close to a Bragg Angle," J. Opt. Soc. Am., 66, 1438-1440 (1976)
3. R. S. Chu, J. A. Kong, and T. Tamir, "Diffraction of Gaussian Beams by a Periodically Modulated Layer," J. Opt. Soc. Am., 67, 1555-1561 (1977)
4. M. G. Moharam, T. K. Gaylord, and R. Magnusson, "Bragg Diffraction of Finite Beams by Thick Gratings," J. Opt. Soc. Am., 70, 300-304 (1980)
5. H. Kogelnik, "Coupled Wave Theory for Thick Hologram Gratings," Bell Sys. Tech. J., 48, 2909-2947 (1969)

Fig. 1 shows schematically the process of Bragg diffraction for each grating subsection with a single incident ray. After successive diffractions by multiple grating subsections, a set of diffracted rays in the \mathbf{k}_d propagation direction and a set of undiffracted rays in the \mathbf{k} propagation direction are obtained. The change in propagation direction and beam amplitude are considered at each interval in the diffraction process. At any diffraction point, P, the incident rays can be characterized by field amplitudes $E_1(x,z)$ propagating in the \mathbf{k} direction and $E_2(x,z)$ propagating in the \mathbf{k}_d direction. Originating from a single incident beam, E_1 and E_2 are coherently coupled inside the grating and, therefore, can make use of coupled wave theory [5,6]. It is assumed that s- and p-polarized waves do not couple in the grating region and can be treated separately. After diffraction at point P, the new E_1 beam can be represented by the summation of beams generated by the undiffracted portion of $E_1(x,z)$ and the diffracted portion of $E_2(x,z)$ which are propagating in phase due to coherent Bragg coupling. Similarly, the new E_2 can be obtained by the summation of beams generated by the diffracted portion of $E_1(x,z)$ and the undiffracted portion of $E_2(x,z)$. After diffraction, the new E_1 will propagate from position (x,z) to $(x+\Delta x_1, z+\Delta z)$ while the new E_2 will propagate from position (x,z) to $(x+\Delta x_2, z+\Delta z)$ for the next subsequent subsection grating diffraction. Each beam diffraction is then weighted by the amplitude coefficients (including complex phase factors) derived from the coupled wave theory [5,6].

A set of spatially resolved diffracted and undiffracted beams from all grating subsections, as shown in Fig. 1, results when an impulse response transfer function of the grating is applied to an incident ray of unit amplitude. Here, we let $G(x')$ represent the spatially digitized impulse response function for beams with wave vector \mathbf{k} , where x' is the axis along which the incident beam profile $f(x')$ is defined. $H(x'')$ represents a similar response function for a beam with wave vector \mathbf{k}_d , where x'' is the corresponding axis perpendicular to \mathbf{k}_d . Lastly, $h(x'')$ and $g(x')$ are the digitized representations for diffracted and undiffracted beam profiles, respectively, which are obtained by convolving the impulse response functions $H(x'')$ and $G(x')$ with the corresponding spatially digitized representation $F(x')$ for the incident beam profile $f(x')$. With these axis orientations and digitized spacings, shown in Fig. 1, the digitized amplitude profile for $h(x'')$ and $g(x')$ can be expressed using the convolution notation $h[n\Delta x'']$ and $g[n\Delta x']$, respectively, and be calculated by the expression:

$$h[n\Delta x''] = \sum_{m=-\infty}^{\infty} F[m\Delta x'] H[(n-m)\Delta x''] \quad (1)$$

$$g[n\Delta x'] = \sum_{m=-\infty}^{\infty} F[m\Delta x'] G[(n-m)\Delta x'] \quad (2)$$

where m and n are integer values for each digitized input, and $F[m\Delta x']$ is the digitized profile for the incident Gaussian laser beam, $f(x') = \exp(-x'^2/\omega_0^2)$, given by

$$F[m\Delta x'] = f(x') \big|_{x' = m\Delta x'} \quad (3)$$

where ω_0 is the spot size of the incident laser beam. The corresponding intensity distribution is proportional to the square of these amplitudes. The diffraction efficiency is obtained by dividing the diffracted beam energy by the incident beam energy, expressed in convolution notation as

6. M. R. Wang, G. J. Sonek, R. T. Chen, and T. Jansson, "Large Fanout Optical Interconnects Using Thick Holographic Gratings and Substrate Wave Propagation," *Applied Optics*, 31, 236-249 (1992)

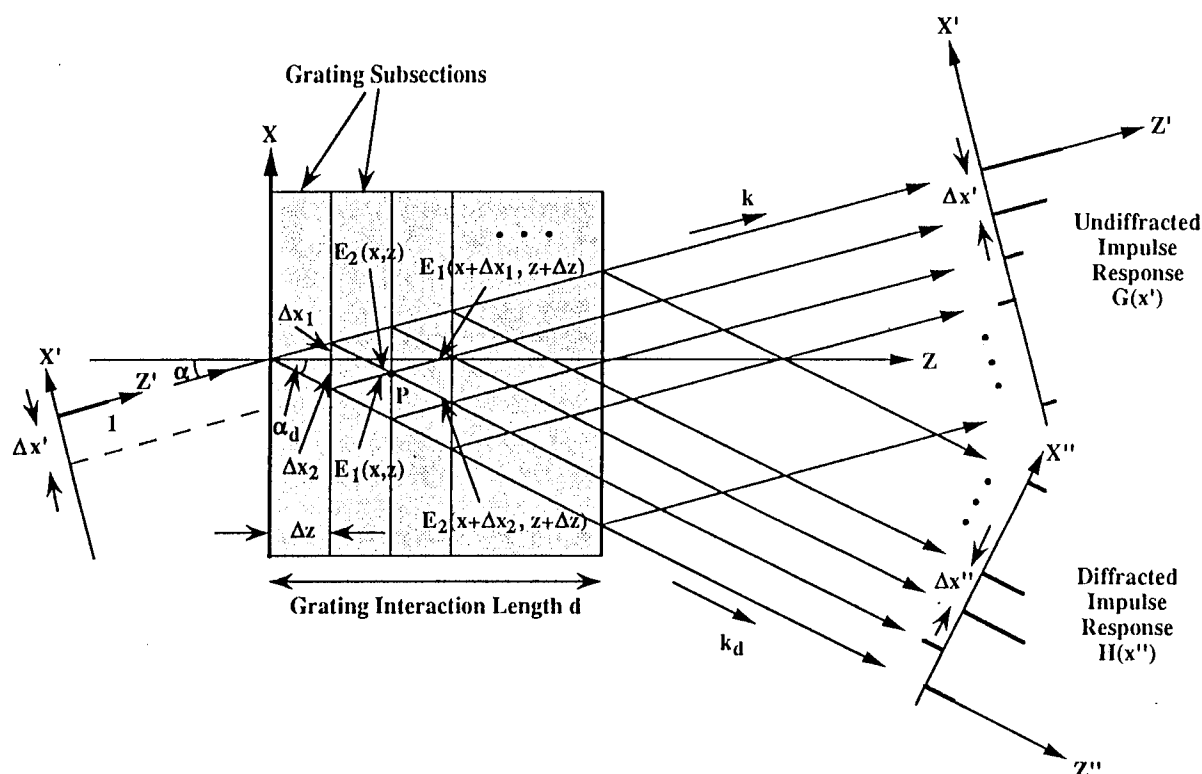


Fig. 1 Model of impulse response technique for finite beam Bragg grating diffraction. The impulse response amplitude functions are obtained by successively weighting diffracted and undiffracted beams at each grating subsection.

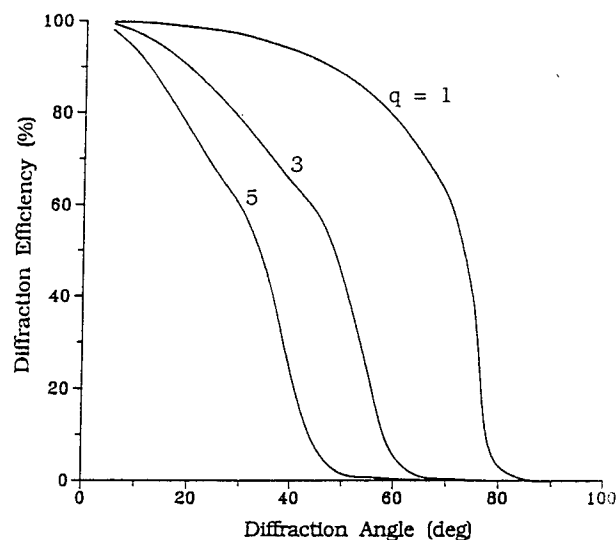


Fig. 2 Diffraction efficiency as a function of q and α_d .

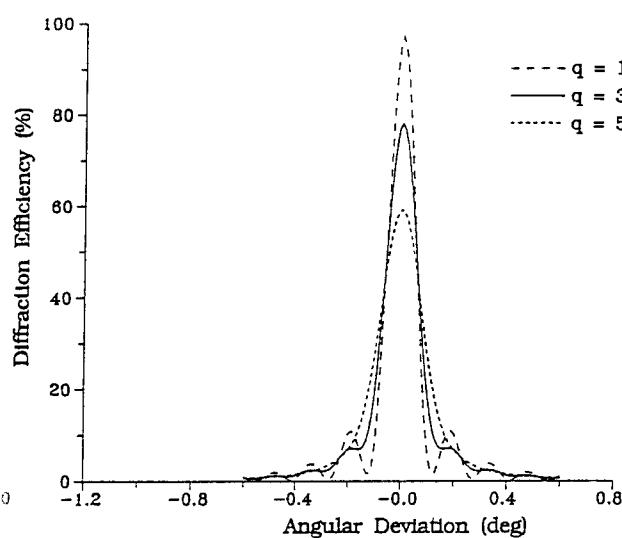


Fig. 3 q dependent angular selectivity.

Diffractive Microoptics in Switzerland

H. P. Herzig

Institute of Microtechnology, University of Neuchâtel, Rue A.-L. Breguet 2,
CH-2000 Neuchâtel, Switzerland, Phone: +41 38 205 121, Fax: +41 38 254 276

Introduction

Planar diffractive microoptical elements are becoming increasingly important for realizing compact and low cost optical systems. Typical elements have multilevel microreliefs ('binary optics') or continuous microreliefs, with features ranging from submicron to millimeter dimensions and relief amplitudes of a few microns. Novel structures can be realized complementing and exceeding the possibilities of traditional lenses, prisms and mirrors. The growing interest of industries in diffractive elements is based on the progress of modern microfabrication technologies. Computer-generated data for arbitrary phase profiles can be transformed into optical elements, which provides optimum design freedom. In contrary to earlier holographic elements, recorded in materials like silver halide or dichromated gelatin, these elements can now be made of rigid materials, such as glass or fused silica, or they can be replicated at low cost into plastic and epoxy materials. The paper presents a review of current activities in diffractive microoptics in Switzerland. Not mentioned are activities in waveguide grating couplers, display holograms and security applications.

An important role in the actual research in diffractive microoptics plays the Swiss Priority Program "OPTIQUE" which supports a project in "binary and continuous-relief microoptics" and a project on "e-beam lithography development". The aim of these projects is to establish a microoptics design and fabrication capability in Switzerland, as well as the fabrication and characterization of selected prototype elements of interest to industry and university groups. It includes the theoretical background and the design modules, as well as the fabrication and replication studies necessary to specify the achievable fabrication tolerances (for design) and identify a route to commercial fabrication. Several interested industries are participating.

We will start with a summary of the fabrication methods and then give some highlights of current activities.

Fabrication of diffractive optical elements

Fabrication techniques for realizing the microstructures resulting from the design of DOEs are based on a variety of high resolution lithographic and optical processes [1,2]. The typical procedure is to generate a mask by e-beam or by laser beam lithography, as shown in the central row of Fig. 1. Then, to get high efficiency, the mask is transformed into surface-relief structures by dry or wet etching. Using several masks, multiple profiles can be generated to improve the efficiency. Another technique is the direct writing of the DOE phase relief in photoresist by e-beam or laser beam. The developed photoresist relief can be converted into a metalized master relief by electroplating to emboss or cast low-cost replica. Of less interest as microoptical elements are actually interferometrically recorded volume holograms (HOEs) in materials like silver halide,

Monday, June 6, 1994

Novel Applications

DMB 10:30am–12:00m
Room B

Joseph N. Mait, *Presider*
U.S. Army

gray levels are created by a varying number of transparent holes in a chromium masks. The holes are small enough so that they are not resolved during the photolithographic step. The CSEM has reported a diffraction efficiency of 75 % for an 8-level microlens manufactured in fused silica (diameter 0.5 mm, focal length 1.5 mm). The lens was designed for a wavelength of 633 nm.

Continuous-relief elements: Continuous-relief elements can be fabricated by direct laser writing in photoresist using a system which has been developed over a number of years at the Paul Scherrer Institute in Zürich (PSIZ). Different types of elements have been produced, such as fan-out elements [4] and diffractive microlenses (Fig. 5). A diffraction efficiency of about 60% has been measured for a high aperture lens with $NA = 0.5$.

Beam shaping: A very interesting application for diffractive optics is the collimation of high-power laser diode arrays (LDAs). A compact demonstrator for coherent beam shaping has been built, which converts efficiently the double lobed far-field of a linear LDA, consisting of ten coupled emitters, into a single-lobed Gaussian mode of collimated light [5]. Two DOEs, a multilevel phase plate in the near-field of the array and a continuous surface relief-grating in the far-field, are needed for the conversion. The theoretical efficiency of the set-up is determined to be 96.7%. On the realized breadboard, one third of the total emitted power was converted into a single Gaussian mode. The critical point in coherent beam shaping is the stability of the transversal mode emitted by the LDA. Using a common external cavity, the stability and the modal separation of the LDA can be increased. This basic principle has been demonstrated for the coherent addition of three fiber lasers [6]. In this case, more than 77% of the output power have been coupled into a single collimated beam.

Hybrid achromat: A hybrid (refractive/diffractive) lens combines two optical elements with opposite dispersion. This enables the realization of an achromat which is about two times thinner than a conventional refractive achromat. IMT Uni-Ne has designed a hybrid achromat for a focal length $f = 8$ mm, a diameter $D = 5.2$ mm and a wavelength range $\lambda = 650 \pm 20$ nm (semiconductor laser). The numerical optimization has shown a wavefront error of 0.39λ for the whole spectrum in the center of the image plane. Additionally, the system (including lens, laser and housing) is insensitive to temperature variations in the range of -20° to $+40^\circ\text{C}$. The diffractive element will be fabricated in optical glass by ion beam milling at IMT-Uni Ne.

References

- [1] H. P. Herzig, R. Dändliker, "Diffractive components: Holographic optical elements" in *Perspectives for Parallel Interconnects*, Ph. Lalanne, P. Chavel, eds. (Springer, Berlin, 1993) pp. 43-69.
- [2] H. P. Herzig, M. T. Gale, H. W. Lehmann, R. Morf, "Diffractive components: Computer generated elements", in *Perspectives for Parallel Interconnects*, Ph. Lalanne, P. Chavel, eds. (Springer, Berlin, 1993) pp. 71-107.
- [3] S. Gray, F. Clube, D. Struchen, "The holographic mask aligner", *Holographic Systems, Components and Applications*, Neuchâtel, CH, Conference Publication No. 379 (Institution of Electrical Engineers, London, 1993), pp. 265-270.
- [4] M. T. Gale, M. Rossi, H. Schütz, P. Ehbets, H. P. Herzig, D. Prongué, "Continuous-relief diffractive optical elements for two-dimensional array generation", *Appl. Opt.* **32**, 2526-2533 (1993).
- [5] P. Ehbets, H. P. Herzig, R. Dändliker, P. Regnault, I. Kjelberg, "Beam shaping of high-power laser diode arrays by continuous surface-relief elements", *J. Mod. Opt.* **40**, 637-645 (1993).
- [6] J. Morel, A. Woodtli, R. Dändliker, "Coherent coupling of an array of Nd^{3+} -doped single-mode fiber lasers by use of an intracavity phase grating", *Opt. Lett.* **18**, 1520-1522 (1993).

dichromated gelatin and photopolymer. In photoresist, the interference pattern is converted into a relief structure, which is more attractive because it can be transferred into glass or quartz.

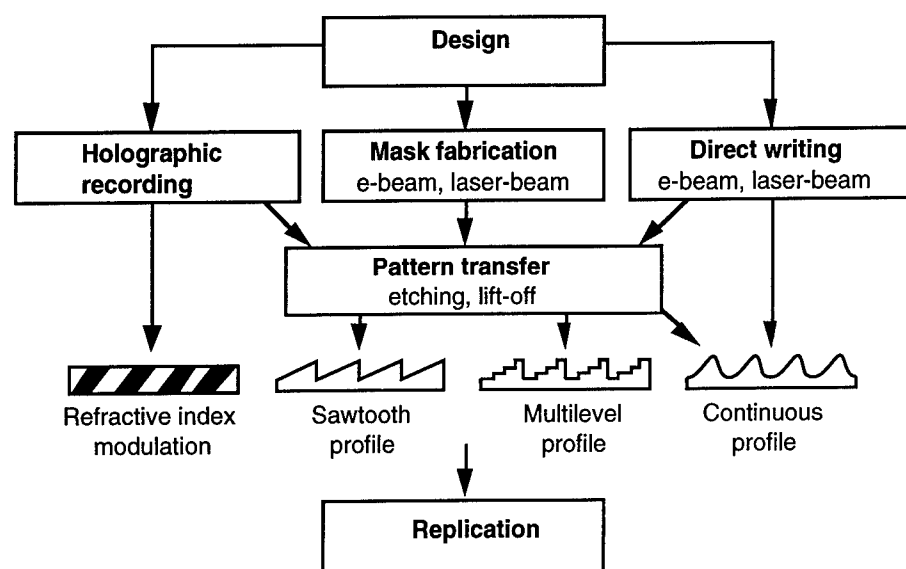


Fig. 1. Fabrication of diffractive optical elements.

The main activities in diffractive microoptics fabrication are at the Institute of Microtechnology Neuchâtel (IMT-Uni Ne), at the Paul Scherrer Institute Zürich (PSIZ) and at the Centre Suisse d'Electronique et de Microtechnique SA, Neuchâtel (CSEM). IMT-Uni Ne is experienced in the design of DOEs, interferometrically recorded holograms and investigates now the fabrication of multilevel phase elements by photolithography and subsequent etching. PSIZ has concentrated its effort on continuous-relief elements fabricated by laser-beam writing, replication of small series, and the interface to large volume industrial replication. CSEM has in its technological workshop a complete line of photolithographic and plasma etching equipment for microelectronics. These installations are also employed for micro- and planar optics. Besides CSEM, also IBM in Rüschlikon is equipped with an e-beam which is used for the development of DOE fabrication.

Current highlights

Modulated submicron structures: High resolution gratings can be written by e-beam into photoresist (Fig. 2). However, for submicron structures it is difficult to realize deep profiles in the order of a micron, as required for transmission elements. An alternative technique is the holographic lithography developed by Holtronic Technologies in Marin [3], enabling deep structures with feature sizes down to $0.3\ \mu\text{m}$ (Fig. 3). In holographic lithography a mask pattern is recorded as a hologram and then reconstructed for copying into photoresist. In collaboration with Holtronic, IMT-Uni Ne has realized an off-axis 9×9 fan-out element with a feature size of $0.5\ \mu\text{m}$ (carrier frequency $\nu = 1000\ \text{lines/mm}$). The diffraction efficiency of the transmission element was measured to be 85% at the wavelength $\lambda = 840\ \text{nm}$. Promising results have also been obtained by interferometric recording of fan-out elements into photoresist ($\nu = 1774\ \text{lines/mm}$).

Gray-tone masks: Multilevel phase profiles, as shown in Fig. 4(a), can be produced by a multiple mask process. The critical point is the alignment between the different steps. Similar elements can be realized with a single gray-tone mask [Fig. 4(b)]. This technology uses one mask, a photolithographic exposure and an etching step to transfer the photoresist relief into quartz. The

Single Element Achromatic Diffractive Lens

Donald W. Sweeney and Gary Sommargren

Advanced Microtechnology Program
Lawrence Livermore National Laboratories
Livermore, CA 94550
Phone: 510-422-5877
FAX: 510-422-8761

Introduction

A single element achromatic diffractive lens would have many unique applications. We are specifically interested in applications that require both the micro-thin character of diffractive optics and broadband imaging. Unfortunately, a diffractive lens tends to exhibit large chromatic aberrations and frequently low diffraction efficiency. For example, across the visible spectrum a zone plate Fresnel lens introduces about one diopter of axial chromatic aberration for every three diopters of power. Fortunately, as discussed in this paper, there are methods for overcoming this problem while retaining the micro-thin character of diffractive optics. The methods and results presented are generally applicable to many applications.

In general, diffractive lenses must be corrected for both field and chromatic aberrations. Single and multiple element diffractive elements are discussed extensively in the literature; see the reviews in Farn and Goodman [1] or Swanson [2]. Buralli and Morris [3] show a good example of the performance degradation of a purely diffractive landscape lens as a function of source bandwidth. It has been shown that single, achromatic planar diffractive elements are limited to those of negative power [4-5].

In this paper, we describe and demonstrate a method for generating an efficient, single element, diffractive lens that forms excellent white-light images. The following section describes the nature of the problem and summarizes the design strategies, the final section reviews the fabrication techniques and presents white-light imaging results.

Basic design strategies

The basic problem with using diffractive optics for broadband imaging is the optical power ($P = 1/f$) depends linearly on wavelength. For example, the power of a Fresnel lens is,

$$P \equiv \frac{1}{f} = \frac{k\lambda}{n'' r_1^2} \quad \text{so that,} \quad \frac{\Delta P}{P} = \frac{\Delta \lambda}{\lambda}, \quad (1)$$

where f is the focal length in meters, n'' is the ambient refractive index, k is the diffracted order, and r_1 is the radius of the first Fresnel zone. A diffractive lens of 20 diopters power at 550 nm shifts to 14.5 diopters at a wavelength of 400 nm and 25.5 diopters at 700 nm.

As we will now show the dispersive spread can be reduced to any level desired by trading the lens thickness for achromatic performance. For simplicity, the paraxial phase distribution created by an imaging lens is

$$\phi(r, \lambda_0) = \frac{2\pi}{\lambda_0} \frac{n'' r^2}{2f}, \quad (2)$$

where r is radius and λ_0 is the design wavelength. The thickness (t) and the optical pathlength (OPL) of

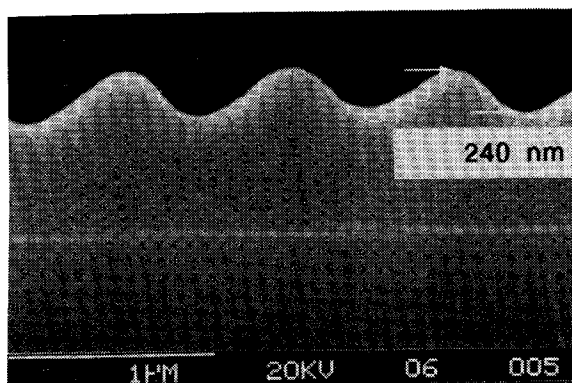


Fig. 2. SEM cross-section showing the profile of a 800 nm period blazed grating (CSEM, Neuchâtel).

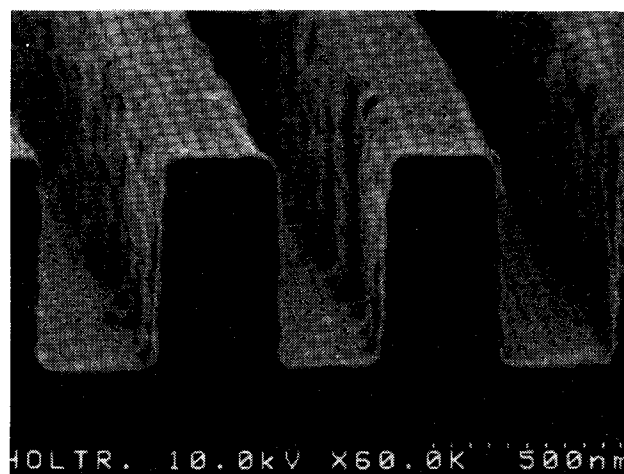
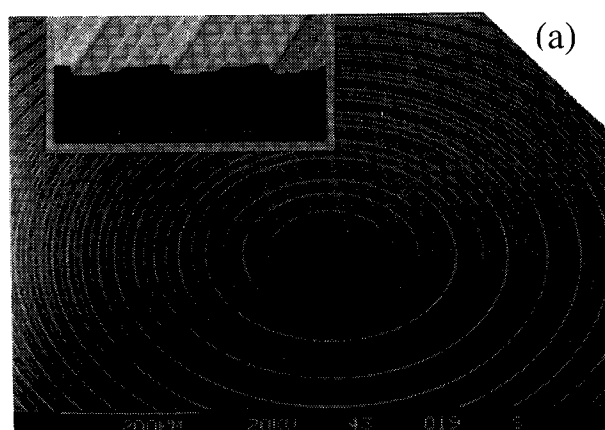
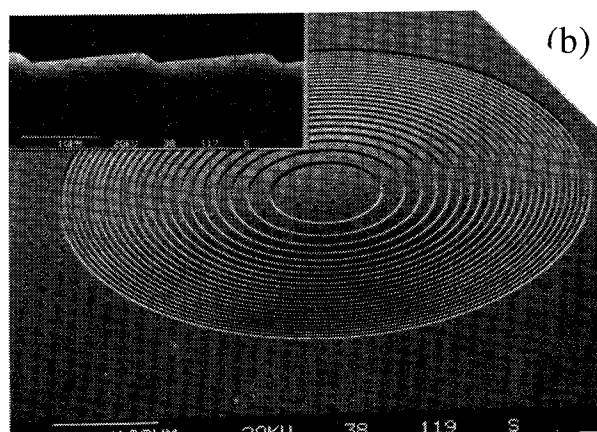


Fig. 3. Holographically printed 0.3 μm lines and spaces (Holtronic Technologies SA, Marin).



(a)



(b)

Fig. 4. Micrographs of a quartz microlens (a) manufactured by multiple etching steps using two conventional masks and (b) by a single etching step using a gray tone mask (CSEM, Centre Suisse d'Electronique et de Microtechnique SA, Neuchâtel).

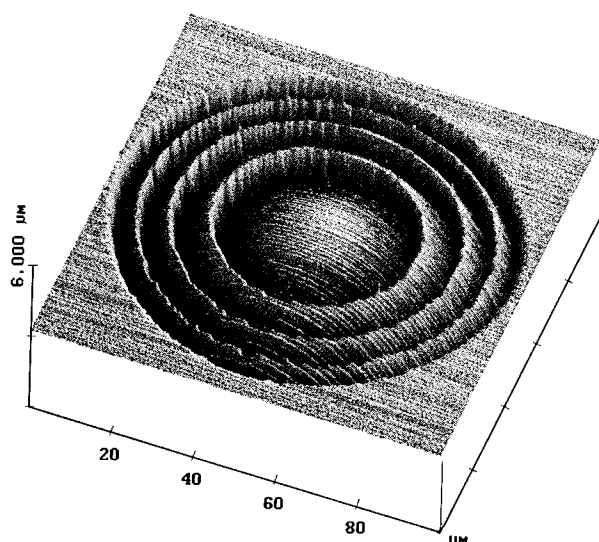


Fig. 5. AFM image of a Fresnel microlens (PSIZ, Paul Scherrer Institute, Zürich).

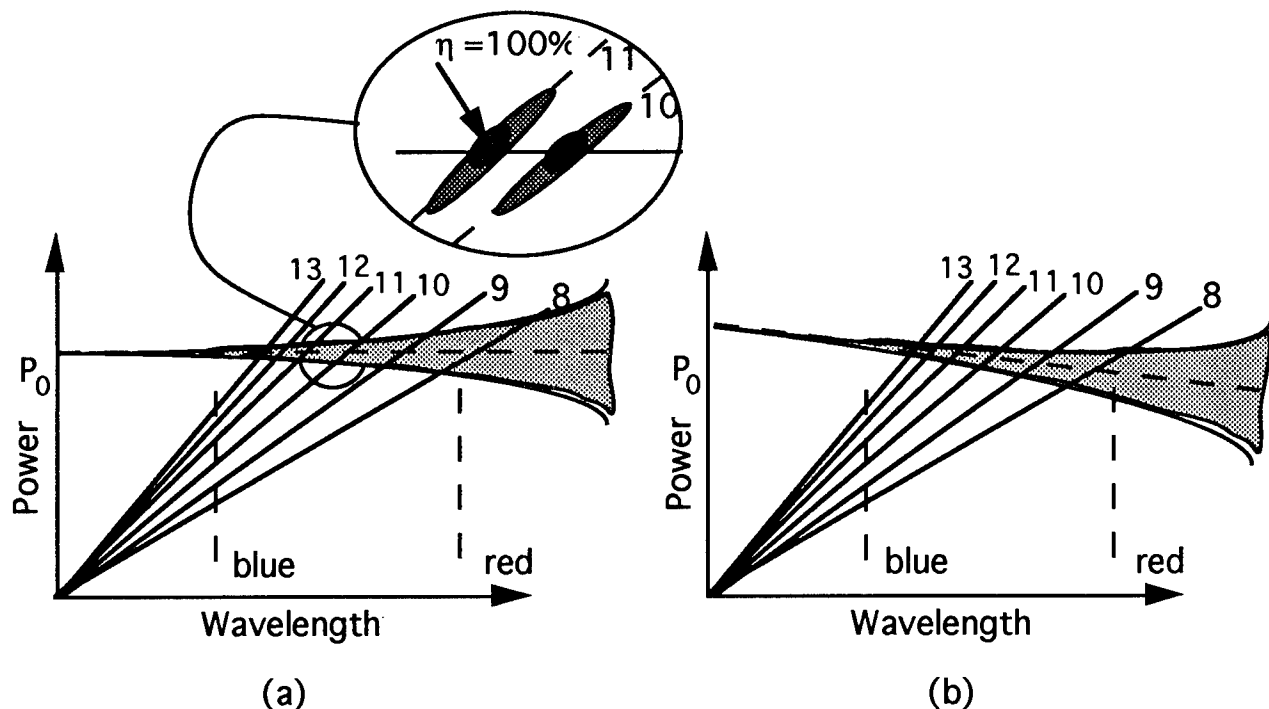


Figure 1. The radial lines from the origin represent the location of diffracted orders given by Eq. (1). Their location is independent of the refractive index of the lens material. The shaded region represents the power distribution determined by the blazing of the grooves. Energy is diffracted into the intersection of these two regions as shown in the insert. In (a) material dispersion is neglected, in (b) material dispersion is included; dispersion causes the shaded region to slope downward. The material dispersion can be corrected by superimposing an $m=1$ Fresnel lens onto the higher-order, harmonic Fresnel lens.

Fabrication and Imaging Results

Any method for generating diffractive optics can be used to generate harmonic Fresnel lenses. We have used both lithographic (i.e., binary diffractive optics) and diamond turning of a master followed by injection molding. The latter method offers the advantage that the groove profile is easily generated. Although diamond turning has difficulty with narrow grooves (standard tool-tips are 40 to 80 microns in diameter), as m increases the narrowest groove width increases proportionally. If the profile is represented by discrete binary levels, there must be at least two phase levels for each 2π phase variation at the shortest wavelength which illuminates the optic.

In the example presented here we have generated an acrylic lens ($n=1.49$) with a power of 25 diopters in air at the design wavelength of 550 nm. Using $m=20$ leads to a discrete step size of 23 microns. Figure 2 shows the aluminum, diamond-turned master and Figure 3 an image of the injection molded acrylic lens. In Figure 3, the lens is held over a US one-dollar note to qualitatively show the image detail.

Fabrication limitations and/or errors affect the final image quality. If the lenses are not manufactured to sufficient accuracy the wavefront segments coming from each region of the lens will not be properly phased. In this case, performance will degrade by an order-of-magnitude to that of a traditional Fresnel lens (e.g., lighthouse-type lens). To determine the required tolerances we use numerical simulation. The lenses have been evaluated using surface scanning profilometry, atomic force microscopy, and phase shift interferometry. Images have been formed in monochromatic and polychromatic white light.

the diffractive lens that creates this wavefront is,

$$t(r, \lambda_0) = \left(\frac{1}{\Delta n} \right) OPL(r, \lambda_0) = \left(\frac{1}{\Delta n} \right) MOD_{m\lambda_0} \left| \frac{n'' r^2}{2f} \right|, \quad m=1, 2, 3, \dots \quad (3)$$

Although this expression is usually written with $m = 1$, the generalization to arbitrary $(m \lambda_0)$ makes the lens an **harmonic** Fresnel lens. Increasing values of m represent the progression from the blazed Fresnel zone plate ($m=1$) with thickness steps of $\lambda_0 / \Delta n$ to an harmonic Fresnel lens with thickness variations of $m\lambda_0 / \Delta n$, through to a purely refractive lens with the final thickness reached as m becomes large (the thickness now also depends on the diameter of the lens).

To understand the effect of m in Eq. (3), think of the lens as a simple blazed Fresnel zone plate made for an effective wavelength $\lambda_{eff} = m\lambda_0$. The OPL step ($m \lambda_0$) created by the modulus operation in Eq. (3) has resonant (or harmonic) wavelengths at $(m \lambda_0)/k$ where $k = 1, 2, 3, \dots$ (i.e., at each of these wavelengths the phase steps of the lens are multiples of 2π). For example, if $\lambda_0 = 550$ nm and $m = 10$, then the resonances in the visible are at 423, 458, 500, 550, 611, and 687 nm.

If this lens is illuminated by λ_{eff} it is well-known that the lens will diffract 100% of the energy into the first diffracted order with a focal position given by Eq.(1). Fourier analysis of Eq.(3) also shows that if the lens is illuminated by $\lambda = \lambda_{eff} / k$, the lens will again diffract 100% of its energy into the k -th diffracted order. Using Eq.(1), the k 's in the numerator cancel leaving the focal length unchanged,

$$P = \frac{k (\lambda_{eff} / k)}{n'' r_1^2} = \frac{\lambda_{eff}}{n'' r_1^2}. \quad (4)$$

This is depicted graphically in Figure 1. If the lens is illuminated with any of the resonant wavelengths each will form a diffraction-limited focus in the same axial plane. The relevant diffracted orders in the example above are 8 through 13. At wavelengths away from the resonant wavelengths, the focal positions for each order follow the grating equation but the diffracted intensity falls quickly. To a good approximation ($m > 5$), the dispersive spread and thickness variations for the harmonic Fresnel lens is,

$$\frac{\Delta P}{P} \cong \frac{1}{m} \quad \text{and} \quad \Delta t_{max} = \frac{m\lambda_0}{\Delta n}. \quad (5)$$

Physically, we are trading between the thickness of the diffractive lens and achromatic performance. The presentation of the nature of the focus has been necessarily brief. The important point is that at any resonant wavelength the focus is diffraction limited. At intermediate wavelengths, the focus has an axial spread which is symmetric with the nominal focal plane.

It is interesting to consider the manner that material dispersion effects the harmonic Fresnel lens; this is depicted schematically in Figure 1(b). The diffracted orders are not a function of the lens material's dispersion, so for example an $m=1$ lens is not affected by this dispersion. Lenses with $m > 1$ are affected by material dispersion as shown in the figure.

The contribution of material dispersion can be corrected by superimposing a second, positive-power grating with $m=1$ onto the thicker grating. The $m=1$ grating has the full dispersion normally associated with diffractive optics and opposed to the material dispersion. Sufficient power is added to cancel the material dispersion.

Wavefront sensing applications of binary optics

D. R. Neal, M. E. Warren, J. K. Gruetzner

Sandia National Laboratories, P.O. Box 5800, Albuquerque, NM 87185-0601

Phone: (505) 844-0854 FAX: (505) 844-3211

1. Introduction

The advent of micro- or binary optics technology has made possible the fabrication of a variety of new optical devices. Optical fabrication is no longer limited by surfaces that can be made by grinding and polishing, or even diamond turning. In fact, optics with no symmetry, no smooth surfaces, and that perform multiple functions can be readily fabricated. While these optics have a large number of applications, they are extremely useful for systems that require arrays of small optics or aperture multiplexing, since these are fabricated using computer controlled photo-lithography and etching processes.

We have applied binary optics technology to construct various wavefront sensing using four mask processes to create 16 level optics. They are binary in the sense that they use discrete phase levels, not in the sense of using only two levels (they might more properly be called digital optics). We have found that 16 levels is adequate for most systems, giving greater than 99% efficiency.

2. Shack-Hartmann Wavefront Sensors

One common application of binary optics is the fabrication of lenslet arrays for Shack-Hartmann wavefront sensors. These usually consist of a lenslet array focussed onto a detector array (usually a CCD). While other researchers have used various methods for making the lenslet arrays, binary optics is the most controllable and straightforward approach [2]. Lenslet arrays for Hartmann sensors do not stress the technology since they use a fairly large $f\#$ (>100). This leads to simple analysis, and to relatively large finest feature size. We have fabricated a number of these arrays, tailored to match the size of various CCD cameras for both visible and IR wavefront sensing. A number of lenslet array patterns will fit onto a single 2 inch substrate, and thus we were able to fabricate lenslet arrays with different spatial resolutions and focal lengths. We have built several linear wavefront sensors that allow much higher speed data acquisition (because of the reduced pixel count)[1].

Figure 1 depicts a profile of a typical lenslet array used for a linear Shack-Hartmann wavefront Sensor. This array consists of 40 0.635 mm diameter cylindrical lenslets across a one inch aperture. The individual levels of the lenslet array can be seen in this figure. Even so, the residual RMS wavefront error is less than $1/20$ wave, and the lenslet elements are $>99\%$ efficient.

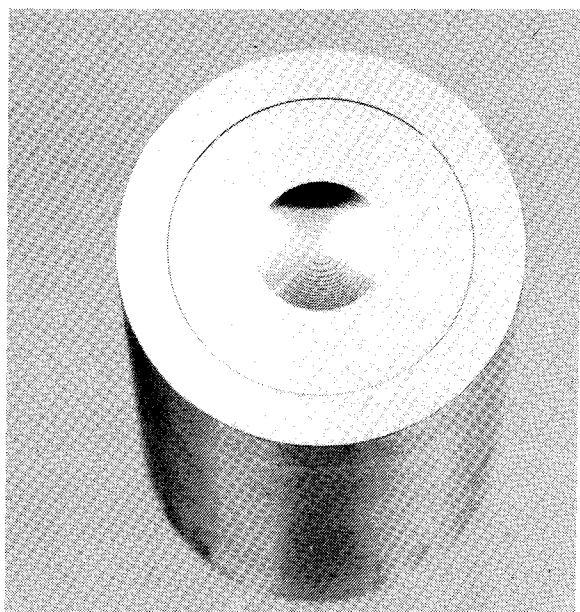


Figure 2. The diamond turned, aluminum Fresnel-lens master. The lens is 6 mm in diameter, has 14 zones, and has a total depth modulation of 23 microns.



Figure 3. The injection molded acrylic lens held over a U.S. one-dollar note.

References

1. M.W. Farn and J.W. Goodman, "Diffractive Doublets Corrected at Two Wavelengths"; JOSA-A, 8, 860 (1991); see also, M.W. Farn, "Design and Fabrication of Binary Diffractive Optics," Ph.D. thesis, Stanford University, Stanford, CA (September 1990).
2. G.J. Swanson, "Binary Optics Technology: The theory and Design of Multi-Level Diffractive Optical Elements," DARPA Technical Report 854 (1989).
3. D.A. Buralli and G.M. Morris, "Design of a wide field diffractive landscape lens," Applied Optics, 28, 3950 (1989).
4. S.J. Bennett, "Achromatic combinations of hologram optical elements," Applied Optics, 15, 542 (1976).
5. W.C. Sweatt, "Achromatic triplet using holographic optical elements," Applied Optics, 16, 1390 (1977).

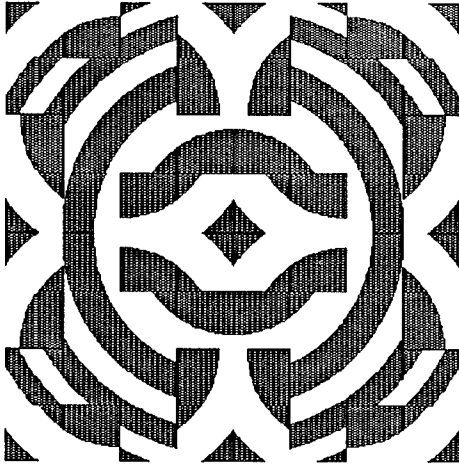


Figure 3: Mask layout for a two-tier wavefront sensor

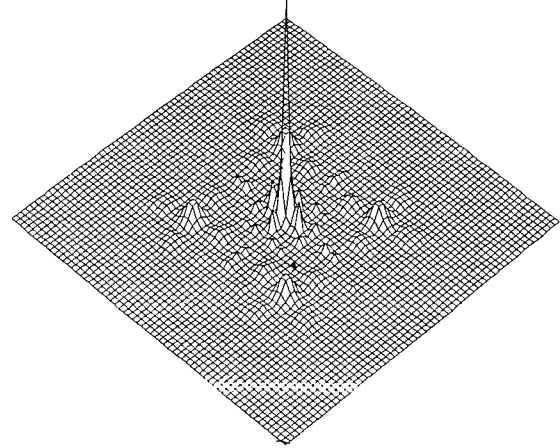


Figure 4: Intensity pattern produced by two tier wavefront sensor

expansion of the wavefront error about the center of the aperture. The terms of the series expansion can be derived by measuring derivatives of the wavefront. This can be accomplished using the multi-tiered wavefront sensor depicted in Fig. 2. The multiplexed binary optic is used to bring light from different parts of the aperture to a focus in different regions on a detector array. The first tier focuses light that is sampled from the entire aperture onto the center of the detector. This provides a measure of overall tip and tilt. It is used to give the second two terms of a Taylor series expansion for the wavefront phase:

$$\begin{aligned} \phi(x, y) = & \quad (1) \\ & \phi(0, 0) + \left. \frac{\partial \phi}{\partial x} \right|_{(0,0)} x + \left. \frac{\partial \phi}{\partial y} \right|_{(0,0)} y + \\ & \left. \frac{\partial^2 \phi}{\partial x^2} \right|_{(0,0)} \frac{x^2}{2} + \left. \frac{\partial^2 \phi}{\partial y^2} \right|_{(0,0)} \frac{y^2}{2} + \left. \frac{\partial^2 \phi}{\partial x \partial y} \right|_{(0,0)} \frac{xy}{2} + \left. \frac{\partial^2 \phi}{\partial y \partial x} \right|_{(0,0)} \frac{yx}{2} + \dots \end{aligned}$$

since the spot centroid position provide a measure of the average wavefront slope over the aperture. The next set of terms in equation (2) are determined from the centroid positions of the next higher tier. This tier brings light from each of the four quadrants to a focus in that quadrant. The second order terms can be derived from the focal spot positions in each quadrant, for example:

$$\left. \frac{\partial^2 \phi}{\partial x^2} \right|_{(0, \Delta y)} = \left. \frac{\partial \phi}{\partial x} \right|_{(\Delta x, \Delta y)} - \left. \frac{\partial \phi}{\partial x} \right|_{(-\Delta x, \Delta y)} \quad \text{and} \quad \left. \frac{\partial^2 \phi}{\partial x^2} \right|_{(0,0)} = \left[\left. \frac{\partial^2 \phi}{\partial x^2} \right|_{(0, \Delta y)} + \left. \frac{\partial^2 \phi}{\partial x^2} \right|_{(0, -\Delta y)} \right] / 2 \quad (2)$$

Figure 4 presents the intensity distribution produced by this system. While the distribution of the lenslets throughout the aperture causes there to be some additional light diffracted into higher orders, the overall Strehl ratio is still quite good since a reasonably large sampling over the aperture was obtained.

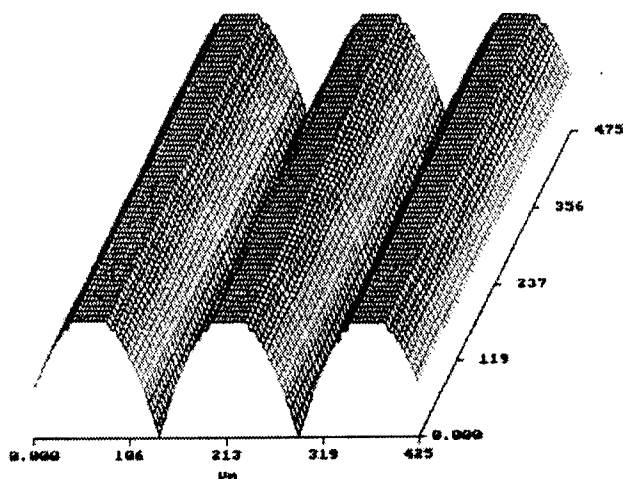


Figure 1: Surface profile of cylindrical lenslet array used to make one-dimensional wavefront sensor

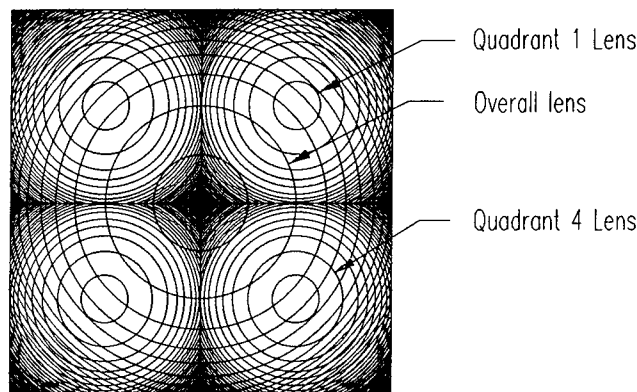


Figure 2: Multi-tiered wavefront sensor - two tier

3. Aperture Multiplexing

Using binary optics technology, we are not limited to producing a simple array of lenslets. It is possible to multiplex the aperture so that one optic can serve the purpose of several different elements. This can be done two ways. The first is diffractive, where gratings or other phase perturbations are written across the aperture to diffract the required amount of light into different orders, and each order performs a specific function. The other method is simply to break the aperture up into a series of smaller sub-apertures, with every other sub-aperture performing a different function. Both of these approaches are feasible using binary optics technology, however, the diffractive approach requires a sophisticated physical optics model (especially for fast optics), whereas ray-tracing is sufficient for the segmented aperture approach.

Aperture multiplexing is useful for a number of reasons. It can be used to reduce the number of optics in a complicated optical system. Beam splitters, gratings, lenses, apertures and other elements are easily multiplexed onto the same optic. For systems where weight or complexity is important, this provides significant advantages. Multiplexing can also be used to build optics that are otherwise inconceivable. Some examples of the applications of aperture multiplexing are presented in the remainder of this section.

3.1 Multi-tiered wavefront sensing

A Shack-Hartmann sensor provides a measurement of the wavefront slope over discrete sub-apertures across the field. In order to determine the wavefront, an integration or reconstruction step must be performed[3]. Often, this reconstruction step introduces a significant amount of noise into the process, or causes is computationally intensive. This can be a significant factor for closed loop control of deformable mirrors in adaptive optics systems or real time wavefront sensing

A more direct interpretation of the wavefront error can be obtained by using a series

New uses of computer-generated holograms for measuring astronomical optics

Jim Burge

Steward Observatory

University of Arizona, Tucson, AZ 85721

602-621-8182 (fax: 602-621-1578)

internet: jburge@as.arizona.edu

Computer-generated holograms (CGH's) have been used for interferometric optical testing of aspheric surfaces for over twenty years, and are now quite common. This paper presents two new applications of circular CGH's that were developed and implemented at the Steward Observatory Mirror Laboratory to support the production of large, highly aspheric telescope mirrors. Null correctors that are used to test large (up to 8.4 m diameter) primary mirrors are tested directly using small CGH's. Large, convex secondary mirrors are tested using full-aperture spherical test plates that have zone patterns written onto the curved reference surfaces.

These two tests use circular CGH's or zone plates that are designed and fabricated to diffract highly accurate wavefronts. Rather than using tilt in the CGH to separate the different orders of diffraction, both tests use power to separate the orders, causing them to come to focus at different axial positions (See Fig. 1). A small aperture is placed at the position where the desired order comes to a sharp focus, allowing only that order to pass. The size of the aperture is chosen to be small enough to reject the unwanted orders, but large enough to pass the high frequency figure information.¹

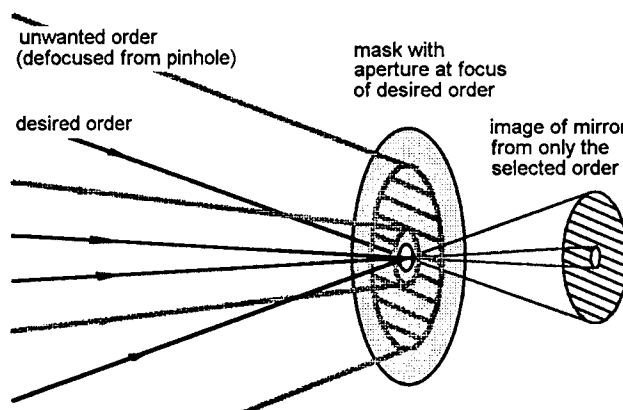


Figure 1. Rejection of stray diffraction orders. The order rejection relies on two principles. (1) The desired order comes to a sharp focus where all other orders are out of focus, and (2) An annular pupil is used.

Verification of null correctors

A new CGH test of null correctors has been designed and implemented for several telescope primary mirrors.² Large primary mirrors for optical telescopes are interferometrically tested using null correctors. In fabricating a primary mirror, the optical surface is polished to match the wavefront generated by the null corrector. In the unlikely event of a flawed null corrector, the final shape of the primary mirror will be incorrect. Two recent telescopes had their primary mirrors made to the wrong shape because of errors in the null correctors -- the Hubble Space Telescope and the European New Technology Telescope. If accurate testing of the null correctors had been performed, the errors would have been discovered and corrected in the shop. Instead, the errors were not discovered until the finished mirrors were operational in their telescopes.

In the CGH null lens test, a computer-generated hologram of the mirror is tested by the null lens. The hologram, which is only 40 mm in diameter for a 3.5-m $f/1.75$ primary mirror, is made so it will appear to the null lens as a perfect primary mirror to the null corrector. The test is easy to perform to high accuracy for several reasons: it is a null test, it is insensitive to alignment errors, and no optics other than the hologram are required. The hologram is designed and fabricated independently from the null corrector, so agreement between the two indicates a high probability that both are correct.

The hologram is simply a circular grating or reflective zone plate on a flat substrate. The holograms used at Steward Observatory were made by etching concentric grooves into fused silica substrates and coating with reflective aluminum. The CGH patterns were fabricated by replicating masks written using electron beam lithography. The ring positions are determined analytically to synthesize the shape of the wavefront that would be

3.2 Specialized Adaptive Optics Sensors

This sensor is also useful for adaptive optics systems. For segmented adaptive optics applications, a portion of the light from each quadrant is focused to a point directly between the quadrants. This produces a distinct interference pattern that can be used to determine the relative phase of the two regions. This is useful for adaptive optics systems where the different regions represent wavefront measurements of a segmented deformable mirror. The center spots in each quadrant are used to provide tip/tilt information to the deformable mirror. The segments are compared two by two to determine the phase around the entire quadrant.

5. Conclusions

We have developed a number of different wavefront sensors for measuring turbulence, fluid flow and for feedback sensors in adaptive optics. We have found that binary optics technology can be used effectively to reduce the number of optics and detectors required for many of these systems. We have developed hierarchical wavefront sensing and control schemes using aperture multiplexing to reduce the computational load required for wavefront reconstruction. Other novel concepts including curvature sensing and phase diversity sensors are also under development.

References

- [1] D. R. Neal, T. J O'Hern, J. R. Torczynski, M. E. Warren and R. Shul, *SPIE* Vol. 2005, pp. 194–203 (1993).
- [2] D. Kwo, G. Damas, W. Zmek, *SPIE* Vol. 1544, pp. 66–74 (1991).
- [3] M. Roggeman, *Computers Elect. Engng* Vol. 18, No. 6, pp. 451–466 (1992).

Unfortunately, several holograms were fabricated with gross errors due to an unsolved problem with the replication by contact printing. Discrete phase steps of up to half a fringe, corresponding to a radial shift of the ring pattern of about $1\text{ }\mu\text{m}$ were seen. This is a factor of 5 larger than what was expected from the printing process. The errors can be avoided by eliminating the replication step from the fabrication process by writing the hologram onto its final substrate with the e-beam writer.

This new test of null correctors will be performed for the 6.5-m $f/1.25$ and 8.4-m $f/1.14$ primary mirrors at the Steward Observatory Mirror Lab.³

Measurement of secondary mirrors

A technique for testing large, highly aspheric convex secondary mirrors is being pursued at the Steward Observatory Mirror Lab. This new test uses a full aperture test plate with a computer-generated hologram (CGH) fabricated onto a concave spherical reference surface.⁴ Fringes of interference are viewed through the test plate, which is supported several millimeters from the secondary (See Fig. 5). The hologram consists of annular rings of metal spaced at intervals as small as $80\text{ }\mu\text{m}$ and as large as $500\text{ }\mu\text{m}$.

In this interferometric test, the diffraction from the zone plate forms the reference wavefront and the reflection from the secondary forms the test wavefront (See Fig. 6). The test plate is illuminated with light that refracts from the reference sphere to strike the secondary mirror at normal incidence. This light reflects back onto itself to form the test beam. Any figure errors in the secondary mirror will be imparted to this test wavefront. The reference wavefront is formed by diffraction from the ring pattern on the reference sphere. The CGH is designed to make this reference beam match the test wavefront so it also retraces the incident path.

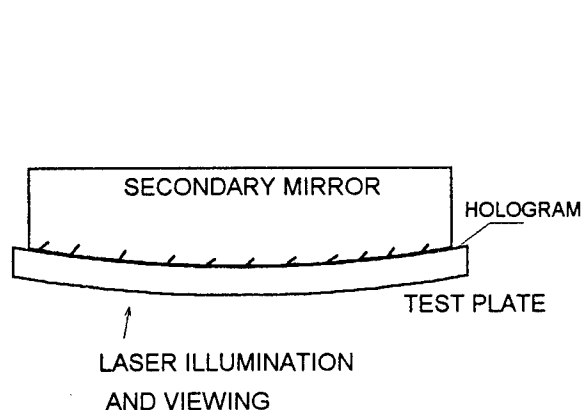


Figure 5. Layout of holographic test of a secondary mirror. The test plate has a reference spherical surface with a ring pattern drawn onto it.

There are several feasible methods currently being studied to fabricate a rotational CGH onto a curved surface. These methods generally use a precise rotary stage to spin the test plate under a focused optical beam (See Fig. 7). Linear stages control the radial and axial position of the writing head. The stages need only several-micron accuracy, which is readily available in coordinate measuring machines. The pattern may be drawn by exposing photoresist, ablating a metallic coating, or by creating a thin oxidation layer by heating with a focused laser.⁵

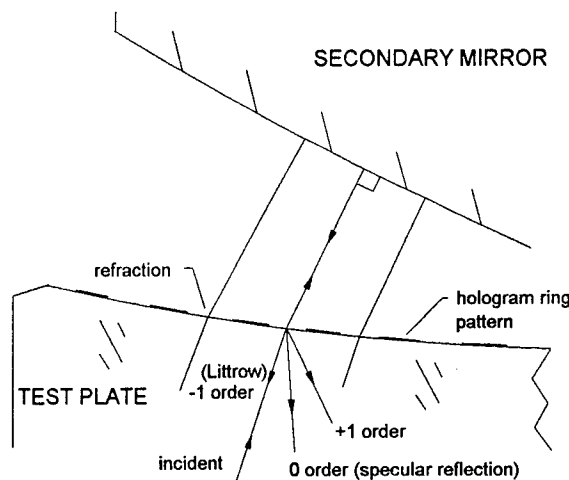


Figure 6. Reference and test beams for a holographic test plate measurement.

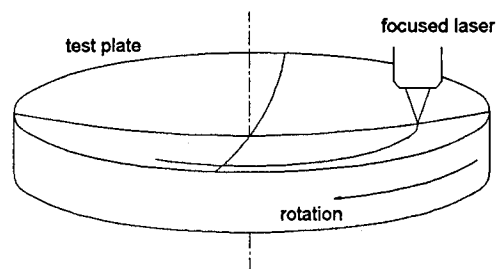


Figure 7. General geometry for optically writing ring patterns onto curved test plates. A focused laser beam is moved radially to expose rings onto the rotating optic.

reflected by a perfect primary mirror. The depth and width of the grooves are optimized to minimize fabrication costs while giving the correct 4% diffraction efficiency to yield high contrast fringes.

A layout of the CGH null test, shown in Fig. 2, depicts an Offner null lens and CGH. No modifications are made to the null lens for performing this test; the null corrector tests the hologram in exactly the same manner used to test a primary mirror. The alignment of the test is surprisingly simple. The CGH is positioned at paraxial focus of the light from the null corrector. Once the CGH is near the correct position, the shape of the fringe pattern viewed in the interferometer is used to align the hologram. Since the CGH appears to the null corrector as a complete primary mirror with the correct shape, the alignment of the hologram is exactly like that of the actual primary. The lateral translation, axial translation, and tilt of the null lens are adjusted to eliminate tilt, focus, and coma from the interferogram.

The holograms are designed to give about 4% diffraction efficiency into the desired order. This matches the intensity from the reference surface to give a high-contrast interference pattern. A pinhole positioned near the Shack cube rejects the stray orders of diffraction and lets only the desired order through.

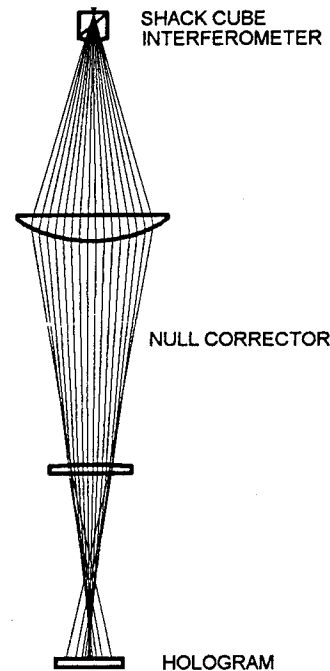


Figure 2. Layout of CGH test of null lens. The use of the CGH involves simply positioning the hologram at the correct location and making the measurement as if testing the mirror itself.

The null correctors for two 3.5-m $f/1.75$ primary mirrors (for the ARC and WIYN telescopes) were successfully tested using computer-generated holograms. Both of these tests confirmed the null corrector conic constants within the test uncertainty of ± 0.000078 . The wavefront errors for the two null lenses were measured to be 0.022λ rms and 0.016λ rms at 632.8 nm. An interferogram and reduced phase data are shown in Figs. 3 and 4.

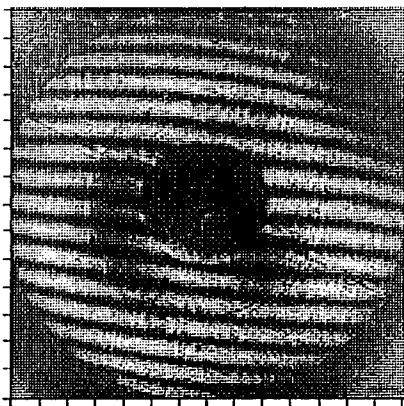


Figure 3. Interferogram of computer-generated hologram through null lens. This single interferogram shows speckle, non-uniform illumination, air motion, and tilt and coma from alignment.

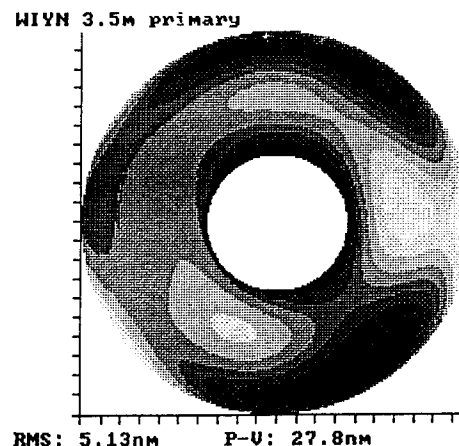


Figure 4. Contour map showing measured null lens error of 5.1 nm rms with contours at 3 nm intervals.

PATTERNED SCHOTTKY BARRIER SOLAR CELLS

H. Grebel, K. J. Fang

Optical Waveguide Laboratory, the department of Electrical Engineering, New Jersey Institute of Technology, Newark, New Jersey 07102. Tel: (201) 596-3533

Additional optics are required to illuminate the test plate such that the rays will be normally incident to the mirror being tested. Low quality illumination optics can be used without degrading the test accuracy because the reference and test beams are coincident and equally affected by the illumination system. Only the difference between the two wavefronts is measured. This fact allows the test to be economical, because the requirements on the large optics are quite loose. It also makes the test insensitive to vibration and air currents. Only the reference spherical surface of the test plate must be figured and measured accurately. That surface is a concave sphere, which is relatively easy to fabricate and measure. The illumination and viewing optics must be of sufficient quality to allow the rejection of stray diffractive orders. This condition allows ray aberrations of about 0.1° .

A 10.25-inch secondary mirror was measured using this method to have a shape error of 44 nm rms, shown below in the contour map and interferogram (Figs. 8 and 9). The hologram, which is made up of a pattern of chrome rings, was written at the Optical Sciences Center by Cindi Vernold. The interference pattern had nearly perfect contrast allowing low-noise measurements. The secondary was pushed using piezo-electric transducers to allow high resolution phase shifting interferometry.

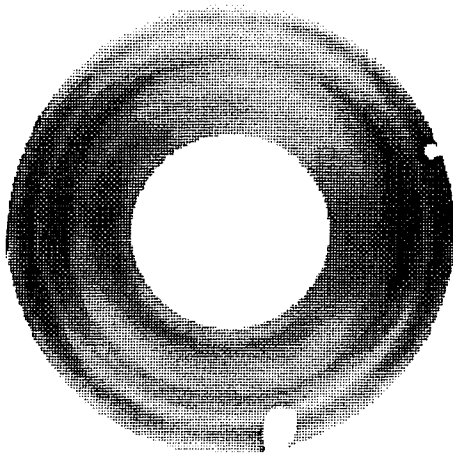


Figure 8. Phase map showing figure of a secondary mirror as measured by a holographic test plate. The surface has 44 nm rms variations, shown as gray scale.

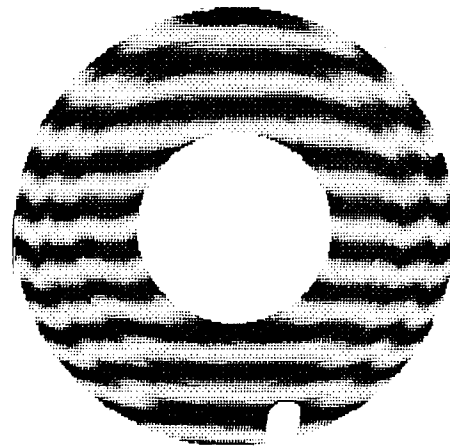


Figure 9. Interferogram corresponding to Fig. 8.

This new test will be implemented at the Steward Observatory Mirror Lab for testing secondary mirrors up to 1.65-m in diameter with over 300 μm departure from the closest fitting sphere. The hologram writer for these tests and the illumination system are currently under construction.

References

1. J. H. Burge, *Advanced Techniques for Measuring Primary Mirrors for Astronomical Telescopes*, Ph. D. Dissertation, Optical Sciences, University of Arizona (1993).
2. J. H. Burge, "Certification of null correctors for primary mirrors," in *Advanced Optical Manufacturing and Testing IV*, J. Doherty, Editor, Proc. SPIE **1994**, in press (1993).
3. J. H. Burge, D. S. Anderson, D. A. Ketelsen, and S. C. West, "Null test optics for the MMT and Magellan 6.5-m $f/1.25$ primary mirrors," in *Advanced Technology Optical Telescopes V*, L. M. Stepp, Editor, Proc. SPIE **2199**, in press (1994).
4. J. H. Burge and D. S. Anderson, "Full-aperture interferometric test of convex secondary mirrors using holographic test plates," in *Advanced Technology Optical Telescopes V*, L. M. Stepp, Editor, Proc. SPIE **2199**, in press (1994).
5. V. P. Koronkevich, *et al*, "Fabrication of kinoform optical elements," *Optik* **67**, No. 3, 257-266 (1984).

In Figure 1 we show a pictorial description of ray tracing in a groove. The groove is assumed to be much larger than the light wavelength. In Figure 2 we show the average reflectivity for a V-groove structure on silicon. It is an average because each portion of the surface possesses a different reflectivity value. The zero reflection point for a randomly polarized light impinging on the grooved surfaces is seen to lie in the sharp, needle-like regime (small inclination angles). The surface area of the cell, and consequently the dark current, is large at these angles. The relationship between the cell size, A_0 , and the total surface area, A , is, $A = A_0 / \sin(\theta/2)$, where θ is the inclination angle. Large dark current may decrease the cell's performances⁷ owing to a reduction in the open circuit voltage. Another aspect to be considered is the apparent change in the effective barrier height between the metal and the semiconductor material. This is owing to a non-uniform current distribution between the electrodes and the introduction of surface states by the photo-ablation process. In this paper, we examine these aspects and their effects on Schottky barrier solar cells.

In the experiment we used a 200mJ/pulse KrF Excimer laser at $\lambda = 248\text{nm}$ in the presence of various solutions and a simple cylindrical lens to ablate V-grooves and M-shape structures. Asymmetric shapes have been fabricated by tilting the laser beam in an angle with respect to the sample.

In the following we compare flat Schottky barrier solar cells with patterned solar cells. We used 15 pulses to engrave large grooves and 5 pulses to engrave small grooves. The dimensions of the large grooves were: depth $11.5\mu\text{m}$ and width $30\mu\text{m}$ so that the opening angle of a deep V-groove is about 75° . The smaller grooves were about $4\mu\text{m}$ deep. Grooves ablated in air were 20% deeper and wider than grooves ablated in solutions. In Figure 3 we show a relative measurement of short circuit current vs incident light angle. We use

Patterning is known to increase the light collection efficiency of solar cells¹⁻². The reason is that a surface relief increases the number of reflections either at the surface or within the cell, thereby, increases the probability of a light beam to be absorbed and be turned into useful current³. Traditional patterning was either relying on naturally occurring pyramids in Si during etching with KOH⁴, or involved complicated patterning techniques⁵. The naturally etched planes in Si, do not possess the required slopes necessary to optimize the light collection process. Other possibilities lie in the area of binary optics where VLSI methods were used to pattern structures finer than the optical wavelength⁶. Light-assisted patterning, such as, laser ablation, may be more efficient than these methods since the laser beam intensity may be tailored by means of holographic masks to achieve a desired three dimensional relieves.

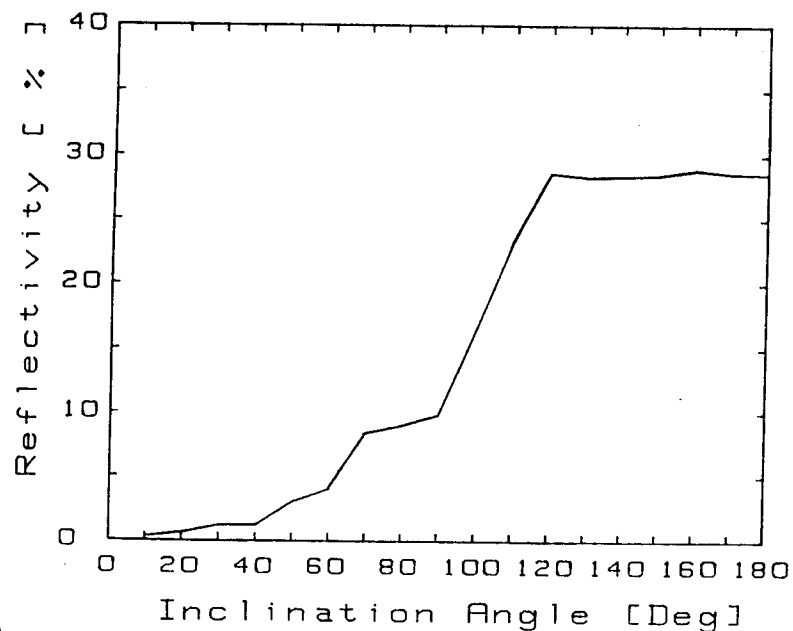
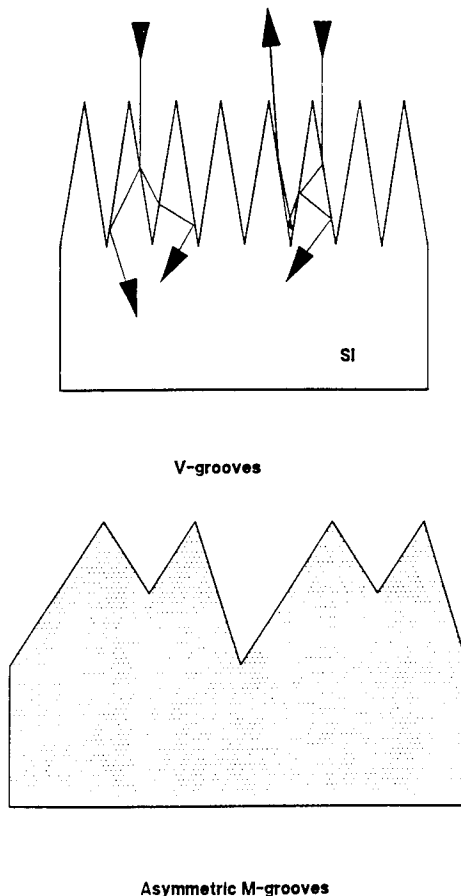


Figure 2 (top). Reflectivity vs θ

Figure 1 (left). Grooves in Si

To summarize, we have used a UV Excimer laser to ablate patterns on Si surfaces in order to increase the light collection efficiency of solar cells. We have noticed that ablation of grooves in various etchants led to improved solar cell performances compared to those of their flat cell counterparts. The photo-ablation patterning technique did not result in a degraded electrical cell's properties. Rather, we were able to enhance the light collection efficiency by 23%.

TABLE 1
 <100> n-Si V-groove vs flat cells for normal incidence,
 5mW HeNe laser light source
 Upper electrode - Cu; Bottom electrode - Al

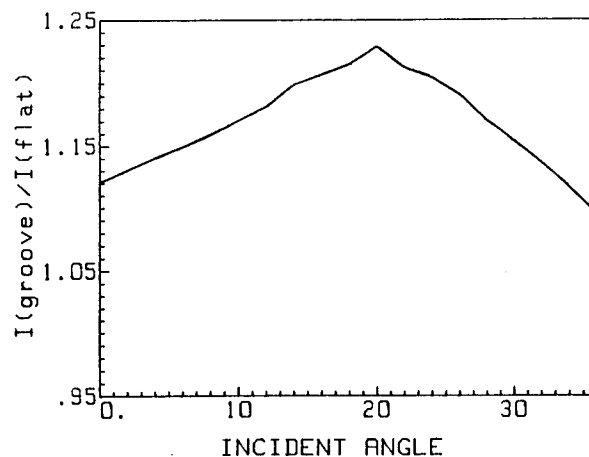
Sample	Short-circuit Current (μA) I_L	Open-circuit Voltage (mV) V_{oc}	Saturation Current (nA) I_s	Barrier Height (eV) Φ_B
V-groove	297	115	40	0.73
flat	259	106	8	0.77

REFERENCES

1. C. Baraona, "V-grooved silicon cells", 11th IEEE Conference on Photovoltaic, 1975, pp 44-48.
2. G. Derrick, App. Opt., 25, 3690-6, (1986).
3. T. Paulik, J. App. Phys., 62, 3016-24 (1987).
4. P. Campbell and M. Green, J. App. Phys., 62, 243-249 (1987). 5. R. Shimokawa, I. Saito and K. Katori, J. App. Phys. 71, 1540-2 (1992).
6. M. Moharam and T. Gaylord, J. Opt. Soc. Am. 72, 1385-90 (1982).
7. S. Sze, "Physics of Semiconductor Devices", 2nd ed., John Wiley & Sons, New York, 1981.

a 5mW HeNe laser as a photo-current source. Flat cells are almost insensitive to the launching angle. A patterned solar cell has a maximum of 23% higher efficiency over its flat counterpart. The etchant was 2:3:100 of $\text{HF}:\text{HNO}_3:\text{H}_2\text{O}$ solution. Asymmetric shapes showed similar performances to symmetric shapes with the exception that the peak performance of asymmetric shapes was near normal light incidence while the peak performance of symmetric shapes was at an oblique incident angle.

In another set of measurements, we have measured the electrical Schottky barrier using I-V curves for flat and patterned surfaces. In general, the barrier height has reduced in patterned cells by $0.04 \pm 0.004 \text{ eV}$. This was true for $\langle 100 \rangle$ n-Si and p-Si samples alike provided that the depths of the grooves were above $2 \mu\text{m}$ and the periodicity of the grooves more than three times the groove's width (more than $60 \mu\text{m}$ in our case). Otherwise, the barrier heights were equal or even larger than the barrier heights for flat cells. Some of the cells parameters are summarized in Table 1. The open circuit voltage values for the patterned Schottky barrier solar cells were equal or slightly larger than for their flat cell counterparts. This may be attributed to the effect of surface states introduced by the etching process. We may conclude that the etching process was not affecting the electrical barrier properties significantly.



Using diffractive lenses in optical design

Dale A. Buralli

Sinclair Optics, Inc., 6780 Pittsford-Palmyra Rd., Fairport, NY 14450

Phone (716) 425-4380 FAX (716) 425-4382

1. Introduction

Diffractive optical elements, which have a history dating back to the work of Lord Rayleigh and R. W. Wood, have been a subject of renewed interest over the past several years, primarily due to advances in manufacturing technology. The purpose of this paper is to provide a basic introduction to some of the features of diffractive optics that are most applicable to optical system design.

In general, the term *diffractive optics* (or *diffractive optical elements*) refers to those optical elements that base their operation on the utilization of the wave nature of light. This broad categorization can be divided into several subsections. *Diffractive lenses* are elements that perform functions similar to conventional refractive lenses, e.g., they form an image. *Kinoforms*¹ are diffractive elements whose phase modulation is introduced by a surface relief pattern. *Binary optics*² are kinoforms produced by photolithographic techniques, resulting in a "stair-step" approximation to the desired surface profile. Each photolithography step increases the number of levels in the surface profile by a factor of two - hence *binary optics*. *Holographic optical elements*³ (HOEs) are devices formed by recording the interference pattern of two or more waves.

Regardless of the name used or method of fabrication, the operation of diffractive optics can be understood with just a few basic tools. The properties of diffractive optics that are shared with conventional elements, e.g., focal length, chromatic dispersion, aberration contributions, etc., do not depend on the specific type of diffractive element. Given a phase function or equivalently, a grating spatial frequency distribution, the influence of the diffractive element on an incident ray for a specified diffraction order is found via the grating equation. The specific element type involved (kinoform, binary lens, HOE, etc.) only influences the diffraction efficiency - how much light is going into each diffracted order.

One factor that has stimulated much of the recent interest in diffractive optics has been the development of manufacturing techniques (e.g., binary optics, diamond machining,⁴ laser

Monday, June 6, 1994

Joint Session on Diffraction Optics Design

(Joint session with International
Optical Design Conference)

JMC 1:30pm–3:30pm
Room A

William C. Sweatt, *President*
Sandia National Laboratories

3. Aberrations

One extremely distinctive feature of diffractive lenses is their chromatic dispersion. The paraxial power of a diffractive lens is a linear function of wavelength. Explicitly, if at the design wavelength λ_0 the lens has a power ϕ_0 , at another wavelength λ , the power of the lens is $\phi(\lambda) = (\lambda/\lambda_0)\phi_0$. This relationship allows us to find an Abbe value v_{diff} , defined over the wavelength range from λ_{short} to λ_{long} :

$$v_{\text{diff}} = \frac{\lambda_0}{\lambda_{\text{short}} - \lambda_{\text{long}}}.$$

Note that the value of v_{diff} depends only on the wavelengths and is independent of any material-type parameters. Hence there are no “crown” or “flint” diffractive lenses. Also, since λ_{long} is greater than λ_{short} , v_{diff} is always negative. Thirdly, the absolute value of v_{diff} is much smaller than the Abbe value for conventional refractive materials. For example, for the visible spectrum defined by the d, F, and C lines, the value of v_{diff} is -3.45.

Since rotationally symmetric diffractive elements behave as lenses, it is clear that aberration coefficients can be derived. Perhaps the easiest way to do this is to use the Sweatt model. The aberration coefficients for a diffractive lens are found as just the limiting forms of the familiar thin lens aberrations.⁷ Thinking of the diffractive lens as just a thin lens with an extremely high refractive index allows for a simple qualitative description of the third-order aberrations. Just as a refractive lens, spherical aberration is a quadratic function of both conjugates and bending, while coma is a linear function of both of these parameters (assuming stop-in-contact). Also, astigmatism depends only on the power of the lens and distortion is zero. The major difference for diffractive lenses is in the Petzval term, which is zero. Diffractive lenses have no contribution to the Petzval sum. Simple design examples will illustrate these points.

4. Diffraction efficiency

The designer must be aware of the effects of “undiffracted” light (actually, light that is diffracted into orders other than the desired order). This is an almost unavoidable situation, particularly for systems that must operate over a finite spectral region. The effect on the image of the undiffracted light is similar to the effects of glare, i.e., an overall lowering of contrast, especially at lower spatial frequencies.⁸ The designer may need to pay close attention to the

writing systems⁵) that give the designer control over the phase function of the lens, and result in an element with a reasonably high diffraction efficiency. In fact, a scalar diffraction theory analysis reveals that a properly designed surface relief profile can have a first-order diffraction efficiency of 100% for the design wavelength. Of course, a scalar treatment is inadequate for gratings with a high wavelength-to-grating-period ratio.

2. Elements of diffractive lens design

The design of the phase function for a diffractive element can be separated from the specific choice of which type of element is used. The implementation of the desired phase function as a particular diffractive element (kinoform, HOE, binary optic, etc.) does not influence the design considerations to be discussed in this paper. Also, the discussion will be restricted to rotationally symmetric lenses, to draw comparisons and contrasts to familiar refractive lenses.

The fundamental description of a diffractive lens is the phase function that defines the OPD introduced by the lens. For a rotationally symmetric lens the phase function $\Phi(r)$ is generally given by a power series expansion:

$$\Phi(r) = \frac{2\pi}{\lambda_0} (s_1 r^2 + s_2 r^4 + s_3 r^6 + \dots)$$

In the above equation, r is the polar radial coordinate. For a lens described by the above equation, the paraxial properties are completely determined by the s_1 coefficient. For example, the focal length for the design wavelength is given by $-1/(2s_1)$. The fourth-order coefficient s_2 affects third and higher order (ray) aberrations; the sixth-order coefficient s_3 affects fifth and higher order aberrations, etc., in a manner akin to aspheric surfaces on a refractive lens.

For optical design purposes, an alternative to the use of phase functions such as the equation given above is the use of the Sweatt model.⁶ Sweatt showed that a diffractive lens is mathematically equivalent to a thin refractive lens, in the limit as the refractive index goes to infinity and the lens curvatures converge to the substrate curvature of the diffractive lens. Thus, the designer can treat a diffractive lens as just a thin lens with a very high refractive index, e.g., 10,001.

propagation of unwanted diffraction orders through the system and allow for vignetting or baffling of the "stray light".

References

1. L. B. Lesem, P. M. Hirsch, and J. A. Jordan, Jr., IBM J. Res. Dev. **13**, 150 (1969).
2. W. B. Veldkamp, G. J. Swanson, and D. C. Shaver, Opt. Commun. **53**, 353 (1985).
3. D. H. Close, Opt. Eng. **14**, 408 (1975).
4. P. P. Clark and C. Londoño, Opt. News **15**, 39 (1989); J. A. Futhy, Proc. SPIE **1052**, 142 (1989).
5. V. P. Koronkevich, in *Optical Processing and Computing*, H. H. Arsenault, T. Szoplik, and B. Macukow, Eds. (Academic, Boston, 1989), pp. 277-313.
6. W. C. Sweatt, J. Opt. Soc. Am. **67**, 803 (1977); W. C. Sweatt, J. Opt. Soc. Am. **69**, 486 (1979); W. A. Kleinhans, Appl. Opt. **16**, 1701 (1977).
7. D. A. Buralli and G. M. Morris, Appl. Opt. **30**, 2151 (1991).
8. D. A. Buralli and G. M. Morris, Appl. Opt. **31**, 4389 (1992).

Modeling of diffractive optics

Michael W. Farn

Lincoln Laboratory, Massachusetts Institute of Technology
244 Wood St., Lexington, MA 02173-91081. INTRODUCTION

With constant advances in both fabrication technology and design innovation, diffractive optics continues to be an area of great interest. However, since diffractive optics is still a relatively new technology, the methods used to model diffractive optics may also be relatively new to many potential users. In this paper, we describe some of the more common methods which are used to analyze surface-relief diffractive optics. We begin by considering the theoretical tools which are available. Then we focus on the particular issue of diffraction efficiency. In the last section, we mention several design examples which illustrate potential pitfalls one may encounter in modeling diffractive optics.

2. MODELING THEORIES

The optical theories used to model diffractive optics can be roughly divided into three regimes: geometrical optics, scalar diffraction and vector diffraction (i.e., Maxwell's equations). In this section, we describe each of these regimes, including the distinguishing characteristics of each theory, the applications which are commonly modeled by each method, and the numerical approach which is used in each regime.

In the geometrical optics regime, rays are used to describe the phase of a propagating wavefront while variations in the amplitude of the wavefront, diffraction due to these variations and the varying efficiencies of different diffraction orders are all neglected. That is, geometrical optics predicts the directions of different diffraction orders but not their relative intensities. Despite these limitations, if a diffractive optic is used in an application which is normally designed by ray tracing, then ray tracing coupled with simple efficiency estimates will usually be sufficient. The majority of these applications are conventional systems (e.g., imaging systems, collimating or focusing optics, laser relay systems, etc.) in which the diffractive optic either provides residual aberration correction (e.g., chromatic, monochromatic or thermal) or replaces a conventional optic (e.g., a Fresnel lens replacing a refractive lens). In most of these cases, the diffractive optic is blazed for a single order and can be thought of as a generalized grating - one in which the period varies across the element.

Regarding the actual ray tracing of the element, there are two common methods which are used: the grating equation and the Sweatt model. In the grating equation, a local grating period is defined for each point on the element. When a ray intercepts the element, it is then diffracted by the local grating according to the grating equation¹, which is the diffractive counterpart to the refractive Snell's law or

the reflective reflection law. In the Sweatt model², the diffractive optic is replaced by a thin refractive equivalent constructed with a material of high refractive index which varies proportional to the wavelength. Snell's law is then used to trace rays through this refractive equivalent of the diffractive element. As the index approaches infinity, the Sweatt model approaches the grating equation. Almost all commercial ray tracing software can handle either of these models.

If amplitude variations are not negligible, if efficiency estimates cannot be separated from the rest of the design, or if the element cannot be considered to be a generalized grating, then the scalar diffraction theory may be appropriate. In the scalar theory, the diffractive optic is normally modeled as an infinitely thin phase plate and the light field is propagated via the appropriate scalar diffraction theory (i.e., Fresnel, angular spectrum, Rayleigh-Sommerfeld, etc.)³. Typical applications include beamsplitter gratings (i.e., gratings in which the diffraction efficiency of each order is tailored to follow a given distribution), laser cavity optics, diffusers, laser beam shapers, lenses with multiple focal lengths and computer generated holograms. Since few, if any, commercial codes are available to simulate the general scalar diffraction case, most designers use their own numerical implementations of the appropriate scalar diffraction integral and their own optimization methods for designing the elements. Common optimization techniques include phase retrieval methods⁴, non-linear optimization and search methods⁵ or linear systems analysis (e.g. eigenmode analysis for the design of laser cavities).

The scalar theory cannot handle all cases. Most notable among its shortcomings is the lack of polarization effects and back-reflected diffraction orders and its inability to handle structures which are on the order of a wavelength or smaller in size. In this regime, the numerical solution of Maxwell's equations is required for a more accurate picture. It is possible to numerically solve Maxwell's equations for arbitrary geometries⁶. However, this is limited in usefulness by computer speed and memory requirements. For example, a cube 10 wavelengths on a side is only a $5\text{ }\mu\text{m}$ cube in the visible but would require a million nodes if sampled at an ordinary rate of 10 samples per wavelength. More common is the solution of Maxwell's equations for periodic structures (i.e., diffraction from a grating). Applications which are commonly analyzed using this method are anti-reflection structures, elements which utilize form birefringence and some optical data storage components. In this case, the field outside the grating is decomposed into plane waves while the field inside the grating is decomposed into either plane waves (the space harmonic approach) or eigenmodes of the grating (the modal approach)⁷. The space harmonic approach is applicable to gratings of any shape. However, it is numerically less stable than and does not converge as quickly as the modal approach, especially if metals are used (e.g., in reflective gratings). The modal approach is numerically better behaved, but it is used only in special cases (e.g., square wave gratings) since the eigenmodes of the grating must be known. If the grating structure is much less than a wavelength, then we may use the Rytov approximations (effective medium theory)⁸. In this approach, the grating structure is so fine that the light only responds to the "average" properties of the structure. Therefore, we can consider the structure to be equivalent to a stack of differing materials (i.e., a stratified medium) with the "average" properties of each material given by the Rytov expressions.

3. EFFICIENCY MODELS

In a large class of problems, the diffractive optic is intended to be used in first order only, with the goal being to maximize the efficiency of this order. As mentioned previously, almost all geometrical optics designs fall in this class. In this section, we discuss several efficiency estimates of gratings, beginning with the scalar model. We discuss only linear gratings because in most cases the diffractive optic can be modelled locally as a linear grating. Therefore, we can use the linear grating model to estimate the local efficiency of the diffractive optic which can then be used to estimate the overall efficiency of the element.

We begin with the scalar theory prediction since these results are easily summarized and are applicable to a large number of applications. In the scalar theory, the grating is modeled as a thin phase plate and a Fourier series analysis of this periodic phase structure gives the efficiency of each diffraction order³. In the simplest scalar approach, a grating of thickness profile $t(x, y)$ is assumed to introduce a phase delay of $2\pi t(\Delta n)/\lambda$, where Δn is the difference in refractive index between the grating and surrounding materials and λ is the wavelength of light. Under this approach, a sawtooth grating of maximum height $t_0 = \lambda_0/(\Delta n)$ will be 100% efficient into the first order at the design wavelength λ_0 and an N step staircase approximation to this ideal sawtooth (as is commonly the result if binary optics fabrication is used) will have an efficiency of $\text{sinc}^2(1/N)$, where $\text{sinc}(x) = \sin(\pi x)/(\pi x)$. This approach yields the often quoted efficiency estimates of 99% for 16 phase levels, 95% for 8 phase levels and 80% for 4 phase levels. Note that this efficiency prediction only accounts for wavelength variations and does not account for effects due to variations in the grating period, index of refraction (the prediction is actually a function of the optical path difference $t(\Delta n)$ rather than of n or Δn), angle of incidence and polarization of the light. The approach becomes more accurate for larger grating periods (typ. periods greater than ten wavelengths), for shallower angles of incidence (typ. less than 30 degrees in air) and, if the Fresnel reflection is accounted for separately, for higher refractive index differences (typ. greater than 0.5).

More accurate predictions are possible either by extending the basic scalar theory prediction⁹ or by using the vector theory⁷. However, these results are more complex and not easily summarized.

Light which does not appear in the first diffraction order must go elsewhere. The majority of this stray light ends up in higher diffraction orders (some consider this to be deterministic scatter) while some of it is scattered in the usual sense of the word. In both cases, the designer must determine the impact of this stray light.

4. DESIGN EXAMPLES

In this section, we mention design examples which illustrate some peculiarities of diffractive optics. In particular, we consider the following:

- Microlens arrays for beam homogenization. In this example, a microlens array is used to homogenize an incoming laser beam, providing a uniform flux at a work piece surface. However, a cursory analysis of this system yields two different predictions, depending on whether a geometrical or scalar analysis is used.
- Beam steering. In this example, we begin with a conventional two-lens telescope. This device can be used to steer a beam by translating one of the lenses with respect to the other. We then construct a device based on shrinking the lenses to microlenses and arraying them. We will examine where the analogies between the two systems are valid and where they are not.
- Beam shaping. In this example, a phase plate is introduced in order to transform the focus of a Gaussian beam into a flat top. Again, geometrical optics and scalar theory predict different outcomes.

5. ACKNOWLEDGEMENTS

This work was sponsored by the Advanced Research Projects Agency. The views expressed are those of the author and do not reflect the official policy or position of the U.S. Government.

6. REFERENCES

1. W. T. Welford, *Aberrations of Optical Systems* (Adam Hilger, Ltd., Boston, 1986), 75-78.
2. W. C. Sweatt, "Mathematical Equivalence between a Holographic Optical Element and an Ultra-high Index Lens," *J. Opt. Soc. Am.* 69, 486-487 (1979).
3. J. W. Goodman, *Introduction to Fourier Optics* (McGraw-Hill, New York, 1968), 30-100.
4. J. R. Fienup, "Reconstruction and Synthesis Applications of an Iterative Algorithm," *Proc. Soc. Photo-Opt. Instrum. Eng.* 373, 147-160 (1981).
5. *Numerical Recipes in C: the Art of Scientific Computing* (Cambridge University Press, New York, 1988).
6. K. S. Kunz, *The Finite Difference Time Domain Method for Electromagnetics* (CRC Press, Boca Raton, FL, 1993).
7. T. K. Gaylord, et. al., "Analysis and Applications of Optical Diffraction by Gratings," *Proc. IEEE* 73, 894-937 (1985).
8. D. H. Raguin and G. M. Morris, "Antireflection Structured Surfaces for the Infrared Spectral Region," *Appl. Opt.* 32, 1154-1167 (1993).
9. G. J. Swanson, *Binary Optics Technology: Theoretical Limits on the Diffraction Efficiency of Multi-level Diffractive Optical Elements*, M.I.T. Lincoln Laboratory Technical Report 914, (1991).

Optical Systems Employing Refractive and Diffractive Optical Elements to Correct for
Chromatic Aberration

C. William Chen

Hughes Aircraft Co.

EO/E01/C109

2000 E. El Segundo Blvd.

El Segundo, CA 90245

Tel (310)-616-9776

Fax (310)-616-5987

A diffractive optical element (DOE) has many unique properties such as high dispersion with an equivalent negative Abbe number and a zero petzval curvature. Consequently, a DOE can simplify the optical design form and improve the image quality of many refractive optical systems.

This paper formulates and discusses the basic theory of chromatic aberration correction of an optical system consisting of conventional optical elements (COE) and a DOE. Several design examples with spectral bands ranging from the visible, mid-wave infrared to long-wave infrared are given to illustrate the advantages of optical systems using a DOE. These examples show that a DOE is very effective in primary chromatic aberration correction for infrared optical systems, and in primary and secondary chromatic aberrations correction for visible optical systems. Generally, a DOE can improve optical system performance while lowering the cost and weight by reducing the number of lens elements by approximately one-third. Additional benefits often include desensitizing the design to rigid body misalignments.

Achromatic and Apochromatic Diffractive Singlets

G. Michael Morris and Dean Faklis, Rochester Photonics Corporation, 330 Clay Road,
Rochester, New York 14623, (716) 272-3010, (716) 272-9374 (fax)

Diffractive optics offers optical system designers new degrees of freedom that can be used to optimize the performance of optical systems. The zone spacing of a diffractive lens can be chosen to impart focusing power as well as aspheric correction terms to the emerging wavefront. The surface (or blaze) profile within a given zone determines how the incident energy is distributed among the various diffraction orders. In a conventional diffractive lens the phase jumps at each zone boundary is taken to be 2π , and the zone radii, r_j , are obtained by solving the following equation: $\phi(r_j) = 2\pi j = s_1 r_j^2 + s_2 r_j^4 + s_3 r_j^6 + \dots$, where $\phi(r)$ represents the desired phase of the wavefront emerging from the element at radius r from the optical axis. The phase coefficient s_1 determines the optical (or focusing) power of the element. The phase coefficients s_2 , s_3 , etc. determine the aspheric contributions to the wavefront. In a given application, the phase coefficients can be optimized using commercial lens-design software.

While it is often useful to think of a diffractive lens as a "modulo 2π " lens at the design wavelength, the spectral properties (or wavelength dependence) of a diffractive lens are drastically different from that of a refractive lens. For a thin refractive lens, the lens power is given by $\Phi(\lambda) = [n(\lambda) - 1] c$, where $n(\lambda)$ denotes the index of refraction of the lens material at wavelength λ , and c represents the surface curvature of the lens. Whereas for a diffractive lens, the optical power (associated with the r^2 phase term) is highly wavelength dependent. In fact, the optical power, Φ , varies linearly with the wavelength of light, i.e., $\Phi(\lambda) = (\lambda/\lambda_0)\Phi(\lambda_0)$. Because of their high dispersion and the fact that a diffractive lens has a negative Abbe v -number, they can be combined with refractive (crown) elements to produce achromatic diffractive/refractive hybrid lenses for use in broadband optical systems. The use of a diffractive/refractive hybrid eliminates the need to use exotic flint glasses and provides a significant reduction in the weight and number of optical elements required to achieve a specified level of performance¹.

In this paper we investigate the imaging properties of multi-order diffractive (MOD) lenses that are used in conjunction with light that has either a broad spectral range or a spectrum consisting of multiple spectral bands. A MOD lens differs from the standard diffractive lenses described above in that the phase jump at the zone boundaries is taken to be a *multiple* of 2π , i.e., $\phi(r_j) = 2\pi p$, where p is an integer ≥ 2 , and the location of the zone radii are obtained by solving the equation $\phi(r_j) = 2\pi p j$, where again $\phi(r)$ represents the phase function for the emerging wavefront. The number of 2π phase jumps, p , represents a degree of freedom for the designer. However, to date most of the reported investigations with diffractive lenses have set $p = 1$, by default.

In the literature one finds only a few articles that consider multi-order (or higher-order) diffractive lenses. In a footnote, Miyamoto² states that one can reduce the problems associated

with small zone spacings by using multiple 2π phase jumps at the zone boundaries. Dammann^{3,4} considered the spectral characteristics of stepped-phase gratings that have arbitrary phase jump at the edge of each grating facet, and the application of these gratings for color separation. Futhey^{5,6} and co-workers have described what they call a "super-zone" diffractive lens. The structure of a super-zone lens is motivated by the desire to keep the zone spacing of the various facets above the resolution limit imposed by the particular fabrication method (diamond-turning, laser pattern generation, or photolithography). Marron⁷ et al. have also reported on "higher-order kinoform" structures. The motivation for their work was, again, to keep surface features large compared to the wavelength of light, even when the f-number of the lens is very low.

While it is important to note that the larger zone structure of a MOD lens is easier to fabricate than a standard "modulo 2π " diffractive lens, to our knowledge we are the first to consider the use of such lenses with light having a broad spectrum or having multiple spectral bands, and we have found the imaging properties of MOD lenses with such illumination to possess a number of interesting and useful properties. For example, as we show in the next section, one can use a MOD lens with light having broad spectral band or multi-spectral bands to form either an *achromatic* or an *apochromatic diffractive singlet* by choosing the appropriate value for p . Such elements may be particularly useful for applications such as color image displays⁸, alignment of optical systems whose wavelength of operation lies outside the visible spectrum, and medical instrumentation, particularly medical laser scalpels.

In the next section, we consider the first-order properties of MOD lenses, namely, the optical power, diffraction efficiency, and the structure of achromatic and apochromatic diffractive singlets. We conclude that a MOD lens is capable of bringing wide-field, multi-color images into focus at the same image plane.

Imaging properties of paraxial multi-order diffractive lenses

We begin by describing the amplitude transmission function of a diffractive singlet. The zone radii, r_j , are defined such that the optical path difference at the j th zone is equal to $(F_0 + jp\lambda_0)$, where λ_0 is the design wavelength, F_0 is the focal length when the illumination wavelength $\lambda = \lambda_0$, and p is an integer that represents the maximum phase modulation as a multiple of 2π . In the paraxial region, the locations of the zones in the plane of the lens are given by

$$r_j^2 = 2jp\lambda_0 F_0 . \quad (1)$$

The optical phase introduced by the diffractive element is given by⁹

$$\phi(r) = 2\pi\alpha p \left[j - \frac{r^2}{2p\lambda_0 F_0} \right] , \quad r_j \leq r < r_{j+1} , \quad (2)$$

where α is defined as the fraction of 2π phase delay that is introduced for illumination wavelengths other than the design wavelength and is given by

$$\alpha = \frac{\lambda_0}{\lambda} \left[\frac{n(\lambda) - 1}{n(\lambda_0) - 1} \right] , \quad (3)$$

where n is the index of refraction of the material in the grating region. The maximum height of the surface relief is given by

$$h_{\max}(r) = \frac{p\lambda_0}{n(\lambda_0) - 1} . \quad (4)$$

In a manner similar to that used in Ref. 12, the amplitude transmission function of the diffractive lens can be expanded as a Fourier series to give

$$t(r) = \sum_{m=-\infty}^{\infty} e^{-i\pi(\alpha p - m)} \text{sinc}(\alpha p - m) e^{\frac{i\pi m r^2}{p\lambda_0 F_0}} , \quad (5)$$

where $\text{sinc}(x) = \sin(\pi x)/(\pi x)$ and m denotes the m -th diffraction order. It is important to note that the transmission function in Eq. (5) represents a diffractive lens within the paraxial approximation and that transmission functions that describe other diffractive lenses are possible. It is interesting to compare Eq. (5) with the transmission function of a conventional refractive lens¹³ given by

$$t(r) = e^{-\frac{i\pi r^2}{\lambda F}} , \quad (6)$$

where F is the focal length, which depends on the material properties of the lens. Comparison of Eqs. (5) and (6) suggests that there are an infinite number of focal lengths given by

$$F(\lambda) = \frac{p\lambda_0 F_0}{m\lambda} . \quad (7)$$

Notice that the focal length in Eq. (7) is proportional to p and inversely proportional to the illumination wavelength and the diffraction order, m . It is interesting to note that when the quantity in Eq. (7), $p\lambda_0/m\lambda$, is set equal to unity, several wavelengths can come to a common focus. Clearly, p is a construction parameter and is usually constant across the lens radius and the wavelengths that are focused to a common point are chosen from a set of diffraction orders. *While a diffractive lens with a maximum phase modulation of 2π can allow a mutual focus for simple harmonics of the design wavelength, the parameter p now offers a mechanism to control specific wavelengths in a given band or bands that will come to a fixed focus. This property allows the design of achromats and apochromats using a single diffractive surface.*

The scalar diffraction efficiency, η_m , of the m -th diffracted order is given by the squared modulus of its Fourier coefficient in Eq. (5), i.e.

$$\eta_m = \text{sinc}^2(\alpha p - m) . \quad (8)$$

The diffraction efficiency given by Eq. (8) is unity when the argument of the sinc function is equal to zero. Notice that this condition can allow for high diffraction efficiency for several wavelengths. For example, consider the case of a multi-order diffractive lens operating in the visible region with $p = 10$. Figure 1 illustrates the wavelength dependence of the diffraction efficiency for a range of diffracted orders neglecting material dispersion. The peaks in diffraction efficiency occur at precisely those wavelengths that come to a common focus [see Eq. (7)], i.e.,

$$\lambda_{\text{peak}} = \frac{p\lambda_0}{m} . \quad (9)$$

Using Eq. (9), it is possible to choose the parameters p and m that can allow high diffraction efficiency for certain bands in a given spectrum. The center wavelength of each of these bands comes to a focus a distance F_0 behind the lens.

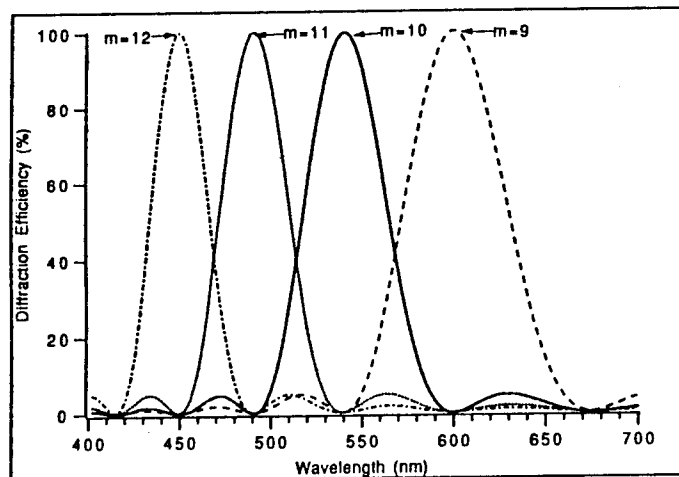


Fig. 1 Diffraction efficiency of the m -th diffracted order versus wavelength for a MOD lens with $p = 10$.

A MOD lens operating with multiple spectral bands may be particularly useful for color display applications⁸. Another important application of MOD lenses with illumination containing multiple spectral bands is as an alignment system for optical systems that operate using wavelengths outside of the visible spectral band. For example, by choosing $p = 5$, sodium D light (589 nm) in the $m = 9$ diffraction order will focus at precisely the same focal position as a ND:YAG laser operating at $\lambda = 1,060$ nm. Preliminary experimental results will also reported.

References

1. D. Faklis and G. M. Morris, "Diffractive lenses in broadband optical system design," *Photonics Spectra*, p. 131-134 (Dec. 1991).
2. K. Miyamoto, "The phase Fresnel lens," *J. Opt. Soc. Am.* **51**, 17-20 (1961).
3. H. Dammann, "Color separation gratings," *Appl. Opt.* **17**, 2273-2279 (1978).
4. H. Dammann, "Spectral characteristics of stepped-phase gratings," *Optik* **53**, 409-417 (1979).
5. J. A. Futhy, "Diffractive Lens," U. S. Patent No. 4,936,666, June 26, 1990.
6. J. A. Futhy, M. Beal and S. Saxe, "Superzone diffractive optics," 1991 Annual Meeting of the Optics Society of America Technical Digest, Paper TuS2 (1991).
7. J. C. Marron, D. K. Angell, and A. M. Tai, "Higher-order kinoforms," in *Computer and Optically Formed Holographic Optics*, I. Cindrich and S. H. Lee, eds., Proc. SPIE **1211**, p. 62-66 (1990).
8. D. B. Judd and G. Wyszecki, *Color in Business, Science and Industry* (Wiley, New York, 1975).
9. D. A. Buralli, G. M. Morris and J. R. Rogers, "Optical performance of holographic kinoforms," *Appl. Opt.* **28**, 976-983 (1989).

refractive elements⁴. For this reason, hybrid eyepieces comprised of all positive elements may be designed. Eyepieces are a close grouping of mostly positive-powered elements with a combined short focal length. As previously mentioned, this case leads to a strong, inward curving image plane. A desirable attribute of diffractive lenses is that they contribute no Petzval field curvature⁵. Fabricated as surface-relief structures, diffractive lenses can offer considerable size and weight reductions. Along with these features, diffractive optics can be used to shape the emerging wavefront to help correct the monochromatic aberrations⁴.

Earlier work in the field of visual instruments incorporating diffractive elements include a hybrid, diffractive-refractive telescope in which a diffractive eyepiece compensates for the color in the refractive objective⁶. Similar designs were also proposed by Wood⁷, who constructed a zone-plate telescope, and by Bennett⁸. These were all first-order proposals in which monochromatic aberrations were left uncorrected. Recently, a biocular magnifier, which is to be viewed with both eyes, employing one diffractive surface was patented⁹. A diffractive-refractive doublet was designed for use as an eyepiece-magnifier¹⁰. In that design one refractive surface was aspheric, and the diffractive element was to be placed on a curved substrate.

3. Hybrid diffractive-refractive wide-field eyepieces

As the field-of-view increases, eyepiece design issues become more significant. Maintaining a sufficient eye relief while increasing the principal ray angle increases the outside diameters and thicknesses of the individual elements. The well-defined exit pupil location and the wide field-of-view require that the system be well-corrected for spherical aberration of the pupil and off-axis aberrations¹¹. At increasing field angles, the intersection of the principal ray with the optical axis becomes nearer to the last lens. This has the unfortunate characteristic that some zones of the field become vignetted by the final pupil of the overall visual system, the eye's pupil. For this reason, spherical aberration of the exit pupil must be kept under control, especially in wide-field eyepieces. Other field aberrations are likewise difficult to correct, and some aberrations are tolerated, ignored, or are corrected by another part of the entire visual instrument. For example, a certain amount of distortion at the edge of the field is considered acceptable due to the fact that the user does not use this area other than to orient himself/herself¹², and often the lateral color is corrected with a dispersive prism.

Two examples of hybrid diffractive-refractive, wide-field eyepieces are presented to demonstrate the effectiveness of diffractive optics in providing eyepieces with fewer elements. These eyepiece designs offer performance equivalent to or better than existing, conventional eyepiece designs. Comparisons with a common wide field-of-view eyepiece design are presented.

The well-known Erfle eyepiece is considered to be a very good compromise of optical performance with size and weight for wide-field use and is probably the most commonly used wide-field eyepiece.¹² An Erfle eyepiece¹³ consists of a five-element design, with strong positive

Diffraction Optics Applied to Eyepiece Design[†]

Michael D. Missig and G. Michael Morris
The Institute of Optics, University of Rochester, Rochester, NY 14627
(716) 275-5140, fax (716) 271-1027

1. Introduction

Eyepieces play an important role in many types of optical systems, such as telescopes and medical instruments. The eyepiece is often the limiting factor in the overall optical performance of the instrument and, due to the requirements for sufficient eye relief and high performance, it presents a difficult design problem. Improvement of existing eyepiece designs is limited using conventional design variables. By introducing a new technology – diffractive optics – to eyepiece design, the performance of today's eyepieces can be enhanced. Advantages of a diffractive optics solution to eyepiece design include smaller lens curvatures, higher numerical aperture achromats, and reductions in the number of elements, overall weight, and system cost, as well as an increase in optical performance compared to an all-refractive eyepiece design.

2. Eyepiece design

Eyepieces are significantly different from photographic objectives. Typical features that are necessary in this type of system include a sufficient eye relief (10 to 20 mm), a wide field-of-view such that the user does not experience tunnel vision, and a well defined exit-pupil location to avoid vignetting. One essential difference is the external aperture stop of the eyepiece. This feature, combined with the large field of view, results in large aperture elements – in comparison to the eyepiece aperture. Dealing with these and other design issues makes eyepiece design quite difficult¹. In particular, the external aperture stop and pupils eliminate the symmetry of the principal ray, which would help to reduce distortion, coma, and lateral color. For example, in some conventional eyepiece designs, each convergent element is coupled with a negative element to provide achromatization². Also, due to the relatively short focal length of the eyepiece, field curvature is inherently strong. Strong meniscus elements placed near the focal plane are often used to combat this problem³. As can be seen, the goals of designing an eyepiece well-corrected for aberrations such as lateral color and Petzval field curvature along with maintaining necessary first order features can be difficult. Solutions for these eyepieces often result in multi-element or exotic configurations, which are extremely heavy and bulky; this significantly reduces their desirability in a number of situations. In such cases, optical performance is often sacrificed to satisfy weight or cost requirements.

As a new, effective design variable diffractive optics offers features which are beneficial to eyepiece design. The effective dispersion of diffractive lenses is opposite in sign to that of

[†] This research was supported in part by the U.S. Army Research Office

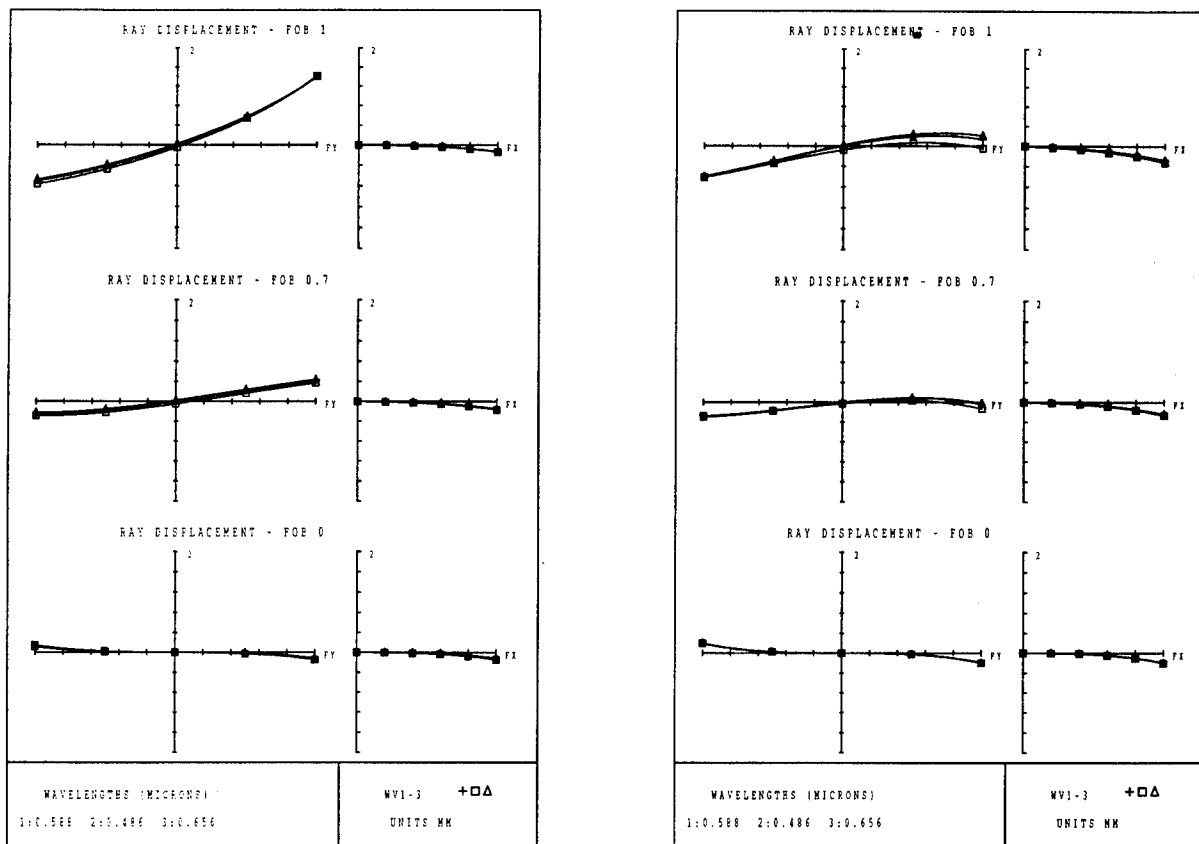


Fig. 2. Transverse ray plots for (a) Erfle eyepiece and (b) for diffractive-refractive eyepiece in Fig. 1(c).[†]

REFERENCES

1. *Optical Design-Military Standardization Handbook MIL-HDBK-141* (Defense Supply Agency, Washington, D.C., 1962), p. 14-1.
2. A. Cox, *A System of Optical Design* (Focal Press, New York, 1964), pp. 563-575.
3. W. J. Smith, *Modern Lens Design* (McGraw-Hill, Inc., New York, 1992), pp. 87-88.
4. D. A. Buralli, G. M. Morris, and J. R. Rogers, "Optical Performance of Holographic Kinoforms," *Appl. Opt.* **28**, 976-983 (1989).
5. W. C. Sweatt, "Describing Holographic Optical Elements as Lenses," *J. Opt. Soc. Am.* **67**, 803-808 (1977).
6. T. W. Stone, "Hybrid Diffractive-Refractive Telescope," in *Practical Holography IV*, Stephen A. Benton, ed. Proc. SPIE, **1212**, 257-266 (1990).
7. R. W. Wood, "Phase-Reversal Zone-Plates and Diffraction-Telescopes," *Phil. Mag. [Series 5]* **45**, 511-522 (1898).
8. S. J. Bennett, "Achromatic Combinations of Hologram Optical Elements," *Appl. Opt.* **15**, 542-545 (1976).
9. C. W. Chen, U.S. Patent no. 5,151,823 (29 September 1992).
10. R. E. Aldrich, "Ultra Lightweight Diffractive Eyepiece," OSA Topical Meeting: Diffractive Optics Design, Fabrication, and Applications, New Orleans, LA, April 13-15, 1992, Presentation: TuD13.
11. R. Kingslake, *Lens Design Fundamentals* (Academic Press, New York, 1978), p. 335.
12. W. J. Smith, *Modern Optical Engineering Second Ed.* (McGraw-Hill, Inc., New York, 1990), pp. 404-407.
13. H. Erfle, U.S. Patent no. 1,478,704 (25 December 1923).
14. S. Rosin, *Applied Optics and Optical Engineering, Vol. III Optical Components*, R. Kingslake, ed. (Academic Press, Inc., New York, 1965), ch. 9, p. 342.

[†] It is standard in evaluating eyepieces that rays are traced from infinity, from the side of the pupil, through the eyepiece to the focal plane, except in the case of pupil spherical aberration¹⁴.

and negative elements, covering up to a sixty degree apparent field-of-view (i.e. the field-of-view in eyespace.) The two hybrid eyepiece designs are compared to the Erfle eyepiece; all three designs have equivalent focal lengths, f-numbers, and fields-of-view.

The first design consists of three refractive lenses and two diffractive surfaces. Two of the refractive elements have a planar side to which the diffractive elements are directly mounted. Planar substrates were chosen for the diffractive optical elements of both hybrid eyepiece configurations to simplify fabrication. The second design consists of three refractive elements also, but only one diffractive element. In Fig. 1 the eye is positioned at the exit pupil location, and x marks the image plane. As can be seen in Fig. 1, the curvatures of the refractive elements of the hybrid designs, Fig.1(b) and (c), are significantly less than those of the Erfle eyepiece, Fig. 1(a).

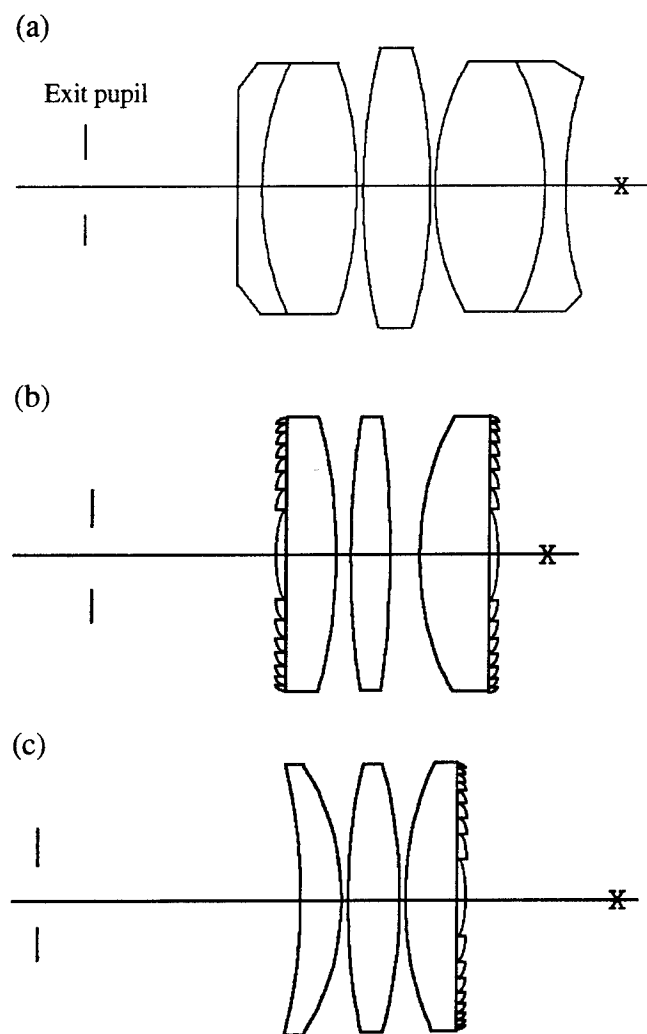


Fig. 1. Eyepiece designs. (a) Erfle eyepiece, (b) hybrid diffractive-refractive eyepiece, (c) hybrid diffractive-refractive eyepiece. All three eyepiece designs have a 25-mm focal length, a 10-mm exit pupil, and a 60° FOV.

In Fig. 2, the transverse ray aberration plots are presented for the Erfle eyepiece and for the hybrid eyepiece in Fig. 1(c), which has aberration correction slightly better than the first hybrid, Fig. 1(b). Both hybrid eyepiece designs exhibit better performance than the Erfle design at the three field positions (0,0.7,1.0.) Furthermore the eye relief of the Erfle design is 15 mm, compared to the eye relief of the two diffractive-refractive eyepiece designs 16 mm and 20 mm, respectively. Also, the pupil spherical aberration is significantly reduced by optimizing the higher order aspheric terms in the phase function of the diffractive elements, which increases the effective eye relief even further. Along with the improved optical performance, the hybrids also have a significant decrease in size and weight compared to the Erfle design. The weight of each of the hybrid designs is approximately 44% less and 72% less than the weight of the Erfle design, respectively.

As an application of the hybrid design, we have fabricated hybrid diffractive-refractive eyepieces for a set of binoculars. Experimental results will be presented.

Computing results:

Fig.1

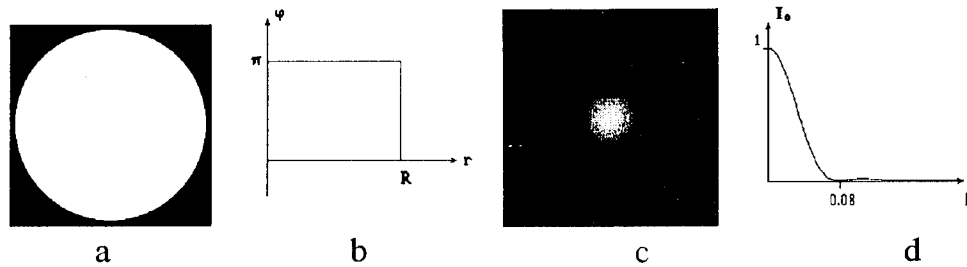


Fig.2

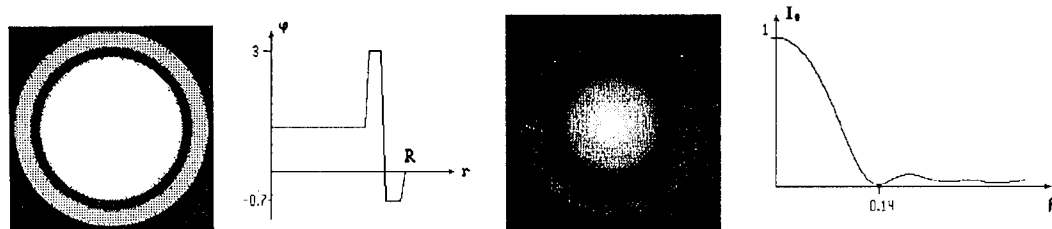


Fig.1 illustrates the results for a lens without DOE: constant phase (a), its radial cross-section (b), the Airy disk (c) and its radial cross-section (d). Fig.2 shows the three-level DOE capable of increasing the Airy disk diameter twofold: the DOE phase (a), its radial cross-section (b), the pattern of diffraction in the focus (c), and its radial normalized intensity distribution (d).

Fig.3

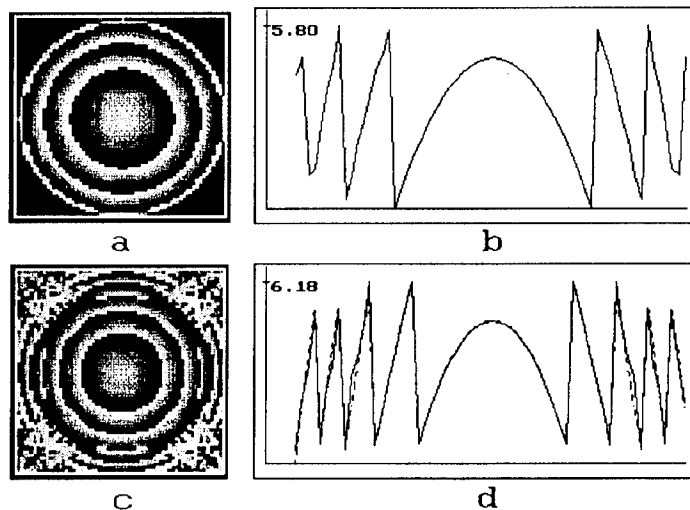


Fig.3 contains: the phase of an optical element (a), the phase cross-section along the x-axis (b), a phase generated at the distance z_0 (c), and the phase cross-section along the ξ -axis: solid line in Fig.3.d; dashed line is the pre-given phase $\psi_0(\xi, \eta) = -\alpha(\xi^4 + \eta^4)$. The difference between the calculated phase (Fig.3.c) and the desired phase amounts to 6%.

Fig.4

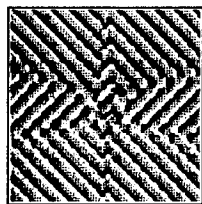


Fig.5

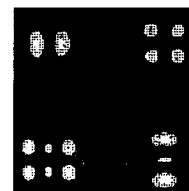


Fig.4 presents the gray-level phase calculated within 10 iterations (module 2π) of an optical element that forms (in the lens's focal plane) four GH's modes of equal energy with the numbers (0,1); (1,1); (2,0) and (1,2) (see Fig.5). The diffractive efficiency is more than 90%.

ITERATIVE METHODS FOR THE KINOFORMS SYNTHESIS

Khonina S.N., Kotlyar V.V., Nikolsky I.V., Philippov S.V., Soifer V.A.

Image Processing System Institute of the Russian Academy of Sciences,
151 Molodogvardejskaya, Samara 443001 Russia.

New iterative methods for computing phase diffractive optical elements have been considered.

The problem of widening a minimum diffraction spot can have a practical implementation in laser printers. We propose that the problem should be solved using an additional phase optical element, which, when introduced in an optical setup, increases the diameter of the Airy disk. In order to calculate such a diffraction optical element (DOE), a novel iterative method has been developed. The method is a modernization of the known iterative Gerchberg-Saxton algorithm and differs from the above in that the sought function is represented as a series sum taken over the Bessel function of first order instead of the plane waves (Fourier's series).

The task of calculating the phase optical elements forming reference wavefronts is considered. This task appears, for example, with reference to a noncontact inspection of the form of aspheric mirrors. In the present work we discuss an iterative algorithm for computing phase optical elements — wavefront formators (WF) that are capable of forming a desired phase distribution at a pregiven distance. The algorithm is a modernization of the well-known Gerchberg-Saxton's algorithm. The problem of the proposed algorithm convergence is discussed. The results of the WF calculation are reported.

The developed iterative method is intended to calculate the phase function of the phase optical element forming several diffraction orders, with the complex amplitude of each of them to be proportional to Gauss — Hermit's (GH) mode with a preset number. The method uses expansion of the sought function into a series with respect to the GH orthogonal functions. Such optical elements can be successfully used to perform the parallel input of laser light into several square fibers, with the desired mode (or a set of modes) characterized by a pregiven intensity to be excited in each fiber.

DIFFRACTIVE OPTIC DESIGN for BOARD-LEVEL FREE-SPACE OPTICAL INTERCONNECTS

Raymond K. Kostuk

**Electrical and Computer Engineering Department and
The Optical Sciences Center
University of Arizona
Tucson, Arizona 85721
kostuk@ece.arizona.edu**

Introduction

The use of diffractive optics in interconnect design is of considerable interest for several reasons. First, micro diffractive optic fabrication processes using microlithography and holographic methods can provide a large variety of optical functions which can be used in both space variant and invariant systems. These fabrication methods can be mass produced which lowers overall system cost. In addition, multiple diffractive optic elements can be cascaded on planar substrates and more readily packaged with planar electronic substrates.

In order to be effective however, the diffractive optical system design must divide and distribute optical signals in three dimensions. The optics must also be readily packaged with standard board substrates, and have sufficient alignment tolerances to allow for board insertion, replacement, and length changes due to temperature variations.

In this presentation we will discuss a distributed free-space optical interconnect system that provides both lateral distribution within a plane, and longitudinal signal transmission between planes or boards¹. The system uses binary optics to collimate and relay signals between planes, and high spatial frequency volume holograms to distribute signals through a small form factor substrate within a plane. The design and performance of several components used in this system are also presented.

SYSTEM DESIGN CONSIDERATIONS

A board level interconnect system must perform several functions. First, a method for bidirectional information transfer is required at each information port. Parallel data transfer is also important to increase information transfer rates. It must be possible to broadcast signals to multiple lateral and longitudinal locations in the processing system, and the system must be expandable to accommodate greater data processing loads. Finally, the optical interconnect system must be competitive in performance and cost with competing electrical interconnect methods.

In order to assess the use of optics for these tasks we are implementing the board level interconnect system shown in Fig.1. In this system data is exchanged between boards in four communication ports. The number of processing elements associated with each port is optimized to minimize timing delays.

Monday, June 6, 1994

Optical Interconnects

DMD 4:00pm–5:30pm
Room B

Jurgen Jahns, *Presider*
AT&T Bell Laboratories

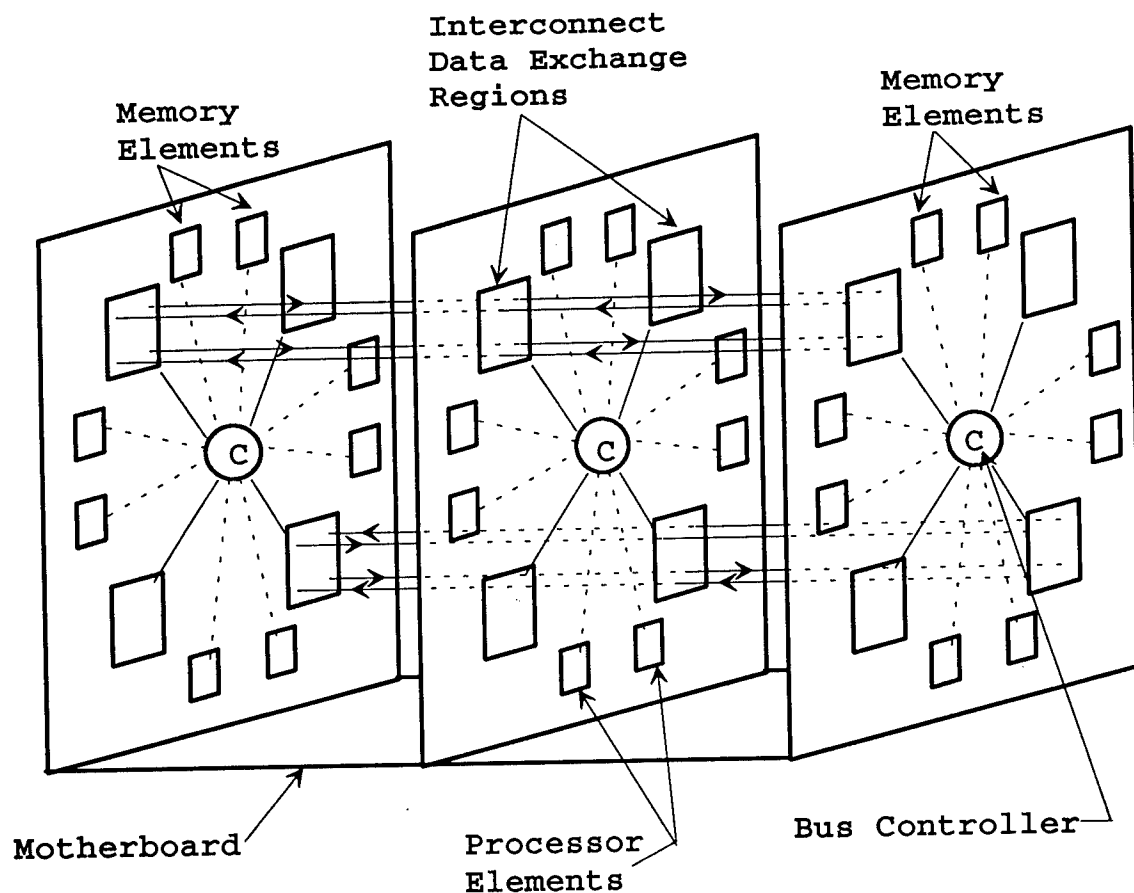


Fig. 1. Distributed optical multi-bus system for evaluating diffractive optic interconnects.

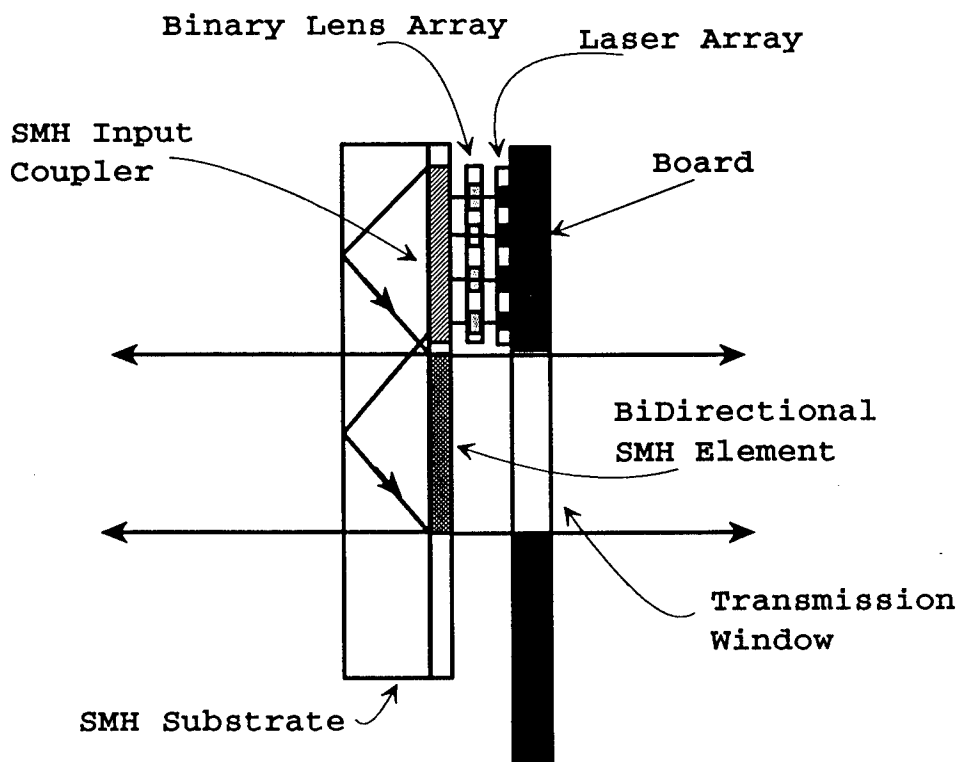


Fig. 2. Bidirectional beamsplitter for sending optical signals to adjacent boards.

DIFFRACTIVE OPTICAL ELEMENTS

Four different types of diffractive optical elements have been designed and fabricated to realize the optical interconnect system required for the configuration of Fig. 1. These include binary optic micro lens arrays to collimate light from surface emitting laser diode arrays and collect and focus light onto detectors; volume type input/output coupler gratings to direct light into and out of guiding substrates; lateral beam splitters for dividing optical signals on a plane; and bi-directional beamsplitters for broadcasting signals to adjacent board planes. In addition, we have also formed a fiber optic tap which diffracts a portion of a signal transferred through a fiber and laterally distributes the tapped signal on a plane. This component is used to connect processing elements which exceed the alignment tolerance for free-space optical interconnects.

The diffractive optical elements are formed with hybrid combinations of lithographically formed binary optics and holographically generated volume gratings. These two forms of diffractive optics complement each other. Lithographic techniques are useful when arrays of accurately aligned components are required, and holographic methods are useful for forming high spatial frequency input/output couplers and beamsplitters.

The bidirectional interface illustrated in Figure 2 is an example of the hybrid diffractive element design. Light from a surface emitting laser array is collimated with an on-axis binary lenslet array which matches the emission properties and spacing of the laser elements. The array of collimated beams are then coupled into an optical substrate using a volume grating and are guided to one of the communication ports. A bidirectional beamsplitter formed with volume gratings diffracts the beam array in two counter propagating directions for data transfer to adjacent boards.

The binary lenses provide high efficiency on-axis beam collimation and focusing. This is not readily achieved with single volume type lenslets because the volume grating condition is not satisfied for on-axis sections of the beam. The input coupler is realized with a slanted volume grating formed in dichromated gelatin. The diffracted beam exceeds the critical angle of the glass substrate, therefore the addition of a reflective surface is not required. The bi-directional beamsplitter consists of two multiplexed transmission gratings which diffract the incident and the total internal reflected beams. Since two transmission gratings are used, the processing is much easier than that required for a transmission/reflection grating pair and results in higher yields. This component was also realized in dichromated gelatin.

The diffractive elements must provide a suitable alignment tolerance for acceptable performance of the processing system. The different types of errors causing beam displacement for diffractive elements are illustrated in Fig.3. These include lateral displacement, longitudinal displacement, angular misalignment, and chromatic dispersion. The affect of these factors on system geometry and operating characteristics will be discussed in the remainder of the presentation.

1. R. K. Kostuk, J-H. Yeh, and M. Fink, "Distributed optical data bus for board-level interconnects," *Appl. Opt.*, 32, 5010-5021 (1993).

Design of Achromatic Holographic Grating Couplers for Backplane Optical Interconnects

Michael R. Wang and Freddie Lin
Physical Optics Corporation
20600 Gramercy Place
Torrance, CA 90501
Tel. (310) 320-3088
FAX (310) 320-4667

Future computers and signal processors will require high-speed interconnection networks for efficient data transfer among electronic modules. Holographic backplane optical interconnects for multi-board three-dimensional packaging have been the subject of recent investigation. The use of transparent backplane substrates as beam propagation media can take advantage of the dimensional freedom, compact device packaging, and planar fabrication economy the backplanes offer. An optical backplane packaging architecture with couplings from and to board-level waveguide interconnect networks has recently been proposed [1]. However, laser diode sources for the backplane interconnects change their wavelengths by several nm because of variations in environmental temperature and bias fluctuations. As a result, in a conventional grating pair design, as shown in Fig. 1, the diffraction angles and beam positions in the substrate vary with the laser wavelengths. This will affect the performance of the backplane interconnects since waveguide end-fire coupling has stringent requirements for the direction of the focused incident beam.

A grating-pair structure is sensitive to laser wavelength fluctuation which causes a shift in substrate beam spot position. To describe the effect, the well known Bragg grating dispersion equation is written in general form as

$$\sin \alpha = \sin \theta \pm \frac{\lambda}{n\Lambda} \sin \phi \quad (1)$$

where \pm is used when $\phi - \theta > 90^\circ$ ($< 90^\circ$), respectively. λ is the free-space laser wavelength, n is the refractive index of the bulk holographic material, Λ is the grating fringe spacing, and θ , α , and ϕ are incidence, diffracted, and grating slant angles, respectively, as shown in Fig. 1. All of these angles are in the medium of the diffraction grating, and Fresnel equations can be used to translate these angles to those outside the emulsion area. The translation in angle from a dichromated gelatin hologram to a soda-lime glass substrate, for example, in the following discussion, can be ignored since the two media have similar refractive indices.

Taking the derivative of Eq.(1) with respect to wavelength λ and ignoring the material dispersion within the laser wavelength fluctuation range (typically less than 7 nm), the chromatic sensitivity of a single grating diffraction is given by

$$\Delta \alpha = \frac{\Delta \lambda}{\lambda} \tan \alpha \quad (2)$$

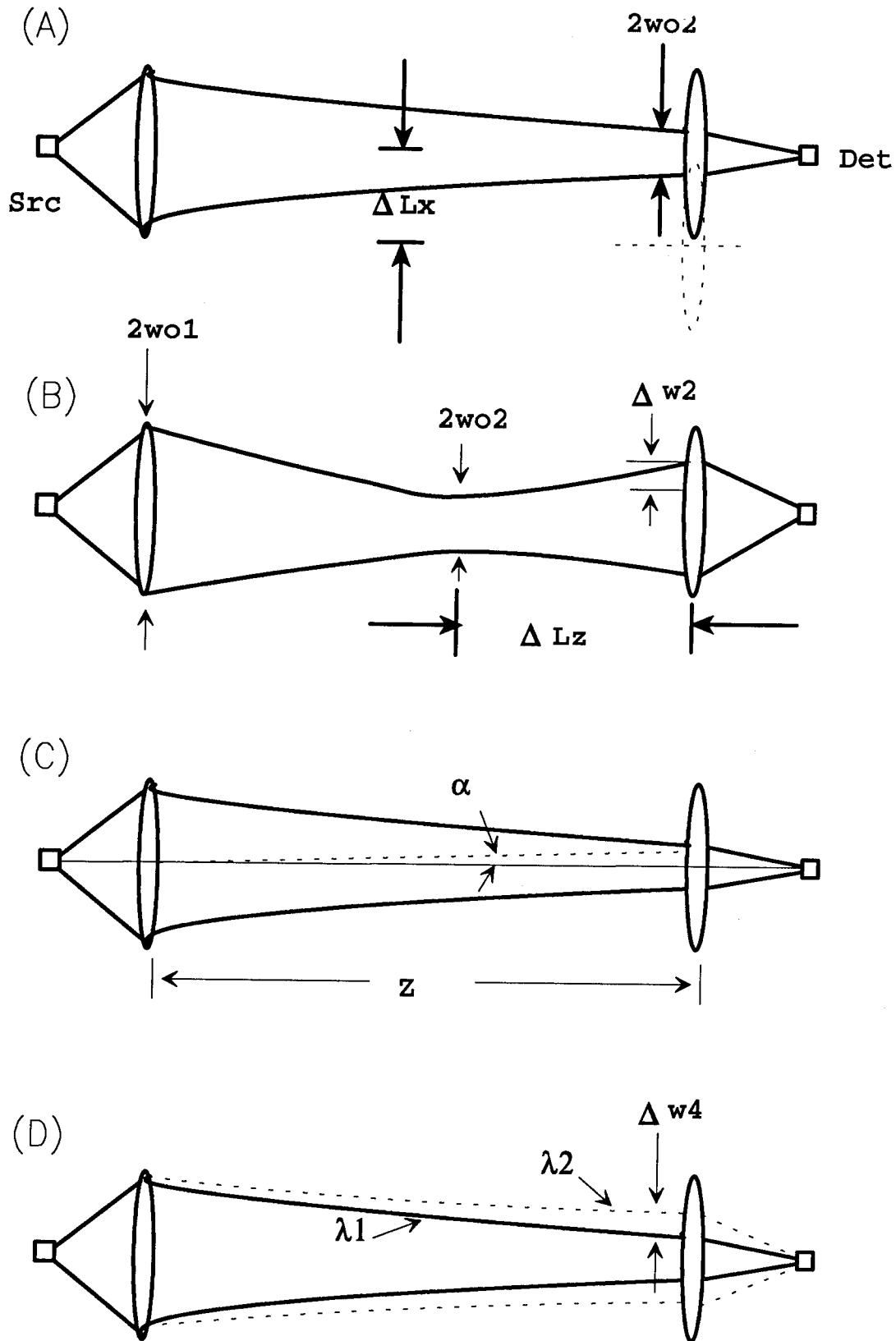


Fig. 3. a) Lateral misalignment; b) Longitudinal misalignment; c) Angular misalignment; d) chromatic dispersion factors which affect optical system performance.

$$\begin{aligned}
\Delta \ell &= 2m_1 t \frac{\Delta \alpha}{\cos^2 \alpha} - 2m_2 t \frac{\Delta \beta}{\cos^2 \beta} \\
&= \left(2m_1 t \frac{\sin \alpha - \sin \theta}{\cos^3 \alpha} - 2m_2 t \frac{\sin \beta - \sin \theta}{\cos^3 \beta} \right) \frac{\Delta \lambda}{\lambda} \\
&\quad + \left(2m_1 t \frac{1}{\cos^3 \alpha} - 2m_2 t \frac{1}{\cos^3 \beta} \right) \cos \theta \Delta \theta
\end{aligned} \tag{7}$$

Neglecting angular misalignment ($\Delta \theta \approx 0^\circ$), the spatial spot shift can be compensated by finding β and β' that satisfy

$$m_1 \frac{\sin \alpha - \sin \theta}{\cos^3 \alpha} = m_2 \frac{\sin \beta - \sin \theta}{\cos^3 \beta} = m_2 \frac{\sin \beta' + \sin \theta}{\cos^3 \beta'} \tag{8}$$

and make Eq.(7) equal to zero. For normal incidence ($\theta = 0^\circ$), Eq.(8) simplifies to

$$m_1 \frac{\sin \alpha}{\cos^3 \alpha} = m_2 \frac{\sin \beta}{\cos^3 \beta} = m_2 \frac{\sin \beta'}{\cos^3 \beta'} \tag{9}$$

Since both sides of Eqs.(8) and (9) are monotonic increasing functions with respect to angles within the angular range of interest, single value solutions for β and β' can always be found for $m_1 \neq m_2$ to provide a stable beam spot location at the output holographic grating.

Further design issues are focused on reducing the ratio $f = \ell_2/\ell$ that can minimize the total propagation distance in the substrate for low propagation loss. Calculations show that f decreases with decreasing $g (= m_1/m_2)$ and decreases with increasing α , for small α . For a large α angle, the α dependence is weak, especially for $\alpha > 70^\circ$.

The achromatic coupling range is determined by comparing three factors: the wavelength selectivity of grating diffraction [2], the achromatic wavelength range for angle γ , and the achromatic wavelength range for the substrate spot shift. Results indicate that the achromatic wavelength range for substrate spot shift is the dominant factor and is expressed as

$$R_{\lambda, \ell} = 2 \sqrt{\frac{2\Delta \ell_{\text{tol}} \lambda^2 \cos^2 \beta}{3f\ell |\tan^2 \alpha - \tan^2 \beta|}} \tag{10}$$

Minimizing f , and using a short distance ℓ , can reduce total propagation distance in the substrate and, therefore, widen the achromatic wavelength range.

The achromatic coupling technique is particularly useful for optical coupling between free-space beams and guided waves. It can also be extended to other visible and infrared diode

For a given laser wavelength shift, a small $\Delta\alpha$ can cause diffracted beam position shift $\Delta\ell$ in the substrate by

$$\Delta\ell = \left(1 - \frac{\tan(\alpha + \Delta\alpha)}{\tan\alpha}\right)\ell \quad (3)$$

where ℓ is the substrate beam planar propagation distance. Small laser wavelength shifts can produce significant optical spot shifts at the output coupling hologram. For example, under normal and collimated incidence on an optical backplane, a 1 nm laser wavelength shift at a center wavelength of 780 nm can change the diffracted beam angle in the backplane substrate by as much as 0.127° for α near 60° . This translates to a spatial beam spot shift of about $257\ \mu\text{m}$ at the output coupling hologram, after a 50 mm planar propagation in the backplane substrate. Increasing $\Delta\lambda$, ℓ , and angle α will further increase the spot shift values, possibly to several mm, which could cause the substrate beam to miss the output holographic grating or to produce a large focusing angle error unacceptable to the waveguide end-fire coupling.

Obviously, a two-grating system is not suitable for spatial shift compensation because the second grating has no effect at all on the shift. A three-grating structure, as shown in Fig. 2, can, however, provide a stable output diffraction angle γ and a stable output beam position. Three local coordinate systems, at corresponding gratings, are used to define the beam incidence and diffraction angles.

A simple derivation for the shift compensation grating and the output grating results in the following dispersion relationships:

$$\Delta\beta = \frac{\cos\theta}{\cos\beta}\Delta\theta + \frac{\Delta\lambda}{\lambda} \frac{\sin\beta - \sin\theta}{\cos\beta} \quad (4)$$

$$\Delta\gamma = -\frac{\cos\theta}{\cos\gamma}\Delta\theta + \frac{\Delta\lambda}{\lambda} \frac{\sin\gamma + \sin\theta}{\cos\gamma} \quad (5)$$

When the output coupling angle is designed at $\gamma = -\theta$, the angle γ will be insensitive to laser wavelength variations. Under normal incidence, with $\Delta\theta = 0^\circ$, the achromatic output coupling requires $\gamma = 0^\circ$, i.e., normal output coupling, which is desirable for board-to-board interconnect applications.

The spatial location of the beam spot at the output coupling hologram is calculated by the expression

$$\ell = \ell_1 - \ell_2 = 2m_1t \tan\alpha - 2m_2t \tan\beta \quad (6)$$

where t is the backplane substrate thickness and m_1 and m_2 are the numbers of propagation bounces from the input grating to the shift compensation grating, and from the shift compensation grating to the output grating, respectively. Both ℓ_1 and ℓ_2 are positive in value for the designated angles. The physical spot shift in this case can be written as

Design and fabrication error analysis of input couplers for integrated planar micro-optic systems by rigorous diffraction theory

Seung Gol Lee, Tae Wan Kim

Department of Electronic Materials and Devices Engineering, Inha University,
253 Yonghyun-Dong, Nam-Gu, Incheon, South Korea 402-751
(032) 860-7433

Seok Ho Song

Electronics and Telecommunications Res. Inst., Research Department,
P.O. Box 106, Yusung, Taejeon, South Korea 305-606
(042) 860-6033

I. Introduction

Since the new concept of planar integration was introduced by J. Jahns et al.^[1], individual components such as input/output couplers, beam splitters, and beam deflectors have been studied extensively^[2] in order to construct micro-optic systems. Most of individual components have been based upon kinoform, Fresnel lens, and surface relief gratings with continuous profiles or multiphase levels^[3,4].

Recently, the use of high spatial frequency grating becomes attractive since high diffraction efficiency can be easily obtained with relatively simple shape. The rigorous diffraction theory^[5,6] has been applied for the analysis of components in this area instead of conventional diffraction theory.

In this paper, two-way input couplers with high spatial frequency are designed by applying the rigorous diffraction theory based on the coupled wave approach^[5] and their fabrication errors are analyzed numerically also. Though the similar work^[2] was performed in order to design high spatial frequency gratings for beam splitters and beam deflectors, the rigorous diffraction theory based on the modal theory^[6] was applied.

II. Two-way input coupler

Two-way input coupler is defined as an input coupler which couples a signal beam into two integrated planar micro-optic systems simultaneously in the case that two micro-optic systems may be placed on the same substrate. The function and the structure of two-way input couplers are shown in Fig. 1, schematically.

When a signal beam is normally incident on the two-way input coupler in Fig.1, only two of symmetrically diffracted beams should be generated. It is convenient to define the sum of two diffracted beam as the diffraction efficiency of two-way input coupler. For optimal design, ± 1 st-order diffracted beams are chosen to have the maximum diffraction efficiency. And the high spatial frequency grating with rectangular grooves is adapted in

laser wavelengths, including 0.6 μm , 0.8 μm , 1.3 μm , and 1.55 μm center wavelengths, for use in wafer scale interconnects, backplane interconnects, integrated disk pickup devices, and optical computing and fiber communication systems that require optical coupling with minimal chromatic sensitivity.

References:

1. Michael R. Wang, "Optically Assisted Three-Dimensional Packaging for Multichip Module Applications," Army SBIR contract No. DAAL01-93-C-3318 (1993)
2. M. R. Wang, G. J. Sonek, R. T. Chen, and T. Jansson, "Large Fanout Optical Interconnects Using Thick Holographic Gratings and Substrate Wave Propagation," *Applied Optics*, 31, 236-249 (1992)

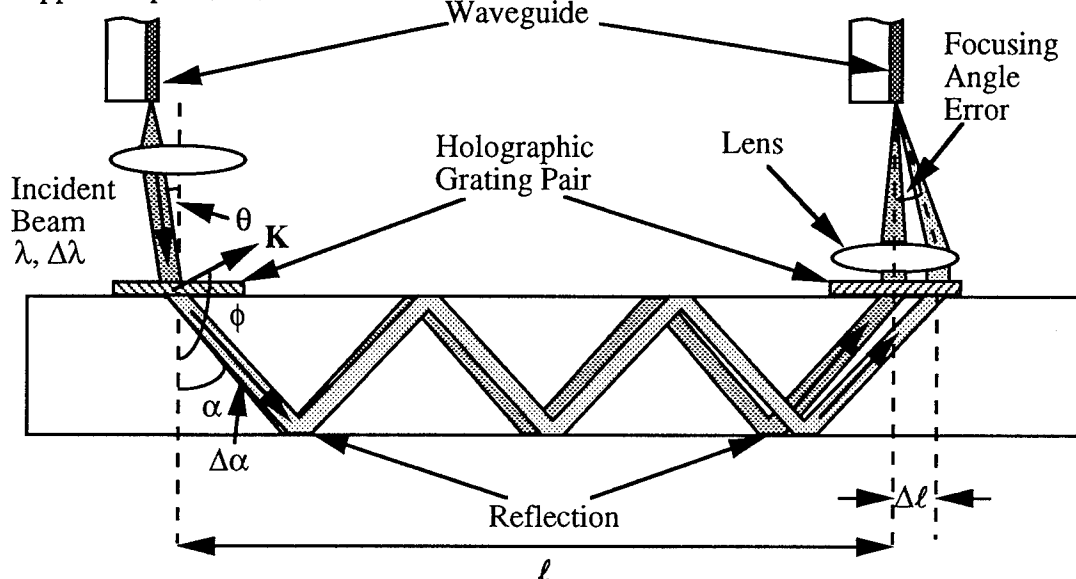


Fig. 1 Wavelength variation causes a substrate beam spot shift at the output coupling hologram in a two-grating structure. The spot position shift will affect the efficiency of coupling to a waveguide.

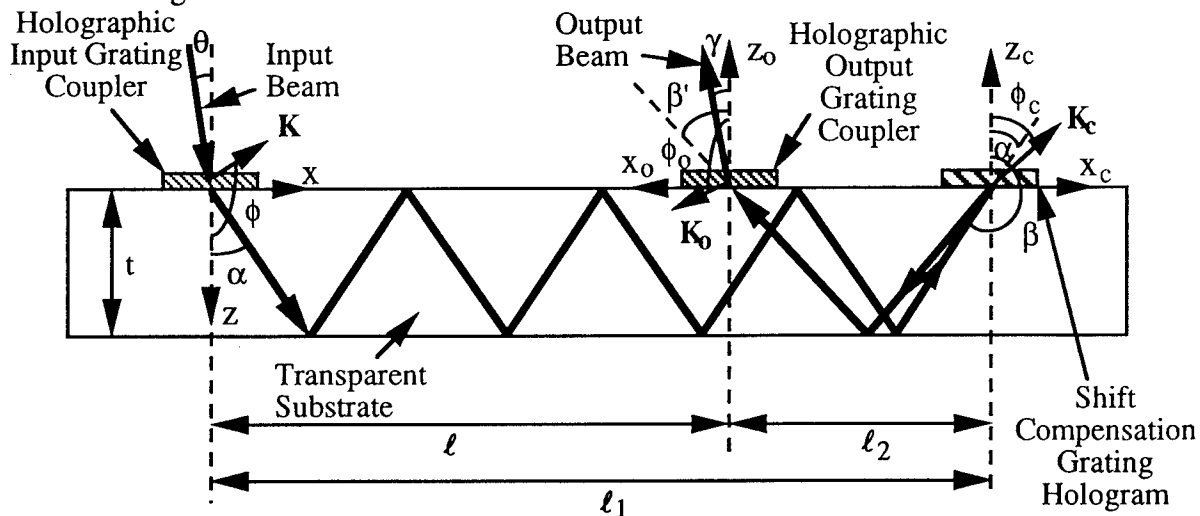


Fig. 2 A three-grating structure for backplane substrate interconnects, providing a stable output diffraction angle γ and a stable output beam position over the entire laser diode wavelength shift range.

is limited to 1 %. Therefore the undercut effect will not degrade the efficiency of micro-optic components, if the wet etching process is not utilized in the fabrication process.

IV. Conclusions

The optimal design of two-way input coupler with rectangular grooves is accomplished by using the rigorous diffraction theory. The diffraction efficiency of 93.2 % can be obtained with the binary structure. And fabrication errors such as etch depth error and the undercut effect is evaluated numerically.

< REFERENCES >

1. J. Jahns and A. Huang, "Planar integration of free-space optical components," *Appl. Opt.* **28**, 1602 (1989).
2. S. J. Walker, J. Jahns, L. Li, W. M. Mansfield, P. Mulgrew, D. M. Tennant, C. W. Roberts, L. C. West, and N. K. Ailawadi, "Design and fabrication of high-efficiency beam splitters and beam deflectors for integrated planar micor-optic systems," *Appl. Opt.* **32**, 2494(1993).
3. J. M. Miller, M. R. Taghizadeh, J. Turunen, and N. Ross, "Multilevel-grating array generators: fabrication error analysis and experiments," *Appl. Opt.* **32**, 2519(1993).
4. E. Noponen, J. Turnen, and A. Vasara, "Electromagnetic theory and design of diffractive-lens arrays," *J. Opt. Soc. Am. A* **10**, 434(1993).
5. M. G. Moharam and T. K. Gaylord, "Diffraction analysis of dielectric surface-relief gratings," *J. Opt. Soc. Am.* **72**, 1385(1982).
6. L. C. Botten, M. S. Craig, R. C. McPhedran, J. L. Adams, and J. R. Andrewartha, "The dielectric lamellar diffraction grating," *Opt. Acta* **28**, 413(1981).
7. L. Li and C. W. Haggans, "Convergence of the coupled-wave method for metallic lamellar diffraction gratings," *J. Opt. Soc. Am. A* **10**, 1184(1993).

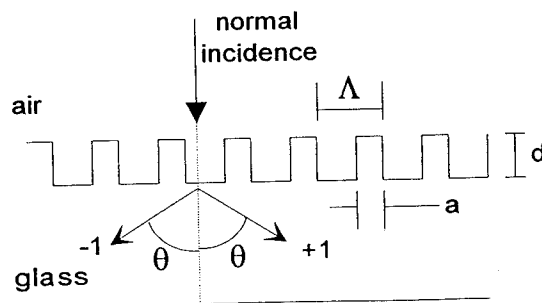


Fig. 1. The schematic diagram of two-way input coupler with rectangular grooves.

order that single mask technology may be utilized.

Three design parameters of two-way input couplers are period, thickness and duty cycle and they are denoted as Λ , d , and a in Fig. 1, respectively. In order to obtain the efficient input coupler, undiffracted beam may be reduced by destructive interference. From the rule of thumb, the thickness of input coupler can be estimated to be the same value as incident wavelength.

III. Design and Results

The design procedures are as follows: At first, the period is iterated for initial values of the thickness and the duty cycle, and then its optimal value is found. Secondly, the next parameter is optimized by the similar method and third parameter is done also. The above procedures are repeated to optimize three design parameters until the maximum diffraction efficiency is saturated. During design procedure, the diffraction efficiencies of diffracted beam are calculated by using the rigorous diffraction theory, where only TE mode is considered for convenience. The convergence of the rigorous diffraction theory^[7] is confirmed for the number of eigenvalues of more than 20.

The wavelength and the angle of incident beam are assumed to be $0.85 \mu\text{m}$ and 0° , respectively. Since the incident beam travels from air into glass plate, refractive indices of two regions are assumed to be 1.0 and 1.46, respectively.

The optimized values of two-way input coupler are $\Lambda = 1.90\lambda$, $a = 0.325\Lambda$, and $d = 1.10\lambda$ and then the diffraction efficiency of two-way input coupler has the maximum value of 93.2 % for TE mode. Fig. 2(a) and 2(b) represent the variation of the diffraction efficiency according to the period and the duty cycle, when the thickness of the input coupler is 1.10λ . The central small region in Fig. 2(a) shows the parameter condition having the diffraction efficiency of more than 90 %. The similar region is shown in detail from Fig. 2(b).

In the fabrication process using VLSI technology, much undesirable errors may happen and degrade the characteristics of micro-optic components strongly. Therefore the influence of the fabrication errors on the diffraction efficiency must be evaluated in design process. Etch depth error and undercut effect can be considered as key factors in the fabrication error analysis, since single mask technology is enough for the fabrication of two-way input couplers.

Fig. 3 shows the variation of diffraction efficiency with the etch depth error of maximum 10 %. It can be known from Fig. 3 that the etch depth allows $\pm 10\%$ error at the cost of 2 % diffraction efficiency reduction.

The undercut effect in the etching process is represented in Fig. 4(a) and the structure change due to that effect can be simply modeled by the trapezoidal shape as shown in Fig. 4(b). The slope error s is defined as the ratio of Δ to the thickness d in order to describe the structure change quantitatively. The variation of the diffraction efficiency to the slope error s is shown in Fig. 5. Within the 10% slope error, the deviation of diffraction efficiency

A selective cell-based algorithm for designing high efficiency beam array generators

Rick L. Morrison and Mike J. Wojcik
AT&T Bell Laboratories
Naperville, IL 60566

Introduction

Current free-space digital optical systems require optical power supplies that generate two dimensional arrays of uniform intensity light beams¹. The resultant spot arrays are used to illuminate opto-electronic logic device arrays to optically encode and transfer information. The favored method for creating these regularly spaced beam arrays is to illuminate a computer designed Fourier-plane hologram using a collimated laser source.

Phase holograms are desired in optical systems due to their higher diffraction efficiency. These surface relief gratings, also referred to as multiple beamsplitters, are designed using scalar diffraction theory via a computer optimization process to create a uniform intensity array of beams. The quality of the hologram is quantified by its diffraction efficiency for coupling light into a set of designated orders and the relative deviation of the beam intensities from their targeted values. The quality is expressed via a merit function calculated during the optimization process. The inclusion of arbitrary intensity orders can also be incorporated in the process through the merit function.

In this paper, we describe an algorithm that uses a pixelated, discrete phase level representation of the hologram to examine and modify only those cells that form the boundary between phase transitions, thereby substantially reducing processing requirements. An additional feature of the algorithm is the capability to increase the spatial bandwidth of the hologram during the design process. Using this algorithm, we have designed holograms with up to 4096x4096 cells per period that couple light into arrays containing up to 16,000 spots. We have fabricated a number of smaller designs for use in our free-space photonic switching program.

Although rectangular, uniform intensity arrays can be designed by partitioning the problem along the two dimensions and solving each dimension separately, higher efficiencies are obtained when a nonseparable, two dimensional approach is used. Unfortunately, the computational complexity grows exponentially, making it difficult to design larger arrays.

The algorithm presented here is similar in nature to the IDO (iterative discrete on-axis) encoding algorithm². In the basic IDO algorithm, one period of the Fourier-plane hologram is divided into an array of rectangular cells where each cell imparts one of two fixed phase delays to the incident wavefront. The contribution of each cell to an order intensity is independent of the other cells, thus, each test requires calculation of only a small fraction of the full set of diffraction equations. During a series of iterations, each cell phase is reversed and this new value is retained based on its contribution to the merit function and a probabilistic simulated annealing process.

By examining the mathematical framework of this problem, it can be seen that (once the phase levels are fixed) it is the locations of the level transitions that determine the order intensities. Therefore, in this new algorithm, it is necessary to examine and modify only cells along phase transition boundaries. This results in a significant reduction in processing since only a fraction of the cells are tested during each iteration. In addition, by calculating and storing the trigonometric and complex exponential values before the iterative process, the number of arithmetic operations is drastically reduced.

An additional strength of this algorithm is the ability to increase the spatial resolution of the phase array during the optimization process. When the merit function value stagnates at an unacceptable value, each phase cell is subdivided into 4 parts with each new cell given the original cell's phase value. The additional cells provide higher frequency components that aid, primarily, in improving the intensity uniformity.

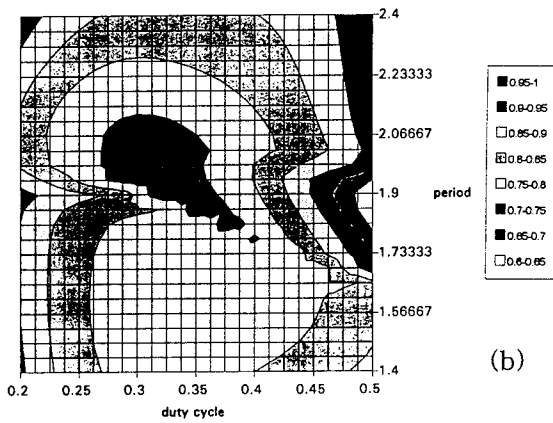
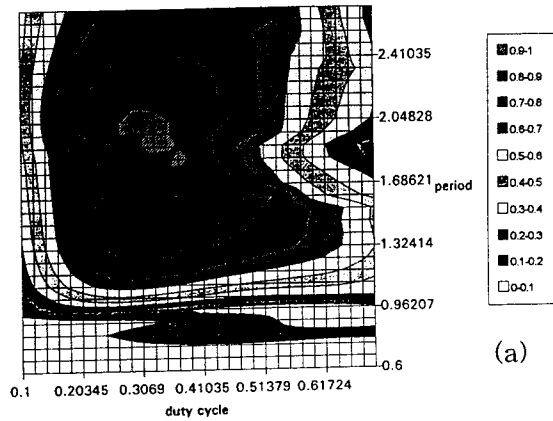


Fig. 2. Contour map viewing the variation of the diffraction efficiency.

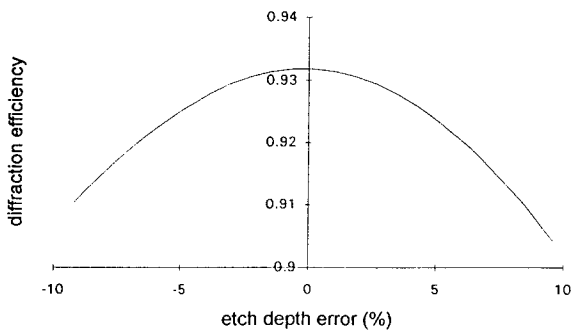


Fig. 3. The influence of the etch depth error on diffraction efficiency

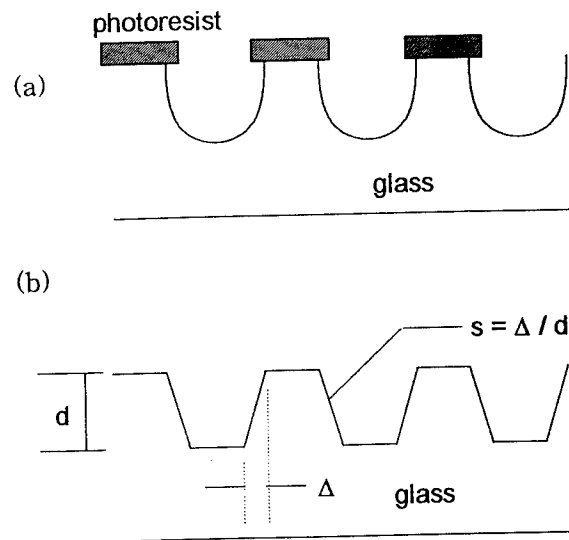


Fig. 4. (a) Conventional etching pattern and (b) its model

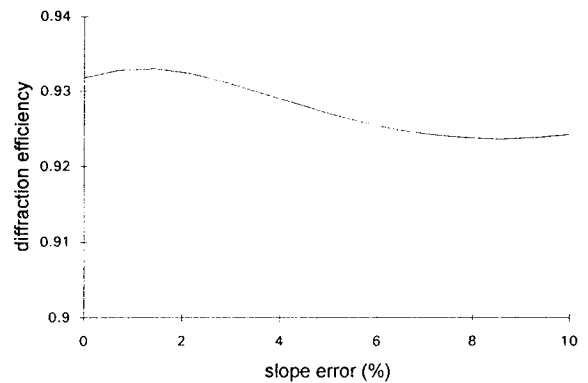


Fig. 5. The influence of the slope error on diffraction efficiency.

levels in the design. We have also included the ability to load the phase array with values generated by a separate application based on the Gerchberg-Saxton algorithm³. In this case, the Gerchberg-Saxton program rapidly generates a rudimentary solution whose intensity deviations are then reduced by the new algorithm. We have observed that this dramatically reduces the design time and avoids the stagnation problems associated with the Gerchberg-Saxton algorithm, especially with binary level designs.

Next, the amplitude of each designated order is calculated using values from the phase array. After the amplitude arrays have been initialized, the algorithm examines cells with the objective of improving the merit function value. A series of four comparisons are performed where all phase values, θ_{jk} , are compared against $\theta_{j+1,k}$, $\theta_{j,k+1}$, $\theta_{j-1,k}$, and then $\theta_{j,k-1}$ respectively. Cells along the array boundaries whose neighbors lie outside the standard array are exempt from this process. If the two phase values are equal, no action is taken. If, however, the phase values differ, the neighbor's value is inserted and its contribution to the order amplitudes and, consequently, the merit function are calculated. If the merit value is improved, the new phase value is inserted into $\theta_{j,k}$. If not, the original value is retained. The IDO method used a probabilistic scheme to occasionally choose a phase value that produces a higher value merit value in order to avoid local minima during the optimization process. We have found this to be unnecessary here.

The algorithm repeats the cell examination and update sequence until one of the following conditions are achieved. When the merit value or order intensity deviation reaches its target value, the solution is stored and the process is terminated. If no quality objectives are met within the number of specified iterations or if the improvement of the merit function stagnates, the algorithm may either terminate, or, subdivide the phase array to attain higher resolution. During subdivision, each cell is replicated along both dimension to form an array that is four times larger. All stored values are recalculated according to the new array format and the search process is revisited. The number of allowed subdivisions is a parameter that is specified in the application. When the program terminates the phase array is stored in a data file and is later used to create the lithographic mask(s) that will transfer the pattern into an optical surface.

A further reduction in processing effort is achieved by integrating symmetries into the algorithm⁴. For example, when an even numbered array design is required it is necessary to calculate only one quadrant of the array. This quadrant, when replicated by shifting and adding an additional π phase shift to two diagonal quadrants, automatically generates suppressed even numbered orders. Also, for binary phase gratings, it is unnecessary to calculate $A_{-m,-n}$ since it is equal in value to $A_{m,n}$.

Results

Uniform intensity, binary phase array generators producing an 8x8 spot array were designed in about 12 seconds on a SUN Sparcstation 10. An equivalent 16 phase level 8x8 generator required about 18 seconds. Both tests began with an initial randomly generated phase array with a quadrant size of 32x32 cells eventually dividing into 128x128 cells.

A 32x32 spot array binary phase design with a final size of 512x512 cells per quadrant took 42 minutes to generate. When the Gerchberg-Saxton application was used to create an initial phase distribution, the design time for the total optimization was reduced to 16 minutes. A 128x128 binary phase array generator using an initial Gerchberg-Saxton starting array with a final 2048x2048 cell quadrant required 71 hours to complete. Typically, the binary phase solutions had a diffraction efficiency of about 75%. In each of the above cases, the standard deviation of the spot intensities was reduced to under 2% of the average spot intensity. If this condition is relaxed, for example in designs that generate pictures using arbitrary intensity spots, the optimization time can be substantially reduced.

Figure 1 shows the hologram designed used to generate an irregularly spaced spot array used in a free-space photonic switching system. A picture of the resulting spot array from a fabricated grating is shown in figure 2.

In summary, this new algorithm in conjunction with the application of design symmetries, substantially reduces processing time and makes the design of moderate size array generators feasible. The algorithm accomplishes this goal by selectively examining only cells located adjacent to a phase transition. In addition, the spatial resolution is increased as needed allowing the design to begin from a much simpler initial distribution.

The designs described in this paper have been used to create periodic binary level and multiple discrete level phase gratings that can be fabricated using contact microlithography and reactive ion etch techniques. Although the multilevel designs have higher diffraction efficiencies than the binary phase counterparts, rigid submicron alignment tolerances must be maintained during the multistep fabrication process to avoid potentially large fluctuations in beam intensities. Therefore, binary phase designs are still highly regarded.

Algorithm

Scalar diffraction theory is used to calculate the complex amplitude of the n th order in the m th row as given by the sum of the contributions from each of the $J \times K$ phase cells,

$$A_{m,n} = B_{m,J} \cdot B_{n,K} \cdot \sum_{j=0}^{J-1} \sum_{k=0}^{K-1} F_{m,j,J} F_{n,k,K} \cdot \exp(i\theta_{j,k}),$$

where, θ_{jk} is the phase delay associated with cell (j,k) , and

$$B_{m,J} = \frac{1}{2\pi m} \cdot \sin\left(2\pi \frac{m}{J}\right) \cdot \exp\left(-i\pi \frac{m}{J}\right), \text{ and}$$

$$F_{m,j,J} = \exp\left(-2\pi i \frac{mj}{J}\right).$$

The intensity of the order is given by the complex square of $A_{m,n}$. The designated orders are also described by other sets of parameters. One array holds the target value for the relative intensity. All orders in uniform intensity arrays have value one. Suppressed intensity orders are given values of zero. Other integer values may also be provided within the range $[0...R]$, where for this demonstration we limit R to 15. Another array contains the weights describing the relative importance of each order in reaching its targeted intensity.

The quality of this solution is measured using a merit function given by,

$$C = \eta - \alpha(s) \cdot \sigma,$$

where η , the diffraction efficiency for the T orders, is given by,

$$\eta = \sum_{t=1}^T (A_{mn})^2,$$

and the intensity deviation is given by,

$$\sigma = \sum_{t=1}^T w_t \cdot (I_t - I_{i0})^2.$$

I_t is the calculated intensity, I_{i0} is the desired intensity, and w_t is the weighting factor of each order. The merit function includes a variable, $\alpha(s)$, that is a function of the iteration number, s . It is a linearly increasing function starting at an initial value of about 0.1, rising to about 0.2 after about 20 iterations and then retaining this value. This form of the merit function initially emphasizes the diffraction efficiency, while eventually increasing the importance of reducing the deviation of the order intensity from its target value. Other merit functions could also be considered. The parametrization of this function has been seen by us to significantly influence the completion time of a design.

First, a two dimensional data array is defined that contains the $J \times K$ pixel phase values of one period of the hologram. This array is filled with a random distribution of values within the set $[0, 1, ..., L-1]$ where L is the number of phase

Coupled Kinoforms for Space Variant Optical Interconnect Systems

David Zaleta, Michael Larsson, Walter Daschner, Sing H. Lee
 Electrical and Computer Engineering
 University of California at San Diego
 9500 Gilman Drive
 La Jolla, CA 92093-0407
 Phone: 619-534-2699, Fax: 619-534-1225

1.0 Introduction

Space variant optical interconnect systems have the benefit of permitting fully random interconnections between input and output optoelectronic devices in two arbitrary located processing elements (PEs) as shown in Figure 1. Due to the fact that diffractive optical elements (DOEs) can support random interconnect patterns, they are attractive to implement space variant types of systems. However, the small apertures (≤ 1 mm), the limited space bandwidth product, and the high efficiency specifications required of these systems conflict with the desire to maintain large distances (> 1 cm) between the input and output optoelectronic devices. The small DOE apertures found in these types of systems make diffraction a dominant consideration. Likewise, the limited space bandwidth product makes it difficult to achieve large angles in folded planar systems. Several papers have addressed techniques to increase the angle by multiple DOEs [1] or by special encoding techniques [2]. However, these angles are still relatively small ($< 25^\circ$) resulting in the need to increase longitudinal distances in order to realize the desired lateral interconnect distance. Thus, there is a need to develop design methods that permit one to maximize the distance traversed by the interconnect while maintaining as high efficiency as possible. In this paper, the authors present three methods utilizing the Gerchberg-Saxton (GS) [3] algorithm to design coupled kinoforms that are capable of maximizing the optical power on the detector while maintaining diffraction-limited distances for many types of space variant systems. These designs are compared to a "standard" space variant design.

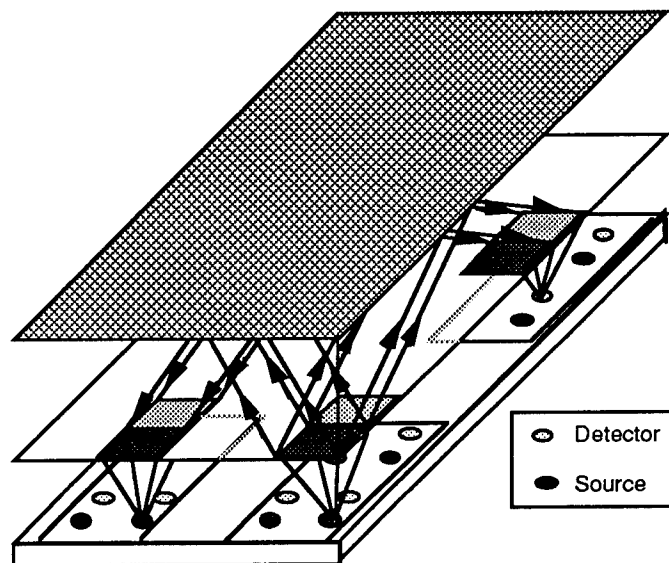


Figure 1. Schematic diagram of space variant optical interconnect system.

2.0 Standard Space Variant Optical Design

Our goal in this paper is to increase the lateral interconnect distance in a planar space variant optical system by increasing the propagating distance between the two elements to some diffraction limited level that permits the maximum optical throughput. Figure 2 shows a modified optical interconnect that was recently proposed for achieving diffraction limited performance in space variant optical systems[4]. In this system, we wish to transfer as much light as possible to the opposite side by forcing the focal length of DOE #1 (Fresnel lens) to be

References

1. R. L. Morrison, S. L. Walker, and T. J. Cloonan, "Beam array generation and holographic interconnections in a free-space optical switching network," *Appl. Optics* **32** 2512-2518 (1993).
2. M. R. Feldman and C. C. Guest, "Iterative encoding of high-efficiency holograms for generation of spot arrays," *Optics Letters* **14**, no. 10, 479-481 (1989).
3. R. W. Gerchberg and W. O. Saxton, "A practical algorithm for the determination of phase from image and diffraction plane pictures," *Optik* **35**, no. 2, 237-246 (1972).
4. R. L. Morrison, "Symmetries that simplify the design of spot array phase gratings," *J. Opt. Soc. Am A* **9**, no. 3, 464-471 (1992).

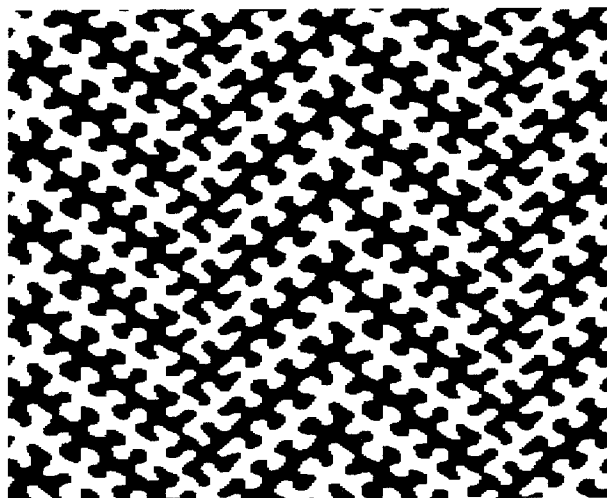


Figure 1. Nonseparable design used to generate irregularly spaced spot array of 32 spots.

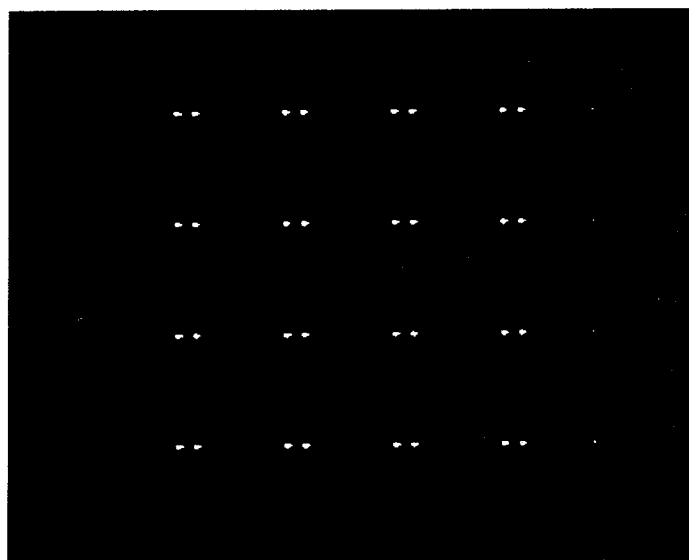


Figure 2. Picture of spot array generated by grating fabricated with design shown in figure 1.

rather than fully optimize the 2nd half of the optical relay, we only partially optimize it by reducing the number of iterations of the GS algorithm. The result yields an amplitude and phase pattern at the kinoform #2. The phase is used to determine kinoform #2's phase distribution while the amplitude pattern is imposed upon the illumination in order to adjust the phases of kinoform #1. This process continues until a maximum number of iterations is reached or until little improvement is realized during an iteration.

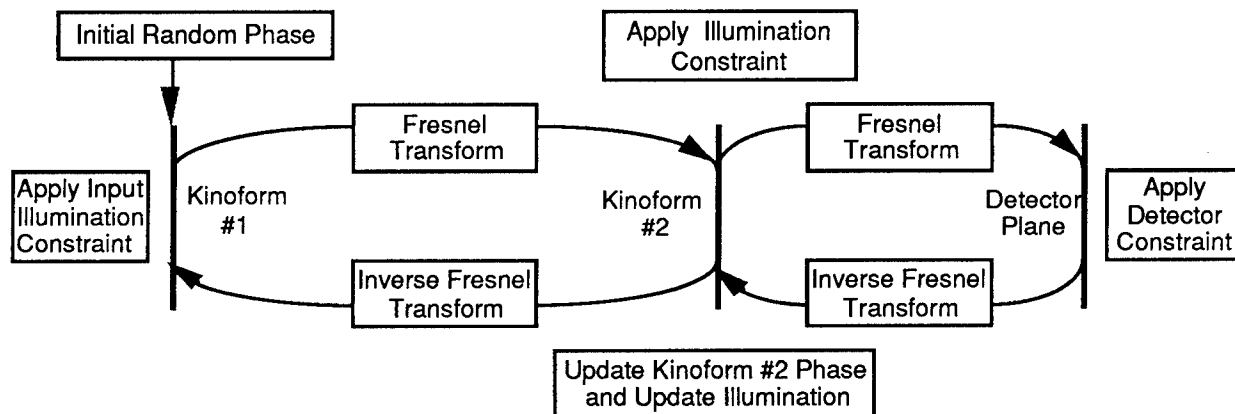


Figure 3. Flow chart for coupled Gerchberg-Saxton algorithm.

4.0 Comparison between the Standard Design and Three Gerchberg-Saxton Designs

In order to compare the four designs discussed in this paper, we ran numerical simulations on the different design methods for parameters. The physical parameters used for comparison are set by the standard design and are shown along with the optical throughput (expressed as a percentage of the input intensity) in Table 1. Of primary interest is to determine the tradeoff between the lateral distance separating the elements and the optical throughput. One would expect that this distance is inversely related to the optical throughput. However, as Table I shows that for the standard optical design this intuition fails. This is due to the fact that although by including more side lobes of the *sinc* diffraction pattern inside the aperture of kinoform #2 (increasing n) more light is captured, the resultant phase distribution on the kinoform #2 is inappropriate to effectively focus the light onto the detector. In all the systems studied, we increase the aperture size of the DOEs (with the assumption that the kinoform #1 and #2 are of the same size) while increasing the distance according to Eqn 1 and maintaining a fixed f-number (ratio of kinoform aperture to distance between kinoform #2 and the detector) for kinoform #2 (in our case $f/10$).

The results for the optical throughput for all 12 cases (4 designs methods for $n=1,3$, and 5) as a function of the distance is shown in Table 1. The results show that the coupled GS provides the most favorable designs in almost all cases with the largest increase (a factor of 16) over the standard design occurring when $n=5$ and $D=1.0$ mm. What is disappointing is that while the coupled GS design method is better than the $n=1$ standard design case, it is only marginally improved. Unfortunately, it is this very case that is actually the most attractive for optical interconnect applications since the propagation distances are the greatest allowing the largest lateral interconnection distances. However, this situation is only important in the one to one interconnection case. For general fanout elements, the coupled GS algorithm permits one to design fanout elements that maximize the optical throughput to the detector for diffraction limited cases found in space variant optical interconnect systems.

equal to the distance between the two DOEs. Note that the amount of power captured by DOE #2 is limited by diffraction by the aperture size and the distance between the elements. Typically, if we desire to capture ~90% of the input intensity, we need to adjust the distance so that the main lobe of the resultant *sinc* is captured by DOE #2. The relationship between the distance (z), the aperture size (D), and the number of *sinc* side lobes captured (n) is given by:

$$z = \frac{D^2}{2n\lambda} \quad (1)$$

where λ is the wavelength of light. Note that in Figure 2 the system is arranged in a linear fashion for simplicity of discussion. Although, in general, we need to achieve an off-axis transfer of energy which can be accomplished by using either an extra linear grating next to each element or equivalently an off-axis DOE.

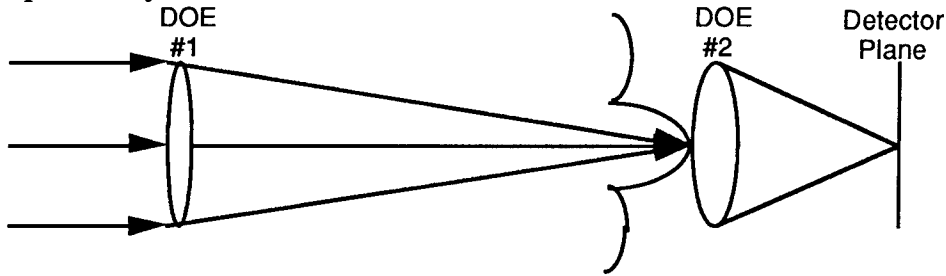


Figure 2. Modified optical design presented in Ref. 4 for achieving diffraction limited interconnect distances.

3.0 Kinoform Designs based on Gerchberg-Saxton Algorithm

In order to increase the throughput, it is necessary to design both input and output kinoforms so that maximum throughput is achieved. To accomplish this three different design algorithms have been employed and compared to the above standard design. All three designs require the use of the GS algorithm modified for application in the near field (replacement of the Fourier transform with a Fresnel transform)[5,6]. Briefly, the GS algorithm is an iterative technique used to match the intensity constraints at two planes separated by some distance by adjusting the phase at each plane. This section will summarize the three kinoform design methods discussed in this paper.

3.1 Single Kinoform designed by Gerchberg-Saxton Algorithm

The first method, referred to as the single GS design, retains DOE #1 described above in the standard design. However, kinoform #2 is designed by a single application of the GS algorithm. In other words, by letting the illumination from DOE #1 be the input constraint and the detector area be the output constraint, one can utilize the GS algorithm to specify the phase necessary for kinoform #2 in order to achieve maximum intensity at the detector.

3.2 Two Kinoforms designed by repetitive Gerchberg-Saxton Algorithm

The second design method applies the GS algorithm in a repetitive fashion (which we refer to as the repetitive GS design). In this design the GS algorithm is first used to determine the phase of the kinoform #1 by using the input illumination and the aperture of the kinoform #2 as the input and output constraints, respectively. After completing this phase of the design, the resultant illumination from kinoform #1 and the detector area are used by a second application of the GS algorithm as the constraints to maximize the power falling on the detector.

3.3 Two Kinoforms designed by coupled Gerchberg-Saxton Algorithm

The third design method attempts to couple the design of the two elements to achieve a higher optical throughput. A flow chart is shown for this method in Figure 3. A single iteration consists of Fresnel propagating the illuminated kinoform #1's output to the input of kinoform #2. This then becomes the illumination constraint for a short GS algorithm. By short, we imply that

Table 1. Physical parameters set by the standard design method and optical throughput for the 12 cases studied.

Aperture Size (mm)	n=1 (standard design)				
	Distance (mm)	Standard	Single GS	Repetitive GS	Coupled GS
0.125	9.765	81.1%	83.5%	80.0%	84.2%
0.25	39.06	78.2%	83.7%	77.6%	81.1%
0.5	156.25	81.0%	80.5%	78.7%	83.1%
1.0	625	78.5%	81.3%	77.8%	81.7%
Aperture Size (mm)	n=3 (standard design)				
	Distance (mm)	Standard	Single GS	Repetitive GS	Coupled GS
0.125	3.255	35.1%	53.8%	80.0%	84.2%
0.25	13.02	26.3%	49.6%	81.3%	82.3%
0.5	52.08	34.3%	56.4%	76.7%	87.3%
1.0	208.33	34.3%	56.4%	76.7%	82.9%
Aperture Size (mm)	n=5 (standard design)				
	Distance (mm)	Standard	Single GS	Repetitive GS	Coupled GS
0.125	1.953	10.0%	31.2%	78.3%	86.3%
0.25	7.812	6.5%	28.9%	78.5%	83.0%
0.5	31.25	7.9%	36.3%	76.3%	85.0%
1.0	125	5.7%	33.9%	74.1%	86.4%

5.0 Summary and Conclusions

This paper has attempted to summarize the authors' research into the design of DOEs for space variant optical interconnect systems. Three design methods based on the GS algorithm were proposed and compared with a standard design for systems with many different parameters. It was shown that the coupled GS algorithm generally outperformed all other design methods, however only marginally when compared to standard designs for the $n=1$ case. However, the coupled GS approach is flexible enough to design general fanout systems that are typically required. Currently, we are fabricating the kinoforms designed and experimental verification of the numerical results will be presented at the meeting. Future work will concentrate on application of the coupled GS algorithm to fanout situations where the standard design is no longer applicable.

6.0 References

1. W. Daschner, R. Stein, and S.H. Lee, "Alignment and assembly of diffractive optical elements for optical system packaging", OSA Annual Meeting Technical Digest, Albuquerque, NM, 183, (1992).
2. M. Nakkar, J. Stack, W.H. Welch, M.R. Feldman, "Computer generated holograms for large deflection angle optical interconnects", OSA Annual Meeting Technical Digest, Albuquerque, NM, 189, 1992.
3. R.W. Gerchberg and W.O. Saxton, "A Practical Algorithm for the Determination of Phase from Image and Diffraction Plane Pictures", OPTIK, **35**, 237-246, (1972).
4. K.S. Urquhart, P. Marchand, Y. Fainman, S.H. Lee, "Diffractive optics applied to free-space optical interconnects", Submitted for publication to Applied Optics, 1993.
5. B. Kress, D.E. Zaleta, S.H. Lee, "Iterative Design of CGH for Free-Space Optical Interconnections", OSA 1993 Topical meeting on Optical Computing, 22-25, 1993.
6. D. Zaleta, J. Fan, B.C. Kress, S.H. Lee, C.K. Cheng, "Optimum placement for optoelectronic multichip modules and the synthesis of diffractive optics for multichip module interconnects", Accepted for Publication in Applied Optics, 1994.

X-Ray Lithography: Applications to Fabrication of Diffractive Optics

Franco Cerrina, Azalia A. Krasnoperova

Department of Electrical Engineering and Center for Xray Lithography,
University of Wisconsin-Madison, WI 53706

Planar optical elements fabricated using lithographic techniques have recently received wide interest ¹. We can distinguish between two types of binary optics: those approximating a lenslet by a staircase (Fresnel lens), and those based on diffractive optical elements (Fresnel Zone Plates (FZP), gratings and so on). Lenslets are often formed in polymers, silicon and AlIII-B V materials (where reflow is also used to "smooth" the lens surface. The use of lithographic techniques opens the way to the development of optical elements which are economical, high-resolution and of flexible design. These ideas are utilized in many systems (laser beam extraction from solid state lasers and multiplexers are two examples ²) at optical or near-infrared wavelengths. Because of our interest in hard X-ray microscopy, we have developed FZP lenses for the region from 8 keV to 20 keV ³. In a FZP, the lateral resolution is determined by the width of the highest number zone. To achieve high focusing efficiency, it is necessary to maintain an optical thickness of the absorber equivalent to a π phase shift. This represents a very challenging manufacturing process, since the small linewidth (0.2 μm) coupled with high thickness of the absorber (3 - 4 μm) yields aspect ratios up to 20. We have developed an efficient fabrication process based on the replication by X-ray lithography of a master mask patterned by e-beam lithography. The high resolution, penetration power and large depth of focus of X-rays allows us to pattern a thick layer of polymethylmetacrylate (PMMA) which is then used as a mold for electroplating of gold or nickel. Figure 1 shows the smallest lines (0.25 μm) of the FZP designed for the photon energy of 20 keV and the focal length of 10 cm. To obtain the electroplated gold thickness of 3.5 μm , it was necessary to pattern PMMA with the aspect ratio of about 20. Those, one-level, FZPs have the theoretical limit of focusing efficiency about 40%.

The very nature of diffractive optics leads to the formation of orders, which lower the contrast and reduce the usable flux. The intensity in the various orders is proportional to the Fourier transform of each "groove" or "facet" profile at the corresponding spatial frequency ⁴; hence, by deliberately introducing assymetries in the "groove" we can control the position of the maximum intensity in the orders sequence, i.e., we can blaze the optical element. While more complex profiles are possible, a simple triangular lineshape produce a good blaze. Clearly, it is very difficult if not impossible to produce a variable linear profile by planar microfabrication techniques; however, it is possible to approximate the linear slope with a binary staircase. For additive (i.e., plating) lithographic processes, this has the additional advantage that each layer is thinner than the final structure, and hence the aspect ratio at each exposure level is reduced. The structures must be maintained with a resolution equal to $d/2n$, where d is the smallest linewidth, and n is the number of quantization levels. The structures must also be placed in registry to the previous ones by a fraction of $d/2n$ (we notice that placement errors will affect the efficiency but not the resolution of blazed FZP). Hence, an exposure system with adequate resolution and alignment capabilities is

Tuesday, June 7, 1994

Fabrication Methods

DTuA 8:30am–10:00am
Room B

M.C. Hutley, *Presider*
National Physical Laboratory

5. E. Difabrizio, M. Gentili, A. A. Krasnoperova, F. Cerrina, W. Yun, B. Lai, E. Gluskin. High-Performance Multilevel Blazed X-ray Microscopy Fresnel Zone Plates Fabricated Using X-ray Lithography, The 38-th International Symposium on Electron, Ion and Photon Beams, New Orleans, May 31 - June 3, 1994.

necessary. At resolution of $0.2\ \mu\text{m}$ and below, the requirements are comparable to those of ULSI and indeed the experiments can be performed using exposure tools developed for quarter micron lithography, i.e., X-ray steppers.

Using proximity X-ray lithography, we have developed the technology for fabrication of multilevel zone plates⁵. We have fabricated circular and linear bi- and tri-level zone plates, with gold structures as thick as $0.75\ \mu\text{m}$ per level. The structures were formed on silicon nitride membranes since those FZPs will be used for transmission X-ray microscopy. All levels of the blazed FZP were located on one master X-ray mask, so the inter-mask errors were minimized. We designed the zone plates for use at the wavelength of $1.54\ \text{\AA}$. The theoretical efficiency of the tri-level blazed FZPs is 82%. Some examples of the multilevel FZP are shown in Figure 2 (circular tri-level FZP), Figure 3 (linear FZP) and Figure 4 (side view on the linear FZP). The finished zone plates exhibit very steep sidewall profiles, with resolution down to $0.25\ \mu\text{m}$. With all levels aligned to one side, the staircase structure of each zone provides the blazing effect.

In fabricating the blazed FZP's, we employed standard tools, such as the IESS Leica Cambridge EBMF 10/cs 120 e-beam writer for the master X-ray mask fabrication, and a SUSS X-ray stepper XRS-200/1 installed on the synchrotron radiation beamline of the storage ring Aladdin at the UW-Madison. The processing was carried out at the Center for X-ray Lithography's microelectronics facility. Once the infrastructure is in place, X-ray lithography technology is an economical and efficient process. The fabrication of the blazed FZPs represents a challenging task and provides an excellent test vehicle for the X-ray stepper.

We will present a review of the status of X-ray Lithography, and its applicability to diffractive optics manufacturing. In particular, we will stress the characteristics of resolution, depth of focus and process latitude that can provide unique solutions to fabrication problems. We will discuss in details the fabrication process and the results of the characterization experiments at Brookhaven National Laboratory. We will discuss the limitations of the methods, and the feasibility of extension the technology to the sub 100 nm domain. We expect that these FZP will provide new applications in X-ray microscopy and microprobing. We notice that while the process developed to date is an additive one (based on the metal plating), there is no reason for which we could not transfer the patterns in a substrate by a subtractive process (i.e., etching the material). In this case, X-ray lithography will help considerably in the imaging of the finest and deepest zones. The combination of e-beam and X-ray lithography will allow the design and manufacture of arbitrary multi-level, blazed diffractive optics for a range of wavelength from the infrared and visible up to hard X-rays.

This work is supported by the Department of Energy (Argonne National Laboratory, 60988), while the Center for X-ray Lithography is supported by ARPA/ONR.

1. W. B. Veldkamp, *Binary Optics : the Optics Technology of the Decade*, The 37-th International Symposium on Electron, Ion and Photon Beams, San Diego CA, June 1993.

2. P.Unger, V. Boegli, P. Buchmann, and R. Germann, *Journal of Vac. Science and Technol.*, B11(6), 2514 (1993).

3. A. A. Krasnoperova, J. Xiao, F. Cerrina, E. Difabrizio, L. Luciani, M. Figliomeni, M. Gentili, B. lai, W. Yun, E. Gluskin, *Journal of Vac. Science and Technol.*, B11(6), 2588 (1993).

4. J. Goodman, *Introduction to Fourier Optics*, McGraw-Hill, 1968.

roch2 - 3

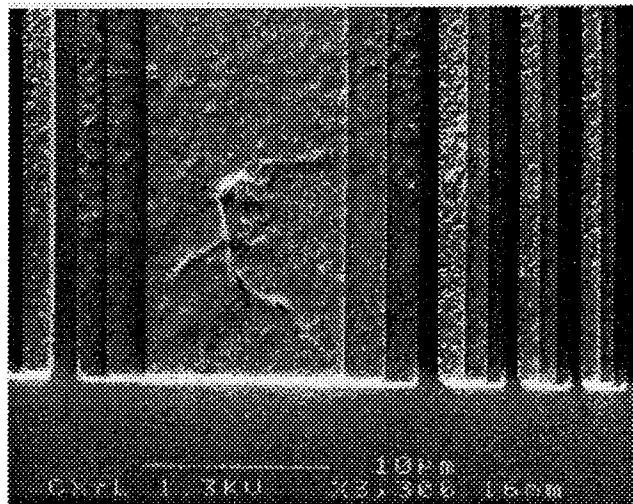


Figure 3: Tri-level linear FZP

roch4.tif

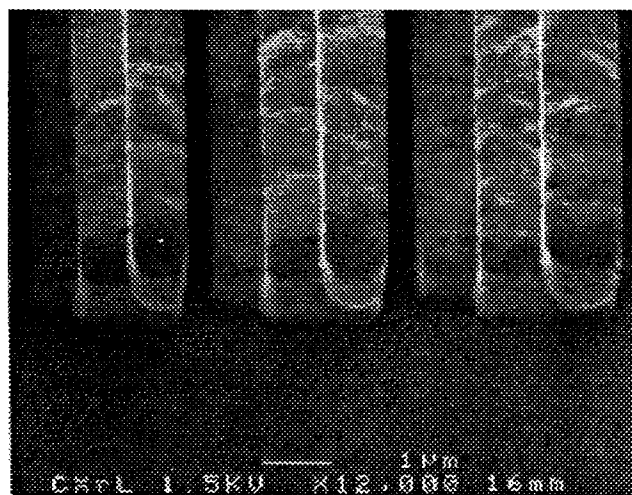


Figure 4: Tri-level linear FZP, side view

roch1 - 2

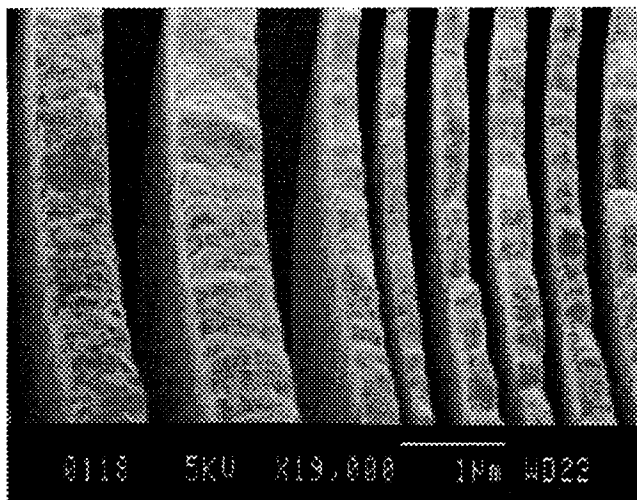


Figure 1: High aspect ratio FZP with the smallest linewidth of $0.25\ \mu\text{m}$ and feature thickness of $3.5\ \mu\text{m}$

roch3 - 1

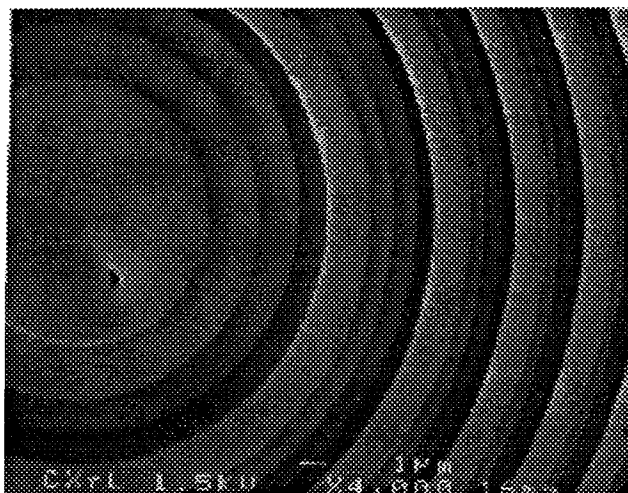


Figure 2: Tri-level circular blazed FZP

In our experiment, we start with a single 100 nm period parent grating and expose 50 nm period gratings in photoresist. The soft x-ray source is the X1A undulator [4] at the National Synchrotron Light Source, $\lambda=20\text{\AA}$. Undulators are the brightest source of soft x-rays available [5]. The X1A undulator has a coherently illuminated area of about $5000\text{ }\mu\text{m}^2$. Total coherent power is $\sim 1\text{ nW}$. The exposure time for the single grating using PMMA is 10-20 minutes. An atomic force microscope filtered image of a 50 nm period grating recorded in PMMA is shown in Fig. 2. The total area of the grating is $1800\text{ }\mu\text{m}^2$.

The 100 nm period parent gratings have been written with e-beam lithography and consist of 1000-1500 \AA of Ni electroplated on a silicon nitride membrane. A maximum first order diffraction efficiency of 13% at $\lambda=20\text{\AA}$ is shown in Fig. 3, using rigorous electromagnetic calculations [6]. Greater nickel thickness would yield higher diffraction efficiency, but the achievable aspect ratio of individual grating bars is less than 4:1. Nickel has a refractive index very close to unity at these wavelengths, and the diffraction efficiency can be modeled using Fraunhofer diffraction theory taking into account transmission through the grating bars. Good agreement with full EM calculated results is seen for Ni grating thicknesses below about 1800 \AA .

This work was supported in part by the Department of Energy.

- [1] N.M. Ceglio, R.L. Kauffman, A.M. Hawryluk, H. Medeck, *Applied Optics* 22, 318 (1993).
- [2] C.R. Canizares, M.L. Schattenburg, H.I. Smith, *Proc. Soc. Photo-Opt. Instrum. Eng.* 597, 253 (1985).
- [3] E.H. Anderson, K. Komatsu, H.I. Smith, *J. Vac. Sci. Technol. B* 6, 216 (1988).
- [4] H. Rarback, C. Buckley, H. Ade, et. al, *J. X-Ray Sci. Technol.* 2, 274 (1990).
- [5] D. Attwood, K. Halbach, K.-J. Kim, *Science* 228, 1265 (1985).
- [6] E.H. Anderson, Ph.D. Thesis, Massachusetts Institute of Technology, (1988).

Fabrication of Ultrahigh Resolution Gratings for X-Ray Spectroscopy

Max Wei^{†,*}, Erik H. Anderson[†], and David T. Attwood^{†,æ}

[†]Center for X-Ray Optics
Lawrence Berkeley Laboratory
Berkeley, CA 94720

*Department of Electrical Engineering and Computer Sciences
^æApplied Science and Technology Graduate Group,
University of California, Berkeley 94720

High resolution gratings are an important component in x-ray optics and spectroscopy and are used in x-ray spectrum analyzers [1], x-ray interferometers, and as dispersive elements in x-ray astronomy satellites [2]. In many applications, the smaller the grating period the better the performance. For example, the dispersion of an x-ray diffraction grating is proportional to the line density (spatial frequency), and in most x-ray spectrometer configurations the energy resolution is proportional to the dispersion.

Typically holographic lithography or electron beam lithography is used to fabricate fine-period gratings. Conventional holographic lithography requires a coherent source but can pattern large area gratings with periods down to 200 nm. E-beam lithography can write 100 nm period gratings but is limited by the proximity effect for more finely spaced features.

In this paper, we report the patterning of large area (90 μm x 20 μm) gratings of 50 nm period in PMMA by soft x-ray achromatic holographic lithography using a synchrotron undulator source. This technique has the ability to write large area gratings with twice the spatial frequency of the finest-period gratings that can be written by electron beam lithography.

The geometry for soft x-ray achromatic holographic lithography is shown in Fig. 1. In both the single and two grating case, a periodic intensity pattern is set up at the recording plane by the interference of two beams. For a parent grating of period d , the overlap of the $+n$ and $-n$ diffracted orders will produce an intensity pattern whose period is $d/2n$ (Fig. 1a). The two grating configuration (Fig. 1b) has the advantage of being insensitive to the source spatial coherence and has been employed previously using deep UV illumination [3]. However the required exposure time can be two orders of magnitude larger than the single grating case since second order diffraction is required. Existing soft x-ray sources lack sufficient brightness to expose the two grating geometry, but reasonable exposure times will be available using undulators at the new Advanced Light Source in Berkeley.

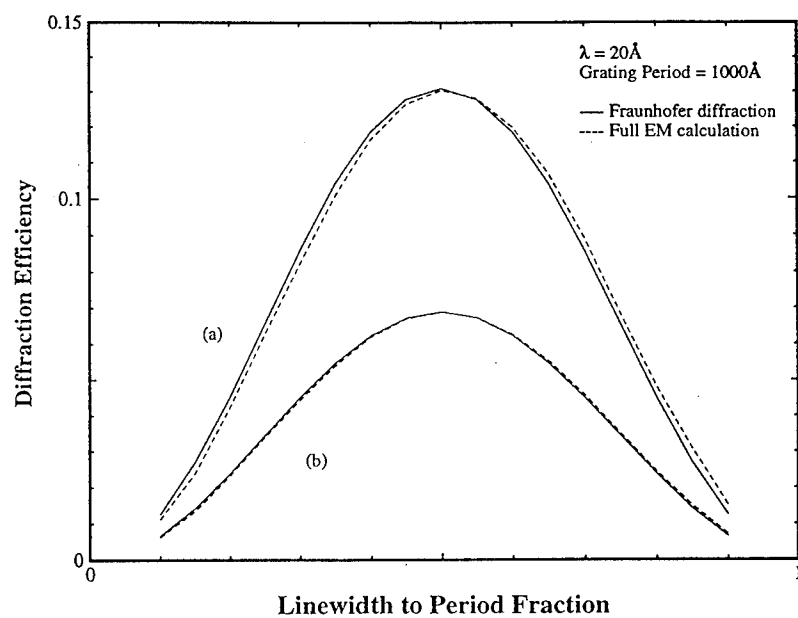


Figure 3. First order diffraction efficiency of soft x-ray phase gratings as a function of linewidth to period fraction, for two different nickel absorber thicknesses. (a) Ni thickness = 1500 Å; (b) Ni thickness = 1000 Å.

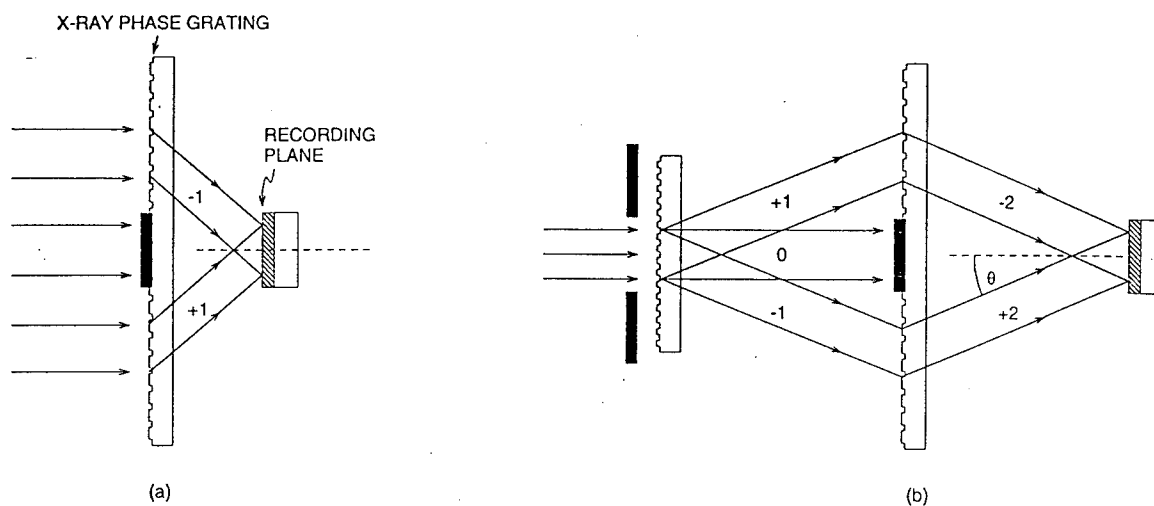


Figure 1. Soft x-ray achromatic holographic lithography using (a) single grating; (b) two grating geometry.

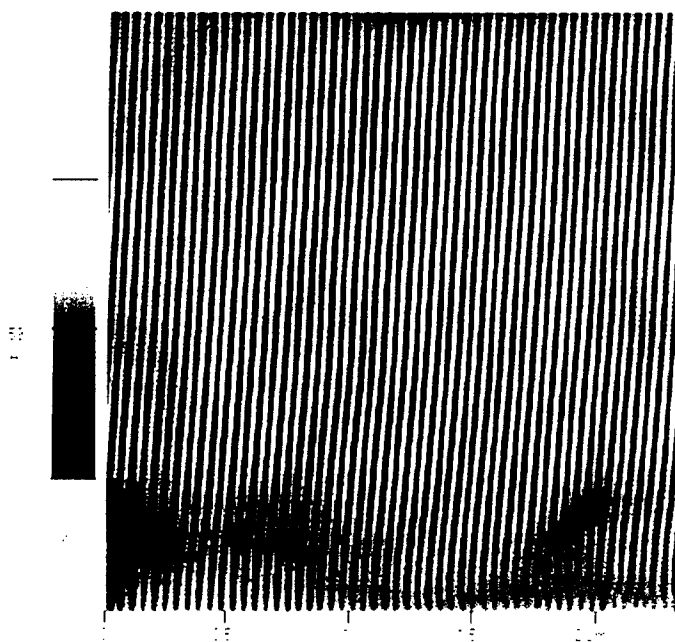


Figure 2. AFM filtered image of 50 nm period grating recorded in PMMA. Total area of grating is $20\text{ }\mu\text{m} \times 90\text{ }\mu\text{m}$.

where each wave is characterized by its amplitude A_n , its wavevector \mathbf{k}_n and its relative phase ϕ_n .

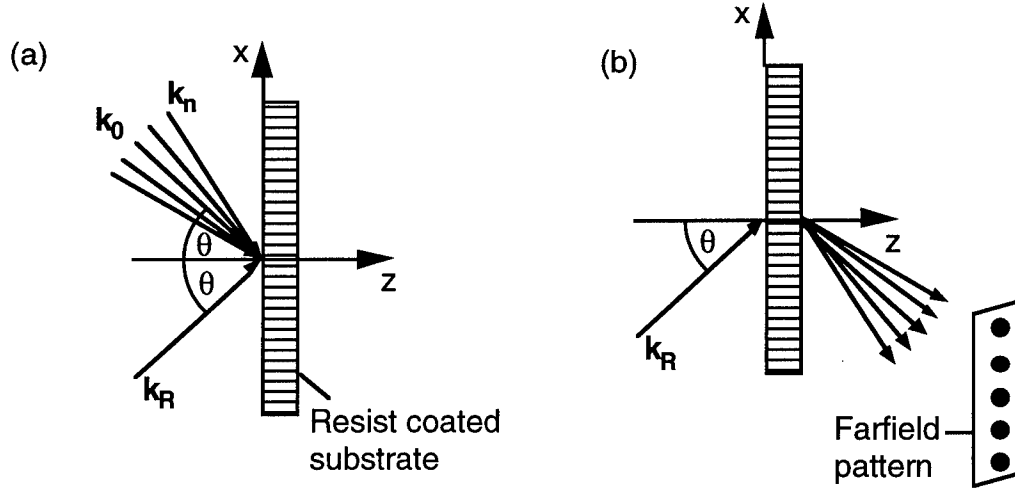


Fig. 1. Recording (a) and read-out (b) of high carrier-frequency DOEs.

For our application, the object wavevectors \mathbf{k}_n must have equally spaced components in the x -direction. By introducing a grating vector \mathbf{K} along the x -axis, this condition can be written as

$$k_n^x = k_0^x + nK; \quad n = -M \dots N, \quad (2)$$

where k_0^x is the x -component of the central object wave. Using Eq. (2), the object wave spectrum (1) can be rewritten as

$$O(\mathbf{x}) = \exp(-ik_0^x \mathbf{x}) A_O(\mathbf{x}) \exp(i\Phi(\mathbf{x})), \quad (3)$$

and the interference pattern of the reference wave and the modulated object beam takes now a form similar to the two-wave case

$$I(\mathbf{x}) = |R(\mathbf{x}) + O(\mathbf{x})|^2 = A_R^2 + A_O^2(\mathbf{x}) + 2A_R A_O(\mathbf{x}) \cos(Qx + \Phi(\mathbf{x})), \quad (4)$$

where $Q = 2\beta \sin \theta$ is the carrier frequency with $\beta = 2\pi n / \lambda$. The object phase $\Phi(\mathbf{x})$ modulates the carrier frequency Q . Therefore, the period in the hologram plane is defined by the grating vector \mathbf{K} and is equal to $\Lambda = 2\pi / K$. Optimized recording conditions are obtained if the intensity fluctuations of the object amplitude $A_O(\mathbf{x})$ are minimized in the hologram plane $z = 0$. The optimization criterion can be formulated as

$$\int_0^\Lambda dx (A_O^2(x, z=0) - \langle A_O^2 \rangle)^2 \rightarrow \min., \quad (5)$$

where $\langle A_O^2 \rangle$ is the mean object intensity. The optimization parameters are the relative phases ϕ_n of the object beam, defined in Eq. (1). The calculation of the optimum phases for a given object far-field intensity distribution is identical to the design of a phase only on-axis DOE [4]. Figure 2 shows one period of the optimized interference pattern (Eq. (4)) for the case of a 9-beam array generator. The remaining intermodulations can be eliminated afterwards by using a strongly nonlinear development. As a result, the sinusoidal interference pattern is then transformed into a rectangular shaped surface-relief grating. The whole object information is now encoded by the

Interferometric and TIR holographic fabrication of high carrier-frequency surface-relief elements

P. Ehbets, H. P. Herzig, P. Blattner, P. Nussbaum

Institute of Microtechnology, University of Neuchâtel, Rue Breguet 2,
CH-2000 Neuchâtel, Switzerland, Tel. (41) 38 205 121, Fax (41) 38 254 276

F. S. M. Clube, S. Gray, J. C. Tisserand

Holtronic Technologies SA, Champs-Montant 12b,
CH-2074 Marin, Switzerland, Tel. (41) 38 336 800, Fax (41) 38 336 501

1. Introduction

Off-axis diffractive optical elements (DOEs) have grating-like structures with submicron carrier frequency. Since at read-out only the zero and the minus first diffraction orders are generated, diffraction efficiencies over 90% can be reached with a binary relief [1]. These grating structures clearly show Bragg diffraction behavior, but are not very selective because of their small thickness. The submicron features require electron beam lithography or interferometric recording methods for their fabrication. Electron beam lithography offers high flexibility for generating arbitrary structures. However, for submicron features this approach is limited by the positioning accuracy during the writing process (typically 50 - 100 nm). Interferometric recording allows a better positioning accuracy. Using an active fringe stabilization system, positioning errors in the order of $\lambda/40$ are possible. Unfortunately, this technology has up to now been limited to simple surface-relief gratings [2]. We show in this paper that almost any object intensity distribution can be interferometrically recorded and transferred to a binary surface relief. In the following sections, we first explain the design of high carrier-frequency surface-relief elements and introduce the principles of interferometric recording. Experimental results have been obtained for a two-dimensional (2-D) off-axis array generator. In a second experiment, we have first fabricated an e-beam mask of a similar element and copied the high-resolution structure very accurately into photoresist using a holographic mask aligner [3].

2. Optimum interferometric recording

The basic configuration for the interferometric recording is shown in Fig. 1 (a). The interference pattern of a plane reference wave and a modulated object beam is recorded. Symmetric incidence of the two beams is necessary, in order to produce fringes perpendicular to the substrate surface. The read-out is shown in Fig. 1 (b). The modulated object beam is generated around the minus first diffraction order of the carrier frequency and produces the desired intensity pattern in the far-field. The reference beam is a plane wave $R(\mathbf{x}) = A_R \exp(-i\mathbf{k}_R \mathbf{x})$ and the modulated object beam can be described by a superposition of plane waves

$$O(\mathbf{x}) = \sum_{n=-M}^N A_n \exp(-i[\mathbf{k}_n \mathbf{x} + \phi_n]), \quad (1)$$

amplitude function of the mask is obtained from the interference pattern of Eq. (4) by neglecting the amplitude variations of $A_0(x)$ and hard clipping the cosine-function to 0 and 1. Using the method of total-internal reflection (TIR) holography, high resolution structures can be photolithographically reproduced by proximity printing. We have used a commercially available holographic mask aligner from Holtronic Technologies SA [3], to copy a grating with a carrier-frequency of 1000 lines/mm into a 1.3 μm layer of photoresist. This holographic mask aligner offers 0.25 μm feature size over an area of 150 mm in diameter from a single printing exposure. Due to the holographic imaging of the structures directly into the resist layer, much sharper transitions of the relief function can be achieved than by direct write methods. Using this technology, we have been able to fabricate high quality off-axis fan-out elements. The measured diffraction efficiency of the elements at a wavelength of $\lambda = 840$ nm was 85%, which is close to the optimized value of 89%. The loss of 4% can be explained by the fact that the resist layer was about 5% too thick. An intensity profile through the generated spot array is shown in Fig. 5. A uniformity error of about $\pm 8\%$ has been measured. We have verified that the uniformity error of the array has not been introduced during the copying process. The original e-beam written mask produces the same errors, which are due to the finite positioning accuracy of the e-beam.

In conclusion, we have shown that interferometric recording offers the resolution and the flexibility for the fabrication of high carrier-frequency surface-relief elements. Holographic lithography has clearly demonstrated its viability for the industrial fabrication of high quality submicron binary gratings.

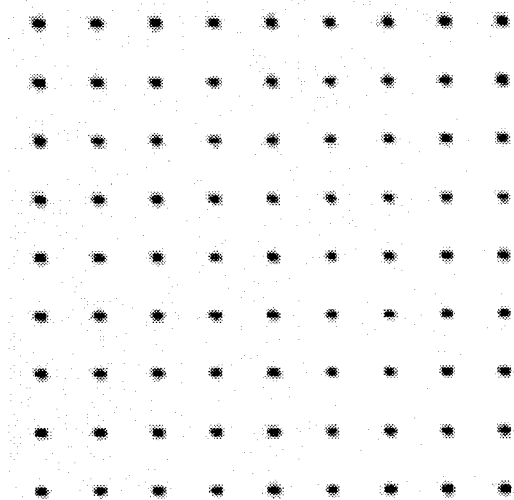


Fig. 4. Generated 9x9 off-axis spot array.

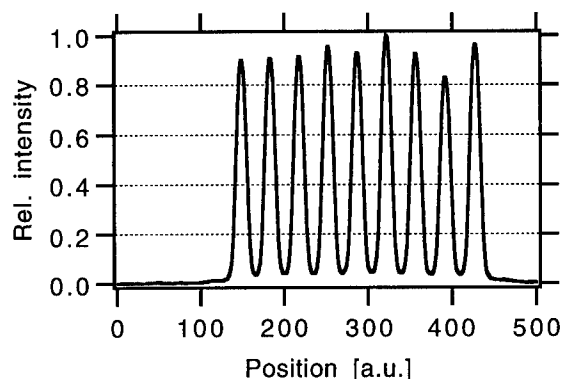


Fig. 5. Intensity profile of the off-axis 9x1 spot array generated by a photolithographic copy in photoresist.

References

1. J. Turunen, P. Blair, J. M. Miller, M. R. Taghizadeh, E. Noponen, "Bragg holograms with binary synthetic surface-relief profile", *Opt. Lett.* **18**, 1022-1024 (1993).
2. M. G. Moharam, T. K. Gaylord, G. T. Sincerbox, H. Werlich, B. Yung, "Diffraction characteristics of photoresist surface-relief gratings", *Appl. Opt.* **23**, 3214-3220 (1984).
3. F. S. M. Clube, S. Gray, D. Struchen, J. C. Tisserand, "Holographic mask aligner", *Opt. Eng.* **32**, 2403-2409 (1993).
4. P. Ehbets, H. P. Herzig, D. Prongué, M. T. Gale, "High efficiency continuous surface-relief gratings for 2-D array generation", *Opt. Lett.* **17**, 908-910 (1992).

continuous phase function $\Phi(x, z=0)$, which locally shifts the carrier frequency.

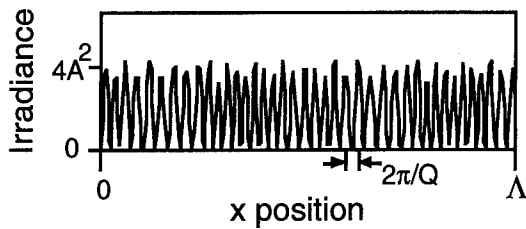


Fig. 2. Optimized interference pattern for a 9-beam off-axis array generator.
($A_R^2 = \langle A_O^2 \rangle = A^2$).

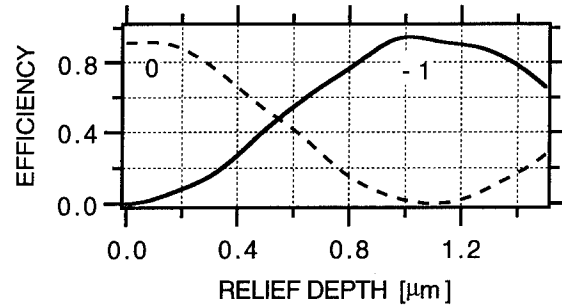


Fig. 3. Overall diffraction efficiencies of the 0 and -1 transmitted orders for a rectangular grating vs. relief depth.

In order to introduce only weak perturbations of the carrier frequency, the period Λ and the total number of object orders ($M+N$) have to satisfy the following relation

$$\Lambda \gg \frac{\lambda(M+N)}{2n\sin(\theta)}. \quad (6)$$

Turunen et al. [1] have shown that if Eq. (6) is satisfied, high diffraction efficiencies can be obtained by optimizing the relief depth of the unperturbed carrier grating. Since the carrier grating has submicron period, rigorous diffraction theory has to be applied. We have used a model based on rigorous coupled wave theory [2] and calculated the optimum thickness of the grating in photoresist for TE polarization. A typical efficiency curve for the minus first diffraction order is shown in Fig. 3 for a transmission grating with a frequency of 1317 lines/mm, calculated for a wavelength of $\lambda = 840$ nm and for a refractive index of $n = 1.63$. The maximum efficiency of 94.8 % is reached for a relief depth $d = 1.02$ μm .

3. Experimental results for interferometric recording

Experimental results have been obtained for 2-D array generators. Different possibilities exist in order to generate the optimized object beam $O(x)$ in the substrate plane. We have used our previous published continuous surface-relief elements for this operation [4]. The phase function of the continuous surface-relief grating is imaged onto the substrate plane using a 4-f lens system. The high carrier-frequency gratings are recorded with an Ar-laser at $\lambda = 488$ nm and then measured at a longer wavelength $\lambda = 840$ nm, which shifts the Bragg angle from 18.7° to 33.6° . Figure 4 shows a CCD picture of the 9x9 off-axis spot array generated by a first grating recorded without any fringe stabilization. Efficiency and uniformity of the array are not yet satisfactory, but with our new fringe stabilization system and improved photoresist processing much better results are expected soon.

4. Copying of submicron gratings using holographic lithography

An alternative fabrication method for high carrier-frequency gratings is first to write an e-beam mask of the desired structure and then transfer the structure using an optical mask aligner. The

it was felt would be the greatest sources of defects in the production of diffractive lenses including the power of the diffractive lenses and hence the number of zones created. One group were designed to simulate the diffractive surfaces on typical hybrid elements, with between 10 and 30 zones, to study the defects introduced when considering the optimisation of elements for broadband applications. A second group were purely diffractive lenses in the range $F/1$ to $F/2$, with hundreds of zones. Due to the high levels of chromatic aberrations and poor off axis performance, the use of fast, purely diffractive lenses is limited to a small number of applications. However, fast, blazed zone plates were chosen as they were considered to be the most demanding lenses to manufacture accurately.

For the two groups of devices it was found that the optimum manufacturing conditions were very different. As the number of materials which are suitable for use in the mid to far infrared is limited, this was also chosen as a variable. Devices were produced using germanium, zinc selenide and zinc sulphide. The tool feedrate was also chosen as a variable. A small number of hybrid achromatic singlets were also produced incorporating the lessons learnt during the production of the slow, planar devices.

To assess the quality of all the devices it was decided to investigate both the macroscopic and microscopic defects. An important periodic, microscopic defect which was investigated was the effect of the tool geometry upon the surface finish, which would force the trade-off with shadowing. In addition to tool geometry another very important source of microscopic, random defects was due to the vibrations of the tool due to the finite stiffness of the machine. To investigate both of these aspects it was decided to machine a number of flat samples and then complete both contact and optical non-contact surface profilometry measurements of the surface roughness. Comparative scatter measurements were also completed, to study the radiation lost due to scatter from random, aperiodic structures and to investigate whether it was possible to observe energy being lost to spurious diffracted orders due to a periodic surface structure. The flat samples were also compared with a standard high quality polished mirror.

Having studied the microscopic defects, the planar, diffractive lenses were diamond turned. For the blazed zone plates a number of qualitative and quantitative measurements were completed to study the accuracy of the surface structure. To do this both contact and non-contact profilometry measurements were completed. Studies were made to investigate any limitations which existed because of the surface gradient at the facet edges, dependent upon the form of the of the shadowing region. The surface quality was assessed using high power optical microscopy and scanning electron microscopy.

The theoretical investigation of the diffractive effects of diamond turned blazed structures.

For a diffractive optical element it is often the aim to design the diffractive surface to direct as much of the incident radiation as possible into the first diffracted order. If the fabrication of the device is not perfect, radiation will be diffracted into other orders, which will not only cause image degradation but also lower the system signal to noise ratio. Having completed the investigation into the defects introduced when diamond turning diffractive surfaces, this information was then incorporated into a theoretical study of optical performance and tolerancing of these elements. To do this it was necessary to calculate the diffraction efficiency of real blazed profile structures. A variety of methods are available for calculating the diffraction efficiency of grating structures, the accuracy is dependent upon any approximations which are made in their formulation [6,7]. Thin regime grating theories can be used to predict the behaviour of grating structures, the amplitude transmittance theory is a good example [8]. This method is accurate for thin gratings, i.e. those with Q values which are very much less than one, where Q is a measure of the optical thickness of the grating,

$$Q = \frac{2\pi\lambda d}{n_0 L^2 \cos\theta}$$

where λ is the free space wavelength, n_0 is the average refractive index, L is the grating period and θ is the angle of incidence inside the medium. However, if the ratio of the free space wavelength to the grating period tends to one, this approximation becomes invalid and the accuracy of the predicted diffraction efficiency decreases. In the work described here, the approximations required for the thin regime expressions had been called into question,

There also exist rigorous methods of calculating the diffraction efficiency of gratings which contain no

An investigation of the defects introduced when diamond turning hybrid components for use in infrared optical systems.

Andrew J. McDowell¹, Patrick B. Conway¹, Andrew C. Cox²,
Richard A. Parker², Chris W. Slinger¹, Andrew P. Wood².

1. Defence Research Agency, St. Andrews Road, Great Malvern, Worcestershire, WR14 3PS, England, U.K.,
Tel: 44 684 89 2733, Fax: 44 684 89 4498, Email: ajmcdowell@dra.hmg.gb

2. Precision-Optical Engineering, 42 Wilbury Way, Hitchin, Herts., SG4 0TP, England, U.K.,
Tel: 44 462 44 0328, Fax: 44 462 44 0329.

Introduction.

The advantages offered by hybrid refractive-diffractive elements are particularly attractive in infrared systems where the material forms a significant proportion of the overall cost and mass and space are often at a premium.

Development of uncooled hand held thermal imagers operating over 8-14 micron waveband [1,2], require optics to be consistent with advantages offered by this camera technology. Hybrid elements allow, for example, passive athermalisation of a lens in a simple aluminium mount to be achieved with the minimum number of elements. For this system, two of the elements will perform the athermalisation and the dispersive properties of a diffractive surface are used effectively as a third material to achromatize the system

In order to realise their full performance potential, hybrid elements must comprise a conventional aspheric lens with a surface relief diffractive structure on one surface [3,4]. Diamond turning permits the aspheric profile and diffractive features to be machined on the same surface in a single process. In principle, the process for the manufacture of hybrid elements is no more complex than that employed for aspheric lenses, which are produced reliably and routinely by diamond turning.

A considerable number of publications over recent years have dealt with the design of hybrid refractive-diffractive optical systems operating in the infrared. By comparison, relatively little has been written about the practical realisation of these systems using, for example, single point diamond turning. This study examines the defects introduced by the diamond turning process and assesses their influence on the performance of surface relief diffractive elements. The results from rigorous coupled wave theory are compared with scalar models and with experimental measurements.

The investigative study of diamond turned diffractive lenses.

Using single point diamond turning it is now possible to produce blazed zone plate structures on aspherical components. However, studies have shown that this method of producing these structures results in the creation of additional unwanted defects [5]. For example, a fast, blazed zone plate with diffraction limited performance may require a large number of zones, typically hundreds. At the centre of such a device, a circular tool of relatively large radius can be used to accurately cut blazed profiles with good surface finish. However, the transitional steps at the boundary of one zone and the next can not be cut accurately due to the tool's finite size. It is not possible for a large radius tool to cut away all the material down to the substrate and retain both the blaze and the vertical step. This has been called the effect of "shadowing". Away from the centre of the zone plate, as the spatial frequency of the grating increases, the inability of the tool to accurately cut the steps grows in importance. This effect limits the size of the smallest facet which can be cut and hence limit the performance of the lens. Conversely, if a circular tool of smaller radius were used to complete the same task, smaller facets could be cut, the effect of shadowing is reduced, but, this leads to the creation of an additional unwanted periodic surface structure, most obvious in the centre.

The aim of this study was to ascertain and quantify the greatest sources of periodic and random defects due to diamond turning diffractive surfaces. To investigate this thoroughly a number of planar, blazed zone plate lenses were produced using controlled manufacturing and design parameters. It was decided to vary those parameters that

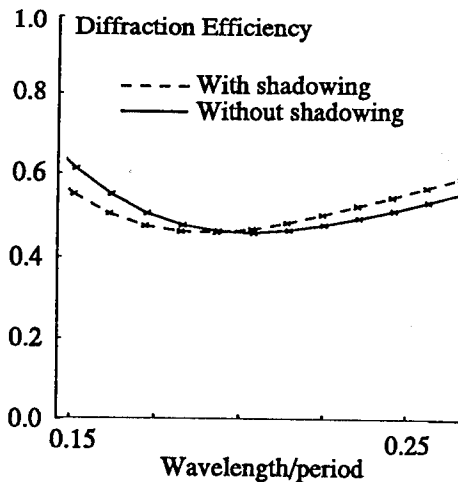


Figure (5).

for the far infrared region (8 μm to 14 μm). The profile chosen was the 100th zone (see figure(2)) with and without the effects of shadowing. Figure (5) shows the sum of the energy being directed into all other orders except for the first, transmitted, diffracted order ($m=-1$). This is for the 100th zone (see figure (2)), with and without the effect of shadowing. A surprising observation is that the shadowing actually improves the elements performance over some of the waveband. These results do not include the effects of anti-reflection coatings, which will enhance the performance accordingly.

Summary.

The results show that the rigorous coupled wave theory can accurately predict the behaviour of diffractive elements, and it has been shown that these defects have a profound effect upon the optical performance of real diamond turned elements. The theoretical results show how the effect of shadowing becomes more important with radial distance from the centre of the lens, and that this defect will have a very serious effect upon lens performance. The results also show how this method of analysis can be used to accurately predict the performance of lenses for a given surface finish, over a given bandwidth. Even a small amount of shadowing has effects on the efficiency and spectral response of the elements. The cases we have highlighted in this summary were designed to show the limitations of diamond turned diffractive elements. Generally speaking, the diffractive surfaces on hybrid (as opposed to purely diffractive) elements have, of course, fewer zones and some of the detrimental effects due to machining will be smaller. However, it is clear that in calculating manufacturing tolerance budgets, these must include accurate diffraction analyses if they are to give realistic predictions of optical system performance.

References.

1. R. Watton, *Ferroelectrics*, Vol. 91, 1989, pp. 87-108.
2. R. Watton and P.A. Manning, *SPIE*, Vol. 807, 1987, pp. 98-105.
3. A.P. Wood, *Applied Optics*, Vol. 31, No. 13, 1 May 1992, pp 2253-2258.
4. A.P. Wood, *Proc. SPIE*, Vol. 1573, Nov. 1991, pp 122-128.
5. M.J. Riedl, *SPIE Vol. CR41, Proceedings of Lens Design conference*, Jan. 1992, L.A., California, pp 140-156.
6. T.K. Gaylord and M.G. Moharam, *Proc. IEEE*, Vol. 73, No. 5, May 1985, pp 894-937.
7. M.G. Moharam and T.K. Gaylord, *J. Opt. Soc. Am.*, Vol. 71, No. 7, July 1981, pp 811-818.
8. R. Magnusson and T.K. Gaylord, *J. Opt. Soc. Am.*, Vol. 68, No. 6, June 1978, pp. 807-809.
9. M.G. Moharam and T.K. Gaylord, *J. Opt. Soc. Am.*, Vol. 72, No. 10, Oct. 1982, pp 1385-1392.

approximations. One such method is the rigorous coupled wave theory which was formulated by Moharam and Gaylord [9]. In this method, a surface-relief grating of arbitrary profile is divided into a large number of thin layers parallel to the surface, within each layer the grating is described as a periodic distribution of two dielectrics, for example, air and germanium. Each thin grating is then analysed by using the state-variables method of solution of the rigorous coupled-wave equations. A computer program was developed to model the diffraction effects of real blazed zone plate facets, together with profiles which also contained the additional unwanted structures such as the periodic turning features and the shadowing at the zone boundaries.

Having developed the code it was then possible to compare the diffraction efficiency of ideal blazed zone plate structures as predicted by the first-order theory, with the results obtained from the rigorous coupled wave analysis, and hence determine the point of breakdown of the scalar approximation. The quantitative data obtained from the diamond machining study were then used to define the profiles of the non-ideal blazed structures and the diffraction efficiencies were calculated using the rigorous coupled wave analysis. By assessing the effects upon the efficiencies of varying the size of the defects on the non-ideal structures, it was possible to ascertain which of the unwanted structures had the most detrimental effect upon the optical performance of the surface. It was then possible to predict for a given performance what would be a tolerable surface quality and hence the optimum machining parameters.

The following graphs show the effect upon the diffraction efficiency of including only a small amount of shadowing at a zone boundary. Two blazed profiles typical of those modelled are shown in figures (1) and (2). The gratings were specified as having a refractive index of 4, a depth of 3.53 μm , which assumed a design wavelength of 10.6 μm . The rigorous coupled wave analysis included in this summary is for the H-mode polarisation only.

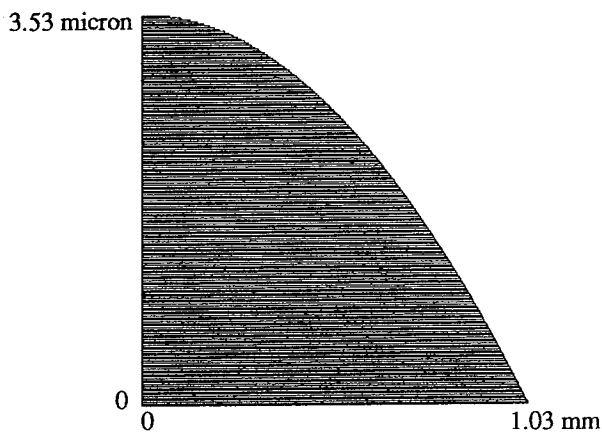


Figure (1). Central zone, blazed profile structure.

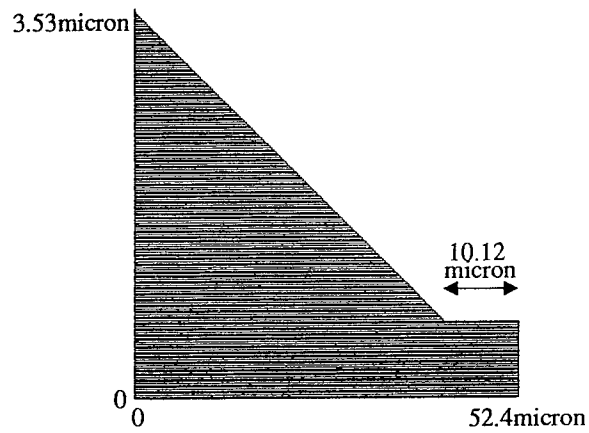


Figure (2). Zone 100, blazed profile with shadowing.

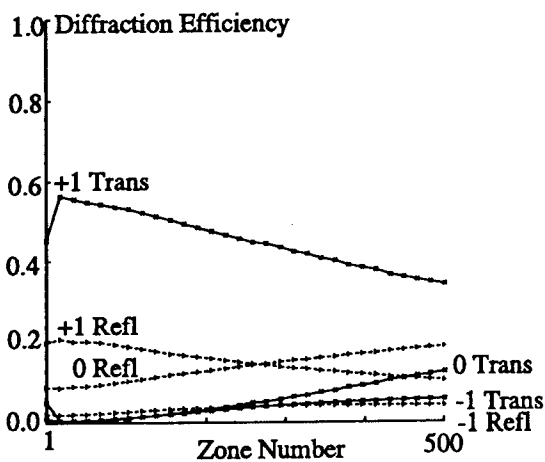


Figure (3).

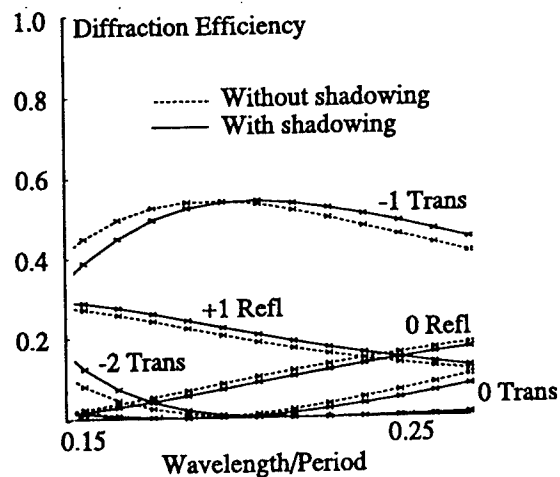


Figure (4).

are near a maxima. Near the maximum, variations in the profile depth would affect the predicted characteristics less than at other depths. Depth error is usually well-controlled and is often not significant. The effect of linewidth error was investigated by designing gratings with three duty cycles ($f=.25,.5,.75$). The depth was set to maximize the efficiency of the +1 order for the given fill factor; two grating periods were analyzed. Results show that the effects of linewidth errors on performance predictions is dependent on the normalized grating, Figure 4. Scalar diffraction efficiency predictions of the diffraction characteristics of binary gratings are independent of the grating period. Thus, it is expected that variations in the fabricated grating period would not significantly affect the predicted performance of binary grating when in the scalar regime. Results confirm this, Figure 5. Gratings were designed from the rigorous to the scalar regime ($\Lambda/\lambda = 1-25$) for maximum efficiency in the +1 order. It is clear from the results that variations in grating period could severely affect the predicted performance in the vector regime. Of course, variations in grating period will affect the angular distribution of the diffracted orders, regardless of the regime. The most detrimental effect of grating period error results from inconsistent grating periods across the element. These inconsistencies cannot be currently modelled accurately at small periods.

NON-SQUARE PROFILES

No fabrication technique is capable of producing crisp, square profiles. Though using a trapezoid to model this error, Figure 6, is only a first-order approximation, it is often in good agreement with actual fabricated profiles⁶. Preliminary, first-order results show that the diffraction characteristics are least affected when the duty cycle of the grating is 50%, Figure 7 ('Trapezoidalness' is defined as half the ratio of the total width of the slanted portion of the profile to the width of the ridge). Another common form of fabrication error is the 'scalloped' profile, Figure 8. Current work is being done with these profiles. For higher-order accuracy, models could be enhanced by forming a piece-wise linear approximation of the error created by the process.

SUMMARY

Recent advances in fabrication technology have yielded an improvement in the quality of binary gratings. Subsequently, binary gratings with feature sizes that are large enough to be analyzed with scalar diffraction theory can also be fabricated without significant error. By investigating the process errors associated with small featured gratings, it is anticipated that *a priori* information may be used in the design stage to compensate for specific fabrication process errors.

Effects of Fabrication Errors on the Performance of Binary Gratings

Drew A. Pommet, M. G. Moharam, and Eric B. Grann
 Center for Research and Education in Optics and Lasers
 University of Central Florida, Orlando, FL 38286
 (407)658-3983 Fax: (407) 658-6880 dap@sphinx.creol.ucf.edu

INTRODUCTION

A myriad of tools exist, ranging from scalar/Fourier theories to rigorous electromagnetic techniques, to design and analyze binary gratings. Regardless of the accuracy of the tool, the diffraction characteristics predicted are dependent on the exact dimensions of the profile analyzed, i.e., deviations from these dimensions will yield different diffraction characteristics. Thus, when a grating is fabricated, the diffraction characteristics must change from those desired, since all fabrication processes produce some error in the dimensions of the grating profile. Previous work exists¹⁻³ detailing the effects of processing errors. However, due to recent advances in fabrication technology, gratings that can be analyzed in the scalar regime⁴ are minimally affected by fabrication errors. Therefore, it is important to investigate fabrication errors for gratings with small features, since it is these gratings that are the most difficult to fabricate. In this paper, effects of fabrication errors will be rigorously analyzed for small grating features. In addition, the effects of the inability to etch or mill a crisp, square edge on the predicted performance will be investigated. Finally, we look to see if *a priori* information about the fabrication process may be used in the design stage for error compensation.

EFFECTS OF FABRICATION ERRORS

Errors involved in the fabrication of surface-relief gratings, Figure 1, include depth, d , duty cycle (linewidth), f , and grating period, Λ . To analyze the effect of depth error on the predicted performance, single-level binary gratings were designed to yield maximum scalar diffraction efficiencies in the +1 order, ($f = .5$, $d/\lambda = .5/(n-1)$) for various normalized grating periods ($\Lambda/\lambda = 2,5,10$), where λ is the wavelength of light. The profiles were then analyzed with depths that strayed from optimal depth by $\pm 5\%$. The analysis technique used was the well-established Rigorous Coupled Wave Technique (RCWT)⁵. Results show that variations in grating depths significantly affect the predicted performance when the normalized grating period is small, Figure 2. In addition, gratings were designed and analyzed at depths that did not maximize the diffraction efficiency. The purpose of this was to show that fabrication errors at these depths would affect the diffraction predictions more than at the optimal depth, Figure 3. This is because the slope of the diffraction efficiency curves are close to zero since they

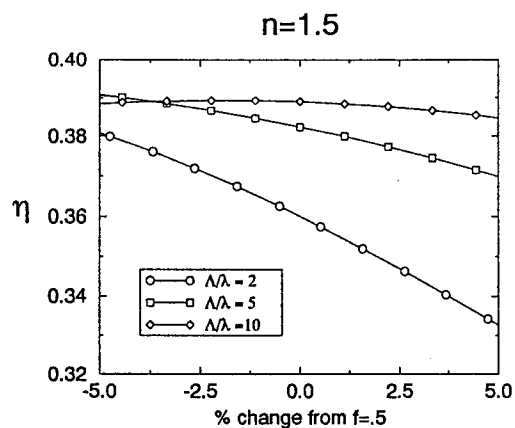


Figure 4: Error in fill factor (linewidth).

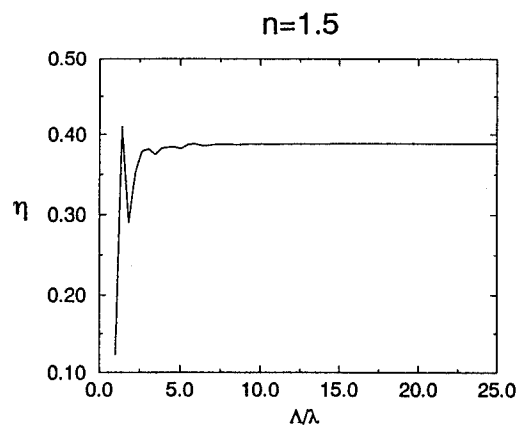


Figure 5: Error in grating period.



Figure 6: Trapezoidal model.

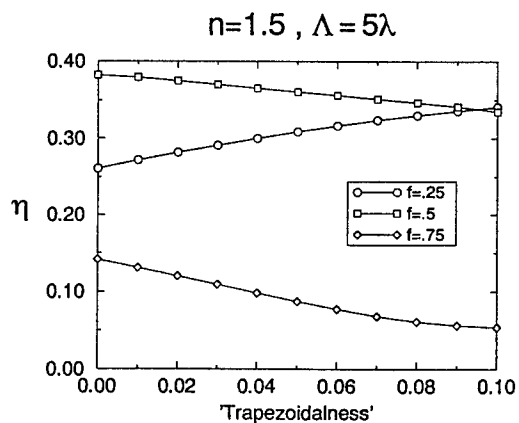


Figure 7: Effect of trapezoidal profile on predicted performance.

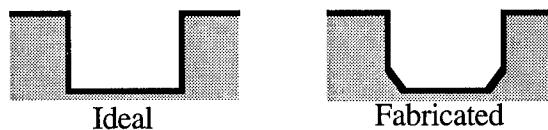


Figure 8: Scalloping model.

REFERENCES

1. J. A. Cox, "Processing error limitations on performance of diffractive optical elements", in *Diffractive Optics: Design, Fabrication, and Applications Technical Digest*, 1992 (Optical Society of America, Washington, DC, 1992), Vol. 9, pp. 143-145.
2. J. A. Cox et al., "Diffraction efficiency of binary optical elements," *Proc. SPIE*, Vol. 1211, pp. 116-124, 1990.
3. M. W. Farn and J. W. Goodman, "Effect of VLSI fabrication errors on kinoform efficiency," *Proc. SPIE*, Vol. 1211, pp. 125-136, 1990.
4. D. A. Pomet, M. G. Moharam, and Eric. B. Grann, "Limits of scalar diffraction theory for diffractive phase elements", *J. Opt. Soc. Am. A* 7, pp. xx-xx, April 1994.
5. M. G. Moharam and T. K. Gaylord, "Diffraction analysis of surface-relief gratings," *J. Opt. Soc. Am.* 72, pp. 1385-1392, 1982.
6. S. J. Walker et al., "Design and fabrication of high-efficiency beam splitters and beam deflectors for integrated planar micro-optics systems," *Appl. Opt.* 32, pp. 2494-2501, 1993.

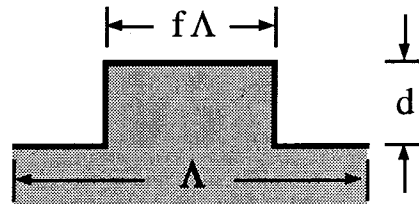


Figure 1: Unit cell of a binary gratings (depth, d , fill factor, f , period, Λ).

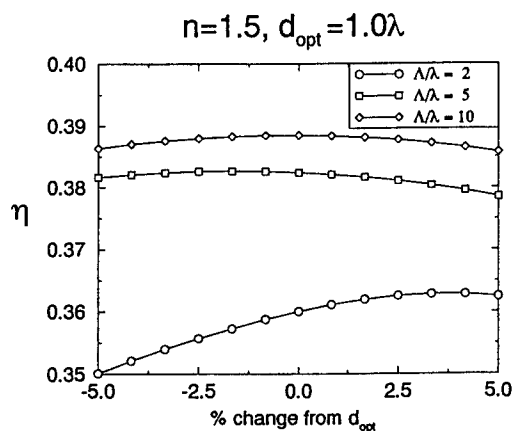


Figure 2: Depth error at optimal depth, d_{opt} .

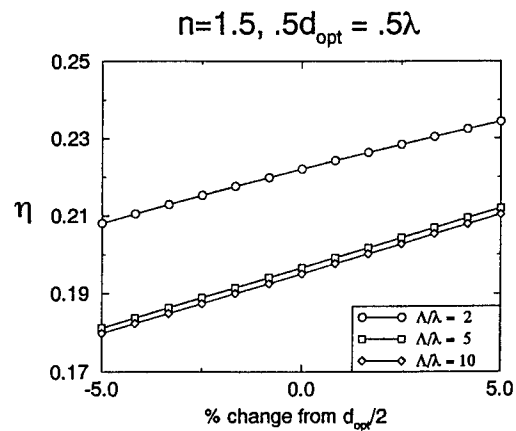


Figure 3: Grating not at optimal depth.

New Developments in the Diffraction Behavior of Echelle Gratings

By Erwin G. Loewen	Daniel Maystre	Evgeny K. Popov	Lyubomir Tsonev
Milton Roy Co.	Lab.d'Optique Electromagnetique	Institute of Solid State Physics	Inst.of Solid Sate Phys.
820 Linden Ave	Univ.d'Aix-Marseille III	Bulgarian Academy of Sciences	Bulg. Acad.of Sciences
Rochester NY	Marseille,France	Sofia, Bulgaria	Sofia, Bulgaria
Tel. (716)248-4205		(Currently Marseille,France)	
Fax (716)248-4014	33-9167-4428	33-9167-4428	

Introduction

Echelle Gratings find increasing use in modern spectrographs, especially in astronomy, because of their unique ability to provide high dispersion combined with high efficiency over a large spectral range. Available in ruled widths upto 408 mm, with blaze angles upto 76° , sometimes even greater, they provide near perfect wavefronts. This means high resolution, and minimal ghost intensities and stray light. Typically used in orders 10 to 150 it is a long held tradition that their diffraction behavior can safely be considered to lie in the scalar domain.

Recent work, both experimental and theoretical, has shown that this is not always true. Especially when diffraction angles are at the high end, and when orders are at the low end, some peculiar effects can be seen. Whether these are harmful or not depends on the application. Particularly gratifying was to find that rigorous electromagnetic theory could, for the first time, be extended to accurately represent these gratings, for which computational barriers had seemed insurmountable. Correspondence between theory and experiment was good enough so that discrepancies could be largely blamed either on insufficient knowledge of the exact groove geometry or of the the complex refractive index of the thin metallic film that makes up the surface of a replica grating.

Experimental Work

Since spectrographs typically operate at constant angles of incidence it would have been ideal to test echelle behavior similarly and vary the input wavelength. To do this properly requires a source whose monochromaticity matches the high dispersion, and has the ability to determine wavelength to the nearest 0.1 \AA . In other words a super dye laser. Since none was available to us we used instead a collection of gas and ion lasers covering a wavelength span of 441 to 676 nm, and at each wavelength observed the diffracted output as the angle of incidence was varied in small increments over a span of about 16° . Groove frequency varied from 31.6 to 316 per mm. A solid state detector picked up all the orders within the 16° range. Groove angles were either 63.5° and 76° nominal. A series of experimental examples are shown below, some compared with theoretical calculations for which perfect right angle triangular groove profiles were assumed. It seems too difficult to measure groove geometry to the accuracy required to really make a difference.

Theoretical Work

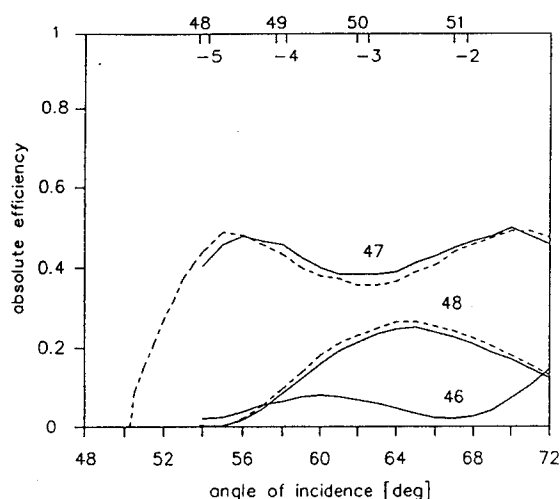
The problem with applying Maystre's integral formalism for efficiency calculations of echelles has been the need to invert much larger matrices that correspond to the unusually large number, of diffracted orders, all of which receive at least some energy. A new approach has circumvented this difficulty, at least as far as grooves $31.6 \mu\text{m}$ wide. The surprising evidence of Woods anomalies with echelles was discovered first on the computer and then verified by experiment.

Tuesday, June 7, 1994

Poster Preview and Poster Session

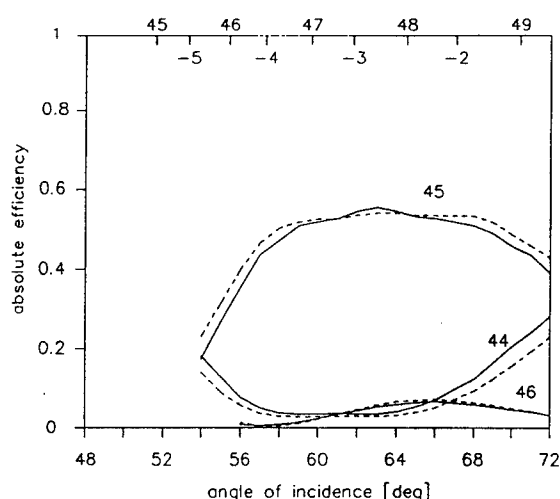
DTuB 10:30am–12:30pm
Room B

G. Michael Morris, *Presider*
University of Rochester



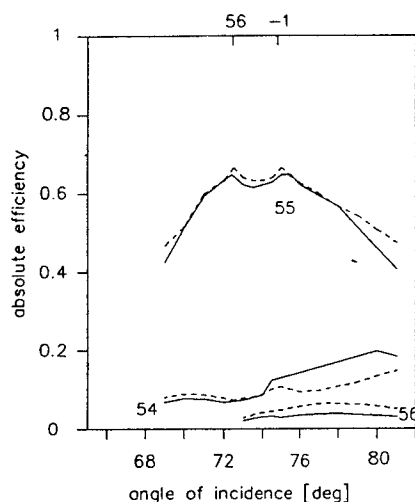
Absolute efficiency of 79 g/mm Echelle, 63.0° Blaze angle, as a function of α . — TE and TM designate planes of Polarization. Orders are labeled, as are pass off limits.

EXPERIMENTAL at 476.5 nm



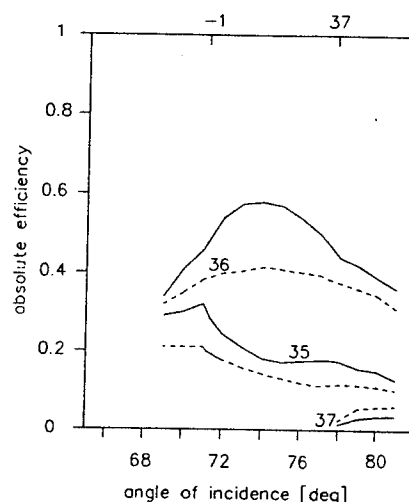
EXPERIMENTAL at 501.7 nm

At 476.5 nm we are in the half-order position, which explains the drop in efficiency at the nominal blaze angle. Latter can be accurately determined from the approximate locations of the two peaks of the main diffracted order (56° and 71°). The 501.7 nm wavelength happens to fall within 0.1° of the blaze angle. Passing off order effect is barely detectable.



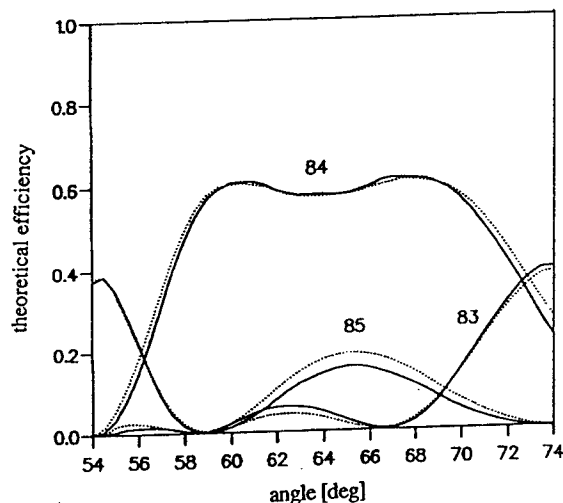
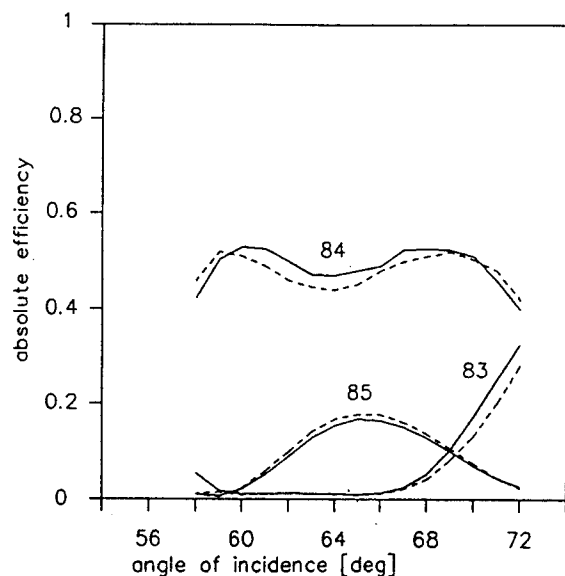
Absolute efficiency of 79 g/mm Echelle, 73° blaze angle, measured as function of α . — TE, and TM designate planes of polarization. Diffraction and pass off orders are labeled.

EXPERIMENTAL at 441.6 nm



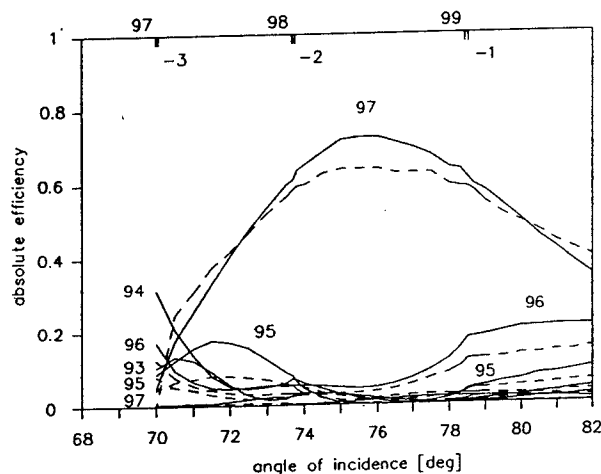
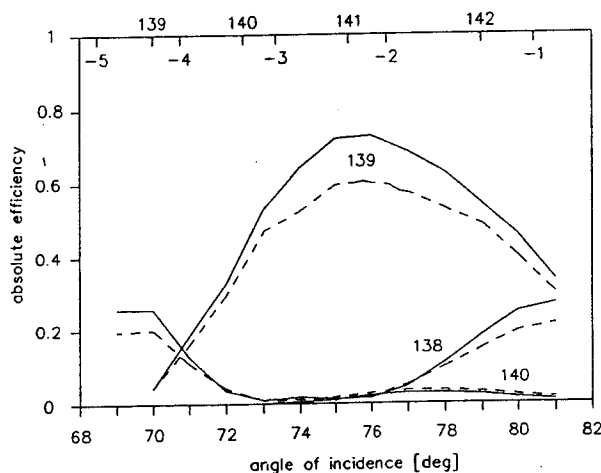
EXPERIMENTAL at 676.4 nm

Unusual is the pronounced trough in efficiency near the blaze peak at 441.6 nm, which is caused by a central 2° wide band where both the -1 and +56th order can diffract. The opposite holds at 676.4 nm, where between 71° and 77° incidence neither the adjacent -1 nor the +37th orders can diffract, thus making extra energy available. However, it shows up strongly only in the TE plane, leading to high polarization that was not confirmed by theoretical calculations.



Absolute efficiency at 676.4 nm of 31.6 g/mm Echelle, 64.48° Blaze Angle, as a function of α , the angle of incidence. — TE and TM designate planes of Polarization. Orders are labeled.
EXPERIMENTAL **THEORETICAL**

Note the low level of polarization and close match between experiment and theory. The saddle shape indicates that the Littrow condition is not near the center of the (84th) order (1/3 order position).



Absolute efficiency of 31.6 g/mm Echelle, 75.6° Blaze angle. as function of α . Boundaries of passing-off orders is indicated at top. — TE and TM designate Planes of Polarization
EXPERIMENTAL $\lambda = 441.6$ nm **EXPERIMENTAL $\lambda = 632.8$ nm**

Note fairly strong polarization at this high order and blaze angle. The - order pass off shows angle to the right of which the order cannot diffract and + orders show limits to the left of which that order cannot diffract. The effect of passing off orders is small but detectable, a manifestation of Woods anomalies where they were not expected.

Edge Diffraction Theory for Phase Apertures

William H. Southwell
Rockwell International Science Center
1049 Camino dos Rios
Thousand Oaks, California 91360
(805) 373-4485 phone
(805) 373-4775 fax

It is a correct model to consider light propagating around an abrupt edge as consisting of the original beam in the exposed region (this component is zero in the shadow region) plus a diffraction term that makes the edge appear as a radiating source. In the past several years this edge diffraction function has been refined using contour integration in the complex plane and asymptotic methods. For rectangular aperture geometries the amplitude of the diffracted wave from an illuminated edge is given by¹

$$D(x', z, x) = i(i/2)^{1/2} \Phi(h) \exp(-i\pi h^2/2), \quad (1)$$

where

$$h = [2/(\lambda/z)]^{1/2} |x' - x|, \quad (2)$$

$$\Phi(h) = f(h) + ig(h), \quad (3)$$

$$f(h) = (1 + 0.926h)/(2 + 1.792h + 3.104h^2) \quad (4)$$

$$g(h) = 1/(2 + 4.14h + 3.492h^2 + 6.67h^3). \quad (5)$$

As shown in Fig. 1, x' is the position of the diffraction edge, z is the distance to the field point or observation plane along the direction of the incident wavefront, and x is the position in the field plane.

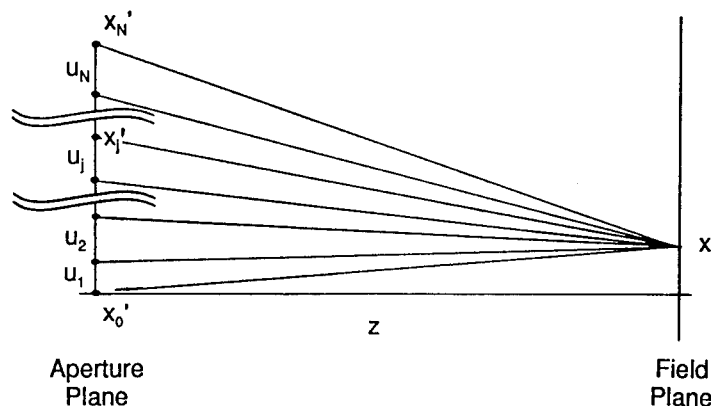
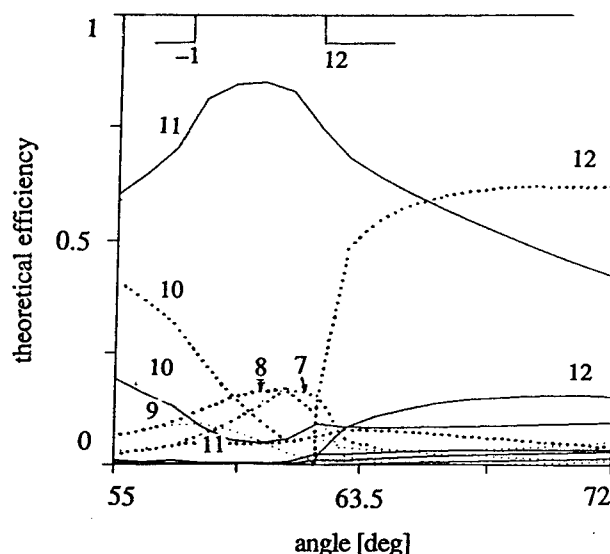
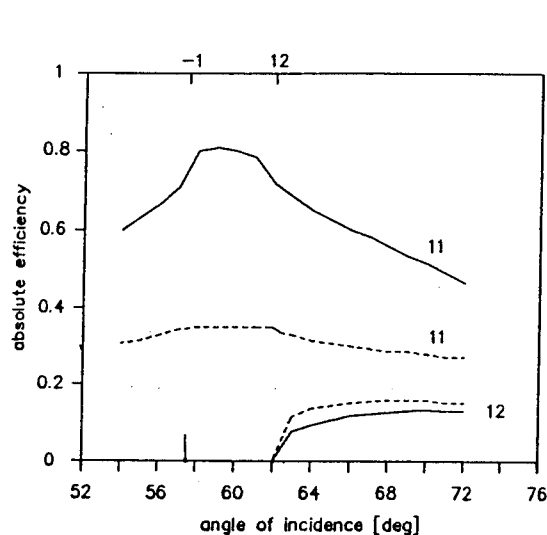


Fig. 1. Sketch showing the summation of edge diffraction terms from boundaries between each zone having a different aperture field u_j .

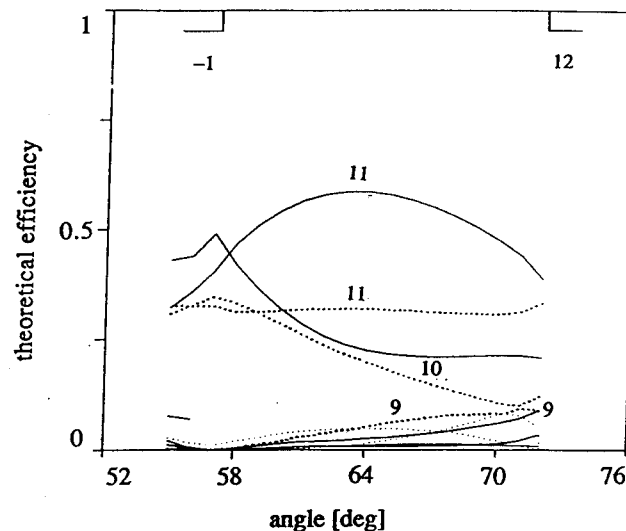
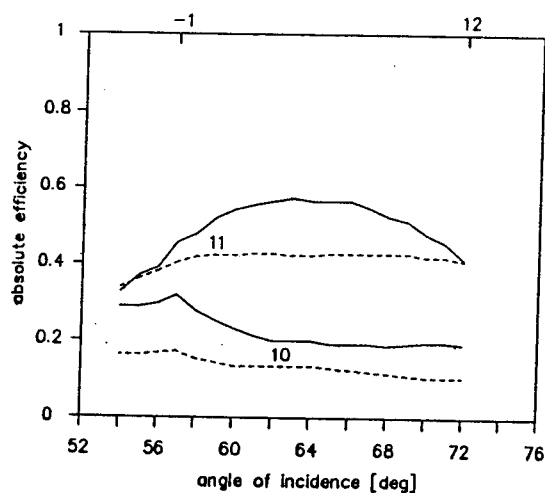


Absolute efficiency of 316 g/mm Echelle, 63.4° Blaze angle, as a function of α , at 496.5 nm
 — TE and TM designate planes of Polarization. Orders are labeled, as are pass off limits.

EXPERIMENTAL

THEORETICAL

Clearly evident is the close match in the TE plane (electric vector parallel to the grooves) between experiment and theory, which is typical. In the TM plane the behavior is quite different, and not yet explained. At this wavelength we are near the half order position (0.4).



Absolute efficiency of 316 g/mm Echelle, 63.4° blaze angle, measured as function of α , at a wavelength of 514.5 nm — TE, and TM designate planes of polarization. Diffraction and pass off orders are labeled.

EXPERIMENTAL

THEORETICAL

At this wavelength we are right in the center of order 11, which leads to quite different behavior. Polarization is seen to be reduced compared to the previous data, and the efficiency match between theory and experiment, even in the TM plane, is good. The influence of the -1 order passing off is clearly expressed in both the 10th and 11th orders.

and to demonstrate its accuracy. For convenience we define the fields in the aperture zones as

$$u_i = [T_i]^{1/2} \exp(i\pi\phi_i), \quad (10)$$

since T_i and ϕ_i are often unity.

As a first example we propagate a uniform field from a single aperture in the near field using the Fresnel-Kirchhoff integral. The result is shown on the left of Fig. 2. On the right side in Fig. 2 is the result using the diffraction from the two edges.

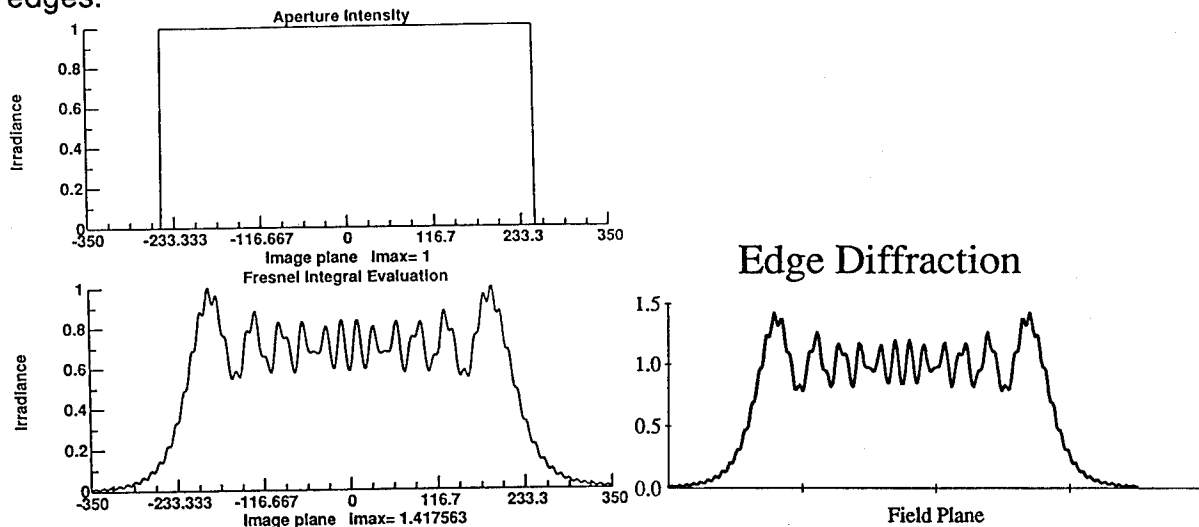


Fig. 2. Comparison of edge diffraction with Fresnel integral calculation.

The Fresnel integral requires the evaluation of the field throughout the aperture, whereas the diffraction approach consists of a constant plus two diffraction function evaluations, no matter how large the aperture is. An internal edge is shown next.

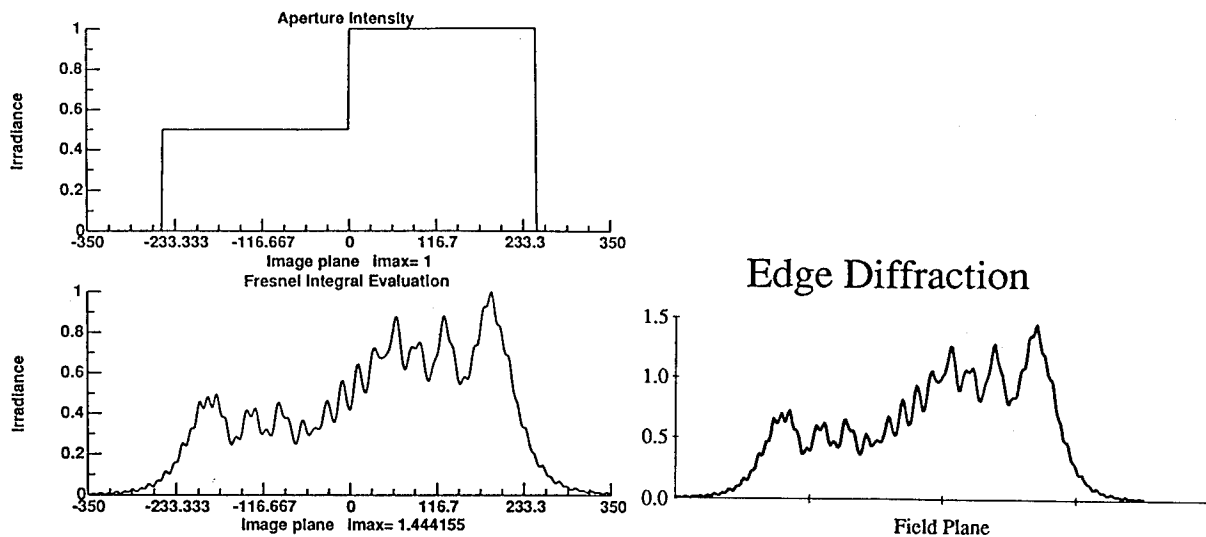


Fig. 3. An example to verify the diffraction approach for an internal edge.

This D function has the property that when it is combined with the incident field in the exposed region and in the shadow region the incident field is zero and D changes sign, that the total field is continuous across the shadow.

In this paper we extend this concept of edge diffraction to include other regions of an aperture (besides the limiting stop edges) that consist of lines across which the transmissivity changes either a little or a lot or the phase changes either a little or a lot. This includes phase gratings, binary optics surfaces, and apertures that have apodized transmission.

The general case under consideration is the line separating two zones in an aperture wherein each zone has a different complex electric fields u_a and u_b . We assume an incident uniform wavefront is propagated through this aperture and the shadow position in the field plane is identified. The approach is to consider the wavefront from the aperture as consisting of a superposition of two apertures, one for each zone. That is, each zone transmits inside itself and zero elsewhere. Thus in the field plane to the left of the shadow line, the propagated electric field e_a consists of its incident field u_a plus the diffracted field from its edge $u_a D$ (the strength of the diffracted field is proportional to the strength of the incident field), plus the shadow diffraction of the other zone, $-u_b D$. We can therefore write the fields in each region in the field plane,

$$e_a = u_a(1 + D) - u_b D = u_a + (u_a - u_b)D, \quad (6)$$

$$e_b = u_b(1 + D) - u_a D = u_b + (u_b - u_a)D. \quad (7)$$

The right hand sides of these equations may be interpreted as saying that the propagated field from an aperture containing a zone boundary is equal to the incident field plus a diffraction term that is proportional to the *difference* of the field amplitudes across the zone. This difference is computed as the field in the zone you are in minus that of the zone across the boundary.

For an aperture of N zones as shown in Fig. 1, there are N + 1 edges. The first step is to determine which zone J exposes the current field point x. That is, find J such that

$$x_{J-1}' < x \leq x_J', \quad (8)$$

where the x-primes are the zone boundaries in the aperture. The total field in the field plane is given by

$$e(x) = u_J + \sum_{k=1}^J (u_k - u_{k-1})D(x_{k-1}', z, x) + \sum_{k=J}^N (u_k - u_{k+1})D(x_k', z, x). \quad (9)$$

Equation (9) is our final result. We show some examples to illustrate its usefulness

FRESNEL INTERFERENCE OBSERVED BY MEANS OF ZONE PLATES

V.P.Koronkevitch

Institute of Automation & Electrometry of Russian Academy of Science, Siberian Branch.

Universitetskij Prospekt, 630090 Novosibirsk, Russia.

Fax: (3832) 35 48 51. E-mail: koronkev.@iae.nsk.su

I.G.Pal'chikova

Institute of Automation & Electrometry of Russian Academy of Science, Siberian Branch.

Universitetskij Prospekt, 630090 Novosibirsk, Russia.

Fax: (3832) 35 48 51. E-mail: palchikova@iae.nsk.su

When a zone plate (ZP) [1] is illuminated by a point light source, non-localized Fresnel fringes [2] are formed in the image space behind the plate. The zone plate acts as a interferometer forming the interference field in some respects much as Fresnel's or Lloyd's mirrors. In ZP-interferometer a recombination of interfering beams is realized without any additional optical components.

The present communication concerns the properties of interference fringes observed by means of Fresnel, Soret and Rayleigh – Wood zone plates.

A basic optical scheme for the observation of interference fringe pattern, and the path of rays of +1st, -1st and 0 diffractive orders through a ZP are shown at Fig. 1. Special properties of the wave front division by ZP [1], and sharp differences in the magnitudes of order intensities [1] result in formation of the peculiar interference pattern. Thus, for Fresnel ZP, if the distance L from ZP to the observation plane ten times as much as the focal length f , $L > 10f$, then two-beams [+1st, -1st] order interference prevails. As the screen gets closer to the ZP, the number N of interfering beams increases, and at $L < 2.5f$, multibeam fringes are always observed. The peaks existing in the two-beams pattern are preserved, although each of them shrinks into more narrow angular region. Between two-beam peaks, $N-2$ additional peaks corresponding to new supplementary two-beams patterns appear.

The calculation of beam travel differences and estimation of radial coordinates of two-beams interference peaks is considerably simplified if the path from S to source images S' and S'' is not taken in to account because it is constant. Then spherical waves from S, S' and S'' interfere in P . When $L > f$, the calculation of path differences is reduced to estimation of differences between sags of wave fronts from S, S' and S'' . In Fig. 1, S and S' are source images in the +1st and -1st diffraction orders.

For arbitrary distances l and L , and arbitrary pairs (n, i) of interfering beams, the following relation for radii of maximum intensity rings is valid:

$$R_k = \sqrt{\frac{2k\lambda f}{\delta(n, i)}}, \quad k = 1, 2, 3 \dots \quad (1)$$

where λ is the wavelength, $\delta(n, i)$ is a constant depending on the numbers n and i of diffraction orders and on

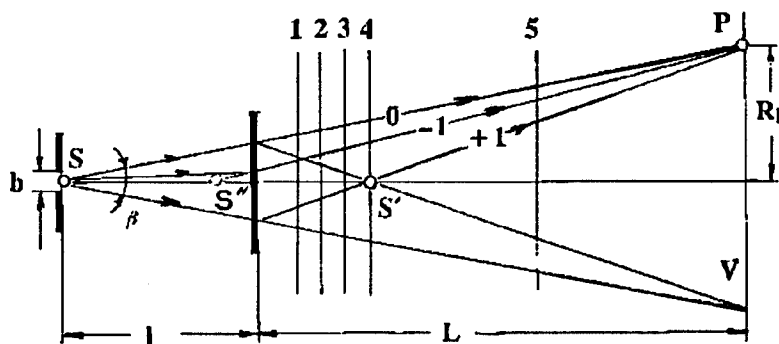


Fig. 1.

A Fresnel zone plate is shown in Fig. 4. It is evaluated in one case with alternate zones zero transmission and with alternate zones having a pi phase shift.

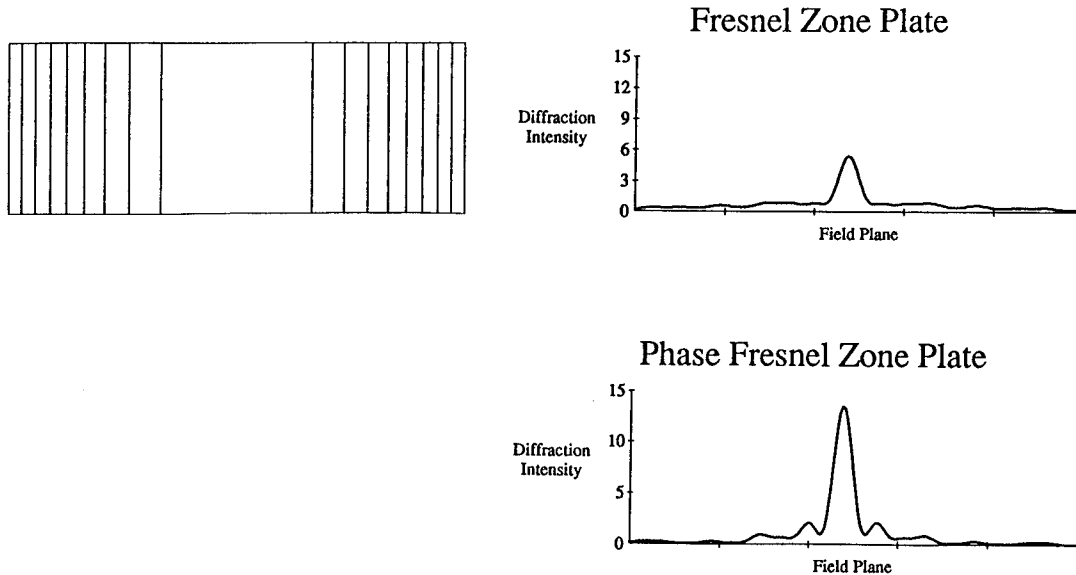


Fig. 4. Fresnel and a phase Fresnel plate evaluated using edge diffraction.

The last example is six slit diffraction to compare with a common result.

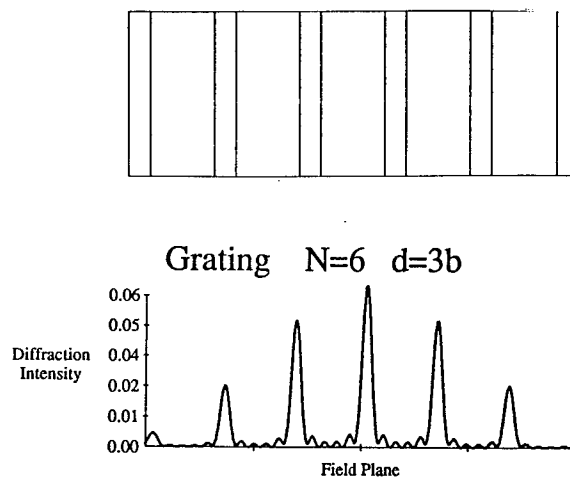


Fig. 5. Six slit diffraction grating evaluated using edge diffraction theory.

1. W.H. Southwell, "Unstable-resonator-mode derivation using virtual-source theory," J. Opt. Soc. Am. **3**, 1885-1891 (1986).

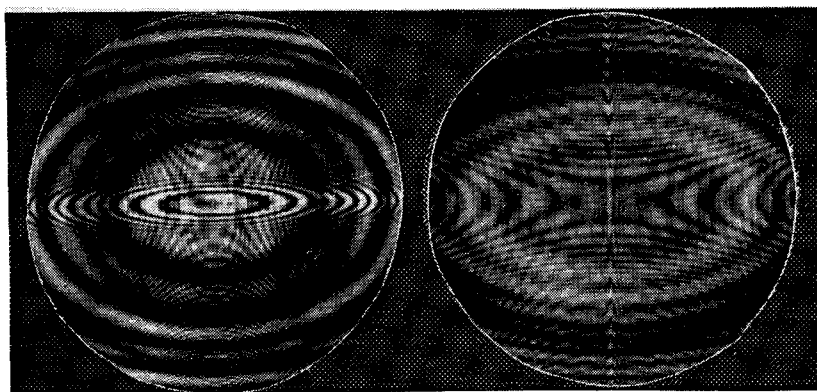


Fig. 4.

the wave length λ and the angular size β of the source must be associated by the relation

$$b \leq \lambda / \sin \beta.$$

This is a usual condition for observing the Fresnel interference which is not strict for laser sources or illumination by means of optical fibers.

The distinction of the pattern is determined by the enormous ZP chromatism ($\Delta f/f = \Delta\lambda/\lambda$). The focal point for the red region of the spectrum is formed on blue-green background, and for the violet one - on red background. Respectively, interference fringes are observed on a colored background. An interesting distinction is also color inversion in the fringe coloring when it passes through the focus.

The interference field under consideration carries a complete information about parameters and quality of the ZP and about the spectral and modal structure of the light. By the coordinates, contrast and brightness of fringes one can determine the focal length and ZP's aberrations, the correctness of fabrication of the diffraction structure and of its phase depth. A characteristic example is shown in Fig. 4, where interference field was obtained with a help of elliptic ZP. Astigmatic beam structure can be easily identified. The use of ZP-interferometer for the synthesis of diffraction elements with a high spatial frequency for operation in the X-ray region of the spectrum is well known [3]. From our studies it follows that ZP-interferometer is a good tool for the estimation of a quality of zone plates, for the investigation of a modal structure of radiation sources, and for the demonstration of the light interference phenomena in large auditoria during lectures.

REFERENCES

1. Koronkevich V.P., Pal'chikova I.G., Modern zone plates, *Optoelectronics, Instrumentation & Data Processing*, 1992, no. 1, p. 86-101.
2. Shmahl G., Rudolph D., Guttman P., Christ O., Zone plates for X-ray microscopy, in: *X-ray Microscopy*, Springer Series in Optical Sciences, vol. 43, p. 87-101, Springer-Verlag, 1984.
3. Vavilov S.I., Complete Works, vol. II, *Academy of Sciences of USSR*, Moscow, 1952, p. 466-477.

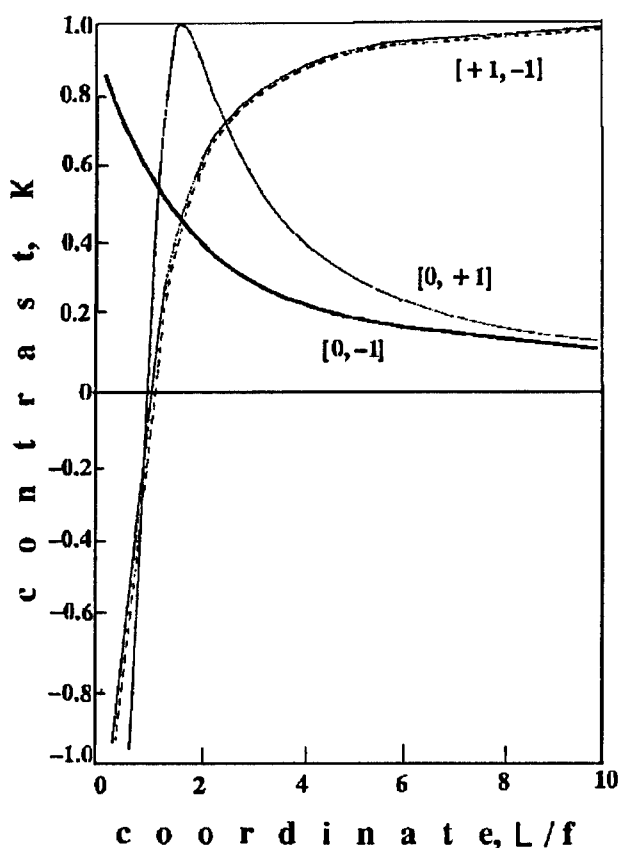


Fig. 2.

In sections 1, 2 and 3 in the field center, $[+1, -1]$ type two-beams fringes are visible. The position of planes is chosen so as to demonstrate the formation of a dark central fringe (contrast inversion) due to Gui effect. In section 5, the field center corresponds to two-beam fringes of $[+1, -1]$ type which dominate in the interference field during the screen gets further from the ZP. An important peculiarity of the interference pattern is the fact that central fringes are formed at path differences close to zero (see Fig. 1). They are achromatic and can be observed in white light.

The brightness and the contrast of interference fringes depend on the light source size, i.e., the slit width b ,

positions of the screen and of the source. The relation (1) corresponds to the Newton's rule: "...the radii of the rings are related to each other as square roots of integers."

The contrast of two-beams interference patterns K is

$$K = 2\sqrt{m} / (m + 1) \quad (2)$$

where m is the ratio of intensities of interfering beams which depends on the ZP type, the screen and source position, and the distance of the observation point from the optical axis.

In Fig. 2, calculated curves of contrast changes depending on the position of the screen L/f for zero and ± 1 st order interfering beams are shown. From the graphs it follows that at the distances $L > f$, the main contribution to the interference pattern is made by two-beams fringes of $[+1\text{st}, -1\text{st}]$ orders. The change of the contrast sign indicated the inversion of light and dark fringes after the light wave has passed through the focus. The calculation results are well corroborated by experimental data.

In Fig. 3, photographs of interference field in sections marked in Fig. 1 by numbers from 1 to 5 are presented. In the plane 4, a beam of the $+1$ st order is focussed into a bright central spot S' . In this way, $+1$ st order beam is filtered out of the interference pattern. The field is filled by two-beams fringes of zero and -1 st orders. They are well observed also in other planes.

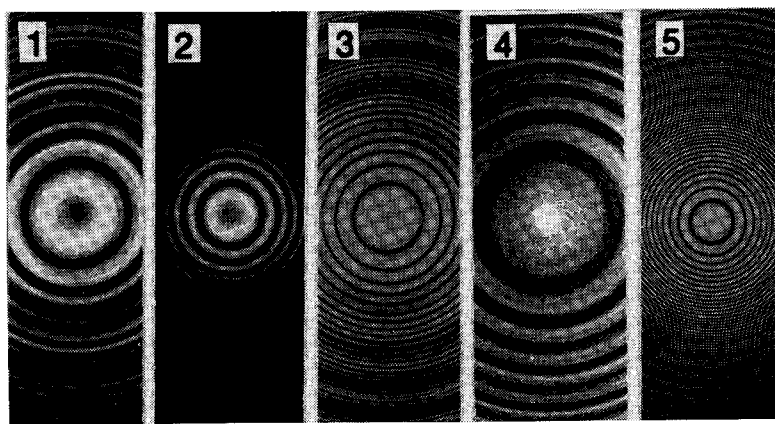


Fig. 3.

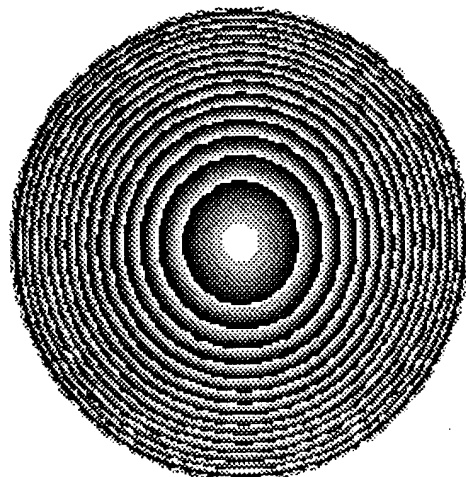


Fig. 1. PostScript output of a 32 gray level lens generated in *Mathematica*.

This halftone screen can be converted to a smooth gray scale by recording a spatially filtered image of the halftone. This was done using the set up in Fig. 2. A reticle, which is a 10X reduction of the original transparency, is located at the center of radius of curvature of a spherical mirror. A beamsplitter is inserted in the light path between the mirror and the focal length. The image in this unity magnification system is reflected off-axis by the beamsplitter to a high resolution holographic plate (8E75). An aperture at the image of the pinhole source in the image arm blocks the spatial frequencies responsible for the grating image and passes the low frequency components which represent the smoothly varying gray pattern we wish to capture. To reduce coherent ringing that occurs with a low power laser, we use a tungsten-halogen lamp surrounded by aluminum foil with a pinhole in it to limit the extent of the source. In Fig. 3 is shown two images of section of a reticle of a 10X reduction of an transparency

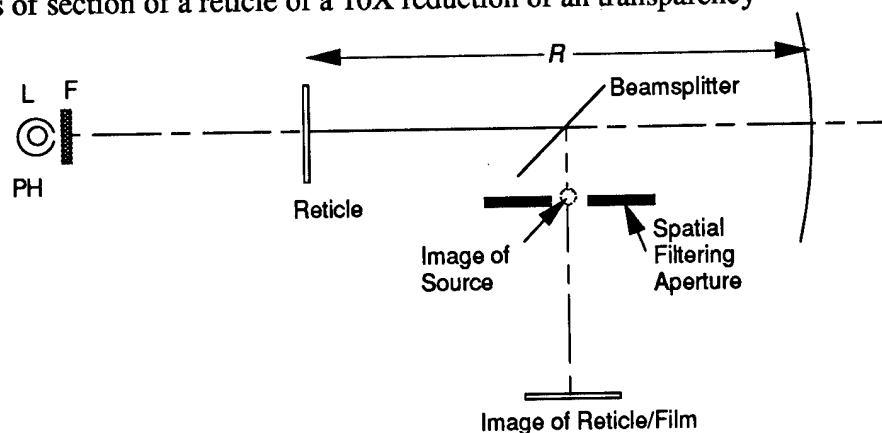


Fig. 2. Optical schematic of halftone filtering geometry. L: Lamp; PH: pinhole; F: Filter

Grayscale masks for diffractive optics: I. Spatially filtered halftone screens

Donald C. O'Shea, Patrick L. Thompson, and Willie S. Rockward
School of Physics and
Center for Optical Science and Engineering
Georgia Institute of Technology
Atlanta, GA 30332-0430

Binary masks for diffractive optics can be generated using commercial imagesetters, printers that generate high resolution images on paper or film. They are usually controlled by PostScript™, a standard page composition language from Adobe Systems. Output directed to a laser imagesetter can produce high resolution (3600 dpi) graphics, which yields patterns with 30 micron features¹. The image on this film is then reduced by a factor of 10 with a Rodenstock Rodagon projection lens. Because of lens aberrations the smallest feature that can be reliably recorded upon reduction is about 8 microns.

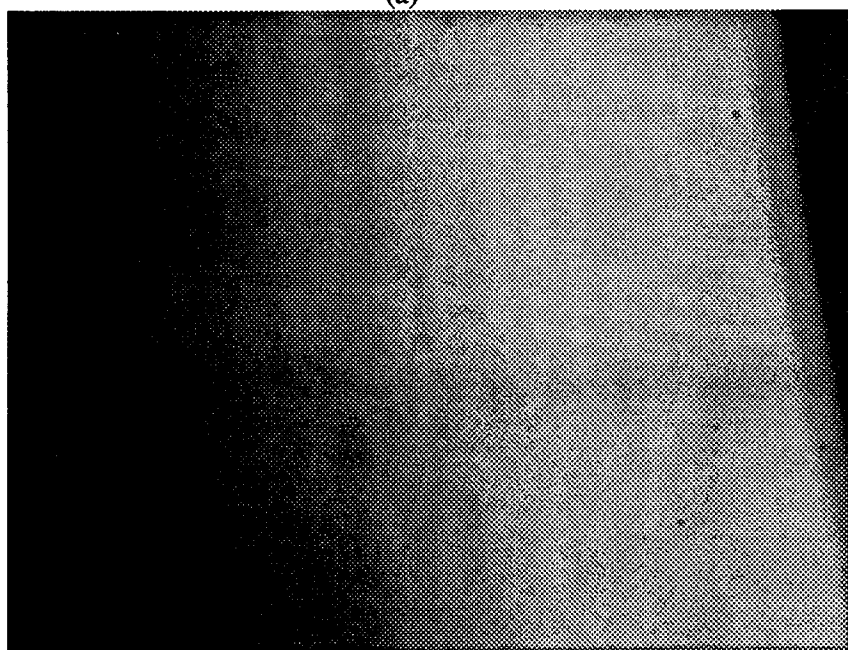
In conjunction with this mask generation effort, we use *Mathematica*, a standard computational mathematics package to plot the binary masks needed to generate the diffractive optical element. Since the graphics output of *Mathematica* is expressed in PostScript, the graphic can be copied as an Encapsulated PostScript File and placed in a commercial illustration program for desktop publishing (Aldus *Freehand*) for imagesetter output.

The difficulty in fabricating a diffractive optical element from a set of binary masks is that the alignment, photoresist exposure and development, and reactive ion etching steps must be repeated for each mask. Each step puts all previous work in jeopardy. If a profile can be rendered into photoresist so that a series of gray levels correspond to depths in phase surface, then there is no need for multiple masks. This eliminates mask alignment fiducials and alignment procedures². The time and cost of fabricating diffractive optics will be reduced substantially.

The standard technique to render gray scale in publishing is with halftone screens. These are variable dot patterns of a specific spatial frequency. The light grays are rendered as a rectangular array of black dots on a white background; dark grays are the same with the colors reversed. For example, a diffractive lens was generated from a spherical phase profile and represented as gray levels in *Mathematica* (Fig. 1). This is the PostScript output of a 32 gray level lens.



(a)



(b)

Fig. 3. Micrograph of sections of the diffractive lens. (a) Image of the lens with filtering aperture open. The halftone screen is 3000 lpi. (b) Image of the lens with filtering aperture closed to eliminate the halftone screen.

This technique is valuable because it uses widely available desktop publishing equipment and simple optical components. A gray scale pattern can be generated without resorting to modulatable lasers writing to a plate on a precision transport. Preliminary results appear promising, but additional work is needed to determine the limits posed by the reduction lens resolution, the contrasts of the reticle containing the halftone screen and the gray-image plate, and the choice of halftone screen frequency. The paper will discuss details of the technology, tradeoffs in the choice of line screen, and achievable resolution.

REFERENCES

1. D. C. O'Shea, J. Beletic, and M. Poutous, "Binary-mask generation for diffractive optical elements using microcomputers," *Appl. Opt.* **32**, 2566 (1993).
2. H. Andersson, et. al., "Single photomask, multilevel kinoforms in quartz and photoresist: manufacture and evaluation," *Appl. Opt.* **29**, 4259 (1990).

Somewhat better results have been obtained by reducing the 4"x5" format. In all cases, there are a set of incoherent transfer processes that must be modeled. Starting backward with the photoresist that requires a preexposure to move the exposure curve into the linear region, one must then model the contrast of the film for the reticle and the range of optical densities possible with the color film. Through contrast stretching and an appropriate lookup table to generate the correct grays in the original computer image, it should be possible to generate a relief in photoresist that faithfully reflects the original computation. A profile of several transitions of the reduced gray scale image of a diffractive lens rendered in photoresist is shown in Fig. 1. The non-linearity of the photoresist was not compensated properly with the necessary preexposure.

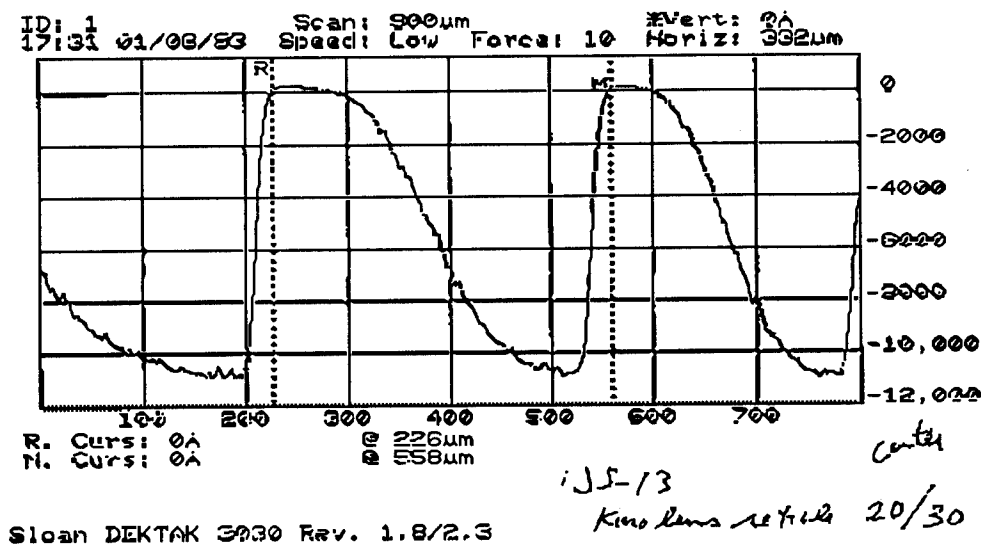


Fig. 1. Profile of a segment of a diffractive lens made by exposure to photoresist of a photoreduced gray scale image generated from a commercial slideimager.

The limits of resolution are not known since neither the device nor the film has been optimized. A high resolution black and white film is needed. Currently, to write a black line on a white background, the film must be exposed to a CRT image three times through different color filters. Since the slides are generated at a commercial slide processing house, it is not possible to optimize the system yet. A range of high resolution, low contrast films must be assessed to determine the ultimate resolution of these devices. We believe research into diffractive optics mask generation through these low cost slide generation devices could have significant impact in fabricating cheap diffractive optics.

Gray scale masks for diffractive optics: II. Commercial slide imagers

Donald C. O'Shea and Thomas J. Suleski
School of Physics and
Center for Optical Science and Engineering
Georgia Institute of Technology
Atlanta, GA 30332-0430

Our laboratory has exploited pattern generation technology based on the PostScript page generation language and raster image processors used in desktop publishing. Until recently we have generated sets of binary masks to produce an efficient diffractive optical element that approximates the smoothly varying fractured phase surface, called a kinoform. Since the masks must each be correctly aligned and etched to achieve this approximation, any technology that can capture and record a gray scale should be considered as a possible alternative to multiple mask technology.

Another type of pattern generation technology that is available to the users of desktop publishing programs is that of slide imagers. Using the same software for presenting patterns generated by computational programs, such as *Mathematica*, to a commercial imaging companies, we have been able to generate gray scale patterns that can be used in making one step gray level masks. The grays generated in these devices are true gray scale created by variable illumination of a relatively high resolution color positive film (Ektachrome 100 Plus Professional), rather than simulated grays using a halftone technique.

All images were prepared in both native file formats (usually Aldus *Freehand*) and as encapsulated PostScript files by "printing" to file. The PostScript printer device (PPD) file that we used varied between commercial houses. Most images were rendered, but not all. However, images that refused to print at one place would print at another. There are two formats available. (1) A standard 35 mm slide image (36 x 24 mm) and (2) a 4" x 5" transparency. The first of these is produced on Solitaire 4 or 8 slide imagers. The model number indicates the thousands of lines in the long (36 mm) direction. Thus a Solitaire 4 has a 9 micron spacing and the Solitaire 8, half that. The 4"x5" format is generated by a Solitaire 16, which, using the same relation, yields an 8 micron line spacing. The 35 mm slides cost \$5 each and the 4"x5" transparencies, about \$100.

We have examined a number of techniques that use these gray scale transparencies to produce diffractive optical elements. A simple contact print of the 35 mm slides yields a very poor image in photoresist with a great deal of scatter. This we attribute to small grains in transparent areas. Rephotographing these patterns removes this scatter, but it introduces another transfer mechanism to be determined.

developer reflection takes place of beams the phase difference of which depends on the resist thickness. All other reflected beams are excluded according to fig. 2. The ray trajectory was chosen in that way, as the light has to pass by no means the developer but runs through the glass substrate exclusively. Therefore, the influence of fluctuations of the refractive index generated during the development process in the developer is avoided. As a resist PMMA was used, the developer consisted of MIBK and IPA 1:1. The resist thickness decreasing during the development process causes in turn a constructive and destructive interference of both reflected beams. The resulting interference signal is detected by a photodiode, the photo current varying in time is recorded by a plotter. As an example, fig. 3 shows an interference signal measured. The development process starts at $t = 30\text{s}$, at $t = 220\text{s}$ the resist film is dissolved completely. In the experimental arrangement used the distance between two neighbouring interference maxima is according to a decrease of the resist film thickness of 240nm .

3 Applications

The energy given from the electrons to a volume element of the resist (deposited energy density) is highly depending on the depth. It causes there a change in solubility with respect to the developer. In this way during the development process a certain dependence of the dissolution rate on the depth is produced, which may be detected by means of the measuring procedure given above. Therefore, from the detected interference signal a conclusion may be drawn about the depth efficiency of the exposure.

Fig. 4 shows the distribution of the dissolution rate as a function of depth for various energies of the primary electrons. The *shape* fits well with the results of model calculations [1]. However, the *position* of the maximum of the dissolution rate (as a characteristic point of the distribution) is different from the theoretically expected one. As the main reason for this the influence of a copper film deposited on the resist on the electron motion was found. In principle, such kind of

fig. 2

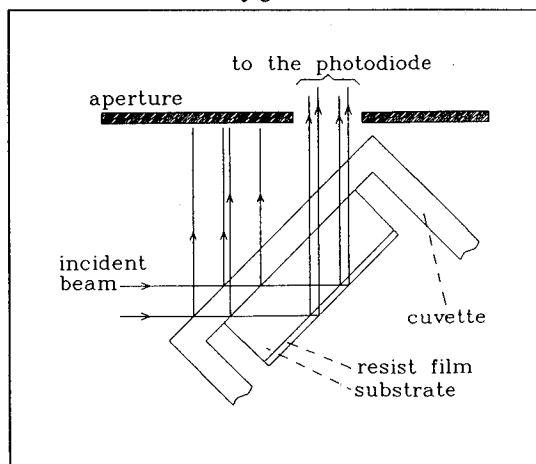
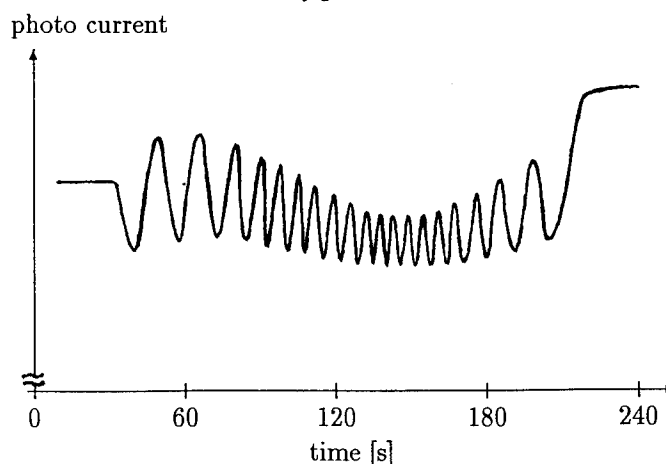


fig. 3



In-situ Measurement of Resist Development Process in Electron Beam Lithography

E.-B. Kley, B. Schnabel

Friedrich-Schiller-Universität Jena, Institut für Angewandte Physik
Max-Wien-Platz 1, 07743 Jena, Germany, Tel.: ++49 3641 657648

1 Introduction

Recently, the realization of resist profiles in order to produce microoptical elements (Fresnel lenses, gratings, kinoforms for example) has developed as an interesting field of lithography. The thickness of the resist film the structure of which has to be changed may be some μm according to the profile depth of the optical elements. Crucially, the efficiency of those elements depends on the shape and quality of the resist profiles. Blazed and multilevel diffractive optical elements can realize seriously higher efficiency than binary optical elements. A preliminary condition for the possible precision of the resist profile required is to know the depth efficiency of the exposition. We have applied an interferometric measuring procedure to characterise the resist development process *in situ*. By this procedure we have measured the depth efficiency of the exposition in e-beam lithography and we have investigated chances to influence its dependence. Furthermore, the development process can be stopped definitely at a certain depth.

2 Measuring Procedure

A laser beam ($\lambda = 633\text{nm}$) is collimated and comes to a cuvette containing the glass substrate covered with the resist and the developer (fig. 1). At the interfaces substrate-resist and resist-

fig. 1

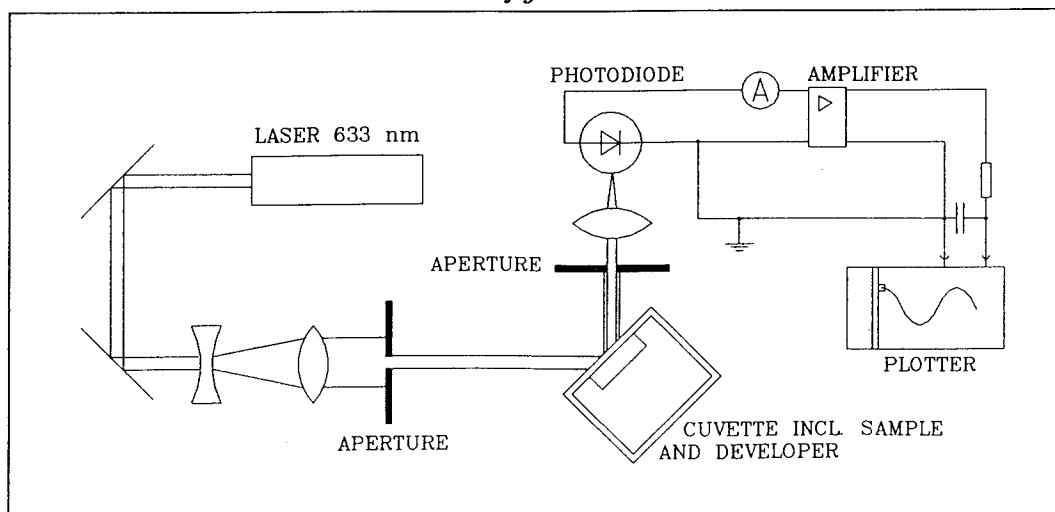
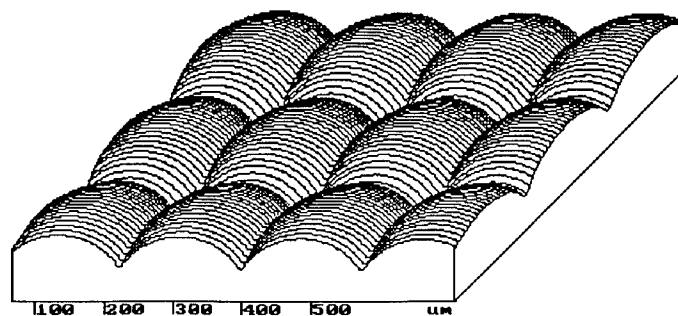


fig. 8



depth (fig. 4) is the use of a film system consisting of several resists with different sensitivity to exposition by electrons. As an example, fig. 6 shows the detected interference signal for a resist film system of SK 6000 (above) and PMMA (below). At equal values of the exposition dose the resulting dissolution rate is higher in SK 6000 than in PMMA. Thus, at the interface between the resists a stepwise behaviour of the dissolution rate occurs. By a proper choice of the parameters of the resist films very different shapes of the dissolution rate as a function of depth may be realized.

The realisation of a well-defined resist profile requires precisely to know the relation between exposure dose D , development time t_e and resist thickness z . This relation can be determined by the measuring procedure given above very efficiently. As an example, fig. 7 shows this relation for the resist PMMA covered with a thin copper film. By means of this characteristics a working point may be fixed, that means to select a proper development time and hence a dependence of the resist thickness (or the loss in thickness) on the exposition dose for the selected development time. Furthermore, the working point may be controlled during the development process by means of the measuring procedure given. The development procedure can be stopped at a certain depth within $\pm 30\text{nm}$ error.

We have used the results given above in order to realize optical elements with well-defined surface profiles. As an example, fig. 8 shows the surface profile of a lens array produced with electron beam lithography. The profile depth is $1.3\mu\text{m}$, 72 dose steps were used.

References

- [1] H.-W. Thümmel: Durchgang von Elektronen- und Betastrahlung durch Materieschichten. Akademie-Verlag Berlin, 1974

fig. 4

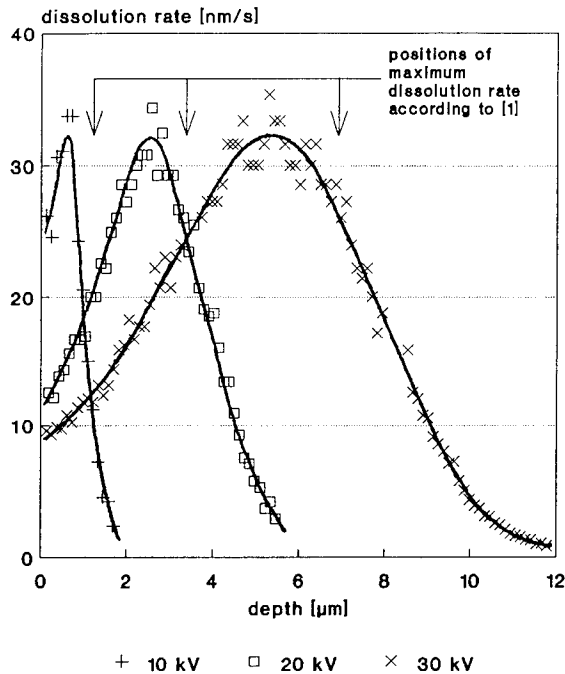
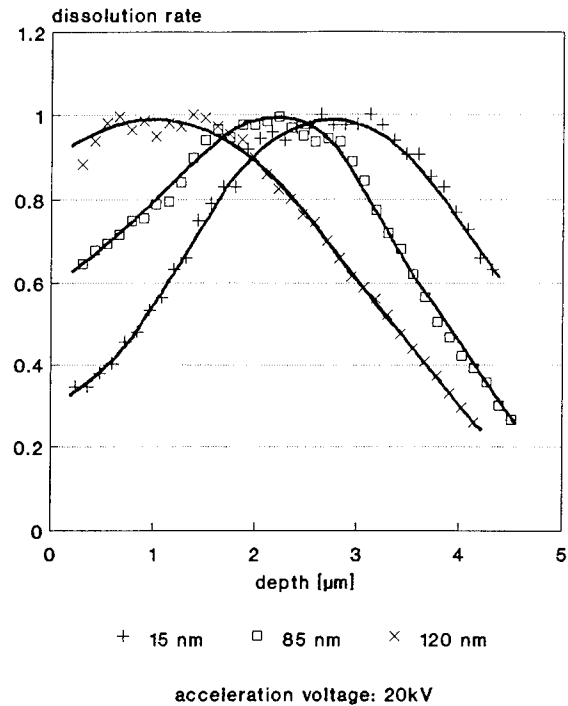


fig. 5



electrically conductive film is required in order to prevent electrical charging of the sample during the exposition. However, the thickness of this film may be chosen within a wide range.

Therefore, in the following the influence of the different thickness of copper films on the distribution of dissolution rates was measured (fig. 5). As to be seen, the position of the maximum of the dissolution rate distribution is at lower depth with increasing thickness of the copper film. At a certain thickness of the copper film (about 120nm) the dissolution rate is constant within $\pm 5\%$ in a range of about $2\mu\text{m}$ thickness beginning with the resist surface. Therefore, within this range there is a rather linear relation between development time and thickness loss of the resist.

Another opportunity to modify the initial distribution of the dissolution rate as a function of

fig. 6

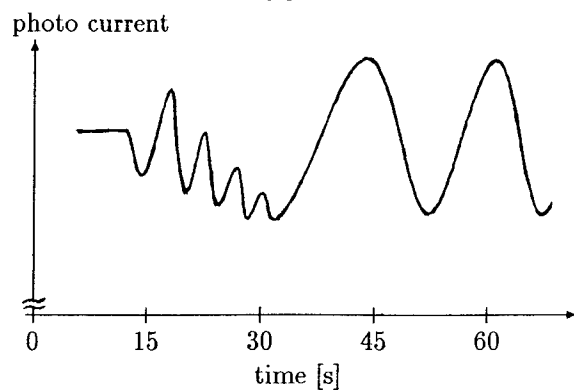
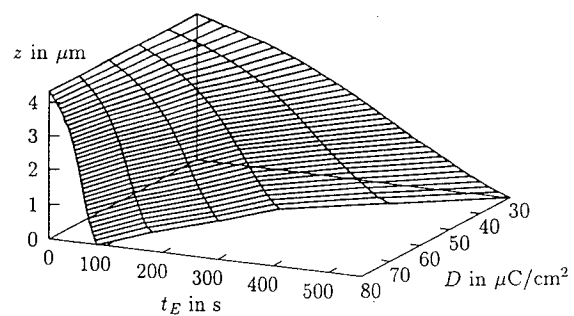


fig. 7



It is well known that high-intensity pulsed lasers can uniformly ablate material from the surface of a wide range of substrates.^{1, 2} Proper choice of laser wavelength and careful control of fluence permit precise control of depth. Ultraviolet (uv) wavelengths are particularly attractive because many materials absorb strongly in this region of the spectrum. By using a high-power excimer laser as the light source, "dry" lithographic etching techniques have been developed and applied to both semiconductor processing and phase grating fabrication. However, lithographic techniques still require generation, positioning, and maintenance of a set of masks.

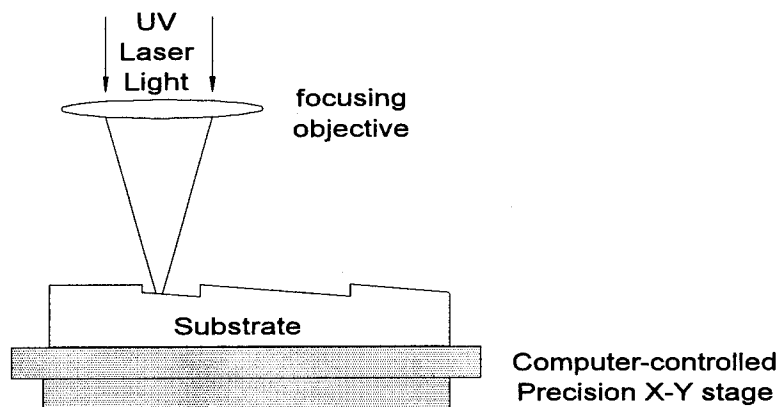


Figure 1. Direct-write photoablation of the substrate allows a computer-generated relief pattern to be directly etched onto the surface.

Our approach is to use a small, high repetition-rate pulsed excimer laser, focusable to micron-diameter spot sizes to directly ablate and etch the grating into the substrate material. Figure 1 is a schematic of the process. We note that this process is significantly different from other "direct-write" schemes for production of phase gratings that have been described in the literature.^{3, 4} These reports involve direct-writing of a *resist* which eliminates the mask, but still requires many additional steps to arrive at a finished piece.

We use our own commercial microfabrication workstation, diagrammed in Fig. 2, to ablate structures into the substrate. Excimer wavelengths of 248 nm or 193 nm with pulse energies generally $\lesssim 20 \mu\text{J}$ are used for these studies. The laser radiation is directed through a microscope-like optical train that allows illumination of a worksurface, viewing with a video camera, and laser exposure of selected area in the view field. The laser is focused onto the work surface with uv-transmitting microscope objectives and a uv optical system capable of producing focal spot diameters that are adjustable between 1 and 100 microns. Laser fluence levels at the worksurface can be adjusted from 0 to $>10 \text{ J/cm}^2$ to accommodate controlled ablation of a wide range of materials. The workpiece is mounted on motorized X-Y stages that are interfaced to a personal computer and driven by a CAD/CAM program. Laser pulsing is synchronized to motion of the X-Y stages to assure that sample exposure is independent of stage velocity. The X-Y stages themselves are specified for 0.25- μm addressability and 0.5- μm reproducibility.

Micromachining of Diffractive Optics with Excimer Lasers

Michael T. Duignan

Potomac Photonics, Inc.
4445 Nicole Drive
Lanham, MD 20706

Phone: (301) 459-8093 Fax: (301) 459-3034
e-mail: 76217.1357@compuserve.com

Widespread applications for diffractive optical devices include sensors, analytical instruments, fiberoptic distribution and communication, neural networks and optical computing, lasers and laser instrumentation, pattern recognition, displays, and information storage. Incorporation of diffractive optical elements (DOEs) into the design of optical instruments offers the modern optical engineer an abundant array of potential solutions to long-standing problems. With the cost of high-power personal computers and engineering workstations continuing to plummet, manufacturers of optical design software are providing sophisticated optical-design programs that now incorporate tools for generating and analyzing diffractive or holographic elements. This has opened the field to optical engineers at every level. Well-developed lithographic methods from the semiconductor industry and stamping techniques similar to those used in the production of compact disks have generated excitement about cost reduction and expansion of future markets for diffractive optic technology. However, these manufacturing techniques are complex, time-consuming, capital-intensive and often unsuitable for generation of test-pieces, prototypes and one- or few-of-a-kind diffractive structures. Many optical devices that might benefit by incorporation of phase-correcting structures are, by their nature, individual and highly specialized.

We will report preliminary results from a new approach, using a table-top ultraviolet waveguide excimer laser-based micromachining workstation to etch diffractive structures *directly into the substrate* without masks or intermediate processing steps. The proposed technique will be applicable to a wide spectrum of substrate materials, including glass, diamond, semiconductors, and polymers. Such a system should allow an optical designer to generate diffractive elements in *hours* compared to weeks or months with current methods. At the same time total system cost is expected to be an order of magnitude lower than the conventional equivalent and therefore within the reach of a far greater number of designers, engineers, manufacturers, and optical job shops.

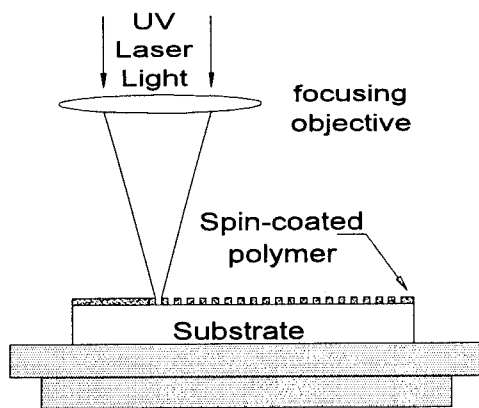


Figure 3. Etching a binary grating into a $\sim 0.5 \mu\text{m}$ thick coating of a spin-coated polymer such as polyimide. If the substrate material is non-absorbing at the laser wavelength (e.g., fused silica), depth accuracy depends only on the thickness of the original polymer layer.

twice that calculated by equation [1], precise depth control must be achieved. Our goal is to identify conditions that will allow reproducible ablation rates of $\lesssim 100 \text{ nm/shot}$.

To show the direct-write micromachining technique to be useful, we must demonstrate that the system is capable of achieving the following:

- (1) required accuracy and precision of grating spacing
- (2) required accuracy and precision of grating depth and smoothness
- (3) application to optical materials of general interest

Our experiments are designed to evaluate each of these criteria. We will report the results of these ongoing studies.

This work is supported, in part, by Small Business Innovative Research contract NAS8-40131 with the National Aeronautics and Space Administration.

1. *Laser Ablation in Materials Processing: Fundamentals and Applications*, B. Braren, J.J. Dubowski, and D.P. Norton, eds., Materials Research Society Proceedings, Vol. 285 (1993)
2. R. Srinivasan and B. Braren, "Ablative Photodecomposition of Polymers by UV Laser Radiation," in *Lasers in Polymer Science and Technology: Applications*, Vol. III, J-P. Fouassier and J.F. Rabek, eds., CRC Press, Boca Raton, FL, 133-179 (1990)
3. K.S. Urquhart, R. Stein, and S.H. Lee, "Computer-generated holograms fabricated by direct write of positive electron-beam resist," *Opt. Lett.* **18**, 308-310 (1993)
4. T. Yatagai, M.H. Geiser, R. Tian, X. Tian, and H. Onda, "CAD systems for CGHs and laser beam lithography," *Computer and Optically Generated Holographic Optics*, I. Cindrich, S.H. Lee, Editors, Proc. SPIE **1555**, 8-12 (1991)
5. G.J. Swanson, "Binary optics technology,: The theory and design of multi-level diffractive optical elements," *MIT/Lincoln Lab Technical Report 854*, 14 Aug 89
6. D.W. Ricks and R. Ajmera, "Light scattering from binary optics," *Computer and Optically Generated Holographic Optics*, I. Cindrich, S.H. Lee, Editors, Proc. SPIE **1555**, 89-100 (1991)

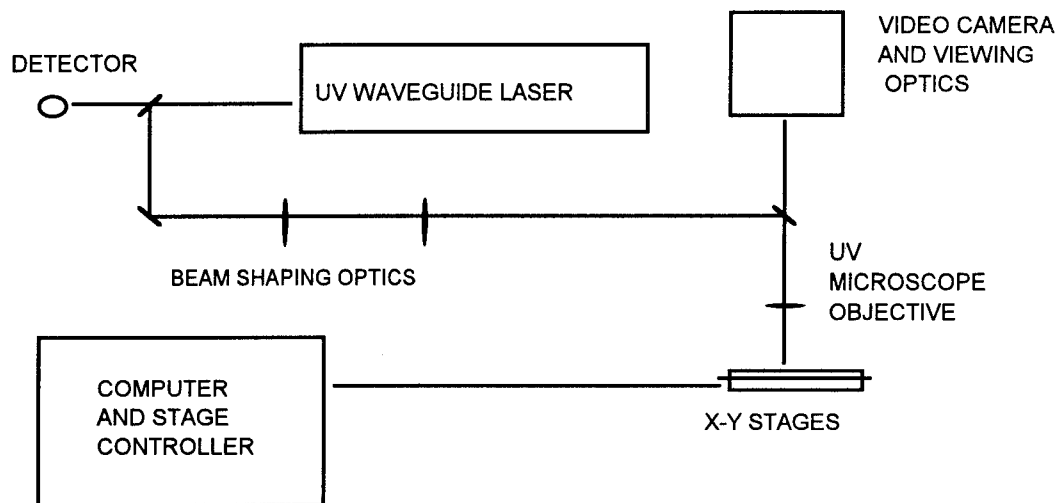


Figure 2. Block diagram of the Potomac laser microfabrication system.

The CAD program accepts standard DXF and G-Code file formats, or structures can be entered directly via a mouse and keyboard. Simple diffractive structures, such as line gratings and Fresnel lenses, are quite easy to describe mathematically.^{5, 6} We have chosen these types of DOEs to be our test structures. An array of line segments or circle radii corresponding to the area to be milled for the required diffractive component is first generated in Mathcad™ or Microsoft Excel™. The output from this initial step is then translated to DXF format and imported by the CAD program. The CAD program, interfaced to both the laser and motion control system, executes the required motion and the structure is written to the substrate much like a pen plotter.

A true binary (2-level) DOE can be achieved in a straightforward manner. A polymer is spin-coated onto a fused silica substrate to a precise depth, d ,

$$d := \frac{\lambda}{2 \cdot (n - 1)} \quad [1]$$

where λ is the design wavelength, and n is the index of refraction of the polymer. For visible wavelengths d is typically of the order of $0.5 \mu\text{m}$. Many polymers are known to ablate cleanly with far-uv sources at fluences of a few hundred millijoules per square centimeter. Fused silica, on the other hand, has a damage threshold more than an order of magnitude higher, and will be unaffected by the laser. Therefore, 2-level diffractive systems with accurate depth can be etched by drilling completely through the polymer layer (Fig. 3). Critical control of fluence and total dose is unnecessary. However, the maximum theoretical efficiency of a 2-level DOE is only ~40%.

To improve diffraction efficiency, smooth ramped or contoured structures must be fashioned. Since peak-to-valley height for such a structure is only

features required by the specification of multi-level diffractive optical element, such as critical dimension, layer to layer registration, etch depth and so on. The GDSII data created use the data type feature to rank data from the multi-level structures and assign each rank with different doses (dwell time) on a Focused Ion Beam machine. The multi-level zone patterns are created in high molecular weight PMMA by 200 Kev Beryllium whose dose (dwell time) was controlled to achieve the multi-level exposure. The exposed resist was then developed to form a multi-level profile and transferred into fused silica by means of reactive ion etching.

Considerable preliminary experiments were conducted to calibrate and decide the optimal conditions to producing uniform and smooth steps. Initial measurement using Dektak showed a linear response can be achieved with a 0.1 microns to 1 micron thick layer of PMMA. From repeated experiments, we have generated calibration curves which would allow us to fabricate multi-level structures with predictable step size (see fig. 1). Additional. Studies involve FIB aperture size from 25nM to 200nM; since larger aperture gives higher current density and therefore shorter write time per pixel. Higher throughput, however, might be achieved at the expense of resolution and quality of the step.

Rapid prototyping of multi-level diffractive optical elements

**Peter Kung & Li Song
QP Semiconductor Technology Inc.**

**217 St. Louis Avenue
Pointe Claire, Quebec
Canada, H9R 5L7**

Tel: (514) 695-5214

Fax: (514) 695-2401

The fast growing demands for multi-level diffractive optical elements in the recent years are the results of their important and unique features. Needless to say, the characteristics, such as, light weight, low cost, high diffraction efficiency (close to 100%), ability to provide any wave front, high optical performance and possibility for chromatic correction make the multi-level diffractive optical elements, the attractive component for many optical and photonic applications.

To fulfil the special needs required by DOE user, we have developed a cost-effective procedure to realize the rapid prototyping of the multi-level diffractive optical elements. One software HOLOCAD™, an internally developed physical layout tool, is used to generate GDS data from user defined component phase function. This tool has greatly reduced data generation time. In fact, this software automatically inserts process control

multi-level resists profile can be transferred with a scaling factor. A factor up to 2.5 has been achieved to scale PMMA step into fused silica.

Using the above procedure; a variety of DOE were fabricated; phase mask, on axis lenses, doublets, off axis output and off axis input.

These DOE were characterized on the optical bench; their performance are correlated with measured process data such as alignment, line width and actual etch depth. The encouraging results obtained thus far showing using Focused Ion Beam can become a reliable technique that provides performance much superior those obtained by lithography-etch methods.

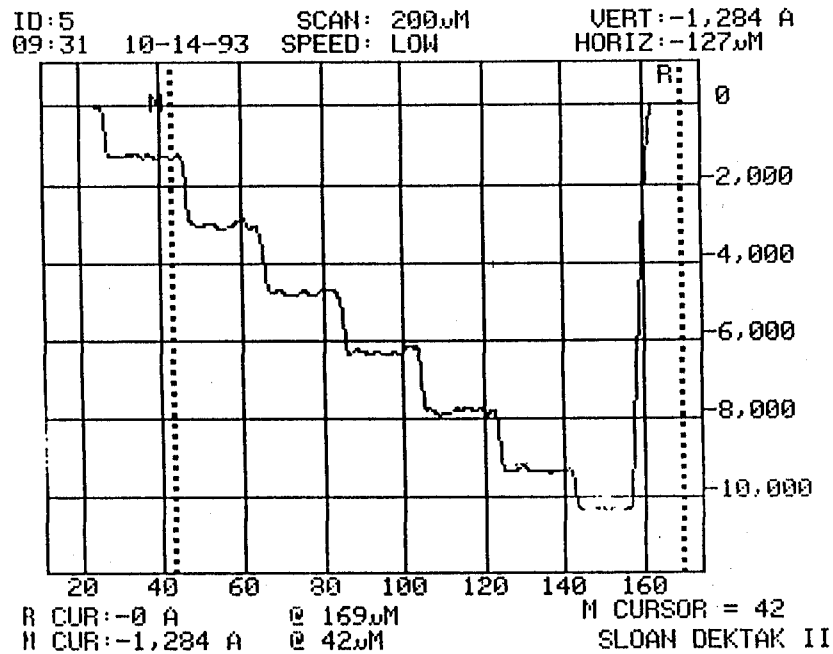


Fig. 1

The data structure used by the FIB machine is available to support a maximum of 64 levels; The size of such data set could reach many megabytes, we expect the added load time to significantly increase general write time. Future experiment will be conducted involving the fabrication of 32 steps and 64 steps versions of the test vehicles; characterizing the data size and write time differences.

Other experiments involving the transfer of multi-level resist profile into fused silica are also conducted. By varying the mixture of Freon and Oxygen in the Ion milling chamber, the

For diffractive optical elements with high spatial frequencies or polarization sensitivity, scalar simulation are inaccurate. Therefore, Maxwell's equations must be implemented to model the resonances present in small structures. The most common technique for this class of simulations is the coupled-mode approach.¹⁰ For 2-dimensional coupled-mode analysis, the unit cell is described as a series of sublayers. Each sublayer is defined by some simple pattern in the dielectrics of that region. The variables which define the pattern in each sublayer are encoded as genes, and the set of genes defining the set of sublayers describe a chromosome. A GA can thus be implemented to optimize the grating for a give field value and diffraction efficiency.

Genetic algorithms are a useful and interesting approach for optimizing diffractive optical elements. Past work has demonstrated their applicability to fanout grating optimization, and new results indicate that the same techniques can be applied to many other types of diffractive elements. Critical to any optimization algorithm is proper operating parameters and weighting to avoid an over-constrained solution space and a non-physical solution. As knowledge of diffractive optics increases, new methods for design optimization will be required to address the problem complexities and more fully utilize the full SBWP of diffractive optical elements.

References

1. Alan Kathman and Eric Johnson, "Binary Optics: New Diffractive Elements for the Designer's Tool Kit," *Photonics Spectra*, pp. 125-132, September 1992.
2. Hamid Farhoosh et al, "An algorithm for computation of large size FFTs in computer-generated holograms by interlaced sampling," SPIE Volume 884, January 1988.
3. Wilfrid Veldkamp and Tom McHugh, "Binary Optics," *Scientific American*, pp. 92-97, May 1992.
4. Eric Johnson et al, "Advantages of Genetic Algorithm Optimization Methods in Diffractive Optic Design," SPIE Critical Review Volume ###, June 1993.
5. Eric Johnson, Mustafa Abushagar and Alan Kathman, "Phase Grating Optimization Using Genetic Algorithms," OSA Optical Design for Photonics Volume 9, March 1993.
6. Alan Kathman and Eric Johnson, "Multi-Beam Grating Structures," OSA Optical Design for Photonics Volume 9, March 1993.
7. Lawrence Davis, *Handbook of Genetic Algorithms*, Van Nostrand Reinhold, New York, 1991.
8. Zbigniew Michalewicz, *Genetic Algorithms + Data Structures = Evolution Programs*, Springer-Verlag, Berlin, 1992.
9. John Koza, *Genetic Programming: On the Programming of Computers by Means of Natural Selection*, MIT Press, Cambridge, 1992.
10. M. Moharam and T. Gaylord, "Diffractive Analysis of a Surface Relief Grating," JOSA A, Volume 72, October 1992.

New Techniques for Genetic Algorithm Optimization of Diffractive Optical Elements

Alan D. Kathman and David R. Brown
Teledyne Brown Engineering

Eric G. Johnson
SY Technologies

Diffractive optical elements are finding new and varied applications.¹ The large space-bandwidth product (SBWP) of binary optics provide a tremendous number of degrees of freedom for wavefront manipulations.^{2,3} Optical designers are sometimes finding this freedom unwieldy due to the inherent complexity and non-linearities that exist in advanced hybrid and diffractive designs. Conventional design techniques are not capable of fully exploiting the SBWP of binary optics; more advanced algorithms are required to achieve global solution strategies. Substantial work has been done to demonstrate the advantages of genetic algorithm optimization methods in diffractive optic design.^{4,5,6} Genetic algorithms (GAs) are non-deterministic optimization algorithms for problems with high dimensionality. This paper documents new techniques for applying GAs to diffractive optics design.

Genetic algorithms are patterned after the natural selection process.⁷ The process manipulates a coding of the independent variables in a population of candidate solutions. These candidates are composed of a set of coded variables which are treated as genes. Therefore, a possible solution can be described as a chromosome. A typical GA utilizes three operators in the optimization of these candidate solutions: parent selection, crossover, and mutation. All three operators are implemented in each iteration to produce a new generation of solutions. As successive generations are formed, this algorithm samples multiple optima in the solution space and, with proper operating parameters, converges to an ideal optimum. The concept of "survival-of-the-fittest" as a species optimization algorithm is not new, nor is it's application in the microcosm of computer simulation.^{8,9} Successful design efforts demonstrated to date suggests that this approach is well suited to the highly dimensional solution space of diffractive optical elements.

Work to date has centered around the design of two- and three-dimensional fanout grating. The applicability of genetic algorithms, however, extend far beyond grating design. A grating is routinely described by a discretely sampled phase function within its unit cell. This encoding inserts well into the genetic algorithm. Other diffractive elements are described by discrete phase and amplitude functions, by continuous phase polynomials, or even by a multiple layers of patterned in dielectrics. The optimization of any one of these concepts is complex and highly challenging even utilizing a GA.

In cases where the diffractive optical element is described by a set of phase polynomials, efficiently encoding the element as a set of genes becomes more complex. The polynomial set should not over-constrain the SBWP of the diffractive optic, or the optimum solution may lie outside the limited solution space. To use the polynomial coefficients as genes it is preferable that they be independent variables, so the polynomial set should be orthogonal. This is not a firm requirement. One strength of GA optimization is that the individual genes need not be completely independent. It is also important that proper weighting be applied to the genes to prevent high frequency terms from causing instabilities.

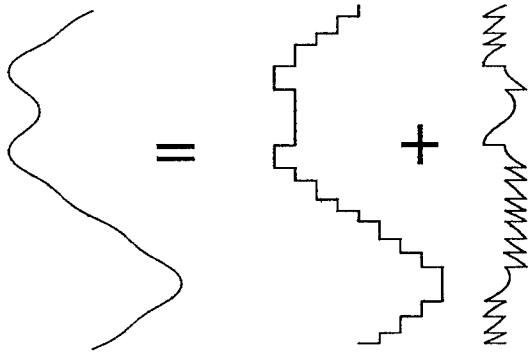


Figure 1: Decomposition of a continuous phase profile into an approximated profile and the associated "error profile".

By

$$t_q(x, \vec{\alpha}) = \exp(ip_q(x, \vec{\alpha})) = \exp(ip(x)) \exp(-ip_e(x, \vec{\alpha})) = t_c(x) t_e^*(x, \vec{\alpha})$$

and the convolution theorem the diffraction amplitudes of the phase-quantized hologram can be expressed by the amplitudes a_m of continuous phase hologram and the amplitudes of the "error profile" hologram: $a_m^q = \sum_{k=-\infty}^{\infty} a_{m-k} a_{-k}^*$. The asterisk denotes complex conjugation. The a_m are the diffraction orders defined by $a_m = \int t_c(x) \exp[-2\pi i m x] dx$ and so forth.

2.2 Figure of Merit for signal distortion

The quantization of continuous phase holograms has to be performed such that the energy loss and the signal distortion is minimized. Thus a figure of merit has to be introduced that judges the change of signal due to quantization. Since the phases of the output signal are supposed to be of no concern, the following condition has to be fulfilled for an optimum quantization: $\sum_{m \in D} (c^2 |a_m|^2 - |a_m^q|^2)^2 \rightarrow \min$, where D denotes the index set of diffraction orders of interest (in the signal window [Wyrowski89]). Applying the convolution theorem the intensities of the quantized phase hologram can be expressed as

$$|a_m^q|^2 = \underbrace{|a_m|^2 |a_0^e|^2}_{A} + \sum_{k \neq 0} \left(\underbrace{|a_{m-k}|^2 |a_{-k}^e|^2}_{B} + \underbrace{\sum_{l \neq 0} a_{m-k} a_{m-k-l}^* a_{-k}^e a_{-k-l}^e}_{C} \right) \quad (1)$$

Obviously an optimum quantization has to maximize term A, since signal distortion and energy loss are then minimized due to energy conservation ($\sum_k |a_k^e|^2 = 1$). The mutual ratios of the diffraction intensities are not affected by this term. However, term B changes the ratio since the diffraction intensities are non-uniformly increased. Term C finally also alters the ratios of intensities since it lowers or increases intensities non-uniformly.

2.3 Optimum quantization rule

Assuming that the "error profile" is bound from above ($|p_e, \vec{\alpha}| \leq \epsilon$) the transmission function can be expanded in a Taylor series: $t_e^*(x) = \exp(-ip_e(x, \vec{\alpha})) \approx 1 - ip_e(x, \vec{\alpha}) - \frac{1}{2} p_e^2(x, \vec{\alpha})$. As a result, the zero diffraction order of the "error profile" hologram scales with the variance of the "error profile" according to:

$$|a_0^{e*}|^2 \approx 1 - \int_0^1 p_e^2(x, \vec{\alpha}) dx + \left(\int_0^1 p_e(x, \vec{\alpha}) dx \right)^2 = 1 - (\Delta p_e(x, \vec{\alpha}))^2$$

Optimum quantization rules for computer generated holograms

U. Krackhardt

Physikalisches Institut der Universität Erlangen — Nürnberg

Staudtstr. 7/B2, 91058 Erlangen, Germany

Phone: +9131/85 8371, FAX.: +9131/13508

1 Introduction

In optical information processing computer generated holograms (CGH) have served as a powerful and versatile tool [Streibl89]. Usually phase-only holograms are required to minimize energy dissipation. The following considerations are restricted to periodic Fraunhofer-holograms for which the Kirchhoff-approximation is supposed to be valid.

A common design procedure starts from a given intensity distribution in the image plane. Suitable algorithms like [Daendliker90] use the phase freedom in the image plane to obtain a phase-only structure. Usually continuous profiles are approximated by multi-level staircase profiles to facilitate fabrication. This influences the reconstruction quality as outlined in [Goodman70, Dallas70]. However, there are more degrees of freedom than the number of phase steps: The positions of the stair steps (transition points) and their heights. Usually the heights are preset by the fabrication process [Jahns89]. In the following analytic expressions are derived that serve to determine the optimum positions of transition points in the sense that the energy loss is minimized. The theory is not restricted to a special profile. The results are illustrated with the help of computer simulations. The accordance of the results presented here with those in literature is shown.

2 Theory

A phase-only hologram of continuous phase is described by its transmission function according to $t_c(x) = \exp[ip(x)]$, where $p(x)$ denotes the phase profile. The aim is to find a quantized profile with a transmission function $t_q(x, \vec{\alpha}) = \exp[ip_q(x, \vec{\alpha})]$, where $p_q(x)$ denotes the phase profile of the quantized structure. The vector $\vec{\alpha}$ describes all degrees of freedom of the quantized structure, e.g., the transition points and the height of the stair steps in case of a staircase profile.

2.1 Decomposition of the phase information

By virtue of the quantization operation an "error profile" is introduced defined by $p_e(x, \vec{\alpha}) = p(x) - (p_q(x, \vec{\alpha}) + p_c)$. For further considerations it is convenient to choose the constant p_c such that the DC-term of the error profile vanishes, i.e. $\int p_e(x) dx = 0$.

Consequently the transmission function of the continuous phase hologram can be decomposed like $t_c(x) = t_q(x, \vec{\alpha})t_e(x, \vec{\alpha})$, where $t_e(x, \vec{\alpha}) = \exp[ip_e(x, \vec{\alpha})]$ describes the transmission function of the "error profile" hologram.

Since the Kirchhoff-approximation is supposed to be valid this factorization can be thought of as follows: A continuous phase hologram placed in a collimated beam of light can be replaced by the phase-quantized hologram together with the associated "error profile" hologram (see fig. 1).

2.5 Consistency with other theories

In [Goodman70, Dallas70] the diffraction efficiency scales like $\tilde{\eta}_q = (\text{sinc}(1/Z))^2$ (with $\text{sinc}(x) := \frac{\sin(\pi x)}{\pi x}$) due to phase quantization by Z equally spaced (in space and phase) phase steps. It can be shown that the lower bound for this scaling parameter obtained by the present model differs by $\frac{1}{Z^2}$ from the value in literature. That is both values agree the better the more phase steps are used for quantization.

3 Numerical and experimental results

By the algorithm given in [Daendliker90] continuous phase profiles for multiple beam splitters with efficiencies close to the theoretical limit [Mait92] were calculated. Expression (1) is evaluated to obtain values for performance parameters (see section 2.4). Furthermore, expression (1) serves for estimations of the lower (upper) bound of signal-to-noise-ratio (variance). Fig. 4 shows these parameters as a function of equally spaced phase steps Z .

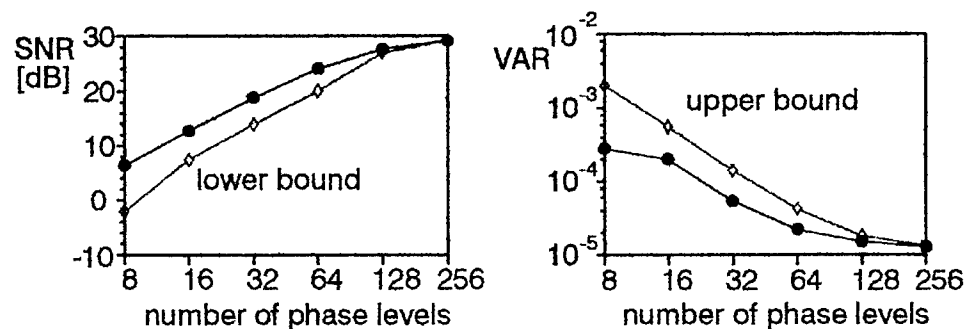


Figure 4: SNR and VAR of a quantized 9-fold beamsplitter as a function of the number of quantization levels. The filled dots represent values of computer simulations, the light dots designate the predicted values.

References

- [Daendliker90] H.P. Herzig, D. Prongue, R. Dändliker: "Design and fabrication of highly efficient fan-out elements", *Jap. Jour. of App. Opt. Phys.* **29**, L1307-L1309 (1990)
- [Dallas70] W.J. Dallas: "Phase Quantization - a Compact Derivation", *Appl. Opt.* **10**, 673 (1970)
- [Goodman70] J.W. Goodman, A.M. Silvestri: "Some Effects of Fourier-domain Phase Quantization", *IBM J. Res. Develop.*, 478-484 (1970)
- [Jahns89] J. Jahns, N. Streibl, S.J. Walker: "Multilevel phase structures for array generation", *Holographic Optics: Optically and Computer Generated*, I.N. Cindrich and S.H. Lee, eds., *Proc. Soc. Photo-Opt. Instrum. Eng.* **1052**, 198-203 (1989)
- [Mait92] U. Krackhardt, J.N. Mait, N. Streibl: "Upper bound on the diffraction efficiency of phase-only fanout elements", *Appl. Opt.* **31**, 27-37 (1992)
- [Streibl89] N. Streibl, K.-H. Brenner, A. Huang, J. Jahns, A.W. Lohmann, D.A.B. Miller, M. Murdocca, M. Prise, T. Sizer: "Digital optics", *Proc IEEE* **77**, 1954-1969 (1989)
- [Wyrowski89] Frank Wyrowski: "Coding and quantization techniques in digital phase holography", in *Holographic Optics II: Principles and Applications*, G.M. Morris, ed., *Proc. Soc. Photo-Opt. Instrum. Eng.* **1136**, 215-219 (1989)

Thus an optimum parameter set $\vec{\alpha}_0$ for the quantized profile is found if the condition

$$\nabla_{\vec{\alpha}}(\Delta p_e(x, \vec{\alpha}))^2|_{\vec{\alpha}_0} = 0 \quad (2)$$

is fulfilled.

2.4 Measure of performance

In order to judge the optical performance of an information processing system application dependent parameters are introduced. A basic parameter is the energy loss or the diffraction efficiency, respectively. The quantization caused energy loss $\tilde{\eta}_q$ scales like $\tilde{\eta}_q = |a_0^e|^2$ according to eqn. 1. Since all the remaining intensity not gathered within $|a_0^e|^2$ contributes to signal distortion (see comments to eqn. 1), the quantization caused signal-to-noise-ratio SNR_q can be defined as $\text{SNR}_q = 10 \log \left(\frac{|a_0^e|^2}{1 - |a_0^e|^2} \right)$.

In the special case of multiple beam splitters (N diffraction orders of the same intensity) a similar measure of uniformity is the variance of the intensities within the signal window: $\text{VAR}_q = \frac{1}{N} \sum_m (|a_m^q|^2 - \frac{1}{N} \sum_k |a_k^q|^2)^2$.

2.4.1 A particular profile

For a special quantization profile, the staircase profile, the quantization rule can be elaborated in more detail. A staircase profile is determined by its transition points x_k and the step heights h_k (see fig. 2). The degrees of freedom $\vec{\alpha}$ thus defined by $\vec{\alpha} = (x_1, \dots, x_Q, h_1, \dots, h_Q)$. The phase profile $p_q(x, \vec{\alpha})$ can be described by $p_q(x, \vec{\alpha}) = \sum_{k=0}^Q h_k \text{rect} \left(\frac{x - (x_k + x_{k+1})/2}{x_{k+1} - x_k} \right)$ with $x_0 = 0, x_{Q+1} = 1$ and

$$\text{rect}(x) := \begin{cases} 1 & : |x| \leq 0.5 \\ 0 & : \text{sonst} \end{cases} \quad (3)$$

Application of the optimum quantization rule given by eqn. 2 yields the simple condition:

$$p(x_k) = h_k.$$

That is the transition points have to be placed at those positions where the (given) step heights of the quantization profile coincide with the height of the continuous profile. Figure 3 shows the profile of a 9-fold beam splitter together with a quantized profile using the optimum quantization rule.

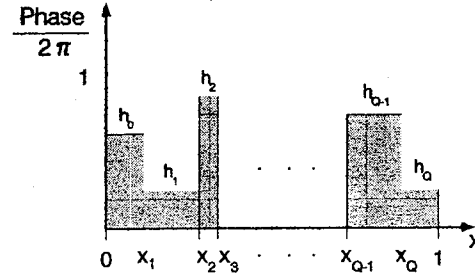


Figure 2: Schematic picture of a multi-level staircase phase profile.

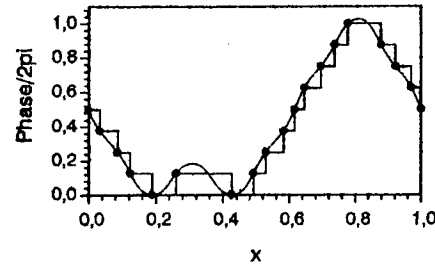


Figure 3: Continuous and quantized phase profiles of a 9-fold beam splitter. The dots indicate the locations where step heights and heights of the continuous profile coincide.

For the two level phase grating the deflection angle varies according to a variation of the relative grating period. Additionally, due to the dispersion of the dielectric material used for the fabrication of the phase grating, the efficiency of the grating is reduced. For wavelengths other than the design wavelength the phase shift caused by the dielectric islands of the grating changes to values other than π , which reduces the efficiency.

Angular Dependences

In the approximation of small prism angles and consequently small deflection angles the deflection by a macroscopic prism is independent of the angle of incidence of the incoming light beam. This is in contrast to a diffractive deflection grating. There the deflection angle as well as the thickness of the phase shift (determining the diffraction efficiency) scales with the cosine of the angle of incidence [2].

Temperature Dependences

The temperature dependence of a refractive prism is described by three main material constants; the thermal expansion coefficient of the prism, and the thermal variation of the refractive indices of the prism material, as well as the surrounding medium. These parameters have immediate effect on the prism angle. For bulk elements like macroscopic prisms also the temperature gradient within the material has to be considered.

Diffractive phase gratings are influenced by the same parameters as refractive elements. The effects, however, are quite different [3] [4]. The thermal expansion coefficient of the dielectric medium causes a change in the grating period and thus the diffraction angle. The variation of the refractive index of the medium, however only has an impact on the zeroth diffraction order i.e. lowers the energy in the diffracted light.

Light deflection by a blazed grating

In the previous section we showed a brief comparison of the behaviour of light deflecting components based on the pure effects of refraction or diffraction respectively. Now we want to develop a picture which allows to investigate blazed components which combine refractive and diffractive effects.

Fig. 2 shows how a blazed grating can be subdivided into a periodic sequence of refractive microprisms. The periodic arrangement of these microprisms is the origin of the diffractive power of the blazed structure. Thus to investigate how diffractive and refractive effects are combined in such a component we look at this prism grating as a convolution of a microprism with a diffractive grating structure:

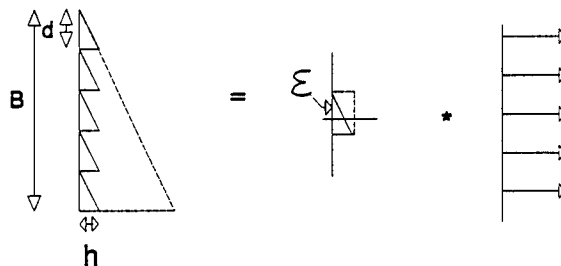


Fig.2: Blazed grating expressed as convolution

The Transition between Diffractive and Refractive Microoptical Components

S. Sinzinger, M. Testorf, W. Singer

Motivation and Plan

For the packaging of optical systems generally two main approaches are discussed. People believing in the advantages of refractive optics try to miniaturise classical refractive optical components. These components are then used to build compact optical systems. The other approach makes use of diffraction, an effect which becomes more and more important as the structures get smaller. Diffractive optical elements (DOEs) offer a unique variety of functionality which allows to build systems with maximum compactness.

There are, however, some problems with the use of DOEs, e.g. the wavelength sensitivity of its properties or the low efficiencies. To achieve higher diffraction efficiencies the designs move away from two level diffraction gratings towards highly efficient multilevel phase elements [1]. This, however, can also be looked upon as adding a certain amount of refractive power to these DOEs. On the other hand, as refractive elements become smaller diffraction plays an ever more important role for their properties. Especially arrays of miniaturised refractive microcomponents show effects typical for diffractive elements. One example is the Talbot imaging of refractive lenslet arrays.

Therefore it is necessary to look at these microoptical components as elements containing both an amount of diffractive power as well as a certain refractive contribution. In this paper we investigate how diffraction and refraction work together resulting in the effect of such hybrid components. On the example of a simple light deflecting component (e.g. refractive prism, diffractive grating or hybridized blazed grating) we illustrate effects of varying degrees of diffraction on efficiency, wavelength-, and angular dependence, as well as temperature dependence. Even for the blazed grating the shares of diffraction and refraction on the total functionality of the component can be varied by different blaze depths.

The pure effects - light deflection by prism or two level diffraction grating

The job of light deflection can be performed by various different components. Examples for the two extreme cases are a purely refractive prism and for the diffractive case a two level phase grating (Fig.1). For these cases the calculation and illustration of the dependences is straightforward:

Wavelength Dependences

The effect of the refractive prism changes under variation of the wavelength is due to the dispersion of the prism material. The diffractive effect at the edges of the prism as well as its variation with the wavelength causes a finite and λ -dependent width of the Fourier transform of the deflected beam. For a macroscopic prisms this effect can be neglected.

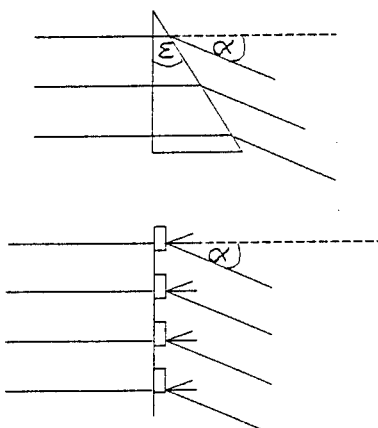


Fig.1: Refraction and diffraction for light deflection

$$\exp[2\pi i x \tan(\epsilon) \frac{n-1}{\lambda}] \cdot \text{rect}\left(\frac{x}{d}\right) * \sum_m \delta(x - md) \cdot \text{rect}\left(\frac{x}{B}\right) \quad (1)$$

The Fourier transform of such an element shows the resulting complex amplitudes:

$$\text{sinc}\left[\left(\nu_x + \tan(\epsilon) \frac{n-1}{\lambda}\right) \cdot d\right] \cdot \left[\sum_m \delta\left(\nu_x \frac{m}{d}\right) * \text{sinc}(\nu_x B)\right] \quad (2)$$

where: $\nu_x = \frac{x}{\lambda z}$ and $\text{sinc}(x) = \frac{\sin(\pi x)}{\pi x}$

Eq. (2) shows that the total complex amplitude in the Fourier plane of such a blazed grating consists of the product of a shifted sinc-function and a sinc-comb. The generally fairly broad, shifted sinc function results from the light deflection on the single microprisms. It therefore represents the refractive part of the element. The width is determined by the lateral extension of a single microprism. The sinc-comb on the other hand is the diffraction pattern of the grating which is due to the periodic alignment of the microprisms. In fig.3 these two parts are plotted independently. Thus it is possible and illustrative to investigate the influence of the various parameters, mentioned in the previous section, on the different parts of the complex amplitude. This gives good insight into the effects on the complete complex amplitude resulting in the Fourier plane behind such a blazed grating. Furthermore our approach allows to investigate the influence of different degrees of refractivity which can be varied e.g. by different blaze depths.

Wavelength dependence

As an example we discuss here the wavelength dependence of a grating which is blazed into the -1st order for a design wavelength $\lambda_0 = 480\text{nm}$. Fig. 3 shows the refractive (broad sinc function) and diffractive (narrow sinc peaks) parts of the light distribution in the Fourier plane. Due to the dispersion of the prism material the refractive peak is slightly inclined to smaller deflection angles for increasing wavelength. Much stronger, however, is the inclination of the sharp diffractive peaks. In fig. 3 only the blaze order and the two neighbour orders are shown (in the case of the -1st order being the blaze order these are the 0th, -1st and -2nd orders).

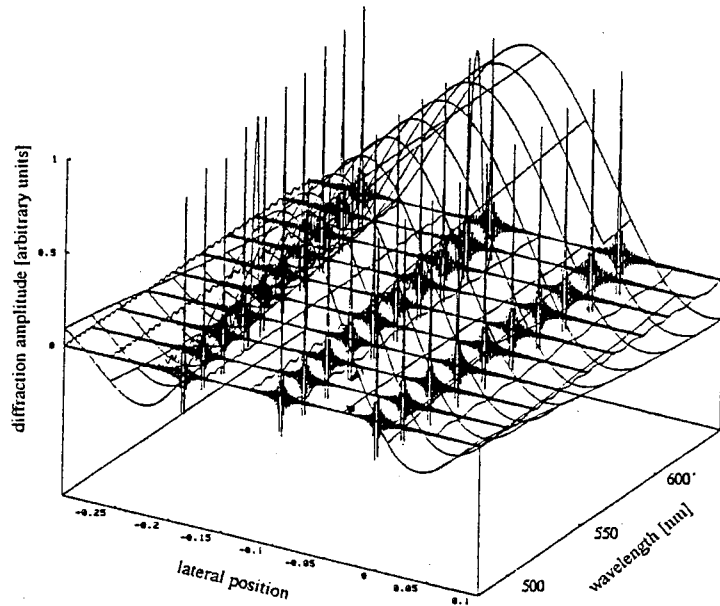


Fig.3: Amplitudes of the refractive and diffractive contributions of a blazed grating

In the example of fig.3 the blazed grating consists of 100 periods. Thus the refractive peak is 100 times wider than the diffractive peaks. Consequently the change in the position of the refractive sinc function has very little consequence on the overall complex amplitude. The blazed grating is in its behaviour with respect to the wavelength dependence very similar to the purely diffractive

grating. This is also illustrated in fig. 4 which shows the product of the refractive and the diffractive parts of the complex amplitudes.

For deeper blaze structures, however, the contribution of refraction to the effect of the blazed structure is increased. Then the individual microprisms become bigger in size and thus the refractive peak gets narrower. As the extension of the grating itself remains the same the relative influence of refraction increases. This is illustrated in fig. 5 where the resulting total complex amplitude of a grating with blaze depth $4\lambda_0$ is plotted. Comparing figs. 4 and 5 it is obvious that the shift in the position of the diffraction amplitude is less with variation over the same wavelength intervall.

There is, however, a bigger variation on the amplitudes. The reason for this is a change from one diffractive order to another which falls under the refractive envelope. This causes a transition through a minimum value at the position of the diffraction order.

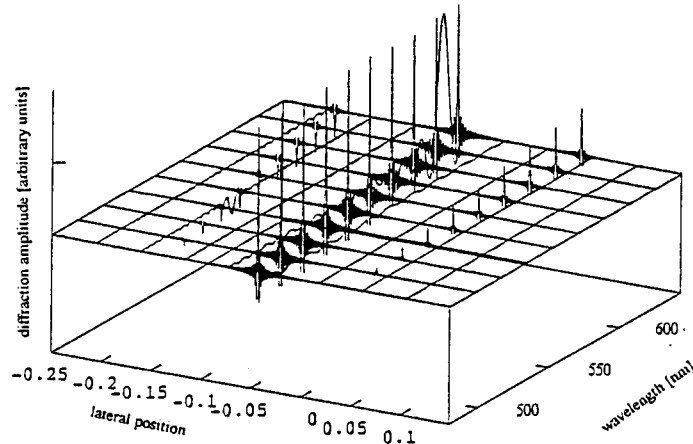


Fig.4: Total diffraction amplitude of a grating (blaze order = -1st order)

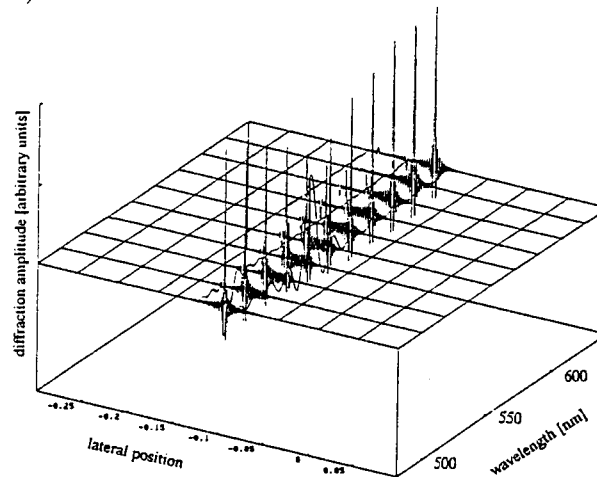


Fig.5: Total diffraction amplitude of a grating (blaze order = -4th order)

Conclusions

This rather simple illustration of the wavelength dependence of blazed structures will be extended to other parameters like angular and temperature dependence. It gives a better understanding of the transition between diffraction and refractive optical elements. We especially focus on the question how the specific dependences develop during this transition. This will eventually lead to the definition of a "degree of refraction" of such hybride elements.

References

- [1] S. J. Walker, J. Jahns et al., Appl. Opt. **32**, 2494 (1993)
- [2] M. C. Hutley, "Diffraction Gratings", Academic Press, New York (1982)
- [3] C. Lodoño, W.T. Plummer, P.P.Clark, *Diffraction Optics*, Tech. Digest (OSA, 1992), Vol.9
- [4] G. P. Behrmann, J. P. Bowen, Appl. Opt. **32**, 2483 (1993)

Exact surface relief profile of kinoform lenses from a given phase function

Y. Han, C.A. Delisle

Centre d'Optique, Photonique et Laser, Université Laval, Ste-Foy, Québec, Canada, G1K 7P4

Tel: (418) 656-5093, Fax: (418) 656-2623

L.N. Hazra

Applied Physics Department, Calcutta University, 92 A.P.C. Road, Calcutta 700 009, India

1. Introduction

Recently, ^{[1]-[2]} we described a geometric method for designing kinoform lenses for stigmatic imaging of an axial object point at finite conjugates. In practice, a diffractive optical element is often represented as a phase function. This is quite appropriate in general when the diffractive element is part, with conventional refractive and/or reflective elements of a multicomponent optical system. Some commercial lens design programs, such as CODE V, have the capability to insert diffractive phase profiles into a lens system. The optimum diffractive phase profile is attained by using the CODE V automatic design feature. A radially symmetric diffractive phase profile is given by the following power series

$$\Phi(r) = \frac{2\pi}{\lambda} (A_1 r^2 + A_2 r^4 + A_3 r^6 + \dots) \quad (1)$$

Once the coefficients of the phase function have been optimised for best performance of the optical system, one is left with the determination of the surface relief profile. This can be done easily by approximating the thickness of the profile as $Z(r) = \Phi(r)_{2\pi} \lambda / [2\pi(\mu-1)]$, where $\Phi(r)_{2\pi}$ is the phase function modulo 2π , λ is the design wavelength, and μ the index of refraction of the material used for the kinoform lens. For a plane kinoform lens, $Z(r)$ is measured along the direction of the optical axis, while for a spherical kinoform, $Z(r)$ is measured radially from the centre of curvature of the surface. The diffractive element being considered as being infinitely thin, the method just described gives approximate results, since thickness and refraction are not taken account of. The thickness of the relief being of the order of the wavelength, the relief obtained with that method should not differ greatly from the exact shape. However, determining the exact relief profile is worth considering and is precisely the goal of this paper.

2. Determination of the exact blaze profile from the phase function

Let $\Phi(r)$ be a known phase function obtained, for example, from a lens design program. It can be the phase function needed to make a single diverging or converging diffractive element or the phase function generated through an optimization routine for the purpose of reducing aberrations in a multi element optical system. With reference to fig.1, let AP be the surface on which a diffractive relief profile is to be added. O is the object point and O' the image point, while $P_m R_m$ is the m th zone of the blaze profile to be found from the phase function. The zone radii of this kinoform lens are determined by solving the following equation

$$\Phi(r_m) = -sm(2\pi) \quad (2)$$

where $s = +1$ for positive focal length, $s = -1$ for negative focal length and m is the zone number.

the total optical path length, $(OPL)_1$, from O to O' through point P' is

$$(OPL)_1 = -\frac{r}{\sin U} + \Delta(r) + \frac{r}{\sin U''} \quad (7)$$

On the other hand, the total optical path length, $(OPL)_2$, from O to O' through points P' and R' on the exact blaze relief profile $P_m R_m$ is

$$(OPL)_2 = -\frac{r}{\sin U} + \mu t_m + \frac{r - t_m \sin \tilde{U}}{\sin U'} \quad (8)$$

The optical path lengths $(OPL)_1$ and $(OPL)_2$ have the same value. Combining (7) and (8), we obtain

$$\Delta(r) + \frac{r}{\sin U''} = \mu t_m + \frac{r - t_m \sin \tilde{U}}{\sin U'} \quad (9)$$

A quadratic relation defining t_m is then obtained from (9) as

$$A t_m^2 + B t_m + C = 0 \quad (10)$$

where

$$A = 1 - \mu^2 \quad (11)$$

$$B = 2 \left\{ \mu \left[\Delta(r) + L' \sqrt{\left(\frac{r}{L'} \right)^2 + \left(\frac{L' - z}{L'} \right)^2} \right] - (r \sin \tilde{U} + (L' - z) \cos \tilde{U}) \right\} \quad (12)$$

$$C = -\Delta^2(r) - 2\Delta(r)L' \sqrt{\left(\frac{r}{L'} \right)^2 + \left(\frac{L' - z}{L'} \right)^2} \quad (13)$$

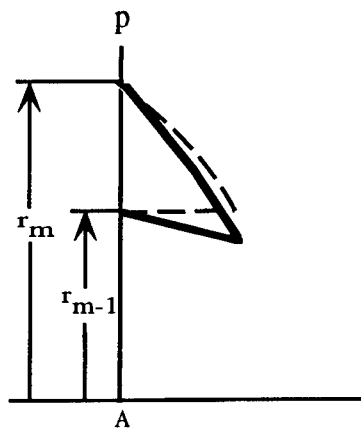
In the above, L is the object distance in the case of a stigmatic object, or the distance (see fig.1) from A to the intersecting point of the ray incident at P' with the optical axis in the case of a non-stigmatic object. Similarly L' is the image distance in the case of a stigmatic image or the distance from A to the intersecting point of the exit ray from P' with the optical axis in the case of a non-stigmatic image.

When one knows the phase function $\Phi(r)$, for example by using the optimisation routine of an optical design software, the shape of the blaze profile, coordinates Z and Y (see fig.1) can be calculated. Indeed, as $Z = t_m \cos \tilde{U}$ and $Y = r + t_m \sin \tilde{U}$ (see fig.1), the exact blaze profile is easily calculated when t_m and \tilde{U} are known. The thickness t_m is obtained from equations (10) to (13), and \tilde{U} from $\tilde{U} = U + I - I'$. The angle U between the incident ray on the diffractive surface and the optical axis is equal to the angle between the exit ray of the preceding element and the optical axis. The angle of incidence I is equal to the negative of angle U in the case of a plane kinoform lens and equal to $\theta - U$ for a spherical kinoform lens, where θ is the angle between the normal at the point of incidence and the optical axis. The angle of refraction I' is calculated using the Snell's law at the point of incidence. The value of L' in equations (10) and (11) is determined from the ray trace of the ray going through P' at height r . This value can normally be obtained as an output when tracing a singular ray with an optical design software. Finally, the value for z in equations (10) and (11) is obtained from r the height of the incident ray and R the radius of the kinoform surface.

It is seen that there is no analytical solution for the exact blaze profile in the case of finite conjugate imaging. The coordinates Z and Y have to be calculated point by point from the values of t_m and \tilde{U} .

We have considered the case when both the object and the image are non-stigmatic. Of course, the calculation are much simpler when the object or the image or both of them are stigmatic. The problem of determining the exact blaze profile from the phase function is also much simpler when one considers a configuration with an infinite conjugate.

Fig. 2 Example of exact and approximate surface relief profile



The approximate method for calculating the blaze profile, which has been mentioned earlier, should bring two differences if one compares with the blaze profile obtained with the exact method. Fig. 2 shows both profiles, the approximate, dashed lines, and the exact, solid lines. The first difference concerns the thickness of the blaze and the second difference the shape of the thick part of the blaze. In the approximate method, the bottom part is perpendicular to the plane face of the kinoform lens, while in the exact method, the higher the order of the zone more inclined is the bottom part.

References

1. Hazra, L. N., Han, Y. and Delisle, C.A., "Curved Kinoform Lenses for Stigmatic Imaging of an Axial Object at Infinity", *Opt. Commun.* **90**, 201-206 (1992).
2. Hazra, L. N., Han, Y. and Delisle, C.A., "Plane Kinoform Lenses for Axial Stigmatism in Finite Conjugate", *Opt. Commun.* **91**,1-4 (1992).

APPLICATION OF THE YANG-GU ALGORITHM TO THE DESIGN OF DIFFRACTIVE PHASE ELEMENTS FOR ACHIEVING MULTIPLE OPTICAL FUNCTIONS

Benyuan Gu, Guozhen Yang, Bizhen Dong

Institute of Physics, Academia Sinica, P. O. Box 603, Beijing 100080, China

Tel: (86)-1-2553101; Textfax: (86)-1-2562605

Ming-Pin Chang, and Okan K. Ersoy

Purdue University, School of Electrical Engineering, West Lafayette, Indiana 47907, USA

As the development of computer-generated holograms and kinoforms, and advances in the techniques of optical and electron lithography, it makes possible to fabricate various high quality diffractive optical elements (DOE's). The studies on the design and fabrication of the DOE's have become active subject in recent years.¹⁻⁵ The goal of this presentation is to propose a new design approach for the diffractive phase elements (DPE's) achieving multiple optical functions in a general linear optical systems. We generalized the previous theory⁶⁻⁸ to the imaging system illuminated by a light beam with multiple wavelength components. We derive a set of equations for determining the profile of the surface-relief DPE. By using the derived equations and an iterative algorithm, the profile of the surface-relief DPE achieving multiple optical functions can be determined.

An optical system considered here is illuminated by a beam of incident light with multiple wavelength components incoherently. P_1 and P_2 are the input and output planes, respectively. The output wave function is linked to the input one at wavelength λ_α by a linear transform function $G(\mathbf{X}_2, \mathbf{X}_1, \lambda_\alpha)$ ⁶⁻⁸ in the form

$$U_2(\mathbf{X}_2, \lambda_\alpha) = \int G(\mathbf{X}_2, \mathbf{X}_1, \lambda_\alpha) U_1(\mathbf{X}_1, \lambda_\alpha) d\mathbf{X}_1. \quad (1)$$

In the general case G may be nonunitary transform.

In the simulations, the every continuous function is approximately assumed to be represented by its values at a set of sampling points (or pixels). Assume the total numbers of the sampling points are N_1 and $N_2 = N_{2s} \times N_\lambda$ for the input and output wave functions, respectively, where N_{2s} is the number of the spatial sampling points on the output plane, and N_λ is the number of different wavelengths. Thus, we have

$$U_{1n}(\lambda_\alpha) = \rho_{1n\alpha} \exp(i2\pi h_{1n}/\lambda_\alpha), \quad n = 1, 2, 3, \dots, N_1, \quad (2a)$$

$$U_{2m\alpha} = \rho_{2m\alpha} \exp(i\phi_{2m\alpha}), \quad (2b)$$

and

$$U_{2m\alpha} = \sum_{n=1}^{N_1} G_{mn}(\lambda_\alpha) U_{1n\alpha}, \quad m = 1, 2, 3, \dots, N_{2s} \quad \alpha = 1, 2, 3, \dots, N_\lambda. \quad (3)$$

It is worth emphasizing that in our calculations we will assume that the DPE is fabricated by surface-relief kinoform. Here, h_{1n} represents the surface-relief local depth in the kinoform at the n th sampling point, independent of the wavelength. Thus, the phase distribution in the DPE is given by $\phi_{1n\alpha} = 2\pi h_{1n}/\lambda_\alpha$.

The design problem of the DPE can be generally addressed as follows: If the leaner transform \hat{G} and amplitude information on $U_{1\alpha}(x_1)$ and $U_{2\alpha}(x_2)$ are known, how can we determine the profile of the surface-relief kinoform so that Eq. (3) can be satisfied to a high accuracy?

To describe the closeness of $\hat{G}U_1$ to U_2 , we introduce a distance measure D^2 in an L_2 norm⁶⁻⁸ as

$$D^2 = \sum_{\alpha} || [U_{2\alpha} - \hat{G}(\lambda_{\alpha})U_{1\alpha}] ||^2. \quad (4)$$

Therefore, the design problem of the diffractive phase element may thus be formulated as the search for the minimum of D^2 with respect to function arguments h_1 and $\phi_{2\gamma}$.

Through evaluating the functional variations in detail, we can derive the following equations for determining the pattern of the DPE :

$$\exp(i2\pi h_{1k}/\lambda_0) = \frac{\tilde{Q}_k^*}{|\tilde{Q}_k|}, \quad k = 1, 2, 3, \dots, N_1 \quad N_1 = N_2 = N, \quad (5)$$

where

$$\begin{aligned} \tilde{Q}_k = & \sum_{\alpha} \left\{ \sum_{j \neq k}^I \rho_{1j\alpha} \exp(-i2\pi h_{1j}/\lambda_{\alpha}) A_{jk}(\lambda_{\alpha}) \right. \\ & \left. - \sum_j \rho_{2j\alpha} \exp(-i\phi_{2j\alpha}) G_{jk}(\lambda_{\alpha}) \right\} (2\pi/\lambda_{\alpha}) \rho_{1k\alpha} \exp[i(2\pi h_{1k}/\lambda_0)(\lambda_0/\lambda_{\alpha} - 1)], \end{aligned}$$

and

$$\begin{aligned} \exp(i\phi_{2k\gamma}) = & \frac{\sum_j G_{kj}(\lambda_{\gamma}) \rho_{1j\gamma} \exp(i2\pi h_{1j}/\lambda_{\gamma})}{|\sum_j G_{kj}(\lambda_{\gamma}) \rho_{1j\gamma} \exp(i2\pi h_{1j}/\lambda_{\gamma})|}, \\ & k = 1, 2, 3, \dots, N_{2s}, \quad \gamma = 1, 2, 3, \dots, N_{\lambda}. \end{aligned} \quad (6)$$

Here λ_0 is the mean wavelength and $\hat{A}(\lambda_{\alpha}) \equiv \hat{G}^+(\lambda_{\alpha})\hat{G}(\lambda_{\alpha})$. No analytical solution to Eqs. (5) and (6) is expected to be available. They can be numerically solved by using the iterative algorithm described in Refs. [6-8].

To verify the effectiveness of the new design approach, we carry out a simulation design for the DPE's capable of both functions of demultiplexing and focusing each partial wave in space. The DPE is placed on the input plane. Optical system performs a linear transform with a transformation kernel as $\hat{G}(x_2, x_1; l, \lambda_{\alpha})$ at wavelength λ_{α} . In the paraxial approximation and measuring x_1 and x_2 in units of $\sqrt{\lambda_0 l}$, $G(x_2, x_1; l, \lambda_{\alpha})$ can then be expressed as

$$G(\bar{x}_2, \bar{x}_1; l, \lambda_{\alpha}) = \sqrt{\frac{\lambda_0}{\lambda_{\alpha}}} \exp(i2\pi l/\lambda_{\alpha}) \exp[i\pi \lambda_0 (\bar{x}_2 - \bar{x}_1)^2/\lambda_{\alpha}], \quad (7)$$

$$\bar{x}_1 = x_1/\sqrt{\lambda_0 l}, \quad \bar{x}_2 = x_2/\sqrt{\lambda_0 l}.$$

The following relevant physical and structural parameters values were chosen : The wavelengths of the illumination light waves are ranged over an interval of $[\lambda_{min} = 4000\text{\AA}, \lambda_{max} = 7000\text{\AA}]$. The spacing between two planes is $l = 20\text{mm}$. We assumed a uniform intensity distribution for all wavelength components, i.e., $\rho_{1\alpha}$ is constant. We chose the following initial phase for $\phi_1^{(0)} = 2\pi h_1^{(0)}/\lambda_0$ in the iterations:

$$\phi_1^{(0)} = 2\theta(\sqrt{\lambda_0 l})x_1/\lambda_0 - x_1^2, \quad \theta = x_{2max} \lambda_0 N_{\lambda} \sqrt{\lambda_0 l}/(N_2 \Delta \lambda l), \quad (8)$$

where x_{2max} is the size of the aperture on the output plane. We set the sizes of the aperture on the input and output planes to be the same as $x_{1max} = x_{2max} = \sqrt{N_1}$ in units of $\sqrt{\lambda_0 l}$. The amplitudes on the output plane are assigned as follows : $\rho_{2\alpha}(x_{2m}) = (1/\sqrt{N_\lambda})\delta_{\alpha,m}$, ($\alpha = 1, 2, 3, \dots, N_\lambda, m = 1, 2, 3, \dots, N_{2s}$). N_λ equals 8, $N_1 = 64$ and $N_{2s} = 8$. The diffraction pattern on the output plane generated by the DPE with the calculated surface-relief profile and the desired pattern are shown in Table 1, where the sequence I represents different positions in space, and γ indexes different wavelength components. As shown in Table. 1, the diffraction pattern obtained with the designed elements is very close to the desired pattern. It indicates that satisfactory design of such multifunction diffractive phase element is indeed possible with the new iterative algorithm.

Table 1. Profile of Relief-Surface of Kinoform and Output Demultiplexed Amplitudes at Eight Different Wavelengths

Position Sequence I	Sequence wavelength γ	Calculated Thickness (μm)	Desired ρ_2	Calculated ρ_2
1	1	0.6114	0.3536	0.3613
	2	0.7928	0.0	0.0118
	3	0.0992	0.0	0.0362
	4	0.1317	0.0	0.0209
	5	0.9974	0.0	0.0191
	6	0.1493	0.0	0.0174
	7	0.2475	0.0	0.0425
	8	0.3188	0.0	0.0403
2	1	0.9367	0.0	0.0225
	2	0.9079	0.3536	0.3469
	3	0.1713	0.0	0.0131
	4	0.3170	0.0	0.0121
	5	0.1986	0.0	0.0174
	6	0.8939	0.0	0.0127
	7	0.8097	0.0	0.0351
	8	0.8669	0.0	0.0627
3	1	0.9858	0.0	0.0153
	2	1.0859	0.0	0.0184
	3	0.0368	0.3536	0.3363
	4	1.0103	0.0	0.0130
	5	1.0309	0.0	0.0162
	6	1.0454	0.0	0.0395
	7	0.9309	0.0	0.0385
	8	0.0126	0.0	0.0400
4	1	0.8879	0.0	0.0105
	2	0.8184	0.0	0.0154
	3	0.7504	0.0	0.0240
	4	0.6831	0.3536	0.3631
	5	0.4558	0.0	0.0363
	6	0.3631	0.0	0.0198
	7	0.1760	0.0	0.0348
	8	0.0839	0.0	0.0312

Table 1. (continue)

Position Sequence I	Sequence wavelength γ	Calculated Thickness (μm)	Desired ρ_2	Calculated ρ_2
5	1	1.0153	0.0	0.0101
	2	0.4997	0.0	0.0138
	3	0.3009	0.0	0.0162
	4	0.2336	0.0	0.0340
	5	0.1663	0.3536	0.3827
	6	0.9673	0.0	0.0541
	7	0.5868	0.0	0.0249
	8	0.3513	0.0	0.0387
6	1	0.0660	0.0	0.0158
	2	0.8249	0.0	0.0188
	3	0.4764	0.0	0.0111
	4	0.0845	0.0	0.0327
	5	0.6597	0.0	0.0259
	6	0.2118	0.3536	0.3049
	7	0.8512	0.0	0.0217
	8	0.1807	0.0	0.0609
7	1	0.8084	0.0	0.0245
	2	0.2969	0.0	0.0214
	3	0.9207	0.0	0.0174
	4	0.9510	0.0	0.0252
	5	0.9149	0.0	0.0248
	6	0.3131	0.0	0.0407
	7	0.0453	0.3536	0.3462
	8	0.4814	0.0	0.0288
8	1	1.0125	0.0	0.0217
	2	0.6230	0.0	0.0170
	3	0.4491	0.0	0.0081
	4	0.0419	0.0	0.0205
	5	0.6363	0.0	0.0216
	6	0.5163	0.0	0.0106
	7	0.2419	0.0	0.0296
	8	0.3368	0.3536	0.3174

REFERENCES

1. M. Bernhardt, F. Wyrowski, and O Bryngdahl, *Appl. Opt.* **30**, 4629-4635 (1991).
2. P. Ehbets, H. P. Herzig, R. Dandliker, P. Regnaul, and I. Kjelberg, *J. Modern Opt.* **40**, 737-645 (1993).
3. F. Wyrowski and O. Bryngdahl, *J. Opt. Soc. Am. A* **5**, 1058-1065 (1988).
4. M. Kato and K. Sakuda, *Appl. Opt.* **30**, 630-635 (1992).
5. Y. Amitai, *Opt. Commun.* **98**, 24-28 (1993).
6. G. Yang, L. Wang, B. Dong and B. Gu, *Optik* **75**, 68-74 (1987).
7. G. Yang, B. Gu, and B. Dong, *J. Modern Phys. B* **7**, 3153-3224 (1993).
8. G. Z. Yang, B. Z. Dong, B. Y. Gu, J. Y. Zhuang and O. K. Ersoy, to be published in *Appl. Opt.* (1994).

Interpolation Approaches to Computer-Generated Holograms

Nobukazu Yoshikawa and Toyohiko Yatagai
 Institute of Applied Physics
 University of Tsukuba
 1-1-1, Tennoudai, Tsukuba, Ibaraki, 305, Japan
 Tel: +81-298-53-5334
 Fax: +81-298-53-5205

Introduction

Computer-generated holograms¹⁻³ (CGHs) have improved significantly the possibilities of optical data processing⁴ and display.⁵ Functional flexibility is the main advantage of CGHs. Its extensive use, however, is limited because of a large amount of computation and plotting time. For reconstructing $N \times N$ resolution points, CGH requires $N \times N$ sampling cells. When an object to be reconstructed contains a large number of degrees of freedom, the hologram must contain this number of sampling cells and needs a large amount of computing time and also a large size of the computer memory. If the amplitude transmittance of each object point is not independent, we can reduce the required memory size with an interpolation technique of reconstructed image points.

In this paper we present an interpolation method of image points reconstructed by Fourier transform CGH, and its computer simulation. We evaluate reconstructed images generated with several interpolation algorithms.

Description of the method

Before describing the method, we consider a property of the discrete Fourier transform (DFT). For simplicity, calculations in this paper are carried out in one dimension. The extension to the two-dimensional situation is trivial because of the linearity of the DFT. We define here the DFT series of a sequence of N sample points in the image domain, $f(p\Delta)$, $p=0, 1, \dots, N-1$, as follows,

$$f(p\Delta) = \frac{1}{N} \sum_{n=0}^{N-1} F(n\Omega) \exp\{inp\Omega\Delta\} \quad (1)$$

where Δ denotes the sampling interval, and $\Omega=2\pi/(N\Delta)$. In the case of Fourier transform CGHs, $F(n\Omega)$ is interpreted as the hologram reconstructing the image $f(p\Delta)$. Its inverse transform is given by

$$F(n\Omega) = \frac{1}{N} \sum_{p=0}^{N-1} f(p\Delta) \exp\{-inp\Omega\Delta\} \quad (2)$$

With this specification of Ω , there are only N distinct and independent values computable by Eq. (1), namely, $n=0, 1, \dots, N-1$.

If the sampling period Δ in the object domain is divided into K -subperiods, then the new period is given by $\delta=\Delta/K$. Since the sequence $f(p\Delta)$ provides samples of the desired remaining samples by making $(k-1)$ -time interlace of N sample sequence $f(p\Delta)$ with the weight factor $p=k\delta$ for interpolation. We have from Eq.(2)

$$\begin{aligned}
 F'(r\Omega) &= \frac{1}{NK} \sum_{p=0}^{N-1} \sum_{k=0}^{K-1} f(p\Delta) \rho(k\delta) \exp\{i(p\Delta + k\delta)r\Omega\} \\
 &= F([r]_N \Omega) w(r)
 \end{aligned} \tag{3}$$

where $[r]_N = r$ modulo N , and $w(r)$ is the weight factor in the Fourier domain. The weight factor in the Fourier domain is written by

$$w(r) = \frac{1}{K} \sum_{k=0}^{K-1} \rho(k\delta) \exp(-ikr\delta\Omega) \tag{4}$$

The DFT of the sequence given by K -time interpolation of the original sequence $f(p\Delta)$ is the product of the sequence $F([r]_N \Omega)$ which is the periodic extension of $F(n\Omega)$ and the weight factor $w(r)$.

In the previous study, the constant interpolation is implemented. Its weight factor in Fourier domain is given by

$$w(r) = \frac{1}{K} \frac{1 - \exp(2\pi ir/N)}{1 - \exp(2\pi ir/NK)}. \tag{5}$$

In this case, the resolution of the image increases because one point sequence of the interpolated image is made by K -time interace.

We consider here the following four types of interpolation weights $\rho(k\delta)$;

- Type A: Separable square interpolation,
- Type B: Separable triangle interpolation (two square convolved),
- Type C: Separable bell interpolation (three square convolved),
- Type D: Separable cubic B-spline interpolation (four square convolved).

In these cases, the weight factors in the Fourier domain are

$$\text{Type A: } \omega_0(r) = \frac{\sin(\pi r/N)}{\pi r/N}, \tag{8}$$

$$\text{Type B: } \omega_1(r) = \omega_0^2(r), \tag{9}$$

$$\text{Type C: } \omega_2(r) = \omega_0^3(r), \tag{10}$$

$$\text{Type D: } \omega_3(r) = \omega_0^4(r), \tag{11}$$

The interpolation types and their weight factor are shown in Figure 1. These interpolation can interpolate smoothly between the discrete values. The simplest interpolation weight is the rectangle function that results in a zero-order interpolation of samples (Figure 1(a)). A triangle function provides the first-order interpolation with triangular-shaped interpolation patterns (Figure 1(b)). The triangle function may be considered to be the result of convolving a rectangle function with itself. Convolution of the triangle function with the rectangle function yields a bell-shaped interpolation weight (Figure 1(c)). Polynomials of order two or greater can be employed as interpolation weights. The cubic B-spline is a particularly attractive candidate for image interpolation because of its

properties of continuity and smoothness at its extremities (Figure 1(d)). The orthogonally separable two-dimensional interpolation function can be defined as $\omega(x,y)=\omega(x)\omega(y)$.

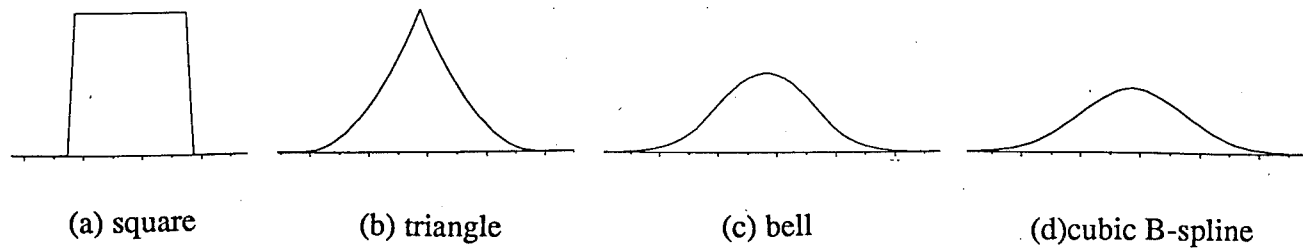


Figure 1. One-dimensional interpolation waveforms.

Synthesis procedure and computational verification

Let us consider a hologram of $N \times N$ sample points. At the first step, its Fourier transformed hologram is plotted. By using a step-and-repeat camera, two dimensional multiplication of the Fourier transform hologram of $N \times N$ sample points provides a mosaic hologram of $K \times K$ subholograms, so that a mosaic hologram of $NK \times NK$ sample points is obtained. On the other hand, a complex filter whose transmittance is $w(r)$ is produced, for example, by using the CGH technique. Superposition of the weight complex filter on the mosaic hologram reconstructs an interpolated image.

Alternative is to make a mosaic hologram which consists of $K \times K$ subholograms with $N \times N$ sampling points multiplied by an appropriate weight factor $w(r)$.

In computer simulation, a normal CGH of 16×16 sample points and its mosaic hologram given by arranging 4×4 subholograms are synthesized to verify the method. Figures 2 and 3 show experimental results. Figure 2 shows the reconstructed image of the CGH of Type A. Same subholograms of 16×16 sample points are arranged. The weight factor for interpolation is rectangular. Each reconstructed point is interpolated as shown in Fig.2. The reconstructed image of the hologram with the weight factor given by Eq.(10) is shown in Fig.3, which is the same as that of a single subhologram. Thus each reconstructed point is interpolated as shown in Fig.3. Image sharpness of Fig.3 is decreased with the interpolation order, but the image is smoothly interpolated.

Concluding remarks

This paper has described that we can reduce the required memory size for computing Fourier transform CGHs whose sampling points are not independent. Four types of the interpolation techniques are employed. The main advantages of the present algorithm is that a sufficiently large size hologram of $NK \times NK$ sample points is synthesized by $K \times K$ subholograms which are successively calculated from the data of $N \times N$ sample points and also successively plotted. This means that the required data size in a computer memory is only $N \times N$ to make a CGH that reconstructs $NK \times NK$ image points.

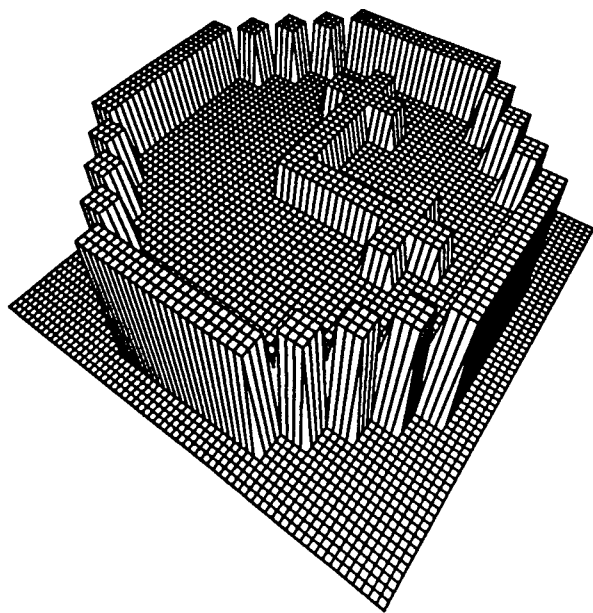


Figure 2. Image interpolation of Type A, Separable square interpolation.

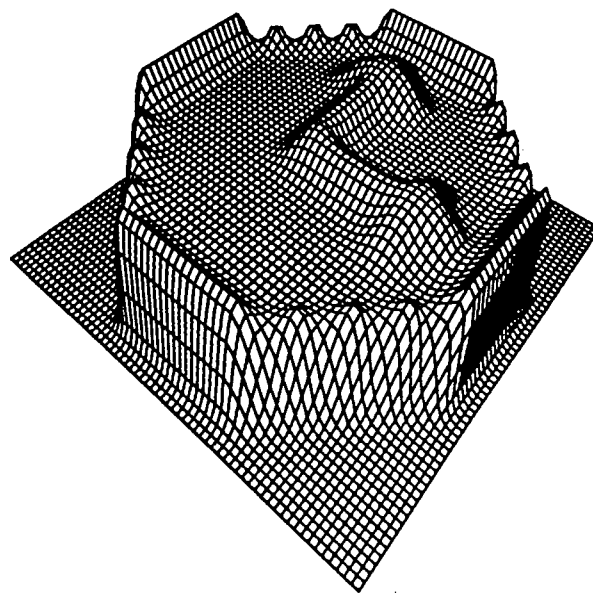


Figure 3. Image interpolation of Type C, Separable bell interpolation.

References

1. Brown, B. R., and Lohmann, A. W., "Complex Spatial Filtering with Binary Masks," *Appl. Opt.*, Vol.5, pp.967-969. 1966.
2. Lohmann, A. W., and Paris, D. P., "Binary Franhofer Holograms Generated by Computer," *Appl. Opt.*, Vol.6, pp. 1739-1748. 1967.
3. Lee, W. H., "Computer-Generated Holograms: Techniques and Applications," *Progress in Optics*, Vol.XVI, E. Wolf ed., North-Holland, pp. 121-232. 1978.
4. Lohmann, A. W., and Paris, D. P., "Computer-Generated Spatial Filters for Coherent Optical Data Processing," *Appl. Opt.*, Vol.7, pp. 651-655. 1968.
5. Yatagai, T., "Stereoscopic Approach to 3-D Display Using Computer-Generated Holograms," *Appl. Opt.*, Vol.15, pp. 2722-2729. 1976.
6. Yatagai, T., "Interpolation Methods of Computer-Generated Filters for Large Object Formats," *Opt. Commun.*, Vol. 15, pp. 347-351. 1977.
7. Bartlet, H., Dallas, W. J., and Lohmann, A. W., "Computer-Generated Spatial Filters for Large Object Formats," *Opt. Commun.*, Vol.20, pp. 50-55. 1977.

A Direct Search Method for the Computer Design of Holograms for the Production of Arbitrary Intensity Distributions.

Matthew Clark, Applied Optics Group, Blackett Laboratory, Imperial College, London SW7 2BZ.
Tel.: 071 589 5111 ext. 6861 Fax.: 071 589 9463 E-mail: matt@op.ph.ic.ac.uk

1. INTRODUCTION TO DESIGN PROBLEM.

A direct search method has been developed to produce high diffraction efficiency single element holograms that when appropriately illuminated produce a close approximation to a specified intensity distribution. Applications include laser machining, optical interconnects and matching sources to detectors.

The design of a hologram must be for a physically realisable device with a quantized phase and limited space bandwidth product. Quantized phase can prove problematic for some design methods such as "Projection on Constraints"^{1 2 3}, as the restraint of quantizing the phase can lock so much phase noise into the hologram phase distribution that the algorithm does not converge efficiently and the reconstructed image is noisy. Attempting to represent a continuous phase with a quantized phase can be problematic even when error diffusing methods⁴ are used.

Direct complex amplitude calculation, such as carried out by Riley and Birkett⁵, produces poor results because the computed complex amplitude distribution contains amplitude variations that are not encoded into the hologram and the subsequent quantization process does not preserve the phase information accurately. This method also fails to exploit the image phase as a partial degree of freedom.

It is desirable that the design method incorporates quantized phase during optimisation so that the design is not disrupted by subsequent quantization.

Space bandwidth Product, Numerical Aperture and Sampling.

It is fairly simple to demonstrate that the hologram must have at least the same space bandwidth product as the required intensity distribution. It is also important that a continuous image intensity distribution is sampled or digitised with the same or higher bandwidth. In some circumstances it may be desirable to sample at a higher rate than given by this bandwidth.

Usually the desired image contains regions of uniform intensity such as lines or patches. For the purpose of computation it is necessary to represent the required intensity distribution as a set of sample points. In order for these uniform intensity regions to appear uniform when reconstructed it is necessary

that sample spacing should be smaller than the minimum feature size. The light at adjacent samples must be "in phase"⁶, to avoid destructive interference leading to low intensity between samples. This destructive interference is seen in some optical reconstructions of Fourier transform holograms designed using the "Projection on Constraints" method, in which the phase in the image is allowed to vary in an unconstrained manner. This is not important for images of well-separated points as used in interconnects, but for uniform areas results in optical reconstructions that are far noisier than the digital reconstructions. It is therefore desirable to restrain the phase variation in the image to some extent. Higher sampling rates could be used to ensure more uniform intensity distributions but would increase the computational effort by a large factor. It is better to control the image phase distribution during the design process. It is not necessary to specify the phase at each point as long as it does not vary too quickly across the image. This flexibility is a useful degree of freedom during the optimisation of the hologram.

3. THE DIRECT SEARCH ALGORITHM.

The hologram can be considered to be made of pixels each of which adds phase to the incident wavefront. The number and sizes of the pixels are determined by considering the resolution and space bandwidth product of the image. The phase at each pixel can take values corresponding to the number of phase levels available (e.g. in binary hologram the phase can have values 0 and π). In the direct search algorithm an initial solution to the phase distribution ϕ_d is chosen: for example this could be random or uniform. The complex amplitude of the image is computed at a set of sample points in the image and an initial "cost" (defined below) is then computed. A change is then made to the phase of a single hologram pixel and the resulting change in the complex amplitude at all the selected image sample points is calculated. The new cost (or the change in the cost) is also calculated. If the new cost is lower than the old cost (or the change in the cost is negative) the new solution is retained, otherwise it is rejected and the previous solution retained. The process is repeated until some stopping criterion is fulfilled.

This process is equivalent to the simulated annealing method^{7, 8} with the notional temperature⁹ set to zero.

The contribution to the image complex amplitude from one hologram pixel is given, using the Kirchhoff approximation, by

$$\Delta U_{image} \cong \frac{-i}{2\lambda} |U_i| \frac{\exp\{-i(k \cdot R + \phi_d + \phi_s)\}}{R} O \Delta S \quad (1)$$

where ΔU_{image} is the complex amplitude contribution at the image, U_i is the amplitude at the hologram pixel, R is the distance between the image sample point and hologram pixel, k is the wave number, ϕ_d is the design phase, ϕ_s is the phase of the incident illumination, ΔS is the area of the pixel and O is an obliquity factor determined by the particular configuration. The obliquity factor is usually considered to be constant over the range of angles subtended by the hologram at the image points.

Design of Cost Functions.

The cost function is made up of a set of contributions which can be given variable weights. For example, the total cost function, C_t might be constructed as

$$C_t = aC_I + bC_\phi + cC_u + dC_{cu} + eC_{fab} \dots \quad (2)$$

where C_I is a cost associated with the required intensity distribution at the image, C_ϕ is a cost associated with the phase distribution in the image, C_u is an amplitude uniformity cost, C_{cu} is a complex uniformity cost, C_{fab} is a cost introduced to help with the fabrication of the hologram and factors $a-e$ are cost balancing weights.

The cost, C_I , associated with the required intensity distribution in the image is a measure of the error between the required intensity distribution and the computed intensity distribution, a convenient form is

$$C_I = \sum_{image} (I_i - I_t)^2 \quad (3)$$

where I_i is the intensity and I_t is the target intensity. A suitable cost associated with the phase distribution can be defined by

$$C_\phi = \iint_{image} |\nabla \phi_i - \underline{I}_\phi|^2 dS \quad (4)$$

where ϕ_i is the phase and \underline{I}_ϕ is the target phase gradient given by

$$\underline{I}_\phi \approx \frac{4\pi}{F\lambda} \underline{r} \quad (5)$$

where \underline{r} is a vector normal to the axis of the hologram, from the axis to the image sample point and F is the distance from the hologram to the image plane.

The range of phase gradients, δT_ϕ , which allows an acceptable representation of continuous image intensity distribution is given approximately by

$$\delta T_\phi \approx \frac{4\pi D_H}{F\lambda} \quad (6)$$

where D_H is the size of the hologram. If the magnitude of the greatest phase gradient is less than the range of phase gradients a target gradient is not needed, i.e., $T_\phi < \delta T_\phi$. This occurs when the size of the image is smaller than the size of the hologram.

The uniformity cost may be defined as

$$C_u = \sum_{image} (|u_i| - \overline{|u|})^2 \quad (7)$$

where u_i is the complex amplitude at the image sample point and $\overline{|u|}$ is the average magnitude of this over the image.

A complex uniformity for the set of image sample points at which the complex amplitude is u_i can be defined as

$$C_{cu} = \sum_{i, image} \left\{ \sum_{k, neighbours} |u_i - u_k| \right\} \quad (8)$$

This is useful and easy to calculate. If the image is fairly uniform it can be shown that the complex uniformity, C_{cu} , can be roughly written as

$$C_{cu} \approx aC_\phi + bC_u \quad (9)$$

The cost C_{fab} associated with fabrication might be used to discourage solutions that are particularly difficult to fabricate, for example assigning a large cost penalty to isolated pixels with a phase level different from all its nearest neighbours.

It is important to note that the cost function can take many other factors into account.

Stopping Functions and Strategies.

The direct search algorithm stopping criteria can be based on factors such as the amount of elapsed computational time, the quality of the solution and the estimated probability of a pixel phase change being accepted. The latter has produced the most satisfactory results. The algorithm is usually stopped when the estimated probability of accepting a change is low, for instance less than one percent. This tends

to ensure that the majority of the pixels in the hologram are set optimally and that time is not wasted pursuing small improvements. It is important not to try to get an absolutely stable solution as there is a chance that the algorithm might drift slowly through a range of very similar solutions.

Computational approach

The direct search method is computationally intensive. If the hologram has N^2 pixels and sampling the whole image plane requires N^2 samples, the procedure becomes an N^4 process. However, it is only necessary to sample the bright regions of the image as dark regions become darker as light is drawn into the brighter regions. Line and point images require typically N image samples making an N^3 process. This significantly reduces the computational time required.

The initial image phase may contain a lot of phase noise which can remain "locked in" to the image during the optimization. This can result in lengthy optimization in an attempt to remove this noise and escape this poor local solution. By including phase in the cost function, especially at early stages of optimization, it is possible to speed up the convergence of the algorithm.

It is advantageous to identify at each stage of the optimisation those pixels which are subsequently unlikely to change and to concentrate on those pixels that are likely to do so. As the solution develops fringe structures appear, pixels that are embedded in the centre of these fringes are unlikely to change. Considering only those pixels that are at the edge of fringes, once an initial solution has developed, can speed the algorithm considerably.

If the wavefront incident on the hologram has a significantly non-uniform intensity distribution, choosing pixels initially in order of decreasing intensity also speeds the convergence of the algorithm.

The direct search method is particularly suited for use with parallel and vector processing computers and the algorithm has been developed to exploit this.

4. RESULTS

The method has been used to design a number of holograms for laser machining with CO_2 ($10.6\mu\text{m}$) lasers. The image is typically made up of narrow lines for laser cutting designs, or rectangular patches with a "top hat" intensity profile for laser heat treatment designs. These holograms are single reflective elements mounted at 45° to the laser beam with the horizontal image plane typically 0.5m below the hologram. Digital reconstructions of the holograms have been made to predict the performance of these elements. A figure of merit for the efficiency of these elements based upon the amount of light in the bright design areas of the

image compared with the amount of light in these areas in an idealised image with sinc^2 line profiles is approximately 92%. The rest of the light is spread as a diffuse background or escapes the target area. Some of these designs have been re-scaled for reconstruction at HeNe wavelength and elements fabricated using electron beam lithography. These chrome on glass masters have been subsequently copied into photoresist to produce phase holograms.

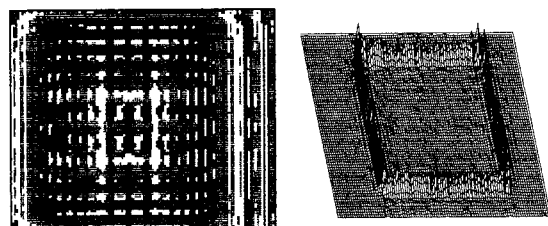


Fig. 1. A hologram design to produce a rectangular line focus from a uniform intensity source and its digital reconstruction.

Figure 1 shows a hologram which has been designed using the direct search method to produce a rectangular line and the digitally reconstructed intensity distribution produced by this hologram. The estimated efficiency of this hologram is $\sim 90\%$.

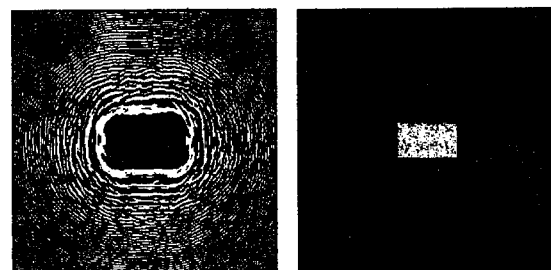


Fig. 2. A hologram designed to produce a rectangular patch of light with uniform intensity from a Gaussian laser beam source and its digital reconstruction.

Figure 2 shows a hologram designed to produce a rectangular patch of light 8 mm by 4.5 mm from a Gaussian laser beam and the digital reconstruction of the image. The hologram contains 350 by 350 pixels and has binary phase. The estimated efficiency of this hologram is $\sim 90\%$.

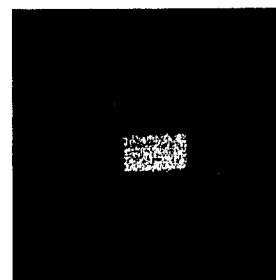


Fig. 3. The optical reconstruction, at 633nm, of the design shown in figure 2.

Figure 3 shows an optical reconstruction of the hologram shown in figure 2 at HeNe wavelength, the focal length or working distance of the element was ~30mm and the size of the patch was ~.5mm by .25mm.

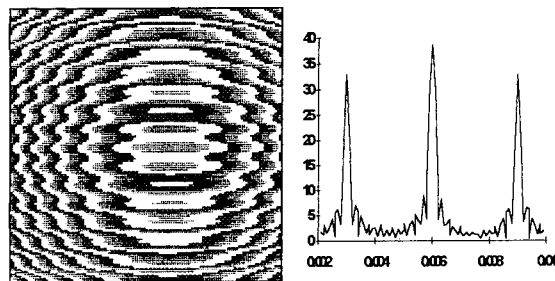


Fig. 4. A hologram designed to produce three dots, note the fringes are continuous resulting in little high frequency noise. The graph shows the intensity profile through the three foci.

Figure 4 shows a simple interconnect hologram. Examination of reconstructions of this and similar holograms confirms that the spot size is determined by the numerical aperture of the hologram. This can produce smaller spots than arrays of separate lenses.

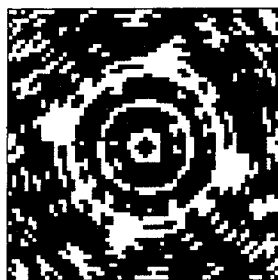


Fig. 5. Shows a hologram design to produce a ring focus at $F=1m$ and a cross focus at $F=14m$ figure 6 shows the digital reconstructions at these planes.

Figure 5 shows the hologram designed, for 633nm, to produce two different images at two different focal lengths. The digital reconstructions of the hologram at these focal lengths are shown in figure 6. This demonstrates the flexibility of the direct search method and the very important feature that the method is not restricted to two dimensional images.

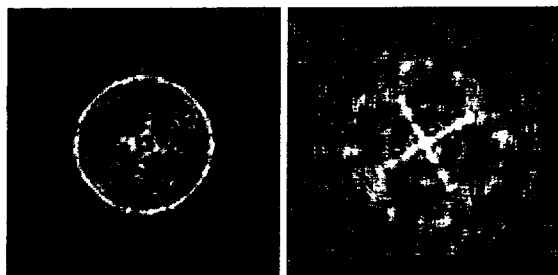


Fig. 6. Digital reconstructions of the hologram shown in figure 5 at $F=1m$ and $F=14m$

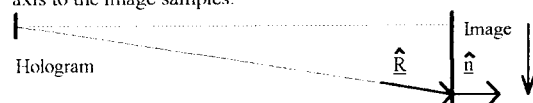
5. DISCUSSION.

The direct search method has been used to design holograms for which traditional methods such as "projection on constraints" are unsuccessful. The method produces high efficiency designs, provided conditions such as the space bandwidth product and the minimum hologram pixel size are correctly set. The method does not use FFT routines and consequently the "stand alone" holograms require no additional optics. The method is not restricted to planar images. The image intensity can be specified over a shaped surface, for example the surface of a cylinder such as an optical fibre.

1. B. Jennison, J. Allebach and D. Sweeney, *Opt Eng* vol. 28 **6**, 629-637 (1989).
2. F. Wyroski and O. Bryngdahl, *J Opt Soc. Am* vol. 5 **7**, 1058-1065 (1988).
3. N. Gallager and D. Sweeney, *Opt Eng* vol. 28 **6**, 599-604 (1989).
4. S. Weissbach, F. Wyroski, O. Bryngdahl, *SPIE* **1136**, Holographic Optics II, 226-227 (1989).
5. J. P. Riley and F. N. Birkett, *OPTICA ACTA* vol. 24 **10**, 999-1009 (1977).
6. "in phase" means the image phase gradient does not vary significantly from the "ideal" phase gradient given by

$$\frac{d\phi}{dr} = \frac{2\pi}{\lambda} |\hat{R} \times \hat{n}| \quad \text{where } \frac{d\phi}{dr} \text{ is the phase gradient. } \hat{R} \text{ is}$$

the unit vector in the direction of a vector between the hologram and the image samples and \hat{n} is the unit normal to the surface of the image and r is the radial distance from the axis to the image samples.



7. Otten and Van Ginneken, "The Annealing Algorithm", Kluwer Academic Publishers (1989).
8. M. Dames, R. Dowling, P. Mackee and D. Wood, *App. Opt.* **30**, 2685-2691 (1991).
9. E. Aarts and Korst, "Simulated Annealing and Boltzmann Machines", John Wiley & Sons (1989).

Diffractive zoom lens based on rotational moiré

U. Krackhardt, A. W. Lohmann

Physikalisches Institut der Universität Erlangen — Nürnberg

Staudtstr. 7/B2, 91058 Erlangen, Germany

Phone: +9131/85 8371, FAX.: +9131/13508

1 Introduction

A Fresnel zone pattern of variable focal power, i.e. the period size, can be formed as a moiré pattern between a pair of suitable grids. The focal power can be controlled by either shifting, rotating or scaling the grids with respect to each other [Lohmann67, Burch77, Kolod93]. This contribution focusses on the variation of focal power by rotation.

A grid $M(x, y)$ with curved lines can be described by means of pseudo-periodic functions $\Phi(x, y)$. Since the desired pattern has axial symmetry, polar coordinates are useful: $M(r, \varphi) = \sum A_n \exp[2\pi i \Phi(r, \varphi)]$. The Fourier coefficients A_n are determined by the groove shape, e.g. amplitude, phase or saw-tooth profiles. Thus we disregard problems of light efficiency and false diffraction orders. In [Lohmann67] $\Phi(r, \varphi) = \frac{r^2}{a^2} \varphi$ is proposed with a scaling parameter a . Similar to shearing interferometry superposition of two patterns rotated by the angle $\Delta\varphi$ reduces the power in φ . The superimposed moiré pattern thus is independent of the angle φ .

One drawback of such rotation induced moiré patterns is the side condition of periodicity in angle. That is the function $\Phi(r, \varphi)$ shows a discontinuity at $\varphi = 2\pi$ (see fig. 1). One effect is that the transmittivity $t(r, \varphi) = M(r, \varphi - \Delta\varphi/2)M(r, \varphi + \Delta\varphi/2)$ of an amplitude mask is low in the vicinity of that discontinuity. An other effect is a sparse sector where no fresnel pattern can be found (see fig. 2).



Fig.1: Single mask with the phase $\Phi(r, \varphi) = \frac{r^2}{a^2} \varphi$.



Fig.2: Moiré between two patterns of fig. 1 with a twist angle $\Delta\varphi = 0.25\pi$.

Modifications of the individual grids are proposed that increase both transmittivity and the useable area of the desired moiré structure.

2 Theory

The superposition of two masks twisted by the angle $\Delta\varphi$ with respect to each other can be described by its fourier representation:

$$\begin{aligned} t(r, \varphi, \Delta\varphi) &:= M(r, \varphi + \Delta\varphi/2)M(r, \varphi - \Delta\varphi/2) \\ &= \sum_m \sum_n A_n B_m \exp\left\{2\pi i \left[\frac{m+n}{2} (\Phi(r, \varphi + \Delta\varphi) + \Phi(r, \varphi - \Delta\varphi)) + \right. \right. \\ &\quad \left. \left. \frac{m-n}{2} (\Phi(r, \varphi + \Delta\varphi) - \Phi(r, \varphi - \Delta\varphi)) \right] \right\} \end{aligned} \quad (1)$$

By proper choice of the groove shape or angular averaging [Lohmann67] the double sum can be reduced to a more handy expression. A ronchi ruled π -phase grid, for example, emphasizes the coefficients A_{-1}, A_1, B_{-1}, B_1 . Whereas — in case of linear angular dependence — by angular averaging only terms with $m = n$ contribute. Consequently terms like $\Phi(r, \varphi + \Delta\varphi) \pm \Phi(r, \varphi - \Delta\varphi)$ are of major interest. Obviously the difference terms serve for the elevation of the angular dependence.

The aim of the present work is to reduce the impact of the angular discontinuity of $\Phi(r, \varphi)$ at $\varphi = 2\pi$. This means that the transmittivity close to the discontinuity has to be enhanced. Furthermore a reduction of the sparse area is desirable.

A particular design of $\Phi(r, \varphi)$ is the better the more transmittivity $T(r)$ of the resulting moiré pattern through a disk of radius r can be obtained. Where $T(r, \Delta\varphi) = \frac{1}{r^2\pi^2} \int_0^r r' dr' \int_0^{2\pi} d\varphi t(r', \varphi, \Delta\varphi)$. Thus as a figure of merit we use contour plots of isotransmittivity curves ($T(r) = \text{const}$) as a function of twist angle $\Delta\varphi$ and the radius of the illuminated disk r (see figs. 5,6,9). The lower the isotransmittivity curve the higher the transmittivity of the total pattern.

To enhance both transmittivity and the portion of usable area we propose three different concepts:

2.1 Angular offset

The concept of angular offset is based on a function $\Phi_o(r, \varphi) = \frac{r^2}{\alpha^2}(\varphi + \varphi_0)$ which is equivalent to introducing a carrier frequency. The resulting moiré pattern, however, is not affected by φ_0 . Fig. 3 shows the corresponding mask with $\varphi_0 = 0.25\pi$



Fig.3: Single mask with the phase $\Phi_o(r, \varphi, \varphi_0)$, $\varphi_0 = 0.25\pi$.

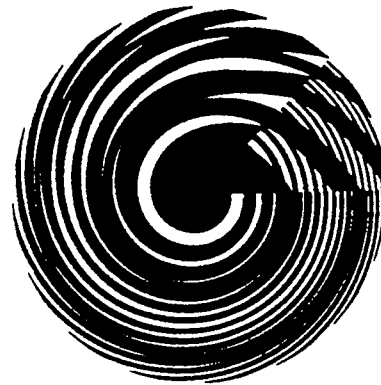


Fig.4: Moiré between two patterns of fig. 3 with a twist angle $\Delta\varphi = 0.25\pi$.

As can be seen from fig. 4 the sparse area is not reduced by the concept of angular offset. Comparing the isotransmittivity curves (figs. 5,6) the transmittivity is substantially increased, however.

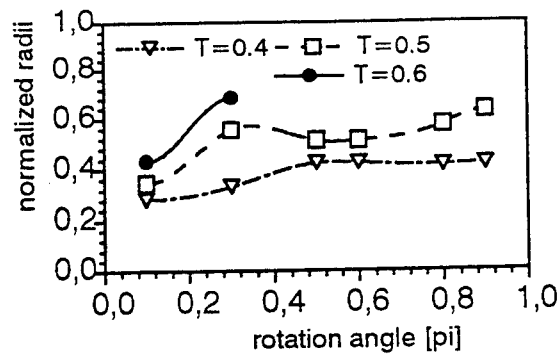


Fig. 5: Isotransmittivity curve for the moiré between $\Phi(r, \varphi)$ with no angular offset $\varphi_0 = 0$. The sparse sector is omitted.

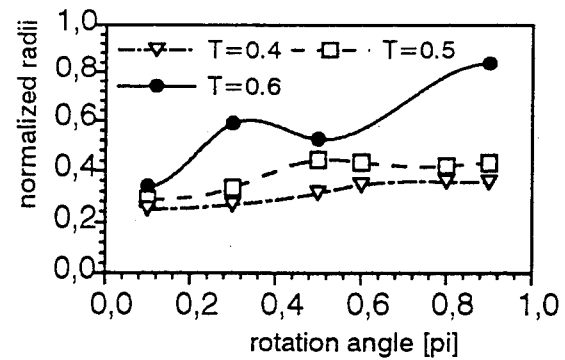


Fig. 6: Isotransmittivity curve for the moiré between $\Phi_o(r, \varphi, \varphi_0)$ with angular offset $\varphi_0 = 0.25\pi$. The sparse sector is omitted.

2.2 Angular symmetry

The concept of angular symmetry is based on a function $\Phi_s(r, \varphi) = \frac{r^2}{a^2}(|\varphi - \pi| + \varphi_0)$. This pattern is symmetric with respect to the $\varphi = 0$ axis. Like in the concept of angular offset φ_0 serves to enhance transmittivity close to $\varphi = 0$ and $\varphi = \pi$. Fig. 7 shows the corresponding mask with $\varphi_0 = 0.25\pi$

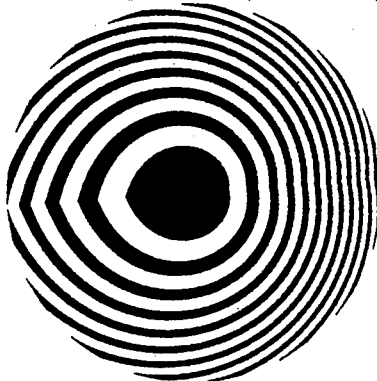


Fig. 7: Single mask with the phase $\Phi_s(r, \varphi) = \frac{r^2}{a^2}(|\varphi - \pi| + \varphi_0)$, $\varphi_0 = 0.5\pi$.

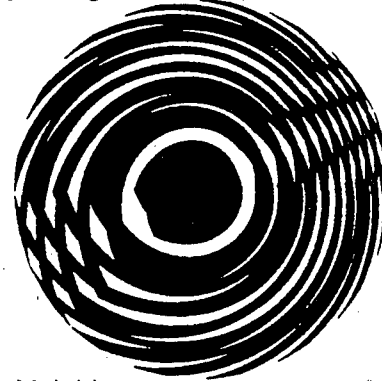


Fig. 8: Moiré between two patterns of fig. 7 with a twist angle $\Delta\varphi = 0.25\pi$.

As can be seen from fig. 8 the sparse area is doubled compared to the concept of angular offset. Comparing the isotransmittivity curve (figs. 5, 6, 9) the transmittivity is even lowered.

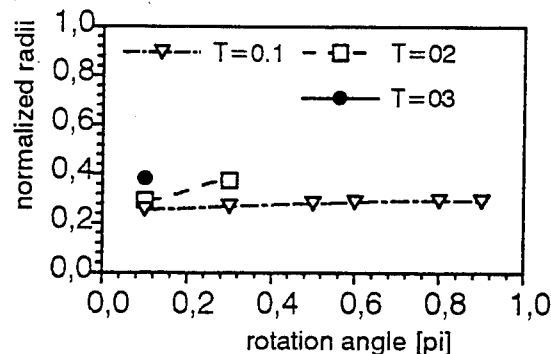


Fig. 9: Isotransmittivity curve for the moiré between $\Phi_s(r, \varphi)$ with angular offset $\varphi_0 = 0.5\pi$. The sparse sector is omitted.

2.3 Separated centres

The concept of separated centres of rotation is based on the moiré of two patterns from the concept of angular offset, whereby the centres of both patterns do not coincide. The centres are rather shifted, say, along the x-axis. Then the single patterns are rotated around their fixed centres. This concept is found heuristically. The incentive was to get the two centres out of the region where the variable Fresnel pattern occurs. A theoretical description is still under research. On the one hand this concept enhances transmittivity by angular offset. On the other hand no sparse area occurs within the resulting desired moiré pattern (see fig. 10).

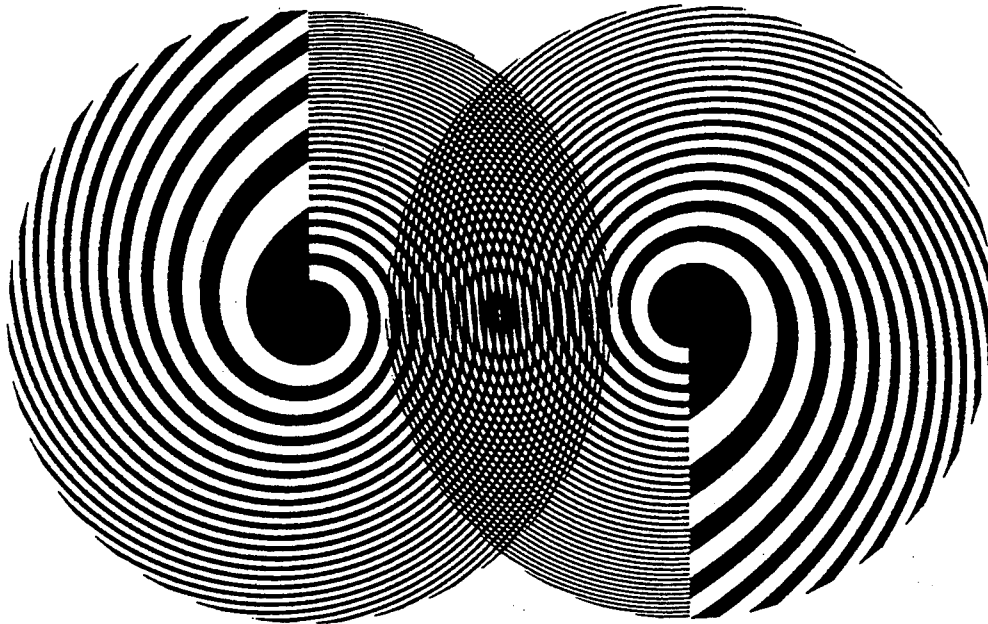


Fig. 10: Moiré of two patterns with angular offset and separated centres with a twist angle of $\Delta\varphi = \pi$.

3 Conclusion

Three different concepts for the generation of varifocal lenses by rotational moiré are proposed. With identical centres of rotation the concept of angular offset increases transmittivity. If additionally the centres are separated the desired moiré pattern can be kept free of sparse area portions.

References

- [Lohmann67] A.W. Lohmann, D.P. Paris: "Variable Fresnel Zone Pattern", Appl.Opt. **6** 1567 (1967)
- [Burch77] J.M. Burch, D.C Williams: "Varifocal moiré zone plates for straightness measurements", Appl.Opt. **16** 2445-2450 (1977)
- [Kolod93] A. Kolodziejczyk, Z. Jaroszewicz: "Diffractive elements of variable optical power and high diffraction efficiency", Appl. Opt. **23** 4317-4322 (1993)

Superimposed grating for use with magneto-optical disk heads

Shigeru AOYAMA and Tsukasa YAMASHITA

Omron Corporation, Central R&D Laboratory

20 Igadera, Shimokaiinji, Nagaokakyou-city, Kyoto 617, JAPAN

Phone:075-951-5111 Fax:075-951-5124

In a magneto-optical (MO) disk system, there is a strong need for small-size and light-weight optical disk heads to allow for high speed track access¹. A superimposed grating fabricated by electron-beam lithography², which simultaneously acts as polarizing beam splitter and cylindrical lens, has been developed for use with MO disk heads. This device includes signal detection functions such as focusing and tracking error and magneto-optical signal detection .

The purpose of the present paper is to propose a superimposed grating, which makes it possible not only to achieve small-size MO disk heads, but also to facilitate axial alignment because of the ease of combining different optical elements. This paper describes the investigation of the superimposed grating with emphasis on clarifying both its fundamental optical characteristics and its use in MO disk heads.

A schematic view of the proposed superimposed grating is shown in Fig. 1. The superimposed grating basically consists of two types of an ultra high spatial frequency grating (UHSFG)³ with mutually different duty ratios . The two types of the UHSFG are periodically formed corresponding to the function of the off-axis cylindrical lens based on binary diffraction grating. The groove direction of the UHSFG is perpendicular to the other. The period is smaller than one-half the wavelength of incident light.

Figure 2 shows the calculated plots of effective refractive indices vs duty ratios⁴. The UHSFG, illuminated by a plane monochromatic light at normal incidence, is described by the refractive indices n_{\perp} and $n_{//}$ for light polarized perpendicular to the groove direction and parallel to that, respectively. The duty ratios t_a and t_b of the superimposed grating can be chosen for the two types of the UHSFG such that the effective index has the same value of n_0 for one polarization. Then, the difference of the effective indices becomes $n_a - n_b$ for the other. Hence, by introducing an appropriate depth of groove, one can recognize that the phase shift difference becomes 0 for one polarization and π for the other. The theoretical efficiency of the diffraction grating, which consists of the periodical series of the two types of the UHSFG, is approximately 40 % at the phase shift of π .

The optical configuration of the MO disk head, using the superimposed grating, is illustrated in fig. 3. The light reflected back from the MO disk is reflected by the polarizing beam splitter and strikes on the superimposed grating after passing through the lens. There, the groove direction of the UHSFG's is set in an about 45 degrees direction with respect to polarization of the light reflected back from the disk. It simultaneously acts as a polarizing beam splitter and cylindrical lens, as required for signal detection. The light polarized parallel to the diffraction grating is transmitted and converged while the perpendicularly polarized light is diffracted and transferred to the converged light with astigmatic characteristics. Focusing error signal and tracking error signals are detected from the quadrant photo detector, using the astigmatism principle and push-pull principle, respectively. A readout signal is detected using the differential detection method.

Figure 4 shows cross sectional SEM photographs of the superimposed grating fabricated by electron beam lithography. The groove depth and

period are $1.5\mu\text{m}$ and $0.3\mu\text{m}$ respectively for a design wavelength of $0.78\mu\text{m}$. The duty ratios are 0.33 and 0.58, respectively.

Figure 5 shows the experimental results of the diffracted beam spot pattern. From these results, one can recognize that excellent astigmatic characteristics were obtained. The diffraction efficiency and transmission efficiency were 4% and 88% respectively for the perpendicularly polarized light, while efficiency was 36% and 3% respectively for the parallel polarized light. The resultant extinction ratios were calculated as -13dB for the diffracted light and -11dB for the transmitted light.

A superimposed grating, which includes the analyzer functions of signal detection and simultaneously acts as a polarizing beam splitter and cylindrical lens, has been developed for use with MO disk heads. The operating principles of the polarizing beam splitter and the cylindrical lens were experimentally confirmed. The superimposed grating promises not only to achieve small-size, light-weight MO disk heads but also eliminate the complex axial alignment procedure.

References

1. A. Ohba, Y. Kimura, S. Suguma, and Y. Ono, in MOC/GRIN'89 Technical Digest, (Tokyo, Japan), 224 (1989).
2. S. Aoyama, S. Ogata, T. Inoue, and T. Yamashita, in Technical Digest, Conference on Laser and Electro-optics (Optical Society of America, Washington, DC, 1988), paper THM49.
3. S. Aoyama, T. Ogaki, and T. Yamashita, Proceedings of SPIE International Conference on the Application and Theory of Periodic Structures, San Diego (1991) pp. 241-250.
4. M. Born and E. Wolf, Principles of Optics (Pergamon, Oxford, 1970), Chap. 14, pp. 705.

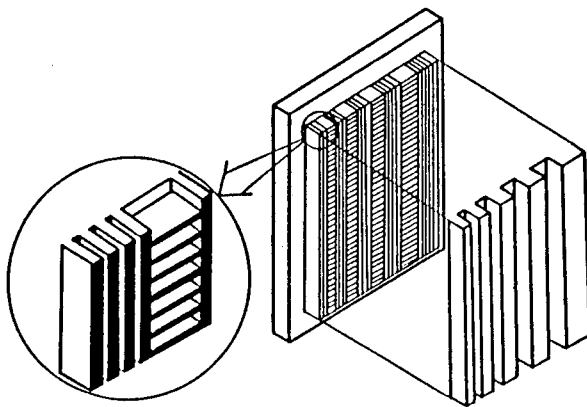


Fig.1. Schematic view of the superimposed grating.

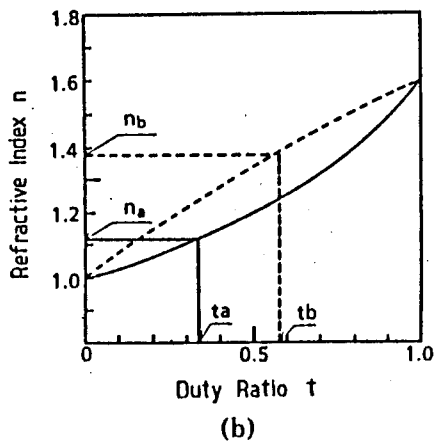
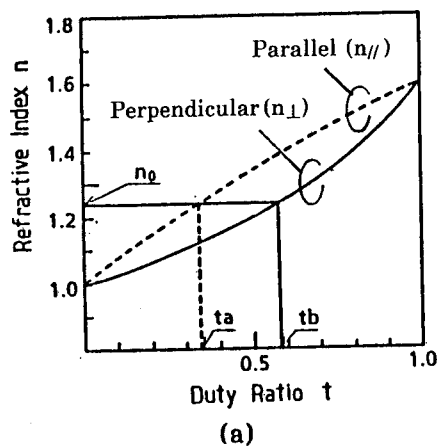


Fig.2. Calculated plots of the effective refractive indices vs. duty ratio: a) transmitted light; b) diffracted light.

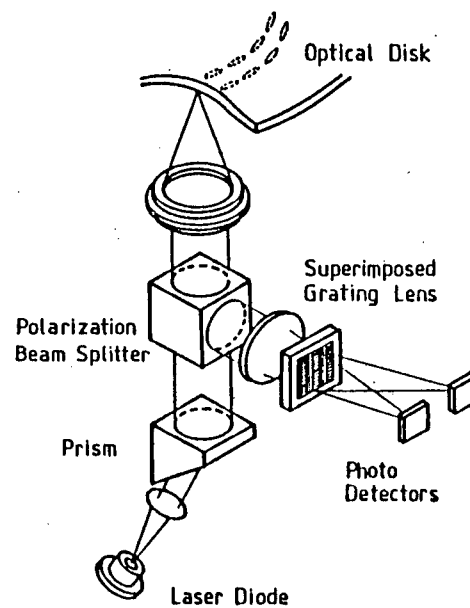


Fig.3. Optical configuration of a magneto-optical disk head.

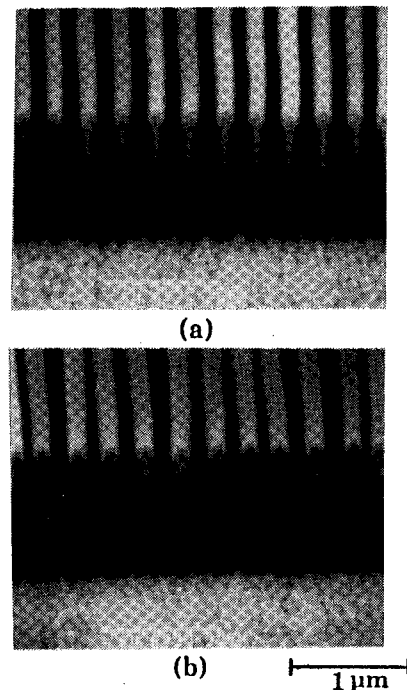


Fig.4. SEM photographs of the fabricated superimposed grating. Duty ratio is (a) 0.31 and (b) 0.51.

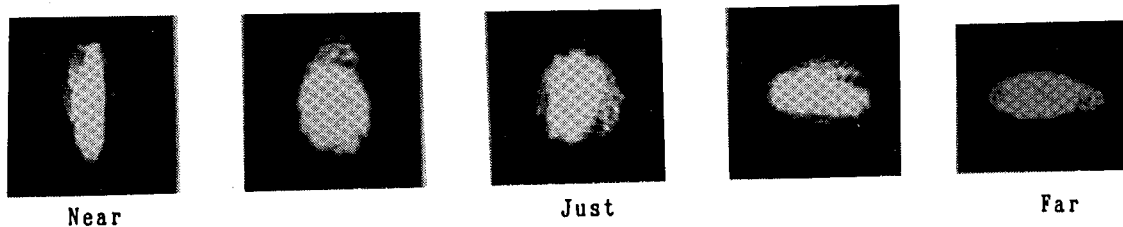


Fig.5. Experimental results of the diffracted beam spot patterns.

Application of Diffractive Optics to Photonic Integrated Circuit Packaging

M.E. Warren, S.H. Kravitz, G.R. Hadley, J.R. Wendt, G.A. Vawter, M.G. Armendariz
J.C. Word, R.F. Corless, R.F. Carson, B.E. Hammons
Sandia National Laboratories, P.O. Box 5800 MS 0603
Albuquerque, NM 87185-0603, ph. (505) 844-7208; fax 844-8985

R.E. Leibenguth
AT&T Bell Laboratories, Route 222
Brenigsville, PA 18031-9359, ph. (215) 391-2579; fax 391-2668

One of the primary challenges in the development and application of complex photonic integrated circuits (PICs) is the packaging of the devices. The coupling of single mode fibers to a semiconductor guided-wave device is an expensive manufacturing step and a major part of the system losses. For complex circuits in which many channels need to be coupled off of the chip, the difficulties are enormous and far from solved. The requirements for a successful packaging technology for multiple channel PICs include low loss coupling from single-mode, rectangular, semiconductor waveguides to single-mode fibers, hermetic sealing of the package against environmental conditions, a means of bringing a large number of optical signal channels out of the chip without greatly increasing its size and an efficient means of aligning each of a large number of single-mode fibers with minimum losses. The losses of coupling semiconductor waveguides to single-mode optical fibers can be large because of the large mode mismatch between the elliptical mode from the rectangular cross section waveguide and the circular mode of the fiber. The elliptical waveguide mode has a very large numerical aperture (0.9 NA for our tightly confined guides) in one axis which is difficult to match to the symmetric mode of the fiber (0.16 NA in our case). Hermetic sealing is important for the utilization of PICs in stressful environments such as military, aerospace and automotive applications. Photonic circuits today are usually coupled to fibers by bringing the output waveguides to the chip edge and butt-coupling. As the number of channels is increased, more and more of the chip real estate is used for routing of the waveguides and to allow sufficient space along the chip edge for coupling. Guided-wave devices with one or two fiber connections are often manually aligned to single-mode fibers. This would be a prohibitively expensive process with a large number of fibers. Consequently, much effort has gone into methods of monolithically aligning a number of fibers at once with techniques like silicon v-groove and solder-bump bonding technology ¹.

The approach being investigated at Sandia is based on bringing the optical signals of a complex PIC off the chip nearly perpendicular to the chip surface. This allows more efficient use of the wafer by not having to route the signals via waveguides to the chip edge. It also eliminates the need for a carefully cleaved chip edge for butt-coupling. The surface-emission out of the waveguides can be accomplished by second-order grating couplers. The vertical coupling of the signals then allows the use of auxiliary optical elements to provide mode matching to the fiber. These optical elements are currently diffractive microlenses and allow the fiber to be placed further from the chip surface. This enables the placement of the optical fibers in a monolithic carrier outside of the transparent package wall with the binary optical elements fabricated in the wall material. The proper center-to-center spacing of all the component groups (waveguide couplers, auxiliary lenses and fiber array holder) is assured by use of photolithography to fabricate each part. The alignment steps are then simplified to the alignment of the two monolithic components (PIC chip and package lid/fiber array holder). A depiction of the entire scheme is shown in Fig. 1.

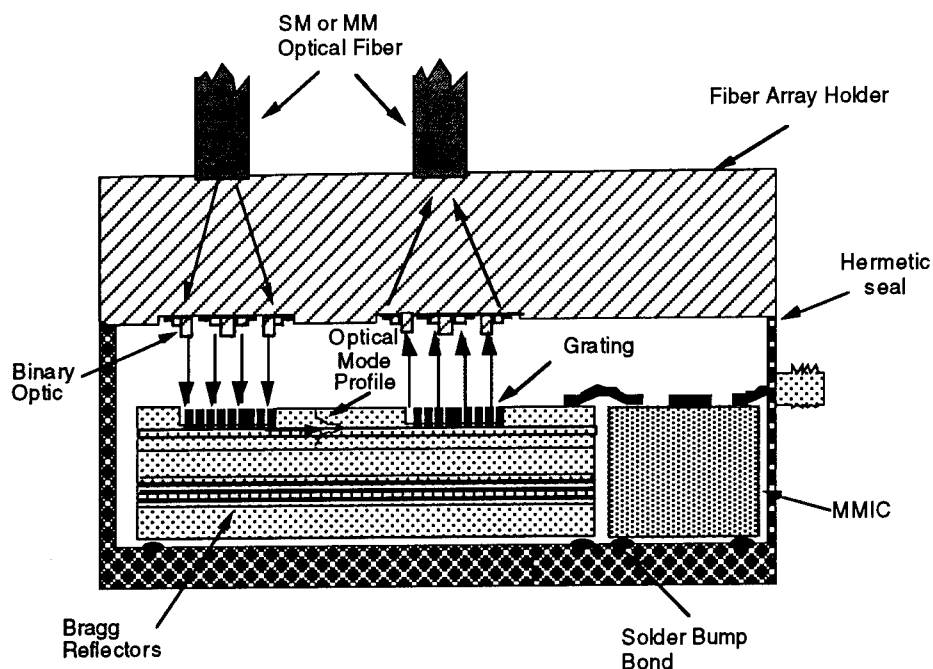


Figure 1. Advanced packaging concept for complex PICs.

The semiconductor waveguide technology in development at Sandia is based on GaAs/AlGaAs etched-rib waveguides for 1.3 microns in which components such as phase-modulators² and directional couplers³ can be fabricated. Typical losses for these waveguides are 1.2 dB/mm. This technology is being developed for complex PICs for applications such as phased-array radar steering.⁴ A basic test structure has been designed for prototype testing of photonic packaging technology that incorporates waveguide segments with phase modulators and second-order grating couplers as shown in Fig. 2.

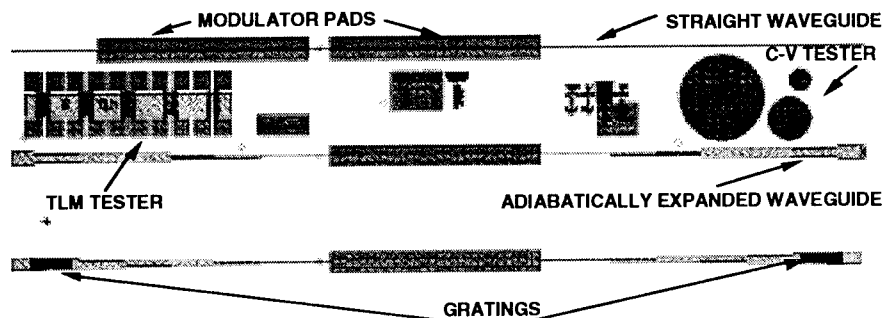


Figure 2. Test structure for development of advanced packaging technology.

A unique combination of second-order grating coupler and adiabatically tapered waveguide segment has been developed for coupling the optical signals out of the waveguides. The waveguide taper goes linearly from 2 to 50 microns in width in 1 mm. This expansion was designed using beam propagation methods to maintain a single-mode output with a reduced lateral divergence. A 200-micron-long grating is etched into the waveguide after the complete expansion. A 2D Helmholtz equation solver was used to model the fields in deeply etched waveguide grating segments to design a short grating with high coupling efficiency.⁵ The short grating length and increased waveguide width improve the beam's aspect ratio. The grating is slightly detuned to minimize back reflections in the waveguide and emits approximately 10

degrees off normal. A distributed Bragg reflector stack is grown below the waveguide cladding to enhance the efficiency of the top-emitted beam from the grating.

The grating coupler was fabricated by e-beam lithography for both the grating and the tapered segment. Special care was taken to ensure a smooth transition between the taper and grating region, smooth sidewalls along the taper, and uniform grating lines. The grating pitch is 0.3825 micron with a 50% duty cycle. The grating is etched to a critical depth using an interferometrically monitored etch process. The grating has a 59% out-coupling efficiency with a beam divergence of 1 degree along the waveguide length and 2 degrees transverse to the waveguide. This reduced divergence decreases the NA requirements for the coupling lenses.

The diffractive lenses were fabricated in silicon. The lenses were 4 and 8 phase-level binary optic designs fabricated by conventional photolithography and dry etching of silicon. The designs included both symmetric Fresnel zone designs and anamorphic designs⁶ to compensate for the remaining astigmatism of the grating output. The surface of a 4-phase-level lens is shown in Fig. 3. A variety of 500-micron-diameter lenses with NAs ranging from 0.10 to 0.32 were fabricated. The 8-phase-level designs were not significantly better in diffraction efficiency (76%) than the 4 level designs, indicating that alignment errors were reducing the diffraction efficiency. Widths of the phase-zones on the photomasks were held to 1 micron or larger, so the third level of the larger numerical aperture patterns were truncated, further limiting the utility of additional phase-levels in the designs. E-beam lithography is being used for a second generation of microlenses to improve the alignment and allow complete fabrication of high NA designs.



Figure 3. A scanning electron micrograph of a silicon 4 phase-level binary optic.

The package concept was demonstrated as illustrated in Fig. 4. A 1.3 micron diode-pumped YAG laser was coupled via a polarization-preserving single-mode fiber into a GaAs/AlGaAs waveguide on a fabricated test chip. The light was then coupled out of the chip surface by the adiabatic taper and grating and collected by a silicon microlens 2 mm away. The silicon microlens focused the light into the same type of single-mode fiber. The waveguide losses, grating output efficiency, and microlens diffraction efficiency were all measured independently. The total loss through the system was -18.5 dB. Neglecting the -8.8 dB loss for butt-coupling into the waveguide, as measured by OTDR, the coupling loss through the waveguide-grating-lens-fiber route was -9.7 dB, including a guiding loss of -2.3 dB in the semiconductor waveguide. The efficiency of coupling through the silicon lens into the fiber was 30% (-5.2 dB) after emission from the grating. We believe this is a promising indication of the potential for this application of diffractive optics to packaging of complex PICs. Some obvious areas of improvement are improving the diffraction efficiency of the silicon microlenses and optimizing the lens design for coupling of the grating output into the fiber mode. The coupling

data indicates the anamorphic lenses bracketed the optimum configuration for this application and improvement is expected for the next generation. The off-axis emission of the grating is necessary because of the need to detune the grating to eliminate feedback problems for the PICs. Consequently, the next lens designs will include optimization for off-axis performance so they can be positioned with their surface parallel to the chip surface as required for the packaging concept.

This work was sponsored by the United States Department of Energy under Contract DE-AC04-94AL85000.

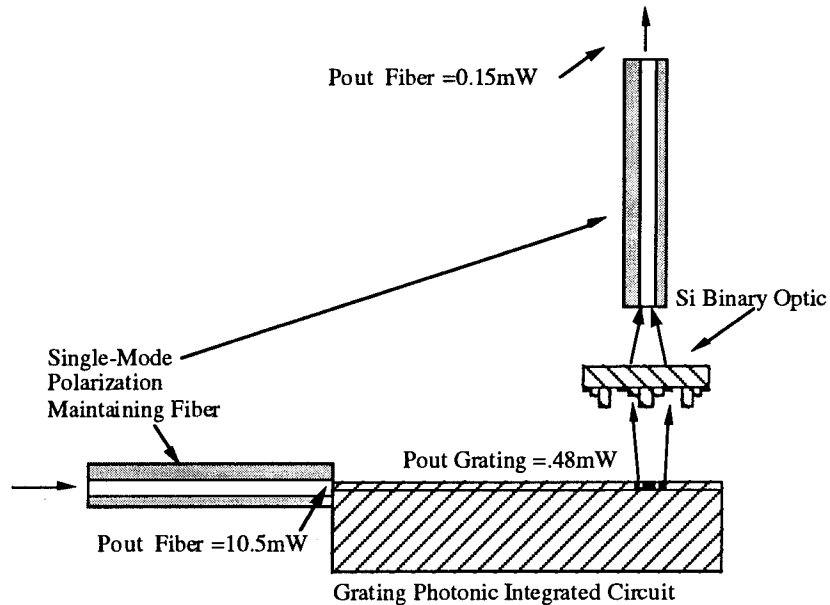


Figure 4. Configuration for coupling from ridge waveguide to single-mode fiber via waveguide grating-coupler and silicon microlens.

REFERENCES:

1. M.R. Matthews, B.R. MacDonald, and K.R. Preston, "Optical Components-The New Challenge in Packaging," *IEEE Trans. on Components, Hybrids and Manufacturing Tech.*, **13**, pp. 798-806, (1990).
2. V.M. Hietala, S.H. Kravitz, M.G. Armendariz, G.A. Vawter, "High-performance GaAs/AlGaAs optical phase modulators for microwave/photonic integrated circuits," to be published in *Proceeding of the SPIE*, **2155**, Jan., 1994.
3. G.A. Vawter, J.F. Klem, G.R. Hadley, and S.H. Kravitz, "Highly accurate etching of ridge-waveguide directional couplers using *in situ* reflectance monitoring and periodic multilayers," *Appl. Phys. Lett.* **62** pp. 1-3, (1993).
4. V.M. Hietala, G.A. Vawter, W.J. Meyer, and S.H. Kravitz, "Phased-array antenna control by a monolithic photonic integrated circuit", *Proceeding of the SPIE*, **1476**, pp. 170-175, (1991).
5. G.R. Hadley, "Numerical simulation of reflecting structures via solution of the 2D Helmholtz equation," to be published in *Opt. Lett.*, Jan., 1994.
6. J.R. Leger, M.L. Scott, P. Bundman, and M.P. Griswold, "Astigmatic wavefront correction of a gain-guided laser diode array using anamorphic diffractive microlenses," *Proceedings of the SPIE*, **884**, pp. 82-89, (1988).

High-Efficiency, Metallic Diffraction Gratings for Laser Applications

B. Boyd, J. Britten, D. Decker, B. W. Shore, B. Stuart, M. D. Perry,
*Laser Program, Lawrence Livermore National Laboratory,
P.O. Box 808, L-493, Livermore, CA 94550*

Lifeng Li
Optical Sciences Center, University of Arizona, Tucson, AZ 85721

New developments in laser technology have resulted in demand for high efficiency diffraction gratings, used in reflection, which produce a high quality wavefront while exhibiting a high threshold for laser damage. Advances in holographic techniques now make possible the manufacture of inexpensive yet high quality gratings, while concurrent theoretical developments provide computational procedures that can reliably predict the behavior of gratings having quite general groove profiles and coatings. We will display examples of predicted diffraction efficiencies for various gratings, describe the techniques we use to construct efficient metallic-coated holographic gratings, and discuss the measured efficiencies and mechanism of laser damage in metallic gratings.

Although the presence and direction of orders diffracted from a planar grating follow from the grating equation, $\sin\vartheta_m - \sin\vartheta_i = m\lambda/d$, relating the incident angle ϑ_i , the diffracted angle ϑ_m for order m , and the ratio of wavelength λ to groove spacing d , the distribution of energy amongst the orders is determined by the wavelength and polarization of the light, the shape of the grooves, and the optical properties of the surface. We have examined reflection gratings used in first-order Littrow mount ($\vartheta_{-1} = -\vartheta_i$) and constrained by the inequality $2 > \lambda/d > (2/3)$ to allow only two propagating orders (0 and -1). It has

been established [1] that under these conditions the diffraction efficiency of a perfectly conducting grating is an oscillatory function of depth, for both TE and TM polarization. More realistic models of metal surfaces are known to exhibit oscillatory depth dependence.

Theory

Our computations used the multilayer modal method [2]. This method replaces the corrugated grating surface by a succession of slices, in each of which the complex-valued dielectric constant alternates periodically between two values, corresponding to the materials above and below the grating surface. Exact normal mode solutions to the vector Helmholtz equation are found within the slices and boundary conditions are matched in moment form, to produce a complete solution. For the present study we approximated the grating profile by a modified sinusoid, in which the height of the air-metal interface at position x is given by the three-parameter function $f(x) = h [\sin(\pi x/d)]^{2p}$ specifiable by depth of modulation h and by exponent p for fixed groove spacing d . A convenient alternative to the parameter p is the duty cycle, which we take to be the fraction of the grating period in which the profile exceeds $h/2$.

We will show computations that predict families of grating profiles having diffraction efficiency (in order -1) of 95% or better. We will show examples in which the shape of the grating profile (i.e. the duty cycle) has a minor effect upon the efficiency of TM polarized light. In other cases efficiencies are strongly affected by duty cycle, for given depth. Our results exhibit a succession of maxima and minima as the groove depth increases, thereby allowing selection of efficiency by suitably choosing the groove depth and shape.

Grating Fabrication

Our gratings are fabricated using a multistep holographic/lithographic process. In brief, we coat a thin layer of photoresist upon an optically flat glass substrate (spin coating

for gratings < 15 cm and meniscus coating for grating substrates > 15 cm) which we then expose to a stabilized interference pattern of laser light at the intersection of two arms of an equal path interferometer. The exposed photoresist is developed and then coated with a thin metal film (Au, Al or Ag).

We examined the profiles of the developed photoresist, and the gold-coated photoresist, with a scanning electron microscope (SEM). When the photoresist is sufficiently deep, the grating profile is sinusoidal and the depth of the grooves is established by the exposure time. As these exposure times become longer, the exposed region reaches the lower boundary of the photoresist and the groove depth becomes bounded by the thickness of the photoresist. Increased exposure then makes the grating ridges narrower. The gold coating may distort the surface by filling in the grooves.

Grating Efficiency and Damage Threshold

We have obtained excellent agreement between our theoretical predictions and experimental measurements of grating efficiency, for a range of groove depths and shape. In particular, we have constructed gratings with a diffraction efficiency greater than 95% (figure 1). Our results demonstrate that it is essential to model deviations from purely sinusoidal profiles and from perfectly conducting surfaces.

We will also describe a systematic study of the relationship between damage threshold and coating thickness, which we believe to be the dominant factor in determining the damage threshold of metallic gratings. We will present a simple model for damage, based on heat flow considerations, that we have found to account for both long-pulse and short-pulse damage to gold films. Specifically, the damage threshold varies strongly with laser pulsewidth over the range from picoseconds to nanoseconds. Although the damage threshold of the gratings is always slightly lower than observed for uniform metal films, we observe the same general dependence on coating thickness.

This work was performed under the auspices of the United States Department of Energy by the Lawrence Livermore National Laboratory under contract no. W-7405-Eng-48.

References

- [1] D. Maystre, M. Cadilhac and J. Chandezon, *Optica Acta* **28**, 457 (1981)
- [2] L. Li, *J. Opt. Soc. Am. A* **10**, 2581 (1993)

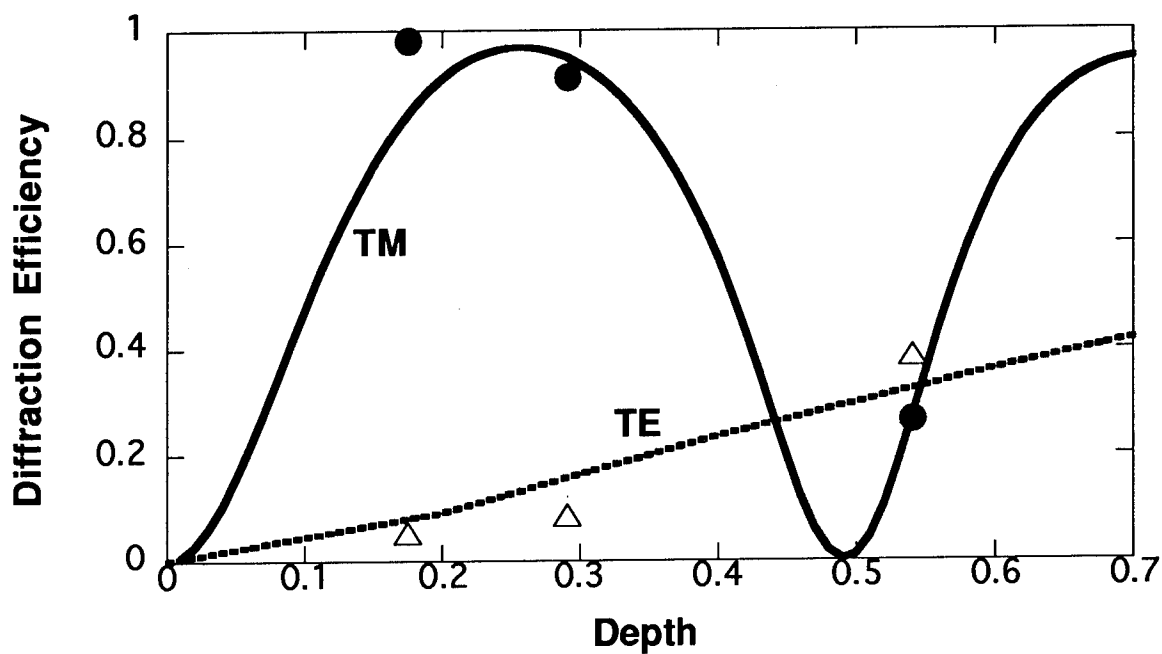


Figure 1. Diffraction efficiency (order -1) versus groove depth (in μm) for sinusoidal gold grating, period 640 nm, wavelength 1064 nm, for TM polarization (solid line = theory, solid circles = experiment) and TE polarization (dotted line = theory, triangles = experiment).

Holographic Couplers for Optical Fibers in On-Axis Off-Bragg and Off-Axis Configurations

Pavel Cheben* and María L. Calvo

Optics Dept., Faculty of Physics, Complutense University, Ciudad Universitaria, Madrid 28040, Spain

*Present Address: Nat'l Aerospace Institute (INTA), Space Instrumentation Lab., Torrejón de Ardoz, Madrid 28050, Spain.

Since a coupled-wave theory for volume holograms have appeared in 1969¹, many extensions, modifications or particularizations of Kogelnik's approach were done within the coupled-wave framework². The alternative approaches like a dispersion equation theory³, an integral equation solution⁴ or a Feynman diagram representation⁵ were used less extensively mainly due to its mathematical complexity in the case of nonuniform gratings. The fact that some optical CAD programs (see e.g. CODE V) still use quasi-one-dimensional theories with locally plane phase grating approximation for HOEs design⁶, shows large applicability and flexibility of coupled-wave approach.

In ref.⁷ it was shown that the low numerical aperture of the monomode fibers causes that it is necessary to approximate the wavefront of the Gaussian beam emerging from the monomode fiber by the spherical (cylindrical in 2D-geometry) function at the place of the holographic emulsion. Rigorous theoretical description of the diffraction process is needed in this case, since not such a treatment was done before.

The solution of the problem was recently published for the on-axis geometry and off-Bragg parameter $B=0$ ⁸.

However, in majority of applications when high diffraction efficiencies is required, it is fundamental to employ off-axis geometries. Hence, the solution for diffraction of off-axis cylindrical wave is required to describe precisely the wavefront conversion process. Moreover, due to the shrinkage of the holographic emulsion for a great number of materials and associated development processes⁹ and due to misalignment errors, it was necessary to create a theoretical model for not strictly on-Bragg reconstruction process (i.e. for $B \neq 0$).

To solve the second order partial differential equation which results from two coupled-wave equations was used the Riemann's method¹⁰. Two-mode approximation was applied in the analysis. To avoid tedious mathematics we present only resulting integral solutions:

a; The case of the conversion between Gaussian beam with cylindrical phase and the plane wave for on-axis geometry and for nonzero value of the off-Bragg parameter B . It can be shown that the solution for the 1-st

diffraction order amplitude Ψ_1 could be expressed in the form:

$$\Psi_1(u, v) = \frac{jk\tau}{2} \exp(j\beta_0 \delta(B)\xi) \int_{f(u)}^v \frac{\exp(-j\beta_0 \delta(B)g(v'))}{v' \sin g(v')} \left(\ln \frac{v}{v'}\right)^{-1/2} \times J_0 \{2[(v-v')(u-f(v'))]^{1/2}\} dv', \quad (1)$$

where: u, v are generalized coordinates,
 ξ is a transformed u coordinate,
 v' is a dummy variable,
 v is a function of u coordinate,
 β_0 is a free-space propagation constant,
 τ is a parameter of Gaussian beam,
 k is a coupling parameter,
 $\delta(B)$ is a virtual transversal shift of the fiber's rear face as a function of the off-Bragg parameter B ,
 $f(v)$ is a function defining the curve where the boundary conditions are given for the mode Ψ_1 ,
 $g(v)$ is a value of ξ coordinate at $u=f(v)$,
 J_0 is a zero-order Bessel function of the first kind.

It can be seen that for the case when the off-Bragg parameter $B=0$ (i.e. $\delta=0$) the formula (1) reduces to the solution of the on-axis on-Bragg problem published in ref.⁸.

b; In the case of the conversion between cylindrical and plane waves for off-axis geometry and for $B=0$ it follows for the amplitude Ψ_1' (1-st diffraction order):

$$\Psi_1'(u, v) = \frac{j}{kc_1 c_{10}} \exp(-\int \frac{\alpha}{\alpha'} d\xi) \int_{f(u)}^v \exp\left\{-\frac{v'}{k^2 c_1 c_{10}} + \int \frac{\alpha}{\alpha'} d\xi\right\} \times (\sin\phi \cos g(v') - \cos\phi \sin g(v'))^{-1} J_0 \{2[(v-v')(u-f(v'))]^{1/2}\} dv', \quad (2)$$

where: c_{10} is an amplitude of a recording cylindrical wave at unit distance from the end of the fiber,
 c_1 is an amplitude of a cylindrical wave used during the reconstruction process at unit distance from the end of the fiber,
 α, α' are specific functions of an off-axis angle ϕ and of the coordinates u, v .

The numerical results shown considerable difference in the behavior of the coupling process for the on-axis⁸, on-axis off-Bragg (1) and off-axis (2) geometries. However, it may be stated, that in all cases both the high diffraction efficiencies and high reconstruction fidelities cannot be accomplished simultaneously. With an increasing amplitude of a refractive index modulation Δn (hence with increasing value of the coupling parameter k) a splitting effect and Bormann-like effects are more pronounced. The effects should be analyzed carefully in design of HOEs based on the materials with large Δn capabilities (e.g. photopolymers).

REFERENCES

1. H. Kogelnik, Coupled wave theory for thick hologram gratings, Bell Syst. Tech. J. **48**, 2909-2947 (1969).
2. L. Solymar and D. J. Cooke, *Volume holography and volume gratings*, Academic Press, Oxford (1981).
3. P. P. Ewald, Zur Begründung der Kristalloptik, Part 1, Ann. Phys. **49**, 1-38, Leipzig (1916).
4. A. Korpel, Two-dimensional plane wave theory of strong acousto-optic interaction in isotropic media, J. Opt. Soc. Am., **69**, 678-683 (1979).
5. T. Ch. Poon and A. Korpel, Feynman diagram approach to acousto-optic scattering in the near-Bragg region, J. Opt. Soc. Am., **71**, 1202-1208 (1981).
6. Advanced topics in CODE V, Holographic and diffractive optical elements, Seminar notes, Optical Research Associates seminar, Pasadena, California, Sept. 20-24 (1993).
7. P. Cheben and M. L. Calvo, Holographical coupler for monomode fibers as a GRIN structure, Tenth topical meeting on gradient-index optical systems,

Technical digest, pp. 84-87, Santiago de Compostela, Spain, October 4-6 (1992).

8. P. Cheben and M. L. Calvo, Wavefront conversion between Gaussian beam with cylindrical phase function, and plane wave in monomode on-axis transmission holographical coupler, J. Opt. Soc. Am., Vol. 10, No. 12 (1993).

9. H. L. Fielding and R. T. Ingwall, Stabilization of holograms, U.S. Patent No. 4.535.041 (1985).

10. S. L. Sobolev, *Partial differential equations of mathematical physics*, pp. 58-71, Dover Publications, Inc., N.Y. (1989).

Hybrid Optics for Deep UVHans-Jörg Heimbeck

FISBA OPTIK AG

Rorschacher Str. 268, CH-9016 St. Gallen, Switzerland

Tel: 0041 - 71 - 35 57 75

Fax: 0041 - 71 - 35 58 95

Currently designing and manufacturing optical systems for the UV is mainly a material problem. At 300 nm only 5 glasses transmit light and only one has an absorption less than 10% at 25 mm thickness. At 250 nm the 2 remaining glasses have about 60% absorption. So the main material for UV is fused silica, that is highly transmissive down to about 180 nm. The only additional materials available are several fluorides. The most commonly used of them is calcium fluoride in spite of its brittleness and considerable absorption below 250 nm.

Optical systems of pure fused silica would be highly appreciated, but the high dispersion in the UV make a colour correction even for small laser bandwidths necessary. The diffractive colour correction is the only possibility to design hybrid lens systems that can replace the limited mirror systems at 250 nm and below.

Hybrid components have been designed, fabricated and evaluated for use below 200 nm. Results are presented and advantages and problems will be discussed.

Tuesday, June 7, 1994

Design I

DTuC 1:30pm–3:30pm
Room B

Dale A. Buralli, *Presider*
Sinclair Optics

Diffractive Optics beyond the Paraxial Domain

Jari Turunen and Eero Noponen

Department of Technical Physics, Helsinki University of Technology, FIN-02150 Espoo, Finland
Phone: +358 0451 3163; Fax: +358 0451 3164

Frank Wyrowski

Department of Diffractive Optics, Berlin Institute of Optics, Rudower Chaussee 5, D-12484 Berlin, Germany
Phone: +49 30 6392 3470; Fax: +49 30 6392 3452

1. Introduction

From being regarded as a limitation to the performance of optical instruments, diffraction has rapidly gained ground as a powerful tool for the synthesis of optical elements in such instruments. Diffractive optics, which has its roots in old concepts such as diffraction grating and Fresnel zone plate, is now one of the most dynamic fields of modern optics. Incidentally, diffractive elements were specifically excluded from the IODC '94 optical design problem.¹ This may be interpreted as an example of the newly-found wide recognition of the power of diffractive optics.

Fabrication of diffractive elements by optical interferometry (holography) is a well-established technique with a wide range of applications. The alternative method based on mathematical synthesis of the diffractive structure and its computer-controlled fabrication has suffered from a 'noisy' public image, but this adverse perception is rapidly being erased by advances in numerical synthesis methods and lithographic microfabrication of surface-relief profiles.

The basic synthesis problem in diffractive optics is illustrated in Fig. 1. The modulated region $0 < z < h$ is illuminated by a plane wave incident at an angle θ , and we specify some properties of the diffracted field in the signal window \mathcal{W} . The specified properties define the optical function of the element, i.e., the desired signal. More general synthesis problems are encountered in diffractive optics: the optical function may depend on the wavelength, the angle of incidence, or the state of polarization of the incident wave, which is not necessarily a plane wave, nor is it always fully coherent. Nevertheless, the situation illustrated in Fig. 1 is central in diffractive optics and sufficiently general for our purposes.

Most of the research on the mathematical synthesis approach has concentrated on the paraxial domain, where the angular extent $\Omega_{\mathcal{W}}$ of the signal window, the central diffraction angle Ω_C , and the incident angle θ are all paraxial, i.e., $\sin \Omega_{\mathcal{W}} \approx \Omega_{\mathcal{W}}$, $\sin \Omega_C \approx \Omega_C$ and $\sin \theta \approx \theta$ (a notable exception is the work on diffractive lenses, where the paraxial approx-

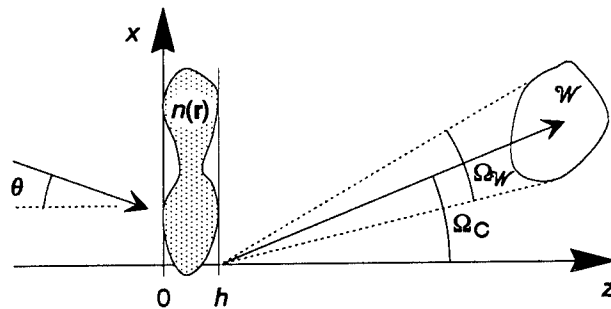


Figure 1: Illustration of the basic synthesis problem in diffractive optics.

imation is of limited use). However, because of the ever more demanding applications and the advances in microfabrication of surface-relief structures, which make these applications feasible, diffractive optics beyond the paraxial domain is gaining significance.

In this paper, we present a review of some recent results of diffractive-optics research in the non-paraxial domain. A number of new synthesis results are given in the resonance domain ($\Omega \lesssim \pi$), and in the region between it and the paraxial domain. We consider in particular the possibility of exceeding the upper bounds of diffraction efficiency² by the use of resonance-domain diffractive structures. Somewhat speculative arguments will be presented to trigger further research on theoretical topics that we consider important.

2. Paraxial-domain diffractive optics

A respectable range of synthesis methods are available in the paraxial domain, whether the signal window \mathcal{W} resides in the Fresnel or Fourier region of the aperture, and whether the signal is two- or three-dimensional, continuous, or discrete.^{3,4}

Paraxial signals can be generated by weakly scattering diffractive elements. This means that either the surface-relief profile (if it is at least nearly continuous) or the index-modulation profile varies slowly compared to λ or, if the profile is severely quantized,

the transverse features are considerably larger than λ . Thus polarization and multiple-scattering effects are not significant and we may use geometrical optics to predict the response of the element (the field at $z = h$ if the field at $z = 0$ is known). Quite generally, the well-known Fresnel and Fraunhofer diffraction integrals can be used to propagate the field from $z = h$ into \mathcal{W} , and also to solve the inverse propagation problem from \mathcal{W} to $z = h$.

Modern synthesis algorithms make full use of the degrees of freedom provided by the optical function of the diffractive element: we have the freedom to choose the complex amplitude outside \mathcal{W} , the freedom to choose the scale factor (diffraction efficiency), and often also the freedom of phase inside \mathcal{W} . These algorithms also accommodate constraints such as fabrication-related requirements to restrict the profile into a phase-only form, or to a quantized structure with Z permitted phase-delay levels.

The design of diffractive elements in the paraxial domain stands on firm foundations, provided that the thin-element approximation also holds.⁵ It is, e.g., possible to give an upper bound η_l for the diffraction efficiency η of any diffractive element that generates the specified signal within \mathcal{W} , with the distinction that η_l does not depend on the actual form of the diffractive structure. If there are no constraints on the profile and the signal is discrete, we typically have $\eta_l \gtrsim 90^\circ$. If the signal is specified off-axis and the element is permitted to have only Z discrete phase levels,⁶ the upper bound is reduced by a factor $\text{sinc}^2(1/Z)$. For inversion-symmetric on-axis signals, high upper bounds ($\eta_l \gtrsim 80\%$) can be achieved for hermitian signals (which can be produced by binary elements).

3. Resonance-domain diffractive optics

Relatively little is known about diffractive optics beyond the paraxial domain. In this non-paraxial domain it is typically advisable to apply rigorous electromagnetic diffraction theory to the analysis and synthesis of diffractive elements, although in certain circumstances (e.g., in diffractive-lens design) simpler theories such as geometrical optics are valuable.

The electromagnetic theory of diffraction gratings is well established.^{7,8} A wide range of numerical methods exist, most of which can be extended to more general diffractive elements. The choice of the method depends on the type of profile. For Z -level quantized profiles with a low value of Z , rigorous coupled-wave methods⁸ and eigenmode methods⁹ are recommended, except for the case of highly conducting gratings in TM polarization, where the conver-

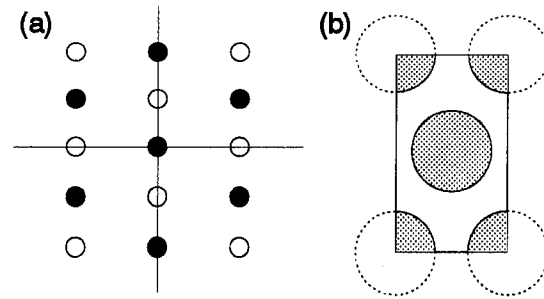


Figure 2: Example of a resonance-domain beam-splitter element with a three-dimensional modulation profile: (a) Far-field signal. (b) Grating structure.

gence is not satisfactory. A Legendre function formalism of Morf seems to overcome the difficulty,¹⁰ as does a rigorous modal formulation.¹¹ For continuous surface-relief profiles, differential and integral methods are available, of which the latter perform better for highly conducting gratings.⁷

It is worth noting that many of the symmetries that apply in the paraxial domain no longer hold beyond it. For example, the signal generated by a binary surface-relief grating is hermitian only if the grating profile itself is symmetric and the incidence is axial. The potential that the breaking of such symmetries may provide in the synthesis problem are not yet fully understood.

In grating theory, there has been considerable interest in the optimization of the profile to obtain a high first-order efficiency (to 'blaze' the grating). Significant results have been obtained by parametric optimization with gradient algorithms.¹² These methods have recently been extended to more general synthesis problems in resonance-domain diffractive optics,¹³ where we have attempted to control the efficiencies of all transmitted or reflected orders. Such multiple-beamsplitter gratings have applications in, e.g., substrate-mode optical interconnection.¹⁴

In Fig. 2 we present a new result, in which the signal is two-dimensional and therefore requires a three-dimensional grating-modulation profile. The signal is a closest-packed array or seven beams, and the grating structure is a hexagonal arrangement of dielectric pillars (refractive index $n = 1.5$, depth $h = 1.181\lambda$, diameter $D = 1.176\lambda$). The grating is synthesized by considering a cartesian period $d \times \sqrt{3}d$, where $d = 1.643\lambda$, using an three-dimensional extension of the eigenmode formulation⁹ and a gradient algorithm. The transmission-mode diffraction efficiency into the seven signal orders is $\eta = 92\%$, and the efficiency variations among the orders are $\pm 11\%$ (with axial polarization).

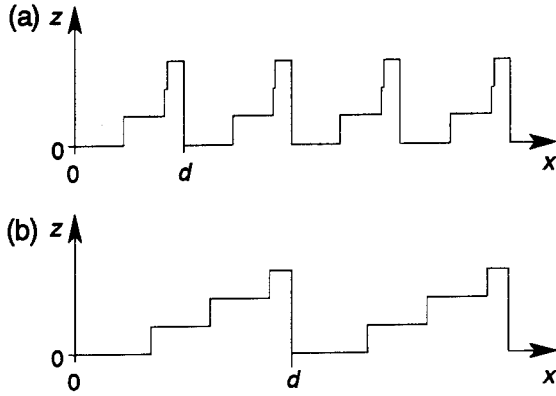


Figure 3: Optimized four-level grating profiles: (a) $d = 2\lambda$. (b) $d = 4\lambda$. The first-order efficiencies η_{opt} of the optimized solutions and the efficiencies η_{stair} of the staircase solutions are: (a) $\eta_{\text{opt}} = 70.1\%$, $\eta_{\text{stair}} = 26.0\%$. (b) $\eta_{\text{opt}} = 75.5\%$, $\eta_{\text{stair}} = 63.5\%$

Other important solutions of the synthesis problem in the resonance domain have been published recently: we wish to draw particular attention to grating antireflection layers, wave plates, and narrow-band filters.^{15–18}

4. Local synthesis by rigorous theory

The use of rigorous electromagnetic approach to synthesize a diffractive element is a heavy computational task if the grating period is an order of magnitude greater than λ in the case of two-dimensional modulation, and even more so if the profile is three-dimensional. Thus exact synthesis appears feasible only in the resonance domain. However, it is often possible to employ ‘hybrid’ design concepts, where we combine an approximate method of determining the optical function with a locally rigorous electromagnetic design of the profile.

Local synthesis results are applicable, e.g., in the design of diffractive lenses. Here the optical function can be determined by geometrical optics, but the thin-element approximation is not valid for high-numerical-aperture lenses.¹⁹ By local optimization of the multilevel grating structure,²⁰ and using the detour-phase principle²¹ to correct the local phase errors, one can synthesize diffractive lenses with a significantly enhanced efficiency.²² Figure 3 illustrates some four-level structures obtained by parametric optimization. They depart quite significantly from the paraxial staircase profile, and the improvement of efficiency is appreciable.

A local use of rigorous theory is valuable also in the parabal region, where $\Omega_W \ll \pi$, but θ and/or Ω_C are non-paraxial. In this region, binary pulse-

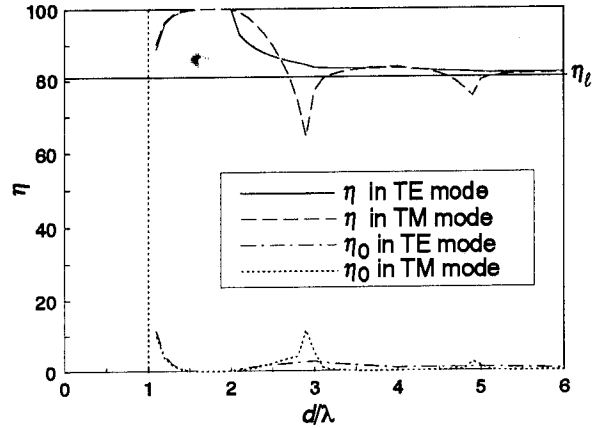


Figure 4: Efficiency of a two-beam fan-out element in the transition domain, compared to η_l .

frequency-modulated surface-relief profiles can be designed with an efficiency comparable to that of unconstrained phase elements in the paraxial domain.²³ Similar efficiencies can be achieved by pulse-width-modulated paraxial-domain elements with a sub-wavelength-period carrier grating.^{24,25}

5. Transition region

Although the above-reviewed investigations reveal a great deal of valuable information on diffractive optics beyond the paraxial domain, they shed little light on the behavior of diffractive elements in the transition region, where $0 \ll \Omega_W \ll \pi$.

Resonance-domain synthesis yields efficiencies significantly in excess of the paraxial upper bounds η_l , because we specify the undesired orders as evanescent. It is of considerable theoretical interest to determine whether η_l can be exceeded also in the transitional domain, or perhaps even in the paraxial domain, by the use of small-scale diffractive structures. We emphasize that such structures are not necessary for the realization of a paraxial optical function, and note that neither the synthesis techniques of Refs. [23–25] nor the analysis of optically recorded elements²⁶ suggests such a possibility.

We consider a simple optical function of splitting a normally incident plane wave into two equal-efficiency orders ± 1 , with the zeroth order suppressed. In this case $\eta_l = 8/\pi^2 \approx 81\%$, and it can be achieved by a single-groove binary surface-relief grating with a 1:1 aspect ratio and a phase delay of π . In Fig. 4 we consider a perfectly conducting substrate and find the first maximum of η as the groove depth h is increased, for a range of periods d . The efficiency increases significantly above η_l only as the element enters the resonance domain.

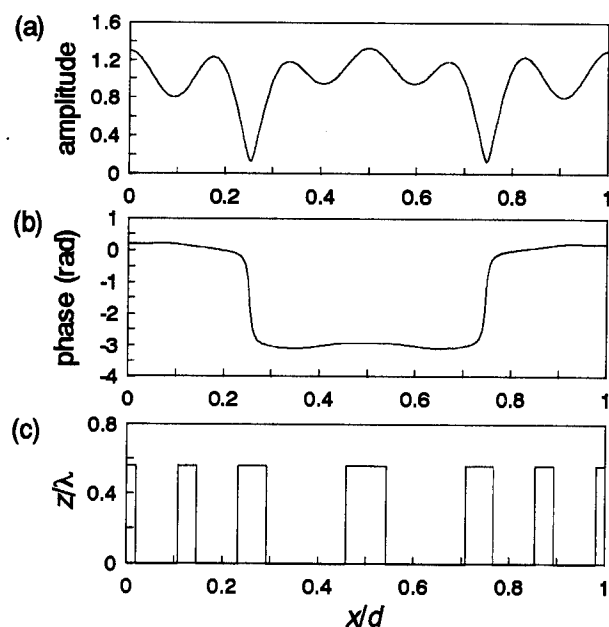


Figure 5: (a) Amplitude and (b) phase of the electric field diffracted by the profile (c).

To evaluate the possible efficiency improvement by the use of smaller transverse features, we consider the two-beam element with $d/\lambda = 3.9, 4.9, 5.9$, and 6.9 . By adding a number of extra grooves, we obtained $\eta = 91.8\%, 89.5\%, 90.0\%$, and 89.6% , respectively. Thus the efficiencies are some $8.5 - 11\%$ above η_1 , and there seems to be no definite decrease of η when Ω_W approaches the paraxial domain.

The phase and amplitude of the propagating part of the electric field at the exit plane of the grating with $d/\lambda = 6.9$ are plotted in Fig. 5(a) and 5(b), and the optimized profile is illustrated in Fig. 5(c). Neither the amplitude (which has values ≥ 1) nor the phase follows the grating profile, as is the case when paraxial-domain diffractive elements are treated using the thin-element approximation.

The case considered above is rather special, and further research is required to determine whether, in general, resonance-domain structures can be used to enhance the efficiency of diffractive elements for paraxial signals.

6. Conclusions

We have demonstrated that parametric optimization of the diffractive structure by exact electromagnetic diffraction theory can significantly enhance the efficiency of diffractive elements in the resonance domain, and provided evidence that small-scale structures may improve the efficiency also in the transition region quite close to the paraxial domain.

References

1. International Optical Design Conference '94 Lens Design Problem: "Camera in a can".
2. F. Wyrowski, *Opt. Lett.* **16**, 1915 (1991).
3. O. Bryngdahl and F. Wyrowski, *Progress in Optics* XXVIII, 1 (1990).
4. F. Wyrowski and O. Bryngdahl, *Rep. Progr. Phys.* **54**, 1481 (1991).
5. F. Wyrowski, *J. Opt. Soc. Am. A* **10**, 1553 (1993).
6. F. Wyrowski, *Opt. Commun.* **92**, 119 (1992).
7. R. Petit, Ed., *Electromagnetic Theory of Gratings* (Springer, Berlin, 1980).
8. T. K. Gaylord and M. G. Moharam, *Proc. IEEE* **73**, 894 (1985).
9. K. Knop, *J. Opt. Soc. Am. A* **68**, 1206 (1978).
10. H. P. Herzig, M. T. Gale, H. W. Lehmann, and R. Morf, *Prospects for Parallel Optical Interconnects* (Springer, Berlin, 1993), 79.
11. A. Roberts and R. C. McPhedran, *J. Mod. Opt.* **34**, 511 (1987).
12. E. G. Loewen, M. Nèviere, and D. Maystre, *Appl. Opt.* **18**, 2262 (1978).
13. E. Noponen, A. Vasara, J. Turunen, J. M. Miller, and M. R. Taghizadeh, *J. Opt. Soc. Am. A* **9**, 1206 (1992).
14. S. J. Walker, J. Jahns, L. Li, W. M. Mansfield, P. Mulgrew, D. M. Tennant, C. W. Roberts, L. C. West, and N. K. Ailawadi, *Appl. Opt.* **32**, 2494 (1993).
15. T. K. Gaylord, W. E. Baird, and M. G. Moharam, *Appl. Opt.* **25**, 4562 (1986).
16. D. H. Raguin and G. M. Morris, *Appl. Opt.* **32**, 2582 (1993).
17. S. S. Wang and R. Magnusson, *Appl. Opt.* **32**, 2606 (1993).
18. C. W. Haggans, L. Li, and R. K. Kostuk, *J. Opt. Soc. Am. A* **10**, 2217 (1993).
19. T. Shiono, M. Kitagawa, K. Setsune, and T. Mitsuyu, *Appl. Opt.* **28**, 3434 (1989).
20. E. Noponen, J. Turunen, and A. Vasara, *Appl. Opt.* **31**, 5010 (1992).
21. A. W. Lohmann and D. P. Paris, *Appl. Opt.* **6**, 1739 (1967).
22. E. Noponen, J. Turunen, and A. Vasara, *J. Opt. Soc. Am. A* **10**, 434 (1993).
23. J. Turunen, P. Blair, J. M. Miller, M. R. Taghizadeh, and E. Noponen, *Opt. Lett.* **18**, 1022 (1993).
24. W. Stork, N. Streibl, H. Haidner, and P. Kipfer, *Opt. Lett.* **16**, 1921 (1991).
25. M. W. Farn, *Appl. Opt.* **31**, 4453 (1992).
26. H. Ichikawa, J. Turunen, and M. R. Taghizadeh, *J. Opt. Soc. Am. A* **10**, 1176 (1993).

Optical Waveguide Gratings Having Double-Surface Corrugation for Highly Efficient Input Coupling

John C. Brazas, Stephen Barry, and Jeffrey Hirsh

Imaging Research and Advanced Development, Eastman Kodak Company, Rochester, New York 14650-2014 (716)722-9461, Fax (716)722-9503

Lifeng Li

The Optical Sciences Center, University of Arizona, Tucson, Arizona 85721

Amanda L. McKeon

The Institute of Optics, University of Rochester, Rochester, New York 14627

Planar optical systems are attractive because they perform unique operations on confined optical beams, reduce the size and weight of an optical system, allow for manufacturing methods similar to those in the micro-electronics industry and potentially reduce the cost of an optical system by minimizing the quantity of specialty materials. Despite the increase in available power from diode lasers, two applications requiring high efficiency of input coupling are optical recording heads and second-harmonic blue light generation.

To obtain high input-coupling efficiency η using waveguide gratings, the percentage of total guided-wave power exiting the waveguide in the direction of the cladding or substrate, branching ratio BR, should be maximized. Methods of increasing the BR include: (1) shaping the grating-groove profile,¹ (2) incorporating a highly reflecting substrate,² and (3) fabricating gratings on both the upper and lower surfaces of the waveguide,³ referred to as double-surface corrugation.

Here we present a method similar to that of Ref. 3, but rather than forming the waveguide by sputtering, the film was formed by evaporation. As with sputtering, the deposited layer conformed to the corrugation of the grating at the substrate-waveguide boundary to produce a second grating of the same period at the cladding-waveguide surface. However, by using the evaporation technique, a preferential angle-of-deposition ϕ_d can be selected allowing a shift of the upper-grating pattern relative to that of the lower grating; the final deposited thickness will determine the upper grating lateral shift. A grating coupler having double-surface corrugation is schematically shown in Fig. 1. The gratings have identical periods Λ , but distinct groove depths h_1 and h_2 and duty cycles (L/Λ) dc_1 and dc_2 . The lateral shift Δz between the gratings is also illustrated.

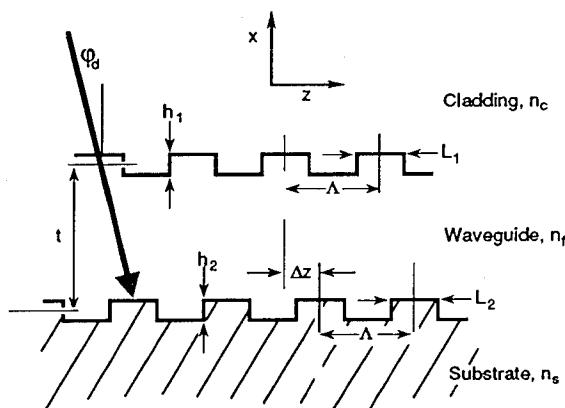


Figure 1. Geometry and coordinate system of a grating coupler having double-surface corrugation.

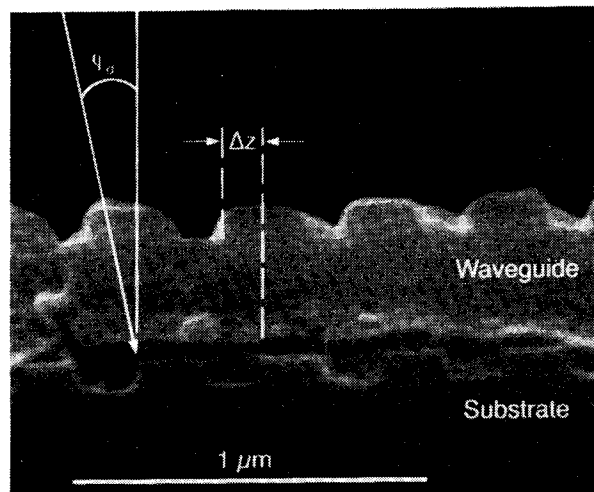


Figure 2. SEM of the double-surface corrugation for a waveguide of thickness $0.42 \mu\text{m}$ showing the angle-of-deposition ϕ_d and the lateral shift Δz .

When a guided wave enters the grating region, both gratings will diffract light into the cladding or substrate. The light that is coupled out of the waveguide into the cladding or substrate is the result of optical interference between the two first orders diffracted by the two gratings. The relative strength of the two interfering waves depends primarily on the ratio of the two grating groove depths, h_1 and h_2 , and the index difference at the boundaries. The phase difference between these two waves can be changed by a lateral shift Δz of the upper grating. A key to understanding this interference phenomenon is to realize that a first-order diffracted plane wave undergoes a phase change of $-K\Delta z$, where $K = 2\pi/\Lambda$, while the zero order suffers no phase change with the lateral shift. In comparison to all other dimensions of the grating system, the adjustment of Δz has the most significant effect on the phase difference of the interfering diffracted waves and the resulting BR.

Our approximate model, to be presented elsewhere, produces a simple analytical formula for the dependence of the BR on the waveguide-grating assembly. The model assumes that both grating groove depths are shallow and the profiles are sinusoidal. For the following equations, c, f, and s denote the quantities associated with the cladding, waveguide film, and substrate, respectively. The expression for BR (TE polarization) into the cladding is

$$BR = \frac{\beta_{-1}^{(c)} |f_c|^2}{\beta_{-1}^{(c)} |f_c|^2 + \beta_{-1}^{(s)} |f_s|^2} \quad (1)$$

where

$$f_c = \frac{1}{(\beta_{-1}^{(f)} + \beta_{-1}^{(c)})} \left[\frac{(\beta_0^{(f)} - \beta_0^{(s)})}{(\beta_0^{(f)} + \beta_0^{(c)})} (n_f^2 - n_c^2) h_1 e^{i(K\Delta z + \beta_0^{(f)} t)} - \frac{2\beta_{-1}^{(f)}}{\beta_{-1}^{(f)} + \beta_{-1}^{(s)}} (n_f^2 - n_s^2) h_2 e^{i\beta_{-1}^{(f)} t} \right], \quad (2)$$

$$f_s = \frac{1}{(\beta_{-1}^{(f)} + \beta_{-1}^{(s)})} \left[\frac{(\beta_0^{(f)} - \beta_0^{(s)})}{(\beta_0^{(f)} + \beta_0^{(c)})} \frac{2\beta_{-1}^{(f)}}{\beta_{-1}^{(f)} + \beta_{-1}^{(c)}} (n_f^2 - n_c^2) h_1 e^{i(K\Delta z + \beta_{-1}^{(f)} t + \beta_0^{(f)} t)} - (n_f^2 - n_s^2) h_2 \right], \quad (3)$$

$$\beta_m^{(k)} = k_0 \sqrt{n_k^2 - \left(N + m \frac{\lambda}{\Lambda}\right)^2}, \quad k = c, f, s \quad \text{and} \quad m = 0, -1, \quad (4)$$

and N is the effective refractive index of the waveguide. In the case where $m = 0$, and $k = c$ or s , the sign of $\beta_m^{(k)}$ should be chosen so that $\beta_m^{(k)} = \pm |\beta_m^{(k)}|$ (we assume n_k , $k = c, f, s$, are lossless). Similar to the case of blazed gratings, the behavior of waveguide grating couplers with double-surface corrugation are sensitive to guided-wave propagation directions. In Eqs. (1)-(4), we have assumed that the guided wave propagates in the $+z$ direction.

The relief grating at the substrate surface was fabricated by forming a photoresist mask and then ion milling the grating grooves into the substrate in combination with positive photoresist image-reversal techniques.⁴ Three adjacent grating areas were formed to allow BR and η measurements in either direction of propagation. The waveguide was formed by thermal evaporation of an organic glass.⁵ Using high-vacuum coating conditions, a specific angle of deposition can be selected by tilting the substrate normal relative to the direction of material deposition and the corrugation on the substrate was transferred to the surface of the waveguide. A consecutive series of waveguide thicknesses were deposited at a constant angle ϕ_d onto a substrate during a single coating cycle by moving a deposition mask. This fabrication procedure ensured identical deposition parameters and substrate conditions for each region of different thickness. Figure 2 shows a cross-sectional view of the waveguide grating for $\phi_d = 13.5^\circ$. The growth of the film distorts the duty cycle dc_1 and groove depth h_1 , and causes a lateral shift Δz . Approximate

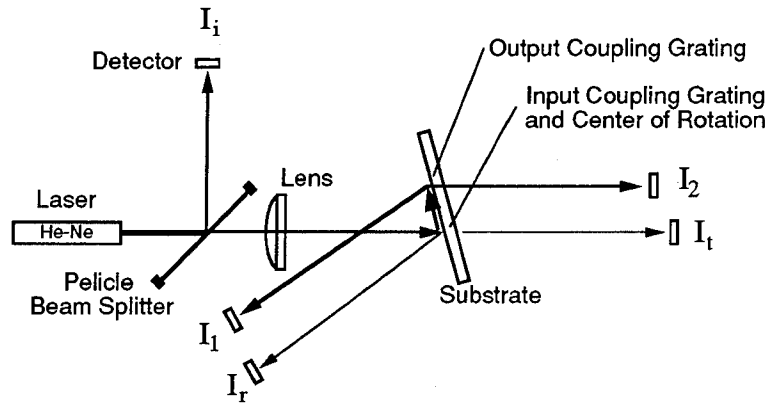


Figure 3. Optical system for measuring the BR and η .

relations between these grating parameters and the waveguide thickness were determined and used in the model to best describe the upper grating characteristic.

Experimental BR and η were obtained using the optical system of Fig. 3. The sample was mounted on computer-controlled stages that provided sample rotation and translation while monitoring the beam intensities to optimize the sample position. The selection of the lens to focus the Gaussian beam onto the sample was critical to maximize the η value. The regions of the grating chosen for optimization were those that exhibited the highest η values. Background intensities I_1' and I_2' were collected by displacing the sample along the direction of the x-trans stage enough to move the incident beam off the grating area. The BR is then obtained from the expression

$$BR = \frac{(I_i - I_1')}{(I_i + I_2) - (I_1' + I_2')} \quad (5)$$

The input coupling efficiency η is the ratio of the power coupled into the guided mode to the power of the incident beam. The input coupling efficiency was determined indirectly by measurement of the non-guided beams originating from the input-coupling grating surface and subtracting them from the incident beam intensity. A fraction of the incident intensity was scattered from the grating surface and unavailable for input coupling. The intensity of scattered light I_s was determined by rotating the grating until light was no longer input coupled, then reading intensities I_i , I_r , and I_t for the incident, reflected, and transmitted beams, respectively. The scattered intensity is then expressed

$$I_s = [I_i - (I_r + I_t)] \Big|_{\text{no coupling}} \quad (6)$$

and the expression for input coupling efficiency becomes

$$\eta = \frac{(I_i - I_s) - (I_r + I_t)}{(I_i - I_s)} \quad (7)$$

The scatter term was included to account for non-uniformities in the grating and waveguide, and removes the effect of scattered intensity from this data for comparison to model values. Also, the thicker waveguide regions supported two modes (TE_0 and TE_1), however, only the TE_0 mode was observed to be excited and no substrate modes existed for this waveguide-grating design.

For +z and -z propagation, the experimental BR values into air (see Fig. 4) ranged between 4% and 98%. These data points illustrate the dramatic effect of Δz on the BR and that a high BR could be selected by a specific waveguide-grating design. There was good agreement between these experimental and model results (see Fig. 4) and the thickness for the intersection for the + Δz and - Δz cases. Despite the lower amplitudes, the approximate model provides a means of selecting a high BR for a specific material system using the angle-of-depositon.

By virtue of reciprocity, an efficient output grating coupler is also an efficient input coupler. The output coupling efficiency (into cladding or substrate) of a grating coupler is essentially given by the branching ratio, provided the grating is sufficiently long. The input coupling efficiency is directly proportional to BR, so an increase of BR directly improves input coupling efficiency. This is demonstrated in Fig. 5 where experimental efficiency curves are overlayed with the corresponding experimental BR curves. The theoretical limit of input coupling efficiency into a single leakage channel grating coupler (100% BR) using a Gaussian incident beam is about 80%. Input coupling efficiencies near the theoretical limit were obtained for thicknesses where the BR was near 100%. The maximum input coupling efficiency observed in this work was 78%, the highest value reported to date for optical wavelengths.

In this work we have demonstrated a new method of fabricating a double-surface corrugation advantageous for input coupling when the over-all efficiency of a device must be considered. In a simple way, a thermally deposited waveguide layer on a surface relief grating can be used to significantly enhance the BR and corresponding η of the grating coupling process.

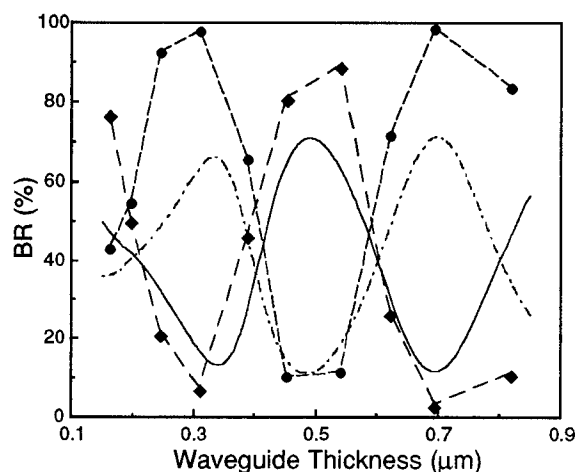


Figure 4. Experimental (plotted points) and theoretical (lines) BR results into air for propagation in the +z (\bullet and —) and -z (\blacklozenge and - - -) directions where the model results are from Eq. 1 using measured waveguide-grating parameters.

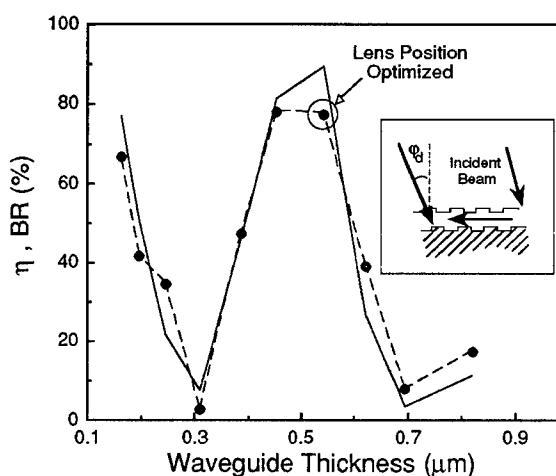


Figure 5. Experimental η for air-incidence using a 300 mm focal length lens (\bullet) for the sign of the deposition angle as depicted with the experimental BR from Fig. 4 (—).

1. T. Aoyagi, Y. Aoyagi, and S. Namba, "High-efficiency blazed grating couplers," *Appl. Phys. Lett.*, **29**, 303-304 (1976).
2. R. L. Roncone, L. Li, and J. C. Brazas, "Single-leakage-channel grating couplers: comparison of theoretical and experimental branching ratios," *Opt. Lett.*, **18**, 1919-1921 (1993).
3. I. A. Avrutshy, A. S. Svakhin, V. A. Sychugov, and O. Parriaux, "High-efficiency single-order waveguide grating coupler," *Opt. Lett.*, **15**, 1446-1448 (1990).
4. L. Li, M. Xu, G. I. Stegeman, and C. T. Seaton, "Fabrication of photoresist masks for submicrometer surface relief gratings," *Proc. SPIE* **835**, 72-82 (1988).
5. J. C. Brazas, G. Kohnke, and J. P. McMullen, "A mode-index waveguide lens with novel gradient boundaries developed for application to optical recording," *Appl. Opt.*, **31**, 3420-3428 (1992).

Design of non-periodic diffractive elements with respect to illumination wave

Harald Aagedal^a, Thomas Beth^a, Stephan Teiwes^a, and Frank Wyrowski^b

^a) Institut für Algorithmen und Kognitive Systeme, Universität Karlsruhe,
Am Fasanengarten 5, 76128 Karlsruhe, Deutschland
Tel.(0049)-721-6084213, Fax:(0049)-721-696893

^b) Berliner Institut für Optik (BIFO)
Rudower Chaussee 5, 12484 Berlin, Deutschland
Tel.(0049)-30-63923470, Fax:(0049)-03-63923452

1 Introduction

The optical function of a diffractive element (DE) is to transform an impinging wavefront into a diffracted wavefront being defined in a signal window. A fundamental objective in diffractive optics is to design DEs capable of performing such a transformation according to some specification. In the paraxial domain of diffractive optics, optical systems can be described by Fourier optics [1, 2, 3].

The published literature normally considers plane illumination waves. This simplification is usually sufficient for periodic DEs, e.g. gratings, leading to discrete diffraction patterns. If the modulation scale of an illumination wave is large compared to the grating period, "only" the shape of the diffraction orders is influenced. However, the situation changes drastically if non-periodic DEs are used. An illumination wave deviating from a plane wave influences the diffraction pattern and thus the optical function of the DE. Applications can be found for instance in beam shaping, optical pattern recognition, pattern projection in material processing, and display.

The effect of the illumination wave on the optical function of non-periodic DEs should be analysed without restriction to a special application. Examinations in this paper are based on the standard $4f$ -configuration. The system input is an optical field denoted by $a_I(x)$, $x \in \mathbb{R}^2$. Its Fourier-transform $A_I(u) = (\mathcal{F}a_I)(u)$ is modulated by the transmittance function $F(u)$, $u \in \mathbb{R}^2$, of the DE. A second Fourier-transform yields the system output

$$a_O(x) = a_I(x) * f(x), \quad (1)$$

disregarding a coordinate inversion; $*$ denotes a convolution. In this case, the function of a DE can be interpreted as a convolution with its impulse response $f(x) = (\mathcal{F}F)(x)$.

For many applications the system input $a_I(x)$ is completely specified by the illumination wave, whereas only the intensity of the system output $\iota_O(x)$ is defined in a signal window W . The problem of designing a DE capable of performing a specified function on an incoming wavefront can be solved for the coherent and incoherent case. For these two cases the system outputs are, respectively,

$$\begin{aligned} \text{coherent illumination} &: \iota_O(x) = |a_I(x) * f(x)|^2 \\ \text{incoherent illumination} &: \iota_O(x) = \iota_I(x) * |f(x)|^2, \end{aligned} \quad (2)$$

with $\iota_I(x) = |a_I(x)|^2$ [4].

In section 2, the impulse response $f(x)$ for non-periodic DEs is defined in terms of $a_I(x)$ and $a_O(x)$ for the coherent and the incoherent case. It will be shown that this definition is not unique and thus, there are several degrees of freedom which may be used to satisfy constraints on $F(u)$. Section 3 deals with the synthesis of $f(x)$ and finally in section 4 examples are given to demonstrate the applicability of the proposed methods.

2 Description of impulse response

Assuming that the system input and output are given, an expression for the impulse response $f(x)$ of the DE can be derived directly. In the case of coherent illumination, we get

$$f(x) = \mathcal{F}(A_O(u)/A_I(u)), \quad (3)$$

with $A_O(u) = (\mathcal{F}^{-1}a_O)(u)$ and $A_I(u) = (\mathcal{F}a_I)(u)$. The deconvolution of two positive real-valued functions does not necessarily lead to a *positive* real-valued function. Thus in the case of incoherent illumination, the impulse response function may be defined by

$$f(x) = \left(\mathcal{F} \frac{\mathcal{F}^{-1}\iota_O(x)}{\mathcal{F}^{-1}\iota_I(x)} + \beta \right)^{\frac{1}{2}} \exp(i\varphi(x)), \quad (4)$$

where $\varphi(x)$ is a free parameter and the bias term β is given by

$$\beta = \max \left\{ 0, -\min_x \mathcal{F} \frac{\mathcal{F}^{-1}\iota_O(x)}{\mathcal{F}^{-1}\iota_I(x)} \right\} \quad (5)$$

The value of the bias term strongly depends on the application.

Since a DE does not amplify an incoming wavefront, its function is restricted by the relation $|F(u)| \leq 1$. However, division by $A_I(u)$ in (3) or by $(\mathcal{F}^{-1}\iota_I)(u)$ in (4), respectively, will introduce large values if the denominator is close to zero. Additionally, singularities appear at the zero crossings of the denominator. In order still to obtain a good approximation for $f(x)$, the distributions $A_O(u)/A_I(u)$ and $(\mathcal{F}^{-1}\iota_O)(u)/(\mathcal{F}^{-1}\iota_I)(u)$, respectively, can be clipped to a suitable maximum value followed by a normalization operation [5, 6]. One further practical restriction is the finite size of the DE being equivalent to the desire for a band-limited $f(x)$.

Equations (3) and (4) do not specify $f(x)$ completely. Considering coherent illumination in (3), the phase $\arg(a_O(x))$ is a free parameter influencing $f(x)$ indirectly via $A_O(u)$. In the incoherent case represented by (4), the phase $\arg(f(x))$ is a free parameter which is only restricted to bandlimitation.

3 Design of diffractive element

In principle, degrees of freedom can be used to fulfil constraints on the distribution $F(u)$ of the DE. This idea was first proposed by Liu and Gallagher [6] for the case that only the intensities of the coherent system input and output are specified. In this paper, the effect of a modulated illumination wave on the optical function of a DE is examined. Therefore, the phase of a coherent system input $a_I(x)$ is not free.

Since a DE is finite in size, a band-limit constraint is fundamental for its design. Depending on the element type, e.g. amplitude- or phase-only element, further design constraints have to be taken into account. As an example we discuss the design of a diffractive phase element (DPE), starting from a band-limited distribution $f(x)$.

Equation (4) is a basis for synthesizing the impulse response $f(x)$ of the DE in the incoherent case. The phase $\arg(f(x))$ can be chosen in such a way that $f(x)$ fulfils the band-limit constraint [8]. The problem of generating DEs realizing other constraints can be solved by iterative methods [7, 2].

The coherent case is more complicated, since the free phase parameter $\arg(a_O(x))$ influences $f(x)$ indirectly. In principle, equation (3) offers a solution for $f(x)$ that can be modified by iteration techniques in order to fulfil additional constraints. But this approach does not allow to make use of the indirect phase freedom which is a significant disadvantage.

We present a version of the iterative Fourier-transform algorithm [7] which gives us the possibility to influence constraints on the DE function $F(u)$ directly via $\arg(a_O(x))$. An implementation for generating band-limited DPEs is given by the following steps:

- Let $(A_O)_j(u) = (\mathcal{F}^{-1}(a_O)_j)(u)$ after j iteration steps. We define the function of the DE by

$$\bar{F}_j(u) = \begin{cases} (A_O)_j(u)/A_I(u) & : |A_I(u)| \neq 0 \\ 0 & : \text{otherwise} \end{cases} \quad (6)$$

- $\bar{F}_j(u)$ has to fulfil a band-limit and a phase-only constraint. Both constraints can be introduced by an operator \mathcal{U} which is defined as follows:

$$(\mathcal{U}\bar{F}_j)(u) = \begin{cases} \exp(i \arg(\bar{F}_j(u))) & : u \in D \\ 0 & : \text{otherwise} \end{cases}, \quad (7)$$

where D is a window which size is half of the size of the spectral bandwidth $\Delta(A_O)_j(u)$ of $(a_O)_j(x)$. Other constraints, e.g. a quantization, may also be introduced.

- The coded DE distribution $F_j(u) = (\mathcal{U}\bar{F}_j)(u)$ multiplied with $A_I(u)$ is required to reconstruct $a_O(x)$ in the output plane. Thus, the iteration moves back to the output domain by a Fourier-transform of $\bar{A}_O(u) = F_j(u)A_I(u)$.
- A correction of the resulting distribution $(\bar{a}_O)_j(x)$ in a signal window W is performed by an operator \mathcal{X} defined by

$$(\mathcal{X}(\bar{a}_O)_j)(x) = \begin{cases} \alpha |a_O(x)| \exp(i \arg((\bar{a}_O)_j(x))) & : x \in W \\ (\bar{a}_O)_j(x) & : \text{otherwise} \end{cases}, \quad (8)$$

The scaling factor α can be used to optimize the diffraction efficiency of the DE [2].

- The distribution $(a_O)_{j+1}(x) = (\mathcal{X}(\bar{a}_O)_j)(x)$ represents the system output for the next iteration cycle.

The iteration starts in the output domain with a band-limited complex distribution $(a_O)_0(x)$ being defined in a signal window W and fulfilling $(a_O)_0^2(x) = i_O(x)$. In order to interrupt the procedure, an error criterion or the number of iterations may be used. The result after n iterations is a coded DE distribution $F_n(u)$.

An error criterion may be defined by

$$\sigma^2 = \int_W (\alpha |f(x)| - |\bar{a}_O(x)|)^2 dx \quad (9)$$

with the scaling factor

$$\alpha = \left(\int_W |f(x)| |\bar{a}_O(x)| dx \right) / \left(\int_W |f(x)|^2 dx \right) \quad (10)$$

This scaling factor is introduced in equation (8) of the iterative Fourier-transform algorithm. It is chosen in such a way that in each iteration step the error criterion is minimized.

4 Examples

The proposed version of the iterative Fourier-transform algorithm can be applied for almost arbitrary situations, where practical system inputs and outputs are specified. To show the flexibility and practical usefulness of the algorithm, we give two examples depicted in figure 1.

The upper row in figure 1 illustrates a beam shaping application, where the DPE in *a*) is generated to transform a broad super-gaussian into a narrow one. The intensity profiles of the impulse response of the DPE, the illumination wave which is a broad super-gaussian, and the system output are shown in *b*), *c*), and *d*), respectively. Sometimes a DPE is required focussing as much energy as possible into a smoothed distribution approximating a narrow super-gaussian. The DPE in *a*) is optimized to fulfil this desire.

In the lower row of figure 1 a display application is presented. The DPE in *a*) is designed to reconstruct a speckle-free intensity signal *d*), considering the illumination wave *c*). The impulse responses of the DPE is shown in *b*).

5 Conclusion

The incorporation of the illumination wave turns out to be important for non-periodic DEs in various applications. The cases of coherent and incoherent illumination are examined separately. A version of the iterative Fourier-transform algorithm is presented, allowing direct control of constraints on the function of the DE in the coherent case. The algorithm may serve as a general concept for the design of non-periodic DEs with the modulation of practical illumination waves taken into consideration.

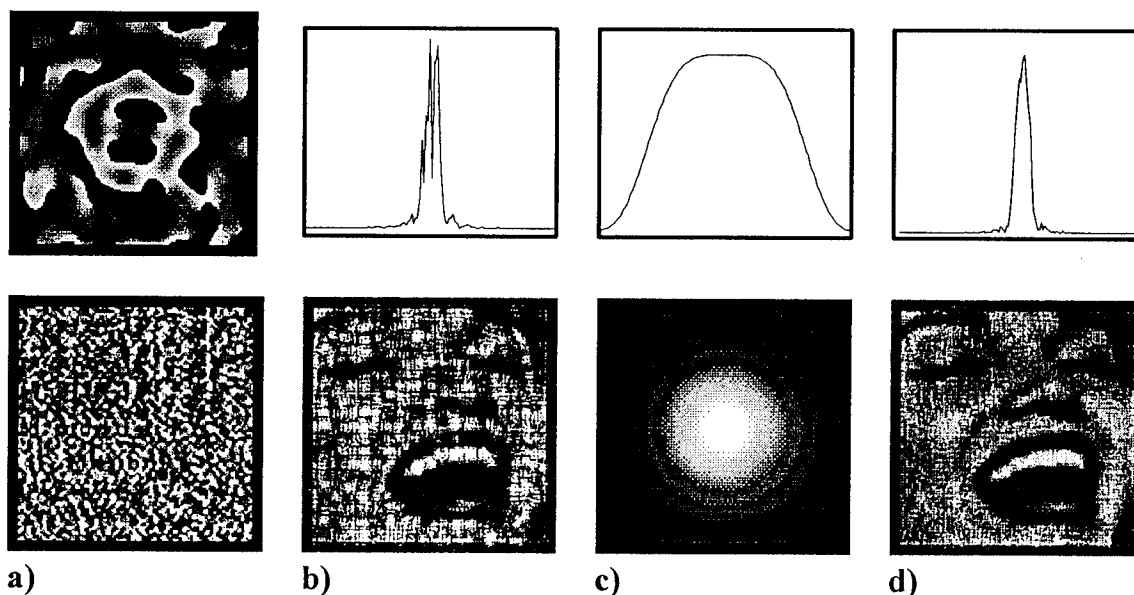


Figure 1: The upper row shows a beam shaping example and the lower row a display example. a) depicts the phase distribution of the DE, b) the impulse response of the DE, c) the illumination wave and d) the system response, respectively.

References

- [1] J. W. Goodman, *Introduction to Fourier Optics* (McGraw Hill, New York, 1969), pp. 141-197.
- [2] F. Wyrowski, "Design theory of diffractive elements in the paraxial domain," *J. Opt. Soc. Am. A* 10, 1553-1561 (1993).
- [3] E. Noponen, A. Vasara, J. Turunen, J.M. Miller and M.R. Taghizadeh, "Synthetic diffractive optics in the resonance domain," *J. Opt. Soc. Am. A* 9, 1206-1213 (1992).
- [4] J. W. Goodman, *Introduction to Fourier Optics* (McGraw Hill, New York, 1969), pp. 108-136.
- [5] F. Wyrowski, "Digital phase-encoded inverse filter for optical pattern recognition," *Appl. Opt.* 30, 4650-4657 (1991).
- [6] B. Liu and N.C. Gallagher, "Optimum Fourier-transform division filters with magnitude constraint," *J. Opt. Soc. Am.* 64, 1227-1236 (1974).
- [7] J. R. Fienup, "Iterative Method Applied to Image Reconstruction and to Computer-Generated Holograms," *Opt. Eng.* 19, 297-305 (1980).
- [8] F. Wyrowski and O. Bryngdahl, "Iterative Fourier-transform algorithm applied to computer holography," *J. Opt. Soc. Am. A* 5, 1058-1065 (1988).

Aperiodic Gratings in Waveguides

TANVEER UL HAQ, KEVIN J. WEBB, and NEAL C. GALLAGHER

School of Electrical Engineering

Purdue University

West Lafayette, IN 47907-1285

Tel No. 317-494-3518 , Fax No. 317-494-6440

I. INTRODUCTION

Free space gratings are typically periodic structures that convert a free space incident mode into a particular set of exit modes. The free space propagating modes in this case are identified as plane waves incident at various angles on the grating. Apart from free space applications, the mode transducing properties of gratings have also been utilized in guided wave devices. One such device is a periodic grating structure used in metallic waveguides to transform one waveguide mode into another [1, 2, 3]. In this application the grating is known as a mode converter. The grating in this case is formed by periodically varying the transverse dimension of the waveguide. When a waveguide mode is incident from any side on the grating, it is converted to another mode. The period of the grating is related to the propagation constants of the input and the exit modes. In this paper we report that in waveguides, there exist gratings that are not periodic but have the same effect as that of the periodic gratings. These aperiodic structures are shorter in length than the periodic gratings, yet they achieve comparable conversion efficiencies. To find the shape of these non-periodic gratings a scattering optimization scheme is developed in which the surface profile of an arbitrary scatterer is optimized for maximum conversion of power from one mode to another.

II. SCATTERING OPTIMIZATION METHOD

To demonstrate the method of designing a non-periodic grating in a waveguide, let's consider a simple parallel plate waveguide. A scatterer is formed within this waveguide through z-dependent variations in one of its walls and is modelled as a staircase in terms of a finite number of step discontinuities (Fig. 1). Mode matching is a well documented technique for analyzing waveguide step discontinuities [4, 5, 6]. Using the mode matching method, a scattering matrix is formed for each of the steps in the staircase model. These scattering matrices are later combined to form a composite scattering matrix, S , representing the effect of the whole length of the scatterer. Considering a field incident on the scatterer, the output mode coefficients (vector B) are related to the input mode coefficients (vector A) by the matrix S ($B = SA$). Using B , the power in each mode at the exit plane of the mode converter can be calculated. To lose the least information while keeping the calculations manageable, the step width (ΔL) is restricted to be greater than or equal to 0.1λ for each step. The total length of the scatterer then is $L=k\Delta L$, for k steps. For the purpose of designing an aperiodic grating, we identify a general scatterer by a set of variables which are the heights of steps in the scatterer. The power excited by this scatterer in a particular mode at the exit plane is a function of the surface profile of the scatterer and can be written as *Power in mode n* $= P_n(h_1, h_2, \dots, h_k)$, where h_i is the height of the i^{th} step. The required grating surface can now be found by optimizing the power P_n in the output mode n as a function of k step heights. This optimization is carried out by implementing a 'global' optimization strategy.

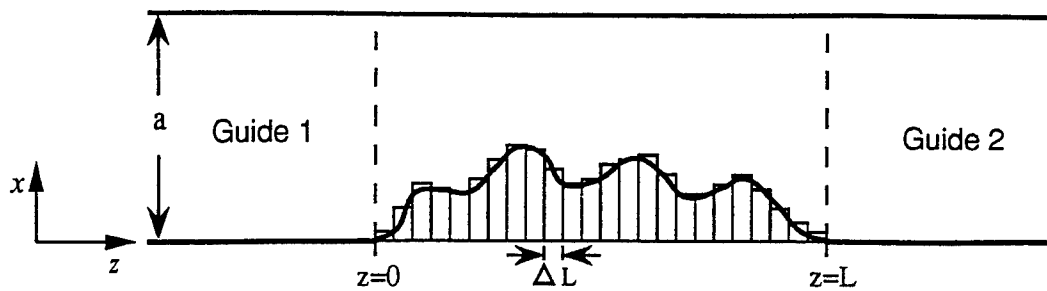


Figure 1: Staircase model for an arbitrary scatterer.

III. RESULTS

Various gratings have been designed using the above method. A summary of four of them is given in Table 1. In each of these designs the IMSL routine BCPOL is utilized for global optimization and a total of twenty evanescent modes are used in the mode matching calculations. The structure obtained for the TE_1 to TE_2 mode converter at 3.5Ghz is shown in Fig. 2. Two more designs for the same converter are shown in Fig. 3 and are drawn on the same axis for comparison.

Converter Type	Frequency (GHz)	'a' (cm)	Efficiency (%)	Aperiodic Grating Length	Periodic Grating Period
TE_1-TE_2	3.5	15	99.78	59.40 cm	62.6 cm
TE_1-TE_4	4.5	15	98.62	58.96 cm	12.9 cm
TE_1-TE_2	10.0	15	98.56	111.9 cm	197.4 cm
TE_3-TE_1	10.0	15	98.31	151.5 cm	73.08 cm

Table 1: Summary of grating designs

The salient features of aperiodic gratings designed by scattering optimization are summarized below :-

1. The general shape of these gratings comprises a primary scatterer in the center, flanked on both sides by smaller scatterers that act as tuning elements. The heights of the tuning elements and their locations are critical; a change in them can greatly affect the mode pattern at the output of the grating.
2. The mode conversion efficiency achieved in each of the designs in Table 1 is $> 98\%$, which is comparable to that achieved by periodic gratings in waveguides [1, 2, 3, 7, 8].
3. The length of the grating in each case is not very large in comparison to the waveguide height. These lengths are much smaller than those obtained for "periodic" gratings. In Table 1, the grating period for comparable periodic gratings is also shown for comparison. A periodic grating generally consists of two or more such periods [1, 2].
4. It can be seen from Figs. 2 and 3 that the grating structures obtained through this method are not unique, i.e., more than one solution can be found having an

acceptable conversion efficiency. The three structures in these figures for TE_1 to TE_2 mode conversion have comparable efficiencies of 99.78%, 99.77% and 99.47% respectively, yet their shapes are entirely different. An important parameter in our design procedure is the height increment used while carrying out the optimization sequence. This determines the coarseness of the grid used for optimization. A coarser grid implies that most likely the solution is in a larger valley and therefore is not very sensitive to small changes in heights of elements. The Designs 1, 2 and 3 in Figs. 2 and 3 are obtained by using height increments of 3mm, 2mm and 0.1mm, respectively. It is found that the first of these designs is the least sensitive to variation in height elements while the last one is the most sensitive. The sensitivity to operating frequency variations also increases from Design 1 to Design 3.

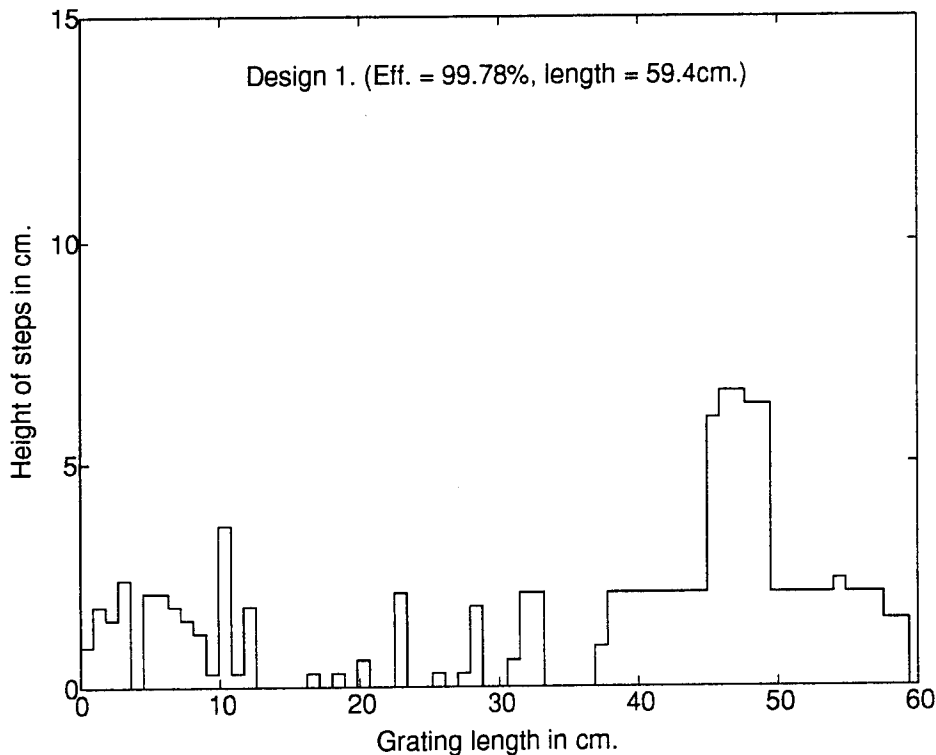


Figure 2: Grating design for TE_1 to TE_2 mode conversion at 3.5 GHz in a waveguide with $a=15$ cm. Wavelength λ is 8.6cm., stepwidth (ΔL) is 9mm and step height increment is 3mm.

IV. CONCLUSION

We have developed a technique for the design of aperiodic gratings used for mode conversion in over-moded waveguides, wherein the profile of a scattering surface is optimized for maximum conversion of power into the required mode. Gratings designed using this approach are highly efficient and their overall length is smaller than the usual periodic gratings in waveguides. The structures obtained from this technique are not unique and their sensitivity to fabrication and frequency errors depends upon the size of step width and height increments used in the staircase model. The scattering optimization method not only generates shorter gratings, but it also provides the advantage of designing structures in which more than one mode at the input can be converted into a single mode at the output.

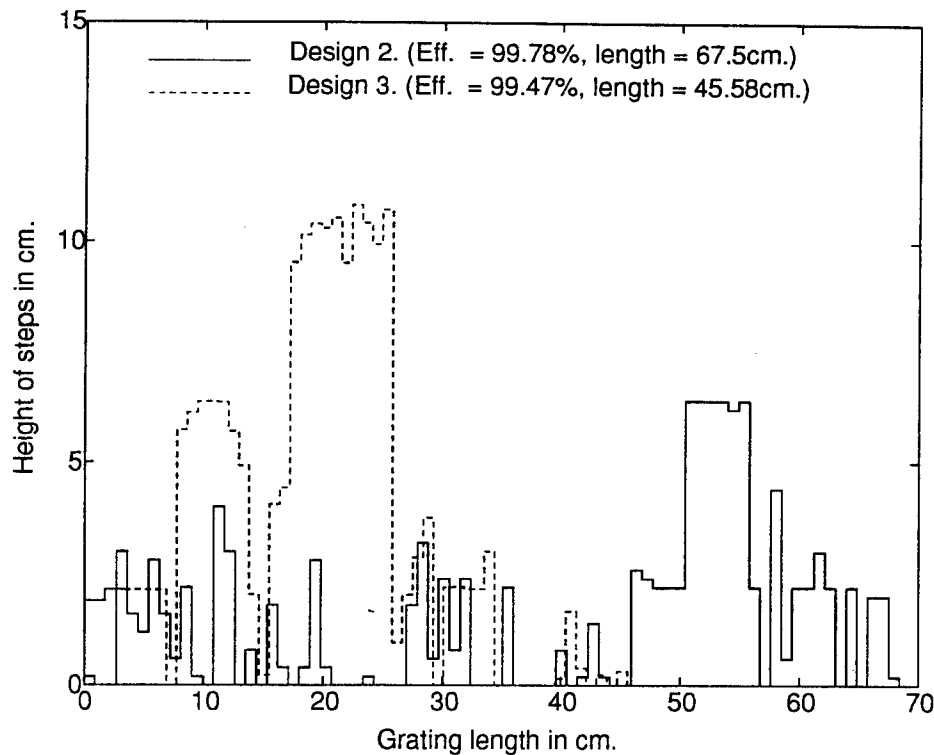


Figure 3: Two more designs for TE_1 to TE_2 mode converter of Fig. 2. For Design 2, ΔL is 9mm and Ht. increment is 2mm. For Design 3, these are 8.6mm and 0.1mm respectively

REFERENCES

- [1] M. Thumm, "High-power millimetre-wave mode converters in overmoded circular waveguides using periodic wall perturbations", *Int. J. Electronics*, vol. 57, pp. 1225-1246, 1984.
- [2] J. S. Levine, "Rippled wall mode converters for circular waveguide", *Int. J. Infrared and Millimeter Waves*, vol. 5, pp. 937-952, 1984.
- [3] M. J. Buckley and R. J. Vernon, "Compact quasi-periodic and aperiodic TE_{on} mode converters in overmoded circular waveguides for use with gyrotrons", *IEEE Trans. MTT*, vol. 38, pp. 712-712, June 1990.
- [4] A. Wexler, "Solution of waveguide discontinuities by modal analysis", *IEEE Trans. MTT*, vol. 15, pp. 508-517, Sep. 1967.
- [5] P. J. B. Clarricoats and K. R. Slinn, "Numerical solution of waveguide discontinuity problems", in *Proc. Inst. Elect. Eng.*, vol. 114, pp. 878-885, July 1967.
- [6] L. Carin, K. J. Webb, and S. Weinreb, "Matched windows in circular waveguide", *IEEE Trans. MTT*, vol. 36, pp. 1359-1362, Sep. 1988.
- [7] K. Kumric, M. Thumm, and R. Wilhelm, "Optimization of mode converters for generating the fundamental TE_{01} mode from TE_{06} gyrotron output at 140 GHz", *Int. J. Electronics*, vol. 64, pp. 77-94, Jan. 1988.
- [8] M. Thumm and H. Kumric, " TE_{03} to TE_{01} mode converters for use with a 150 GHz gyrotron", *Int. J. Infrared and Millimeter Waves*, vol. 8, pp. 227-240, 1987.

Holographic Optical Interconnects

H. Grebel and Su Chiou Tsay

New Jersey Institute of Technology, 323 Martin Luther King Blvd., Newark, NJ 07102-1824

Novel holographic planar structures for optical interconnects employing transverse Bragg waveguides[1] were proposed recently. The gratings, which laterally confine the optical wave, are patterned transversely, as shown in Figure 1. The advantages of these planar structures are: 1. Spectral selectivity allows us to combine many grating patterns (holograms) on top of each other. 2. By use of higher orders of the Bragg condition, mode shaping of the propagating beam may be achieved. 3. These holograms are easily molded in plastics.

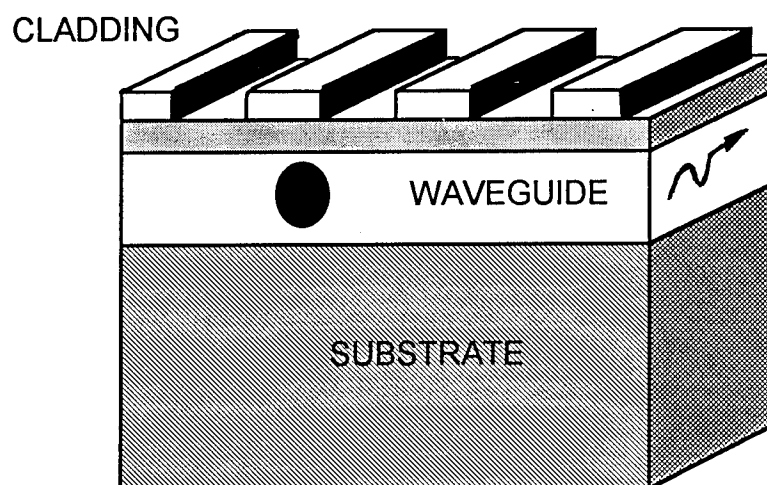


Figure 1. Transverse Bragg Waveguide

In this paper we employ the concept of transverse Bragg reflectors in order to design $N \times 1$ and $1 \times N$ interconnections. We use a ray tracing technique in two design procedures: 1. The Shortest Path (SP) and, 2. The Single Input Maximum Output (SIMO) procedure. It should be noted that since there are virtually infinite number of ways to design a specific connection, simplicity and efficiency of the computation method is of great importance.

We have used ray tracing method to design Nx1 and 1xN optical interconnects. The optical beam was diffracted by grating in each pixel according to the Bragg reflection rule. The grating of the pixel would be engraved along the beam propagation if the beam is to propagate in a straight line. This engraving will confine the beam in its transverse dimension. On the other hand if the beam is to be blocked then the grating will be engraved perpendicularly to the beam direction. The Shortest Path approach maximizes the power at the targeted pixels by minimizing the number of turns in the optical path between an input pixel and an output pixel. It is superior to the other design scheme whenever maximum intensity at the target pixel is needed. The phase though, was found to be distributed non-uniformly amongst the non-targeted pixels compared to the Single Input Maximum Output approach. The latter approach maximizes the power flow into the nearest neighboring pixel by an appropriate choice of a Bragg reflector. Considering Nx1 optical interconnect, the cross talk was -24dB for the SP design approach compared to -44dB for SIMO. The loss for the SP approach was 9.8dB compared to 17.8 dB for SIMO. A sample design of 20x1 interconnection using SP approach is shown in Figure 2. A similar design may be used to fabricate 1x20 interconnection.

The design of an Nx1 interconnection was successful when using the Shortest Path design approach. The light intensity was distributed quite uniformly among the 10 target pixels. The power variation between the target pixels was about 2dB compared to 3.5 for SIMO. The average loss per pixel was about 2dB for SP and 24dB for SIMO.

The difference between the present design approach and past designs is in the usage of the Bragg reflectors. Past designs used the patterns simply to fabricate mirrors by which the optical beams are reflected according to Snell's law. Here we use the engravings to confine and direct the optical beam in the a two dimensional planar structure using Bragg waveguide concepts.

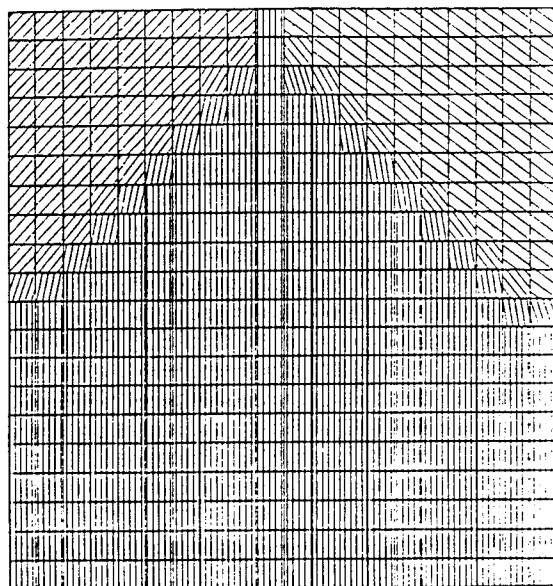


Figure 2. 20x1 interconnection

1. H. Grebel and W. Zhong, Optics Letters, 18, 1123 (1993).

Diffractive Coupling Lenses : Design, Calculation and CAD-Data Generation

Helmut Zarschizky, Otto-Hahn-Ring 6,	Siemens, D-81739 Munich,	Corporate Research and Development, Tel. 49-89-636-44609, FAX: 49-89-636-46426
Albert Stemmer, Hansastraße 27d,	Siemens, D-80686 Munich,	Corporate Research and Development, c/o IFT der Fraunhofergesellschaft, Tel. 49-89-54759092, FAX: 49-89-54759100
Alfons Daiderich, Carl-Wery-Straße 22,	Siemens-Nixdorf, D-81739 Munich,	Computer Aided Engineering, Tel. 49-89-636-48763 FAX: 49-89-636-43939

1. Introduction

The use of diffractive lenses for laser diode to single mode fibre coupling is attractive even for binary on-axis elements. This is due to the excellent imaging properties, the possible mass production using advanced semiconductor technologies and easy handling of the final elements. The possibility to fabricate arrays of lenses with appropriate sizes, shapes and any desired pitch makes diffractive optical solutions superior to bulk miniature optics. The lens patterns may exhibit simple circular fringes but, nevertheless, the feature sizes for practical elements are readily in the submicron range. This is especially true for e.g. off-axis elements which combine functions like deflection and focussing. The first step of the procedure to realise a specific diffractive lens is the design and calculation phase which should be done by a (CAD-) software tool which enables the user to construct the lens under feedback information about the required minimum feature size as well as shape and position of the effective aperture, both facts strongly dependent on the lens substrate.

2. Design

Requirements for coupling set-ups may include mounting tolerances, minimum reflection towards the laser diode, beam shaping and a minimum number of components. Figure 1 gives three examples of possible geometries. Fig.1a is the conventional on-axis geometry, Fig.1b shows a tilted lens for minimum reflection and Fig.1c is an off-axis arrangement which enables an additional shaping of the laser diode beam. The shape of the laser diode beam cross section "X" is assumed to be elliptical, its projection to the surface of the lens substrate "P" may be circular, as illustrated in Figures 1b and 1c.

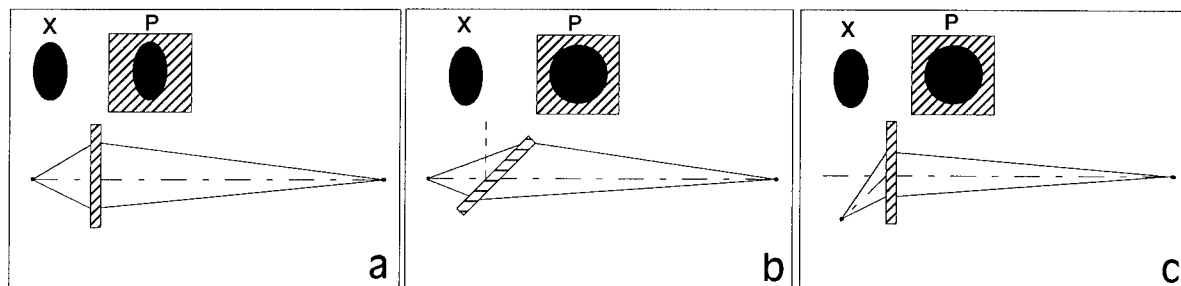


Fig.1: Different Coupling geometries for laser diode-fibre coupling. Laser diode with elliptical beam cross section.

X=perpendicular beam cross section of laser diode, *P*=projection at substrate surface.

a: On-axis-geometry, elliptical beam cross section at substrate surface.

b: On-axis geometry with tilted lens, circular beam cross section at substrate surface.

c: Off-axis-geometry, circular beam cross section at substrate surface.

3. Design and basic data calculation

Basic calculations of the diffraction patterns of the specific lenses are carried out with a development environment, which allows for the investigation of various imaging situations. The principles have already been discussed in [1, 2]. The program is based on a method which gives a sampled intensity pattern of the interference field at the lens plane. The binarisation is done with the help of an intensity histogram, a tracking algorithm produces closed fringes and a final tool gives the desired data output in GDSII-format. The calculations could be time consuming, for example to find the lens pattern for a tilted lens to be realised on a substrate of thickness "d" and refractive index "n", but important results can be derived. Current investigations indicate for example that the fringe patterns of tilted and off-axis lenses with thick substrates are no longer composed of elliptical fringes as is the case for thin lenses. Especially the fringes of the off-center lens region tend to be distorted to egg-shaped patterns.

The knowledge of the fringe shapes belonging to elements of certain geometries finally allows for a much faster pattern calculation as it can be done by the development program. This is due to the fact that one only has to calculate two perpendicular intersections of the basic interference pattern instead of carrying out a complete two-dimensional calculation. The output of such an advanced program is for example a number of data sets (x, y, a, b) describing ellipses of semi-axis a and b, centered around the point (x,y).

4. CAD Data Generation

Programs derived from basic results obtained from the development environment are included in the CAD-program SIGRAPH[®]-Optik [3] in order to establish a professional fast and comfortable tool for the calculation of diffractive lenses. An important feature is the suitable data output, especially the GDSII-Files which can be postprocessed from common lithographic systems. SIGRAPH[®]-Optik was originally a layout editor for integrated optics. It has been extended to calculate diffractive "thin" on-axis- lenses, tilted on-axis-lenses and off-axis-lenses. The consideration of the lens substrate is currently possible for the on-axis case and non-tilted elements, solutions for "thick" tilted and "thick" off-axis lenses are under development.

The calculation of the fringes is rapidly carried out by the calculation of data sets (x, y, a, b) which call the CAD-primitive "ellipse". The elliptical fringes are then generated with a predefined angular accuracy, for example 0.1 degree. The calculation times for thin lenses last about a few seconds, the GDSII-data conversion may last some minutes.

Figures 2a, 2b and 2c give examples for lens patterns calculated with SIGRAPH[®]-Optik. The patterns correspond to the respective situations depicted in Figure 1. Fig.2a shows the pattern of an on-axis lens, which images a light source of 1.3 μm wavelength located in a distance of 300 μm from the lens to an on-axis image point of 3 mm distance. The lens aperture is matched to an elliptical beam cross section. Fig.2b shows the pattern for the same point distances but the lens tilted by an angle of 45 degree. The fringes are now elliptical and the fringe system is decentered. Due to the oblique beam incidence the elliptical beam cross section may be projected to a circular shape as demonstrated. Fig.2c is an example for the off-axis situation of Fig.1c. Depending on the degree of the off-axis geometry the lens center will be shifted outside of the aperture and the fringes may turn from circular to elliptical shape.

During lens parameter calculation and pattern construction SIGRAPH[®]-Optik first generates closed fringes and in a second step makes use of a clipping routine to achieve the desired lens aperture. This clipping routine is important if arrays with very densely packed lenses are of interest. Figure 3 shows two examples of such arrays. The one-dimensional array in the upper row might serve for laser diode array to fibre array coupling. The apertures fit to the laser beam cross section of the single laser diodes of the array allowing maximum capture of the light but minimum cross talk between the neighbouring channels. The square elements of the bottom row might serve for applications where also maximum light capture is required but cross talk is of little interest.

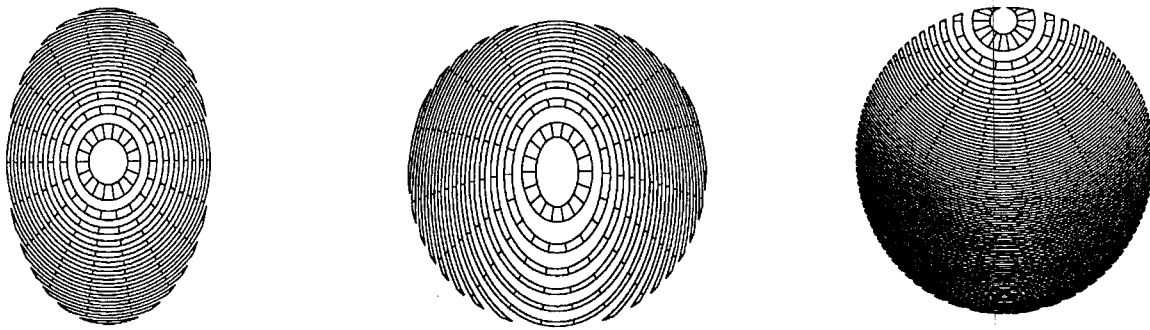


Fig.2: Examples of diffraction patterns and aperture shapes according to the geometries of figures 1a, 1b and 1c, respectively. Calculation are carried out with the CAD-program.
 a) Thin binary on-axis lens with elliptical aperture.
 b) Thin tilted binary on-axis lens with circular aperture.
 c) Thin binary off-axis lens with circular aperture.

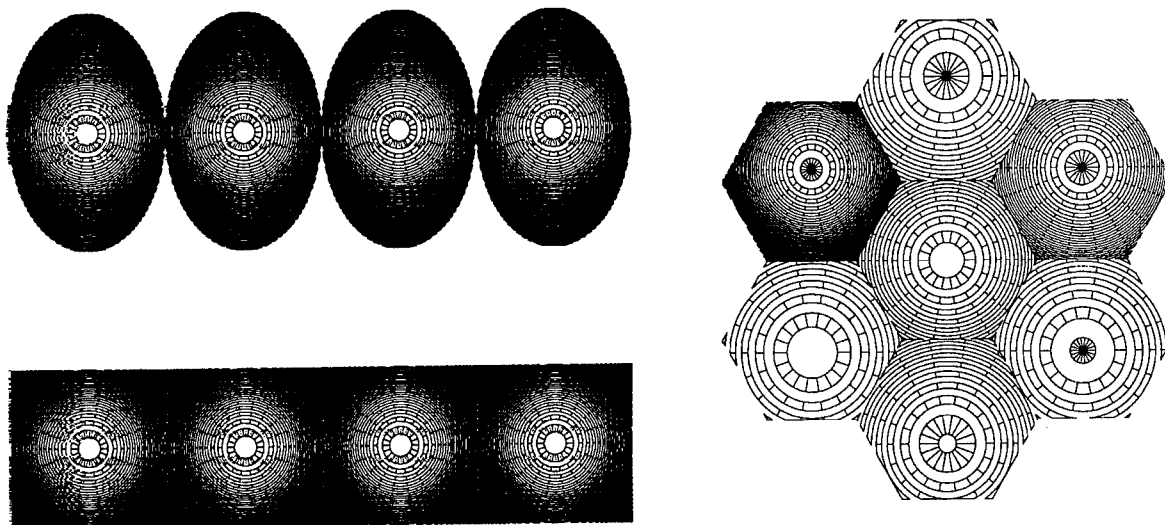


Fig.3: Binary 1-D-lens arrays with different apertures. Pitch is $200\text{ }\mu\text{m}$, focal lengths are $270\text{ }\mu\text{m}$. Ellipses have semi-axes of $200\text{ }\mu\text{m}$ and $300\text{ }\mu\text{m}$, respectively. Size of apertures is $200\text{ }\mu\text{m}$ square

Fig.4: Binary 2-D-lens array composed of hexagonal facets of $100\text{ }\mu\text{m}$ side length. Each facet contains a distinct diffractive lens with a certain focal length

SIGGRAPH[®]-Optik offers another interesting tool for the generation of two-dimensional lens arrays. Up to 63 different lenses can be generated and stored in different layers of the CAD-system. Then a rectangular or hexagonal mesh can be superposed onto the used layers and the mesh facets may be filled with parts of the different single lenses. Fig.4 gives an example of a hexagonal two-dimensional lens array with 7 lenses combined to build a multifocal element.

The lenses discussed so far are of binary type, requiring only one mask for the lithography step resulting in a binary surface profile after fabrication. Binary optical elements, however, suffer from a low diffraction efficiency of 40% at maximum. Higher efficiencies require more sophisticated profiles of the diffraction pattern. Figure 5 gives a schematic of typical profiles. The bottom figure corresponds to a interferometrically recorded element (bleached hologram), then the binary (2-level), the quaternary (4-level), the octernary (8-level) as well as the micro-FRESNEL-lens and the miniature bulk lens are depicted together with their maximum theoretical diffraction efficiencies.

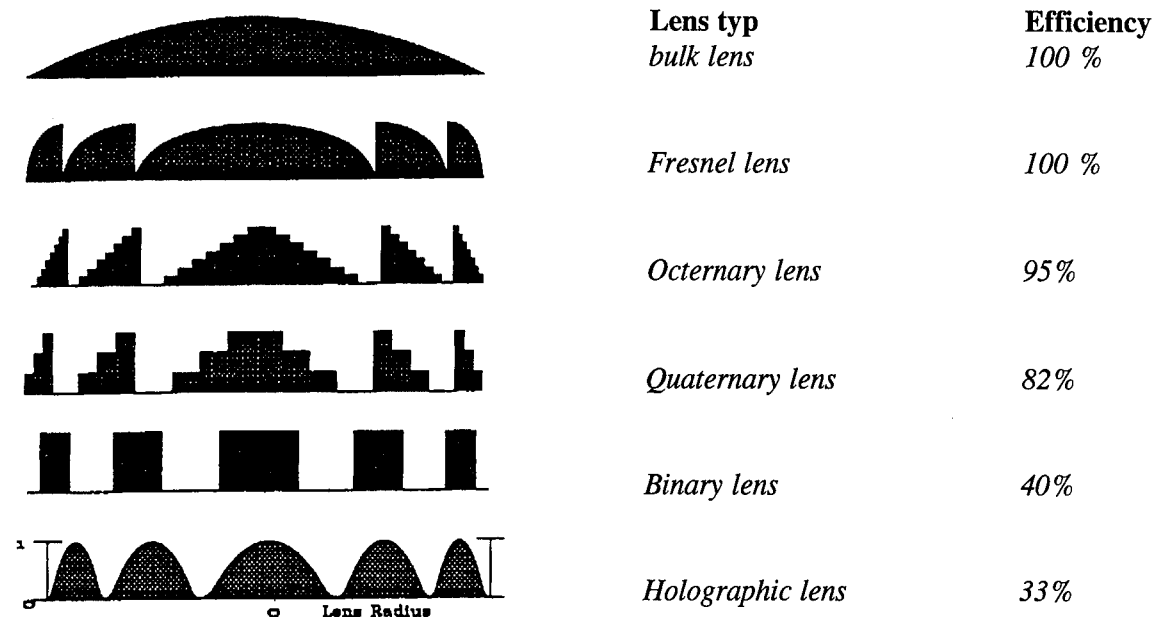


Fig.5: Cross sections of possible phase profiles of synthetic lenses. The continuous profile at the bottom corresponds to a holographically recorded lens of 30 μm diameter. The binary and multilevel profiles correspond to synthetic elements which require one, two or three masks. The maximum theoretical diffraction efficiencies are listed next to the respective profile.

The realisation of the quaternary or the octernary lens requires a two-layer or a 3-layer lens pattern data file, respectively. In case of direct E-beam lithography the layer data can be converted for direct write data for resist profiling [4], in case of photolithography a set of two or three masks has to be produced from the respective GDSII-files. SIGRAPH[®]-Optik allows the generation of multilevel elements from the data originally generated for the basic binary fringes. The higher lens levels may be generated optionally by linear ramp approximation, as is indicated in Fig.5 or by an approximation of spherical curvatures.

4. References

- [1] H.Zarschizky, Ch.Gerndt, A.Stemmer, H.W.Schneider, "A Multifacet Diffractive Mirror for Optical Clock Signal Distribution", SPIE vol.1732, Londonm (1992), 297-306.
- [2] A.Stemmer, H.Zarschizky, F.Mayerhofer, G.Lefranc, H.W.Schneider, P.Galloway, "Design and Fabrication of Synthetic Lenses in Silicon", SPIE vol.1732, London (1992), 77-88.
- [3] A.Daiderich, G.Perrone, "New Programs help the Waveguide Design Team", Opto & Laser Europe OLE, July 1993.
- [4] A.Stemmer, H.Zarschizky, F.Mayerhofer, G.Lefranc, W.Gramann, "Diffractive Coupling Optics: Fabrication and Measurements of Silicon Elements", Rochester (1994), this issue.

Diffractive optical elements for laser and fiber mode selection

V.A. Soifer, M.A. Golub, V.S. Pavelyev

Image Processing Systems Institute, Molodogvardejskaya 151, Samara 443001, Russia

Tel. 7(8462)351826 Fax. 7(8462)322763

Diffractive optics and the digital holography give the opportunity to generate rather complicated optical elements that are not simple substitutes for conventional refractive lenses. This paper is dedicated to *modans*- novel diffractive optical elements for laser and fiber optics, that are matched to coherent modes. Special attention is paid to the generalized methods for diffractive coding of complex transfer function to the phase-only one.

Each wave-field in fiberoptic waveguide can be treated as containing the composition of orthogonal base-functions called modes. Representation of wave-fields by modes is adequate to physical nature of fibers and laser cavities but the practical problem of selective mode excitation seems to be very severe. It is suggested here to reconstruct modes from special holograms. The problem arises of where to find the mode-type object for hologram recording. The solution presented uses mathematical formulae of modes instead of real objects in computer generation of holograms.

The task is the development of "multibeam" optical element, which splits illuminating light beam into L branches and allows parallel and selective excitation of required modes in each branch. We choose angular separation of the branches. Thus the beam $t(\mathbf{x})$ reconstructed by modan must contain partial beams superimposed with proper tilts. The function $t(\mathbf{x})$ appears to be complex-valued. Modan's transfer function $t(\mathbf{x})$ is also complex-valued and must be coded into phase-only form.

A. Coding-method problem in digital holography

The appropriately synthesized thin holograms have a phase microrelief on the plane substrate. Thus, in terms of digital holography, development of the modan is the development of the phase synthesized hologram.

The problem of recording the complex light field on the phase-only medium is well known in digital holography and reviewed in [1,2,3,4]. "Tandem" optical components [5] as well as "dual-phase" optical components have high energy efficiency, but they imply the use of the complicated two-stage optical systems.

Special coding methods are available in digital holography. The methods are aimed at creating the phase-only holograms providing the required amplitude-and-phase transfer function. A method of kinoform complemented by the special methods for making the amplitude more uniform [3] are powerful tools in phase-only holography. The digital holography methods for introducing a random or deterministic additional phase into the reconstructed image [3] are interesting for intensity-type images but are of no use upon forming the complex(amplitude-phase) object. The most appropriate approach for coding the modans is the diffraction redistribution of a beam energy. Such an approach has found use in the method of detour phase with the binary-phase cells [6], in the method of parity elements [7] and in the Kirk-Jones method as well as in the theory of the phased antenna arrays. We introduce and also substantiate a general method to perform diffractive coding of the complex transfer function into the form of the phase-only function. The foregoing methods of digital holography are shown to be specific cases.

Let us consider a modan as a thin digital hologram on the plane substrate. The orthogonal Cartesian coordinates $\mathbf{x}=(x,y)$, with z -axis perpendicular to \mathbf{x} and with the light aperture defined in the domain G of the \mathbf{x} -variables are introduced.

Let us request the beam $t(\mathbf{x})$ to be reconstructed directly behind the holograms plane upon the illuminating beam $w_0(\mathbf{x})$. Thus, a "mathematical" hologram should perform point-by-point transform of light field with the complex (amplitude-phase) transfer function $T(\mathbf{x})$ proportional to $t(\mathbf{x})/w_0(\mathbf{x})$. Let us denote a coefficient of proportionality as $c\sqrt{E_0/E}$, where

$$E_0 = \int_G |w_0(\mathbf{x})|^2 d^2\mathbf{x}, \quad E = \int_G |t(\mathbf{x})|^2 d^2\mathbf{x}$$

are the total powers of the w - and t -fields, respectively. Thus, required complex transfer is given by the formula

$$T(\mathbf{x}) = c \sqrt{E_0/E} \cdot \frac{t(\mathbf{x})}{w_0(\mathbf{x})}, \quad c^{-1} = \max_{\mathbf{x} \in G} \left| \frac{t(\mathbf{x}) / \sqrt{E}}{w_0(\mathbf{x}) / \sqrt{E_0}} \right| \quad (1)$$

In terms of mathematics, the coding represents the change over from the calculated function of the complex transfer

$$T(\mathbf{x}) = |T(\mathbf{x})| \exp(i\varphi_T(\mathbf{x})), \quad |T(\mathbf{x})| \leq$$

to the "coded" phase-only transfer function

$$\Gamma = \exp(i\varphi) \quad (2)$$

where $\varphi = \varphi(\mathbf{x})$ is the coded phase.

B. Encoding procedures based on modulation theory

The idea of coding from complex to phase-only transfer is allowing some "parity" or auxiliary elements in the reconstructed image. These parity elements correspond to parasite diffraction orders and are indeed separated from the main operating order. They are only redistributing the input beam power and reduce respectively the power of main image.

A formal description of "coded" phase holograms is based on the phase-modulation theory, well known in radio-engineering. Of course, an optical application has peculiarities related with 2-D spatial coordinates present instead of the temporal 1-D variable. For this purpose we choose a spatial carrier function that is some basic phase diffraction grating, or another periodic structure.

One of the cases for spatial carrier structures is a 1-D phase diffraction grating with a period of d_0 and a spatial frequency of $\nu_1 = 1/d_0$. Such a 1-D grating can be sinusoidal, binary-stepped, sawtooth-type or the other type described by a dimensionless function $q_0(t)$ taking values on the $[-0.5, 0.5]$ interval and periodic with the period 1 with respect to the dimensionless variable t . We can call $q_0(t)$ function as groove-shape function. One can simply superimpose two crossed 1-D gratings and obtain 2-D gratings as spatial carriers for coding.

Other special types of 2-D periodic structures are really wide spread in digital holography [1]. They are called "coding cells" and include Lohmann's cells and Ichioka's cells [1]. The cell with the size d_x, d_y will be characterized by the 2-D groove-shape function $q(\mathbf{t}) \equiv q(t_1, t_2)$, $\mathbf{t} = (t_1, t_2)$ with values on the $[-0.5, 0.5]$ interval. The function q is assumed to be periodic with the periods 1 with respect to each of t_1, t_2 variables. One period of the $q(t_1, t_2)$ function on the t_1, t_2 plane occupies the unit square $0 \leq t_1 \leq 1, 0 \leq t_2 \leq 1$ and describes single coding cell.

Maximum height of microrelief in the coding cell also can be modulated by multiplying q by factor a that is slowly varying from cell to cell. Thus $aq(t_1, t_2)$ term will be present in "coded" phase (See Fig. 1).

Furthermore, the cell can be shifted from the regular position by using the function $q(t_1 - \alpha_1, t_2 - \alpha_2)$ where detour parameters $\alpha = (\alpha_1, \alpha_2)$ are modulated and thus slowly varying from cell to cell. The function $q(\mathbf{t})$ and the structure of the cell may depend on some additional parameters designated as τ vector. Window size τ could be considered as an example of additional parameters. The parameters τ can be slowly varying (modulated) within the plane of optical element. We are introducing τ parameters into the function q as $q(\mathbf{t}; \tau)$.

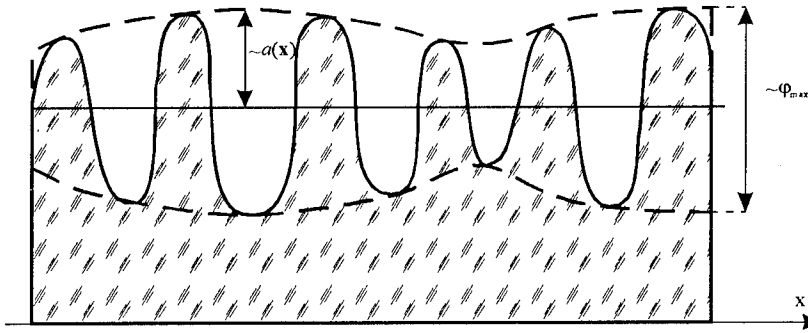


Figure 1 Diffractive coding with maximum-height modulation. $a(x)$ - modulation amplitude, φ_{\max} - maximum phase delay introduced by modulated phase grating

It is clear that the slow variations of any of the parameters listed above change the diffraction conditions and thus result in a beam power redistribution between diffraction orders, that is equivalent to directing light into parity elements. Thus, the main operating diffraction order uses different parts of power from different coding cells. This effect is equivalent to introduction of implicit amplitude transfer by phase-only structure. Such an effect is the core of coding mechanism.

It must be emphasized once more that all modulated parameters must vary slowly so that their spatial featuresize $\Delta x_T, \Delta y_T$ is much more than the period d_0 (or d_x, d_y) of spatial carrier grating.

Let the basic diffraction grating have the carrier spatial frequencies $\hat{S} = [S_{ij}, i = 1, 2; j = 1, 2]$ and the maximum height of the groove equal to φ_{\max} (in terms of the phase delay). The eigenvalues v_{1x}, v_{1y} of the \hat{S} matrix correspond to spatial frequencies that we have with respect to x and y axis. Thus sizes of single coding cell will be $d_x = 1/|v_{1x}|$; $d_y = 1/|v_{1y}|$;

Now we are building some generalization of the Kirk-Jones method [8]. Diffractive optical element has a spatially modulated phase function [2,9] in the form

$$\varphi(\mathbf{u}) = b(\mathbf{x}) + \varphi_{\max} \beta a(\mathbf{x}) q[\hat{S}\mathbf{x} + \alpha(\mathbf{x}); \tau] \quad (3)$$

that corresponds both to the grooves' relative detour the $\alpha(\mathbf{x})$ and to the decrease in the grooves' maximum height by the factor $\beta a(\mathbf{x}) \in [0, 1]$ as compared with the basic grating, where β is a coefficient of the depth of modulation, $\beta \in [0, 1]$, $\alpha_1(\mathbf{x}) \in [0, 1]$, $\alpha_2(\mathbf{x}) \in [0, 1]$, $b(\mathbf{x})$ is a non-modulated component of the phase function that corrects the phase of reconstructed beam. Parameters τ of the q function are also modulated, $\tau = \tau(\mathbf{x})$, if present. Certainly, the functions $b(\mathbf{x})$, $a(\mathbf{x})$, $\alpha(\mathbf{x})$, $\tau(\mathbf{x})$ must be slowly-varying as compared with the basic diffraction grating.

The equation of coding (3) really describes a non-regular phase diffraction grating that becomes a regular one at the special case $b \equiv 0$, $\alpha \equiv 0$ and $a \equiv 1$.

Such a cross-grating modan represents, in effect, a phase hologram of a modal beam that is described by the complex amplitude $t(\mathbf{x})$ in the modal plane and reference beam $w_0(\mathbf{x})$. Note that the phase hologram can be realized in both transmission and reflection variants. It is shown that using suitable selection of the $b(\mathbf{x})$, $\alpha(\mathbf{x})$ and $a(\mathbf{x})$ functions, in Eq.(3), one can ensure the required amplitude-phase transfer T in the \mathbf{n} -th diffraction order ($\mathbf{n} = (n_1, n_2)$ is a 2-D multiplex).

If the following equations are satisfied

$$|B_n[\beta a, \tau]| = g_n |T|, \quad b(\mathbf{x}) + 2\pi \mathbf{n} \alpha(\mathbf{x}) + \arg B_n[\beta a(\mathbf{x}), \tau(\mathbf{x})] = \varphi_T(\mathbf{x}), \quad (4)$$

where

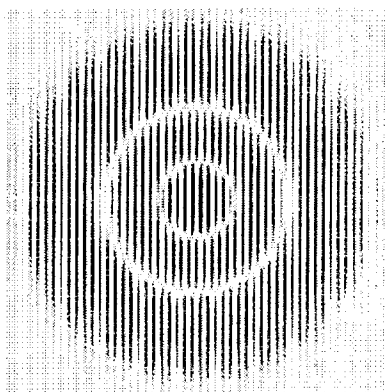
$$g_n = \max_{a \in [0,1]} |B_n[\beta a, \tau]|, \quad B_n(A, \tau) = \int_{-0.5}^{0.5} \int_{-0.5}^{0.5} \exp[i\phi_{\max} A q(\mathbf{t}; \tau) - i2\pi \mathbf{n} \mathbf{t}] d^2 \mathbf{t} \quad (5)$$

then the required amplitude-phase transfer T is available the n -th operating diffraction order in the form including the constant factor g_n and the carrier frequency \mathbf{v}_n :

$$\Gamma_n(\mathbf{x}) = g_n T(\mathbf{x}) \exp(i2\pi \mathbf{v}_n \mathbf{x}), \quad \mathbf{v}_n = \hat{S}^* \mathbf{n} \quad (6)$$

Various special coding methods are suggested.

C. Computer generation of modans.



Gauss-Laguerre modan matched to the mode $(p,l) = (2,0)$ and having the carrier v of 10 lines/mm was generated. A photowriter with a resolution of $25 \mu\text{m}$ was used to generate a mask (see Fig. 2). Six-beam modan also have been generated with the aid of photolithographic technology and tested in experiment. Kirk-Jones-type method of coding was used in both cases. Experimental investigation with He-Ne laser beam have shown good reconstruction of modes from diffractive modan.

Figure 2. Magnified mask for a singlemodal phase modans of Gauss-Laguerre (2,0) mode with the carrier of 10 lines/mm

References

1. Huang T. S., Digital Holography, Proc. IEEE, 59(9), 1335, 1971.
2. Yaroslavskii L. P., Merzlyakov N. S., Methods of digital holography, Plenum Publishing Corporation, New York-London, 1980.
3. Dallas W. J., Computer-generated holograms, in *The computer in Optical Research, Topics in Applied Physics*, vol. 41, Frieden B. R. ed., Springer Verlag, Berlin, 1986, p.291.
4. Wyrowski F., Bryngdahl O., Digital holography as part of diffractive optics. *Reports on Progress in Optics*, 54(12), 1481, 1991.
5. Bartelt H. O., Applications of the tandem component: an element with optimum light efficiency, *Applied Optics*, 24(22), 3811, 1985.
6. Bergeron A., Arsenault H. H., Gauvin J., Gingras D. J. Computer-generated holograms improved by global iterative coding. *Optical Engineering*, 32(9), 2216, 1993.
7. Chu D.C., Goodman J.W., Spectrum shaping with parity sequences, *Applied Optics*, 11(8), 1716, 1972.
8. Kirk J.P., Jones A.L., Phase-only complex-valued spatial filter, *Journ. Opt. Soc. Amer.*, 61(8), 1023, 1971.
9. Adzhalov V.I., Golub M.A., Karpeev S.V., Sisakyan I.N., Soifer V.A., Multi-channel computer optics components matched to mode groups, *Soviet Journal of Quantum Electronics*, 20(2), 136, 1990.

Tuesday, June 7, 1994

Light Propagation and Diffraction

DTuD 4:00pm–5:30pm
Room B

Adolf W. Lohmann, *Presider*
University of Erlangen-Nürnberg, Germany

Space-time duality: diffraction, dispersion, and temporal imaging

Brian H. Kolner

*Electrical Engineering Dept., University of California, Los Angeles
405 Hilgard Avenue, Los Angeles, CA 90024-1594*

Phone: (310) 206-9202 FAX: (310) 206-8495 email: kolner@ee.ucla.edu

The problem of the free-space diffraction or propagation of electromagnetic waves can be cast in a form that is remarkably similar to the problem of pulses propagating in a dielectric medium if certain simplifying assumptions are made. These simplifications are the usual paraxial approximation in the spatial case and the narrowband approximation in the temporal case. The resulting parabolic differential equations admit wave solutions for the envelope profiles and describe the well known phenomena of beams spreading out in space and pulses spreading out in time.

The action of a thin lens can be described by a simple phase transformation where the phase is a quadratic function of the space variables transverse to the direction of propagation. In the time domain, a quadratic phase modulation applied to a pulse performs the same function as a space lens but across the temporal profile of the pulse. Thus, we can consider the quadratic phase modulator as a "time lens." With this in mind, we can imagine that by combining the elements of dispersion, time lens, and more dispersion, we have created the temporal analog of the conventional spatial imaging system composed of diffraction, space lens, and more diffraction. We call such an arrangement a "temporal imaging system."¹ In this talk, I will discuss the theoretical basis for the system, the dualities between its characteristics and those of its spatial counterparts, and suggest some applications ranging from communications to fundamental measurements.

The duality between the equations describing diffraction and dispersion has been known for some time, specifically in the context of nonlinear optics.²⁻⁴ In the linear case, it is most easily arrived at by making a pair of approximations that form a duality in their own right. In the spatial case, we use the paraxial approximation which says, physically, that we concentrate on waves with energy mostly confined adjacent to and in the direction of propagation. In the temporal case, we consider pulses propagating in a dielectric with bandwidth narrow enough so that the dispersion of the dielectric can be adequately accounted for by a Taylor series expansion to second order in the propagation constant β . In the sense that the paraxial approximation deals with spatial Fourier spectra and the limitation thereof, these two simplifications are really the same.

Both the diffraction and dispersion problems describe the evolution of envelope profiles. In the diffraction problem it is the transverse beam profile that we are describing and in the dispersion problem it is the pulse envelope that is of interest. For the diffraction problem, let the beam be described by the z -directed wave

$$\mathbf{E}(x, y, z, t) = E(x, y, z)e^{i(\omega_o t - k(\omega_o)z)}, \quad (1)$$

where $E(x, y, z)$ is a slowly varying envelope function for the transverse beam profile. In the paraxial approximation, the envelope function satisfies the differential equation

$$\frac{\partial E}{\partial z} = -\frac{i}{2k} \left(\frac{\partial^2}{\partial x^2} + \frac{\partial^2}{\partial y^2} \right) E \quad (2)$$

For the dispersion problem, we begin with the same format; an envelope wave equation

$$\mathbf{E}(x, y, z, t) = A(z, t)e^{i(\omega_o t - \beta(\omega_o)z)}, \quad (3)$$

where $A(z, t)$ is a slowly varying envelope function that describes a wave-packet propagating in the z -direction. However, in order to arrive at the desired differential equation, we must make a transformation to a traveling-wave coordinate system moving with the wave-packet. We introduce the following change of variables

$$\begin{aligned} \tau &= (t - t_o) - \left(\frac{z - z_o}{v_g} \right) \\ \xi &= z - z_o, \end{aligned} \quad (4)$$

where t_o and z_o are arbitrary reference points and $v_g = (d\omega/d\beta)$ is the group velocity of the wave-packet. It can then be shown⁵ that the envelope function $A(\xi, \tau)$ satisfies the differential equation

$$\frac{\partial A(\xi, \tau)}{\partial \xi} = \frac{i}{2} \frac{d^2 \beta}{d\omega^2} \frac{\partial^2 A(\xi, \tau)}{\partial \tau^2} \quad (5)$$

which is identical in form to the paraxial wave equation. The general solution to each of these initial value problems is most easily handled in the Fourier domain.⁶ The initial spectrum is multiplied by a phase term quadratic in the Fourier variable and linear in the propagation variable. For the diffraction problem, the solution is

$$E(x, y, z) = \frac{1}{(2\pi)^2} \int \int_{-\infty}^{\infty} \mathcal{E}(k_x, k_y, 0) e^{i(k_x^2 + k_y^2)z/2k} e^{i(k_x x + k_y y)} dk_x dk_y, \quad (6)$$

where $\mathcal{E}(k_x, k_y, 0)$ is the initial spatial Fourier spectrum. For the dispersion problem, the solution is

$$A(\xi, \tau) = \frac{1}{2\pi} \int_{-\infty}^{\infty} \mathcal{A}(0, \omega) e^{-i\frac{\xi}{2} \frac{d^2 \beta}{d\omega^2} \omega^2} e^{i\omega \tau} d\omega. \quad (7)$$

where $\mathcal{A}(0, \omega)$ is the initial temporal Fourier spectrum.

The other necessary element in a temporal imaging system is the time lens. We know that conventional space lenses produce a quadratic phase transformation across the plane transverse to the direction of propagation. In the time domain the phase modulation must be produced across the equivalent to the transverse coordinate which is the local time variable τ . One way to achieve a quadratic phase modulation in the time domain is to use an electro-optic phase modulator driven with a pure sinusoid. If an optical pulse copropagates with any cusp of the sinusoid, it will obtain a quadratic phase modulation over the envelope of the pulse with modulation index proportional to the strength of the modulating field, the interaction length, and the magnitude of the electro-optic coefficient.⁷ Since any cusp of a sinusoid is locally quadratic, the net phase modulation can be described by

$$H_l(\tau) = \exp[-i\Gamma_o] \exp\left[i \frac{\Gamma_o(\omega_m \tau)^2}{2}\right] \quad (8)$$

where Γ_o is the peak phase deviation and ω_m is the frequency at which the modulator is driven. In keeping with the spirit of the space-time duality, we can rewrite (8) grouping the scale factor on the quadratic phase;

$$H_l(\tau) = \exp[-i\Gamma_o] \exp\left[i \frac{\omega_o \tau^2}{2f_T}\right], \quad \Rightarrow \quad f_T = \frac{\omega_o}{\Gamma_o \omega_m^2}, \quad (9)$$

where f_T is the "focal time" of the time lens and serves the same function as that of the focal length of the space lens. We can even go further and define a temporal f -number. Since only a portion of the sinusoidal modulator drive is predominantly quadratic, we can consider the modulator to have a useful time aperture $\tau_a \approx T/2\pi = 1/\omega_m$. We can now define the f -number as the ratio

$$f_T^\# \equiv \frac{f_T}{\tau_a} = \frac{\omega_o}{\Gamma_o \omega_m}. \quad (10)$$

We now have the two essential ingredients for an imaging system; dispersion and a time lens. These are fully equivalent to diffraction and a space lens. To combine these into a useful system we must analyze the combination of dispersion+lens+dispersion and apply a criterion from which we will obtain the specifications for the performance of the elements. Figures 1a and 1b show the arrangements of the elements of both a spatial and a temporal imaging system, while Figure 1c shows the analytical consequences of the system elements in the temporal case. By concatenating the effects in the three domains, we arrive at an integral equation for the output waveform that takes the form⁸

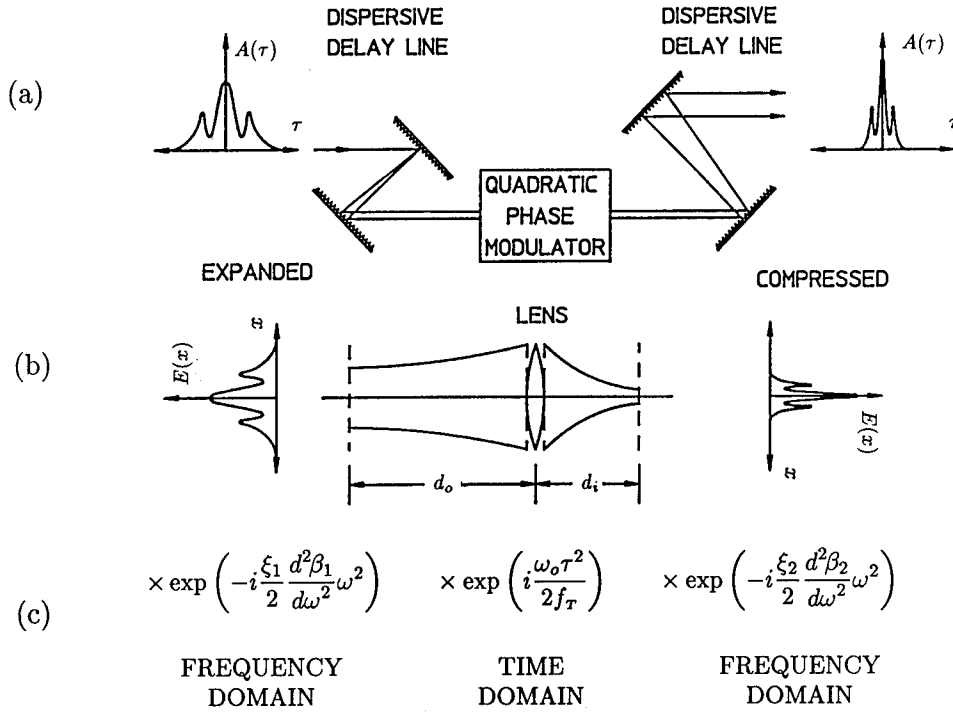


Figure 1. Temporal imaging system as the time domain analog of conventional spatial imaging. a) Temporal imaging system comprised of input dispersion, quadratic phase modulation, and output dispersion. b) Conventional spatial imaging system comprised of input diffraction, lens, and output diffraction. c) Mathematical effects on waveforms in temporal imaging.

$$A(\xi, \tau) \propto \int_{-\infty}^{\infty} A(0, \omega) e^{i\phi\omega^2} e^{i\omega\frac{\tau}{M}} d\omega, \quad (11)$$

where $A(0, \omega)$ is the spectrum of our input waveform $A(0, \tau)$ and ϕ is a function of the input dispersion $\xi_1 d^2\beta_1/\omega^2$, output dispersion $\xi_2 d^2\beta_2/\omega^2$, and the phase modulation represented by the focal time f_T . Equation (11) is an inverse Fourier transform integral. The factor M appears as a scaling on the time variable τ . In order for the output function to be a legitimate "image" of the input function, the quadratic phase term must be unity, or equivalently, $\phi = 0$. Using this as a criterion for imaging results in the expression relating the dispersions and the focal time,

$$\frac{1}{\xi_1 \frac{d^2\beta_1}{d\omega^2}} + \frac{1}{\xi_2 \frac{d^2\beta_2}{d\omega^2}} = -\frac{\omega_o}{f_T}, \quad (12)$$

which is our *temporal imaging condition*. It bears a remarkable resemblance to its spatial counterpart. The minus sign has its origin in the coefficient $-i/2k$ in (2). When (12) is satisfied, the time scale factor M becomes

$$M = -\frac{\xi_2 \frac{d^2\beta_2}{d\omega^2}}{\xi_1 \frac{d^2\beta_1}{d\omega^2}}. \quad (13)$$

which is the *magnification* of the system and also reminds us of the familiar expression $M = -d_i/d_o$ from conventional optics.

All of the expressions presented so far have strong ties with their spatial counterparts, as one would expect from the parallel development of the theory. An additional and very important relationship is that governing the resolution of a temporal imaging system. As one would imagine, the time window or temporal aperture of the time lens sets the resolution. Just as in spatial optics it is the Fourier transform of the aperture function, in suitable coordinates, that gives the impulse response of the system.⁸

The potential applications of temporal imaging systems present some exciting possibilities and some have already been demonstrated. For example, in the ultrafast laser pulse community, we are forever trying to obtain shorter optical pulses. The long standing technique of fiber/grating pulse compression was originally conceived as being accomplished with an electro-optic phase modulator as the chirping source.⁹ The space-time duality suggests that this is equivalent to a lens focusing a beam in space¹⁰ and recently this view has led to active pulse compression with time lenses.^{7,11}

Another important application for temporal imaging will be in the preparation of optimum waveforms on long time scales for subsequent compression to shorter time scales. Since it is not yet feasible to directly modulate optical waveforms on a picosecond or femtosecond scale, these waveforms could be crafted on a long scale with conventional modulators and then demagnified in time to the desired scale for use in laser selective photochemistry, for example.¹²

With optical fiber data links rapidly taking over the telecommunications industry, temporal imaging may prove to be useful as well. The enormous bandwidth of fibers is difficult to exploit by direct modulation with current technology. With a temporal imaging system, data encoded at nominal rates (1-20 GB/s) could be compressed to shorter time scales (20-200 GB/s) and multiplexed onto fibers. At the receiving end, the data could be demultiplexed and detected at the nominal rates. This approach would leverage current optoelectronic technology without requiring dramatic improvements in the performance of lasers, modulators, and detectors.

Still another area where temporal imaging may become important is in high speed signal processing. There has been extensive work done for several decades on the problem of image processing using the Fourier transform properties of lenses. With the space-time duality, one can envisage systems where electromagnetic waveforms are processed using the Fourier transform properties of time lenses. This idea has been investigated theoretically by Lohmann and Mendlovic.¹³

REFERENCES

1. B. H. Kolner and M. Nazarathy, "Temporal imaging with a time lens," *Opt. Lett.*, vol. 14, pp. 630-632, 1989.
2. S. A. Akhmanov, A. S. Chirkin, K. N. Drabovich, A. I. Kovrigin, R. V. Khokhlov, and A. P. Sukhorukov, "Nonstationary nonlinear optical effects and ultrashort light pulse formation," *IEEE J. Quantum Electron.*, vol. QE-4, pp. 598-605, 1968.
3. S. A. Akhmanov, A. P. Sukhorukov, and A. S. Chirkin, "Nonstationary phenomena and space-time analogy in nonlinear optics," *Soviet Phys. JETP*, vol. 28, pp. 748-757, 1969.
4. A. Papoulis, *Systems and Transforms with Applications in Optics*, McGraw-Hill, New York, 1968.
5. H. A. Haus, *Waves and Fields in Optoelectronics*, Prentice-Hall, Englewood Cliffs, NJ, 1984.
6. P. W. Berg and J. L. McGregor, *Elementary Partial Differential Equations*, Holden-Day, San Francisco, CA, 1966.
7. B. H. Kolner, "Active pulse compression using an integrated electro-optic phase modulator," *Appl. Phys. Lett.*, vol. 52, pp. 1122-1124, 1988.
8. B. H. Kolner, "Space-time duality and the theory of temporal imaging," *IEEE J. Quantum Electron.*, to be published.
9. J. A. Giordmaine, M. A. Duguay, and J. W. Hansen, "Compression of optical pulses," *IEEE J. Quantum Electron.*, vol. QE-4, pp. 252-255, 1968.
10. E. B. Treacy, "Optical pulse compression with diffraction gratings," *IEEE J. Quantum Electron.*, vol. QE-5, pp. 454-458, 1969.
11. A. A. Godil, B. A. Auld, and D. M. Bloom, "Time-lens producing 1.9 ps optical pulses," *Appl. Phys. Lett.*, vol. 62, pp. 1047-1049, 1993.
12. W. S. Warren, H. Rabitz, and M. Dahleh, "Coherent control of quantum dynamics: the dream is alive," *Science*, vol. 259, pp. 1581-1589, 1993.
13. A. W. Lohmann and D. Mendlovic, "Temporal filtering with time lenses," *Appl. Opt.*, vol. 31, pp. 6212-6219, 1992.

The Effects of Diffractive Optical Elements on Ultrashort Pulses Analyzed Using the Finite-Difference Time-Domain Method

Diane H. Hochmuth (205) 726-1466
Alan D. Kathman (205) 726-2542
Teledyne Brown Engineering
P.O. Box 070007, MS/200
Huntsville, Alabama 35807-7007
FAX: (205) 726-3735

Eric G. Johnson (205) 722-2774
SY Technology, Inc.
4900 University Square, Suite 8
Huntsville, AL 35816
FAX: (205) 722-9097

Ultrashort pulses are of interest in the area of high-density communications as well as in the study of short-lived electronic and molecular phenomena [1]. Now, as diffractive optics are being used in an ever-increasing number of optical applications, it is important to understand the behavior of ultrashort pulses in systems employing diffractive optics.

As the name implies, the finite-difference time-domain (FDTD) method allows the detailed simulation of time-varying phenomena [2]. Thus, it is ideally suited to modeling ultrashort pulses and other transient effects.

The FDTD method for solving Maxwell's time-dependent curl equations is accurate, computationally efficient, and simple to implement. Since both time and space derivatives are employed, the propagation of an electromagnetic wave can be treated as an initial-value problem. Second-order central-difference approximations are applied to the space and time derivatives of the electric and magnetic fields providing a discretization of the fields in a volume of space, for a period of time [3]. The solution to this system of equations is stepped through time thus simulating the propagation of the incident wave.

In analyzing the dielectric gratings, a mesh is applied only to the area of interest. The size of the mesh is then proportional to the electric size of this region. Doing this, however, imposes an artificial boundary around the calculation area. An absorbing boundary condition must be applied along the artificial boundary so that the outgoing waves are absorbed as if the boundary were absent. Many such boundary conditions have been developed that give near-perfect absorption. In this analysis, the Mür absorbing boundary conditions are employed [4].

Several grating geometries representing various grating periods and depths were analyzed using the FDTD method. Both square and Gaussian pulses on the order of 10^{-14} seconds were used and the results were compared to continuous-wave

scenarios. Figure 1 shows the electric field for a 50 femtosecond square pulse after passing through a dielectric grating with a period of two waves and a depth of one wave. Figure 2 shows the continuous electric field acting on the same grating. Also, in Figure 1 the pulse broadening that occurs can be seen. As a further experiment, a far-field transformation can be applied in order to compare the far-field diffraction patterns.

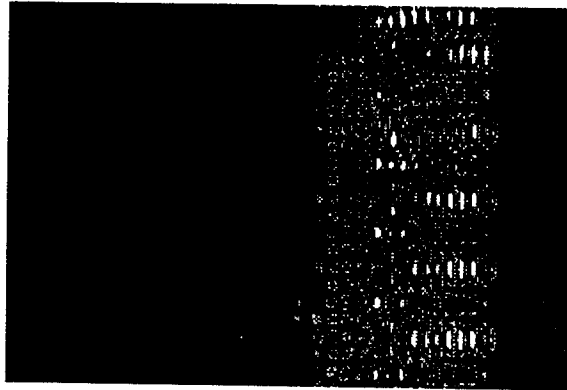


Fig. 1 Electric field of 50 fs pulse after passing through dielectric grating.

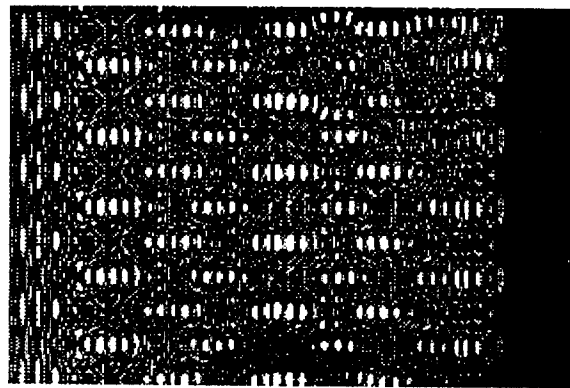


Fig. 2 Electric field of continuous wave after passing through dielectric grating.

References

- [1] A. Yariv, *Optical Electronics*, Third Edition, Holt, Rinehart and Winston, New York, p. 173 (1985).
- [2] K.S. Yee, "Numerical Solution of Initial Boundary Value Problems Involving Maxwell's Equations in Isotropic Media," *IEEE Trans. on Antennas and Propagation*, vol. AP-14, pp. 302-307 (1966).
- [3] A. Taflov and M.E. Brodwin, "Numerical Solution of Steady-State Electromagnetic Scattering Problems Using the Time-Dependent Maxwell's Equations," *IEEE Trans. Microwave Theory Tech.*, vol. MTT-23, pp.623-630 (1975).
- [4] G. Mür, "Absorbing Boundary Conditions for the Finite-Difference Approximation of the Time-Domain Electromagnetic-Field Equations," *IEEE Trans. Electromagn. Compat.*, vol. EMC-23, pp. 377-382 (1981).

White-light optical information processing with achromatic processors

P. Andrés, J. Lancis*, E. Tajahuerce*, V. Climent*, and G. Saavedra

Universidad de Valencia, Departamento de Optica, 46100 Burjassot, Spain.

**Universitat Jaume I, Departamento de Ciencias Experimentales, 12080 Castellón, Spain.*

1. INTRODUCTION

Optical information processing techniques developed with incoherent illumination are becoming more and more common as they do not suffer from the annoying coherent artifact noise associated with coherent processors. In particular, the use of spatially coherent but temporally incoherent illumination allows to employ broadband spectrum sources, such as gas discharge lamps, light emitting diodes, ..., and to deal with color input signals. Nevertheless, the recording of a diffraction pattern of an input object under white-light point-source illumination is chromatic blurred, due to the wavelength dependence of the diffraction phenomenon. Thus, coherent processing systems are not suitable for white-light processing.

One way to overcome this drawback is to develop achromatic processors, which are designed for compensating the chromatic dispersion introduced by the broadband illumination. In this way, a wavelength-independent diffraction pattern results from the incoherent superposition in a single plane, and with the same scale, of its multiple monochromatic versions generated by the different spectral components of the incident light [1]. Some appropriate combinations of diffractive optical elements (DOEs) and refractive achromatic lenses allow to obtain achromatic imaging setups [2], achromatic Fourier transformers [3-5], and achromatic Fresnel diffraction patterns [6,7].

In this contribution, we describe an achromatic Fourier transformer, constituted by two on-axis kinoform zone plates, working under white-light spherical wave illumination. The scale factor of the achromatic Fraunhofer pattern can be varied by moving the input along the optical axis of the system. The residual chromatic aberration is low, even for white-light illumination.

We also discuss, with the same operation principles, an optical configuration for achromatizing a selected Fresnel diffraction pattern of an input signal illuminated by a white-light converging spherical wavefront. The optical device simply consists of a single blazed zone plate, and the axial position of the input allows to select the Fresnel diffraction pattern to be achromatized.

The above achromatic setups are solely constituted with DOEs, and thus they can be used in other ranges of the electromagnetic spectrum, say for instance soft X-rays.

As an application of our achromatic Fourier transformer, we report an achromatic joint transform correlator for color pattern recognition. The use of white-light sources in joint transform correlator (JTC) experiments is sometimes limited due to the chromatic blurring in the recording of the joint Fourier spectrum. However, some white-light JTC have been suggested [8-9]. We claim that our two-zone-plate achromatic Fourier transformer allows the register of the joint power spectrum in an achromatic manner. In a second stage, the correlation signal is obtained by performing a conventional Fourier transformation of the above achromatic intensity pattern. A high-intensity correlation peak is obtained for signals with identical chromatic distribution and identical shape.

As an example of a polychromatic optical information processing operation working in the Fresnel region, we use our achromatic Fresnel transformer for implementing white-light array illuminators. Microlens arrays have been widely used to implement array illuminators, i.e., for implementing a device which transform a wavefront into a 2-D array of bright spots of uniform intensity. Optical array generators based on the Talbot effect have also been proposed [10-12]. The property of a glass lens array to generate a set of replicas of the focal intensity distribution along the optical axis of the system, with different multiplicity, has recently been used to design a versatile monochromatic array illuminator [13].

Here, the chromatic blurring of the above Fresnel diffraction patterns, under white-light illumination, is compensated by using our achromatic Fresnel transformer. Thus, we obtain a flexible optical array illuminator with variable density of bright white-light spots at the output plane. Finally, we have recognized that these ideas can also be applied to design a white-light array illuminator based on a 2-D zone plate array.

Experimental results for our different proposals will be shown.

2. SCALE-TUNABLE ACHROMATIC FOURIER TRANSFORMER

The achromatic Fourier transformer we propose is depicted in Fig.1. The input transparency is illuminated by a broadband spherical wavefront beam converging towards the point source S placed at a normal distance z beyond the aperture. ZP_1 and ZP_2 are two zone plates, with image focal lengths Z_0 and Z'_0 , for a reference wave number σ_0 , respectively, and ZP_2 is inserted at the virtual source plane. This optical system provides, in a first-order approximation, the achromatic Fraunhofer diffraction pattern of the input signal if the separation, d , between the zone plates is

$$d = \sqrt{\alpha} Z_0 \quad (1)$$

where $\alpha = |Z'_0/Z_0|$. In this way, the first-order achromatic Fourier transform of the input is obtained at a distance D'_0 such that

$$D'_0 = \frac{\alpha}{\sqrt{\alpha} - 2} Z_0 \quad (2)$$

To obtain a real achromatic Fourier transform, i.e. $D'_0 > 0$, ZP_1 and ZP_2 should be a diverging and a converging zone plate, respectively, and α must satisfy the inequality $0 < \alpha < 4$.

Since we develop a first-order theory, the setup suffers from residual chromatic aberrations. In fact, for each σ , the Fraunhofer pattern is achieved at a distance, $D'(\sigma)$, from ZP_2 such that

$$D'(\sigma) = \frac{D'_0}{1 + \frac{1}{2 - \sqrt{\alpha}} \frac{(\sigma - \sigma_0)^2}{\sigma \sigma_0}} \quad (3)$$

and the scaling factor is given by

$$\frac{x}{u} = \frac{y}{v} = \frac{z D'(\sigma)}{\sigma_0 \alpha Z_0} \quad (4)$$

where x and y are Cartesian coordinates and u and v spatial frequencies. It is possible to show that both the axial and the lateral chromatic aberrations, expressed as a percentage, and referred to the plane D'_0 , have an identical analytical expression. For $\sigma_0 = \sqrt{\sigma_1 \sigma_2}$, being σ_1 and σ_2 the end wave numbers of the incoming radiation, the greatest value of the chromatic aberration CA_M is

$$CA_M = \frac{100}{1 + \beta(2 - \sqrt{\alpha})} \quad (5)$$

where $\beta = \sqrt{\sigma_1 \sigma_2} / (\sqrt{\sigma_1} - \sqrt{\sigma_2})^2$.

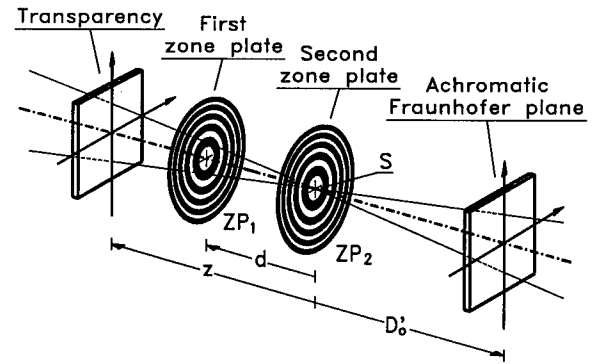


Figure 1.

From Eqs.(4) and (5) we conclude that the scale factor is proportional to z , and therefore can be varied by simply changing the position of the input along the optical axis, but CA_M only depends on the value of α . It appears that α less than 1 is enough to achieve a chromatic error less than 5% even with white light.

3. VARIABLE ACHROMATIC FRESNEL DIFFRACTION PATTERN

Let a black-and-white input transparency be illuminated by a polychromatic point source S , located at a normal distance z . It is straightforward to demonstrate that the different wavelengths produce diffraction patterns identical in form but different in location and size. Thus, the Fresnel diffraction pattern located, under monochromatic parallel illumination with wave number σ_0 , at a distance R_0 from the diffracting aperture, now appears both axially and laterally chromatic dispersed. It is possible to show that a blazed zone plate, ZP , inserted at the source plane (something that implies converging spherical wave illumination; i.e. $z < 0$), is able to recombine all of the monochromatic versions of the above diffraction pattern, in a first-order approximation, in a single picture, if the following constraint is fulfilled

$$z = \frac{-1}{\sqrt{\alpha}} Z_0 \quad (6)$$

where Z_0 represents the focal distance, for the wave number σ_0 , of ZP and now the dimensionless parameter α is defined as

$$\alpha = Z_0 / |R_0| \quad (7)$$

The first-order achromatic diffraction pattern is obtained at a distance D'_0 from ZP such that

$$D'_0 = \frac{1}{2 - \sqrt{\alpha}} Z_0 \quad (8)$$

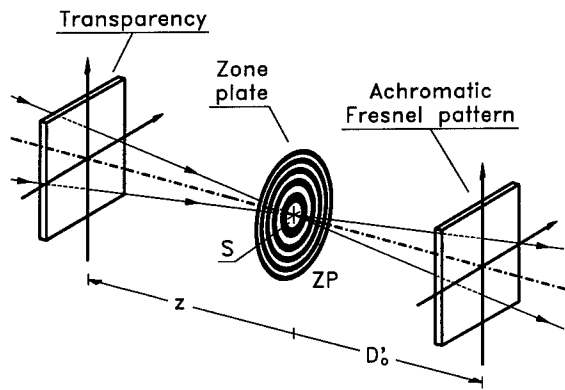


Figure 2.

The outline of our suggested setup is shown in Fig.2. In order to obtain a real achromatic Fresnel diffraction pattern, from Eq.(8) we infer that we are only able to achromatize virtual Fresnel diffraction patterns such that $R_0 < z/2$ and, then, from Eq.(6), ZP must be converging ($Z_0 > 0$).

Since we develop a first-order theory, a partially achromatic version of the selected diffraction field is achieved. It is possible to show that, with the definition of α given by Eq.(7), Eq.(5) hold for the present case.

Once a zone plate is chosen to build the transformer, a change in the value of α is equivalent to select a different pattern R_0 to be achromatized. Thus, Eq.(6) states that our optical setup achromatizes a single, but different, diffraction pattern R_0 by changing the position of the input along the optical axis. Eq.(8) and (5) provides the axial location of the achromatic pattern and the maximum value of its chromatic error, respectively.

4. ACHROMATIC JOINT-TRANSFORM CORRELATOR

Consider the JTC shown in Fig.3, in which the upper part is the optical setup for recording the achromatic joint Fourier spectrum. Both the test scene and the reference pattern are colored signals with amplitude transmittance, for the wave number σ , $f(x,y;\sigma)$ and $g(x,y;\sigma)$, respectively. A polychromatic, converging spherical wavefront beam illuminates the input plane with amplitude transmittance $t(x,y;\sigma) = f(x+x_0,y;\sigma) + g(x-x_0,y;\sigma)$, for the wave number σ .

The achromatic Fourier transformer depicted in the upper part of Fig.3 is constructed following the prescriptions in Section 2. In this way, we obtain a real representation of the Fraunhofer diffraction pattern of all $t(x,y;\sigma)$, in an achromatic

manner. Thus, the irradiance distribution, $I(x,y)$, at the achromatic Fraunhofer plane is

$$I(x,y) = \int_{\sigma_1}^{\sigma_2} |\tilde{t}(Ax,Ay;\sigma)|^2 S(\sigma) d\sigma, \quad (9)$$

where \tilde{t} denotes the Fourier transform of t , $S(\sigma)$ represents the source spectral distribution, and the scale factor A is such that $A = -(2 - \sqrt{\alpha})\sigma_0/z$.

In particular, if we deal with two objects with the same shape and chromatic distribution, i. e. $f(x,y;\sigma) = g(x,y;\sigma)$ for all σ , $I(x,y)$, consists of a set of modulated interference fringes with approximately the same spatial period for each σ .

In a second stage, the achromatic joint power spectrum recorded onto a black-and-white CCD camera is sent to a liquid crystal TV (LCTV). The LCTV is illuminated with a parallel monochromatic light beam, with wave number σ_R . A second Fourier transformation is achieved by using a conventional lens, of focal length f , for obtaining the correlation peak at the back focal plane, as is shown in the lower part of Fig.3.

It is straightforward to show that for each σ we obtain, at the output plane, the cross-correlation of $f(xB,yB;\sigma)$ with $g(xB,yB;\sigma)$ centered around the points $(\pm 2x_0/B, 0)$, where $B = \sigma_R/Af$. We recognize that both the position and the scale factor of the cross-correlation function are σ -independent. Moreover, if we deal with a test scene and a ref-

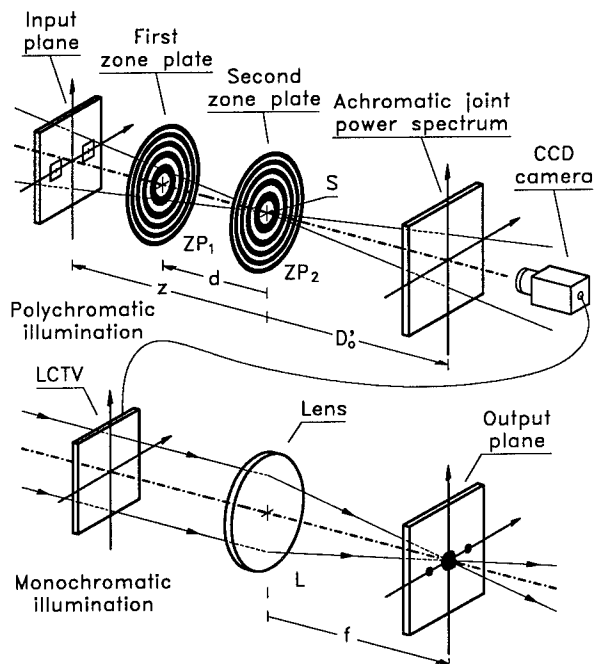


Figure 3.

erence object with the same shape and chromatic composition, then each monochrome cross-correlation becomes an autocorrelation. In this case an off-axis high correlation peak is achieved.

5. ACHROMATIC WHITE-LIGHT TALBOT ARRAY ILLUMINATOR

Let us consider an input object formed by a unit cell repeated periodically in two orthogonal directions illuminated by a parallel monochromatic beam. It is possible to show that a set of periodic patterns in which the unit cell remains undisturbed, but the array function has a reduced period compared to the original, are obtained along the optical axis of the system. These Fresnel diffraction patterns are known as Fresnel images. The reduction factor of a Fresnel image is defined as the ratio of the period of the original periodic structure to that of the Fresnel image.

Following Ref.[13], we recognize that the amplitude distribution at the back focal plane of a 2-D square periodic lenslet array illuminated by a monochromatic plane wave of wave number σ_0 is also periodic and, thus, provides Fresnel images. It is apparent that the above Fresnel pattern and its Fresnel images are in turn pinhole arrays.

The Fresnel images are obtained at distances R_0 from the focal plane given by

$$R_0 = 2 p^2 \sigma_0 \left(Q + \frac{N}{M} \right), \quad (10)$$

where p is the period of the lenslet array, Q is an integer, and M and N ($N < M$) are natural numbers with no common factor. The reduction factor r is equal to M when M is odd, or $M/2$ when M is even.

Under polychromatic illumination, it is clear that the above patterns appears chromatic dispersed along the optical axis. Next, we claim that the achromatic Fresnel transformer depicted in Fig.2 can be used to achromatize a selected Fresnel image. The proposed optical architecture is shown in Fig.4. The system is built following the prescriptions of Eq.(6) and, thus, the lenslet array must be placed, approximately, at a distance h from the zone plate given by

$$h \approx -f - \frac{1}{\sqrt{\alpha}} Z_0, \quad (11)$$

where f is the focal length of the individual microlenses of the array and Z_0 is the focal length of the zone plate for the wave number σ_0 .

In this way we obtain at the output plane an array of bright white light spots. The period p' for

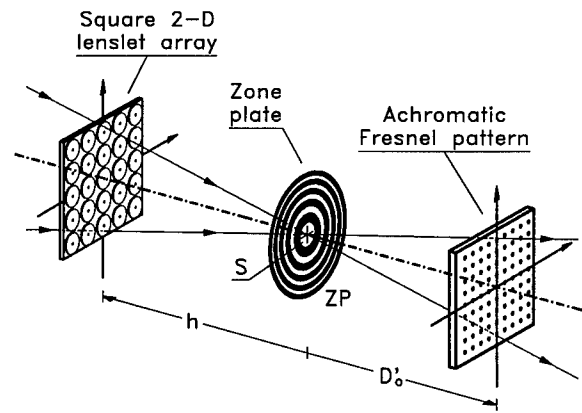


Figure 4

the achromatic white-light array illuminator results, in a first-order approximation

$$p' = \frac{D_0' p}{h + f r} \quad (12)$$

where D_0' is given by Eq.(8). Note that p' can be modified by selecting different Fresnel images.

We want to point out that the achromatic Fresnel transformer in Section 3 can also be applied to achromatize the amplitude distribution at the back focal plane of a diffractive 2-D zone plate array under white-light illumination. In this case, the value of α is given by Eq.(7), where R_0 stands for the focal length for σ_0 of an individual zone plate of the array.

6. REFERENCES

- [1] J.L. Horner, *Optical Signal Processing* (Academic Press, New York, 1987), Ch. 1.2.
- [2] D. Faklis and G.M. Morris, *Opt. Eng.* **28**, 592 (1989).
- [3] R.H. Katyl, *Appl. Opt.* **11**, 1255 (1972).
- [4] G.M. Morris, *Appl. Opt.* **20**, 2017 (1981).
- [5] P. Andrés, J. Lancis, and W.D. Furlan, *Appl. Opt.* **31**, 4682 (1992).
- [6] R.H. Katyl, *Appl. Opt.* **11**, 1248 (1972).
- [7] P. Andrés, J. Lancis, and E.E. Sicre, *Opt. Commun.* **104**, 39 (1993).
- [8] F.T.S. Yu and Y.S. Cheng, *Opt. Lett.* **15**, 192 (1990).
- [9] Y.S. Cheng, *Opt. Commun.* **99**, 252 (1993).
- [10] A.W. Lohmann and J.A. Thomas, *Appl. Opt.* **29**, 4337 (1990).
- [11] J.R. Leger and G.J. Swanson, *Opt. Lett.* **15**, 288 (1990).
- [12] A.W. Lohmann, *Opt. Commun.* **89**, 167 (1992).
- [13] E. Bonet, P. Andrés, J.C. Barreiro, and A. Pons, *Opt. Commun.* (accepted).

Partially Coherently Illuminated Uniform-Intensity Holographic Axicons

Ari T. Friberg and Sergei Yu. Popov

Department of Technical Physics, Helsinki University of Technology, FIN-02150 Espoo, Finland

tel: 358 - 0451 3150 fax: 358 - 0451 3164

1. INTRODUCTION

Recently there has been considerable interest in holographic axicons that produce a focal line image of uniform axial intensity and of narrow transverse width over a given extended region [1–5]. The phase transmittance function of this generalized axicon or axilens, for fully coherent illumination of radially symmetric intensity, was derived on the basis of holographic ray tracing and the geometric law of energy conservation [4] (see also [2,3]). Within the paraxial approximation the result is a logarithmic function, in contrast to the linear phase function of an ordinary axicon leading to a linear growth of the on-axis intensity. The derivation ignores the effects of diffraction and interference on propagation. Numerical calculations indeed indicated large on-axis intensity oscillations and increased spot size near the paraxial focus [5a]. The latter problem could be remedied by suitable annular aperture [5b], whereas the axial oscillations were smoothed by apodization [5c] in analogy with the technique applied previously to non-diffracting beams [6,7].

The axial intensity oscillations arise from interference, and therefore it is natural to expect that the fluctuations could be substantially diminished if the incident radiation had a reduced degree of coherence. Such a situation raises, however, a new and fundamental question concerning the operation of holographic axicons, and of diffractive optical components in general, under partially coherent illumination. This problem is much akin to the focusing of partially coherent light which is known to differ from that of coherent or incoherent light [8]. The assessment of optimized diffractive elements in controlled-coherence radiation is becoming increasingly important since many practical sources, including diode and multimode solid-state lasers, emit well-characterized spatially partially coherent beams [9].

In this paper we analyze partially coherently illuminated uniform-intensity holographic axicons within the space-frequency representation of coherence theory. After a theoretical formulation of the problem, the on-axis intensity in varying states of spatial coherence is evaluated numerically for apodized annular logarithmic axicons (off-axis intensity requires e.g. spline techniques). Both the axial and transverse intensity distributions are further examined in the asymptotic sense as the wavelength becomes short. The analyses lead to several new results on the design and performance of partially coherent diffractive elements.

2. THEORETICAL FORMULATION

We consider a holographic axicon at $z = 0$ represented by a phase transmission function $\exp[ik\varphi(\rho)]$, where k is the wavenumber and ρ is a transverse variable. Optimally, the phase $\varphi(\rho)$ is calculated so as to produce a uniform concentration of light between d_1 and d_2 on the z -axis (Fig. 1). Each realization of the ensemble characterizing the stationary incident wavefield is subjected to the axicon transmission function and so the combined effect, expressed by the cross-spectral density of the focused light, is obtained by statistical averaging [10]. If the dimensions of the effective coherence area exceed several wavelengths and if the phase of the cross-spectral density is sufficiently planar, the field can be expected to locally obey geometric optics (as evidenced e.g. by refraction of thermal

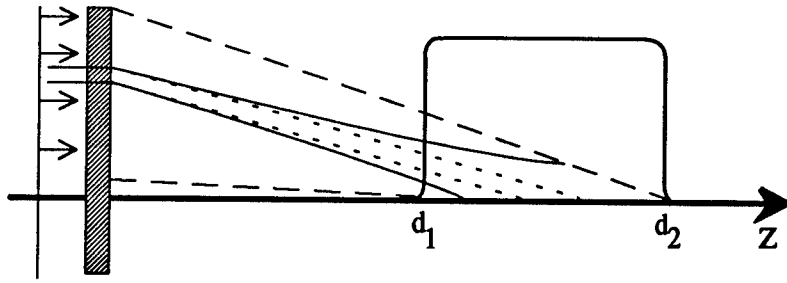


Figure 1: Line-focusing geometry and illustration of diffractive spreading.

light). Hence in this work we use the phase functions calculated previously for uniform coherent waves [4,5]. We emphasize, though, that this is an approximation that demands further study. In particular, our analysis suggests that this approach fails to account for the partial interference and increased diffractive spreading caused by the reduced coherence (Figs. 1 and 2).

Taking an incident cross-spectral density of the Schell-model form [11] with an exponential degree of coherence of rms width σ_g , and using the polar coordinates for integration, the optical intensity at point (ρ, z) behind the axicon in the paraxial approximation is expressible as

$$I(\rho, z) = (k/2\pi z)^2 \iint [I_a(\rho_1)I_a(\rho_2)]^{1/2} C(\rho_1, \rho_2; \rho, z; \sigma_g) \exp[-(\rho_1^2 + \rho_2^2)/2\sigma_g^2] \\ \times \exp[-ik(\rho_1^2 - \rho_2^2)/2z] \exp\{-ik[\varphi(\rho_1) - \varphi(\rho_2)]\} \rho_1 \rho_2 d\rho_1 d\rho_2, \quad (1)$$

where

$$C(\rho_1, \rho_2; \rho, z; \sigma_g) = \iint \exp[\rho_1 \rho_2 \cos(\theta_1 - \theta_2)/\sigma_g^2] \exp[-ik\rho(\rho_1 \cos \theta_1 - \rho_2 \cos \theta_2)/z] d\theta_1 d\theta_2 \quad (2)$$

and $I_a(\rho)$ is a radially symmetric input intensity. We note that the transverse variable ρ appears only in the factor C and that on-axis ($\rho = 0$) Eq. (2) readily yields

$$C(\rho_1, \rho_2; 0, z; \sigma_g) = (2\pi)^2 I_0(\rho_1 \rho_2 / \sigma_g^2), \quad (3)$$

where I_0 is the modified Bessel function. When $\sigma_g = \infty$, Eqs. (1) and (2) are seen to factor and to reduce to the usual fully coherent result [5]. It is also obvious that any axicon apodization can be replaced by appropriate incident-intensity variation.

3. NUMERICAL AND STATIONARY-PHASE RESULTS

With a uniform illuminating wavefield, the transmission phase function of the so-called (forward) annular-aperture logarithmic axicon is (for $r < \rho < R$) [5]

$$\varphi(\rho) = -(2a)^{-1} \log[d_1 + a(\rho^2 - r^2)], \quad (4)$$

where $a = (d_2 - d_1)/(R^2 - r^2)$ and R and r are the outer and inner aperture radii, respectively. Optimally the meridional rays from the aperture's two edges are parallel and so $r = (d_1/d_2)R$. For ease of comparison, we consider first numerically a line focusing situation analogous to that presented in [5]. We take $d_1 = 100$ mm, $d_2 = 200$ mm, $r = 2.5$ mm, and $R = 5.0$ mm. Geometrically

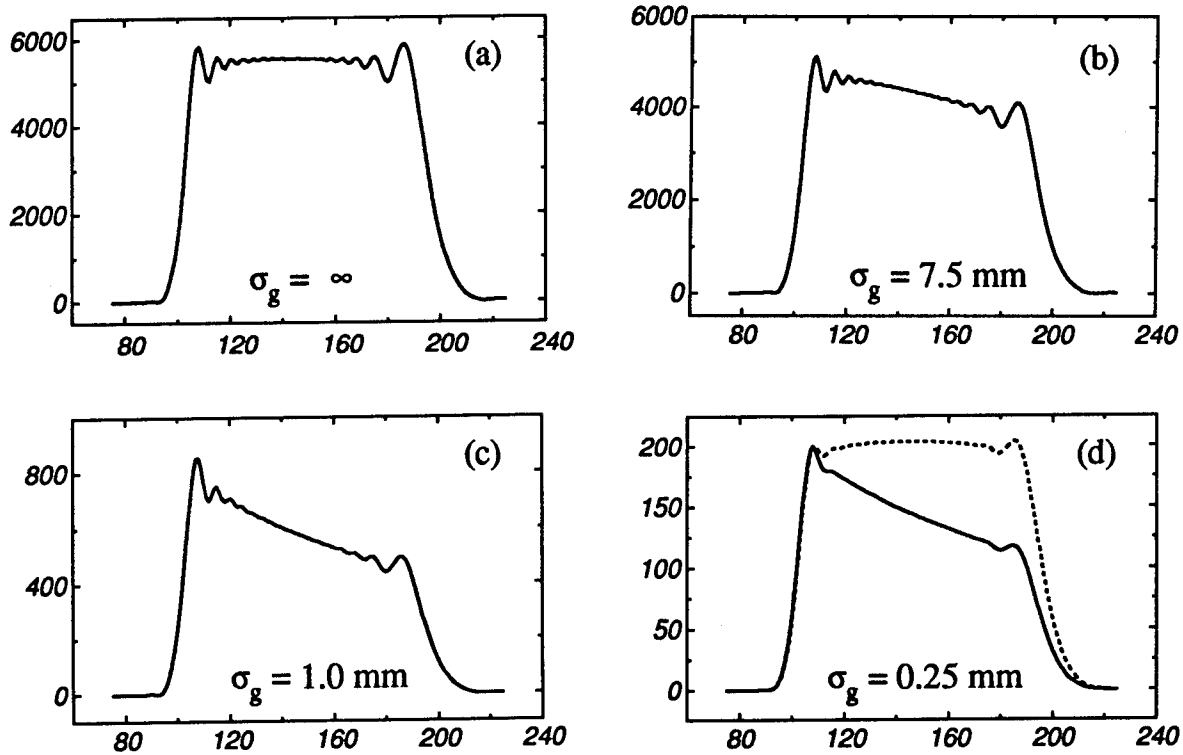


Figure 2: Axial intensity curves produced by illuminations of different degrees of coherence.

the phase (4) corresponds to an axial ‘ray density’ of $z(\rho) = d_1 + a(\rho^2 - r^2)$ and this must be taken into account in apodization, but for simplicity we employ here a weakly truncated (at 1.5 mm and 6 mm) intensity of the form $\{0.5 + \arctan[20(\rho - r)]/\pi\}\{0.5 + \arctan[20(R - \rho)]/\pi\}$. Hence the fully coherent plot in Fig. 2a shows a slight asymmetry. The ripples (compare with Fig. 2 in [5c]) arise because of the steep apodization edges.

The shapes of the partially coherent plots in Figs. 2b–d clearly indicate that the axicon functions in partially coherent light. The overall intensity level drops as the coherence length decreases since rays from the opposite sides of the aperture increasingly add incoherently. In Figs. 2b and 2c the field is still locally sufficiently coherent so as to produce oscillations near the edges. The intensity slope within the focal range is also partly attributed to the diffractive loss of ‘ray strength’, but yet other effects may contribute. A substantially incoherent (1D) Gaussian Schell-model beam of waist intensity and coherence widths σ_I and σ_g decays on far-field axis as $\sim k\sigma_I\sigma_g/z$ [11]. Applying the ray density, the superposition and propagation loss can be compensated by the incident intensity at the holographic axicon. A preliminary numerical result generated through such a radially linear compensation is shown by the dashed line in Fig. 2d.

At optical wavelengths it is convenient to evaluate Eqs. (1) and (2) by the method of stationary phase [12]. Customarily it is taken for granted that the stationary-phase result corresponds to geometrical optics — and we show that to a degree it indeed does — but even the leading contribution carries information about diffraction and interference.

Since (after integration) the factor C is expected not to contain exponential phases proportional to k , consecutive asymptotic evaluation in ρ_1 and ρ_2 can be performed directly in Eq. (1). In both cases the critical points (of the first kind) are $\rho_c = [r^2 + (z - d_1)/a]^{1/2}$, which corresponds to the

mapping mediated by geometrical rays. No stationary point exists inside the annular aperture if $z < d_1$ or $z > d_2$. For points (ρ, z) located within this (geometrical-optics) focal range the leading asymptotic contribution is

$$I(\rho, z)_{\text{sp}} \sim (k/4\pi a) I_a(\rho_c) C(\rho_c, \rho_c; \rho, z; \sigma_g) \exp(-\rho_c^2/\sigma_g^2), \quad (5)$$

where $C(\rho_c, \rho_c; \rho, z; \sigma_g)$ is obtained from Eq. (2). The axial variation of the intensity comes from the stationary point in $I_a(\rho_c) I_0(\rho_c^2/\sigma_g^2) \exp(-\rho_c^2/\sigma_g^2)$, suggesting an exact (asymptotic) method for intensity compensation. The fully coherent limit corresponds evidently to the purely geometric axially constant result. For a unit-intensity He-Ne illumination Eqs. (3) and (5) lead to a numerical value of $I(0, z)_{\text{sp}} \approx 5850$, in excellent agreement with Fig. 2a.

For arbitrary σ_g the transverse variation $C(\rho_c, \rho_c; \rho, z; \sigma_g)$ of the above stationary-phase result is integrated from Eq. (2). When $\sigma_g = \infty$ we find that $I(\rho, z)_{\text{sp}} \sim J_0^2(k\rho[r^2 + (z - d_1)/a]^{1/2}/z)$, indicating a sharp and axially relatively uniform line image. This result also explains the increased spot-size near the paraxial focus of a circular axicon [5a]; when $r = 0$ and $z \rightarrow d_1$, the Bessel function $J_0 \rightarrow 1$ (i.e. a constant). For comparison we recall that a coherent linear axicon of phase $\varphi(\rho) = -\rho/\gamma$ produces, asymptotically, an exact non-diffracting Bessel beam $J_0^2(k\rho/\gamma)$ but with linearly increasing axial intensity [13].

4. CONCLUSIONS

In this paper we have set forth the important issue of designing diffractive elements to be used in partially coherent illumination. We have shown that the design criteria for coherent and incoherent components must be modified appropriately. In the context of variable-coherence diffractive optics, the validity of concepts such as phase and ray as design tools (cf. radiometric ray tracing [14]) are assessed by comparisons against exact numerical and leading asymptotic results.

REFERENCES

- [1] L.M. Soroko, in *Progress in Optics XXVII*, ed. E. Wolf (Elsevier, Amsterdam, 1989), p. 109.
- [2] N. Davidson, A.A. Friesem, and E. Hasman, *Opt. Lett.* **16**, 523 (1991).
- [3] J. Sochacki, S. Bara, Z. Jaroszewics, and A. Kolodziejczyk, *Opt. Lett.* **17**, 7 (1992).
- [4] J. Sochacki, A. Kolodziejczyk, Z. Jaroszewics, and S. Bara, *Appl. Opt.* **31**, 5326 (1992).
- [5] L.F. Staronski, J. Sochacki, Z. Jaroszewics, and A. Kolodziejczyk, (a) *J. Opt. Soc. Am. A* **9**, 2091 (1992); (b) *J. Opt. Soc. Am. A* **10**, 1765 (1993); (c) *Opt. Lett.* **18**, 1893 (1993).
- [6] A.J. Cox and J. D'Anna, *Opt. Lett.* **17**, 232 (1992).
- [7] R.M. Herman and T.A. Wiggins, *Appl. Opt.* **31**, 5913 (1992).
- [8] Q. He, J. Turunen, and A.T. Friberg, *Opt. Commun.* **67**, 245 (1988).
- [9] P. Spano, *Opt. Commun.* **33**, 265 (1980); H.J. Eichler, G. Enterlein, and D. Langhans, *Appl. Phys.* **23**, 299 (1980); S. Lavi, R. Prochaska, and E. Keren, *Appl. Opt.* **27**, 3696 (1988); R. Gase, *J. Mod. Opt.* **38**, 1107 (1991); R. Martinez-Herrero, *Proc. SPIE* **1983**, 513 (1993).
- [10] E. Wolf, *Phys. Rev. D* **13**, 869 (1976); L. Mandel and E. Wolf, *J. Opt. Soc. Am.* **66**, 529 (1976).
- [11] A.T. Friberg and R.J. Sudol, *Opt. Commun.* **41**, 383 (1982); *Opt. Acta* **30**, 1075 (1983).
- [12] J.J. Stamnes, *Waves in Focal Regions* (Adam Hilger, Bristol, 1986), Part III.
- [13] A. Vasara, J. Turunen, and A.T. Friberg, *J. Opt. Soc. Am. A* **6**, 1748 (1989).
- [14] T. Jansson and I. Tengara, in *Proc. Tenth Symposium on Energy Engineering Sciences* (Argonne National Laboratory, Chicago, IL, 1992).

Polychromatic illumination of logarithmic annular-aperture diffractive axicon.

Z. Jaroszewicz* and Juan F. Román Dopazo

Laboratorio de Optica, Departamento de Fisica Aplicada, Facultade de Fisica,
Universidade de Santiago, 15706 Santiago de Compostela, Galicia, Spain
Phone/Fax: +34 81 521984

* on leave from: Institute of Applied Optics, Kamionkowska 18, 03-805 Warsaw, Poland

According to the geometrical law of energy conservation axicons with logarithmic phase function should exhibit a constant level of the axial intensity along the focal segment [1], [2]. Exact solutions obtained by numerical evaluations of the diffraction integral, however, show a presence of fluctuations; thereby the constant intensity level can be understood only as an average approximation. Even then, the averaged energy flows in direct neighborhood of the optical axis turn out to be nonconstant [3]. This inconvenience can be eliminated by an application of the annular aperture, but the oscillatory character of intensity distributions remains almost unchanged [4]. Obviously, oscillations appear due to the truncation of the illuminating beam on the sharp edges of the aperture and can be suppressed by an application of smooth apodization function [5]. Similar approach was proposed for the fluctuations damping of the so-called nondiffracting beams [6-9].

The apodization can be realized in two different ways: or by using an absorbing screen, which softens the aperture boundary [5], [8], [9], or by illumination the element with the Gaussian beam [6], [7]. The first way requires an elaboration of difficult to produce amplitude-only apodizing transmittance. In turn, the second one offers rather limited possibilities of the axial intensities (in particular there are not possible the constant ones), since they are directly related, *via* the phase function of the element, to the transversal intensity distribution of the Gaussian beam.

Both solutions concern the case of monochromatic illumination. Similar result, however, can be obtained, if a logarithmic axicon with clear annular aperture is illuminated by a polychromatic source. A laborious preparation of apodizing transmittance as well as losses of energy due to its presence are avoided in this way. On the other hand the axial intensity can be almost constant. The uniformization is obtained thanks to a incoherent superposition of mutually displaced focal segments produced by particular wavelengths. In following only the easier to produce kinoform version of the annular-aperture logarithmic axicon will be considered. Since the dispersive power of diffractive elements is roughly one order of magnitude greater than that of the refractive ones, narrowband sources are sufficient for good uniformization of the focal segment.

The axial intensity distribution of the logarithmic annular-aperture diffractive axicon illuminated by perpendicularly incident plane wave of wavelength λ within the scope of paraxial approximation is given by the following Fresnel diffraction integral

$$I(\lambda, z) = S(\lambda) \eta(\lambda) \left(\frac{2\pi}{\lambda z} \right)^2 \left| \int_p^R \exp \left\{ \frac{2\pi i}{\lambda} \left[\frac{r^2}{2z} + \frac{\lambda}{\lambda_0} \varphi(r) \right] \right\} r dr \right|^2 \quad (1)$$

where phase function $\varphi(r)$ of the annular-aperture logarithmic axicon is equal to

$$\varphi(r) = -\frac{1}{2a} \ln(d_1 + a(r^2 - \rho^2)), \quad a = \frac{d_2 - d_1}{R^2 - \rho^2}, \quad (2)$$

$S(\lambda)$ is the normalized wavelengths distribution of the source, $\eta(\lambda)$ is the diffraction efficiency of the kinoform in the first diffraction order, λ_0 is the central wavelength of the spectral band (and the wavelength for which the element is adjusted), R is the outer radius of the aperture and $\rho = Rd_1/d_2$ is the inner radius of the aperture.

For the spectral characteristics of the source a gaussian function is taken, which in the case of narrowband sources assumed here can be represented as a gaussian distribution of the wavelengths as well

$$S(\lambda) = \exp\left(-\ln 2 \frac{(\lambda - \lambda_0)^2}{\sigma^2}\right), \quad (3)$$

where σ is the wavelength separation between the central point and the point where $S(\lambda)$ is down to half its peak value.

The diffraction efficiency $\eta(\lambda)$ of a kinoform axicon forming the focal segment in the first diffraction order is given by

$$\eta(\lambda) = \text{sinc}^2\left(\frac{\lambda - \lambda_0}{\lambda}\right), \quad (4)$$

The final axial intensity distribution results from the incoherent superposition of focal segments produced by all wavelengths and is equal to

$$I(z) = \int I(z, \lambda) d\lambda \quad (5)$$

where the integration is extended over the whole spectral region.

In the numerical analysis we have assumed a monochromatic illumination with the wavelength $\lambda_0 = 600$ nm (Fig.1) and a polychromatic illumination with the λ_0 being the central wavelength and half-width value σ equal to 5 nm (Fig.2), 10 nm (Fig.3) and 20 nm (Figs.4 and 5) respectively. The integration given by Eq.(5) was executed over the region $(\lambda_0 - 3\sigma, \lambda_0 + 3\sigma)$. The value of the normalized distribution of the wavelengths $S(\lambda)$ falls at the border of this region to 0.002 of its peak value and more distant wavelengths do not give significant contribution into the focal segment. The diffraction efficiency $\eta(\lambda)$ was approximated by 1 (over the whole spectral range its value does not fall below 98.3%). The parameters of the axicon were: $R = 5$ mm, $\rho = 2.5$ mm, $d_1 = 100$ mm, and $d_2 = 200$ mm.

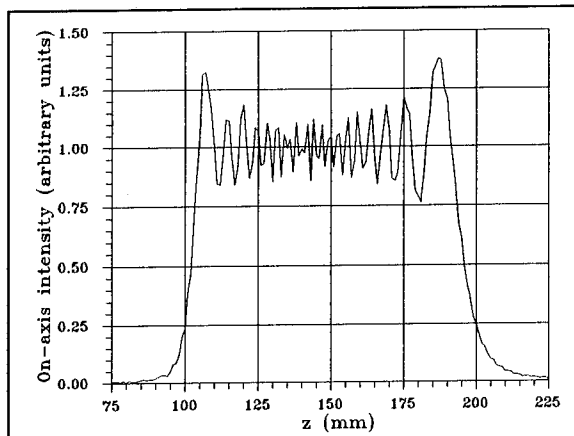


Fig. 1. On-axis intensity distribution for the diffractive annular-aperture axicon illuminated by a monochromatic source with $\lambda_0 = 600$ nm, calculated with the help of Eq.(1).

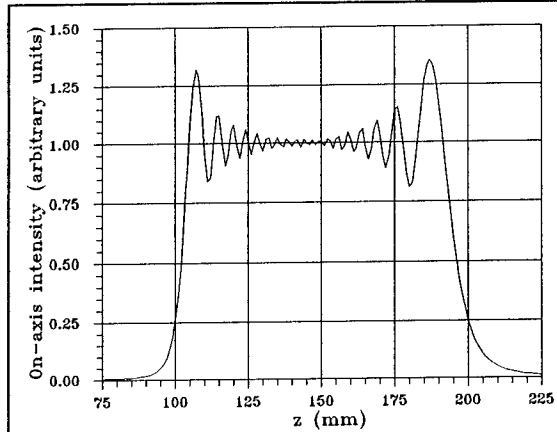


Fig. 2. On-axis intensity distribution for the diffractive annular-aperture axicon illuminated by a polychromatic source with $\lambda_0 = 600$ nm and $\sigma = 5$ nm, calculated with the help of Eq.(5).

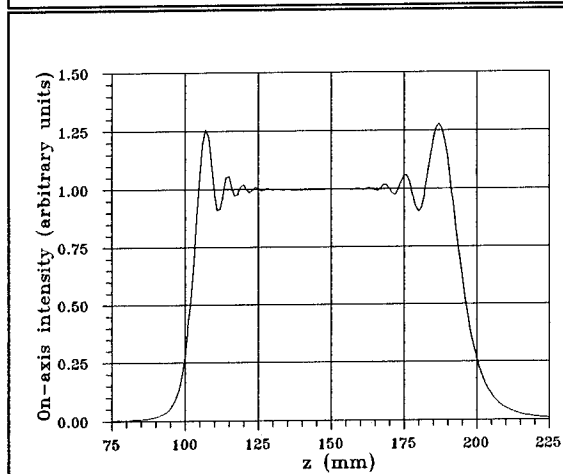


Fig. 3. On-axis intensity distribution for the diffractive annular-aperture axicon illuminated by a polychromatic source with $\lambda_0 = 600$ nm and $\sigma = 10$ nm, calculated with the help of Eq.(5).

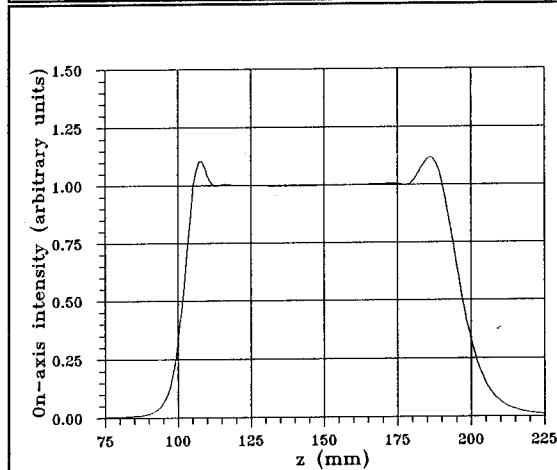


Fig. 4. On-axis intensity distribution for the diffractive annular-aperture axicon illuminated by a polychromatic source with $\lambda_0 = 600$ nm and $\sigma = 20$ nm, calculated with the help of Eq.(5).

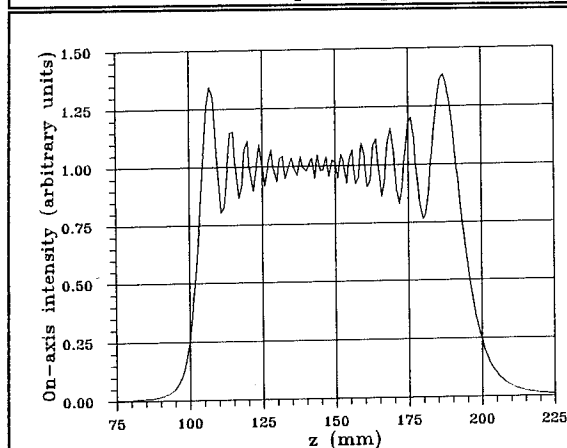


Fig. 5. On-axis intensity distribution for the refractive annular-aperture axicon illuminated by a polychromatic source with $\lambda_0 = 600$ nm and $\sigma = 20$ nm, calculated with the help of Eq.(5). The dispersion of the axicon material over the spectral range is neglected.

The set of figures, from 1 to 4 illustrates the proceeding uniformization of the axial intensity distribution, starting from the monochromatic case (Fig.1), through the narrow bands of the wavelengths distribution (Fig.2, $\sigma = 5$ nm, Fig.3, $\sigma = 10$ nm), till the widest one (Fig.4, $\sigma = 20$ nm). For the comparison, there is presented also the axial intensity of the focal segment produced by the refractive axicon, where the dispersion of the element's material was neglected (Fig.5, $\sigma = 20$ nm). This plot confirms that for the efficient cancellation of the oscillations the most important factor are mutual displacements of the focal segments; other factors, like different frequency of oscillations for different wavelengths are of minor importance.

The first overshoot at the ends of the focal segment is maintained to some degree, even for the incident beam with widest spectral region, however, other oscillations are canceled with good accuracy, comparable to those obtained by the apodization techniques. The slopes at the ends of the uniformized axial intensity become less steep, but this phenomenon takes place in the case of the apodization as well and cannot be avoided.

The application of an annular aperture does not mean that a part of the energy of the illuminating beam must be lost. Two element axicon systems can be applied in order to redistribute it properly. The first of them should be a refractive one (the linear cone at best) and would sent all wavelengths into the annular aperture of the second one. The second one should not only to have an logarithmic phase function, but also to compensate the linear phase of the incident beam. For this reason its dispersive power will be greater, and more narrow spectrum will be sufficient for the uniformization of the axial distribution.

This work was supported by CICYT, Ministerio de Transporte y Turismo y Comunicaciones (TIC 93/0606), Spain.

References

1. J. Sochacki, A. Kolodziejczyk, Z. Jaroszewicz, and S. Bará, "Nonparaxial designing of generalized axicons," *Appl. Opt.* **31**, 5326-5330 (1992).
2. J. Sochacki, S. Bará, Z. Jaroszewicz, and A. Kolodziejczyk, "Phase retardation of the uniform-intensity axilens," *Opt. Lett.* **17**, 7-9 (1992).
3. L.R. Staronski, J. Sochacki, Z. Jaroszewicz, and A. Kolodziejczyk, "Lateral distribution and flow of energy in uniform-intensity axicons," *J. Opt. Soc. Am.* **A9**, 2091-2094 (1992).
4. J. Sochacki, Z. Jaroszewicz, L.R. Staronski, and A. Kolodziejczyk, "Annular-aperture logarithmic axicon," *J. Opt. Soc. Am.* **A10**, 1765-1768 (1993).
5. Z. Jaroszewicz, J. Sochacki, A. Kolodziejczyk, and L.R. Staronski, "Apodized annular-aperture logarithmic axicon: smoothness and uniformity of intensity distributions," *Opt. Lett.* **18**, 1893-1895 (1993).
6. G. Roy and R. Tremblay, "Influence of the divergence of a laser beam on the axial intensity distribution of an axicon," *Opt. Commun.* **34**, 1-3 (1980).
7. A.J. Cox and D.C. Dibble, "Nondiffracting beam from a spatially filtered Fabry-Perot resonator," *J. Opt. Soc. Am.* **A9**, 282 (1992).
8. A.J. Cox and J. D'Anna, "Constant-axial-intensity nondiffracting beam," *Opt. Lett.* **17**, 232-234 (1992).
9. R.M. Herman and T.A. Wiggins, "Apodization of diffractionless beams," *Appl. Opt.* **31**, 5913-5915 (1992).

Wednesday, June 8, 1994

Design II

DWA 8:30am–10:00am
Room B

J.R. Leger, *Presider*
University of Minnesota

OPPORTUNITIES FOR DIFFRACTIVE OPTICAL SYSTEMS

A.W. Lohmann *and J. Ojeda-Castañeda**

*Universität Erlangen, Staudtstrasse 7-B 2, Erlangen D-91058, Germany.

**INAOE, Apdo. Postal 216, Puebla 72000, Pue., México.

An ideal diffractive optical system, which may be a part of a hybrid information processing system, should have the following properties:

Fast, highly parallel, reliable, compact, IC compatible , cheap and easy to manufacture, to test and to assemble as part of the overall system. The relative significance of those properties will differ from case to case. Here we will emphasize SIMPLICITY as most desirable.

We consider two jobs: illumination of a 2-D cartesian array of detectors or modulators ; and the generation and processing of complex 1-D signals.

Specifically we will compare two classes of array illuminators, termed Dammann and Talbot. Furthermore, we will present several 1-D systems which use simple binary masks as crucial components.

The two array illuminators are based on Fraunhofer diffraction and Fresnel diffraction, respectively . For Fraunhofer diffraction one needs a Fourier transform lens with demanding qualifications. Otherwise, the price / performance of the two approaches is comparable.

The second set of projects to be described is based on the concept, that the sacrifice of one of the two lateral dimensions (x,y) leads to very simple systems, which can accomplish among others: a) parallel display and processing of Bessel functions, Laguerre polynomials and Airy functions; and b) novel family sets of apodizers. Our first experimental verifications are included.

A Fresnel Lens Array For Optical Fibre Semiconductor Laser Coupling

P. Mckee, J. Towers, A. Thurlow and D. Wood

B.T. Laboratories

Martlesham Heath

Ipswich

Suffolk

U.K.

Tel. 0473 646574

Fax 0473 637692

The efficient coupling of light between the various components in optical communications systems will be an important factor in the widespread roll out of low cost optical telecommunications networks. Of particular interest is the efficient coupling of semiconductor lasers to optical fibres or waveguides. Because the output of a semiconductor laser is widely diverging compared to the acceptance angle of a single mode fibre, high coupling efficiency is difficult to achieve.

At present lensed fibres are a popular method for fibre/laser coupling, with efficiencies as high as 60%. When extended to arrays of lasers the fabrication of a lensed fibre array becomes more of an issue, lenses are not always concentric to the fibre cores and so must be very carefully selected before alignment or must be individually aligned to each laser in the array.

In this paper we describe the fabrication of computer optimised, low F/# Fresnel lens arrays to address the requirement for efficient and consistent coupling between arrays of semiconductor lasers and single mode optical fibres. The advantage of this approach is that each lens is positioned with a high degree of accuracy by the lithographic fabrication technique.

Design

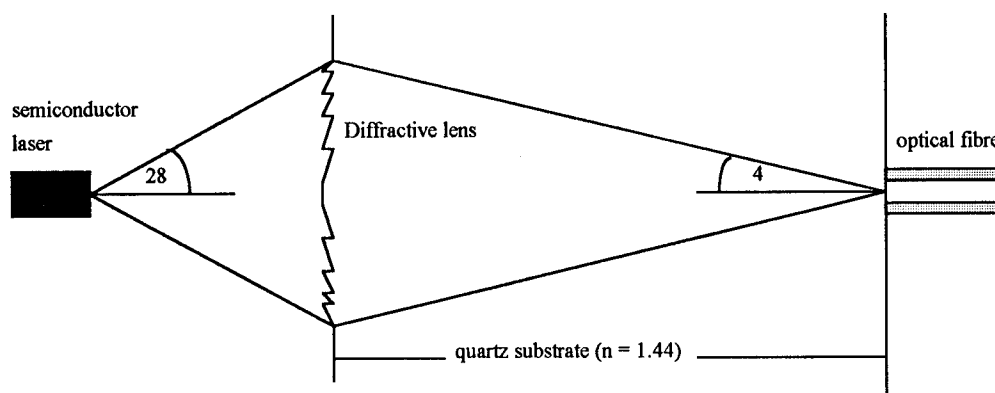


Fig 1 Optical configuration of system
(angles for $\frac{1}{e^2}$ intensity beam radius)

The optical layout of the system is as shown, Fig 1. Each lens array comprises four lenses on a 250 micron pitch, matching the fibre spacing in the four fibre connector. The lenses were designed with the required magnification for transforming a diverging laser beam, NA 0.46, into a converging beam suitable for coupling into a cleaved fibre, NA 0.1. The focal length was

calculated to be 66 microns, resulting from a lens fibre separation equal to the thickness of the quartz substrate, and the laser lens distance was calculated to be 80 microns. These design parameters form the input to a computer program in which the lens surface is represented by a two dimensional array of pixels, each pixel being assigned one of four phase levels. An optimisation algorithm based on simulated annealing (1) is used to optimise the Fresnel-Kirchoff integral that transforms the pixel pattern to produce the desired output pattern.

Fabrication

The $F/\#$ of each lens in the array, defined here as the focal length divided by the effective beam diameter at the lens, is 0.5. Such a low $F/\#$, due to the widely diverging laser beam and the magnification necessary for coupling into a fibre, results in a very small feature size, 0.2 microns, in the outer regions of the lens. A number of different exposure strategies were assessed in order to optimise the fabrication. The choice of quartz substrate also had a major impact on the fabrication process. After an adjustment for non-normal incidence of the light beam, a total etch depth of 2.1 microns was required for an operating wavelength of 1.5 microns, presenting a fabrication challenge. The total etch depth could have been reduced by using a higher refractive index material such as silicon, but the high reflection losses associated with such materials necessitate anti-reflection coating of both surfaces (2).

The other advantage of a quartz substrate is its transparency allowing the positioning of fibre alignment structures on the rear face of the substrate by a straightforward projection method (3).

The lenses were fabricated using direct write electron beam lithography and reactive ion etching as previously reported(4). The basic process is outlined in Fig 2. Two different resist strategies were used for the initial high resolution structure definition, a thick negative tone bi-level resist, and a thin positive tone process forming a metal etch mask by lift-off. After etching and planarisation of the first level topography, the second level was exposed, and a second etch step carried out resulting in the 2.1 μ total etch depth.

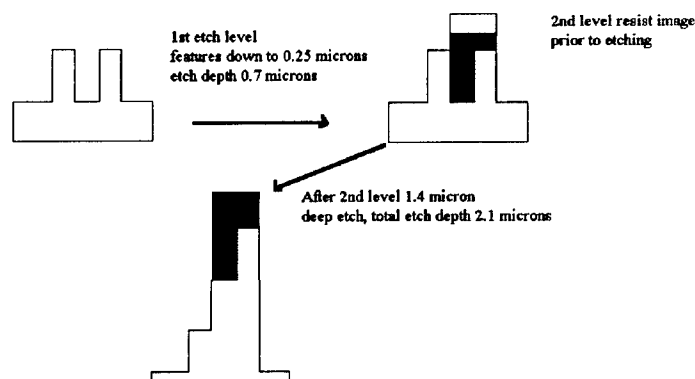


Fig 2 Basic fabrication sequence

Characterisation

a) Structural

One of the major problems encountered in the fabrication of high resolution diffractive optical elements is the assessment of etch depth and pattern fidelity in the deeply etched sub-micron regions since these cannot be measured using conventionally available non-destructive techniques. We have employed focused ion beam sectioning to study the profile and dimensions of the four phase levels. The ability of the focused ion beam to image and machine with the same

beam provides accuracy in the placement of cross-sections that approaches the resolution of the image, ca 30nm.

The ion beam was used to deposit a platinum line over the topography of interest, to preserve edge detail and increase image contrast. A sloping profile etch pit was then prepared adjacent to the line see, Fig 3. Tilting the sample allowed examination of the cross-section and acted as an aid to process development. Although the technique is destructive, the section is small and localised, and the technique can therefore be performed on finished substrates with little impact on the device performance .

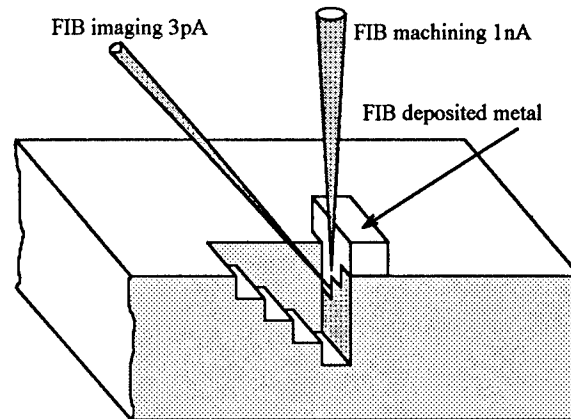


Fig 3 Schematic of ion beam sectioning process

b)Optical

Three sets of measurements were taken to assess the performance of the Fresnel lens array in its intended operating configuration. The first was coupling efficiency of a semiconductor laser to a cleaved fibre through the Fresnel lens array ,Table 1.

	Lens 1	Lens 2	Lens 3	Lens 4	Average
efficiency %	33.8	34.0	34.9	34.2	34.23

Table 1 Coupling of 1.55 μ laser, 30° FWHP to fibre

The second set of measurements investigated the half power coupling efficiency tolerances between the optical fibre and the Fresnel lens array, index matching being used between the fibre and the array.Table 2.

	Lens 1	Lens 2	Lens 3	Lens 4	Average	Tolerance (microns)
Lateral	+6.2 -5.9	+5.1 -6.5	+6.1 -3.7	+6.5 -5.8	+6.5 -5.5	± 5.7
Vertical	+5.4 -5.6	+5.5 -7.3	+6.0 -7.2	+6.1 -6.9	+5.8 -6.8	± 6.3

Table 2 Half power point fibre to lens positioning tolerances in microns

The third set of measurements investigated the half power coupling efficiency tolerances of the semi conductor laser to the Fresnel lens array. Table 3.

	Lens 1	Lens 2	Lens 3	Lens 4	Average	Tolerance
Lateral	+1.2	+1.2	+1.2	+1.2	+1.2	± 1.1
	-0.9	-1.0	-1.1	-1.1	-1.0	
Vertical	+0.8	+1.1	+1.3	+1.3	+1.1	± 1.1
	-0.4	-1.3	-1.2	-1.2	-1.0	
In Gap Out	4.7	6.1	5.5	5.3	5.4	± 5.2
	5.3	3.7	5.5	5.6	5.0	

Table 3 Half power point laser to lens positioning tolerances in microns

Conclusions

We have designed and fabricated sub micron feature sized Fresnel lenses in quartz. The use of focused ion beam sectioning as a fast and potentially an in process, diagnostic tool has been demonstrated. Using the fabricated arrays of Fresnel lenses coupling efficiencies of 34% have been achieved between a 30° FWHP laser and a cleaved standard system fibre. Although this is less than the 60% coupling achievable with a good lensed fibre the use of a lens array has significant advantages. Arrays of lensed fibres are difficult to fabricate due to the process of lens formation on the fibre. However extremely uniform arrays of Fresnel lenses have been produced that exhibit positional tolerances, when aligned to a semiconductor laser, similar to lensed fibres. A further advantage of the Fresnel lenses is the relatively lax positional accuracy required for the cleaved fibre, typically plus or minus 6 microns, making lens/fibre arrays readily achieved.

Acknowledgements

The authors would like to thank John Whitney and Nick Dawes of FEI Europe Ltd for their invaluable help on the focused ion beam cross-sectional analysis of the finished lenses.

References

1. M. R. Feldman and C. C. Guest, Optics Letters, **14**(10), 479(1989)
2. E. Pawlowski, IEE conference publication 379, "Holographic Systems Components & Applications", **54**, (1993)
3. J. Jahns, W. Dascnher, Optics Letters, **17**(6), 390(1992)
4. D. Wood, P Mckee and M. Dames, SPIE Proceedings Vol **1732** (1992)

Design and Fabrication of Multi-Level Phase Holograms for On-Axis Optical Interconnects

Arthur F. Gmitro
Department of Radiology and Optical Sciences Center
University of Arizona
Tucson, AZ 85724
(602) 626-4720

Paul E. Keller
Pacific Northwest Laboratory, K1-87
P.O. Box 999
Richland, WA 99352

Christopher Coleman
Optical Sciences Center
University of Arizona
Tucson, AZ 85721

Paul D. Maker
Jet Propulsion Laboratory
California Institute of Technology
4800 Oak Grove Drive
Pasadena, CA 91109-8099

Introduction

There are a number of important applications for holographic optical interconnects including their use in digital computers, optical neural networks, and optical preprocessing systems. In virtually all of these applications, the overall system architecture is greatly simplified if the interconnections can be made in an on-axis geometry. Additionally, the on-axis geometry provides the potential for higher diffraction efficiency and, in many cases, improved accuracy in the interconnects. In order to realize interconnections in this geometry, holograms are typically designed by computer and fabricated as multi-level phase masks. Many techniques exist for the design of off-axis binary-amplitude holograms. These include cell-based techniques like the Lee¹ and Lohmann² methods, point-based techniques like the error-diffusion approach^{3,4}, and iterative methods like the Gerchberg-Saxton algorithm^{5,6} and simulated annealing^{7,8}. Many of these methods, however, are not applicable to the design of multi-level phase structures - only the iterative techniques can be used to design phase-only holograms with adequate performance. The fabrication of multi-level phase holograms is by no means a trivial task. The standard approach, based on the e-beam fabrication of multiple binary transmission masks and multiple exposure/etch cycles of a glass substrate, is extremely tedious, expensive, and sensitive to fabrication error. In this work we describe an iterative design procedure, developed by our group, that yields holograms with improved performance relative to other design strategies, and a direct e-beam fabrication method that avoids many of the difficulties of the standard fabrication technique.

The Design Algorithm

The design algorithm we have developed is a two-step procedure consisting of a combination of the Gerchberg-Saxton technique followed a random search error-minimization step. The latter is equivalent to simulated annealing at zero temperature. This combination, which we term the Gerchberg-Saxton preconditioned random search (GSPRS) algorithm, yields holograms with high diffraction efficiency and low error in the interconnection intensities⁹.

The Gerchberg-Saxton (GS) technique is an iterative technique, which attempts to find a solution that simultaneously satisfies constraints in both the hologram plane and the output plane. For many applications (all that we have considered), the hologram is designed as a Fourier transform hologram, and as such, the relationship between the hologram and the output plane is a particularly simple one (i.e. just a Fourier transform relationship). In this case the GS procedure consists of repeated application of the following loop: apply the output constraints, inverse Fourier transform to the hologram plane, apply the hologram constraints, Fourier transform back to the output plane. The output constraint is typically that there be a specified intensity pattern in some portion of the output plane. For example, in neural network applications one desires a particular pattern of weighted interconnects at a given set of detector locations. The hologram constraint is that the transmission function of the hologram be multi-level phase. In other words, the magnitude of the amplitude transmission is unity across the hologram and the phase at any pixel is quantized to be one of N levels. The start point of the algorithm entails specification of an output optical amplitude with a magnitude equal to the square root of the desired intensity pattern and a random phase distribution. Although there is no guarantee that a solution can be found because there is no guarantee that a solution even exists, the GS algorithm works reasonably well in practice if there are enough degrees of freedom (pixels) in the hologram. A characteristic of holograms designed by GS is that they have high diffraction efficiency because one starts the design procedure by placing all the energy in the desired interconnection pattern and zero energy outside the pattern.

Although the GS algorithm works reasonably well in its own right, significant improvement in the accuracy of the interconnections can be achieved by incorporating a random search procedure into the design algorithm. In this case one starts with the hologram produced by the GS algorithm; then pixels in the hologram are chosen at random and their phase values randomly changed to one of the N quantized phase values. This change is evaluated and accepted only if it produces a better output. The evaluation of what constitutes a better result is done in terms of a merit function that measures the RMS error between the desired output and the actual output. This procedure is equivalent to simulated annealing at zero temperature (i.e. only changes that improve the accuracy of the interconnects are accepted).

A comparison of the GSPRS algorithm to other holographic design methods was performed. The task for this comparison was the design of a Fourier transform hologram producing an 8×8 binary interconnect pattern centered in a larger array of 32×32 pixels. The fundamental space-bandwidth product (SBWP) of the hologram is, therefore, 1024. Figure 1 (reprinted from Fig. 3 of Ref. 9) shows a plot of the performance of the holograms in terms of the RMS error in the output versus the SBWP product in the hologram. Additional SBWP was incorporated by replicating the hologram. As expected, adding SBWP to the hologram increases the performance (decreases the error). Very similar results are obtained if zero padding is used rather than hologram replication. It is seen that the GSPRS algorithm clearly out performs the other algorithms tested. Results in Ref 9 also shows that the diffraction efficiencies for the GS and GSPRS holograms are approximately six times higher than those for holograms designed by the other methods. This particular analysis used a 4-level phase holograms, but the same general results are seen with binary amplitude holograms as well as phase holograms with different numbers of phase quantization levels.

Hologram Fabrication

The standard approach to fabricating an N -level phase holograms requires the e-beam fabrication of m binary transmission masks, where $m = \log_2 N$, and m processing cycles. Each processing cycle consists of spin-coating resist, resist exposure, resist development, etching of the substrate to the appropriate depth for the given mask, and residual resist removal. Accurate spatial alignment of the m cycles as well as accurate control of the etch depth at each cycle is required to produce a satisfactory hologram. The performance of the holograms relative to errors in both alignment and etch depth has been analyzed by our group¹⁰.

A much more direct method of fabricating multi-level phase holograms is to employ variable e-beam exposure with accurately controlled development to produce a surface relief structure in a single layer of resist. Paul Maker at the Jet Propulsion Laboratory has recently developed and demonstrated a technique employing PMMA as the resist with acetone development¹¹. The e-beam exposure effectively breaks bonds in the highly cross-linked PMMA material altering its solubility in acetone. By controlling the e-beam exposure and development time, a specified surface relief structure (i.e. phase hologram) can be produced. Fresnel lenses with excellent performance have been produced by this technology by Maker and colleagues at JPL. As described in the next section, this technique was used to fabricate multi-level phase holograms designed via the GSPRS algorithm.

Experimental Results

A simple problem was chosen to demonstrate the ability to design and fabricate multi-level phase holograms for use in systems requiring on-axis optical interconnects. A set of nine holograms were designed to encode the numeral 1 thru 9. The numerals were represented as a binary pattern of on and off pixels on a 64 x 64 pixel grid, which was centered in a larger 128 x 128 pixel array. The holograms were designed using the GSPRS algorithm as Fourier transform holograms with a fundamental array size of 128 x 128 pixels and 64 quantized phase levels. Each hologram was replicated 16 times (4 x 4 pattern of replication) to confine the energy in each interconnect to the center of the output cell (detector), which improves the accuracy of the interconnects by reducing cross talk of light from one interconnect to the next. Thus, each hologram consists of 512 x 512 pixels quantized to 64 phase levels. The pixel size was specified as 1 μ m, which yields a hologram of approximately 0.5 mm on a side. The number of phase levels was chosen to match the capability of the fabrication technology, although little improvement in performance is realized for quantization above 8 phase levels. The holograms were fabricated at the e-beam facility at JPL.

Figure 2 shows an example of the output of one of the holograms. The pattern of on and off pixels is clearly seen. The square surrounding the numeral represents the outer border of the 64 x 64 pixel pattern. The fact that this is an on-axis interconnection pattern can be appreciated by the central bright pixel, which represents the zero order diffraction. This pixel should be of equal intensity with the other on pixels in the pattern, but is approximately seven times as bright because of slight errors in the fabrication process. Still, this is an impressive result considering that the on-axis light would be approximately a thousand times brighter with no hologram in the beam.

The performance of this hologram is quite good. The overall diffraction efficiency is about 46%, which is about 10% less than predicted. If one normalizes the output to correspond to values of one (bright) and zero (dark), the bright pixels have an average value of 1.0 (by definition) and a standard deviation of 0.49. The dark pixels in this pattern have an average value 0.029 and a standard deviation of 0.017. This yields an overall contrast ratio of approximately 34, which is within a factor of two of the predicted performance. The slightly reduced performance appears to arise from the an overly active etching process that cuts into the side walls of "tall" PMMA pixels. Future work will be directed to reduce this problem and that of the residual zero-order light signal.

Conclusions

The GSPRS design algorithm appears to be a very good method for the design of multi-level phase computer-generated holograms. Fabrication of multi-level phase structures by direct e-beam exposure and development of PMMA is possible and produces holograms with good performance. Combined, this design technique and fabrication method can be used to make holograms for a variety of on-axis optical interconnect applications.

References

1. W.H. Lee, "Sampled Fourier Transform Holograms Generated by Computer," *Appl. Opt.* **9**, 639 (1970).
2. A.W. Lohmann and D.P. Paris, "Binary Fraunhofer Holograms Generated by Computer," *Appl. Opt.* **6**, 1739 (1967).
3. R.W. Floyd and L. Steinberg, "An Adaptive Technique for Spatial Grayscale," *Proc. Soc. Inf. Disp.* **17**, 78 (1976).
4. S. Weissbach, F. Wyrowski, and O. Bryngdal, "Quantization Noise in Pulse Density Modulated Holograms," *Opt. Commun.* **67**, 167 (1988).
5. R.W. Gerchberg and W.O. Saxton, "A Practical Algorithm for the Determination of Phase from Image and Diffraction Plane Pictures," *Optik* **35**, 237 (1972).
6. J.R. Fienup, "Iterative Method Applied to Image Reconstruction and Computer-Generated Holograms," *Opt. Eng.* **19**, 297 (1980).
7. N. Metropolis, A. Rosenbluth, M. Rosenbluth, A. Teller, and E. Teller, "Equations of State Calculations by Fast Computing Machines," *J. Chem. Phys.* **21**, 1087 (1953).
8. M. Feldman and C. Guest, "Iterative Encoding of High-Efficiency Holograms for Generation of Spot Arrays," *Opt. Lett.* **14**, 479 (1988).
9. P.E. Keller and A.F. Gmitro, "Design and Analysis of Fixed Planar Holographic Interconnects for Optical Neural Networks," *Appl. Opt.* **31**, 5517 (1992).
10. P.E. Keller and A.F. Gmitro, "Computer-Generated Holograms for Optical Neural Networks: On-axis versus Off-axis Geometry," *Appl. Opt.* **32**, 1304 (1993).
11. P.D. Maker and R.E. Muller, "Phase Holograms in PMMA," Submitted to *J. Vac. Sci. Technol.* (1993).

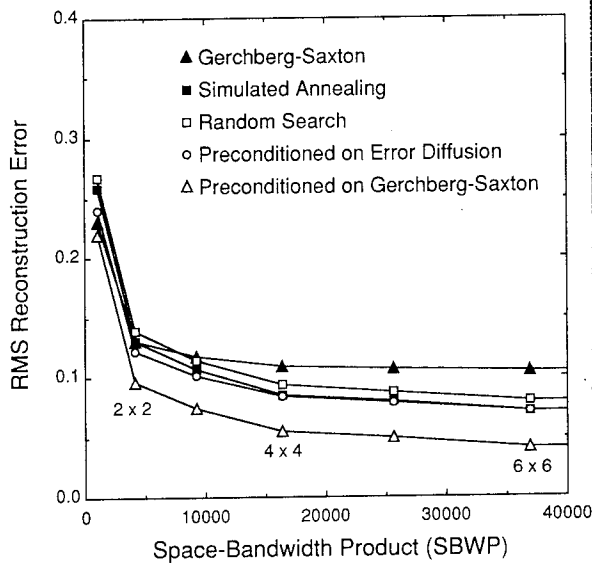


Fig1. Output error of interconnection vs SBWP for various 4-level phase holograms

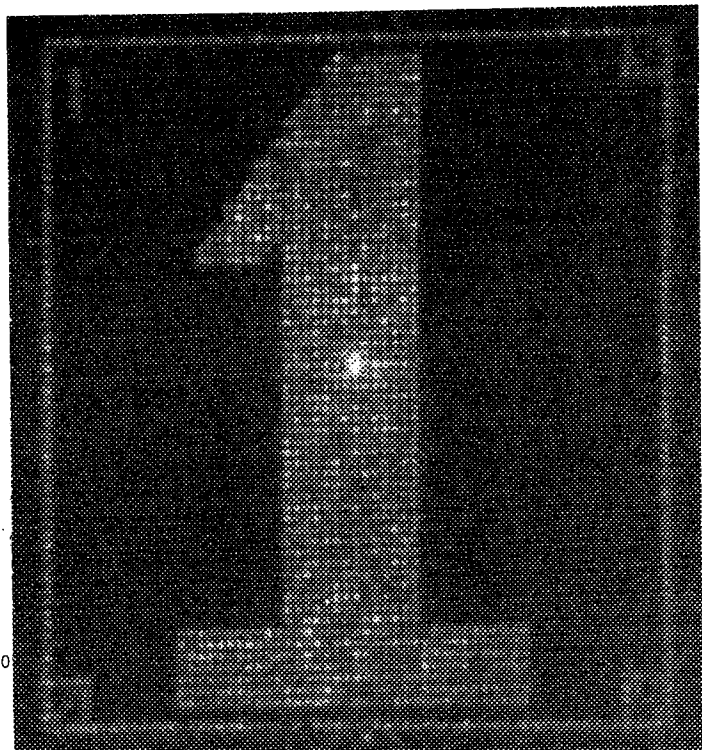


Fig. 2. Output of a 64-level phase hologram designed via the GSPRS algorithm and fabricated by variable e-beam exposure of PMMA. The interconnects are on a 64 x 64 pixel on-axis pattern.

An Algorithm for the Generation of Reduced Ebeam Fabrication Data for General Aspheric Diffractive Optical Elements

Jiao Fan, David Zaleta, Sing H. Lee
Dept. of ECE, University of California, San Diego
La Jolla, CA 92093-0407
Phone: (619) 534-2699 Fax: (619) 534-1225

I. Introduction

Diffractive optical elements (DOEs) can be used in many industrial and military applications including optical interconnections for the next-generation highly parallel computing systems. One of the most general DOEs for such applications is the aspheric DOE. Typically an aspheric element is defined as an optical element whose phase function can be specified by a polynomial of some specified type. Thus aspheric elements can be designed in standard optical design programs such as CODEV that will optimize the coefficients of the polynomial to satisfy the designer's specifications. Once these coefficients are generated the problem is to generate the data necessary to fabricate the aspheric DOE. However, current ebeam pattern generators for vector based machines (such as Cambridge) place stringent limitations on the types of shapes that can be generated. For instance only trapezoids with horizontal tops and bottoms and with a fixed set of angles for the trapezoid's sides are allowed. As the number of trapezoids grow, the ebeam data size grows proportionally. Thus, there is a tradeoff in data generation between pattern fidelity and data size or between optical noise and fabrication cost/time. Therefore, there is a need for general algorithms that generate reduced data size for general aspheric DOEs.

Arnold[1] first proposed the use of the ebeam writer in generating DOEs, however only sketchy algorithms were given on how to take specification data such as the coefficients of an aspheric DOE and generate the ebeam data. Later, two general methods were proposed to generate aspheric DOEs: fringe tracing based algorithms that trace fringe boundaries [2], and pixel based algorithms that draw small areas (pixels) based on the average wavefront values[3]. Fringe tracing based algorithms are not stable nor general enough to ensure successful data generation but they produce far less data than pixel based approaches. In this paper, we present a new algorithm based on modified subdivision techniques[4] that possesses the stability of pixel-based approaches but at the same time significantly reduce the amount of data by using fringe tracing.

II. Algorithm

In this section we will formally describe the problem to be solved and present an algorithm capable of providing a general solution to the problem.

A. Problem formulation

Let A be the aperture region of a DOE: $x_0 < x < x_1$ and $y_0 < y < y_1$.

Let $S = \{E \mid E \text{ is an allowable ebeam shape}\}$ be the allowable ebeam shapes.

Let $P(x,y)$ be a polynomial phase function defined in region A , which represents the desired wavefront of interest. Given the fractional fringe phase value, $2\pi/m$, where m is the number of phase levels, and a phase error bound e . Our problem is to partition A into a set of fringes A_i such that

$$A_i = \{(x,y) \mid (i-1) \times (2\pi / m) < P(x,y) \leq i \times (2\pi / m)\} \quad \forall i. \quad (1)$$

For each A_i , a number ϕ_i is assigned to indicate the quantized phase of this area. For example, when DOEs are L phase level direct write, $\phi_i = 2\pi \times (i \bmod L)$ for all i . The task of the algorithm is to approximate A_i efficiently with a subset S'_i of S , such that the phase errors caused by under-covered or over-covered areas are bounded by e . That is, for any i we want to find S'_i , such that

$$(i-1) \times (2\pi/m) - e < P(x_a, y_a) < i \times (2\pi/m) + e, \text{ for all points } (x_a, y_a) \text{ in } S'_i. \quad (2)$$

B. Algorithm Description

To solve this general aspherical data generation problem, we developed the algorithm described below. This algorithm is based on modifications of subdivision methods found in computer science for surface-to-surface intersections [4]. These methods are known to be both reliable and accurate. The algorithm can be divided into the following steps:

- step 1:** Divide aspheric element A into N regions, R_1, R_2, \dots, R_N (Figure 1a).
- step 2:** Divide each region R_i into G_i grids (Figure 1b), where G_i is dependent on the minimum feature requirement in that region R_i . To ensure the accuracy, there should not be more than one fringe boundary crossing a grid.
- step 3:** Trace each fringe within each grid with Cambridge ebeam angles (Figure 1c). These angles should be the closest one to the fringe section in the grid. The error of the trace is bounded by e .
- step 4:** Form trapezoids shapes based on these traced fringes inside a grid (Figure 1d).
- step 5:** Within each region R_i , we combine shapes so that the total number of shapes is reduced in that region (Figure 1e).

Notice that two extreme cases of this algorithm will result in either pure fringe tracing or pixel based methods. When N is set to 1 and ignore step 5, we have the case of pixel-based methods. In this case, the data size will be quite large (see Section III). When region R_i is set to A_i (those regions covered by the fringes of interest) for all i , and we ignore Step2, we have fringe tracing methods. The problem in this case is that it is very difficult to divide the elements into these type of regions, except for a few special cases such as Fresnel zone plates. In this paper, we present results in which A is uniformly divided into equal rectangular regions (R_i 's). Adaptively dividing A into regions of different sizes will be more effective in reducing the data size, but is a topic of future research.

It is the combination between methods of fringe tracing and using grids that ensure stability, accuracy and smaller data size. There are two aspects of optimization in this algorithm. The

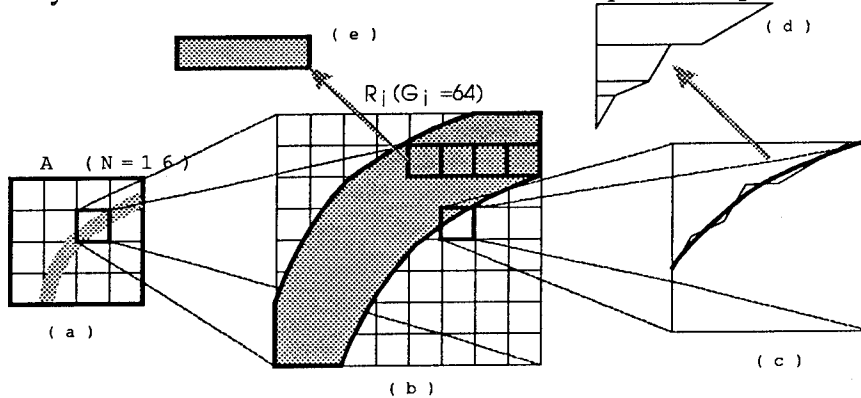


Figure 1. Algorithm for general aspheric element E-Beam fabrication.

first aspect is the combination of the neighboring grids (Step 5) in a given region to form a larger ebeam shape (the identical size of the grid inside the region make this possible). Secondly, the use of regions allows the grids in each of these

regions to be of different sizes to accommodate the varying spatial frequencies in the DOE (small fringes require a small grid size whereas large fringes can accommodate larger grid sizes). Using this algorithm the data size can be controlled by adjusting two parameters: the number of regions and the phase error. Briefly the phase error is a number that is related to the fringe tracing accuracy. The next section will discuss the trends in data size as these two quantities vary.

III. Results

We have applied this algorithm to different types of aspheric elements. Although the algorithm is capable of generating multilevel e-beam data for direct write, for simplicity in this paper we will only show the results for binary masks. Figure 2 shows a picture of the ebeam patterns generated for a 5th order aspheric DOE which corrects for off-axis aberrations for a bulk refractive lens. Its size is 0.6×0.6 mm. Figure 2a shows the result of $N=1$ without Step 5, as a basis of comparison (pixel based approach). For this case, the ebeam data file has 129 kbytes. When Step 5 is performed (Figure 2b), the data size is reduced to 90 kbytes. When the number of the regions N increased, and the grid size in each of the region is adaptively set depending upon the error requirement in that region (Step 2), we can see the data size is reduced further. Figure 2c shows the case where $N=12$. The data size in this case is 73 kbytes. It should be noted that this reduction in the ebeam data will also result in a reduction in ebeam fabrication time (which directly relates to the cost). However, our experiment shows that it is the DOE's area that dominates the ebeam exposure time. For our cases, we noticed only a modest reduction in the estimated exposure time since our elements all have the same area. It should be mentioned that one method of reducing the ebeam writing time is to use variable resolution techniques but is beyond the scope of this paper.

To observe the trends as we vary the number of regions and the phase error, we generated five aspheric DOEs with f-numbers varying between 10 and 50. Figures 3 and 4 shows the relationship between the ebeam data size from the algorithm and different region sizes and phase error requirements. Notice that the results of the pixel based algorithm for the f/10 case are

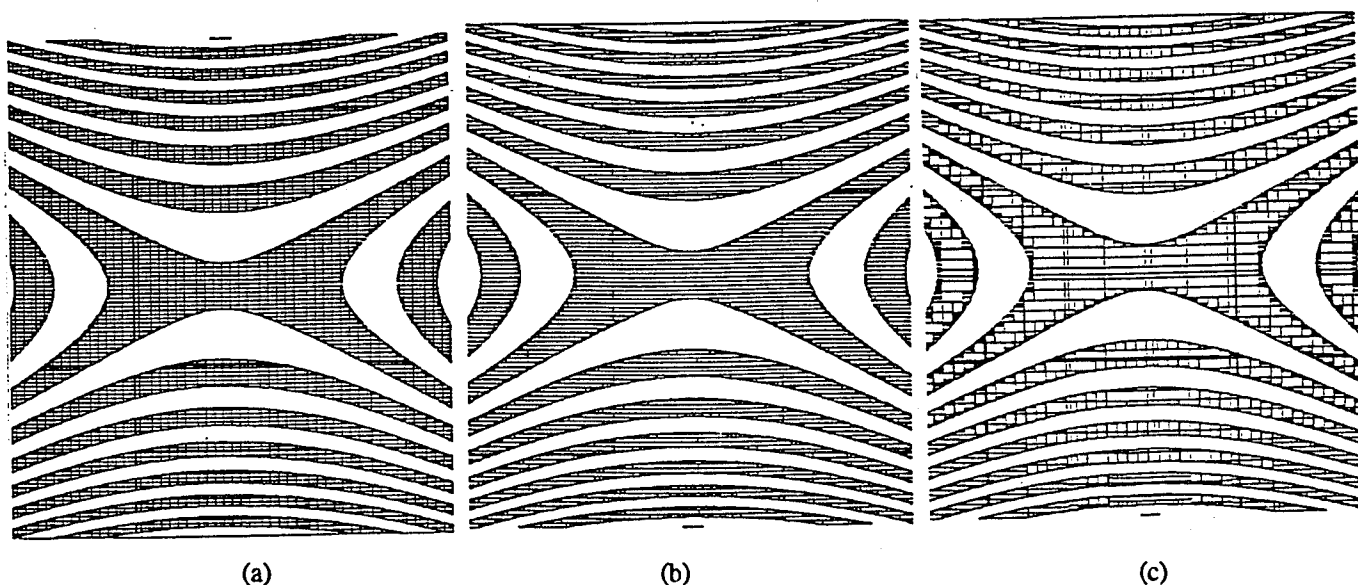


Figure 2. Aspheric DOE ebeam data generated by (a) pixel based approach (b) with optimization (c) with more regions ($N=12$).

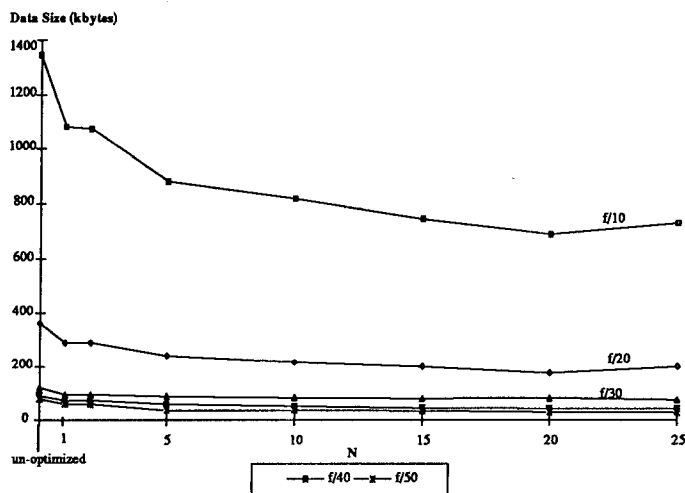


Figure 3. The relationship between the number of regions and the data size for 5 different aspheric DOEs.

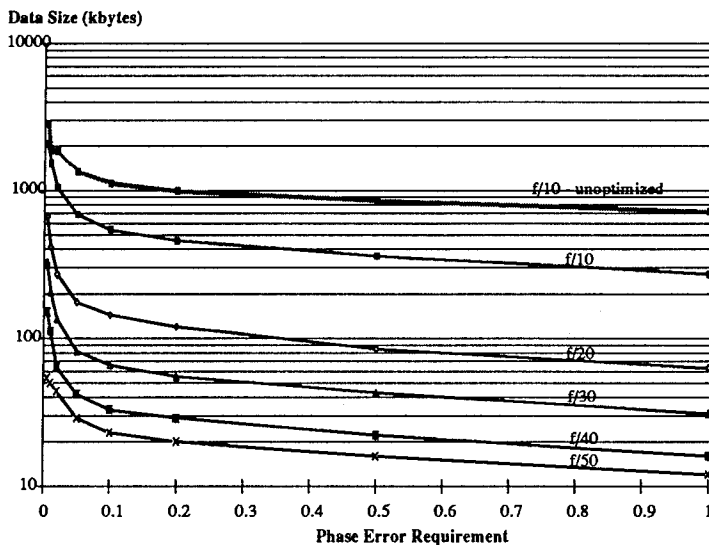


Figure 4. The relationship between the phase error and the data size for 5 different aspheric DOEs.

indicated as "unoptimized". Figure 3 shows the graph of the data size vs. the number of regions for a fixed phase error. It shows that by varying the region size at least 40% reduction in the data size can be realized. In general, as N increases, the data size begins to decrease until an optimal point is reached (in this case $N=20$), after this point the data size increases. Figure 4 shows the relationship between the phase error and the data size. It shows that if the design allows a larger phase error, the data size will become smaller. The optimum phase error is at the elbow of the curve

(phase error $\sim 0.1-0.2$, in 0.1 of the wavelength) where pattern fidelity is still very good and the data size is close to a minimum.

IV. Conclusion

In this paper, we have described a stable algorithm for e-beam fabrication of general aspheric diffractive elements. More than 40% improvement in data size can be achieved over the past published algorithms.

V. References

1. S. M. Arnold, "Electron Beam Fabrication of Computer Generated Holograms," *Opt. Eng.* **24**, 803-807 (1985).
2. H. Farhoosh, "A Knowledge-Based System for Electron-Beam Fabrication of Computer Generated Holograms," Ph.D. Dissertation, Dept. of Elec. Eng., Univ. of California, San Diego (1991).
3. J. Logue and M. L. Chisholm, "General Approaches to Mask Design For Binary Optics," *Proc. SPIE* **1052**, 19-24 (1989).
4. N.M. Patrikalakis, "Surface-to-surface intersections," *IEEE Computer Graphics and Applications*, **13**, 89-95 (1993)

Generation of binary, phase-only, holograms by on-line feedback of output plane intensity

E.G.S.Paige and R.H.Scarbrough

Department of Engineering Science, University of Oxford,
Parks Road, Oxford, OX1 3PJ, England
Telephone +44-865-273113, Facsimile +44-865-278905

Introduction

It is usual to design computer generated holograms (CGH), whether modulating amplitude or phase or to be implemented as fixed or programmable, using a computer alone. In this "off-line" approach, the hologram and the rest of the optical system is modelled and is incorporated in an iterative optimization algorithm for the design of the hologram. The resulting CGH is subsequently fabricated or displayed for assessment [1]. The optical components need to be of high quality because aberrations have not formed part of the modelling procedure.

It has been recognized that computer controlled spatial light modulators (SLM) provide a means whereby the optical system can be incorporated in the design process [2,3]. In this "on-line" approach, the measured intensity in the output plane is fed back to a computer which performs the iterative optimization and controls the SLM pixel pattern, so forming a feedback path from the output to the SLM. This has the virtue that system defects are included into the optimization process and has the possibility of giving faster optimization than the "off-line" approach when the number of SLM pixels is very large.

In this paper results are presented for an on-line feedback system. The system differs from that used earlier [2,3] in that (i) the SLM performs as a binary, phase-only, modulator and (ii) the system operates with a single detector in the output plane. The results show optimal (correct to a single pixel) and near optimal design in Fourier and Fresnel transform optics and demonstrate correction for an aberration deliberately introduced into the system.

Experimental System

Fig. 1 shows the experimental set up used to implement on-line feedback in this work. At the heart of the system is a commercially available 128 x 128 pixel ferroelectric liquid crystal spatial light modulator (FLCSLM) [4], which, in combination with polarisers, achieves inherently binary, phase-only modulation. We refer to the

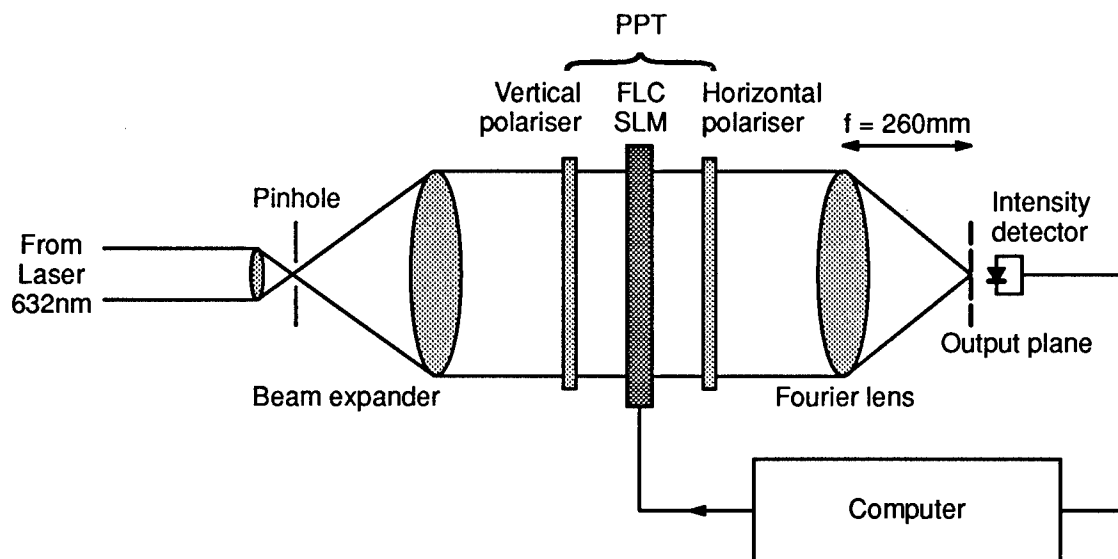


Figure 1 Experimental set up for design of CGH using on-line feedback

SLM plus polarisers as a programmable phase transformer (PPT). Good performance with the system has previously been reported [5,6]. The PPT is controlled via a computer, which also monitors the intensity in the output plane detected by a single photodiode via an analogue to digital converter (ADC) board and computer controlled preamplifier. The arrangement shown in Fig. 1 is for generation of a Fourier transform hologram. Fresnel transform holograms are formed with the detector displaced out of the Fourier plane.

The design procedure starts with a random arrangement of PPT pixels states. A single PPT pixel is then selected at random by the computer, and its phase state switched by $x(-1)$. This is followed by measurement of the corresponding intensity change at the photodiode. The pixel change is retained if the detected intensity increases and rejected if it is reduced, according to the direct binary search (DBS) algorithm. The whole process is then repeated until all pixels have been tested twice.

At present, the overall system performance is limited by ADC quantization noise. This is a problem because measurement of the effect of switching one pixel in up to 128×128 pixels is being attempted using 12 bit quantization. With the current system, the time to carry out a complete optimisation is about $2N$ seconds, where N is the total number of pixels. There is considerable scope for reducing this time.

Performance

Fourier plane, centre spot. The simplest situation to which on-line feedback can be applied is to optimise the PPT to produce a central spot in the Fourier plane of a lens. This means placing the detector at that position. It is then anticipated, for the better-than- $\lambda/2$ phase flatness of the PPT, that the feedback will attempt to put all PPT pixels into the same phase state. Fig. 2 indicates how successful the feedback procedure is, with different numbers of active PPT pixels (the remaining pixels in each case being configured so their output does not contribute to the intensity at the detector).

For up to about 1500 active PPT pixels, the feedback loop puts *all* pixels into the same state. However, as the number of pixels is increased further, a gradual degradation of performance can clearly be seen, so that around 500 pixels are in the 'wrong' state when all 128×128 PPT pixels are used. This figure excludes the contribution made by a number of malfunctioning lines of pixels, arising from defective addressing electrodes on the SLM.

Fig. 3 (a), shows the final phase pattern produced by on-line feedback for the detector located at the centre of the Fourier plane. The defective lines of pixels are clearly visible to the left of the pattern and to a lesser extent in the top right hand corner. Fig. 3 (b) shows an image of the output spot produced by the pattern in 3 (a). The clearly visible side-lobe structure supports the claim of near diffraction limited performance.

Fourier plane, off-centre spot. In this assessment the detector is moved off-centre while still in the Fourier plane. As expected, this produces a grating as is shown in Fig. 3 (c), with 3 (d) showing the corresponding output

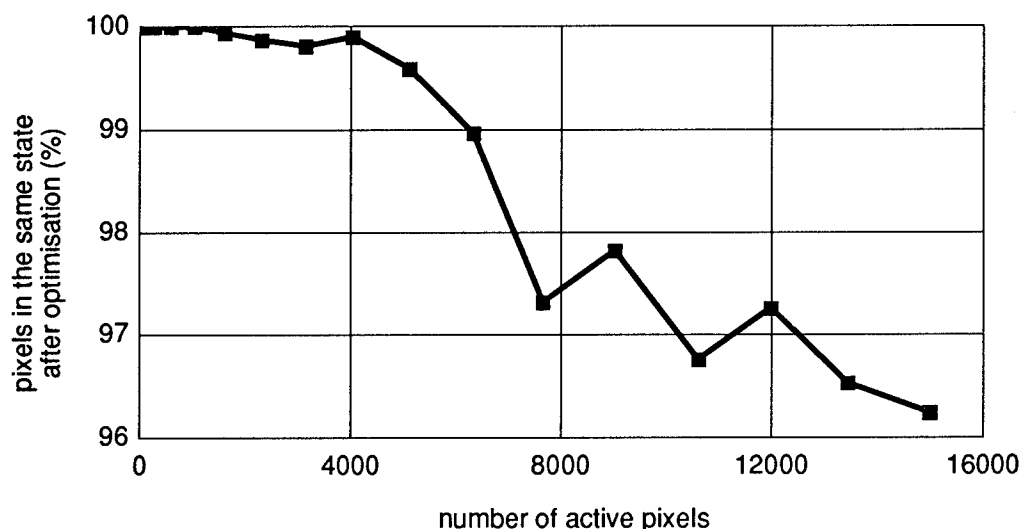


Figure 2 Generation of a Fourier plane central spot: percentage of pixels in the same state as a function of active number of PPT pixels

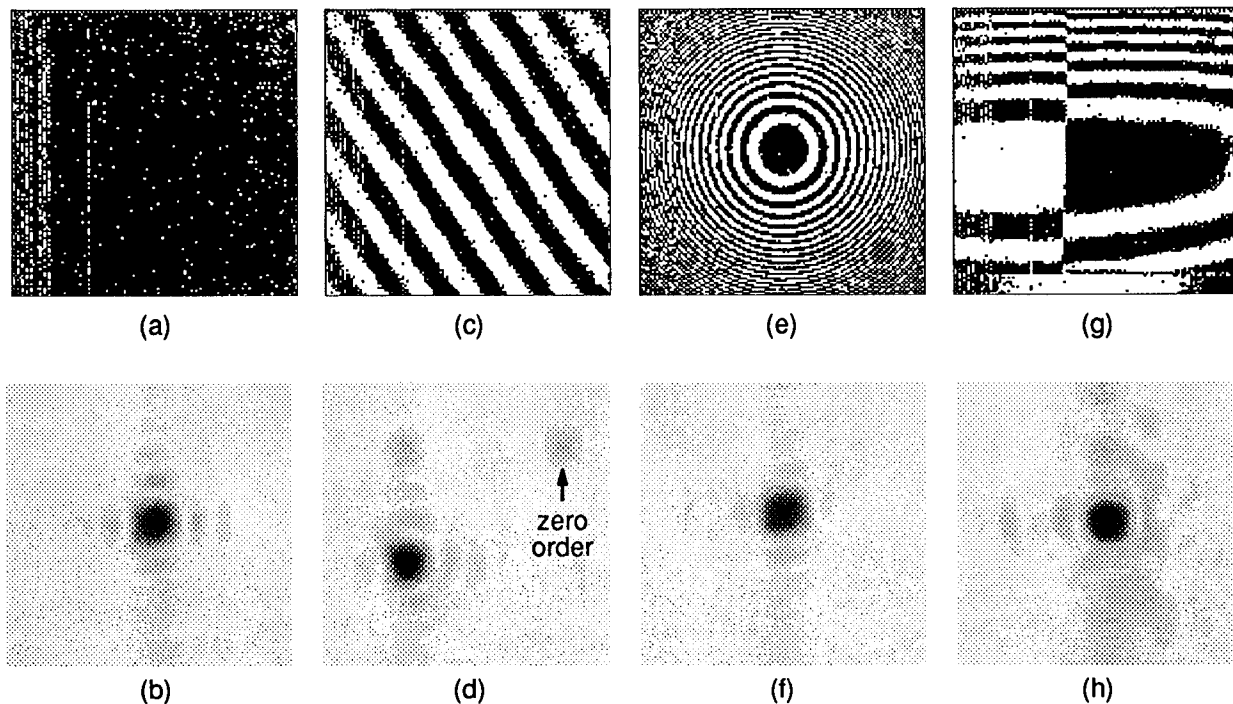


Figure 3 PPT and output plane patterns produced by on-line feedback for different optical configurations

image. It can be seen that the phase boundaries in the PPT pattern are not straight. This is attributable to very minor phase aberration in the system. The output again shows near diffraction limited performance.

Off Fourier plane, centre spot. Moving the detector along the optic axis a distance of 1.7mm from the Fourier plane resulted in the optimised pixel pattern in Fig. 3 (e). It closely approximates a pixelated Fresnel zone plate with first order focal length of 5.7m. The near diffraction limited performance is shown in Fig. 3 (f).

Fourier plane, centre spot, aberration correction. With the detector placed at the centre of the Fourier plane, on-line optimization was performed with a strongly aberrating component introduced into the system. The aberrator was a glass microscope slide which showed a multi-wavelength phase retardation variation in one direction and a sharp step of about half a wavelength in the other (due to the edge of a photoresist layer on the slide). It was placed about 6cm in front of the PPT. Fig. 3 (g) shows the optimized PPT pixel pattern and Fig. 3 (h) the resulting output. The pixel pattern closely resembles the known phase variation introduced by the aberrator with the step in phase correctly positioned and shown with striking clarity. As shown in Fig. 3 (h), a focal spot is clearly seen whereas, in the absence of correction the output is spread over the output plane.

Discussion and Conclusions

The DBS algorithm performs adequately in the relatively simple optimization problem that the single target spot poses. Even in more complex problems of this type the more time consuming algorithms such as the simulated annealing algorithm shows little improvement over DBS. Our results demonstrate that the on-line design method can perform as well as off-line for small pixel numbers and show only small degradation compared with off-line for up to 128×128 pixels. This is mainly attributed to quantization noise though aberration in the system plays a minor role. The malfunctioning pixels are evident in all PPT patterns shown in Fig. 3. The correction of a deliberately aberrated system demonstrates that on-line optimization can compensate automatically for some degradation in the quality of optical components. Our results can be regarded as demonstrating the system "tracking" a target with a spot of light, in principle at least, showing the capability of adaptively compensating for time dependant aberrations. Also, in performing a correction for a phase aberrator located near the PPT, the pixel pattern generated is a good approximation to the complex conjugate of the phase aberration within the limits of phase-quantization of the system. It therefore constitutes a new, direct means of determining phase aberration.

Acknowledgments

The authors would like to acknowledge valuable discussions with Professor G.G. Yang and the support of the UK Science and Engineering Research Council and the Ministry of Defence. One of us (RHS) wishes to acknowledge the provision of an SERC research studentship.

References

- [1] M.P.Dames, R.J.Dowling, P.McKee and D.Wood, "Efficient optical elements to generate intensity weighted spot arrays: design and fabrication," *Applied Optics*, vol. 30, no.19, pp. 2985–2691, 1991.
- [2] U.Mahlab, J.Rosen and J.Shamir, "Electro–optic hologram generation on spatial light modulators," *Journal of the Optical Society of America*, vol. 9, no. 7, pp. 1159–1166, 1992.
- [3] K.J.Weible and H.P.Herzig, "Optical optimization of binary phase fan–out elements," presented at the Fourth International Conference on Holographic Systems, Components and Applications, Neuchatel, IEE Conference Publication No.379, pp. 129–134, 1993.
- [4] Ferroelectric Liquid Crystal SLM, model 2DX128, manufactured by Smectic Technology Group, Thorn EMI Central Research Laboratories, Hayes, Middlesex, England.
- [5] S.E.Broomfield, M.A.A.Neil, E.G.S.Paige, and G.G.Yang, "Programmable binary phase–only optical device based on ferroelectric liquid–crystal SLM," *Electronics Letters*, vol. 28, no. 1, pp. 26–28, 1992.
- [6] S.E.Broomfield, M.A.A.Neil, E.G.S.Paige, R.H.Scarbrough, and G.G.Yang, "Programmable diffractive optics with a ferroelectric liquid crystal SLM in a binary phase–only mode," presented at Holographics International '92, London, Proceedings SPIE 1732, pp. 187–296, 1992.

Wednesday, June 8, 1994

Subwavelength and Coated Structures

DWB 10:30pm–12:00m
Room B

Thomas Keith Gaylord, *Presider*
Georgia Institute of Technology

Subwavelength structured surfaces: design and applications*

Daniel H. Raguin

Rochester Photonics Corporation, Rochester, NY 14623

G. Michael Morris

Institute of Optics, University of Rochester, Rochester, NY 14627

1. Introduction

One promising new aspect of diffractive optics is subwavelength structured (SWS) technology. Applications for SWS surfaces are numerous and can be divided into four basic categories: antireflection (AR) coatings, manufacture of polarization components, fabrication of narrowband filters, and production of phase plates, see Fig. 1.

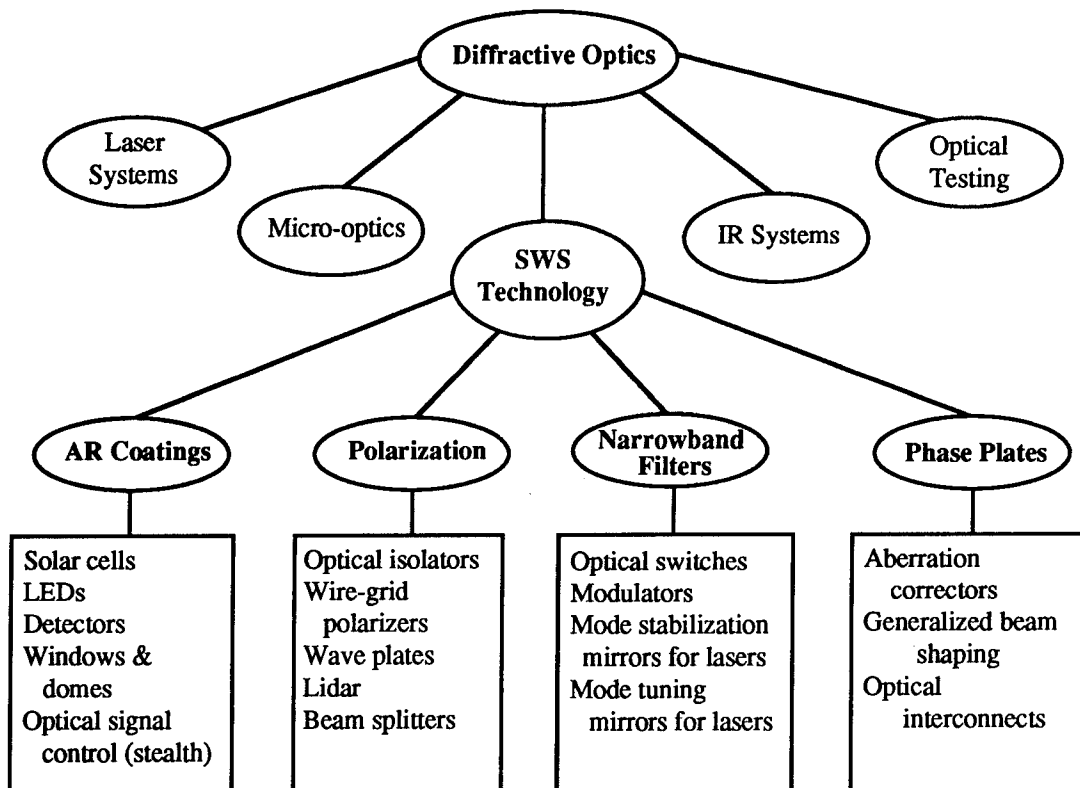


Fig. 1. Diagram illustrating several applications of diffractive optics. SWS technology is an important and promising new component of the field of diffractive optics. Some potential applications for SWS technology are listed.

SWS surfaces can take multiple forms. The grating can be of any type (e.g., surface-relief, phase or amplitude) provided the period is sufficiently fine so that no diffraction orders propagate other than the zeroth reflected and transmitted orders. Because of the fine periods involved, the fabrication of such surfaces for applications in the visible and infrared (IR) portions of the spectral regime has only recently been considered. With refinements in holographic procedures and the push of the semiconductor industry for submicron lithography (both through optical and electron beam techniques), production of SWS surfaces is increasingly

* This research has been sponsored in part by NASA, Jet Propulsion Laboratory, as well as by the Army Research Office.

viable. Replication procedures have also improved to the point whereby SWS surfaces can be mass-produced for specific applications.

As antireflection components, SWS surfaces are called antireflection structured (ARS) surfaces and have been studied extensively both theoretically and experimentally (see for example, Refs. 1-5). By structuring a surface with a subwavelength-period pattern, one can synthesize an appropriate index of refraction distribution so that surface reflections (for polarized or unpolarized radiation) are minimized. When designed properly, these structures can operate over large spectral bandwidths and fields of view.⁶ Because foreign materials are not being added to the substrate surface, problems commonly encountered in thin-film technology, such as adhesion and thermal expansion mismatches, are non-existent in the design of these structured surfaces..

As polarization components, SWS operate on the fact that unlike in the scalar diffraction regime (where the surface period is large compared to the incident wavelength), when feature sizes are on the order of a wavelength, radiation will react to the surface differently depending on the electric field's polarization orientation. Consequently, through SWS technology, polarization components such as wave plates and polarizers can be fabricated using solely isotropic material. SWS surfaces can be used to fabricate wire-grid polarizers, beam splitters, wave plates and retarders, and polarizing mirrors (see, for example, Refs. 5,7-9). Since the magnitude of an SWS surface's effective birefringence Δn (equal to $n_e - n_o$, where n_e and n_o are the structure's effective extraordinary and ordinary indices of refraction, respectively) can be quite large, see Fig. 2(a), the grating of the SWS surface need not be deeper than the wavelength of the incident radiation. Consequently, SWS surfaces are less bulky than conventional polarization devices and offer the possibility of replacing several conventional elements with a single structured one (e.g., beam splitter wave plates or mirror wave plates).

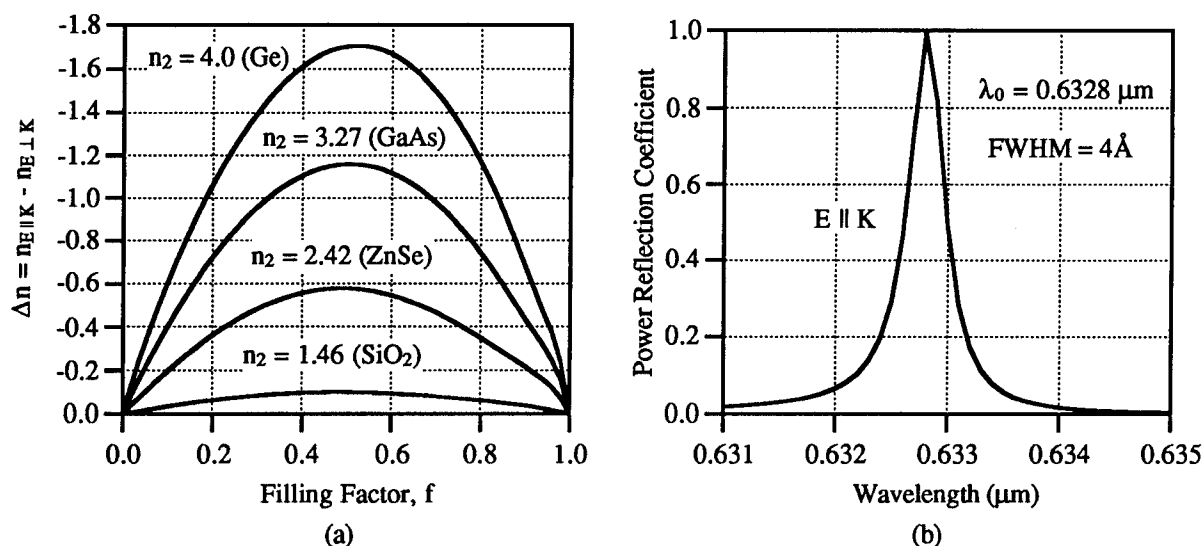


Fig. 2. Examples of SWS surface performance. In (a) we diagram the effective birefringence of 1-D binary SWS surfaces. These birefringent SWS effects allow one to fabricate wave plates and retarders from isotropic materials. In (b) we diagram a 4- \AA bandwidth SWS optical filter designed to operate at the HeNe wavelength of $\lambda_0 = 0.6328 \mu\text{m}$.

SWS surfaces can be used as narrowband filters (see, for example, Refs. 10,11). By fabricating the grating region so that its effective index of refraction is larger than that of the surrounding region, the structure has the potential to support the propagation of leaky (i.e., weakly-bound) waveguide modes. Coupling between the incident field and these leaky modes results in extremely sharp changes in the structure's spectral characteristics as a function of angle of incidence and wavelength, see Fig. 2(b). It is due to the highly-selective

coupling criterion of the waveguide mode that these structures can exhibit filter linewidths that are extremely narrow ($\Delta\lambda/\lambda = 10^{-7}$).¹⁰ These filters do not require the use of multi-layer film stacks as conventional film filters do, and are less bulky than Lyot filters.

SWS surfaces can also be used as an alternative method of fabricating phase plates.^{12,13} A specific form of phase plate, the zone plate, imparts a quadratic phase front on the incident radiation. This quadratic phase is achieved through an annular series of zones in which each zone contains a curved or multi-level profile designed through the use of scalar diffraction theory. With SWS surfaces, the zone plate can be replaced with a binary (two-level) structure.¹² This subwavelength binary structure should not be confused with the scalar binary approximation of a zone plate that achieves only 40.5% diffraction efficiency. By changing the duty cycle of the binary subwavelength structure as a function of the radius, the necessary phase delay to produce near 100% diffraction efficiency can be achieved. The advantage of using SWS surfaces is that a high-efficiency phase plate can be fabricated by using a single mask where otherwise multiple masks would be needed to achieve the same diffraction efficiency. The more masks used, the greater the risk of degrading the device's diffraction efficiency through errors in mask alignment.

SWS surfaces do not rely upon multi-layer thin-film coatings or birefringent materials in order to satisfy a specific system requirement (e.g., AR characteristics, polarization properties, beam splitting, or narrow-band filtering). Consequently, SWS surfaces give optical designers new degrees of freedom in the design of optical systems.

2. Subwavelength structured surface design

There are two basic methods of analyzing SWS surfaces: vector diffraction theory and effective medium theory (EMT). For accurate modeling of SWS surfaces, the use of vector diffraction theory is required since due to the feature sizes involved, scalar diffraction theories are completely invalid. The vector analysis we generally use is a rigorous coupled-wave analysis (RCWA) proposed by Gaylord and Moharam.¹⁴ Like most numerical techniques however, RCWA, due to its intensive computational requirements, offers little opportunity for intuitive insight into the diffraction mechanisms. An alternative method for analyzing SWS surfaces is through effective medium theory (EMT). By relying on the fact that the structures have feature sizes smaller than the incident wavelength, an approximate description of the interaction of radiation with such structures can be obtained. The results are analytic and offer a great deal of insight towards the radiation's behavior. The EMT we utilize is based upon work performed by Rytov.¹⁵

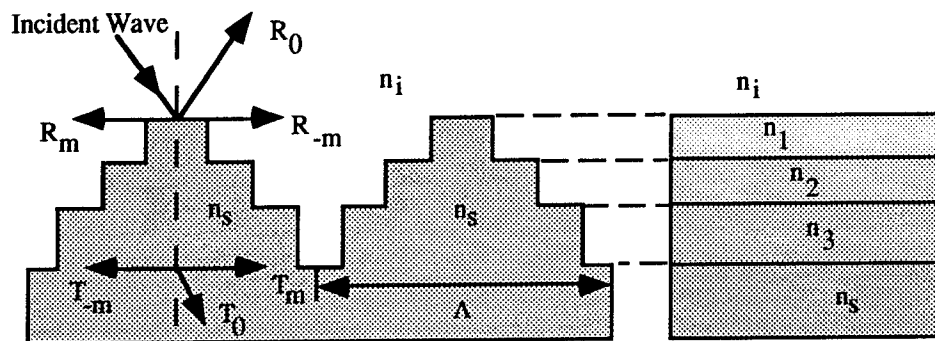


Fig. 3. A multi-level SWS surface profile with its corresponding film stack. Each layer of the film stack corresponds to a distinct level of the profile. Note that the grating period Λ is fine enough that only the zeroth orders, R_0 and T_0 , are propagating; higher diffraction orders are evanescent.

Effective medium theories (EMTs) rely on the fact that when light interacts with periodic structures much finer than its wavelength, it does not diffract, but instead reflects and transmits as if it is encountering a non-structured medium. EMTs describe the interaction of light with such subwavelength structures by

representing regions of subwavelength heterogeneity in terms of a homogeneous material possessing a single set of effective optical constants: permittivity ϵ , permeability μ , and conductivity σ . This is sensible since no energy is lost to diffracted orders; all the energy is contained in the zeroth transmitted and zeroth reflected orders. The optical properties of the effective medium are governed by the specific structural intermixing between the incident and substrate material, but in general, the more substrate material present as compared to incident material in a given region, the closer that region's optical properties are to those of the substrate. In other words, when light interacts with subwavelength structures, it reacts to them as if it were encountering an effective medium whose optical properties are a weighted spatial average of the profile region's optical properties.

For the specific case of a multi-level surface-relief profile, see Fig. 3, the effective medium will be a film stack where each layer of the film stack corresponds to a distinct level of the surface-relief profile. For a continuous profile, the effective medium will be a gradient film. Because the effective medium results from the weighted spatial averaging of the profile region's optical properties, the optical properties of the effective medium must be bound by the properties of the incident medium and those of the substrate medium. Therefore, assuming $n_i < n_s$ in Fig. 3, $n_i < n_1 < n_2 < n_3 < n_s$.

By using EMT, one gains intuition regarding the interaction of radiation with SWS surfaces. Through the use of EMT, one can obtain preliminary designs with regard to SWS surfaces used as AR coatings, polarization components, narrowband filters, or as phase plates. These preliminary designs can be fine-tuned and analyzed using more rigorous vector diffraction theories.

References

1. M. C. Hutley, "Coherent photofabrication," *Opt. Eng.* **15**, 190-196 (1976).
2. R. C. Enger and S. K. Case, "Optical elements with ultrahigh spatial-frequency surface corrugations," *Appl. Opt.* **22**, 3220-3228 (1983).
3. Y. Ono, Y. Kimura, Y. Ohta and N. Nishada, "Antireflection effect in ultrahigh spatial-frequency holographic relief gratings," *Appl. Opt.* **26**, 1142-1146 (1987).
4. N. F. Hartman and T. K. Gaylord, "Antireflection gold surface-relief gratings: experimental characteristics," *Appl. Opt.* **27**, 3738-3743 (1988).
5. D. H. Raguin, *Subwavelength Structured Surfaces: Theory and Applications*, Ph.D. Dissertation, University of Rochester, 1993.
6. D. H. Raguin and G. M. Morris, "Antireflection structured surfaces for the infrared spectral region," *Appl. Opt.* **32**, 1154-1166 (1993).
7. L. H. Cescato, E. Gluch and N. Streibl, "Holographic quarterwave plates," *Appl. Opt.* **29**, 3286-3290 (1990).
8. E. N. Glytsis and T. K. Gaylord, "High-spatial-frequency binary and multilevel stairstep gratings: polarization-selective mirrors and broadband antireflection surfaces," *Appl. Opt.* **31**, 4459-4470 (1992).
9. C. W. Haggans, L. Li, T. Fujita and R. Kostuk, "Lamellar gratings as polarization components for specularly reflected beams," *Journal of Modern Optics* **40**, 675-686 (1993).
10. R. Magnusson and S. S. Wang, "New principle for optical filters," *Appl. Phys. Lett.* **61**, 1022-1024 (1992).
11. S. Norton, D. H. Raguin and G. M. Morris, "Effective medium theory approach to guided-mode resonances," *Optical Design for Photonics* (OSA, Palm Springs, CA, 1993), vol. 10, pp. 143-146.
12. H. Haidner, P. Kipfer, W. Stork and N. Steibl, "Zero-order gratings used as an artificial distributed index medium," *Optik (Stuttgart)* **89**, 107-112 (1992).
13. M. W. Farn, "Binary gratings with increased efficiency," *Appl. Opt.* **31**, 4453-4458 (1992).
14. T. K. Gaylord and M. G. Moharam, "Analysis and applications of optical diffraction by gratings," *Proc. IEEE* **73**, 894-937 (1985).
15. S. M. Rytov, "The electromagnetic properties of finely layered medium," *Soviet Phys. JETP* **2**, 466-475 (1956).

Design of ideal reflection filters using resonant waveguide gratings

R. Magnusson and S. S. Wang
 Department of Electrical Engineering
 The University of Texas at Arlington
 Box 19016
 Arlington, TX 76019
 Phone: (817) 273-3474
 Fax: (817) 273-2253

The design of polarized reflective filters based on the guided-mode resonance properties of planar dielectric waveguide gratings is the topic of this paper. Theoretical analysis of these structures reveals sharp resonance phenomena where efficient transfer of light energy between forward and backward propagating waves occurs over small parameter ranges. This resonance effect is due to coupling of external diffracted fields with the modes of the waveguide. The theory and applications of planar waveguide-grating resonant devices have been presented in previous papers.¹⁻⁴ The purpose of the present contribution is to show that resonant waveguide-grating filters with symmetrical line shapes and low sidebands over wide wavelength regions can be designed and to give examples.

Experimental realization of planar dielectric waveguide grating filters has been reported by Gale *et al.*⁵ (embedded planar dielectric structure, optical region) and by Magnusson *et al.*⁶ (planar dielectric waveguide grating, microwave region). The characteristics measured have thus far exhibited non-ideal filter behavior, i.e. efficiencies that are too low for many applications, relatively high sidebands, and asymmetrical or split resonant lines.

A general multilayer model including interspersed spatially modulated and unmodulated layers has been analyzed using rigorous coupled-wave theory.⁷ An example embedded waveguide grating with a rectangular profile in a three-layer dielectric structure is shown in Fig.1. The modulated layer consists of alternating rectangular regions with relative dielectric permittivities ϵ_H and ϵ_L . It is required that the modulated layer be a waveguide grating and thus $\epsilon_{eff} = (\epsilon_H + \epsilon_L)/2 > \epsilon_1$ and ϵ_3 . Calculated reflectivity results for the TE polarization case are given in this paper.

In general, the spectral filter response has an asymmetrical line shape with respect to the central resonant wavelength for any waveguide-grating geometry. To produce a single-layer filter [as shown in Fig. 1(a)] with symmetrical spectral response, the thickness should be chosen as $d = m\lambda_{res}/2\sqrt{\epsilon_{eff}}$ where $m = 1, 2, 3, \dots$ and λ_{res} is the free-space resonance wavelength. An example for an asymmetric ($\epsilon_a \neq \epsilon_s$) waveguide grating is shown in Fig. 2 with the thickness equal to the wavelength (i. e., $m = 2$). If additionally $\epsilon_a = \epsilon_s$ the sidebands are brought down according to the classical antireflection (AR) condition for a half-wave layer. Thus the net result is an efficient reflection filter at the resonant wavelength but with the reflected power outside of the resonance region suppressed by the AR design. The guided-mode resonance effect and the classical single- or multilayer antireflection effect are seen to operate independently even with respect to the same layer since, in this example, the same layer serves as the waveguide grating supporting the resonance and as the antireflection layer suppressing reflection around the resonance.

A waveguide-grating filter in a double-layer design is given in Fig. 1(b). An AR design is obtained for $d_1 = \lambda_{res}/4\sqrt{\epsilon_1}$ and $d_2 = \lambda_{res}/4\sqrt{\epsilon_{eff}}$. Figure 3 demonstrates the symmetrical line shape of the filter when the resonance is within the near-zero reflection corridor. In contrast to

the single-layer filter, this shows that the grating thickness does not have to be a multiple of a half-wavelength to provide symmetrical lines. The reflectivity around the resonance peak is suppressed to remain less than 0.2% for $540 \text{ nm} < \lambda < 580 \text{ nm}$.

To achieve broad-band reflectivity suppression, additional antireflection layers can be used as in Fig. 1(c). The spectral response of a three-layer design is illustrated in Fig. 4. In this case, $d_1 = \lambda_0/4\sqrt{\epsilon_1}$, $d_2 = \lambda_0/4\sqrt{\epsilon_{\text{eff}}}$, and $d_3 = \lambda_0/4\sqrt{\epsilon_3}$ where λ_0 is chosen as 550 nm. A broad low-reflectance covering the entire visible region is shown [solid curve in Fig. 4 (a)] except at the filter resonance wavelength $\lambda_{\text{res}} = 553.3 \text{ nm}$. This example shows that it is not necessary that the design wavelength λ_0 be identical to λ_{res} . In fact, the filter resonance peak can be placed anywhere within the AR region by properly varying the grating period while still producing a symmetrical line shape and low sidebands. If region 1 is not a quarter-wave layer, this is no longer an antireflection design and the filter response has an asymmetrical line shape and high reflective sidebands [dashed curve in Fig. 4 (b)]. Again, the guided-mode resonance effect and the effect of the antireflection layer are independent with the resonance effect overriding the AR conditions at the resonance wavelength. Here, the waveguide-grating layer was selected to be a $\lambda/4$ layer to conform to the particular AR design illustrated.

As long as the guided-mode resonance waveguide-grating layer is a part of a proper AR design, based on the effective thin-film character of the waveguide grating, symmetrical-line ideal reflection filters can be designed. The central (resonance) wavelength, the line width, the width of the AR region within which the resonance peak lies, the reflectivity values adjacent to the resonance, and the resonance line shape, are all under the control of the designer. The principles introduced in this paper are applicable in general to planar waveguide gratings with arbitrary grating profiles and arbitrary angles of incidence and to TM polarized incident waves.

1. S. S. Wang, R. Magnusson, J. S. Bagby, and M. G. Moharam, "Guided-mode resonances in planar dielectric-layer diffraction gratings," *J. Opt. Soc. Am. A* **8**, 1470-1475 (1990).
2. S. S. Wang, R. Magnusson, J. S. Bagby, and M. G. Moharam, "Waveguide mode-induced resonances in planar diffraction gratings," *Optical Society of America 1989 Annual Meeting Technical Digest*, 117 (1989).
3. R. Magnusson and S. S. Wang, "New principle for optical filters," *Appl. Phys. Lett.* **61**, 1022-1024 (1992).
4. S. S. Wang and R. Magnusson, "Theory and applications of guided-mode resonance filters," *Appl. Opt.* **32**, 2606-2613 (1993).
5. M. T. Gale, K. Knop, R. H. Morf, "Zero-order diffractive microstructures for security applications," *Proc. SPIE on Optical Security and Anticounterfeiting Systems* **1210**, 83-89 (1990).
6. R. Magnusson, S. S. Wang, T. D. Black, and A. Sohn, "Resonance properties of dielectric waveguide gratings: Theory and experiments at 4-18 GHz," to appear in *IEEE Transactions on Antennas and Propagation* in April 1994.
7. T. K. Gaylord and M. G. Moharam, "Analysis and applications of optical diffraction by gratings," *Proc. IEEE* **73**, 894-937 (1985).

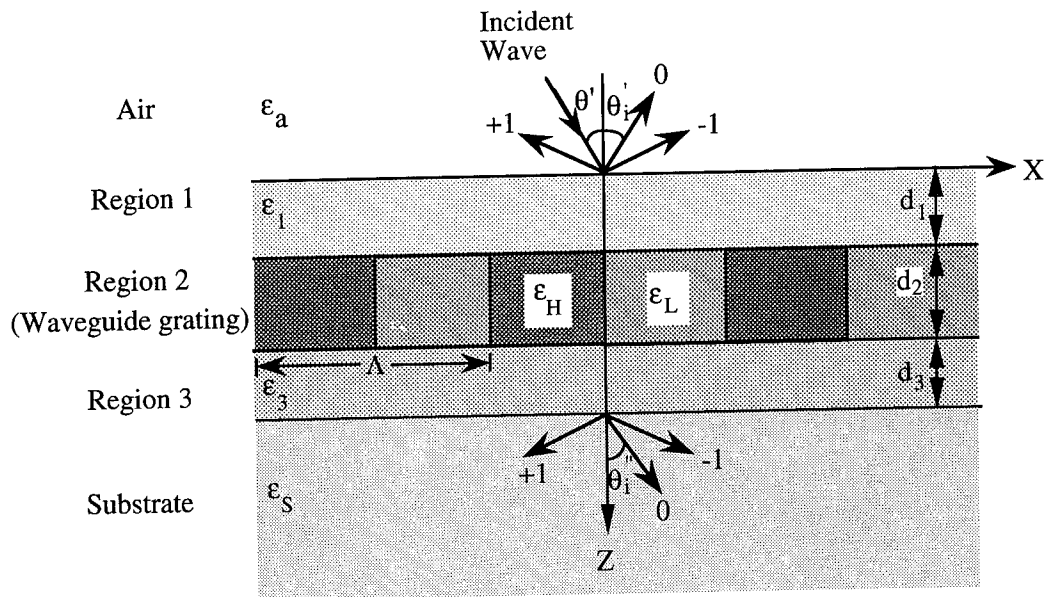


Figure 1. The multi-layer, square-wave profile waveguide grating model used. (a) Single-layer waveguide grating geometry where $d_1 = 0$, $d_2 \neq 0$, and $d_3 = 0$. (b) Double-layer waveguide grating geometry where $d_1 \neq 0$, $d_2 \neq 0$, and $d_3 = 0$. (c) Triple-layer waveguide grating geometry where $d_1 \neq 0$, $d_2 \neq 0$, and $d_3 \neq 0$.

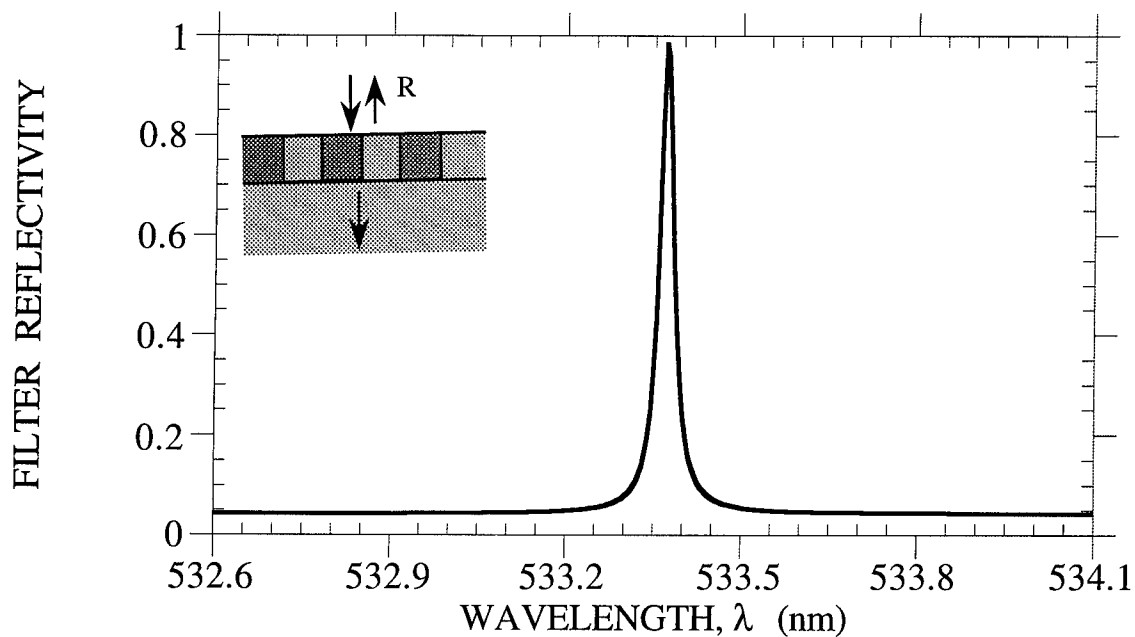


Figure 2. The TE spectral response of a single-layer waveguide-grating filter where the thickness $d_2 = 355$ nm (half-wavelength) is determined at the resonance wavelength $\lambda_{\text{res}} = 533.4$ nm. The other parameters are $\epsilon_a = 1.0$, $\epsilon_H = 2.62$, $\epsilon_L = 2.31$, $\epsilon_s = 2.31$, $\Lambda = 350$ nm, and $\theta' = 0^\circ$.

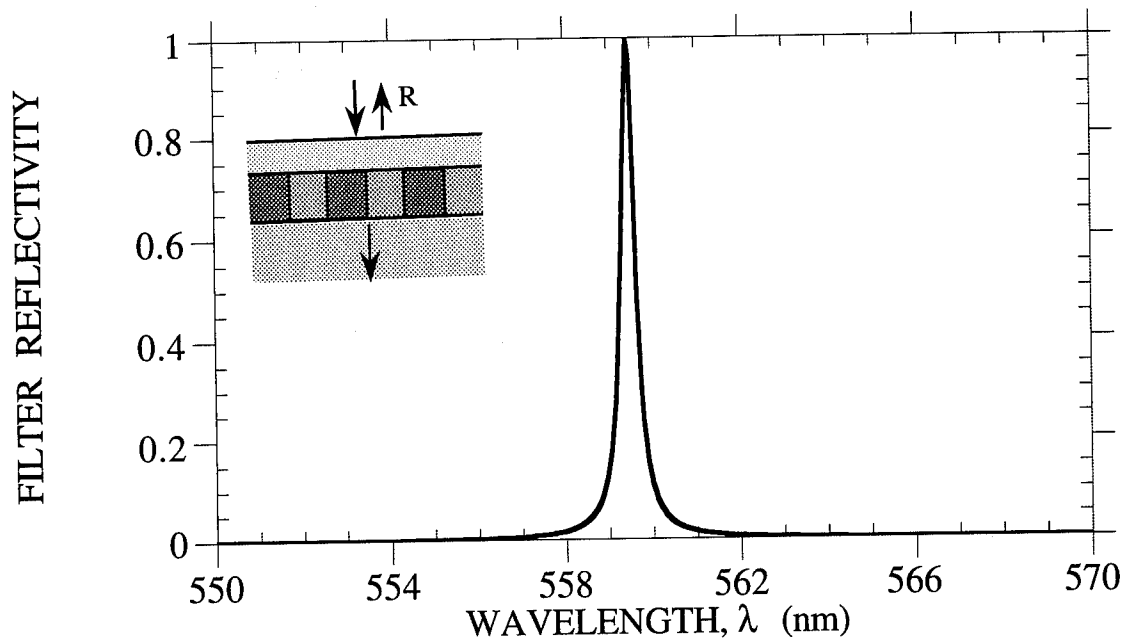


Figure 3. The TE spectral response of a double-layer waveguide-grating filter where the thicknesses $d_1 = 88.4$ nm (quarter-wavelength) and $d_2 = 71.7$ nm (quarter-wavelength) are determined at the resonance wavelength $\lambda_{res} = 559.5$ nm. The other parameters are $\epsilon_a = 1.0$, $\epsilon_1 = 2.5$, $\epsilon_H = 4.0$, $\epsilon_L = 3.61$, $\epsilon_s = 2.31$, $\Lambda = 350$ nm, and $\theta' = 0^\circ$

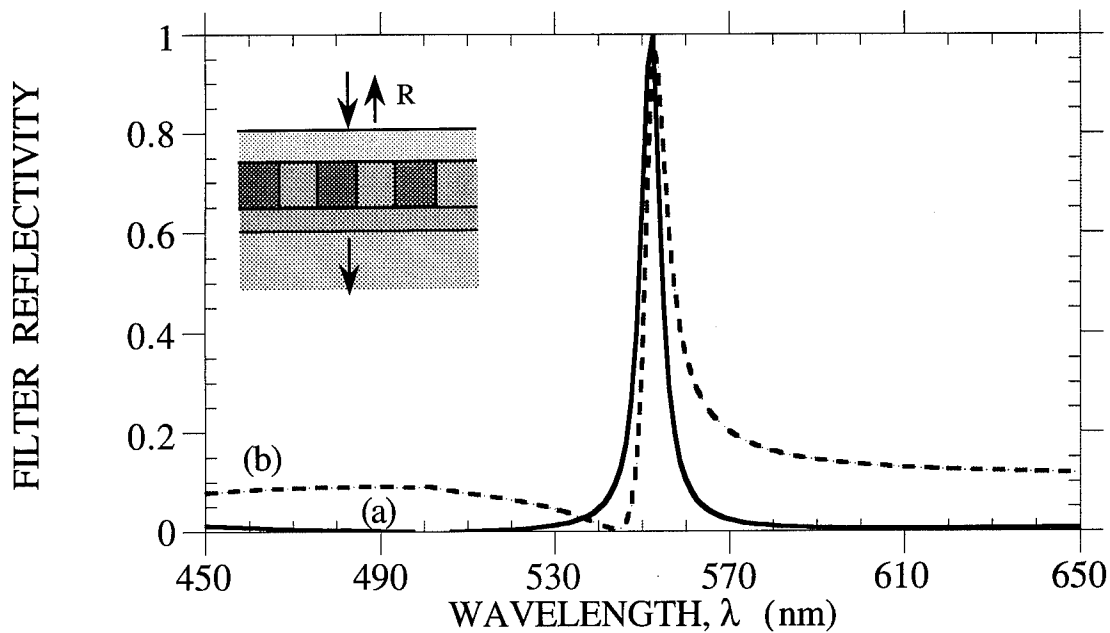


Figure 4. The TE spectral response of a triple-layer waveguide-grating filter. The parameters are $\epsilon_a = 1.0$, $\epsilon_1 = 1.904$, $\epsilon_H = 4.93$, $\epsilon_L = 3.24$, $\epsilon_3 = 3.24$, $\epsilon_s = 2.31$, $\Lambda = 330$ nm, $\theta' = 0^\circ$, $d_2 = 68$ nm (quarter-wavelength), and $d_3 = 76$ nm (quarter-wavelength). The thicknesses are determined at the wavelength of 550 nm. (a) AR design; $d_1 = 100$ nm (quarter-wavelength). (b) non-AR design; $d_1 = 200$ nm (half-wavelength).

Two Dimensional Subwavelength Gratings as Artificial Anisotropic Media

Eric B. Grann, M.G. Moharam, and Drew A. Pommet

Center for Research and Education in Optics and Lasers

University of Central Florida, Orlando, FL 32826

Tel: (407) 658-3983 Fax: (407) 658-6880

Introduction

Light propagates through subwavelength gratings in approximately the same manner that light travels through homogeneous non-corrugated mediums. Effective Medium Theory (EMT) relates the parameters of a stratified layer to that of an effective homogeneous uniaxial or biaxial thin film, depending on the grating structure.

A symmetric two dimensional subwavelength grating is analogous to a uniaxial thin film ($L_x/\Lambda_x = L_y/\Lambda_y$) while an asymmetric two dimensional subwavelength grating is analogous to a biaxial thin film (see Fig.1).

While the properties of one dimensional subwavelength gratings have been analyzed in great detail¹⁻⁹, there has been limited work done in the area of two dimensional gratings. An approximate closed form static EMT solution for a symmetric 2-D grating was proposed by Southwell¹⁰. This predicted solution significantly differs from exact effective index results obtained by the rigorous coupled wave technique (RCWA)². Raguin et. al.¹², designed 2-D symmetric pyramidal structures for reducing reflections. There is still very little known about the behavior of 2-D gratings and all the effective optical properties they possess.

In this paper, we will be focusing on 2-D symmetric and asymmetric subwavelength structures. We will describe a method for determining the effective dielectric constants, using RCWA, as a function of the refractive indices of the substrate, and the duty cycle (fill factor) of the 2-D grating. A theoretical formalization for $n_{\text{eff}}(z)$, effective index in the normal direction, is presented, as well as RCWA results to show the validity of this expression. Using these 2-D effective properties, we will synthesis a multi-level antireflection structure for unpolarized light over a broadband.

Zeroth Diffracted Order Two Dimensional Gratings

An electromagnetic wave that is incident upon a subwavelength grating, will behave as if it is incident on a uniform homogeneous medium, in that there will only be a reflected and

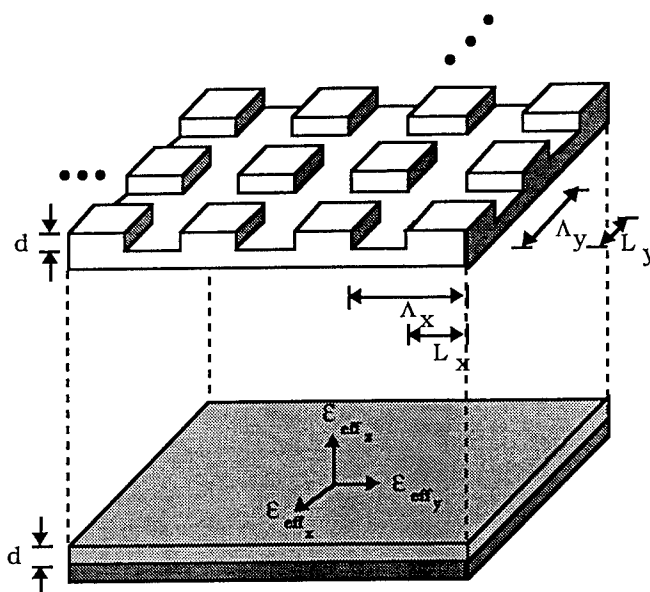


Figure 1 2-D Subwavelength Grating.

transmitted wave. Such a grating is called a zeroth diffracted order grating. The creation of a zeroth order grating is dependent on forcing all of the higher order diffracted fields to be evanescent. In order for this condition to be satisfied, the normalized grating periods along each axis must be

$$\frac{\Lambda_x}{\lambda} < \frac{1}{\max[n_s, n_i] + |n_i \sin \theta_i \cos \phi_i|} \quad (1)$$

$$\frac{\Lambda_y}{\lambda} < \frac{1}{\max[n_s, n_i] + |n_i \sin \theta_i \sin \phi_i|}, \quad (2)$$

where max refers to the maximum value of either n_s , the refractive index of the substrate medium, or n_i , the refractive index of the incident medium.

Effective Medium Theory for 2-D binary grating

Attempts at deriving a closed form solution for the effective permittivities of a 2-D subwavelength grating have not been successful with even a zeroth or static case solution. Due to the rectangular nature of a 2-D grating, a useable characteristic dispersion equation is very difficult to derive. Therefore, the effective permittivities of the structure can not be expressed in a closed form. However, the relationship between the two fill factors and the resultant effective axial permittivities can be determined numerically using RCWA.

The reflected or transmitted power for a given grating structure may be obtained using RCWA. The effective index at normal incidence can then be found by solving the transmission line equation. By scanning the fill factor from $0 \rightarrow 1$, one may obtain a design curve for each particular substrate of interest. In order to obtain the two indices perpendicular to the normal, two separate cases must be examined. Propagating a wave along the z-axis, with the electric field polarized along the x-axis, will produce a reflection which corresponds to that produced by an effective index n_x . Similarly, propagating a wave along the z-axis, with the electric field along the y-axis, will produce a reflection which corresponds to that produced by an effective index n_y . Figure 2 shows the effective index n_y , for $n_s = 3.0$ as a function of the asymmetrical fill factor with the following parameters: $n_i = 1.0$, $n_s = 3.0$, $\Lambda/\lambda = 0.001$. In order to find the effective index, n_x , one needs only to switch the axis labels ($f_x \rightarrow f_y$ and $f_y \rightarrow f_x$).

In order to completely define the effective homogeneous medium, the third

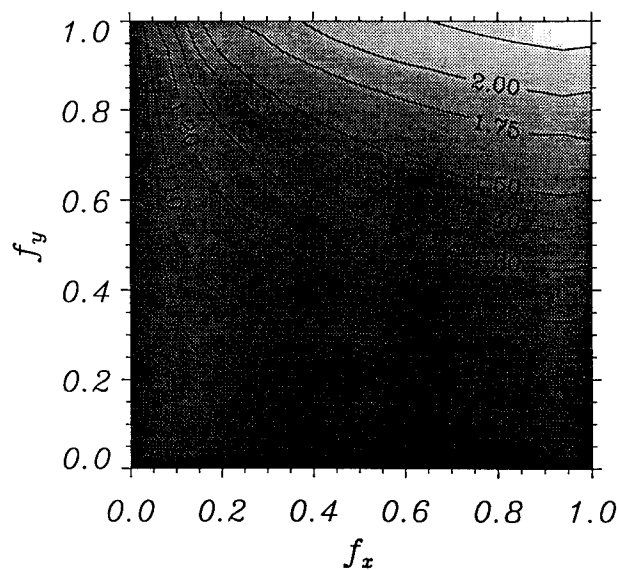


Figure 2 Effective Index n_y .

index n_z , corresponding to the axis perpendicular to both the grating vectors, must be defined. This result can be derived using 1-D EMT.

$$\epsilon_{eff} = \epsilon_s f_x f_y + \epsilon_i (1 - f_x f_y) = \epsilon_z^{(0)} \quad (3)$$

Figure 3 shows a comparison between an effective homogeneous biaxial thin film and RCWA at oblique incidence for $\phi = 45^\circ$. The asymmetric 2-D grating is defined by the following parameters: $n_1 = 1.0$, $n_s = 3.0$, $f_x = 40\%$, $f_y = 80\%$, $\Lambda/\lambda = 0.001$, and $d = 0.20\lambda$. The effective biaxial indices were found to be $n_x = 1.2464$, $n_y = 1.5312$ and $n_z = 1.8868$. The results obtained from the figure, indicates that an asymmetric 2-D subwavelength grating is in fact analogous to a biaxial thin film.

Design of Broadband Antireflection Surfaces

Let us consider an air-substrate interface of $n_i = 1.0$ and $n_s = 3.0$. We are interested in designing an antireflection surface for operation from $8\mu\text{m}$ to $12\mu\text{m}$, using two layers. From the Tschebyscheff synthesis technique¹², we find that the first layer has $n_1 = 2.247$ and $d_1 = 1.068\mu\text{m}$ and the second layer has $n_2 = 1.335$ and $d_2 = 1.797\mu\text{m}$. Let us compare this design for a thin film, a 1-D polarized subwavelength grating, a 1-D unpolarized grating, and a 2-D unpolarized grating. For a 1-D grating with $E \perp K$, the fill factors are $f_1 = 50.20\%$ and $f_2 = 9.73\%$. For $E \parallel K$, the fill factors are $f_1 = 89.98\%$ and $f_2 = 48.98\%$. For the 2-D, the symmetrical fill factors are $f_1 = 89.03\%$ and $f_2 = 55.98\%$. All of the subwavelength grating designed had a grating period of $\Lambda/\lambda = 0.05$. Figure 4 shows the thin film results versus the RCWA results for each two layer subwavelength grating designed.

Summary and Conclusions

It has been demonstrated that the normal incident effective indices of a two dimensional subwavelength grating could be found through the use of Rigorous Coupled Wave Analysis. It was shown, that the effective index parallel to the normal could be derived. A symmetrical 2-D

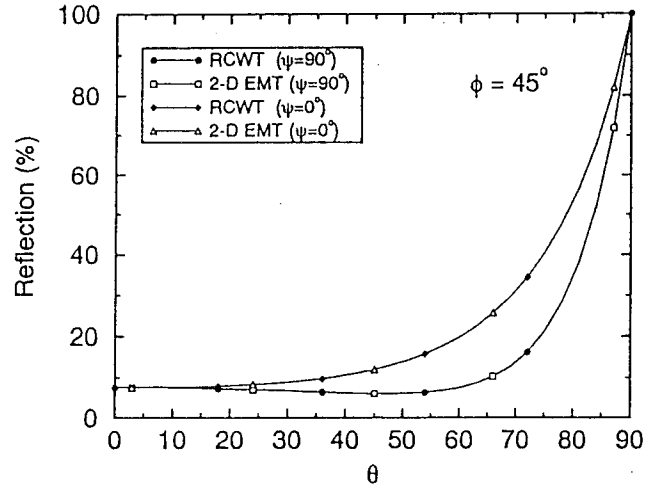


Figure 3 Comparison of 2-D EMT to RCWA

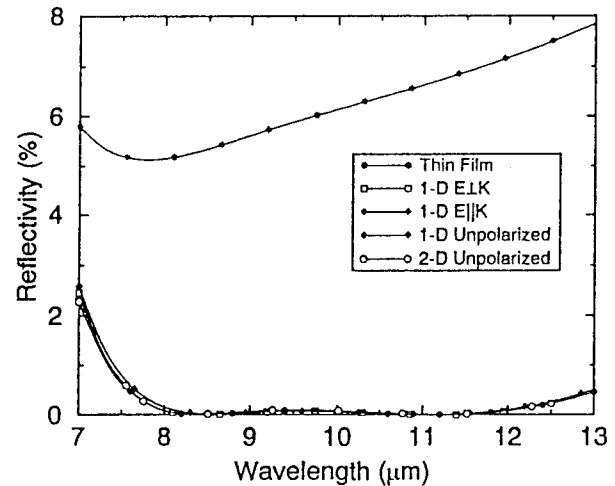


Figure 4 2-layer AR results.

grating has been shown to exhibit uniaxial properties, while an asymmetrical 2-D grating had been shown to exhibit biaxial properties. Using these results, it was possible to design a multi-level symmetric 2-D subwavelength grating to reduce reflections over a broadband.

References

- 1) D. Raguin and G. M. Morris, "Antireflection structured surfaces for the infrared spectral region," *Applied Optics*, vol. 32, pp. 1154-1167, 1993.
- 2) D. Raguin and G. M. Morris, "Analysis of antireflection-structured surfaces with continuous one-dimensional surface profiles," *Applied Optics*, vol. 32, pp. 2582-2598, 1993.
- 3) W. Stork, N. Striebl, H. Hainer, and P. Kipfer, "Artificial distributed-index media fabricated by zero-order gratings," *Optics Letters*, vol. 16, pp. 1921-1923, 1991.
- 4) Y. Ono, Y. Kimura, Y. Ohta, and N. Nishida, "Antireflection effect in ultrahigh spatial-frequency holographic relief gratings," *Applied Optics*, vol. 26, pp. 1142-1146, 1987.
- 5) T. K. Gaylord, W. E. Baird, and M. G. Moharam, "Zero-reflectivity high spatial-frequency rectangular-groove dielectric surface-relief gratings," *Applied Optics*, vol. 25, pp. 4562-4567, 1986.
- 6) E. N. Glytsis and T. K. Gaylord, "High-spatial-frequency binary and multilevel stairstep gratings: polarization-selective mirrors and broadband antireflection surfaces," *Applied Optics*, vol. 31, pp. 4459-4470, 1992.
- 7) D. C. Flanders, "Submicrometer periodicity gratings as artificial anisotropic dielectrics," *Applied Physics Letters*, vol. 42, pp. 492-494, 1983.
- 8) C. W. Haggans, L. Li, and R. K. Kostuk, "Effective medium theory of zeroth order lamellar gratings in conical mountings," To be Published.
- 9) S. M. Rytov, "Electromagnetic properties of a finely stratified medium," *Soviet Physics JETP*, vol. 2, pp. 466-474, 1956.
- 10) M. E. Motamedi, W. H. Southwell, and W. J. Gunning, "Antireflection surfaces using binary optics technology," *Applied Optics*, vol. 31, pp. 4371-4376, 1992.
- 11) M. G. Moharam, "Coupled-Wave Analysis of Two-Dimensional Dielectric Gratings," in *Holographic Optics: P Design and Applications*, I. Cindrich, ed., Proc. of the Photo-Opt. Instrum. Eng. vol. 883, pp. 8-11, 1988.
- 12) Henry J. Riblet, "General Synthesis of Quarter-Wave Impedance Transformers," *IRE Transactions on Microwave Theory and Techniques*, MTT-5, pp. 36-43, 1957.

Numerical Modeling of Multilayer-Coated Gratings

Lifeng Li

Optical Sciences Center, University of Arizona, Tucson, Arizona 85721

Tel: (602) 621-1789, Fax: (602) 621-4358

I. Introduction

In many applications, surface relief gratings are coated with one or more dielectric layers to enhance diffraction efficiency and, in the case of metallic gratings, to prevent the metal surface from tarnishing. Coated gratings, as compared to bare gratings, present certain analytical difficulties that not every grating method is equipped to deal with. Only those methods, such as the integral method¹ and the extinction-theorem method², that explicitly take the grating contour into account are naturally suited for coated gratings. In the early 1980s, Chandezon *et al.*^{3,4} presented a new differential formalism for multi-coated gratings that was applicable in the entire optical region. Subsequently, the method was generalized to the conical mountings by Popov and Mashev⁵, and at a much later time by Elston *et al.*⁶ In this paper, following Popov and Mashev⁷, the method of Chandezon *et al.* is referred to as the C method.

Chandezon *et al.* acknowledged in their paper⁴ that numerical problems prevented them "from achieving the computations when the total thickness of dielectric exceeds one wavelength, or when the number of layers exceeds eight." The present work makes two major improvements to the existing C method. First, the limitations mentioned above are completely removed by the use of the *R* matrix propagation algorithm. Second, the computation time that is required for gratings in conical mountings is greatly reduced by a mathematical reformulation of the C method.

II. The Differential Method of Chandezon *et al.*

1. Review

Figure 1 illustrate the grating diffraction configuration. A monochromatic plane wave is incident on a multilayer coated grating at polar angle θ and azimuth angle ϕ . The notation for the medium permittivities and interfaces are shown in Fig. 2 where $Q \geq 0$ is the total number of coatings. The grating profile function $f(x)$ can be arbitrary, provided that it is a continuous and single-valued function of x . All corrugated surfaces are assumed to have the same functional form except for their vertical offsets.

The ingenuity of the C method is to solve Maxwell's equations for the grating problems in a curvilinear coordinate system $Ox_1x_2x_3$ that is defined by

$$x_1 = x, \quad x_2 = y - f(x), \quad x_3 = z, \quad (1)$$

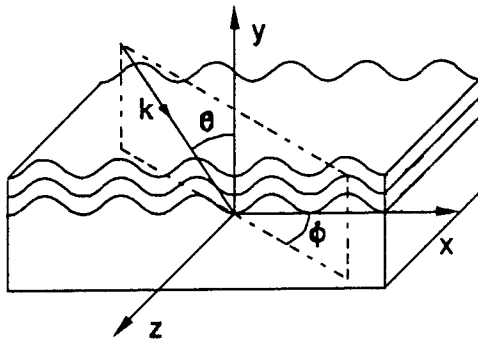


Figure 1. Conical Diffraction Geometry

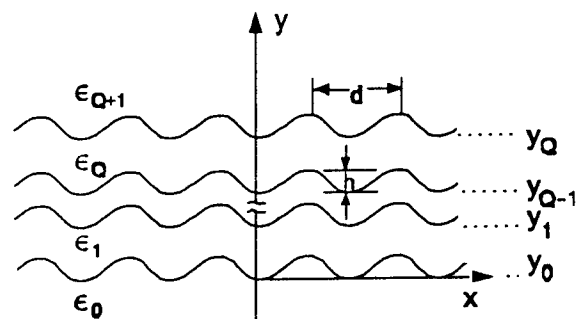


Figure 2. Notation .

where $Oxyz$ is the Cartesian coordinate system in Fig. 1. By writing Maxwell's equations in this coordinate system and expanding the fields in Fourier series, the following equation can be derived for the vector components of the fields:

$$\frac{1}{i} \frac{d}{dx_2} F = M F, \quad (2)$$

where

$$F = (E_3^T, H_3^T, \frac{k_0}{i} H_1^T, \frac{k_0}{i} E_1^T)^T, \quad (3)$$

with k_0 being the length of the wavevector in vacuum, and M is an x_2 -independent square matrix whose expression can be found in Refs. 5, 6 and 8. In Eq. (3), each vector entry is also a vector whose elements are the Fourier expansion coefficients of the corresponding field. In a spatial region that is bound above and below by two curved surfaces, the solution of Eq. (2) can be written as

$$F(x_2) = W \exp[i(x_2 - x_2^*)D] W^{-1} F(x_2^*), \quad (4)$$

where W is the matrix formed by the eigenvectors of M , D is the diagonal matrix formed by the eigenvalues of M , and x_2^* is an arbitrary constant. According to Chandezon *et al.*⁴ it is best to compose the field in the two semi-infinite regions by two distinctive parts. The first part consists of the incident and the propagating diffracted waves, both expressed as the usual Rayleigh expansions. The second part consists of those solutions of Eq. (2) that decay exponentially away from the grating. Upon decomposing the Rayleigh part of the field along directions of x_1 and x_3 , the fields on the top and bottom grating surfaces can be written as

$$F(x_2 = y_Q) = Z_f^{(Q+1)} (\tilde{R}^T, \tilde{I}^T)^T, \quad F(x_2 = y_0) = Z_f^{(0)} (\tilde{J}^T, \tilde{T}^T)^T, \quad (5)$$

where \tilde{R} , \tilde{I} , \tilde{T} , and \tilde{J} are the diffracted and incident field amplitude vectors in the top and the bottom media, respectively, and $Z_f^{(Q+1)}$ and $Z_f^{(0)}$ are two matrices. The exact definitions of all these quantities are given in Ref. 8.

Since the coordinate surface $x_2 = \text{constant}$ is parallel to the grating surfaces, all vector components on the right hand side of Eq. (3) are continuous across the medium interfaces. It then follows that

$$Z_f^{(Q+1)} (\tilde{R}^T, \tilde{I}^T)^T = \left[\prod_{j=1}^Q W_j \exp(i e_j D_j) W_j^{-1} \right] Z_f^{(0)} (\tilde{J}^T, \tilde{T}^T)^T, \quad (6)$$

where $e_j = y_j - y_{j-1}$. In principle, the solution to the grating problem is completed at this point. Indeed, as has been done in Refs. 4-6, the matrix multiplications on the right hand side of Eq. (6) can be performed first, and then a system of linear equations having the complex diffraction amplitudes as unknowns can be derived and numerically solved with a standard technique. In reality, however, it turns out to be a non-trivial matter as to how the linear system is derived from Eq. (6), when a finite word-length computer is used. This point shall be returned to in Subsection II.3.

2. Reduction of Computational Time

Suppose the truncation order, i.e., the number of spatial harmonics retained in the computation, is N . Then the dimension of matrix M in Eq. (2) is $4N$ and $2N$ in conical and classical (assuming the incident light is purely TE or TM) mountings, respectively. Numerical testing shows that the bulk of the execution time of a computer program based on the C method is spent on the calculation of the eigenvalues and eigenvectors of matrix M and this amount of time is roughly proportional to the cube of the dimension of M . Therefore, the computation time for a grating in a conical mounting would be about eight times of that for the same grating in a classical mounting.

However, a careful analysis of the eigenvalue problem associated with the C method uncovers the following important result: *The eigenvalues of matrix M in Eq. (2) for a conical mounting can be deduced from the eigenvalues of matrix M' for a related classical mounting (in TE or TM polarization). Furthermore, the eigenvectors of M can be constructed from the eigenvectors of M' without further matrix computation.* Therefore, the computation time for gratings in conical mountings can be greatly reduced. A mathematical proof of the statement above is given in Ref. 8. Here, only the procedure for constructing the eigensolutions is outlined.

For a given grating, a conical mounting is uniquely defined by the wavevector of the incident plane wave, $\vec{k}_0 = \alpha_0 \mathbf{x} - \beta_0 \mathbf{y} + k_z \mathbf{z}$, where $k_z \neq 0$. For each conical mounting, an induced classical mounting can be defined by the incident wavevector $\vec{k}'_0 = \alpha_0 \mathbf{x} - \beta_0 \mathbf{y}$. Suppose the set of eigenvalues of matrix M' associated with \vec{k}'_0 (for TE polarization) is $\{\lambda\}$ and its eigenvectors are $(p_\lambda^T, q_\lambda^T)^T$, where p_λ and q_λ are N dimensional column vectors after truncation. Then each eigenvalue λ of M' is also a doubly degenerate eigenvalue of matrix M associated with \vec{k}_0 , and the two eigenvectors $v_{1\lambda}$ and $v_{2\lambda}$ of M corresponding to λ are related to p_λ and q_λ as follows,

$$v_{1\lambda} = \left(p_{m\lambda}, 0, \frac{k_0^2 \epsilon \mu}{\tilde{k}^2} q_{m\lambda}, \frac{k_0 k_z}{\tilde{k}^2} \alpha_m p_{m\lambda} \right)^T, \quad v_{2\lambda} = \left(0, p_{m\lambda}, \frac{k_0 k_z}{\tilde{k}^2} \alpha_m p_{m\lambda}, -\frac{k_0^2 \mu^2}{\tilde{k}^2} q_{m\lambda} \right)^T, \quad (7)$$

where $\alpha_m = \alpha_0 + 2\pi m/d$, $\tilde{k}^2 = k_0^2 \epsilon \mu - k_z^2$, and representative vector elements with subscript m have been used to denote the respective N dimensional column vectors.

The procedure described above reduces the computation time for computing the eigenvalues and eigenvectors of matrix M in conical mountings to little more than what is needed for a classical mounting in TE or TM polarization.

3. Removal of Limitations on Layer Thicknesses and Number of Layers

As hinted at the end of Subsection II.1, convergence difficulties may arise if the linear system of equations for determining the unknown diffraction amplitudes is derived by first performing the matrix multiplication in Eq. (6). The cause of the difficulties is a combination of the presence of the very large imaginary part of the eigenvalues in the diagonal matrices D_j and the finite precision of the digital computer. The situation here is exactly the same as the situation where the classical modal method was used to treat arbitrary grating profiles by the use of the multilayer lamellar grating approximation⁹. There, the R matrix propagation algorithm was used with spectacular success to remove numerical instabilities that occurred for deep gratings. This algorithm can be used here without any change. For information about the R matrix propagation algorithm, the reader is referred to Ref. 9.

However, there is a subtlety in applying the algorithm to the present situation that the reader should be made aware of. In order to apply the R matrix propagation algorithm, the matrix product in the square brackets in Eq. (6) has to be factored appropriately into products of what are called the sector t matrices. The factorization as it stands now in Eq. (6) has been numerically proven to yield inferior results⁸. *It is absolutely essential that the exponential term, if it appears in a t matrix, be exposed on the left side of the t matrix.* The following factorization seems to be a good choice:

$$\prod_{j=1}^Q W_j \exp(i e_j D_j) W_j^{-1} = W_Q \cdot \prod_{j=2}^Q \left[\exp(i e_j D_j) W_j^{-1} W_{j-1} \right] \cdot \exp(i e_1 D_1) W_1^{-1}. \quad (8)$$

When the R matrix propagation algorithm is properly implemented, a computer program based on the improved C method should produce convergent results without any of the numerical difficulties that have been experienced by the previous authors regarding the total layer thickness and the total number of layers.

III. Numerical Examples

In this section, two examples are given to demonstrate the effectiveness of the improved C method in modeling gratings having a large number of coatings of varying thicknesses. In these examples, the (vertical) optical thicknesses of all layers are the same and they are measured in normalized thickness which is defined by $r_j = (e_j \sqrt{\epsilon_j})/\lambda$, where $1 \leq j \leq Q$, and λ is the vacuum wavelength. All gratings in the examples are used in first order Littrow mount in TM polarization.

The first example, shown in Fig. 3, is for an eight-layer-coated sinusoidal aluminum grating. The parameters are: $\lambda = 0.59 \mu\text{m}$, $d = 0.3333 \mu\text{m}$, $\epsilon_0 = (1.15 + i7.15)^2$, $\epsilon_{2j-1} = 1.39^2$, $\epsilon_{2j} = 2.61^2$, $j = 1, 2, 3, 4$, $Q = 8$, and $\epsilon_{Q+1} = 1.0$. The grating groove depth h is set to be $0.12 \mu\text{m}$ which gives a peak efficiency of 88.7% for the bare grating. Note that the maximum efficiency reaches about 99.8% at $r = 0.305$. This curve was calculated with truncation order $N = 19$.

The second example, shown in Fig. 4, is for a 15-layer-coated sinusoidal grating in fused silica. The parameters are: $\epsilon_0 = 1.46^2$, $\epsilon_{2j-1} = 2.61^2$, $1 \leq j \leq 8$, $\epsilon_{2j} = 1.39^2$, $1 \leq j \leq 7$, and $Q = 15$. All the other parameters are the same as in the first example. Note that although the bare grating's efficiency for $h = 0.12 \mu\text{m}$ is only 3.3%, the maximum efficiency of the coated grating is more than 99.9% at $r = 0.305$. This curve was calculated with truncation order $N = 17$ and the error in the sum of efficiencies was smaller than 1.0×10^{-10} for all points calculated.

IV. Conclusions

The differential method of Chandezon *et al.* for multilayer coated gratings has been improved so that the computation time for gratings in conical mountings is greatly reduced and the previously existed limitations on the total coating thickness and on the total number of coatings are removed.

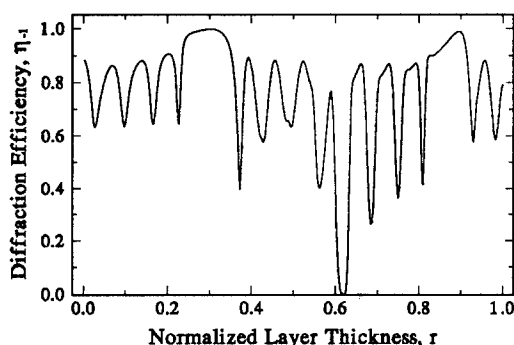


Figure 3. Dielectric-coated aluminum grating.

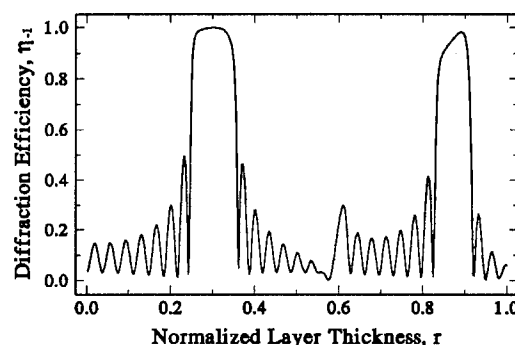


Figure 4. Dielectric-coated fused silica grating.

V. References

1. D. Maystre, *J. Opt. Soc. Am.* **68**, 490 (1978).
2. L. F. Desandre and J. M. Elson, *J. Opt. Soc. Am.* **A 8**, 763 (1991).
3. J. Chandezon, D. Maystre, and G. Raoult, *J. Optics (Paris)* **11**, 235 (1980).
4. J. Chandezon, M. T. Dupris, G. Cornet, and D. Maystre, *J. Opt. Soc. Am.* **72**, 839 (1982).
5. E. Popov and L. Mashev, *J. Optics (Paris)* **17**, 175 (1986).
6. S. J. Elston, G. P. Bryan-Brown, and J. R. Sambles, *Phys. Rev. B* **44**, 6393 (1991).
7. E. Popov and L. Mashev, *Opt. Acta* **33**, 593 (1986).
8. L. Li, "Multilayer coated diffraction gratings: the differential method of Chandezon *et al.* revisited," *J. Opt. Soc. Am.* (to be published).
9. L. Li, *J. Opt. Soc. Am.* **A 10**, 2581 (1993).

POLARIZING PROPERTIES OF DIELECTRIC LAYER WITH
SUBWAVELENGTH STRUCTURED SURFACES.

V.N.Bel'tyugov, S.G.Protsenko, A.V.Leis.

The Institute of Automation and Electrometry.
Universitetski Prospekt 1, 630090, Novosibirsk, Russia.
Phone: (3832)351042, Fax: (3832)354851,
E-Mail: troitski@iaie-phs.nsk.su

In recent years, the dielectric thinfilms with surface-relief gratings have been the subject of a great deal of interest. It has been found that such elements have an interesting optical properties: birefringence [1], antireflection [2,3], resonance anomaly effect [4]. All this properties have found application in different spectral devices as narrow-band spectral filters, spectral-selective laser mirrors and i.e.. The polarizing properties of such elements practically was not investigated. Nevertheless, it have the great importance. In this paper the case of dielectric layer with structured surfaces (DLSS) is considered [5].

The scheme of DLSS is shown in Fig.1. d is a period, h is a deep of the surface-relief grating. Similarly [4], d has to satisfy the condition:

$$\lambda/n < d < \lambda/n_0, \lambda/n_1, (1)$$

where λ is wavelength of incident light. Physical sense (1) is following: at normal incidence in the regions V_0 and V_1 only the zeroth reflected and transmitted orders are diffracted. In the dielectric layer, in addition, there are the first-orders of diffraction. The angles of first-orders reflection from dielectric interfaces is greater than the angle of total internal reflection. The first-order waves give rise to the waves in adjacent to layer media by second diffraction by grating. The propagating

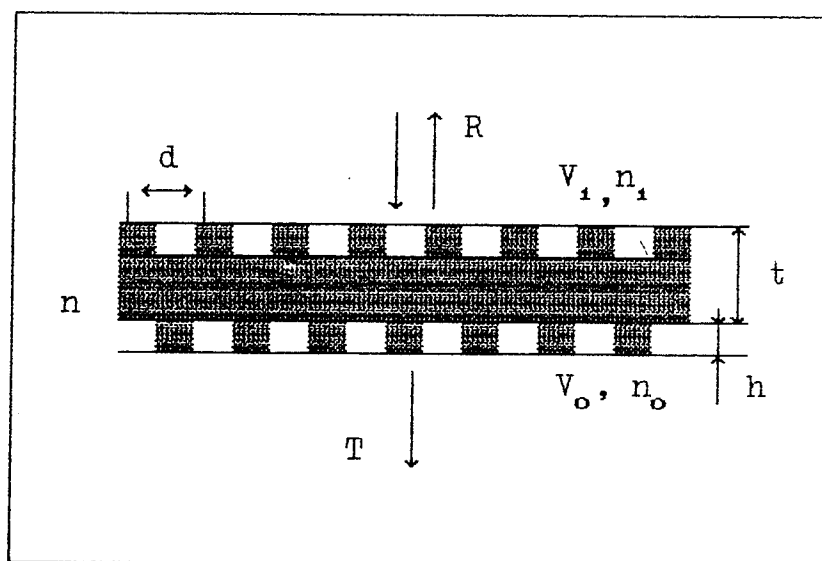


Fig.1. The dielectric layer with structured surfaces.

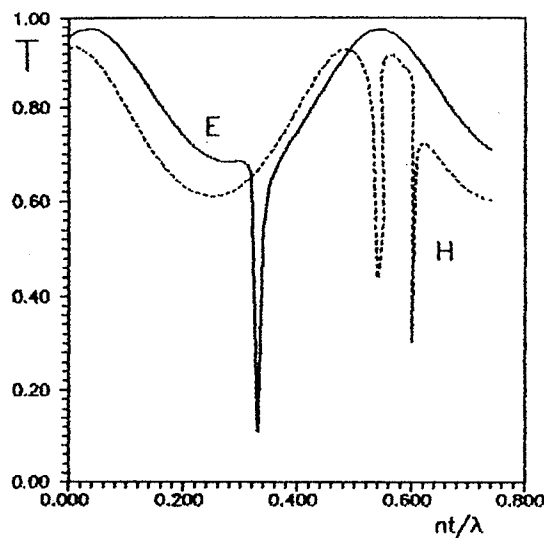


Fig.2. The transmission of DLSS.
 $d=0.375$ mkm, $h_1=0.025$ mkm,
 $h_2=0.00$ mkm, $n=2.32$, $n_1=1.00$,
 $n_0=1.46$.

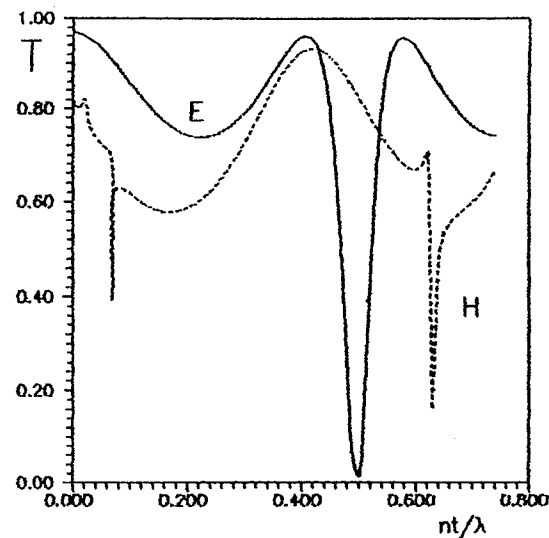


Fig.3. The transmission of DLSS.
 $d=0.328$ mkm, $h_1=0.025$ mkm,
 $h_2=0.025$ mkm, $n=2.32$, $n_1=1.00$,
 $n_0=1.46$.

direction of this waves is normal. The interference-field energy in the regions V_0 and V_1 depends on the polarization of incident light. Hence, polarizing dependence of optical properties of DLSS have to be observed.

Let us consider the resonance anomaly effect as example for the analysis of the polarizing effect (PE). It is common knowledge that the reflectivity in the resonance depend on symmetry of a surface relief, and it can archives 100% under lossless condition. The width of the resonance is determined by the diffractive efficiency of surface-relief grating. Here we examine the dependence of the resonance anomaly conditions from the polarization.

To solve this problem, it was applied the numerical calculation method. The surface-relief grating was consider as set of rectangular dielectric strips with alternate refractive index n and n_1 . The total electromagnetic field in the grating is represented as superposition of the modes of medium with the modulated refractive index [6]. In regions V_0 and V_1 the scattered fields are expressed as series of outward-going plane waves. The necessary continuity conditions electric and magnetic fields on the interfaces lead us to the infinite system of the equations relative to the amplitudes of internal layer modes. In the calculation, the number of modes were selected by required accuracy to the conservation of energy law. The energetic coefficients of reflection, transmission and losses in dependence from wavelength, dielectric layer thickness and incident angle were calculated by this method.

For example, in Fig.2 received results for the transmission of DLSS in dependence from relative thickness of dielectric layer nt/λ are shown. Here is normal incidence. Index "E" correspond to the polarization of incident light, when the electrical vector is directed along the strips of grating. Index "H" correspond to the orthogonal polarization. In this

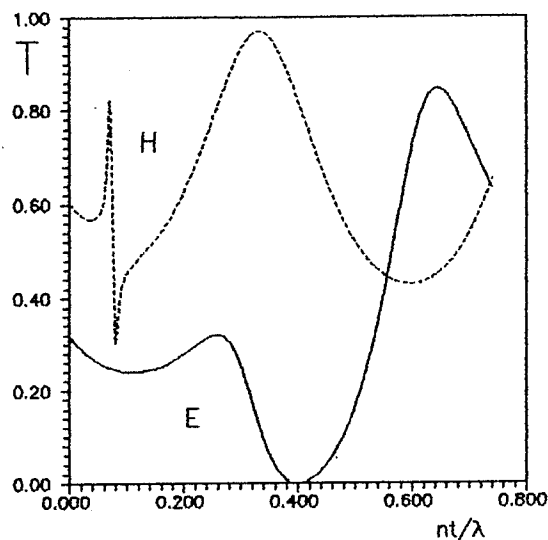


Fig.4. The transmission of DLSS.
 $d=0.330$ mkm, $h_1=0.03$ mkm,
 $h_2=0.03$ mkm, $n=1.98$, $n_1=1.00$,
 $n_2=3.84$, $n_0=1.46$.

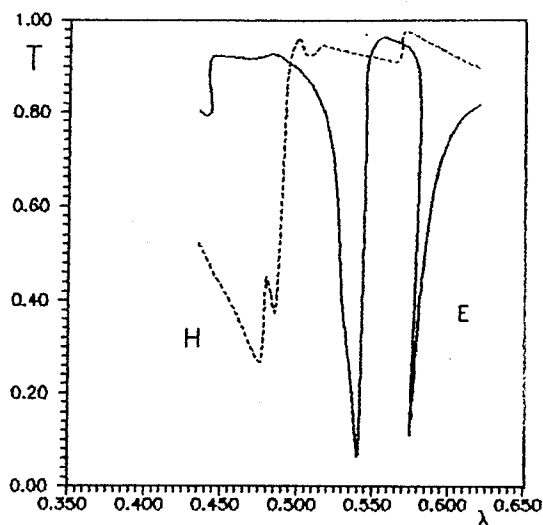


Fig.5. The transmission of DLSS.
 $d=0.330$ mkm, $h_1=0.025$ mkm,
 $h_2=0.025$ mkm, $n=1.98$, $n_1=1.00$,
 $n_0=1.46$, $\phi=0.01$ rad.

case, only one interface of dielectric layer is corrugated. One can see, that the general view of dependence correspond to the transmission of dielectric layer with the plane interfaces except areas where resonances there are. The positions of "E" and "H" polarization on nt/λ axis are different.

The method described above allows to calculate the more complex cases. For example, in practice the creation of the surface-relief grating on optical substrate often is more convenient. After that the substrate is coated by the dielectric. If the thickness of dielectric layer is small enough, its top boundaries repeats the form of substrate surface. In this case, both of dielectric interfaces are corrugated. Since, the light diffracts by two gratings, the efficiency of the interaction of the incident radiation and the field in layer is greater relative one-grating case. Hence, the width of resonances have to be greater. In Fig.3 the dependence of transmission from nt/λ is shown.

In case near to normal incidence of light, the first-orders of diffraction propagate in layer at different angles. There are two different conditions for the resonance anomaly effect. Hence, the double-number of resonances should be observed. In Fig.5 this case is presented.

Let us consider the situation, when in the surface-relief grating the dielectric with refractive index $n_2 \neq n$, n_0 , n_1 is used. The diffractive efficiency of such grating have to be changed. Then the width of resonances must be changed. See Fig.4.

To experimental investigate, the DLSS was made by method of laser lithography and plasma-ion etching. In the course of research of PE, the transmission and reflection in dependence from wavelength were detected. In Fig.6 the transmission at normal incidence is shown.

In such a manner, there is polarizing anisotropy of optical properties of DLSS. Using the resonance anomaly effect as example, we'd like to

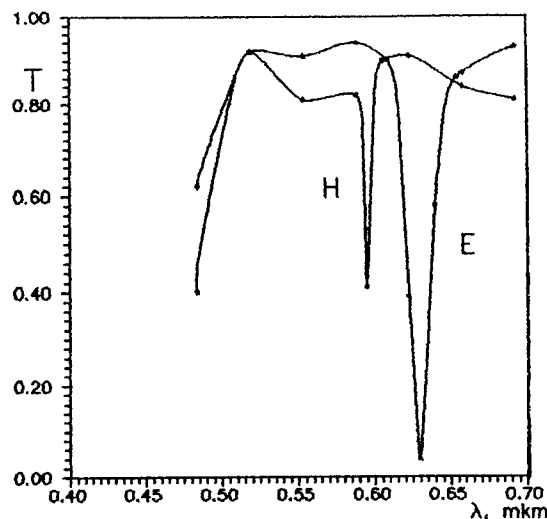


Fig.6. The transmission of DLSS.

$d=0.328$ mkm, $h_1=0.025$ mkm,
 $h_2=0.025$ mkm, $n=2.32$, $n_1=1.00$,
 $n_0=1.46$.

underline the fundamental importance of polarizing effect. DLSS allows to create the polarizing devices, which can work at normal incidence of light: the narrow- band polarizing filter, polarizing- selectivity laser mirror and i.e.. Using of the multilayer dielectric systems allows to create polarizing optical elements with back- characteristic to Fabry-Perot interferometer. Besides, there are other interesting application of DLSS.

References

1. M.Born and E.Wolf, "Principles of Optics" (Pergamon, London, 1980), pp. 705-708.
2. M.G.Moharam and T.K.Gaylord, "Diffraction analysis of dielectric surface- relief gratings", J. Opt. Soc. Am. 72, 1385-1392 (1982).
3. D.N.Raguin and G.M.Morris, "Diffraction analysis of antireflection surface- relief gratings on lossless dielectric surfaces", OSA Technical Digest Series (Opt. Soc. Am., Washington, D.C., 1990) 15, pp. 122-123.
4. E.Popov and L.Machev, "Diffraction from planar corrugated waveguides at normal incidence", Optics Communications 61, pp. 176-180 (1987).
5. This work was partially supported by the Russian Fund of Fundamental Researches (Project code no. 93-02-14296).
6. I.C.Botten, M.S.Craig, R.C.McPhedran, J.L.Adams and J.R.Anderwartha, "The dielectric lamellar diffraction grating", Optica Acta 28, pp. 413- (1981).

Wednesday, June 8, 1994

Applications for Laser Systems

DWC 1:30pm–3:30pm
Room B

J. Allen Cox, *Presider*
Honeywell, Inc.

Applications of Diffractive Optic Design
to Acousto-Optic Signal Processing

Joseph N. Mait, Dennis W. Prather, and Joseph van der Gracht
U.S. Army Research Laboratory
AMSRL-SS-IA

2800 Powder Mill Road
Adelphi, Maryland 20783

phone: (301) 394-2520, fax: (301) 394-4214, e-mail: mait@arl.army.mil

Ravindra A. Athale
Electrical and Computer Engineering
George Mason University
Fairfax, Virginia 22030

phone: (703) 993-1585, fax: (703) 993-1601, e-mail: rathale@sitevax.gmu.edu

For applications in image processing, we have chosen to implement image correlation using the optical processor represented in Fig. 1. To update the reference image dynamically in real-time some form of spatial light modulator (SLM) is required in the pupil plane. Based primarily on technology maturity, space-bandwidth, and device dynamic range, we selected acousto-optic (AO) devices to perform this function as opposed to either magneto-optic or liquid crystal technology [1]. As a consequence, even when coherent illumination is used, system operation is incoherent. Nonetheless, we have also shown that the use of incoherent illumination offers a number of advantages over coherent, e.g., increased immunity to noise sources within the system and increased field of view [2]. We note that Ref. [3] is, to our knowledge, the first reported use of an AO cell to generate Fourier filter functions.

To generate the reference image against which the input is correlated we have relied upon design techniques that are more commonly used for fixed, phase-only diffractive optical elements (DOEs). Before we discuss design, it is necessary for us to present first a one-dimensional system analysis. The unique properties of a two-dimensional system are considered thereafter.

If the input object $f(x)$ is illuminated by a quasi-monochromatic coherent source, the spatially scaled Fourier transform $F(x_f/\lambda f)$ is incident upon the AO cell. The AO cell is driven by the voltage signal $v(t)$,

$$v(t) = |H(t)| \cos[2\pi\nu_{ao}t + \arg\{H(t)\}], \quad (1)$$

which launches a moving, modulated phase grating onto the AO cell, where $H(t)$, the complex driving signal, is

$$H(t) = |H(t)| \exp[j\arg\{H(t)\}].$$

The interaction in the Fourier plane between the AO cell and the object transform produces the Doppler shifted complex-wave correlation image $c(x; t)$,

$$c(x; t) = f(x) \star h\left(\frac{x - a\nu_{ao}}{\lambda f}\right) \exp\left[j2\pi x \left(\frac{t}{a}\right)\right], \quad (2)$$

where $a = \lambda f/V$. Time integration of $c(x; t)$ yields the intensity image $c(x)$,

$$c(x) = |f(x)|^2 \star \left| h\left(\frac{x - a\nu_{ao}}{\lambda f}\right) \right|^2. \quad (3)$$

Note that, although a coherent Fourier plane architecture is employed, an intensity correlation between the input object and filter response results. In other words, the one-dimensional system is incoherent and the use of coherent illumination is unnecessary.

In contrast to the one-dimensional system, the two-dimensional AO system exhibits unique coherence effects that are dependent upon the coherence that exists between the voltage signals $v_x(t)$ and

$v_y(t)$ that drive the cells. The time integrated character of the correlation is now dependent upon the phase coherence between the sources used to generate $v_x(t)$ and $v_y(t)$ [1]. To realize a fully incoherent superposition, the relative phase coherence between the Doppler shifts created by the drive signals $H_x(t)$ and $H_y(t)$ needs to be destroyed.

If separate signal sources are used to drive the two AO cells we can represent the system output image as an intensity correlation

$$c(x, y) = |f(x, y)|^2 \star \left| h_x \left(\frac{x - a\nu_{aox}}{\lambda f} \right) h_y \left(\frac{y - a\nu_{aoy}}{\lambda f} \right) \right|^2. \quad (4)$$

The design problem to be solved is the determination of $H_x(t)$ and $H_y(t)$ such that they generate some desired response $q(x, y)$, where, due to the incoherent nature of the system, $q(x, y)$ is nonnegative and real.

We note that the crossed AO cell architecture, for any instant in time, allows only for the generation of separable point spread functions. An arbitrary point spread function can be synthesized as a superposition of several separable spread functions [4] that are generated time sequentially by the crossed AO cells and time integrated in the detector plane.

We consider the specification of the AO drive signals under the assumptions that the input is presented to the system on an electronically addressed SLM, i.e., it is discrete, and that the AO cells are used to generate a discrete correlation. The desired response $q(x, y)$ is separable and given by

$$\begin{aligned} q(x, y) &= r^2(x) s^2(y) \\ &= \sum_{n=N_1}^{N_2} \sum_{m=M_1}^{M_2} r_n^2 s_m^2 \delta(x - nd_x, y - md_y), \end{aligned} \quad (5)$$

where r_n^2 and s_m^2 specify the intensity of the (n, m) th spot of the response and d_x and d_y are the spacings between spots in the image plane. If

$$r(x) = \sum_{n=N_1}^{N_2} r_n \exp(j\theta_n) \delta(x - nd_x), \quad (6)$$

where θ_n is the phase of the n th spot, then

$$H_x(t) = \sum_{n=N_1}^{N_2} r_n \exp(j\theta_n) \exp(-j2\pi n\nu_x t), \quad (7)$$

where $\nu_x = Vd_x/\lambda f$. A similar expression exists for $H_y(t)$.

Since the generation of each axial component is similar, we consider the generation of only the x -axis response $r(x)$. Our desire is to generate $r^2(x)$ with a minimum amount of error, yet with high diffraction efficiency. To achieve high diffraction efficiency many designs assume use of a phase-only DOE. However, due to the nature of AO technology [see Eq. (1)], this restriction is not necessary. Nonetheless, high diffraction efficiency can be achieved if the desired filter function is approximately phase-only, $|H_x(t)| \approx 1$.

We have used the freedom in the specification of the phases θ_n , which influence the form of $H_x(t)$, to reduce the dynamic range of $|H_x(t)|$, yet still produce the desired response $r^2(x)$. We determined the phases by maximizing the average Fourier magnitude for a given set of r_n [5],

$$|\hat{H}_x| = \int \left| \sum_{n=N_1}^{N_2} r_n \exp(j\theta_n) \exp(-j2\pi n\nu_x t) \right| dt. \quad (8)$$

This expression is derived from the one for the upper bound on the diffraction efficiency with which a phase-only DOE can generate a specified complex response [6]. Other techniques for the determination of spot phases in array generators can also be used [7].

Two drive signals are represented in Fig. 2 for the generation of a nine-spot fan-out; Fig. 2(a) was generated using zero phase for each spot and Fig. 2(b), using the phases that result from maximization of Eq. (8). The magnitude of the fan-out generated by the drive signal of Fig. 2(b) is approximately 2.5 times that of Fig. 2(a). Figure 3 represents nonseparable responses generated by the system.

We presented the design of drive signals for an AO system in the context of DOE design. The analog nature of the AO devices provides considerable degrees of both magnitude and phase design freedom such that uniform and efficient responses can be generated.

References

1. J. N. Mait, D. W. Prather, and R. A. Athale, *Appl. Opt.* **31**, 6820 (1992).
2. R. A. Athale, J. van der Gracht, D. W. Prather, and J. N. Mait, "Incoherent optical image correlators with crossed Bragg cell implementation" *Annual Meeting of the Optical Society of America 1993*.
3. E. Tervonen, A. Friberg, J. Westerholm, J. Turunen, and M. R. Taghizadeh, *Opt. Lett.* **16**, 1274 (1991).
4. R. A. Athale and J. N. Lee, *Proc. IEEE* **72**, 931 (1984).
5. U. Krackhardt, J. N. Mait, and N. Streibl, *Appl. Opt.* **31**, 27 (1992).
6. F. Wyrowski, in *Computer and Optically Formed Holographic Optics*, I. N. Cindrich and S. H. Lee, eds., *Proc. SPIE* **1211**, 2 (1990).
7. H. P. Herzig, D. Prongué, and R. Dändliker, *Japan. J. Appl. Phys.* **29**, L1307 (1990).

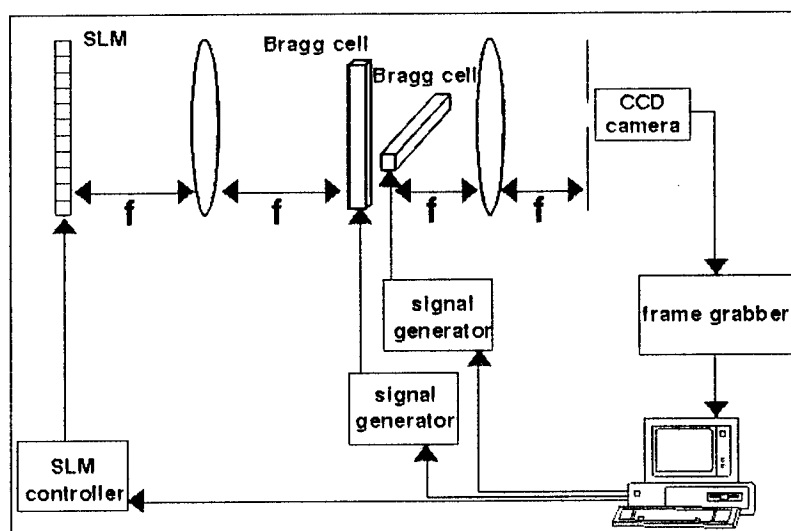


Figure 1. Acousto-optic system for performing two-dimensional Image correlation.

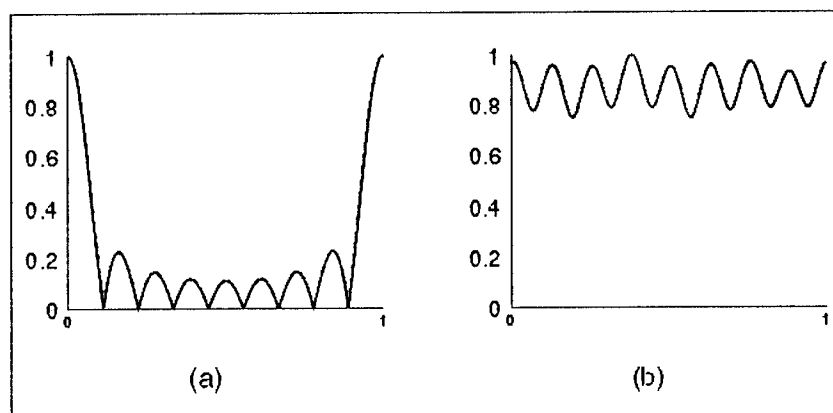


Figure 2. AO drive signals for the generation of a nine-spot fan-out. Drive signal assuming (a) zero phase and (b) optimized phase values.

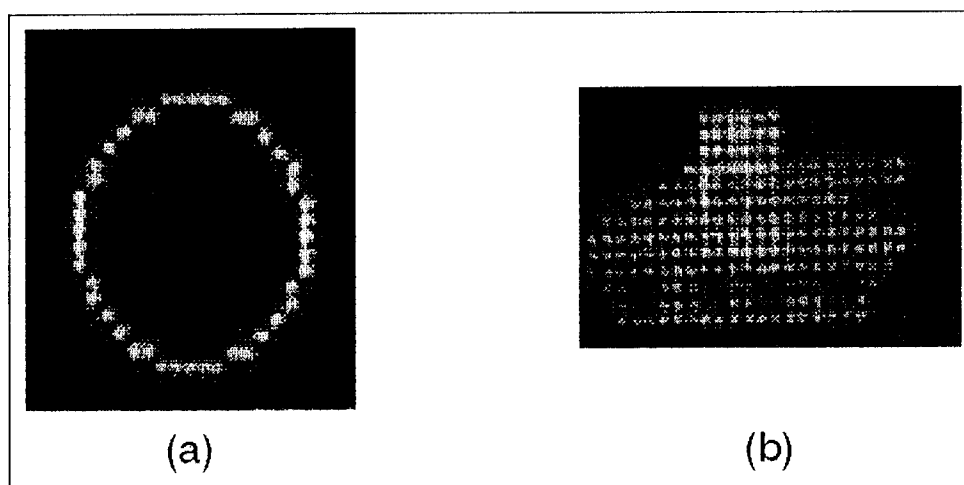


Figure 3. Responses generated by crossed AO cell architecture. (a) Circle and (b) tank.

Use of Diffractive Phase Plates for High Modal Discrimination in Short Laser Resonators

D. Chen
J. R. Leger

University of Minnesota
Minneapolis, Minnesota 55455
(612) 625-0838

The vast majority of commercial lasers utilize a stable Fabry-Perot resonator to establish the laser mode. Although this resonator design produces a low-loss fundamental mode, it has several inherent disadvantages. First, the losses to the higher-order spatial modes are also fairly low, making it difficult to insure operation in a single spatial mode. In addition, the mode diameters are usually small, reducing the amount of power that can be extracted from the gain medium. Increasing the mode diameter reduces the separation in threshold between the higher-order modes to an unacceptable level. Finally, the Gaussian profile of the fundamental mode may not be ideal for applications that require uniform illumination.

Unstable resonators can support a large diameter fundamental mode while simultaneously preserving adequate higher-order mode separation. However, these resonators have inherently lossy fundamental modes, and are not suitable for low-gain laser systems. In addition, they often have an obstructed output aperture that produces an undesirable near-field pattern.

Recently, a variety of laser cavities have been demonstrated that use more sophisticated optics to tailor the fundamental mode shape and increase the separation between adjacent spatial modes. These include variable reflectivity mirrors[1], graded phase mirrors [2], and diffractive mode-selecting mirrors[3, 4]. The last two methods allow the designer to tailor the mode profile to any desired shape, and have been used to generate super-Gaussian fundamental modes with exceedingly flat tops. However, large discrimination between spatial modes occurs when the cavity length is approximately one Rayleigh range of the super-Gaussian. Thus, for large beam diameters, these methods can result in very large cavity lengths, compromising mechanical stability and increasing the pulse length for Q-switched operation.

In this paper, we propose a variation of the diffractive mode-selecting mirror cavity that significantly increases the modal separation while reducing the required cavity length. The cavity to be studied, shown in fig. 1, contains a diffractive mode-selecting mirror on one end and a flat mirror on the other end. A transparent phase plate is placed between these two mirrors to increase the modal separation and decrease the cavity length.

The design of the cavity proceeds in much the same way as the simple diffractive mode-selecting mirror[4]. The designer first chooses the desired amplitude profile of the fundamental mode at the flat output mirror. The resulting field at the phase plate is calculated by the Rayleigh-Sommerfeld diffraction formula, multiplied by the phase transmittance of the plate $\exp[j\phi(x, y)]$, and propagated the remaining distance to the diffractive mode-selecting mirror. The reflectance of the mode-selecting mirror is then chosen to return the phase conjugate of this distribution. The phase

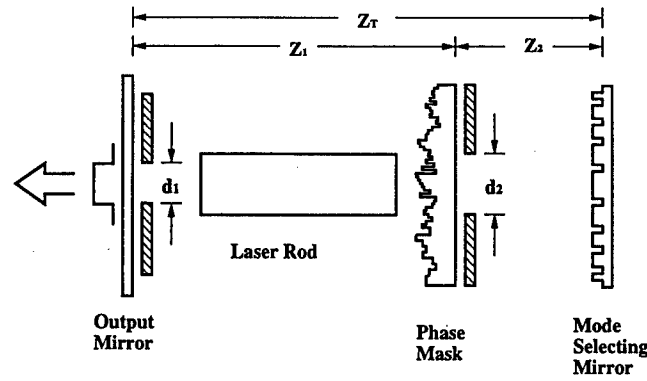


Figure 1: Laser cavity consisting of a flat output mirror, diffractive phase plate, and diffractive mode-selecting mirror.

conjugate wave will propagate back through the phase plate to the output mirror, regenerating the original distribution and establishing it as a mode of the cavity. If the size of the mode-selecting mirror is made sufficiently large and the two aperture sizes d_1 and d_2 are chosen properly, the loss to this mode can be made very small and it becomes the fundamental cavity mode. The higher-order cavity modes are then calculated by solving the integral equation

$$\int K(\bar{x}, \bar{x}') U_\nu(\bar{x}') d^2 \bar{x}' = \gamma_\nu U_\nu(\bar{x}),$$

where the integral kernel $K(\bar{x}, \bar{x}')$ describes the round-trip propagation in the cavity, $U_\nu(\bar{x})$ are the eigenfunctions of the equation, and γ_ν their corresponding eigenvalues. We seek to design a phase plate with a phase function $\exp[j\phi(x, y)]$ that provides the maximum amount of loss to the second-order mode for a given cavity length.

The first modeling experiments were performed using a laser cavity with element spacing $z_1 = 20$ cm and $z_2 = 30$ cm, resulting in a total cavity length $z_T = 50$ cm. The fundamental mode was chosen to be a 20th-order super-Gaussian of square cross-section and beam size of 1.2 mm. The output aperture size $d_1 = 1.3$ mm, resulting in negligible clipping of the super-Gaussian. The phase-plate aperture d_2 was chosen to be 4 mm to pass the diffracted super-Gaussian beam with negligible clipping. The diffractive mode-selecting mirror was assumed to be arbitrarily large.

The first phase plate studied was a simple phase grating with $\phi(x, y) = m \sin(2\pi f_g x)$, where m is the modulation index and f_g is the phase grating frequency. The loss to the fundamental mode in this case was always less than 0.1 %. Fig. 2 shows the laser gain g_{th} required for the second-order mode to overcome the cavity diffractive loss. g_{th} is related to the cavity loss ℓ by $g_{th} = 1/(1 - \ell)$, so that a threshold gain of unity corresponds to a lossless cavity. Threshold gains were calculated for a phase grating with $m = 1$ and a variety of frequency values f_g . A grating frequency $f_g = 0$ corresponds to a simple diffractive mode-selecting mirror cavity, and has a threshold gain $g_{th} = 1.4$ (or a loss $\ell = 28$ %). This value can be improved remarkably by increasing the grating frequency to approximately 4 cycles/mm, where $g_{th} = 3.7$ (corresponding to a loss of 73 %). Increasing the frequency past this point decreases the modal separation. This is expected, since for a sufficiently high frequency the different orders of the grating do not overlap. The diffractive mode-selecting mirror then simply consists of copies of the simple mode-selecting mirror at each of the diffraction orders. The effect of grating translation and modulation depth were also studied. For $m = 1$, the optimal grating had odd symmetry with respect to the mode. Modal threshold gains as large as 6.9 were observed for modulation depth $m = 11$.

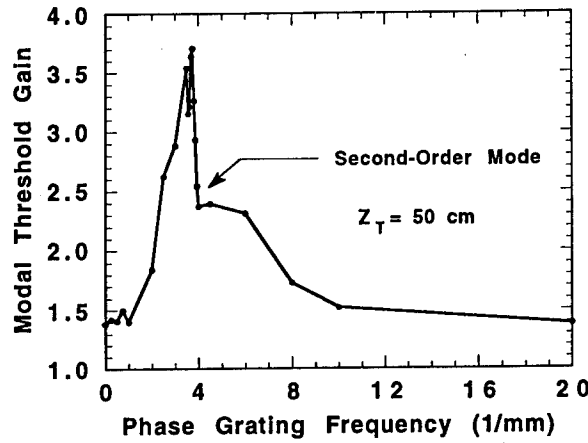


Figure 2: Laser gain required to overcome diffractive losses to the second-order mode for sinusoidal phase gratings of different frequencies. The loss to the fundamental mode is less than 0.1 %.

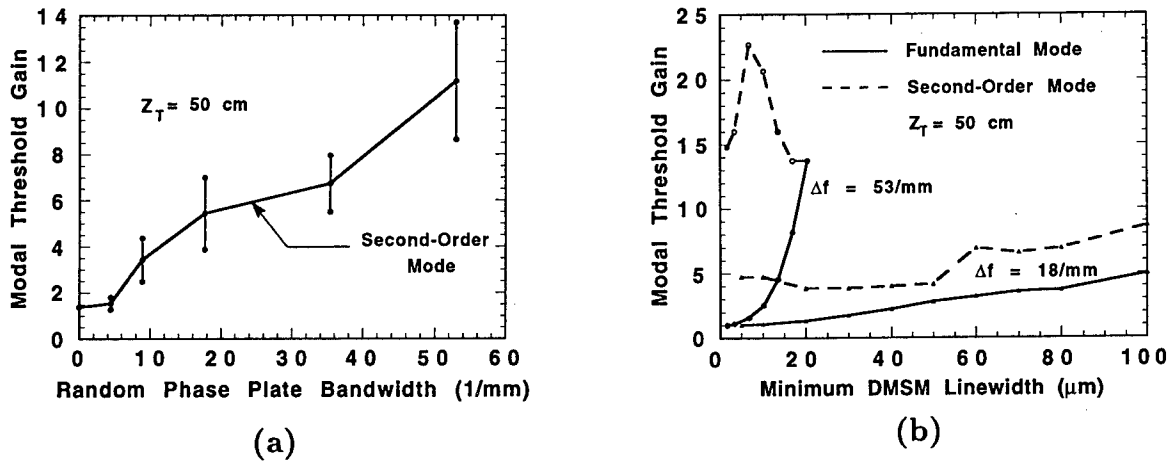


Figure 3: Results from using a phase plate with random phases. a) shows laser gain required to overcome diffractive losses to the second-order mode as a function of the spatial frequency bandwidth of the phase plate. b) shows the effect of finite diffractive mode-selecting mirror linewidth on the threshold gain of the fundamental and second-order modes for two different bandwidths Δf .

It was postulated that the degree of modal separation was related to the angular plane wave spectrum incident on the mode-selecting mirror. To test this, we performed a series of experiments using random phase plates with different angular plane wave spectra. Each phase plate was designed to have a Gaussian angular plane wave spectrum with the power spectral bandwidth defined as the $1/e^2$ point of the Gaussian. Fig. 3a shows the increase of threshold gain to the second-order mode with increasing phase plate bandwidth. The error bars show the statistical variation in the simulation. Very high modal separation can be obtained by presenting the diffractive mode-selecting mirror with a sufficiently complex light field. The price paid for this increased separation is an increase in complexity of the mode-selecting mirror. Fig. 3b shows the effect of mode-selecting mirror linewidth quantization on the modal gains of the fundamental and second-order mode. For fundamental mode losses of approximately 0.1 %, features as large as $5 \mu\text{m}$ can be used for the low bandwidth phase mask (18 mm^{-1}), whereas $1.7 \mu\text{m}$ features are required for a high bandwidth phase mask (53 mm^{-1}).

Finally, we have considered a case study of a very short ($z_T = 10 \text{ cm}$) laser cavity containing a

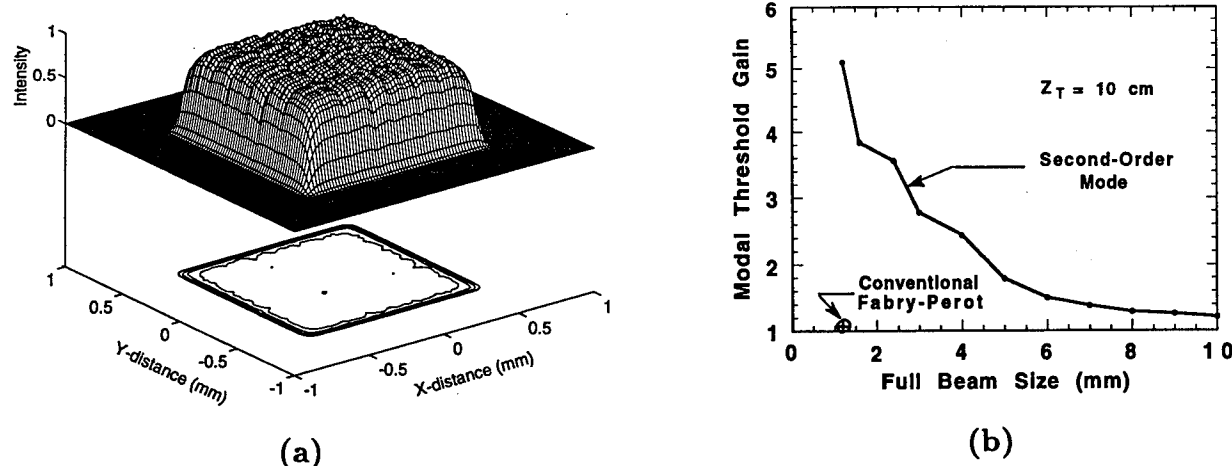


Figure 4: Theoretical performance of a 10 cm laser cavity containing a random phase plate. a) shows the two-dimensional fundamental mode intensity profile. b) shows the laser gain required to overcome the diffractive losses to the second-order mode for various fundamental beam sizes. The result from a conventional Fabry-Perot cavity is shown for comparison.

random phase plate with a bandwidth of 44 mm^{-1} . The phase mask was placed in the center of the cavity ($z_1 = 5 \text{ cm}$, $z_2 = 5 \text{ cm}$), and a 20th-order super-Gaussian chosen as the fundamental mode profile. A mode-selecting mirror was designed with a minimum feature size of $2 \mu\text{m}$ and 16 phase quantization levels. The resulting fundamental cavity mode profile is shown in fig. 4a for a 1.2 mm beam size. The finite linewidth and phase quantization of the mode-selecting mirror produce small nonuniformities in the beam profile and result in a fundamental mode loss of approximately 1.3 %. The gain required to overcome the losses to the second-order mode was 5.1 (corresponding to a loss of greater than 80 %). For comparison, a stable Fabry-Perot cavity with the same cavity length, beam size, and fundamental mode loss has a second-order modal gain of only 1.08, corresponding to a loss of just 7.2 %.

Fig. 4b shows the required second-order modal gain as a function of output beam spot size for this cavity. If a modal gain of 2.0 is sufficient to discriminate against the second-order mode (corresponding to a loss of 50 %), beam diameters of up to 4.5 mm can be used in this 10-cm-long cavity. It is therefore possible to extract a large amount of power from the gain medium, while still maintaining a very small cavity length.

In conclusion, we have studied a new type of laser resonator that employs an intracavity phase plate and a diffractive mode-selecting mirror to produce large-diameter fundamental modes in a short cavity. The intensity profile of the fundamental mode can be chosen to suit the application, and the loss to higher-order modes designed to effectively insure single-spatial-mode operation.

References

- [1] S. De Silvestri, V. Magni, O. Svelto, and G. Valentini, *IEEE J. Quantum Electron.* **QE-26**, 1500 (1990).
- [2] P.A. Belanger, R.L. Lachance, and C. Pare, *Opt. Lett.* **17**, 739 (1992).
- [3] J.R. Leger and X. Li, *Bulletin of the American Physical Society* **37**, 1212 (1992).
- [4] J.R. Leger, D. Chen, and Z. Wang, *Opt. Lett.* **19** (1994).

Apodized diffraction grating as outcoupling element for a 1.06 μm Nd- YAG Laser

A.Mitreiter, J.Guhr, H.-J.Rostalski
Berliner Institut für Optik GmbH
Rudower Chaussee 5, 12484 Berlin, Germany
Tel. (030) 6392 3474, Fax (030) 6392 3452

G. Bostanjoglo
Festkörper-Laser-Institut GmbH
Straße des 17. Juni 135, 10623 Berlin, Germany
Tel. (030) 315 82-0, Fax (030) 315 82-100

1. Abstract

The application of diffractive optical elements (DOE's) as outcoupling components for a 1.06 μm Nd-YAG laser with an unstable resonator was investigated. The laser power should be about 20 W without damaging the DOE. Laser with an unstable resonator can simultaneously provide almost diffraction limited beam quality and high extraction efficiency [1- 3]. Therefore an increasing interest in unstable resonator designs can be observed. On applications of unstable resonators have been reported with regard to various active medias like CO_2 , eximer, and Nd-YAG. In most cases the resonator consists of an unconfined highly reflective (HR) mirror and a variable reflective (VR) mirror as outcoupling element.

We will show that it is possible to replace a variable reflective mirror (VRM) by a holographically produced DOE. The holographic method allows the implementation of the two basic optical functions of the DOE: 1. shaping of the intensity profile of the beam; 2. imaging of the profile. The intensity profile is shaped by a spatial variation of the local diffraction efficiency of the DOE and the imaging properties are realized by a spherical reference wave in the optical fabrication step. With the refining of a copper galvanic replication technique we can present a suitable method to produce radiation resistant DOE's.

2. Introduction

The growing interest in unstable resonators results from their capability to ensure diffraction limited beam quality and high extraction efficiency. A resonator is called unstable if its g- parameter $g_{1,2}$ satisfies

$$g_{1,2} < 0 \quad \text{or} \quad g_{1,2} > 1$$

with $g_{1,2} = 1 - L / r_{1,2}$, L- resonator length, r_1, r_2 radii of mirror curvature

Different schemes of unstable resonators are shown in fig. 1, all consisting of an unconfined highly reflective mirror and a variable reflectivity mirror as outcoupling element. It has been proven that mirrors which possess the maximum reflectivity in the centre and smoothly decrease to zero within a certain radial distance are superior to mirrors with a sharp edge reflectivity profile regarding the beam quality [1,4]. It is therefore possible to use unstable resonators with low round trip magnification. A maximum reflectivity of less than 80% are then sufficient to attain the optimum loss factor. The use of traditional HR outcoupling dot mirrors carries the risk of accidental damage.

Besides dielectric VRM, radially birefringent elements [5] and varying interferometers [6] were used as apodizing outcoupling elements. However they did not become widely used.

Another alternative method for radially dependent outcoupling was published in 1991 [7]. The method is based on the use of a diffractive optical element with a variable efficiency over a certain radial distance. In this work the DOE is called apodized diffraction grating (ADG) and results for a CO_2 - Laser at 10.6 μm wavelength were described.

Our interest was to tackle the application of an apodized diffraction grating for a 1.06 μm Nd-YAG Laser with unstable resonator. The goal was to realize a laser power of about 20 W without damaging the ADG. The experimental results allow a judgement of the use of an ADG in Nd:YAG-laser with unstable resonator.

3. Requirements on the ADG and its fabrication

An ADG has to realize two optical functions. 1. feeding back the beam into the resonator; 2. shaping the intensity profile of the beam. From the description of the beam parameters and the optical path through the system we obtained the requirements on the design of the ADG. The basic setup of the ADG as an outcoupling element in the resonator is shown in fig. 2.

The grating period d was chosen in such a way that only two orders, i.e. the 0th and 1st order, are propagating for the wavelength of 1.06 μm . To use the grating as a resonator mirror it is necessary that the 1st order is in autocollimation, i.e. the light is diffracted in the opposite direction of the incident wave and is therefore fed

back into the resonator. That means that the angle α of incidence and the diffraction angle of the 1st order are identical. The angle of the 0th order, viz. the outcoupling beam, is $\beta = -\alpha$. In order to ensure the shaping of the intensity profile of the beam, the lateral variation of the local grating efficiency of the diffractive structure should be Gaussian. From modelling the properties of two types of unstable resonators we found necessary beam diameters and therefore ADG area diameters of 2 mm to 5 mm. In one case it should be a nonimaging ADG and in another case it should be an imaging with a working radius r of curvature of 0.3 m. According to the grating equation [9]

$$\sin \alpha + \sin \beta = k \lambda / d$$

and with $k = -1$ and $\lambda = 1.06 \mu\text{m}$ we found $\alpha = -\beta = 25^\circ$ and $d = 1.25 \mu\text{m}$ in order to satisfy the requirements.

We produced this ADG interferometrically. Fig. 3 shows the scheme of a special interferometer for this application. As light source an Ar-ion laser with the 458 nm line was used. A glass substrate which had been coated with photoresist was used as recording material. The angle between the two laser beams determines the spacing between the interference fringes and thus the grating period d . The depth of the resulting profile in the resist is controlled by the dose of light.

To realise the Gaussian variation of the local efficiency the relation between the ratio h/d of the grooves and the local diffraction efficiency η , i.e. $\eta = f(h/d)$, is of fundamental concern. By using rigorous diffraction theory we calculated this function to find suitable parameters. Fig. 4 illustrates the calculations.

A symmetrical variation of h/d from 0.05 - 0.35 in the diffractive structure produces the required variation of the local grating efficiency.

One method to realize the variation of the depth h in the structure practically is the exposure with a gradient of the illumination on the resist surface. But it has to be noticed that a good knowledge of the response of the photoresist on the illumination is necessary for this method. This behavior is described by the gradation function.

For the alignments and measurements in the setup a CCD-camera was used in the exposure plane.

With the interferometer configuration a large number of various ADG's were produced. However these gratings were originals in photoresist. To get a higher resistance against high power beams and to increase the damage threshold we applied a replication method in copper. This replication technique is based on a copper galvanic. It is able to produce a copper replica layer with a thickness of nearly 400 μm . In order to get better mechanical stability this copper layer was glued with special epoxyd to a solid copper substrate.

4. Testing

Some of the properties of an ADG were tested first outside a laser resonator and then inside a pumping laser resonator. One of these tests was the measurement of the efficiency profile at 1.06 μm wavelength. The results for s-polarisation is shown in fig. 5 for the 0th and 1st order.

Measurements with a Michelson interferometer showed radial phase shifts of about 1 in the radiation field of the 1st diffraction order.

The entire laser configuration was set up with the special ADG. The Nd-YAG rod was 160 mm long and had a diameter of 10 mm. The laser was run in pulsed operation (pulse duration 2 ms, repetition rate 30 Hz) at a maximum input power of 6.5 KW.

With a 0.8 m long flat - flat resonator 50 W of laser power was obtained at 6.5 KW input power. The beam parameter product was measured to be 10 - 30 mm mrad.

A positive branch unstable resonator yielded 20 W at 4.1 KW input power.

5. Outlook

At this experimental stage of the project the results indicate that apodized diffractive gratings can be used instead of VRM in the medium power range.

A drawback are still the losses due to absorption and scattering which are typical 5 - 15 %. For laser power over 80 W the temperature of the grating exceeds 100° C and causes destruction.

Further development of the manufacturing process could probably reduce the losses and increase the radiation resistance.

7. References

- [1] A.E.Siegman, "Laser" (University Science Books, Mill Valley, CA, U.S.A. 1986).
- [2] S.De Silvestri, V.Magni, O.Svelto and G.Valentini, IEEE J.Quant.Electron. 26(1990)1500.
- [3] N.Hodgson, G.Bostanjoglo and H.Weber, Optics Comm. 99(1993)75.
- [4] K.J.Snell, N.McCarthy, M.Piche and P.Lavigne, Optics Comm. 65(1988)377.
- [5] G.Giuliani, Y.K.Park and R.L.Byer, Optics Lett. 5(1980)491.
- [6] S.De Silvestri, P.Laporta and V.Magni, J.Opt.Soc.Am. A4(1987)1413.
- [7] Ch.Budzinski, R.Grunwald, H.Pinz, D.Schäfer and H.Schönnagel, SPIE Proceedings 1500/25, Den Haag, 1991.
- [8] G.Bostanjoglo, N.Müller, "Erforschung von diffraktiver Laseroptik für Nd-YAG Laser mittlerer Leistung - Optische Prüfung der diffraktiven Optik", Report on BMFT's R&D project 13N60534, Festkörper-Laser-Institut Berlin, June 1993.
- [9] M.C.Hutley, "Diffraction Gratings", Academic Press, London, 1982.

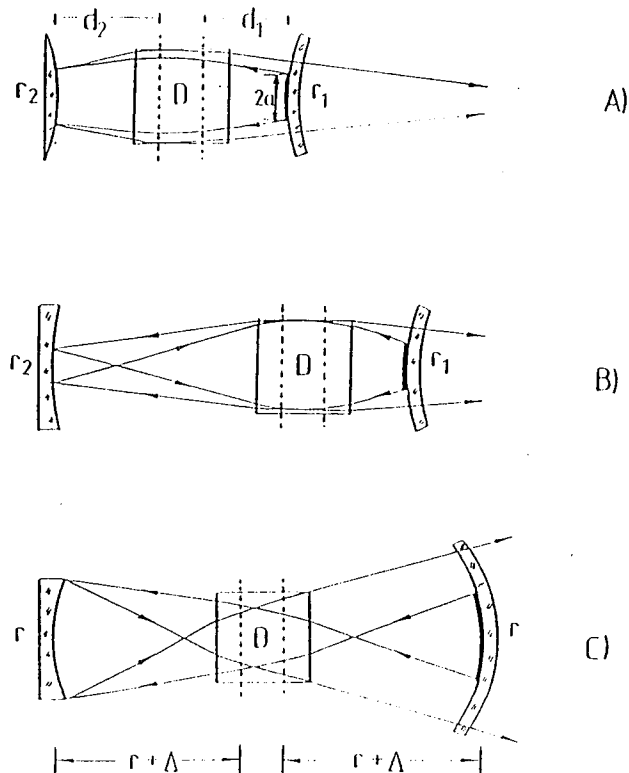


Fig.1 unstable resonators, A) positiv branch 11th quadrant, B) rod-imaging resonator 4th quadrant, C) near concentric unstable resonator 3th quadrant

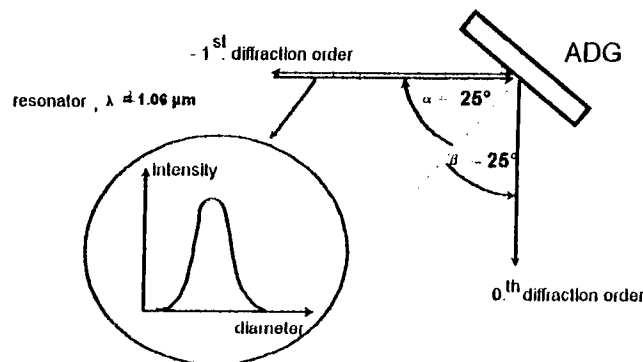


Fig.2 the arrangement for ADG in a laser resonator

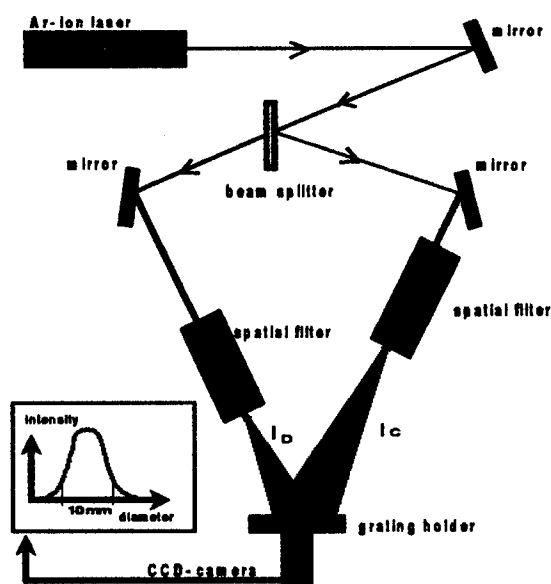


Fig. 3 laser interferometer for exposure

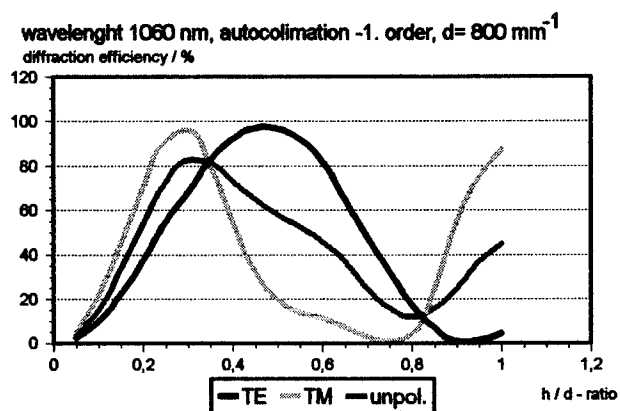
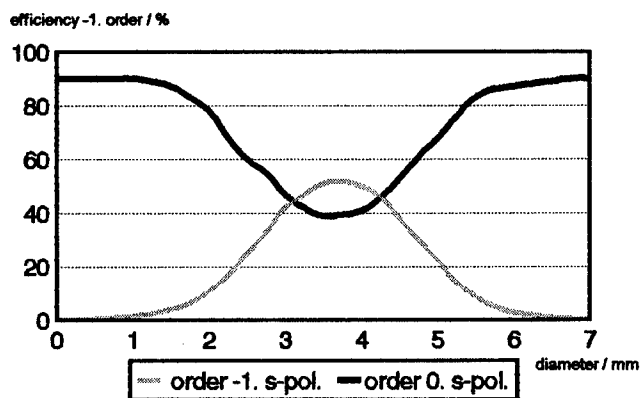
Fig. 4 diffraction efficiency as function of the ratio h / d 

Fig. 5 efficiency profil for -1 th order and 0 th order s-pol., wavelength 1060 nm

Large Aperture Kinoform Phase Plates for Beam Smoothing

S. N. Dixit, M. Rushford, I. Thomas, R. Merrill, M. Perry and H. T. Powell

Lawrence Livermore National Laboratory

P. O. Box 5508, L - 493

Livermore, CA 94551

(510) 423 - 7321

and

K. A. Nugent

The University of Melbourne, Parkville, VIC 3105, Australia

Spatial and temporal beam smoothing has now become an integral part of laser driven inertial confinement fusion (ICF) worldwide. Spatial smoothing is often achieved by using random phase plates (RPP) [1] or lenslet arrays [2]. Temporal smoothing is accomplished using smoothing by spectral dispersion (SSD) [3] or induced spatial incoherence (ISI) [4]. All the RPP's used so far have consisted of random layouts of square, rectangular or hexagonal phase plate elements that impose either 0 or π phase shift on the beam. The far-field intensity pattern of such RPP's consists of an envelope characteristic of the phase plate element and a superimposed speckle pattern resulting from the interference among the various phase plate element contributions. The far-field envelope for square and hexagonal shapes is qualitatively similar to an Airy pattern and it contains roughly 81 to 84% of the incident energy within the central maximum [5]. Even though such regular element, binary phase plates are easy to fabricate and are widely used, they offer little flexibility in our ability to tailor the far-field profile and to increase the energy content in the central maximum beyond the 84% predicted for a circular aperture.

In order to overcome these limitations for the binary RPP's, we have designed and fabricated new phase screens for tailoring the far-field intensity distribution and increasing the energy content therein. These phase screens

consist of smooth, continuous variation of the phase across the aperture and, as such, relax the binary phase and the regular phase element assumptions. We call such continuous contour phase plates kinoform phase plates (KPPs).

The design question for such KPPs can be posed as follows: is it possible to construct a phase screen in the input plane which, for a given input intensity distribution, produces a desired far-field intensity distribution? We have recently developed [6] an iterative algorithm for generating KPP phase screens which produce desired far-field intensity profiles. The algorithm begins by choosing a prescribed near-field amplitude and a random phase screen. Fourier transform of this complex amplitude leads to phase and amplitude modulations in the far-field. At this point, the far-field amplitude is replaced by the desired far-field amplitude leaving the phase unchanged. Inverse Fourier transforming this complex field gives the near-field distribution which has both amplitude and phase modulations. Now, the near-field constraint is applied by replacing the amplitude with the desired near-field amplitude but leaving the phase unchanged. The procedure is repeated again by Fourier transforming to the far-field ...etc. The iteration loop is exited after a satisfactory convergence is reached.

Numerical simulations have been carried out for constructing phase screens that produce supergaussian far-field intensity profiles from supergaussian near-field profiles. We find that the algorithm is rapidly convergent and for the converged solution, greater than 95% of the incident energy is contained within the desired spot in the far-field. This is a significant improvement over the 84% energy content for regular element, binary random phase plates where the element size is chosen such that the size of the central maximum (to the first zero) is equal to the size of the supergaussian profile in the far-field.

The near-field phase screen obtained after the iterative optimization shows a fairly smooth ripply structure resembling waves on a lake surface. Due to the range of the numerical arctangent function, the calculated phase is always in the range $(-\pi, \pi)$. This compression of the real phase by modulo 2π introduces sharp jumps approximately 2π in size. Except for these jumps, the phase screen appears fairly smooth.

KPP fabrication is accomplished by transferring the calculated phase screen on to a substrate such as fused silica. We begin by first discretizing the phase screen to 2^N levels. Calculations indicate that a minimum of 16 levels is necessary to maintain the energy concentration in the far-field. The 2^N phase levels can then be fabricated using photolithographic techniques using N binary masks. We have produced 16 level KPP's on 15 cm diameter substrates in fused silica using acid etching by buffered hydrofluoric acid. Presently we are characterizing the optical performance of such KPPs and are extending the fabrication process to even larger size substrates and more levels.

In this presentation we shall briefly describe the KPP design algorithm which will then be followed by a detailed discussion of the fabrication and characterization of the KPPs.

ACKNOWLEDGEMENT

Work done at LLNL was carried out under the auspices of the U. S. Department of Energy under contract No. W-7405-Eng-48.

REFERENCES

- [1] Y. Kato et al, Phys. Rev. Lett. **53**, 1057 (1984).
- [2] X. Deng et al, Appl. Opt. **25**, 377 (1986).
- [3] S. Skupsky et al, J. Appl. Phys. **66**, 3456 (1989).
- [4] R. Lehmberg and S. P. Obenschain, Opt. Comm. **46**, 27 (1983).
- [5] See, for example, M. Born and E. Wolf, *Principles of Optics* 6th edition (Pergamon, New York, 1980) p. 393.
- [6] S. N. Dixit et al, Optics Letters, to be published.

Excimer laser machining with kinoforms

Anna-Karin Holmér, Fredrik Nikolajeff, Jörgen Bengtsson, Björn Löfving and
Sverker Hård

Chalmers University of Technology
Department of Microwave Technology

S-412 96 Göteborg, Sweden

phone+46-317721897 fax:+46-31164513

Today excimer lasers are finding more and more use in industry for machining polymers and ceramics by ablation (1). Usually the pattern to be machined is obtained by imaging a mask onto the work-piece, the mask being illuminated by a homogenized excimer laser beam. The homogenization is needed to reshape the emitted, roughly Gaussian beam into a uniform top-hat intensity profile. Since the pattern often occupies a minute fraction of the homogenized beam the laser power is inefficiently used with this scheme. By steering the power only to the pattern in the mask the efficiency can be dramatically increased, however. This can be achieved with a kinoform (2), which is furthermore a homogenizer by itself. To ensure sharp edges on the work-piece the kinoform diffracted pattern should overlap the mask pattern with some margin.

In a preliminary experiment we investigated the kinoform/mask concept. The chosen pattern consisted of four circular spots positioned at the corners of a square, the spot diameter to square side being 1:4. This pattern can be realized with two crossed binary phase gratings with duty cycle 1/2, which would yield a diffraction efficiency of ~66%. Better efficiency (~88%) can be obtained with a single, multilevel phase grating. Instead we used a kinoform carrying small, elementary binary gratings of two kinds, every second with horizontal, the other with vertical grooves, both with duty cycle 1/2. The expected efficiency is 81%. To produce the wanted diffraction pattern the coherence areas of the illuminating beam should be roughly square and smaller than an individual elementary grating, whose size was 2 mm x 2 mm. The coherence areas of the KrF beam (wavelength: 248 nm) exiting the laser (Lambda Physik, LPX 100) are vertically elongated, with dimensions ~80 μ m x ~240 μ m. To tailor the coherence areas to the kinoform we compressed the beam in the vertical direction a factor of three with two cylindrical lenses, the resulting beam dimensions being ~22 mm x ~2.5 mm. The kinoform was positioned in the compressed beam after a lens, which focused the beam on the

mask plane, the diffraction limited four spots well matching the mask holes. The mask plane was imaged, demagnified five times, onto the work-piece with a field lens positioned immediately behind the mask. Good results of the machining were obtained, the sharp edged circular machined marks being 200 μm in diameter. We estimate the fraction of the laser power actually delivered to the work piece at ~15% . The number includes reflection losses in twelve optical surfaces, the finite diffraction efficiency of the kinoform and mask losses (~70%).

To withstand the excimer laser beam the kinoform had to be made in quartz. The electron-beam lithography manufactured kinoform was first generated as a binary surface relief in resist on a quartz substrate and then dry-etched into the substrate by Ar ion milling. The fact that the relief was binary helped us better control the etch process and thus to accurately reach the intended depth (244 nm). For manufacture of multi-level or continuous relief kinoforms, which are generally needed to produce more complicated patterns, a higher degree of control in the etch-step is required. This is a problem we are presently facing in our efforts to manufacture continuous relief excimer laser beam homogenizers. We manufacture these homogenizers as fly's eye arrays of square, off-axis micro Fresnel lenses. With this novel design a small unwanted relief depth error will only give rise to a diffraction limited spot located outside of the homogenized area. Measurements show that the quality of the homogenized areas, produced by our diffractive homogenizers, is as good as that obtained by refractive lens array homogenizers (3). An advantage with diffractive homogenizers is that, since they can be replicated, they should be less expensive than conventional homogenizers. Furthermore, they can be made only a few hundred microns thick, which should yield long life-times.

References

1. T. Znotins, "Industrial applications of excimer lasers", Proc. Soc. Photo-Opt. Instrum. Eng., 710, 55-62, 1986.
2. M. Ekberg, M. Larsson, A. Bolle and S. Hård, "Nd:YAG laser machining with multilevel resist kinoforms", Appl. Opt., 30, 3604-3606, 1991.
3. K. Mann, A. Hopfmüller, P. Gorzellik, R. Schild, W. Stöffler, H. Wagner and G. Wolbold, "Monitoring and Shaping of Excimer Laser Beam Profiles", Proc. Soc. Photo-Opt. Instrum. Eng., 1834, 184-194, 1992.

Diffractive Optics for CO₂ Industrial Lasers: Reducing Lens Damage

Russell W. Gruhlke
P.O. Box 5171
Auburn, CA 95604

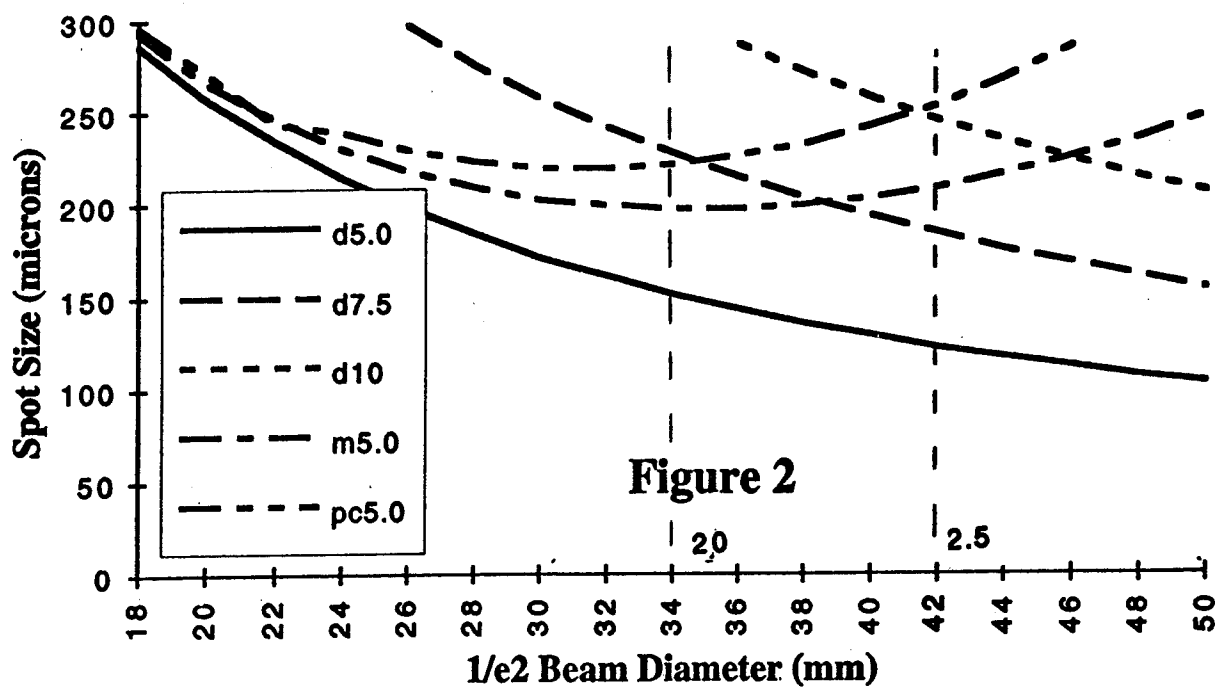
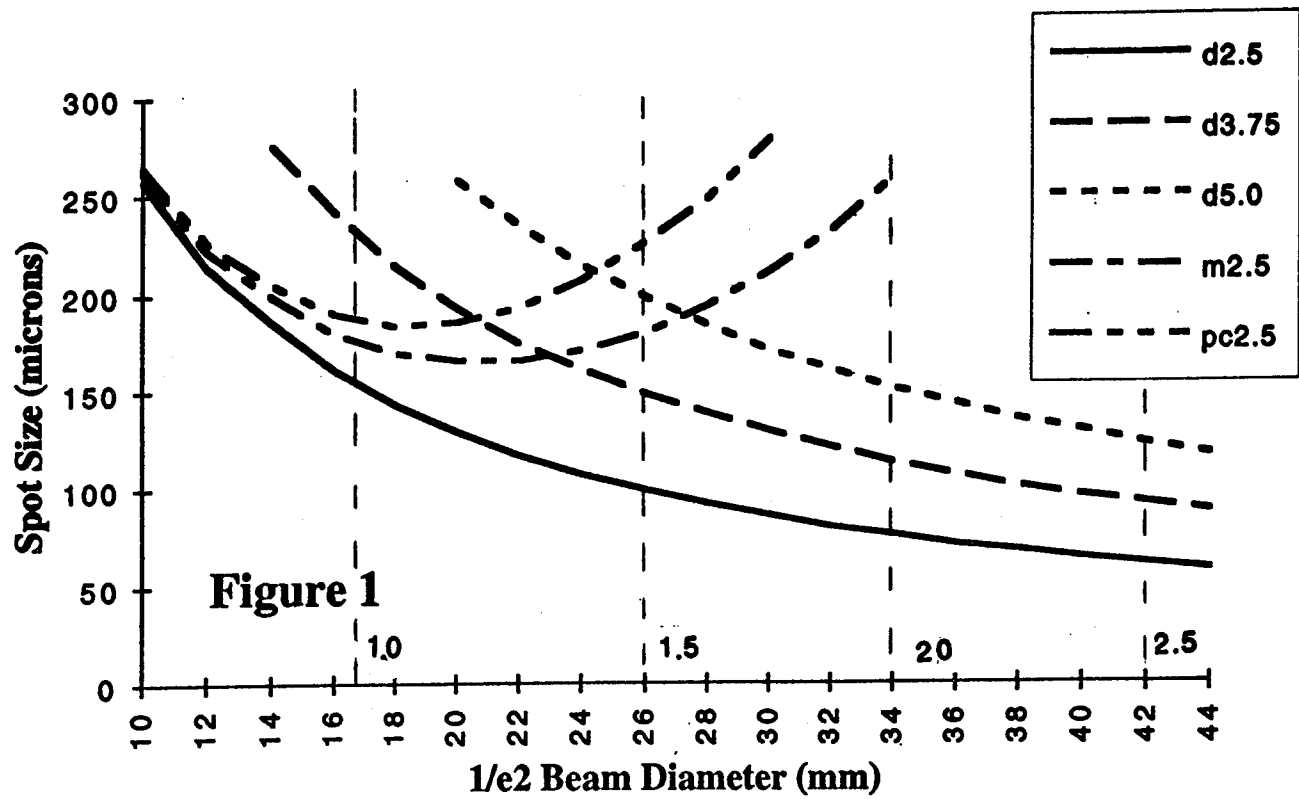
Diffractive elements are utilized in CO₂ industrial lasers to focus laser light to a diffraction limited focal point. Such a focus is smaller in cross-sectional dimensions relative that produced by a conventional, refractive focusing lens. A smaller focus at the workpiece enables more precise laser cutting and allows for a greater energy density to be available for cutting^{1,2}. These improvements are significant, but the key advantage achieved by using diffractive focusing elements is a reduction in the damage to the focusing element caused by "back splatter" and debris coming off the workpiece.

To a good approximation, the focal spot size of a conventional, refractive focusing lens is predicted by³

$$D = (4/\pi) (\lambda f M^2/d) + Kd^3/f^2 \quad (1)$$

where D and d are the 1/e² diameter of the focused and incident, respectively, laser beam (distance between the 1/e² "falloff" points of the intensity distribution), f is the focal length, and λ is the wavelength equal to 10.6 microns. K is a constant that, by industry standards⁴, is equal to .0187 for a ZnSe meniscus lens and equal to .0286 for a ZnSe plano-convex lens (both lenses transmitting light of wavelength equal to 10.6 microns). M² is a measure of the divergence of the laser beam⁵ and is approximated by the value equal to 3.0 for high power (1000-3000 Watts) CO₂ lasers and a value equal to 2.0 for low power CO₂ lasers (<1000 Watts). The second term in Equation 1 is the contribution to the focused laser beam diameter by spherical aberration. Therefore, the focal spot size produced by diffraction limited performance is predicted solely by the first term in Equation 1.

Using Equation 1, the predicted dependence of the focused 1/e² laser beam diameter D (spot size) upon the 1/e² diameter, d, of the collimated laser beam incident a variety of focusing elements is plotted (Figures 1 and 2). In all cases an M² value equal to 3.0 is assumed. In both figures, the dominance of spherical aberration is evident for refractive elements as the eventual increase in focal spot size with increasing incident laser beam diameter. In contrast, the absence of spherical aberration in diffractive elements is manifest by a monotonically decreasing focal spot size with



increasing incident laser beam diameter. As a result, for sufficiently large incident laser beam diameters, diffractive focal spot sizes are smaller than refractive spot sizes produced by refractive lenses with shorter focal length. For example, in Figure 1 a diffractive element having a focal length equal to 3.75 inches focuses incident laser beams with $1/e^2$ diameter greater than 23 mm to a smaller focus point than that of a meniscus lens with a 2.5 inch focal length. If the laser beam diameter is greater than 30 mm, a 5.0 inch focal length diffractive element also produces a smaller focal spot than does the 2.5 inch focal length plano-convex lens (Figure 1). This is a key advantage for diffractive elements. By increasing the separation between the focusing lens and workpiece, the susceptibility of the lens to back splatter and debris coming off the workpiece can be greatly reduced. An example of this is the removal of a lens out of the debris "plume" extending above a ceramic workpiece by replacing a 2.5 inch focal length refractive lens with a 3.75 inch focal length diffractive element. For this case the implementation of this scheme yields a ten to one hundred-fold increase in the lifetime of the focusing element.

In principle, the diffractive spot size can be reduced arbitrarily by increasing the diameter of the incident laser beam. To prevent the "overfilling" of a lens, 99% of the laser energy must pass through the lens aperture. This energy is contained in the beam width equal to 1.5 times the $1/e^2$ diameter of a Gaussian laser beam⁶. Thus the size of a diffractive element limits the arbitrary increase in the laser beam diameter. Diffractive elements for CO₂ lasers currently manufactured have diameters of 1.0 and 1.5 inches. The manufacture of diffractive elements with diameter equal to 2.0 and 2.5 inches is feasible. To exactly "fill" apertures with diameter equal to 1.0, 1.5, 2.0, or 2.5 inches requires Gaussian laser beams of $1/e^2$ diameter equal to 17, 26, 34, or 42 mm, respectively. These values are represented by the vertical dashed lines in Figures 1 and 2. Thus, the 2.5 inch focal length meniscus lens can equivalently be replaced with a 3.75 inch diffractive element with diameter equal to 1.5 inches (see Figure 1). This cross sectional area is large enough to intercept incident laser beams which are diffractively focused to an equal or smaller focal spot than the smallest focal spot possible using the meniscus lens. Even an 5.0 inch focal length diffractive optic with diameter equal to 1.5 inches can be used to produce a smaller focal spot than the 2.5 inch focal length plano-convex lens. In Figure 2, a lens with a diameter of 2.0 inches will be "overfilled" with laser light having cross-sectional area large enough to enable the equivalent replacement of a 5.0 inch focal length meniscus lens with a 7.5 inch focal length diffractive element. In this case, a larger diffractive focusing element with a physical diameter of 2.5 inches is needed.

The use of diffractive elements to achieve superior cutting performance by virtue of diffraction limited focusing has made a considerable impact upon the CO₂ industrial laser industry. A larger impact will be realized by the replacement of conventional, refractive focusing lenses by longer focal length diffractive elements to reduce lens damage and significantly lower operational costs.

References

1. R. Gruhlke, L. Giammona, and W. Sullivan, "Diffractive Optics for Industrial Lasers", in Diffractive Optics: Design, Fabrication, and Applications Technical Digest 1992. (Optical Society of America, Washington, D.C., 1992) Vol. 9, 61-63.
2. R. Gruhlke, L. Giammona, and J. Kedmi, "Medical and Industrial Laser Beam Shaping by Diffractive Optical Elements", in Laser Coherence Control: Technology and Applications, PROC. SPIE Vol. 1870 (1993).
3. G. Ripper and I. Herziger, "Werkstoffbearbeitung mit Laserstrahlung", *Feinwerktechnik and Messtechnik*, **92**, 297-302 (1984).
4. K. Hachfeld, Coherent General Inc., 1 Picker Road, Sturbridge, MA (personnel communication 1993).
5. M. Sasnett, "Propagation of Multimode Laser Beams-The M² Factor", The Physics and Technology of Laser Resonators, Adam Hilger, Bristol and New York, (1989).
6. A. Siegman, An Introduction to Lasers and Masers, McGraw-Hill, Inc., New York (1971).

Serrated Aperture and Its Applications in High Power Lasers

Ximing Deng, Dianyuan Fan, and Liejia Qian
National Laboratory on High Power Laser and Physics
P.O.Box 800-211, Shanghai 201800, P. R. China
Tel. 0086-21-9528355
Fax. 0086-21-9528885

In solid-state fusion lasers, spatially uniform laser beam is required in following two senses, (i). uniform beam with low peak over average ration (less than 1.5 for intensity) can provide large beam filling factor in active media as well as suppressing small scale self-focusing effect, so that more energy can be obtained from amplifiers and laser system can work at a higher energy flux without damage of optical components, and (ii). for laser fusion, uniform illumination of fuel pellets is highly required at or near the focus in order to produce the highly symmetric ablation pressure necessary for high gain. For these purposes, various methods have been developed. Soft apertures with tapered transmission and more recently the serrated apertures have been applied to high power lasers [1]. To achieve high illumination uniformity for target, schemes have been suggested which involve broad-bandwidth laser illumination with SSD [2] and ISI [3], radom phase plate (RPP) [4], and lens array [5]. In this paper we will give out our design procedure for serrated apertures, and discuss the lens array with a serrated edge for each lens element to improve the illumination uniformity further.

Serrated aperture seems quite ideal since it has high damage threshold and is easy to be used in practice, unfortunately, there is no detailed reports on it. Recently, we have designed serrated aperture based on Sommerfeld edge wavelets interpretation of diffraction, it is easy to understand what tends to reduce the in-phase addition characteristic of the circular aperture will tend to damp out the peak amplitude of Fresnel ripples. We find that serrated aperture with a modulated sinusoidal edge can effectively eliminate the near-axis intensity ripples in a large scale of Fresnel numbers(F). The edge shape of serrated aperture is described as follows.

$$r(\theta) = r_0[1 + \alpha \sin m_1 \theta \sin m \theta] \quad (1)$$

where $m_1 \ll m$, normally we can use $m_1 = 5$ and $m = 50$. Typical serrated aperture is given in Fig.1. To have a on-axis intensity variation less than 10%, the Fresnel number F should satisfy the equation (2).

$$ABS(\pi F \alpha - 2.44) \leq 0.5 \quad (2)$$

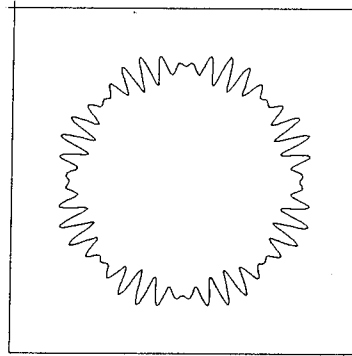


Fig.1 The serrated aperture.

Equation(2) as well as Eq.(1) gives out the design procedure for this kind of serrated aperture. For instance, if we want to place optics (Nd:glass slab) at $F=20$, then $\alpha = 0.04$ calculated from Eq.(2), the range of F is 15 to

25 where the on-axis intensity variation less than 10%, which corresponding to a space range of 3m for a 20 mm diameter aperture. Typical calculated results are shown in Fig.2. One could find that the diffraction behaviors of serrated aperture is very similar to that of supergaussian soft aperture. Furthermore, we should point out that serrated aperture designed here is quite insensitive to the form of modulation (sinusoidal in Eq.(1)), which is important for its use in practice.

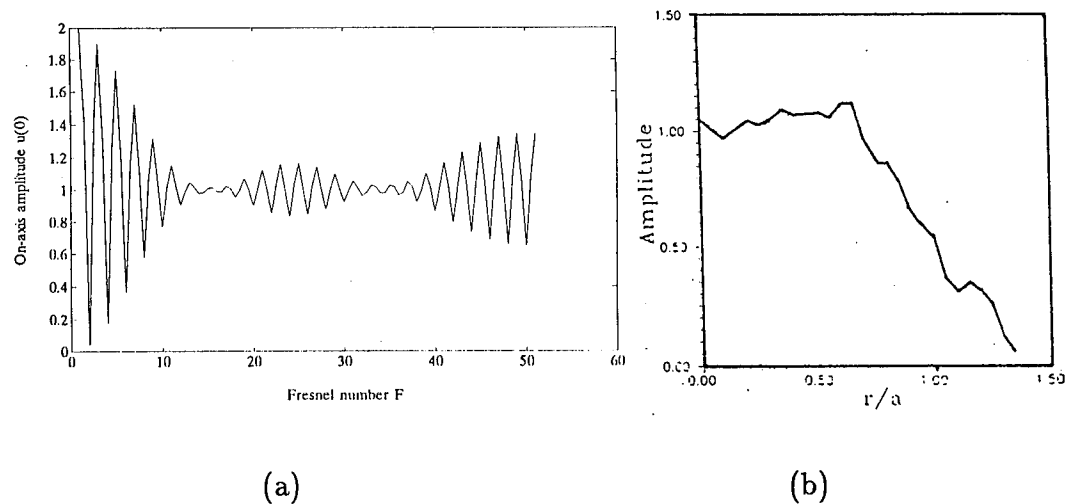


Fig.2(a). The calculated on-axis amplitudes vs Fresnel numbers for $\alpha = 0.05$, and (b). the calculated beam profile at $F = 20$.

As a application of this design, we employ it to the lens array focusing system in order to improve uniformity. Normally, there is still a certain large-scale intensity variation ($\sim 10\%$) by using common lens array, although it can provide much higher uniformity than common focusing lens by reducing the in-phase addition among the beams of all lens elements in the quasi-near-field. This large-scale variation is mainly due to the diffraction ripples of single lens element, therefore it is necessary to eliminate this diffraction ripples. By employing lens array with serrated edge designed, higher illumination uniformity is expected. We are sure that uniformity in a level of 1% could be achieved by using this novel design. Further developments along this direction

are undertook in our laboratory, which involve to use 3-D serrated lens array elements to improve the uniformity furthermore.

References

- [1] C.Bibeau, D.R.Speck, et. al., Appl. Optics, Vol.31, 1992, 5799.
- [2] S.Skupsky, R.S.Craxton, et. al., J. Appl. Phys., Vol.66, 1989, 3456.
- [3] R.H.Lehmberg and S.P.Obenschain, Opt. Commun., Vol.46, 1983, 27.
- [4] Y.Kato and K.Mima, Appl. Phys. B29, 1982, 186.
- [5] Ximing Deng, Xiangchun Liang, et. al., Appl. Optics, Vol.25, 1986, 377.

Wednesday, June 8, 1994

Fabrication by Direct-Write Techniques

DWD 4:00pm–5:30pm
Room B

Jurgen Jahns, *Presider*
AT&T Bell Laboratories

Fast and High Quality Surface Profiling for Microoptical Applications

E.-Bernhard Kley

Friedrich-Schiller-Universität Jena
Physikalisch-Astronomisch-Technikwissenschaftliche Fakultät
Institut für Angewandte Physik
Max-Wien-Platz 1
D-07743 Jena, Germany

Adaptations of lithographic technologies (variable shaped e-beam, variable dose and energy writing) for microoptical applications and new profitable lens profiles (> 10 lenses/s) were described.

FOCUSING DOE FABRICATION
USING VARIABLE SHAPED ELECTRON BEAM LITHOGRAPHY

Sergey Babin, Victor Danilov⁺

Physics and Technology Institute,
Krasikova, 25a, 117218 Moscow Russia

⁺Central Bureau for Unique Instrumentation
Butlerova, 15, 117311 Moscow, Russia

Diffraction optical elements (DOE) for laser beam forming have a spread range of applications. The results are presented on DOE fabrication, which focusing the infrared irradiation into a coil and into two points with required parameters.

The principles of artificial index gratings [1] were used for cylindrical zone plate topology generation. In this case the topology feature size is considerably less than the wavelength.

The results on Fresnel zone plates creation for soft X-ray are also regarded.

The most appropriate technique for diffraction optical elements as well as computer generated holograms fabrication is electron beam lithography (EBL). One of the main problem of EBL application to DOE fabrication is the necessity to treat a large amount of data consist ordinary from some tens of Megabytes to some Gigabytes. The formula for estimation of data volume is presented for DOE exposure depending on DOE parameters, fabrication precision and topology approximation techniques.

A data preparing system was developed. The topology approximation is carried out by rectangular fragments according to available electron beam sizes regarding the dividing into fields and subfields, which are determined by EBL equipment peculiarities.

The electron scattering processes in resist and substrate lead to fabricated topology distortions. On the base of experimental investigation of the effects the correction was provided and undistorted DOE's were created, including DOE's with subhalfmicron feature sizes.

Fabrication of multi-level phase gratings using focused ion beam milling and electron beam lithography

S. M. Shank, M. Skvarla, F. T. Chen, and H. G. Craighead

School of Applied and Engineering Physics and

The National Nanofabrication Facility

Cornell University, Ithaca, NY 14853

607-255-6286, Fax: 607-255-7658

P. Cook, R. Bussjager, F. Haas, and D. A. Honey

USAF Photonics Center, Rome Laboratory

Griffiss AFB, NY 13441

Diffraction optical elements designed for applications such as optical data storage and optical interconnects between VLSI chips in multi-chip modules require high diffraction efficiencies and large numerical apertures. Design specifications with sub-micron feature sizes present exacting requirements on the fabrication technology. In this work, two methods are compared and evaluated for fabricating high-performance diffraction optical elements and surface masters. Linearly blazed reflective gratings in silicon are fabricated with a focused ion beam (FIB) and with direct-write electron beam lithography and reactive ion etching (RIE). The relative simplicity of the fabrication process with a focused ion beam in one lithography step compared to the multiple lithographic exposures and etches used in the electron beam lithography process, is traded off against the relatively slow ion beam write times compared to the electron beam exposure speeds.

Direct-write electron beam lithography and RIE are used to fabricate 8-level gratings. This fabrication process involves four lithography steps and three etches. Exposures are performed on a 90nm thick layer of PMMA. A thin 60nm film of SiO_x between the Si substrate and the resist is used to enhance the RIE selectivity for the transfer of the exposed pattern into the substrate. The SiO_x layer is deposited by thermal evaporation from a SiO source. A smallest feature size of 0.5μm necessitates the correction of proximity effects due to scattered electrons in the resist. It is determined that an area dose of 60μC/cm² at 2nA beam current and 20kV accelerating voltage is near optimal. A 25nm square exposure element size is used to write the desired pattern. For 1mm×1mm gratings, electron beam write times per exposure are approximately

2.5min. A two-step RIE process is used to transfer the exposed pattern into the substrate. In the first step, a mixture of CHF_3 and O_2 is used to pattern the SiO_x and remove the PMMA. In the second step, a mixture of BCl_3 and Cl_2 is used to pattern the Si substrate. RIE parameters (chamber pressure, gas flow rates, and RF power) are adjusted to produce etch rates of approximately 24nm/min for the first step and 40nm/min for the second step. The fabrication process for one exposure and etch is schematically displayed in Fig. 1a. With proper control of dose, etching, and alignment between successive exposures, feature errors less than 50nm wide are achieved. This is shown in Figs. 2a and 2b which display SEM micrographs of one period of the grating and multiple periods of the grating respectively.

A $^{69}\text{Ga}^+$ focused ion beam is used to sputter continuously graded gratings. The linearly blazed surface relief is milled in a single lithography step by linearly varying the sputter yield across a given period. The linear variation in sputter yield is produced by a linear variation in area dose of the ion beam. A schematic representation of the FIB fabrication process is displayed in Fig. 1b. For a reflection grating designed to operate at $\lambda=633\text{nm}$ with $4\mu\text{m}$ wide periods, the area doses used to produce surface reliefs of $\lambda/2$ range from 4×10^{16} to 6×10^{17} ions/ cm^2 . For a given area dose, the FIB is raster-scanned the length of the grating using a 22.5nm square pixel size. The beam diameter is sub-tenth micron and the beam energy is 60keV. To account for the effects of redeposition of material and beam profile, a pattern scheme of 8 overlapping area doses within a given period is used. Atomic force microscopy (AFM) is used to characterize the surface relief profile. An AFM cross-section is shown in Fig. 3a. An 8-level grating fabricated by electron beam lithography is shown in Fig. 3b for comparison. Since the 8-level profile is only an approximation to a linear blaze, FIB gratings can produce superior diffraction efficiencies. Preliminary measurements indicate that both fabrication methods produce gratings with first order diffraction efficiencies exceeding 90%.

The fabrication of a continuously graded periodic surface relief by FIB milling, suggests that diffractive optical elements with binary surface profiles or surface profiles with inaccuracies due to fabrication errors, can be repaired and rendered continuous by FIB milling, thereby producing high-quality surface masters. The effects of surface profile, subwavelength features, and fabrication errors on diffraction efficiency, and the use of FIB for the repair of diffractive optical elements will be discussed.

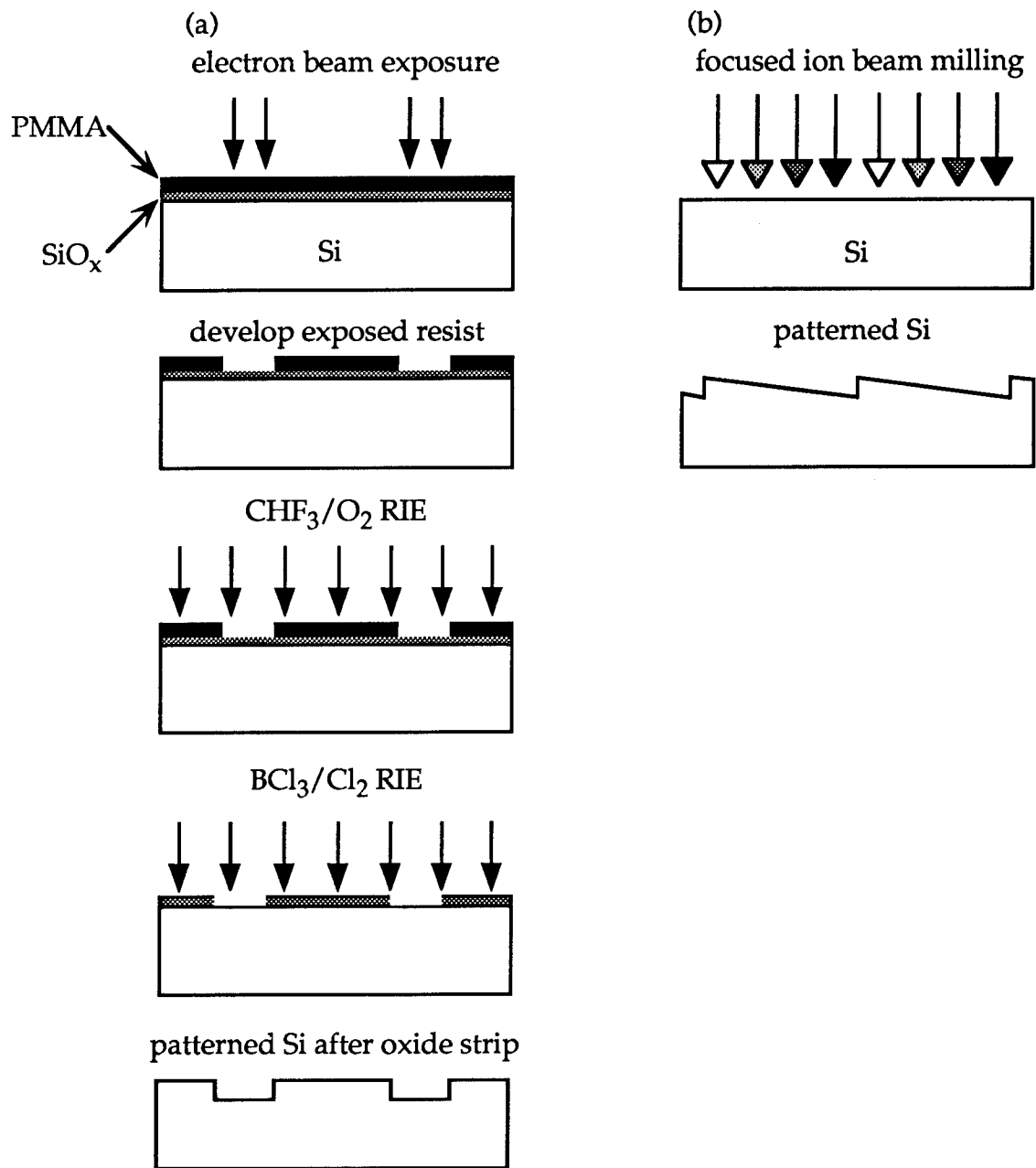


Fig. 1. Schematic representation of grating fabrication processes using electron beam lithography and reactive ion etching (a) and focused ion beam milling (b).

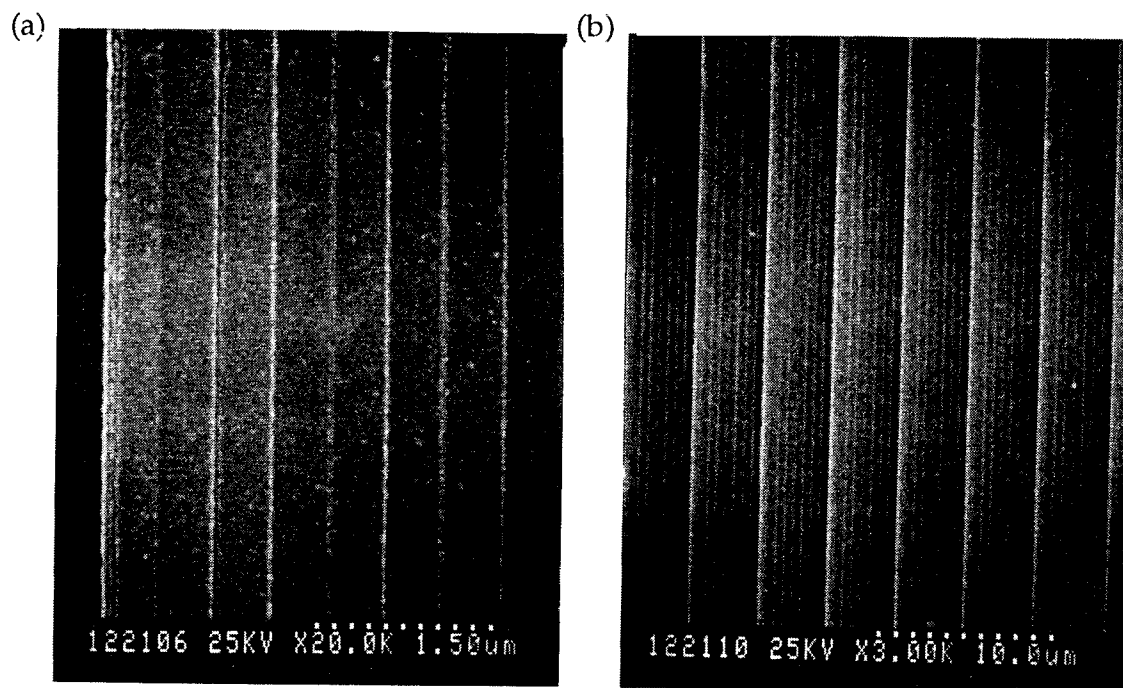


Fig. 2. SEM micrographs of one period (a) and multiple periods (b) of an 8-level linear grating fabricated by electron beam lithography and reactive ion etching.

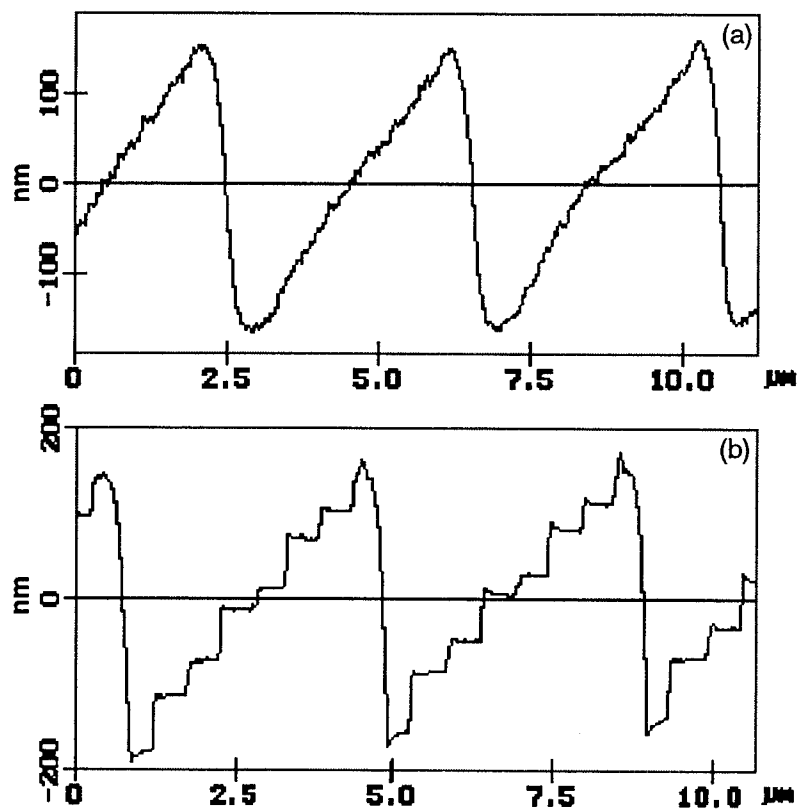


Fig 3. AFM cross-sections of surface profiles for gratings fabricated by (a) FIB and (b) electron beam lithography.

LASER WRITING AND REPLICATION OF CONTINUOUS-RELIEF FRESNEL MICROLENSSES

M.T. Gale, M. Rossi and R.E. Kunz

Paul Scherrer Institute, Badenerstrasse 569, CH-8048 Zurich, Switzerland
Tel. +41-1-492 6350 Fax +41-1-491 0007

G.L. Bona

IBM Research Center, Säumerstrasse 4, CH-8803 Rüschlikon, Switzerland
Tel. +41-1-724 81 11 Fax +41-1-724 17 89

1. INTRODUCTION

Fresnel microlenses and microlens arrays are planar Diffractive Optical Elements (DOEs) which are playing an increasingly important role in modern optical systems. Typical microstructures have surface relief amplitudes of up to about 5 μm , continuous-relief feature sizes down to about 5 μm and apertures varying from about 10 μm up to many millimeters for individual lenslets. They offer significant advantages as compact, lightweight optical elements which can be fabricated in plastic by replication techniques and mass-produced at low cost for industrial applications.

The complexity of Fresnel lenslet microstructures can vary from low aperture, relatively simple forms with only a small number of segments to complex, high aperture lenslets with a large number of Fresnel segments of varying phase numbers (see Figure 1). Modern design techniques enable Phase-Matched Fresnel Elements (PMFEs) to be computed with profiles and height steps optimised to maintain proper phase relationships at the design wavelength [1]. Such microoptical elements combine the advantages of geometrical and diffractive optical components and their optical characteristics can be considered as resulting from a combination of refractive and diffractive behaviour, depending upon the dimensions of the Fresnel segments. Fresnel lenses offer a considerable degree of functional flexibility, with typical applications in monochromatic (laser) or narrow band (LED) imaging and illumination systems.

The fabrication of Fresnel lenslets with continuous-relief surface profiles represents a challenging area of modern optical fabrication technology, in particular for high aperture lenslets with segment sizes in the order of micrometers. In this paper, we describe progress in the fabrication by direct laser writing in photoresist using a system which has been developed over a number of years at the Paul Scherrer Institute in Zurich [2], and describe a number of application examples. Laser writing offers a highly flexible approach for the fabrication of such elements. The photoresist recordings are electroformed to Ni replication shims from which replicas can be produced by embossing or casting techniques. The limitations in microstructure resolution and lenslet numerical aperture as determined by current technology are discussed and the typical performance of Fresnel lenslets fabricated by this technology are presented.



Fig. 1 Examples of simple and complex Fresnel lenslet microstructures :
(a) Basic, single phase number lenslet (b) Multiple phase number lenslet for high apertures.

2. FABRICATION TECHNOLOGY

Continuous-relief Fresnel microlenses are fabricated by laser writing in photoresist. After development of the exposed resist microstructure, the lenslet relief is electroformed to a Ni shim for replication by embossing or moulding techniques.

2.1. Basic Fresnel lenslet microstructure

From the fabrication point of view, Fresnel lenslet microstructures can be characterised by the maximum relief depth and the minimum segment size. In laser writing technology, the maximum depth is given by the resist layer thickness, typically $\sim 5 \mu\text{m}$ for high quality films of commercial, high resolution photoresists. The minimum segment size at the perimeter of the lenslet area is determined by the numerical aperture (NA) of the lenslet, together with the phase (height) step at the segment boundary. Figure 2 shows the relationship between the lenslet NA and the minimum segment size for various phase steps for a Fresnel lenslet designed to focus a parallel HeNe laser beam ($\lambda = 633 \text{ nm}$).

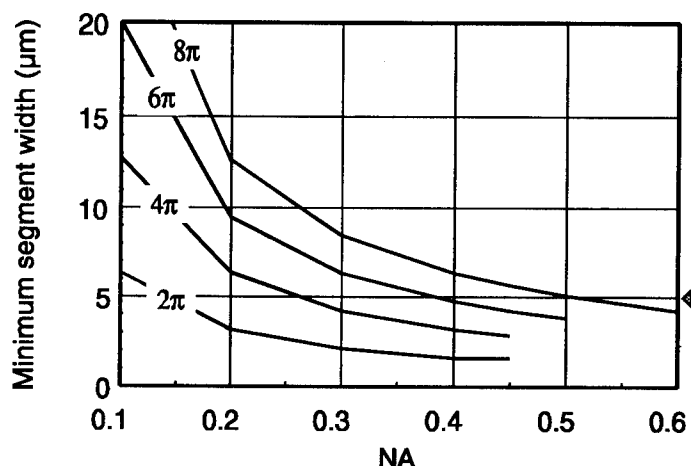


Fig. 2. Dependence of minimum segment size upon Fresnel lenslet NA for various phase steps (data from PMFE design routines for $\lambda = 633 \text{ nm}$).

Low NA lenslets with relatively large segment sizes ($\gg \lambda$) have a dominantly refractive behaviour and can be used in wideband (white light) systems. High aperture Fresnel lenslets with NAs approaching 0.5 require careful design and optimisation. The minimum segment size can be maximised by choosing the largest phase step possible within the limits of the resist thickness. Such lenslets have a dominantly diffractive behaviour and can generally only be used with monochromatic or narrow band (LED) illumination.

2.2 Laser writing and technology limitations

Figure 3 shows the basic laser writing system and the steps involved in fabricating continuous-relief Fresnel lenslets. The system, described in more detail elsewhere [2,3], uses a HeCd laser ($\lambda = 442 \text{ nm}$) to expose a photoresist coated substrate which is raster scanned under the focused beam using a high precision xy-stage. The surface-relief data resulting from the lenslet design are converted to exposure data using a measured resist development characteristic (relief v. exposure). Typical writing parameters are an interline spacing of $1 \mu\text{m}$, a focused spot size of about $1.5 \mu\text{m}$ and a writing speed of 10 mm/sec . The writing of arrays of Fresnel lenslets with zero dead space between lenslets is handled by additional software routines and is straightforward.

Reproducibility in the developed resist profile depth (using Shipley AZ 1400-37 resist and Microposit AZ 303 developer) is about $\pm 2\%$. The surface roughness of the developed resist surface is limited by the precision of the scan lines and is currently in the range $25\text{--}100 \text{ nm rms}$ [3]. The maximum slope at the segment edges is determined by the spot size and is typically greater than 70° . Although the use of a smaller spot size results in higher lateral resolution, it also results in unacceptable surface roughness with the present xy-stage positioning accuracy ($\sim \pm 150 \text{ nm}$). The maximum aperture of Fresnel lenslets is determined by the size of a segment in which the continuous-relief profile can be reasonably attained using

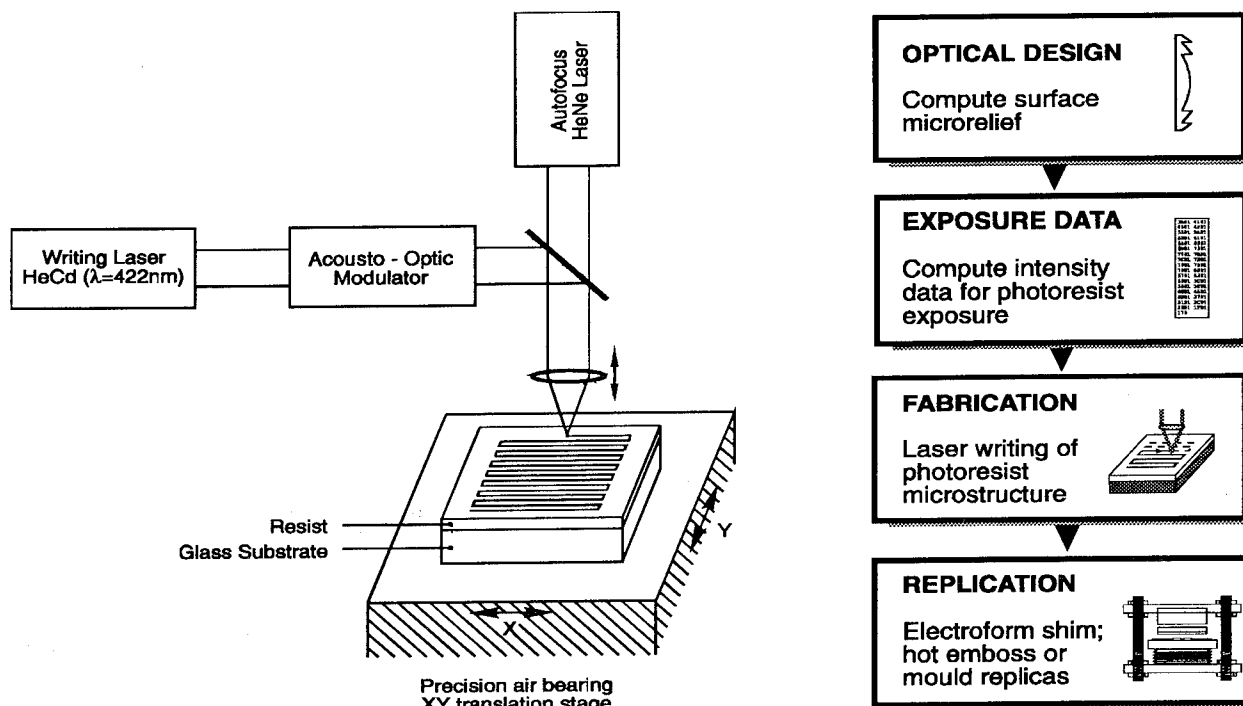


Fig. 3. Laser writing system and process steps for the fabrication of continuous-relief Fresnel lenslets.

the writing spot size, currently about $5\text{ }\mu\text{m}$. For a relief depth of $5\text{ }\mu\text{m}$, this corresponds to a maximum lenslet aperture of $\text{NA} \sim 0.5$ (for a phase step of 8π). Work is in progress to improve the line positioning accuracy in a next generation laser writing system, which should result in reduced roughness in the surface profiles and enable higher NA lenslets to be fabricated.

2.3 Replication

Resist surface-relief microstructures are electroformed to a Ni shim and reproduced by replication in plastic or epoxy materials. Replication technologies which are commercially available include hot embossing (diffractive foil and holograms), injection moulding (plastic optics and Compact Disks) and uv-replication techniques (microstructured foil). Shim fabrication techniques have fidelity much better than 100 nm and add minimal roughness ($< 1\text{ nm}$) to the lenslet surface-relief. The replication of microstructures with relief depth in excess of about $1\text{ }\mu\text{m}$ is generally not standard using the above technologies in an industrial environment and the replication fidelity is currently being evaluated using special test structures.

3. APPLICATION EXAMPLES

A variety of Fresnel lenslets and lenslet arrays have been fabricated over a number of years using the PSI laser writing system. They vary from arrays of more than 80×80 lenslets of low NA (< 0.01) for applications such as Shack-Hartmann wavefront sensors to small arrays of high NA (~ 0.5) for laser diode collimation and imaging. A number of selected examples will be described.

Figure 4 shows an AFM image and measured cross-section of the surface relief of a Fresnel microlens with $100\text{ }\mu\text{m}$ diameter and $\text{NA} \sim 0.1$. The lens has 4 Fresnel segments with a phase step of 2π ($\sim 1.1\text{ }\mu\text{m}$ at a wavelength of $\lambda = 633\text{ nm}$ for a lens replicated into polycarbonate foil). The fine structure on the surface results from line positioning errors in the laser writing process and results in straylight. Typical lenslets of this type have measured efficiencies (transmitted light focused into the central spot) of between 60% and 90%, depending upon the lens design and fabricated microstructure.

Figure 5 shows a more complex Fresnel lens structure with segments of varying phase steps (see Fig. 1b) of 2π up to 8π . The lenslet has a size of $250\text{ }\mu\text{m} \times 300\text{ }\mu\text{m}$ and $\text{NA} \sim 0.5$. The figure shows an AFM image of the fabricated microstructure and the design and fabricated profile of the central section. The measured efficiency of this lenslet was about 60%.

4. CONCLUSIONS

Continuous-relief Fresnel microlenses and lens arrays have been fabricated by laser writing in photoresist. For use in optical systems, the planar microoptical structures have been electroformed to Ni shims and replicated into various plastic and epoxy materials. The quality and performance of the Fresnel lenses is fully adequate for applications in optical illumination and imaging systems in which straylight is not of major significance. Design and fabrication techniques enable a wide range of lenslets and lenslet arrays to be produced, with typical applications in miniature, lightweight optical systems. The main current limitation in the fabrication technology is the limited scan accuracy leading to surface structure and roughness in the lenslet relief. This problem is being addressed in a next generation laser writing system - latest results will be presented at the conference.

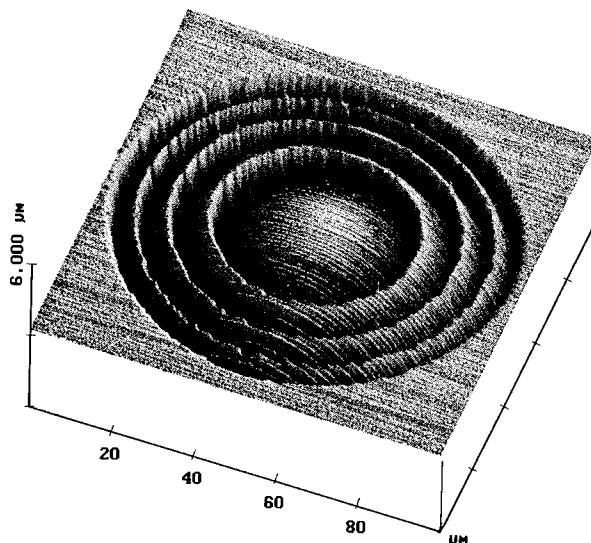


Fig. 4. Fresnel microlens structure (AFM image) and measured profile.

REFERENCES

- [1] R.E. Kunz and M. Rossi, "Phase-matched Fresnel elements", *Opt. Comm.* **97**, 6-10 (1993).
- [2] M.T. Gale, G.K. Lang, J.M. Raynor, H. Schütz and D. Prongué, "Fabrication of kinoform structures for optical computing", *Appl. Opt.* **31**, 5712-5715 (1992).
- [3] M.T. Gale, M. Rossi and H. Schütz, "Fabrication of continuous-relief microoptical elements by direct laser writing in photoresist", *Proc. SPIE* **2045** (1994).

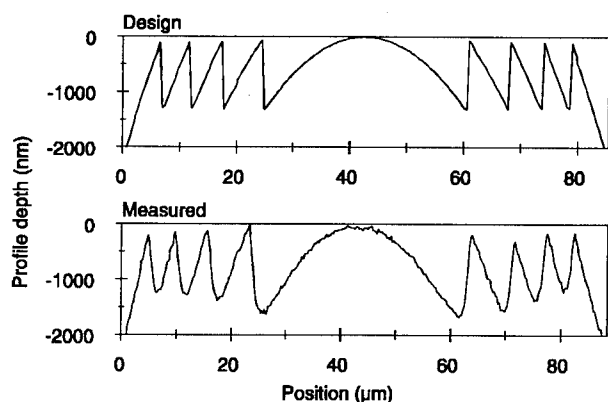
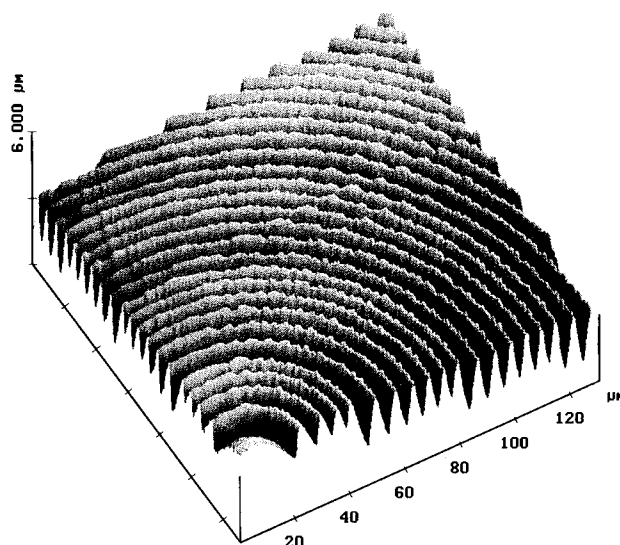


Fig. 5. Fresnel microlens - central area design and measured profile, and AFM image (right) of the fabricated microstructure.



Fabrication of diffractive optical elements by laser writing with circular scanning

V.P.Koronkevich, V.P.Kiryanov, V.P.Korol'kov, G.Poleshchuk, V.A.Cherkashin,
A.A.Kharissov

Institute of Automation and Electrometry Russian Academy
of Sciences, Siberian Branch, 630090 Novosibirsk, Russia
Tel.: 3832-35-59-21. E-mail: koronkevich.v.p@iae.nsk.su

1. INTRODUCTION

One of the problems in the development of diffractive optics is that of reproducibly fabricating topological structures with an overall area up to $(1-3) \cdot 10^4 \text{ mm}^2$ with a minimum dimension of elements less than $1 \text{ }\mu\text{m}$ and with a fabricating accuracy of $0.1-0.2 \text{ }\mu\text{m}$ at the boundaries of elements.

Two basic methods are known for forming microimages - phototype-setting and scanning method. Scanning is carried out in a Cartesian [1] or polar [2,3,4] coordinate system. In the last case, the microimage is formed through a continuous rotation of the substrate, while the focused light beam is simultaneously moved along the radius of the substrate. It is possible to produce a mask of specified configuration [with a amplitude computer-controlled modulation of the laser beam. Specific optical applications (wave front correction, astronomical mirror testing) require the fabrication of circular diffractive structures with size and quality which are difficult of access by x - y pattern generators.

Work on the fabrication of diffractive optical elements by laser beam writing was carried out in early 1980s in The Laboratory of Laser Technology, Institute of Automation and Electrometry of Russian Academy of Sciences.

The circular laser writing system has been designed and thermochemical technology for manufacturing of chromium masks of diffractive elements has been developed [2,4,5]. Direct writing with the high resolution on amorphous silicon films has been investigated [6]. The unique diffractive elements have been fabricated [4,7].

The paper describes the recent results of investigation of new laser writing system, which has been built-up at the Institute of Automation and Electrometry in Novosibirsk. The results of synthesis and test of 2-dimensional diffractive elements and arrays of micro-Fresnel lenslets are presented.

2. LASER WRITING SYSTEM

The circular laser writing system is shown schematically in Fig.1. The Substrate with thin Chromium film on it is fixed on the top of precision Air-bearing Spindle. The turning angle transducer is mounted on the spindle axis. The Angle-code Pick-up system forms the synchronizing pulses for stabilization of rotation speed and synchronizing of laser recording with turning angle of substrate.

Argon laser (488 nm) is mounted on the Granite Base with vibration isolator supports. Laser radiation is modulated by acoustooptical Modulator. Radiation intensity control system ensures the pulse-amplitude type modulation of laser radiation and suppression of it's fluctuations according the signal from light Feedback Photoreceiver. Then the laser beam enters the focusing Objective through the optical system, mounted on the mobile precision Air-bearing Table. The Objective forms a spot on the Substrate surface. The spot diameter is about $0.8 \text{ }\mu\text{m}$ (on the level $1/e$).

Autofocus system with electrodynamic actuator supports the focusing plane in the plane of Substrate during the write process.

Air-bearing Table is moved by means of computer-controlled Linear Motor Drive. Displacement measurement is made by laser Interferometer. The range of Table displacement is equal to 250 mm, positioning precision is near 100 nm rms (discreteness of Interferometer pulses is equal $\lambda/64=10 \text{ nm}$).

During write process the intensity quantity (scale - 10 bits) of writing laser beam is adjusted by computer through universal interface. The forming of pulse modulation signal is made by special adaptor, installed in computer. Adaptor has two RAM buffers that allows to carry out the recording

in continuous mode, alternating the RAM buffers.

Data output is stepped by pulses of Angle-code Pick-up system, that makes it possible to synchronize the laser writing with substrate angular rotation.

Microstructures are written by two methods: continuous spiral scanning and angular raster scanning. In the first case by two motions - substrate rotation and radial displacement of recording beam - the scanning of material surface is fulfilled. For qualitative synthesis of topology elements the spiral step must be smaller than the width of the recorded line. This method gives the maximum speed of writing. In case of circular zone plates or complex structures (when calculations during writing are demanded) writing the second methods is used.

The typical parameters of writing process are the following: substrate rotation speed - 10 r.p.s., written line width: 0.6 - 1 μm (which is given by the writing beam intensity), spiral step or angular raster pitch - 0.3-0.6 μm . The writing laser beam is positioned with precision of 0.1 μm for accurate circular structure's edges recording.

3. WRITING METHODS

The methods for recording of diffractive optical elements without photoresists usage have been developed. The first one [5], based on thermochemical action of laser radiation includes the exposure by laser beam of rotated substrate, covered by thin chromium film (the radiation power is less, than for film melting purposes) and chemical treatment of film in selective etching agent. The possibility of diffractive structures' recording with spatial resolution better, than 1200 mm^{-1} was shown.

Another method is based on amorphous silicon films crystallization and is accompanied by the increase of films transmission depending on exposure [6]. Thus, the continuous-tone recording with high spatial resolution is implemented. The necessary contrast is achieved by the choose of film thickness and exposure and can reach 10. During the writing process the resolution up to 1600 mm^{-1} can be achieved.

4. EXPERIMENTAL RESULTS

Fig.2 shows fragments of chromium masks of lenslet array recorded with raster pitch 0.6 μm . The above described laser writing system was used for different purposes: the microlens array mask recording with the size of some lenses from 10 μm up to several mm; the writing of rastered kinoform masks and synthesized holograms; precision angular scales (with the accuracy up to angular seconds); grids and so on.

REFERENCES

1. W.M. Moreau. «Semiconductor Lithography. Principles, Practices and Materials». Plenum Press. N.Y. and London, 1989.
2. V.P. Koronkevich et.al. «Fabrication of kinoform optical elements».- *Optik*, **67**, 259-266, (1984).
3. M. Haruna et.al. «Laser beam lithographed micro-Fresnel lenses».- *Appl. Optics*, **29**, 5120-5126, (1990).
4. V.P. Koronkevich et.al. «Kinoform optical elements: methods of design, manufacturing technology and practical application».- *Optoelectronics, Instrumentation and Data Processing* (Allerton Press Inc./N.Y.) No 1, 1-20, (1985).
5. V.P. Koronkevich et.al. «Laser thermochemical technology for synthesizing diffractive optical elements in chromium films».- *Kvantovaya Elektronika*, **12**, 755-761, (1985).
6. V.Z. Gotchiyaev et al. «High resolution optical recording on a-Si films».- *J. Non-Crystal Solids*, **137-138**, 1297-1300, (1991).
7. A.G. Poleshchuk. «Fabrication of phase structures with continuous and multilevel profiles for diffractive optics», *SPIE Proc.*, **1574**, (1991).

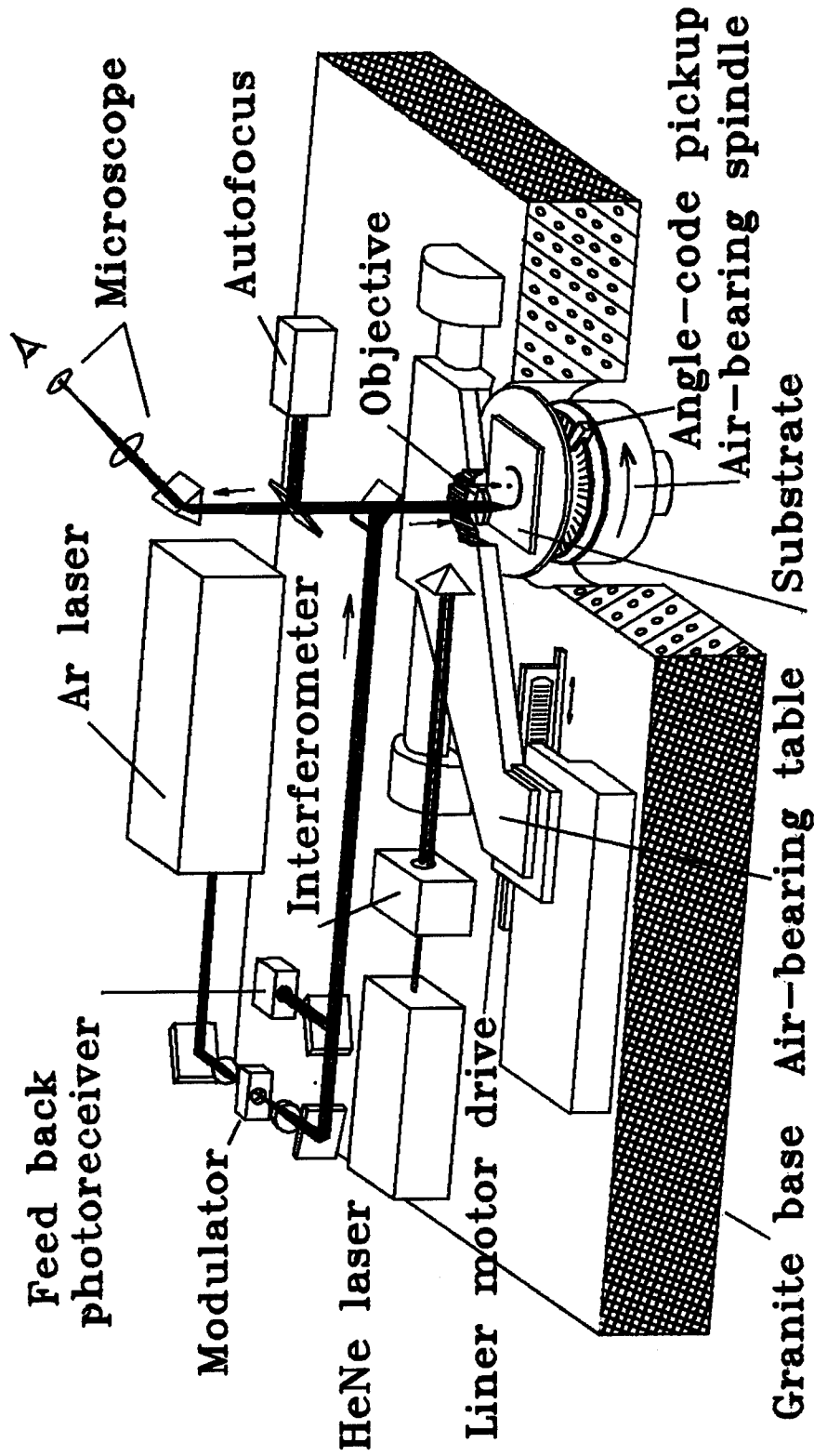
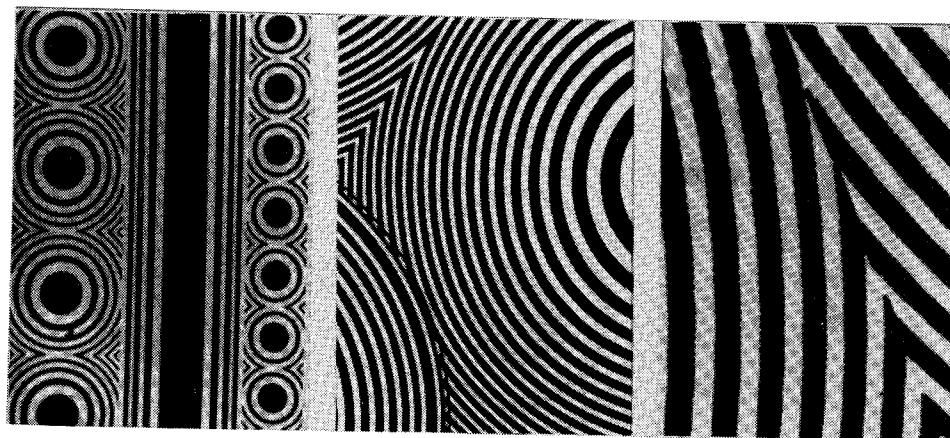


Fig.1. Circular laser writing system.

Technical specification: max. diameter of substrate - 300 mm; spot diameter - 0.8 μm ; laser beam modulation frequency - 0-3.5 MHz; radial coordinate resolution - 0.01 μm ; rotation speed - 1-20 1/sec; angular coordinate resolution - up to 0.1 angular seconds.



(a)

(b)

(c)

Fig.2. Chromium mask fragments of lenslet array fabricated by circular laser writing system:

(a) circular and cylinder Fresnel lenses with $N.A. = 0.15$ and 0.1 for wavelength $0.6328 \mu m$, size of lenses - 50 and $25 \mu m$;

(b) on-axis portion of lenslet array;

(c) spatial quantization error in the zone position of off-axis Fresnel lens caused by $0.6 \mu m$ raster pitch.

Thursday, June 9, 1994

Microlens Fabrication and Applications

DThA 8:30am–10:00am
Room B

Margaret B. Stern, *Presider*
MIT Lincoln Laboratory

The Manufacture of Microlenses

Michael C Hutley

National Physical Laboratory
Queens Road
Teddington, Middlesex
United Kingdom, TW11 0LW

The paper will review a variety of techniques for the manufacture of microlenses and their diffracting equivalents ("micro zone plates"). The relative merits of refracting and diffracting components will be considered from a practical point of view.

Diffractive Coupling Lenses : Fabrication and Measurements of Silicon Elements

Albert Stemmer, Hansastraße 27d,	Siemens, D-80686 Munich,	Corporate Research and Development, c/o IFT der Fraunhofergesellschaft, Tel. 49-89-54759092, FAX: 49-89-54759100
Helmut Zarschizky, Otto-Hahn-Ring 6,	Siemens, D-81739 Munich	Corporate Research and Development, Tel. 49-89-636-44609, FAX: 49-89-636-46426
Franz Mayerhofer, Otto-Hahn-Ring 6,	Siemens, D-81739 Munich	Corporate Research and Development, Tel. 49-89-636-45540, FAX: 49-89-636-46426
Guy Lefranc, Otto-Hahn-Ring 6,	Siemens, D-81739 Munich	Corporate Research and Development, Tel. 49-89-636-45163, FAX: 49-89-636-46426
Wolfgang Gramann, Wernerwerkstraße 2,	Siemens, D-93049 Regensburg	Semiconductors, Opto-Components Division, Tel. 49-941-202-2464, FAX: 49-941-202-2811

1. Introduction

The use of diffractive lenses for laser diode to single mode fibre coupling is attractive due to excellent imaging properties, possible mass production using advanced semiconductor technologies and easy handling of the final elements. High coupling efficiencies require firstly high diffraction efficiencies but also a very good match of image point characteristics to the fibre spot. High diffraction efficiencies should be possible by using multilevel elements to approximate a micro-FRESNEL lens. This leads to lens patterns with feature sizes in the range of well below one micrometer in lateral dimensions as well as in lens profil depth. The elements fabricated are realised in silicon and the techniques used range from CAD-data generation [1], E-beam lithography, reactive ion etching, anti-reflection coating, solder pad evaporation and wafer dicing.

2. Fabrication

The substrates on which the lenses are realised are 3" or 4" silicon wafers which have to be double side polished down to their final thickness. In dependence on the required size of the single lenses, about 1800 and 2500 lenses can be realised per wafer.

2.1 E-Beam Lithography

The patterning of the lenses is performed by direct write E-beam lithography with a Leica-Cambridge EBPG 4V-HR Beamwriter. The EPBG guarantees high performance in pattern transfer with a point to point resolution less than 10 nm. The Beamwriter is controlled by a software especially developed for the transfer of lens data. This software determines the control sequences for binary, quaternary, octernary and blazed patterning based on the calculated basic lens design. This three dimensional profiling of the resist system results from variations of dose, i.e. variations of writing frequencies. The necessary specific dose values are automatically linked to the E-beam data format via a so called profiling software, which calculates the dose from the experimentally measured gradation of the resist. Two coded frequency registers control the way of profiling with eight different frequencies. Blazed profiles can be generated with suitable accuracy by an intelligent combination of these available eight frequencies in each register. Beam diameter, beam current and beam step-size influence the surface-roughness of the resist caused by the development process. Furthermore, the Beamwriter, which works according to the vectorscan principle, cannot only realize rotation symmetry features, but also elliptic as well as arbitrary curved diffractive lenses, e.g. tilted and off-axis lenses. The high writing frequency, which is about 10 MHz, allows sufficient throughput. The target of the mass production of DOEs, however, should be the use of photolithographic systems for the fabrication. That could be done by using a set of reticles or special single masks manufactured by means of E-beam lithography.

After electron exposure, the three dimensional lens profile is developed with a wetchemical process [2, 3]. The new profiling software developed guarantees a more efficient three dimensional pattern transfer. Positive as well as negative resists spun on various substrates can be profiled. The positive tone resist PMMA is preferred due to its low sensitivity and linear gradation, which offers a wide process latitude. New results show that the negative tone resist SAL 601 (Shipley) can also be reliably profiled, though it is much more sensitive and shows a very steep gradation in comparison to PMMA. The high-resolution capacity of the Beamwriter enables the patterning of features of less than 200 nm in the above mentioned resist systems.

2.2 Etching

The developed three dimensional resist profile works as a mask for the dry etch process, which transfers the lens pattern into the substrate. In an MRC 50-RIE, structures of less than 300 nm can be transformed with an anisotropic etch process. An etchant of, SF₆, H₂ and Ar is used in order to etch the fine 3D-steps of the resist profile 1:1 into the substrate. The selectivity of the used resist - and substrate- system guarantees an optimal etch ratio and sufficient process latitude. After wet chemical development, etch depth and etch ratio can be controlled by post exposure bake.

2.3. Coating and Dicing

Both sides of the wafers are coated with antireflective $\lambda/4$ -layers of 160 nm PECVD-Si₃N₄. On the backside of the wafers solder pads are constructed by the evaporation of Ti-Pt-layers for AuSn-soldering. The metallisation layer is patterned by photolithography and a subsequent combined wet- and dry chemical etch process. The final separation is performed by wafer dicing on an adhesive tape for easy pick up and assembly.

Figures 1 show three SEM-micrographs of the centers of the binary (left picture), the quaternary (middle) and the octernary version (right picture) of a coupling lens. The lenses are fabricated for an operation wavelength of 1.3 μm have a numerical aperture of 0.5 and focal length of 270 μm . The smallest feature size of the binary lens is 1 μm , the quaternary and the octernary lenses have considerably smaller features. Figure 2 demonstrates the lens profiles for different sections of the center cross-section of the octernary lens. The left picture is taken near the lens center, the middle shows the region of half the lens radius (about 150 μm from the lens center) and the right picture is taken at the edge of the lens. Obviously the 8-level staircase profile turns to the wanted smooth sawtooth-like profile.

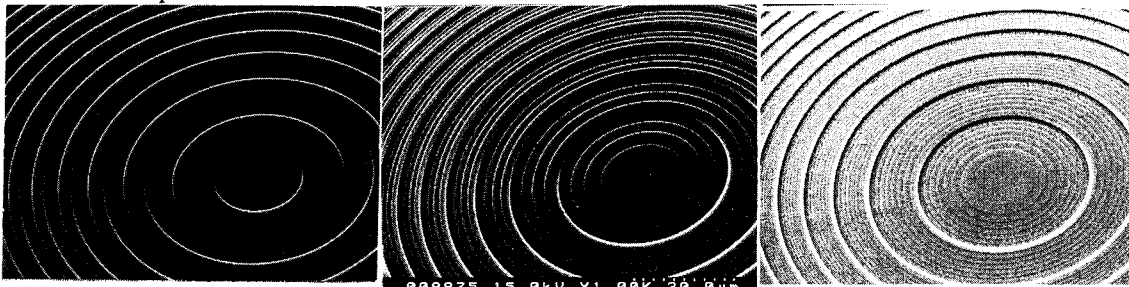


Fig.1: SEM-micrographs showing the centers of a binary lens (left), the quaternary version (middle) and the octernary version (right) of the silicon coupling lens.

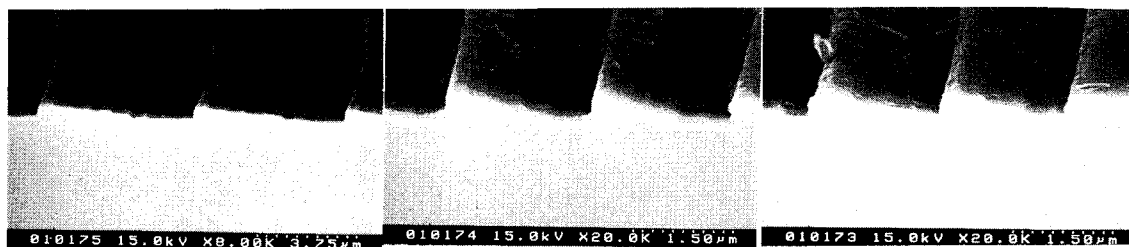


Fig.2: SEM-micrographs of the octernary lens. The side view of a cut through the lens center shows the etched profiles of the lens pattern

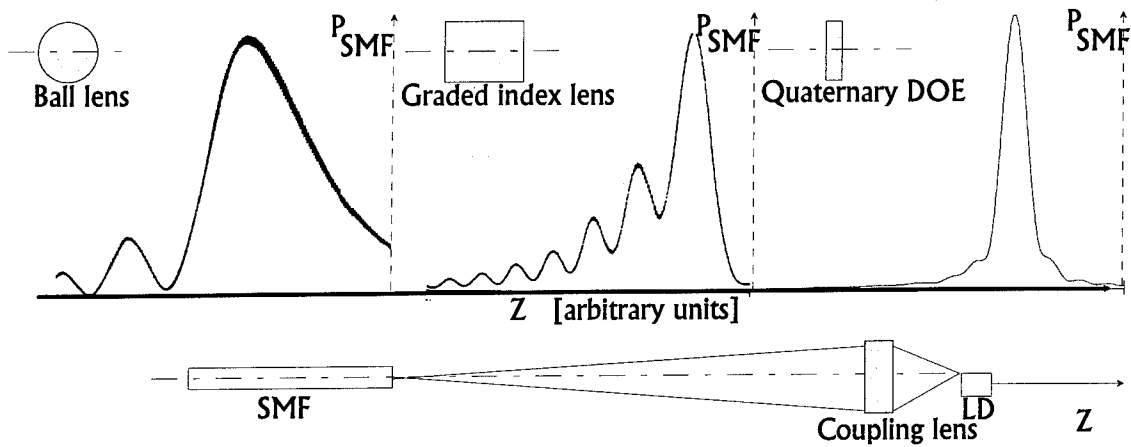


Fig.4: Comparison of different coupling optics with respect to spherical aberration.
The measurements are carried out by moving the laser diode along the optical axis (Z) while the position of the single-mode-fibre and the lenses kept constant.

For the measurement of the diffraction efficiency η_d , the fibre table is replaced by a translation stage carrying a small aperture InGaAs-detector (75 μm sensitive area). After optimum adjustment of the detector, the $P_{\text{Detector}}/I_{\text{Laser}}$ curve is measured and compared to the $P_{\text{Laser}}/I_{\text{Laser}}$ curve. A couple of different binary, quaternary and octernary elements are measured. Basic data from such elements are listed in the table below. An important value is the maximum etch depth T . The table gives the measured etch depth T_m and the depth T_{th} which is assumed to be the optimum depth for maximum diffraction efficiency.

Lens type	T_{th} [nm]	T_m [nm]	η_c [%]	η_d [%]
Binary	260	220	18	26
Quaternary	390	400	38	64
Octernary	455	480	42	72

Table of measured results for different diffractive lenses fabricated for laser diode - fibre coupling

6. Conclusion

Silicon coupling lenses for laser diode - single mode fibre coupling have been realised using techniques and technologies of the semiconductor fabrication. The results of pattern fabrication show the possibility of achieving smooth and staircase patterns of submicron feature size. The measurements of element performance prove that high efficiencies can be reached.

7. References

- [1] H.Zarschizky, A.Stemmer, A.Daiderich, "Diffractive Coupling Lenses: Design, Calculation and CAD-Data Generation", *Diffractive Optics: Design, Fabrication and Applications*, Rochester (1994), this issue.
- [2] A.Stemmer, H.Zarschizky, F.Mayerhofer, G.Lefranc, H.W.Schneider, P.Galloway, "Design and Fabrication of Synthetic Lenses in Silicon", *SPIE vol. 1732*, London (1992), 77-88.
- [3] A.Stemmer, H. Zarschizky, E.Knappek, G.Lefranc, H.Scherer, "Design and Fabrication of Multilevel Diffractive Optical Elements (DOEs) and Holographic Optical Elements (HOE's)", *Microelectronic Engineering* 21 (1993) 471-474

PHASE-MATCHED FRESNEL ELEMENTS FOR OPTICAL INTERCONNECTS

M. Rossi, R.E.Kunz and G.L. Bona*

Paul Scherrer Institute, Badenerstrasse 569, CH-8048 Zurich, Switzerland
Tel. +41-1-492 6350 Fax +41-1-491 0007

* IBM Research Center, Säumerstrasse 4, CH-8803 Rüschlikon, Switzerland
Tel. +41-1-724 8111 Fax +41-1-724 1789

1. INTRODUCTION

Many applications in optics require efficient devices for interconnecting light emitters to different configurations of output ports. In recent years, parallel optical data links have attracted increasing interest in the field of data communications. Typical applications are parallel high-speed and high-capacity interconnects for optical switches, workstation clusters or even between processor chips. Realizing optical crossbar switches and optical clock distribution on a processor board are applications requiring a fan-out operation. In this paper, experimental and theoretical results are presented for novel, single element optical interconnects based on phase-matched Fresnel elements (PMFEs) [1]. These are planar surface microrelief structures which are well suited for low-cost mass replication. Laser diode to fiber connecting lens arrays with high numerical aperture as well as focusing Nx1 fan-out elements have been designed and fabricated.

2. PHASE-MATCHED FRESNEL ELEMENT ARRAYS FOR LASER TO FIBER COUPLING

The design of PMFEs aims at structuring the surface of a thin layer in order to image an object point O on an image point P through an arbitrary number of different media, including curved interface planes and reflective arrangements. For conciseness, we only deal with the specific example of laser to fiber array coupling (see Fig. 1) in this Section. The design procedure starts with a principle ray for which the optical phase Φ_P in the image point is calculated as

$$\Phi_P = \sum_k 2\pi \cdot n_k r_k / \lambda, \quad (1)$$

where λ is the optical wavelength in air, n_k is the index of refraction of the medium k and r_k is the geometrical path length of a ray traversing it. Next, a ray which is shifted by a small increment along a

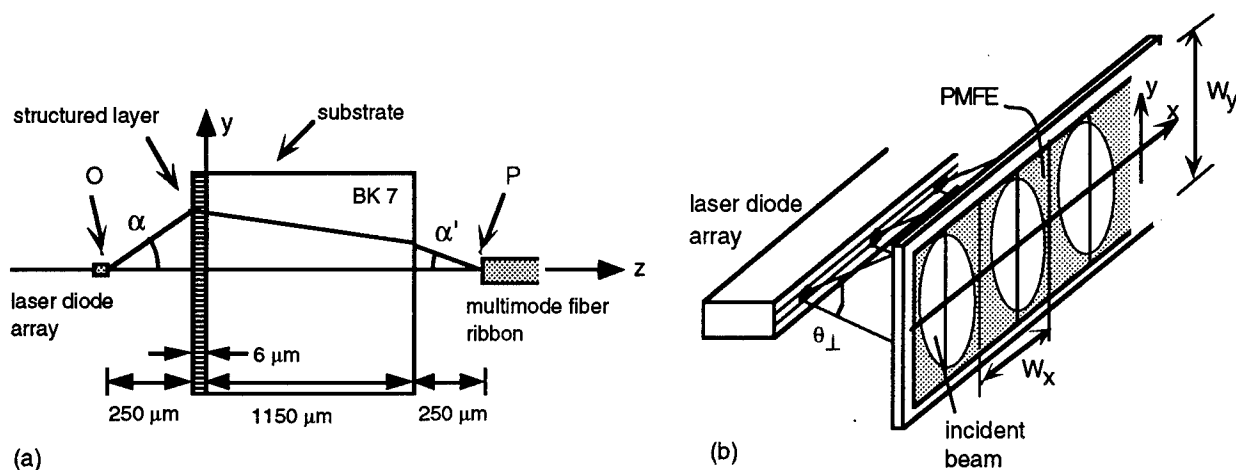


Fig. 1. Optical arrangement for laser to fiber coupling: (a) vertical (y,z) plane cross-section, (b) illumination of PMFE structured layer by the laser diode array

radial line in the yz -plane is propagated from O to P. At the actual ray position, a curved surface element is calculated such that the phase Φ_P in the image point is kept constant up to an integer multiple of 2π . This leads to a segmentation of the surface relief. For the resulting microoptical surface, the phase Φ_P is (i) constant for any two rays which cross the same segment and (ii) differs by an integer multiple of 2π for two rays crossing different segments. The phase difference $M \cdot 2\pi$ between neighboring segments is given by the phase-matching number M which is a powerful design parameter for optimizing the optical performance within the constraints imposed by the fabrication process. To fabricate the PMFEs, a direct laser writing process in photoresist [2] was used which required the size of any individual segment to be $w_i > w_{\min} = 5 \mu\text{m}$. A higher value of M leads to wider and deeper segments. One design strategy was to locally vary the phase-matching number M in order to keep the surface relief depth h_i below the photoresist thickness h_{\max} and maintaining the condition $w_i > w_{\min}$ for segment i . The computer-generated PMFEs can be considered to represent a generalized type of Fresnel microlenses whose zones have a locally varying depth.

A major advantage of the PMFE approach is that arrays of planar elements with very high numerical aperture and an arbitrary clear aperture shape can easily be generated and mass fabricated on a single substrate. Therefore, PMFEs were chosen for accomplishing the compact parallel optical interconnection of a laser diode array to a fiber ribbon cable. Only the most conspicuous facts are discussed here.

The main requirements for this application were a high optical laser-to-fiber throughput $T_n = P_{F,n}/P_{L,n}$ and a low crosstalk $T_{nm} = P_{F,n}/P_{L,m}$, where $P_{F,n}$ is the power incident on fiber No. n in the (x',y') image plane, and $P_{L,m}$ is the total power emitted by laser m . For the single lenslets, optimizing T_n calls for (1) a high numerical aperture NA, (2) adapting the clear aperture shape and size to the laser beam profile at the entrance pupil, and (3) achieving a high efficiency $\eta_n = P_{F,n}/P_{E,n}$ where $P_{E,n}$ is the power incident on the clear aperture of lenslet n . Some important factors for crosstalk minimization in a practical device are (i) a good image quality, (ii) a large tolerance for fiber misalignment, and (iii) proper lenslet entrance pupil locations. For the present example, the most important design parameters and experimental results can be summarized as follows.

Each laser emitted an astigmatic beam with divergence angles $\theta_{\perp} = 8^\circ$ and $\theta_{\parallel} = 28^\circ$ (FWHM) in the horizontal (x,z) and vertical (y,z) planes, respectively, at a wavelength of 831 nm [3]. The MT-connector compatible ribbon cable consisted of 12 multimode fibers with numerical apertures $NA_F = 0.21$ and diameters $\varnothing_{co} = 50 \mu\text{m}$ of the core and $\varnothing_{cl} = 125 \mu\text{m}$ of the cladding.

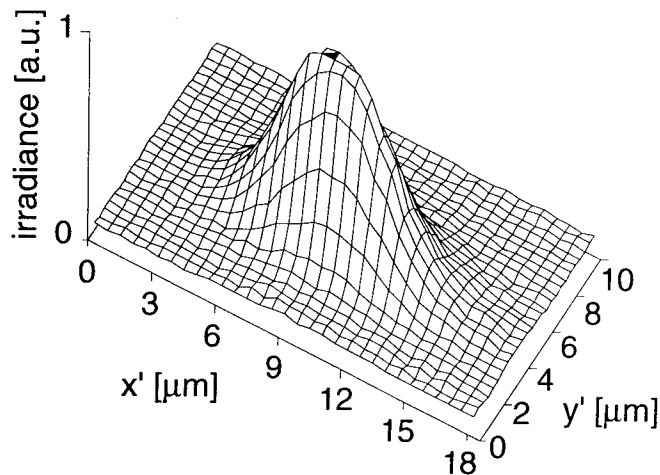


Fig. 3. Output spot irradiance distribution measured by a 2D CCD array.

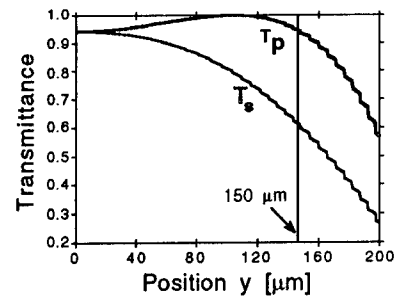


Fig. 2. Position dependent transmittance of s- and p-polarized beams incident at the PMFE surface.

Optimization with respect to the above aspects (1-3) and (i-iii) resulted in the optical arrangement as shown in Fig. 1. A PMFE prototype consisted of a $6 \mu\text{m}$ thick structured photoresist layer on a BK7 substrate. In addition to the parameter values directly given in Fig. 1, widths $W_x = 250 \mu\text{m}$ and $W_y = 300 \mu\text{m}$ were chosen for the rectangularly shaped PMFE lenslets. W_x is equal to the inter-laser and inter-fiber spacing while W_y corresponds to an object side $NA = \sin \alpha = 0.51$ distinctly greater than the laser beam half-maximum $NA_L = 0.24$. For the PMFE, Fresnel reflection losses can cause a decrease of transmittance especially for large angles of incidence. The polarization-dependent transmittance plotted in Fig. 2

shows that the $NA = 0.51$ ($y = W_y/2 = 150 \mu\text{m}$) can be achieved with a still high efficiency even for s-polarized lasers. It also shows the importance of taking into account the strongly inhomogeneous distributions of the irradiance and the polarization state in the entrance pupil. The relevance of these and other factors will be discussed at the conference.

The fiber input coupling efficiency and adjustment tolerance were optimized by a low image side $NA' = \sin \alpha' = 0.13 < NA_F$ still yielding a small image spot size $D'_{//} = 13 \mu\text{m}$ and $D'_{\perp} = 5 \mu\text{m}$ ($< \varnothing_{co}$). The image spot irradiance distribution is shown in Fig. 3. For a first prototype, an overall optical throughput of $T_n = 60\%$ was measured.

3. FOCUSING FAN-OUT ELEMENTS BASED ON INTERLACED PMFES

Other important applications require a fan-out operation, i.e. the optical interconnection of a single light source to N output ports. For typical diffractive optical fan-out elements [4] realized as surface microrelief structures, the input and output beams are collimated. Additional optical elements, which have to be positioned accurately, are therefore required for point-to-point interconnections.

In this Section, results are reported for a novel kind of computer-generated fan-out component, combining the focusing and splitting operation in one single planar microoptical element. The focusing function is implemented by means of PMFES, whereas the desired fan-out effect is accomplished by combining different types of PMFES (e.g. one for each interconnection channel) in a special area sharing arrangement. The basic principle of this approach has been proposed in [5]. The surface microrelief structure of a 5×1 fan-out PMFE fabricated by laser writing in photoresist is shown in Fig. 4. Each type of PMFE, denoted by the letters A..E, is divided into a subarray structure, leading to an array of focused diffraction orders centered around the focal point of the unsplit PMFE. In order to obtain a linear array of image points, the period of the different subarray structures is chosen so that the diffraction orders coincide with the desired image point array. Therefore, in each image point the focused diffraction orders originating from the different types of PMFE subarrays are coherently superposed. This concept can easily be extended for realizing 2D fan-out elements.

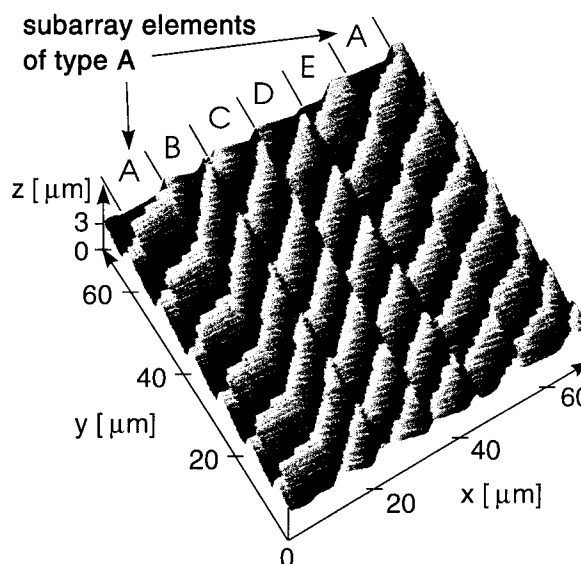


Fig. 4. Interlaced subarray structure of a fan-out PMFE measured by an atomic force microscope.

For optimizing such fan-out PMFES, simple and fast procedures have been developed based on a low number of parameters having a well-defined physical optical meaning. Focusing fan-out elements with a theoretically vanishing uniformity error and an efficiency in the range between 85% and 95% have been calculated. Figure 5 shows theoretical and experimental results for a focusing fan-out element splitting a collimated HeNe laser beam (wavelength = 632.8 nm) into a linear 5×1 point array, equally spaced by a $68 \mu\text{m}$, at a back focal length of 10 mm. The total microrelief area was $1.6 \times 1.6 \text{ mm}^2$. A uniformity error $\gamma = (P_{\max} - P_{\min}) / (P_{\max} + P_{\min}) < 0.1\%$ was calculated. Here, P_{\min} and P_{\max} denote the minimum and maximum powers delivered to the single spots, respectively. The measured uniformity error was $< 1.4\%$, which compares favourably with other results published recently [6,7].

In order to assess the loss in efficiency due to the spatial multiplexing of the PMFES, we define a relative efficiency η_r as the ratio between the total power in the image spot array and the power in the spot of a contiguous single PMFE. The measured values of $\eta_r > 77\%$ are close to the theoretically predicted value $\eta_r = 86\%$.

Table 1. Dependence of uniformity and efficiency on relief depth for a focusing 5x1 fan-out PMFE.

depth scaling	uniformity error γ	rel. efficiency η_r
1.2	4.79%	77.7%
1.1	3.51%	77.3%
1.0	1.37%	77.1%
0.9	2.15%	78.6%
0.8	3.06%	82.4%

A major aspect of this approach is the high tolerance with respect to fabrication errors of the fan-out performance in terms of uniformity. Whereas conventional non-focusing surface relief fan-out elements show a uniformity reduction of up to 10% for a depth scaling error of a few percent [4], fan-out PMFEs showed a good uniformity over a range of $\pm 20\%$ for the depth scaling error. The experimental results reported in Table 1 show that the uniformity error is $< 5\%$ and the relative efficiency is $> 77\%$ for five different elements where the microrelief depth has been intentionally varied in steps of 10% around the design value.

4. CONCLUSIONS

Experimental and theoretical results have been presented for novel, single planar element optical interconnects. It has been shown that phase-matched Fresnel elements are suitable for realizing parallel optical interconnections of a laser diode array to a fiber ribbon cable as well as focusing fan-out elements. By this approach, the optical performance of elements with a high numerical aperture can be optimized taking into account the constraints imposed by the fabrication process. The computer-generated surface microreliefs were fabricated by a direct laser writing process in photoresist. These planar optical elements lend themselves for low-cost mass production by replication in plastic materials. Focusing fan-out elements have been designed and fabricated based on a spatially interlaced arrangement of planar lenses. Excellent uniformity and a high tolerance with respect to fabrication errors have been demonstrated.

5. REFERENCES

- [1] R.E. Kunz and M. Rossi, "Phase-matched Fresnel elements," *Opt. Comm.* **97**, 6-10 (1993).
- [2] M.T. Gale, M. Rossi and H. Schütz, "Fabrication of continuous-relief microoptical elements by direct laser beam writing in photoresist," *Proc. SPIE*, Vol. **2045** (1994).
- [3] H. Jaekel, G.L. Bona et al, "Very high power AlGaAs SQW-GRIN SCH ridge laser with frequency doubled output," *IEEE J. Quantum Electron* **27**, 1560-1567 (1991).
- [4] M.T. Gale, M. Rossi, H. Schütz, P. Ehbets, H.P Herzig, and D. Prongue, "Continuous-relief diffractive optical for two-dimensional array generation," *Appl. Opt.* **32**, 2526-2533 (1993).
- [5] M. Rossi and R.E. Kunz, "Phase-matched Fresnel elements for fan-out applications," *Proc. IEE* **379**, 27-31 (1993).
- [6] G. Hatakoshi and M. Nakamura, "Grating lenses for optical branching," *Appl. Opt.* **32**, 3661-3668 (1993).
- [7] D. Wood, P. McKee and M. Dames, "Multiple-imaging and multiple-focussing Fresnel lenses with high numerical aperture," *Proc. SPIE*, Vol. **1732**, 307-316 (1992).

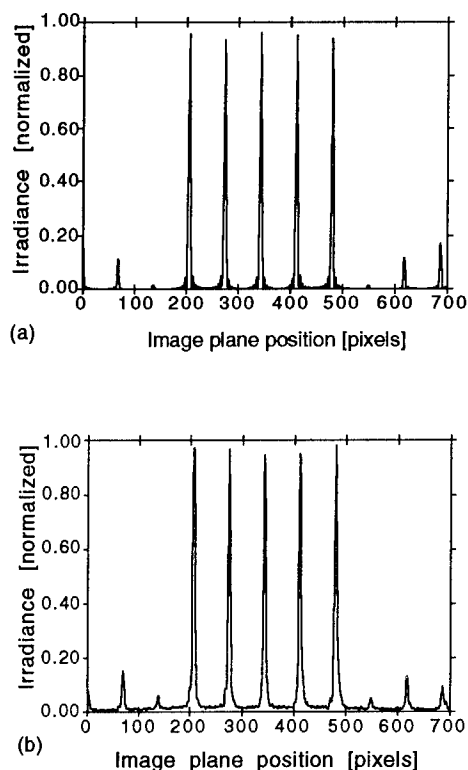


Fig. 5. Theoretical (a) and experimental (b) irradiance distribution in the image plane of a focusing 5x1 fan-out element.

Diffractive Interconnecting Device for Fiber-to-Chip Coupling

Ph. Regnault, H. Buczek*, O. Anthamatten**, G. Voirin, Ch. Zimmer***, H. Gilgen***

CSEM Centre Suisse d' Electronique et de Microtechnique SA
Maladière 71, CH-2007 Neuchâtel, +41 38 205 111, +41 38 205 617 (fax)

*Optique Consulting H. Buczek, Verger en Joran 20, CH 2074 Marin

**Ascom Tech, Morgenstrasse 129, CH-3018 Berne

***Swiss PTT, Ostermundigenstrasse 93, CH-3000 Berne, Switzerland

Introduction

Next generation of optical fiber telecommunication systems will require advanced coupling systems for interconnecting multi-fiber arrays to optoelectronics devices with multiple optical ports. For instance, coupling a pair of optical fibers to a double-channel GaAs modulator is a challenging task. In this case, the spacing of $250\text{ }\mu\text{m}$ between adjacent fibers is ten times the waveguide spacing. Moreover, for optimum coupling, the spherical beams emerging from the fiber outputs must be converted into highly elliptical beams matched to the waveguide mode shape. The desired two-beam adaptation⁽¹⁾ could be performed with an optical set-up composed of two pairs of cylindrical lenses and prisms (Figure 1). However, to miniaturize the coupling system on the appropriate scale, planar diffractive optical elements (DOE) are more suitable than bulk refractive optical elements. A compact coupling system was fabricated, based on the innovative design of a double-side diffractive optical device.

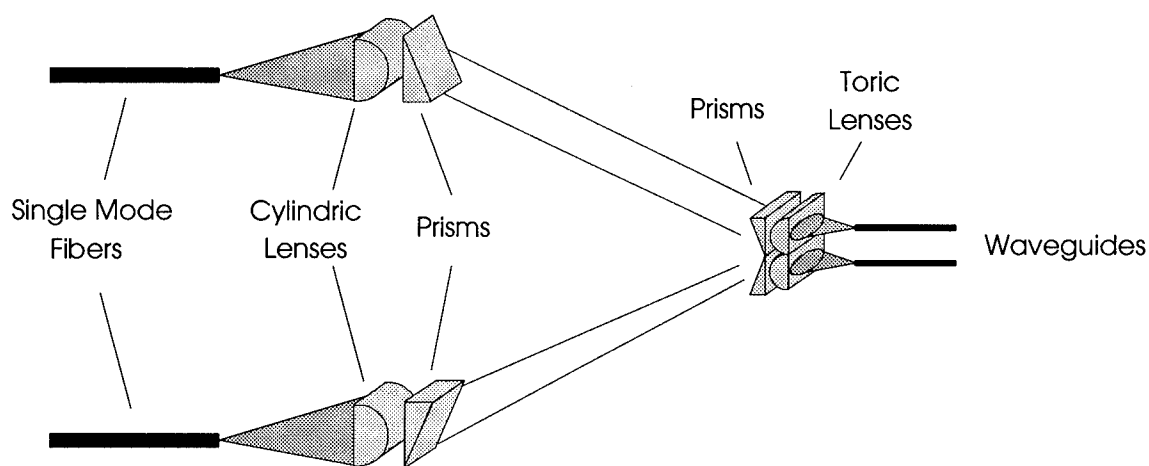


Figure 1 Bulk optics model of the coupling system

the multi-level approximation of the diffractive phase functions of DOE1 and DOE2 to four and two levels respectively with corresponding depths of 2.1 and 1.4 μm at the wavelength of 1.3 μm . Figure 3 shows a scanning electron micrograph (SEM) of DOE1 etched in fused silica using a RIE plasma etcher. DOE1 masks were aligned with a submicron overlay accuracy. DOE2 was aligned with respect to DOE1 on a double-side mask aligner. Side-to-side alignment accuracy was better than 2 μm .

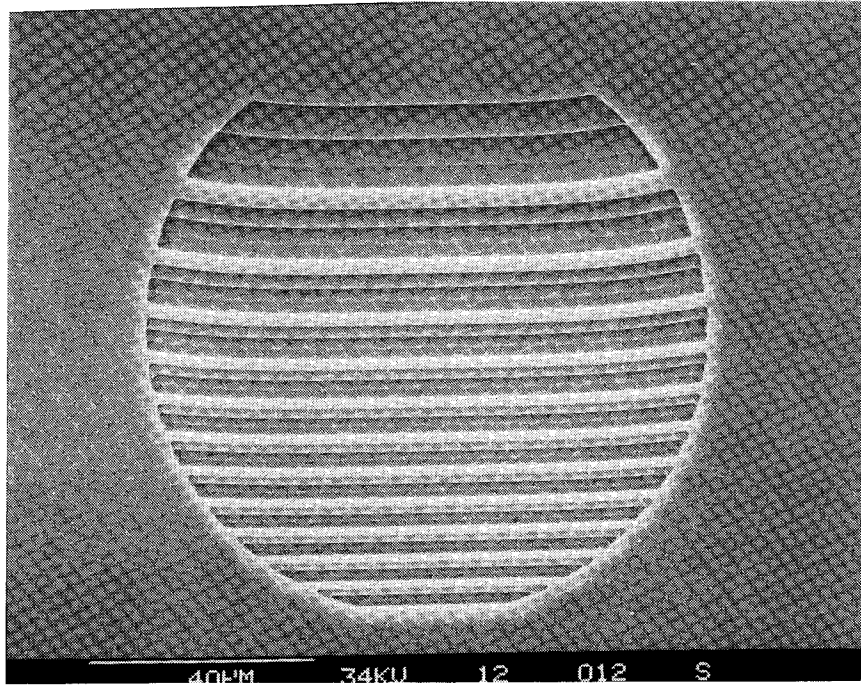


Figure 3 SEM micrograph showing DOE1 four-level structure

Test Results

The optical transmission of the interconnecting device was measured by imaging the optical outputs of the system on a photodetector. It was found to be 18 % including Fresnel reflection losses. This measurement fits the simulated value of the transmission, calculated by taking into account the effects of the DOE manufacturing errors as well as their misalignment. The fiber-to-chip coupling efficiency was experimentally measured on a dedicated test-bench and found to be 13 %. The difference between the transmission and the coupling efficiency indicates that a residual mode mismatch is still present. This leads to an effective loss of 30 %. The DOE alignment tolerance was measured to check for packaging feasibility. A 10% additional loss corresponds to a 2 μm tolerance (Figure 4) which can be achieved with the laser welding technique used for pigtailling optoelectronic devices.

DIFFRACTIVE OPTICAL ELEMENTS WITH HIGH EFFICIENCY FABRICATED BY THIN FILM DEPOSITION

E. Pawlowski, D. Berger, T. Hies, and B. Kuhlow

Heinrich-Hertz-Institut für Nachrichtentechnik Berlin GmbH, Einsteinufer 37, 10587 Berlin, Fed. Rep. Germany, Tel. 004930-31002-489, Fax.-213

1. INTRODUCTION

Diffractive optics will play an important role in optical imaging, optical interconnects and optical interconnection networks^{1,2,3}. The fabrication process of diffractive optics is based on computer-aided design (CAD) and microstructuring techniques. The diffractive optical elements can be fabricated with photolithographic processing techniques and by either etching or thin film deposition^{5,6,7}. For this fabrication process it is necessary to control accurately the level heights, the alignment of the masks and the linewidths of the structures. In order to obtain such control for the level heights, we fabricated the diffractive Fresnel zone lenses by Ion-Beam-Sputter deposition of silicon and controlled the optical thickness by a Reflection-Wideband-Monitoring-System with high accuracy⁸. In order to improve the efficiency of the elements and to reduce reflection losses, possible crosstalk and feedback effects for cascaded elements in an optical interconnection network, the optical elements were coated with a two layer anti-reflection coating of TiO₂ and SiO₂.

2. DESIGN AND FABRICATION OF FRESNEL ZONE LENSES

High diffraction efficiencies can be achieved by approaching a kinoform or blazed profile with multilevel steps⁹. The theory of diffraction by gratings is well known and treated in many papers^{20,21,22}. Near the resonance region, where the grating period and the wavelength are of the same order of magnitude the electromagnetic theory of gratings^{15,22,23} must be used to predict the diffraction efficiency. The calculations revealed that large refractive index differences between the lens material and the adjacent medium moves the resonance region to smaller grating periods. Therefore should be the efficiency for lenses with high refractive index higher than for lenses with small refractive index. We used silicon as high refractive index lens material. In order to reduce thermal effects, we used a substrate with a low thermal expansion coefficient (quartz-glass). For the calculations of the diffraction efficiency of the lenses, we assumed that the electromagnetic field incident to the lens can be approximated by a plane wave. We have fabricated eight level Fresnel zone lenses with focal lengths of 22.8, 5.7 and 2.9 mm for 1.52 μm wavelength. The Fresnel zone lenses have rotational symmetry with a diameter of 2 mm, where the zone radius r_m is given by $r_m = (2m\lambda f)^{\frac{1}{2}}$, where m is the zone index number, λ is the illumination wavelength and f is the focal length. The depth in each zone is $T = \lambda/\Delta n$, where Δn is the difference of refractive index between the lens material and the adjacent medium. The phase profile in each zone was approximated by a discrete multilevel stepped profile, where at least M masks are required for $L = 2^M$ levels (e.g., 3 masks for 8 levels). The discrete levels were realized with the aid of computer generated masks, written by electron-beam and whose patterns were transmitted by means of photolithographic technology. The smallest width w of the annuli radii was $w \simeq (2 \lambda f/d)/L$ (e.g., 1.1 μm for 8 levels, $d = 2$ mm and $f = 5.7$ mm), where d is the diameter of the lens. For test purposes additional Fresnel zone lenses with annuli radii widths down to 0.7 μm have been written on the masks. All features smaller than 2 μm were proximity corrected.

The fabrication process of multilevel Fresnel zone lenses consists of different stages⁷. A critical process is the pattern transfer from the mask into the resist, by optical contact lithography. This involves alignment, exposure, reversal baking, flood exposure and development of the photoresist. The alignment and exposure was carried out on a mask aligner (Süss MA 100M) at the wavelength of 310 nm. An overlay accuracy in the sub- μm range was achieved (0.46 μm). To get a microstructured element, a layer of silicon was sputtered onto the substrate by Ion-Beam-Sputter deposition (IBSD) technology. Layers produced by IBSD have a good adhesion, a high packing density and an amorphous structure. The photoresist was removed with acetone and stripper. For the 8 level Fresnel zone lenses, the lithography- and silicon-coating process was repeated two times with two additional masks. To ensure proper overlay between the various masks, we used diffractive alignment marks and conventionally alignment marks as common in microelectronic technology. The final stage involves IBSD for depositing a two layer AR-coating of TiO₂ and SiO₂ layers at both surfaces. The optical thickness of the layers was monitored in situ by a computer controlled Reflection-Wideband-Monitoring-System (RWMS). The typical measurement accuracy of the optical thickness is better than 0.1%.

3. FABRICATION ERRORS

For an ideal Fresnel zone lens with L levels, without reflection losses from the surfaces and with infinity f /number, the diffraction efficiency is⁸ $\eta = [\sin(\pi/L)/(\pi/L)]^2$. A perfect Fresnel zone lens of 8 levels should have an efficiency of 95%, but several fabrication errors can degrade the optical performance of the lens^{4,15,16,17,18}. The fabrication errors that could occur during the fabrication of binary Fresnel zone lenses can be classified as vertical and lateral errors. Level height errors can be classified as vertical errors and the alignment as well as the linewidth errors as lateral errors. We assume that the level height errors p_m are systematic errors and constant over the whole lens. The total phase shift produced after deposition with the M -th mask is $2\pi/2^M (1+p_m)$. The influence of level height errors on the diffraction efficiency can not be compensated in subsequent steps. Small errors in the desired phase shift, cause only a slight reduction in the efficiency, but the level height errors can cause spurious spots to appear. The effects of lateral alignment errors on the diffraction efficiency of a multilevel Fresnel zone lens are more prominent. To calculate this influence, we resorted to a geometric consideration, where we used a calculation of phasors approach¹⁸. The effects of linewidth errors on the lens efficiency are calculated by the same method. The linewidth errors can occur during the transfer of the pattern from the original mask to the resist on the substrate. Specifically, not correct exposed or developed resist in the lithographic process can alter the linewidth of the structures. Such changes in the linewidth would lead to the appearance of additional focused spots at the higher even orders. The overall diffraction efficiency η_o of a $L=2^M$ levels Fresnel zone lens with level height, alignment and linewidth errors is given by

$$\eta_o = [\sin(\pi/L)/(\pi/L)]^2 \cdot \prod_{m=1}^M \cos^2(\pi p_m / 2^m) \cdot \nu \cdot \sigma \quad (1)$$

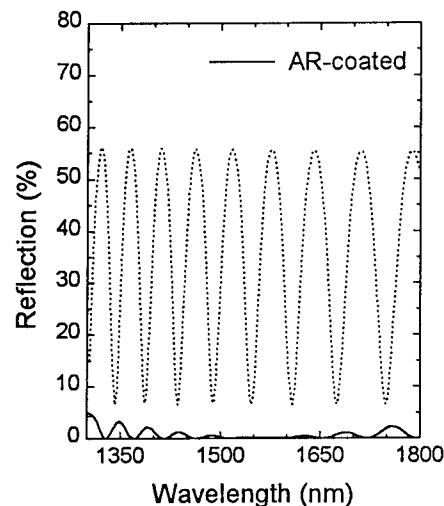
where M is the total number of masks, m is the number of the m -th deposition step starting with the coarse mask, ν is the degrading factor for the overlay errors and σ is the degrading factor for the linewidth errors. For example, a misalignment of $0.46 \mu\text{m}$ and a linewidth error of $0.1 \mu\text{m}$, for a $f/2.9$ -eight-level lens, degrades the diffraction efficiency by a factor of 0.9. Finally, a deviation of the vertical sidewall at the zone borders reduces the diffraction efficiency.

This presented error analysis is adapted for Fresnel zone lenses with relatively large f /number. The validity of this theory is problematic, because the introduced structures are smaller or in the same order of magnitude of the wavelength. However, our calculations are supported by experimental results, so that we believe that the error analysis is useful to optimize the fabrication process.

4. DESIGN AND FABRICATION OF ANTI-REFLECTION (AR) COATINGS

In our calculations we used an angular spectrum approach^{10,11,12,24} and the method of characteristic matrices from Abelès^{13,14}. To get an optimization of the AR-design, we used a numerical iteration process with the geometrical thickness of the layers as a parameter and considering both polarization states (TE and TM). The calculations revealed, that the quartz-glass substrates have to be first coated with a quarterwave index layer of TiO_2 , in order to match the refractive index of the substrate material to the lens material. The multilevel-silicon lens acts without this matching-layer as a mirror with a local reflectivity between 6.5 and 56 %. Figure 1 shows the reduction in reflectivity by applying AR-coatings.

Fig.1 Theoretical reflection curves of silicon-coated quartz-glass substrates without (dash line) and with (solid line) AR-coatings.



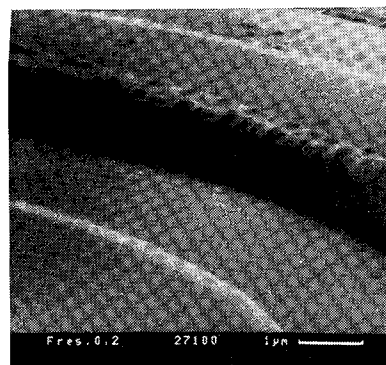
After the lens fabrication process, the lenses were coated with a two layer coating of design 0.705H and 0.771L for $\lambda_0 = 1.52 \mu\text{m}$, where L is a quarterwave index layer of SiO_2 and H is a quarterwave index layer of TiO_2 . The substrate backside is coated with a two layer AR-coating of design 0.305H 1.33L. The measured minimum reflection for these silicon lenses for $1.52 \mu\text{m}$ wavelength was 0.4%. These reflection values were measured with a Perkin-Elmer-Spectrometer (Lambda 19), that operates with an absolute

reflectance accessory, as well as with a laser reflectance measurement system at $1.52 \mu\text{m}$ wavelength. The improvement of the lens efficiency is given by the ratio of the diffracted power at the focus of an AR-coated lens over the diffracted power at the focus of an uncoated lens minus one. The measured improvement of the lens efficiency with the AR-coating of silicon coated quartz-glass substrate lenses is $31 \pm 1\%$ (theor. 32.4%).

5. EXPERIMENTAL RESULTS

The lens structures were analyzed with a Scanning Electron Microscope (SEM) and their surface topography was measured with a mechanical surface profiler (Alpha-Step/ Tencor). Figure 2 shows a SEM of the side wall of the outer zone of an sixteen level second order Fresnel zone lens, designed for the wavelength of $1.52 \mu\text{m}$ and a focal length of 2.85 mm . The height of the side wall ($d_{th} = 1.26 \mu\text{m}$, $n_L = 3.1$) was determined with the Alpha-Step to be approximately $1.29 \mu\text{m}$. Indeed, the overall relief structure has only small deviations from that of an ideal one. The refractive index of the sputtered silicon was determined from reflection and transmission measurements, which were performed with a Perkin-Elmer-Spectrometer (Lambda 19). To measure the focusing characteristics of Fresnel zone lenses, the lenses were illuminated by an expanded laserbeam ($\lambda_0 = 1.52 \mu\text{m}$).

Fig.2 A representative SEM-photograph of the side wall of the outer zone of an eight-level Fresnel zone lens.



The focused spot was magnified with a microscope objective (50x magnification), detected with a vidicon camera (Hamamatsu C1000, $\lambda_0 = 0.4 - 1.8 \mu\text{m}$) and the data were stored in a micro-computer. The measured values of the full width at half maximum (FWHM) intensity for different AR-coated Fresnel zone lenses of different focal lengths are close to the diffraction limited values. Figure 3a shows a representative example of a measured and calculated intensity distribution of a focused spot for a lens with f/number 2.85 at $1.52 \mu\text{m}$ (aperture of 2 mm). The intensity distribution is near to the diffraction limited case and the first order diffraction efficiency is higher than 80% . Figure 3b shows the corresponding modulation transfer function (MTF), indicating a good lens performance.

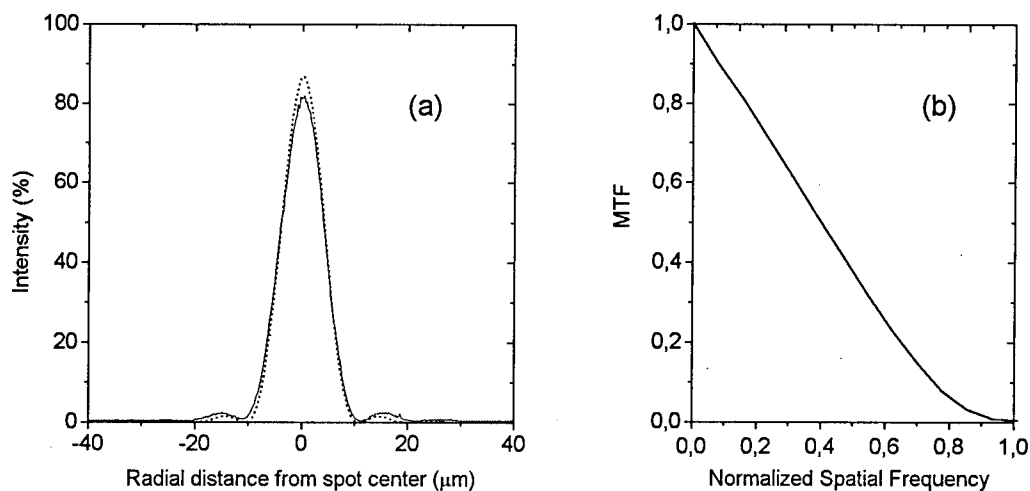


Fig.3 (a) Intensity distribution in the focal plane for a lens with f/number 2.85

(b) MTF of the same lens.

Finally, the detailed results of the full width at half maximum (FWHM) of the intensity distribution at the focal planes for these lenses and operating wavelengths are listed in Table 1. As evident, the experimental and theoretical results are in good agreement.

Lens for $\lambda_0 = 1.52 \mu\text{m}$					
f /number	diam.	FWHM _{exp.}	FWHM _{th.}	Efficiency $\eta_{exp.}$	Efficiency $\eta_{th.}$
11.40	2 mm	21.8 μm	21.2 μm	89%	92%
2.85	2 mm	5.6 μm	5.3 μm	82%	87%
1.43 ^a	2 mm	2.9 μm	2.7 μm	72%	77%

Table 1. Values of measured and calculated FWHM and η of AR-coated 8-level Fresnel zone lenses.
^a second order lens.

To obtain the diffraction efficiency η of the lenses, we measured the ratio of diffracted power at the focus I_F over the incident power I_{air} . To determine the intensity of the first order diffracted light, we introduced at the focalplane f, a pinhole with an aperture of 100 μm . The highest measured diffraction efficiencies were about $89 \pm 1\%$.

6. CONCLUDING REMARKS

Blazed Fresnel zone lenses with high numerical aperture have been fabricated by thin film deposition of silicon on quartz-glass substrates. The effects of fabrication errors, such as level hights, alignment and linewidths errors, on the diffraction efficiency were discussed on the basis of a scalar diffraction theory. Due to the in situ control of the deposited layer thickness, the effect of level high errors can be neglected. The line and alignment tolerances are very critical to achieve maximum diffraction efficiencies. The diffractive optical elements were coated with anti-reflection coatings. The reflection of these elements was optimized on the basis of an angular spectrum approach. As expected, the efficiency of the Fresnel zone lenses was improved by applying AR-coatings. The highest measured diffraction efficiencies for 8 level lenses are close to the expected theoretical values.

7. REFERENCES

1. K. Iga, M. Oikawa, S. Misawa, J. Banno, and Y. Kokubun, *Appl.Opt.*21, 3456-3460, 1982.
2. W. B. Veldkamp and G. J. Swanson, *Proceedings SPIE vol. 437*, pp.54-59, 1983.
3. W. B. Veldkamp; *Optics News* 12/88, 29-30, 1988.
4. B. Kuhlow, M. Ferstl and E. Pawlowski, *Proc. Holographic Systems, Components and Applications*, pp.41-46, 1993.
5. L. D'Auria, J. P. Huignard, A. M. Roy, and E. Spitz, *Opt. Commun.* 5, 232-235, 1972.
6. J. Jahns and S. Walker, *Appl. Opt.* 29, 931-936, 1990.
7. E. Pawlowski, H. Engel, M. Ferstl, W. Fürst and B. Kuhlow, *SPIE vol. 1751*, pp.13-21, 1992.
8. E. Pawlowski, *Le Vide, les Couches Minces*, no. 259, pp.44-46, 1991.
9. H. Dammann, *Optik* 31, 95-104, 1970.
10. F. K. Reinhart, I. Hayashi, and M. B. Panish, *J. Appl. Phys.*, vol.42, pp. 4466-4479, 1971.
11. D. C. Krupka, *IEEE J. Quantum Electron.*, vol. QE-11, no. 7, pp. 390-400, 1975.
12. T. Saitoh, T. Mukai and O. Mikami, *J. of Lightw. Techn.*, Vol.LT-3, No.2, pp.288-293, 1985.
13. F. Abelès, *Ann. Phys.*, Paris 12th series, 5, 1950.
14. H. A. Macleod, "Thin Film Optical Filters", pp. 32-43, Macmillan Publ. Comp., N. Y., 1986.
15. J. A. Cox, T. Werner, J. Lee, S. Nelson, B. Fritz, and J. Bergstrom, *SPIE vol. 1211*, 116-124, 1990.
16. M. W. Farn and J. W. Goodman, *SPIE vol. 1211*, 125-136, 1990.
17. E. Hasman, N. Davidson and A. A. Friesem, *Opt. Lett.*16, pp. 423-425, 1991.
18. M. Ferstl, B. Kuhlow, and E. Pawlowski, *SPIE vol. 1732*, pp. 89-99, 1992.
19. J. D. Gaskill, "Linear Systems, Four. Transf., and Opt.", p. 72, J. Wiley & Sons, N. Y., 1978.
20. R. Petit, "Electromagnetic Theory of Gratings", Springer Verlag Berlin, 1980.
21. T. K. Gaylord and M. G. Moharam, *Proceedings of the IEEE*, vol. 73, pp. 894-937, 1985.
22. N. C. Gallagher, Jr., and S. S. Naqvi, *SPIE vol. 1052*, 32-40, 1989.
23. E. Noponen, J. Turunen, A. Vasara, *J. Opt. Soc. Am. A* vol. 10, No. 3, 434-443, 1993.
24. E. Pawlowski, *Proc. Holographic Systems, Components and Applications*, pp.54-59, 1993.

Thursday, June 9, 1994

Fabrication and Characterizations

DThB 10:30am–12:00m
Room B

Hans Peter Herzig, *Presider*
University of Neuchatel, Switzerland

An Overview of Binary Optics Process Technology*

Margaret B. Stern

MIT Lincoln Laboratory
244 Wood St , Lexington, MA 02173

Telephone: (617) 981-4042; Fax: (617) 981-2922

This paper examines the pivotal role of fabrication in translating diverse optical designs into high-quality optics in a variety of materials. In particular, we evaluate how the alignment precision achieved during photolithography impacts the subsequent optical efficiency of diffractive microlenses as a function of lens speed ($F/2$ to $F/60$) on 200- μm square fused silica microlenses at 633 nm.¹ Next, we describe the multilayer planarization/masking schemes and highly anisotropic Si reactive-ion etching (RIE) processes needed to manufacture high-bandwidth IR binary optics.² Finally, we present a nascent layered system - arrays of CdTe microlenses monolithically integrated with photodetectors on opposite sides of the same substrate.³

1. Fabrication and Optical Efficiency

Binary optics technology conjoins computer-generated optical phase profiles with VLSI photomask and processing technology to form planar surface relief structures that manipulate optical wavefronts.³ Conventional binary optics processing, Figure 1, consists of several iterative steps of photolithographic patterning and phase-relief creation. The relief structures can be constructed by a variety of methods, including etching, deposition, and ion- or photon-induced structural changes in the refractive index or the volume. Dry etching techniques, in particular reactive ion etching (RIE), offer the greatest amount of flexibility and are used to manufacture the optics described below. Binary mask coding greatly reduces the number of process iterations required for highly efficient diffractive elements: only M process iterations result in an optic with 2^M phase steps.

Standard VLSI techniques must be finessed to address the particular requirements of high-quality microoptics fabrication. The nested binary optics structures impose three critical restraints on the fabrication process: (1) to register the mask to the substrate pattern with 0% overlay tolerance; (2) to etch vertical sidewall profiles without lateral undercutting or erosion of the mask edge; and (3) to maintain precise control over the phase-step-heights and widths, often to better than 1%, for both shallow (≈ 10 nm) and deep (≈ 10 μm) structures. Phase-step-width and height errors can significantly reduce the optical efficiency.

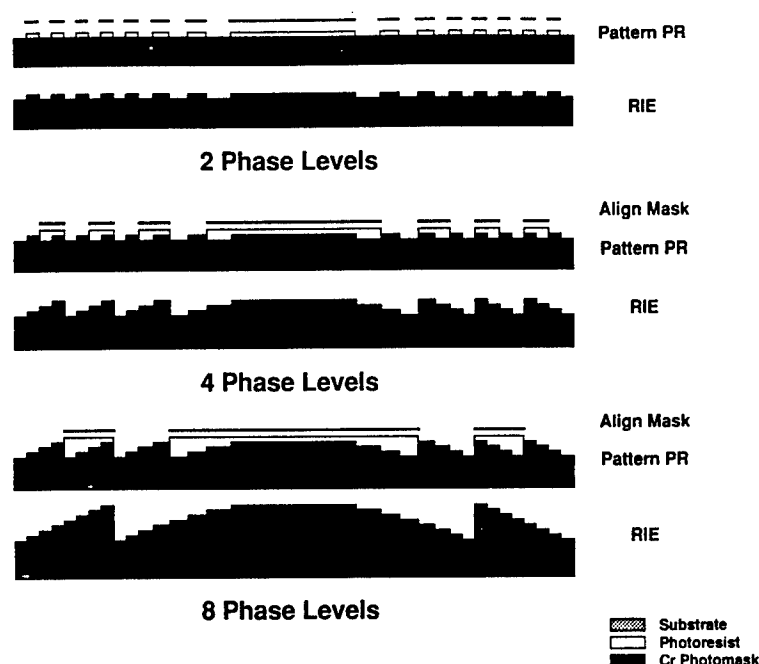


Figure 1: Fabrication steps for an eight-phase-level binary optics microlens. To maximize linewidth control, the mask layer with the smallest features is replicated first. The substrate is coated with photoresist, patterned photolithographically using a contact mask aligner, and then etched in an RIE system. Subsequent mask layers are carefully aligned to the patterned surface. This sequence is iterated until the desired number of phase levels is achieved. The binary coding scheme doubles the number of phase levels after each etch.

To determine where the incremental gain in optical performance justifies the required fabrication effort, we have undertaken a substantial effort to quantify the efficiency limits of diffractive binary-optic microlenses and to correlate losses in optical efficiency with specific fabrication errors. The vehicle for these studies is a fused silica microlens test set comprised of 10 different lenslets having $200\text{ }\mu\text{m} \times 200\text{ }\mu\text{m}$ square apertures and focal lengths between 0.17 and 14 mm at $\lambda = 633\text{ nm}$ (Figure 2). Benchmark optical efficiency measurements have been made on diffractive quartz microlenses as a function of lens speed and then compared with predictions of direct electromagnetic calculations for 2-, 4- and 8- phase levels.¹ For an eight-phase-level F/4.5 microlens having less than $0.1\text{ }\mu\text{m}$ misalignment error, we have measured an absolute efficiency of 0.85; this is, we believe, the highest efficiency reported to date for such a fast, binary optics lens in the visible. This result corresponds to 96% of the predicted value for this lens and implies that net fabrication errors contributed only a 4% efficiency loss.

To quantify the impact of alignment errors on optical efficiency, we have intentionally introduced a $0.35\text{-}\mu\text{m}$ translational error between mask layers 1 and 2 in one set of four-phase level lenslets.⁴ Optical efficiency measured for this "misaligned" set of microlenses are compared with a nominally identical, four-phase level, "well-aligned" set of microlenses. A strong correlation exists between the sizable efficiency losses displayed by the fast lenslets and the fraction of the zonewidth intercepted by the intentional misregistration.



Figure 2: SEM of an eight-phase-level 200- μm square aperture F/6 fused silica microlens. The minimum zone width on level 3 is 0.8 μm .

2. Refractive and Integrated Microoptics

The demand for both visible and IR broadband microoptics has driven our development of fabrication capabilities necessary to create deep, high-resolution, three-dimensional structures. The desired refractive surface contour of the broadband IR microlens is approximated in a stepwise manner. To maintain the high fidelity pattern replication necessary for efficient binary optics structures, we must develop techniques to etch deep anisotropic profiles into the silicon substrate. By judicious choice of the plasma chemistry used in the RIE process, we can induce the in situ formation of a sidewall inhibition layer that prevents lateral undercut and enhances vertical profile

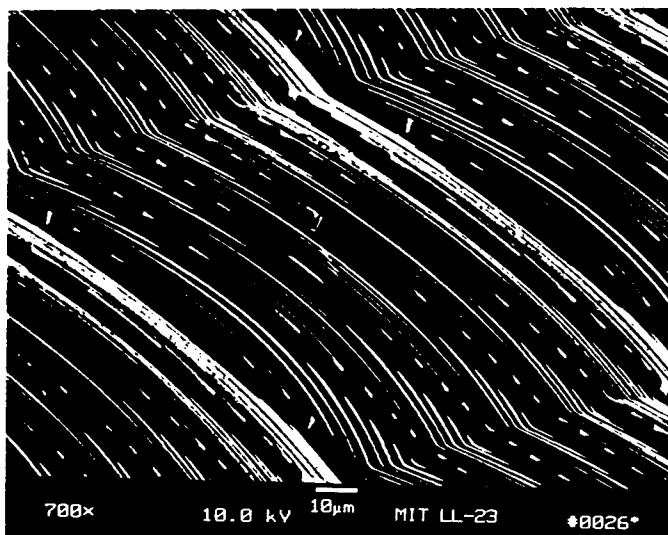


Figure 3: A 16-phase level color dispersing microlens array etched 7.5 μm deep. Shown is one pixel element from a 64 x 64 array.

control. We have achieved vertical sidewalls without mask undercutting and with a 5:1 etch selectivity (ratio of Si:photoresist etching rates) by using an SF_6/O_2 gas mixture in a commercial RIE system (Semigroup TP1000).² The color dispersive microoptic, pictured in Figure 3, is a combination F/2 refractive microlens for focusing and 17 μm period diffraction grating for color separation.⁵ The total depth of this optic, made with four mask levels, is 7.5 μm . There are 64x64 identical pixel elements, each 100 μm x 100 μm square, in this array.

By exploiting the fill factor enhancement made possible by microlens arrays, photodetectors can be made smaller or spaced further apart; the newly available space can be filled with preprocessing circuitry. Monolithic integration of active and passive devices on the same substrate will eliminate difficult and time-consuming alignments between discrete planes of different devices. In a joint project with LORAL IRIS, we have monolithically integrated focal plane arrays of microlenses with epitaxially grown HgCdTe photodetectors on opposite sides of a single CdTe substrate.⁴ The microlens array pattern is registered to the HgCdTe photodetectors on the front side of the substrate to better than 2 μm , using our Karl Suss infrared backside mask aligner, and then etched into the backside of the substrate. In addition, by reducing the needed active detection area, the microlenses result in increased gamma radiation hardening.

3. Conclusion

Fabrication is the cornerstone for the realization of high-quality microoptics. We have highlighted details of the Binary Optics effort at MIT Lincoln Laboratory that lead to significant improvement in optical performance and to new microoptics capabilities.

This work was supported by the Advanced Research Projects Agency.

4. References

1. M.B. Stern, M. Holz, S. Medeiros and R.E. Knowlden, "Fabricating binary optics: Process variables critical to optical efficiency", *J. Vac. Sci. Technol.* **B9**, 3117-3121 (1991); M. Holz, M.B. Stern, S.S. Medeiros, and R.E. Knowlden, "Testing binary optics: Accurate high-precision efficiency measurements of microlens arrays in the visible", *SPIE Proc.* **1544**, 75-89 (1991).
2. M.B. Stern and S.S. Medeiros, "Deep three-dimensional microstructure fabrication for IR binary optics", *J. Vac. Sci. Technol.* **B10**, 2520-2525 (1992). M.B. Stern and T.R. Jay, "Dry etching: path to coherent refractive microlens arrays", *SPIE Proc.* **1992**, 283-292 (1993).
3. M.B. Stern, W.F. Delaney, M. Holz, K.P. Kunz, K.R. Maschhoff, and J. Welsch, "Binary optics microlens arrays in CdTe", *Mat. Res. Soc. Symp. Proc.* **216**, 107-112 (1991).
4. W.B. Veldkamp and G.J. Swanson, "Developments in fabrication of binary optical elements", *SPIE Proc.* **437**, 54-59 (1983); J.R. Leger, M. Holz, G.J. Swanson, and W. Veldkamp, "Coherent laser beam addition: An application of binary-optics technology", *Lincoln Lab. J.* **1**, 225-246 (1988).
5. Margaret B. Stern, Michael Holz, and Theresa R. Jay, "Fabricating binary optics in infrared and visible materials", *SPIE Proc.* **1751**, 85-95 (1992).
6. Michael W. Farn, Margaret B. Stern, Wilfrid B. Veldkamp, and Shirley S. Medeiros, "Color separation by use of binary optics", Michael W. Farn, Margaret B. Stern, Wilfrid B. Veldkamp, and Shirley S. Medeiros, *Optics Lett.* **18**, 1214-1216 (1993).

Metrology of Diffractive Optics

Paul Caber, Don Cohen, and John Podlesny
WYKO Corporation
2650 E. Elvira Road
Tucson, AZ 85706

and

James C. Wyant
WYKO Corporation
and
Optical Sciences Center
University of Arizona
Tucson, AZ 85721
Tel: 602-621-2448
Fax: 602-294-1799
Internet: jcwyant@ccit.arizona.edu

Introduction

The ability to measure the micro-structure of diffractive optics is extremely important in order to optimize the fabrication process. Measuring the micro-structure is challenging because of the accuracy requirements on the height measurement, the high spatial frequencies required, and the steep slopes that must be measured. Both optical interference microscopes and scanning probe microscopes can be used for the measurements. Optical interference microscopes have the advantage that they are easy to use and provide rapid, accurate height measurements. However, as described below, for an optical interference microscope to measure the steep slopes present in diffractive optics special multiple wavelength or white light techniques must be used. Once the steep slope measurement problem is solved the largest limitation of optical interference microscopes is the spatial resolution limit imposed by diffraction. The advantage of the use of a scanning probe microscope for the measurement of diffractive optics is that very high spatial frequencies can be measured. The disadvantage is that the measurement is more difficult to perform and the measurement time is much longer than for optical microscope measurements.

Optical Interference Microscopes

In the measurement of diffractive optics it is possible to use visible light interferometry and computerized phase shifting^{1,2} techniques to measure Angstrom, or even sub-Angstrom, surface height variations. However, the use of a short wavelength creates a problem in the measurement of steep slopes. If a single wavelength is used to make a measurement and the surface height difference between adjacent measurement points is greater than a quarter wavelength, the measurement will have an ambiguity in the height measurement of a multiple of a half-wavelength. One method of removing this height ambiguity is to perform the measurement at two wavelengths, λ_1 and λ_2 , and subtracting the two measurements, resulting in the limitation in the height difference between two adjacent detector points of one-quarter of λ_{eq} , where

$$\lambda_{eq} = \frac{\lambda_1 \lambda_2}{|\lambda_1 - \lambda_2|}.$$

The measurement is essentially performed at a synthesized equivalent wavelength, λ_{eq} . While this approach increases the dynamic range of the measurement, the precision is also degraded by the ratio of λ_{eq}/λ . The precision can be regained by using the equivalent wavelength results to correct the integer half-wavelength height ambiguities in the single wavelength data. In this way, the dynamic range of the equivalent wavelength is obtained, but the precision of the single wavelength data is maintained.³

While the multiple-wavelength interferometry works well on many samples, in the measurement of diffractive optics where fine spatial features are being measured and both the magnification is large and the numerical aperture of the microscope objective is large, the high points and low points of a surface may not be in focus at the same time. In this situation, while multiple wavelength interferometry may give results that initially appear correct, the information about the high spatial frequency structure on the surface may be wrong because portions of the surface are out of focus. The white light scanning interferometry approach described below does not have this problem.

If a white light source is used in an interferometer, the best contrast interference fringes are obtained only when the two paths in the interferometer are equal. Thus, if an interferometer is made such the path length of the sample arm of the interferometer is varied, the height variations across the sample can be determined by looking at the sample position for which the fringe contrast is a maximum. In this measurement there are no height ambiguities and since in a properly adjusted interferometer the sample is in focus when the maximum fringe contrast is obtained, there are no focus errors in the measurement of surface microstructure.^{4,5,6}

The major drawback of this type of scanning interferometer measurement is that only a single surface height is being measured at a time and a large number of measurements and calculations are required to determine a large range of surface height values. One method for processing the data that gives both fast and accurate measurement results is to use conventional communication theory and digital signal processing (DSP) hardware to demodulate the envelope of the fringe signal to determine the peak of the fringe contrast.⁶

The irradiance at a single sample point as the sample is translated through focus, which we can think of as the temporal coherence function, looks like an amplitude modulated (AM) communication signal. To obtain the location of the peak, and hence the surface height information, this irradiance signal is detected using a CCD array. The signal is sampled at fixed intervals, such as every 50 to 100 nm, as the sample path is varied. The motion can be accomplished using a piezoelectric transducer. Low frequency and DC signal components are removed from the signal by digital highpass filtering. The signal is next rectified by square-law detection and digitally lowpass filtered. The peak of the lowpass filter output is located and the vertical position corresponding to the peak is noted. Interpolation between sample points can be used to increase the resolution of the instrument beyond the sampling interval. This type of measurement system produces fast, non-contact, true three-dimensional area measurements for diffractive optics. If smooth surfaces are being measured normal phase shifting techniques can be used to obtain Angstrom, or sub-Angstrom height measurements.⁷

Scanning Probe Microscope

Scanning probe microscopes are becoming popular for the measurement of the microstructure of surfaces.⁸ In the measurement of diffractive optics the force microscope is of particular interest. The force microscope can measure nanometer, or even Angstrom sized structures on non-conducting surfaces. In the force microscope the sample is mounted on a piezoelectric ceramic that is capable of scanning in x, y, and z directions. A thin cantilever (manufactured from silicon nitride) with an integrated tip is brought near the surface of the sample. An optical deflection technique is used to measure the deflection of the cantilever during the scan. The deflection of the cantilever is kept constant by adjusting the z position of the sample using a feedback loop. The x and y coordinates are precisely measured using an optical encoder. The x, y, and z positions of the piezoelectric ceramic are recorded as the surface topography.

Measurement Results

Figure 1 shows typical results for the measurement of a diffractive element using the white light scanning interferometer approach. The ability to measure steep slopes is clearly shown. Figure 2 shows another diffractive optics element measured using a scanning probe microscope. For this element two grating spacings of 5 microns and 10 microns were measured. The grating height range was approximately 1 micron.

In conclusion, the ability to measure the microstructure of diffractive elements is very important. Both optical interference microscope techniques and scanning probe microscope techniques can be used to perform the measurements. For optical interference microscope techniques to be used for the measurement of steep slopes, multiple wavelength techniques, or white light scanning techniques can be used to eliminate half-wavelength height ambiguities that are present with single wavelength measurements.

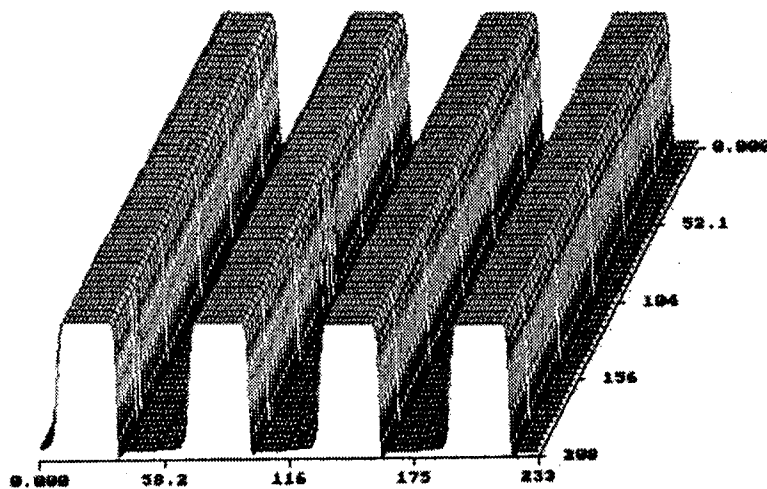


Figure 1. Three-dimensional map of diffractive element obtained using white light scanning microscope. x and y dimensions given in microns. Peak-Valley height 1.3 microns.

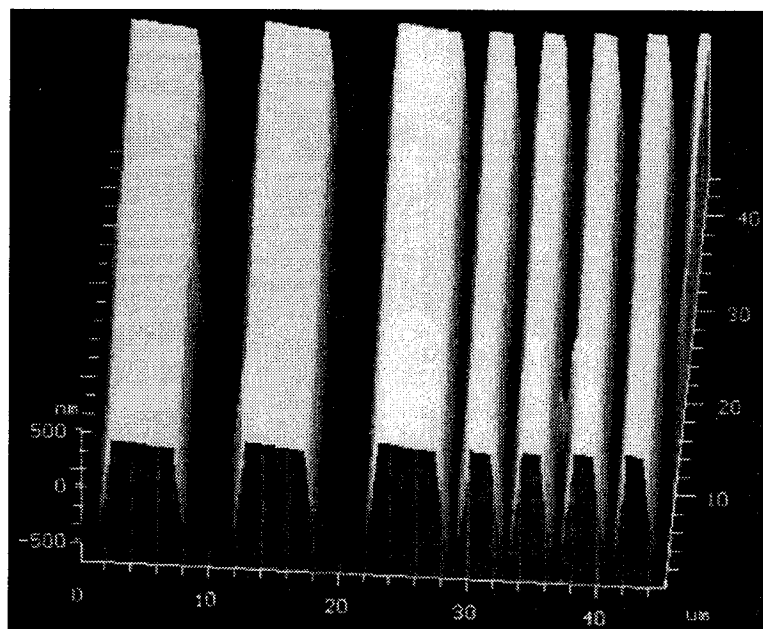


Figure 2. Three-dimensional map of diffractive element obtained using scanning probe microscope. x and y dimensions given in microns. Peak-Valley height is approximately 1 micron.

References

1. K. Creath, "Phase-Shifting Interferometry Techniques," in Progress in Optics XXVI, E. Wolf, ed. (Elsevier Science, 1988), pp. 357-373.
2. J. C. Wyant, "Use of an ac heterodyne lateral shear interferometer with real-time wavefront corrections systems," *Appl. Opt.* **14**(11):2622-2626, Nov. 1975.
3. K. Creath, Y.-Y. Cheng, and J. C. Wyant, "Contouring Aspheric Surfaces using Two-Wavelength Phase-Shifting Interferometry," *Optica Acta* **32**(12):1455-1464 (1985).
4. M. Davidson, K. Kaufman, I. Mazor, and F. Cohen, "An Application of Interference Microscopy to Integrated Circuit Inspection and Metrology," *Proc. SPIE*, **775**, 233-247 (1987).
5. G. S. Kino and S. Chim, "Mirau Correlation Microscope," *Appl. Opt.* **29**, 3775-3783 (1990).
6. P. J. Caber, "An Interferometric Profiler for Rough Surfaces," *Appl. Opt.* **32**, 3438-3441 (1993).
7. J. C. Wyant and K. Creath, "Advances in Interferometric Optical Profiling," *Int. J. Mach. Tools Manufact.* Vol. **32**, No.1/2, 5-10(1992).
8. J. Jahanmir, B.G. Haggar, and J.B. Hayes, "The Scanning Probe Microscope," *Scanning Microscopy*, Vol. **6**, No.3, 625-660 (1992).

Phase Shift Mask Metrology using Scatterometry *

Susan M. G. Wilson, S. Sohail H. Naqvi, B. K. Minhas, John R. McNeil

Center for High Technology Materials

Department of Electrical and Computer Engineering

University of New Mexico

Albuquerque, NM 87131

Herschel M. Marchman

AT&T Bell Labs

600 Mountain Avenue

Murray Hills, NJ 07974

BACKGROUND

Lithography is a critical step in semiconductor manufacturing which involves the faithful transfer of a pattern on a photomask to the wafer. The continued shrinkage of minimum feature size on a wafer have placed unprecedented demands on lithography: demands that can no longer be met by a simple decrease of wavelength of incident illumination. A technique that is currently under investigation for the production of smaller feature sizes, without a decrease in wavelength, is the use of phase shift photomasks. These masks are created by etching the substrate of the chrome-on-glass photomask, thereby creating an amplitude as well as phase structure. Since the fidelity of pattern transfer is critically dependent on the characteristics of the phase etched structure, it is important to develop techniques for the metrology of these structures.

SCATTEROMETRY

Scatterometry is a non-contact, rapid and non-destructive diffraction based metrology technique that involves illuminating a test grating structure with a laser beam and measuring the intensities of the various reflected and transmitted diffraction orders. In a 2Θ scatterometer, illustrated in figure 1, the intensity in a particular diffraction order is continuously monitored as the angle of incidence of the laser beam is varied over a certain range. The shape of the diffraction curves obtained in this manner is shown to be sensitive to the defining parameters of the phase grating, (e.g. sidewall angle, etch depth, top linewidth). An explanation of these parameters is provided in figure 2.

EXPERIMENT

A phase shift mask having both chrome and chromeless phase etched structures was fabricated using e-beam techniques at AT&T. The mask shown in figure 3 had equal line and space

* This work supported by SRC/SEMATECH

gratings with linewidths varying from $0.5\text{ }\mu\text{m}$ to $5\text{ }\mu\text{m}$, and phase etch depth varying from $0.15\text{ }\mu\text{m}$ to $0.4\text{ }\mu\text{m}$. The 2Θ scatterometer was used to make measurements of the fraction of incident power diffracted into 0, +1, and -1 reflected and transmitted orders as the angle of incidence was varied from -60 to 60 degrees. Figure 4 illustrates the change in 0-order transmitted power as the etch depth of the $10.0\text{ }\mu\text{m}$ period grating is varied. It can be seen that for this large period grating the shape of the curve is only slightly influenced by the etch depth and for any angle of incidence there is a monotonic decrease in transmitted 0-order power for increasing etch depth. Figure 5 is a plot of the transmitted +1-order plotted for various etch depths of a $1.0\text{ }\mu\text{m}$ period grating. In this case again the transmitted power at any angle decreases monotonically at any angle with increasing etch depth. In this case however, the curves go through multiple maxima and minima and it appears reasonable to assume that change in linewidth and/or sidewall angle of the structures will influence the shape of the diffraction curves.

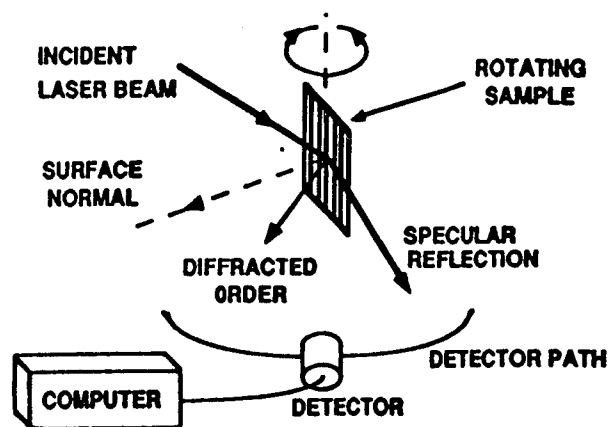
INVERSE DIFFRACTION ANALYSIS

It can be seen from figures 3 and 4 that changes in etch depth of the phase grating structures influences the diffraction curves as measured by the 2Θ scatterometer. The measurement problem is now to predict the parameters of the phase grating, given the diffraction curves. To accomplish this we have utilized rigorous coupled wave theory to solve for the forward diffraction problem. A parameter space is defined for the various grating parameters of interest and the diffraction curves are generated for each parameter set in the parameter space. A partial least square (PLS) based training algorithms is then trained on the theoretical data. PLS techniques exploit correlation between the simulated diffraction curves and the critical parameter of the modeled structures.

We present preliminary results on the use of these techniques for the solution of the inverse diffraction problem. For larger period gratings we obtained good results in the prediction of etch depths using the transmitted 0-order curves. We will discuss problems associated with multiple parameter estimation and also for the measurement of short period (i.e, small pitch to wavelength ratio) gratings.

CONCLUSIONS

We presented preliminary data on the use of scatterometry for the investigation of phase shift grating structures. The 2Θ scatterometer can measure the intensity in any diffraction order as the angle of incidence is varied over a particular range. The curve thus obtained is sensitive to the critical parameters of the diffraction grating and comparison with theoretically obtained curves can provide reasonable estimates of the various parameters of the phase grating.

Figure 1: 2θ Scatterometer

AT&T/ UNM Phase Shift Photomask

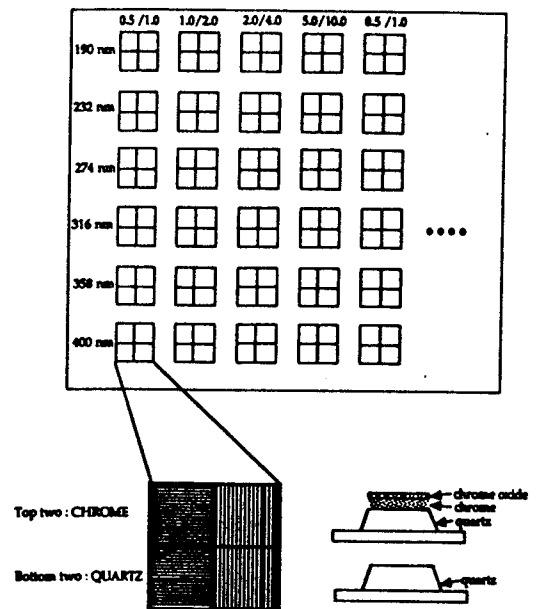


Figure 3: AT&T / UNM Test Photomask

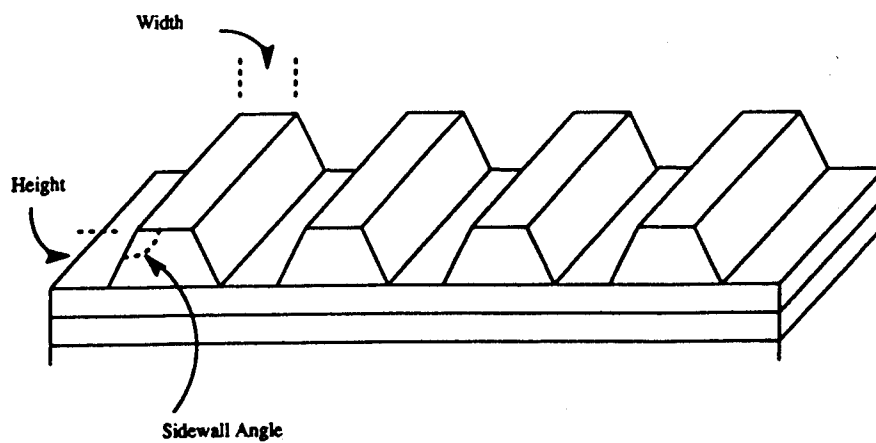


Figure 2: Critical Parameters of a phase shift test grating

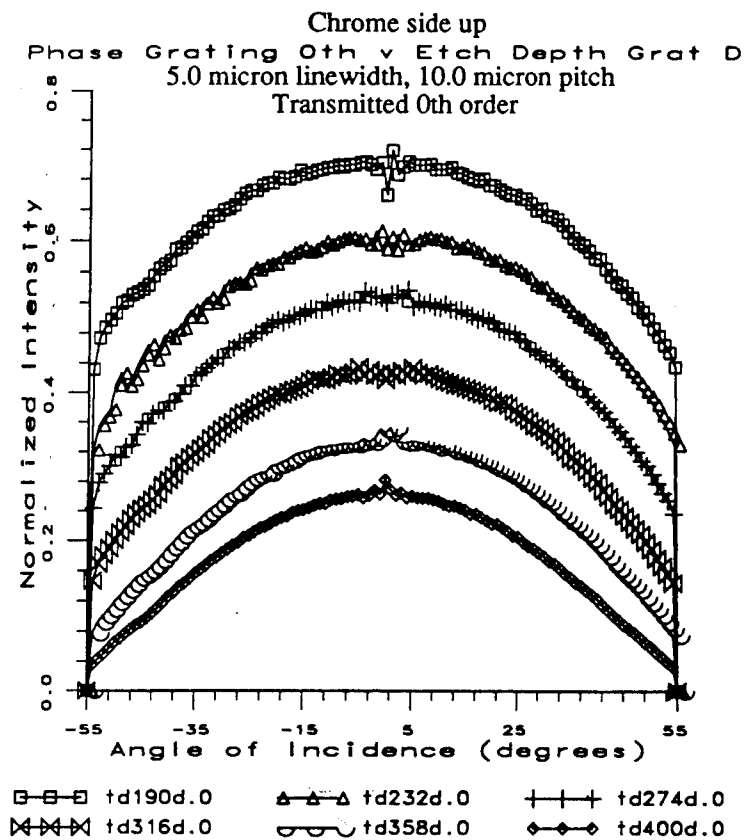


Figure 4:

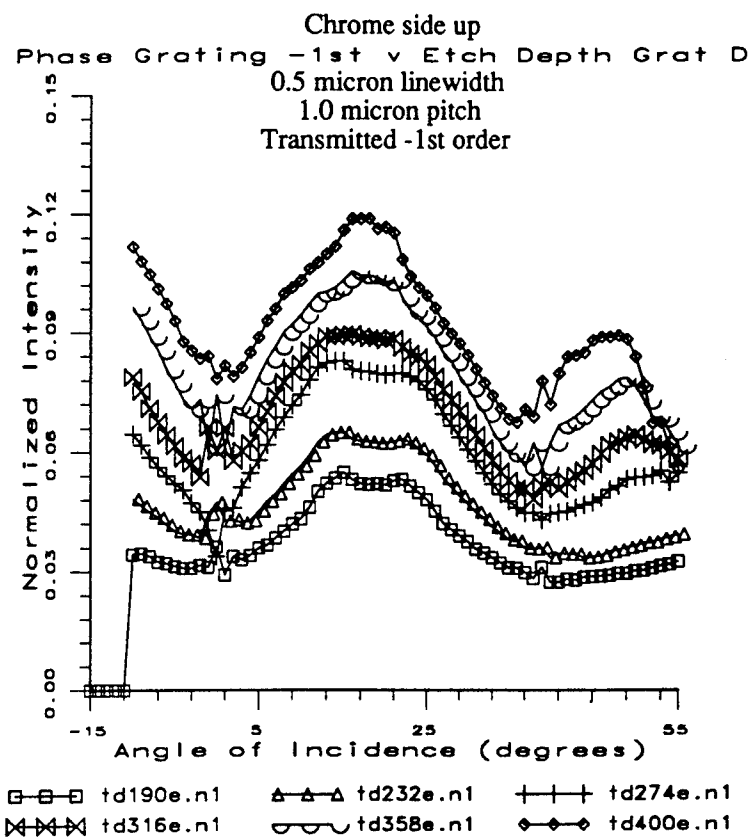


Figure 5

Image Quality Assessment of Diffractive Elements Replicated in SURPHEX™

J. Allen Cox
Honeywell Technology Center
10701 Lyndale Ave S
Bloomington, MN 55420

Felix P. Shvartsman
Datacard Corporation
11111 W. Bren Road
Minnetonka, MN 55345
(formerly at DuPont Imaging Systems
Experimental Station, Box 80352
Wilmington, DE 19880-0352)

1. Introduction.

It is widely believed that the economic viability of diffractive optics will be realized for most practical applications only through a replication procedure capable of yielding both high fidelity and high image quality. Many techniques have been attempted in a variety of materials, and many have found that achieving both fidelity and image quality is quite difficult. The nature of the problem for image quality is illustrated with the three photos in Figure 1 showing the blur spots formed by three f/10 Fresnel phase lenses. On the left is the diffraction-limited image formed by a master element having four phase levels and fabricated in fused quartz. The two remaining photos are the images formed by replicas of the master element, one in a dry photopolymer and one in a liquid photopolymer.

One gradation on the scale in each photo equals $2.5\ \mu\text{m}$. The image quality in both replicas is clearly unacceptable. Currently, we do not have conclusive proof for the cause of the image degradation in each type of replica, but we believe the most likely causes are nonuniformity in the refractive index in the dry material and shrinkage-induced stress (warpage) in the liquid material. Shrinkage in the dry material is quite small (~ 1 percent), and hence fidelity is quite good. Shrinkage in the liquid polymer is ~ 10 percent.

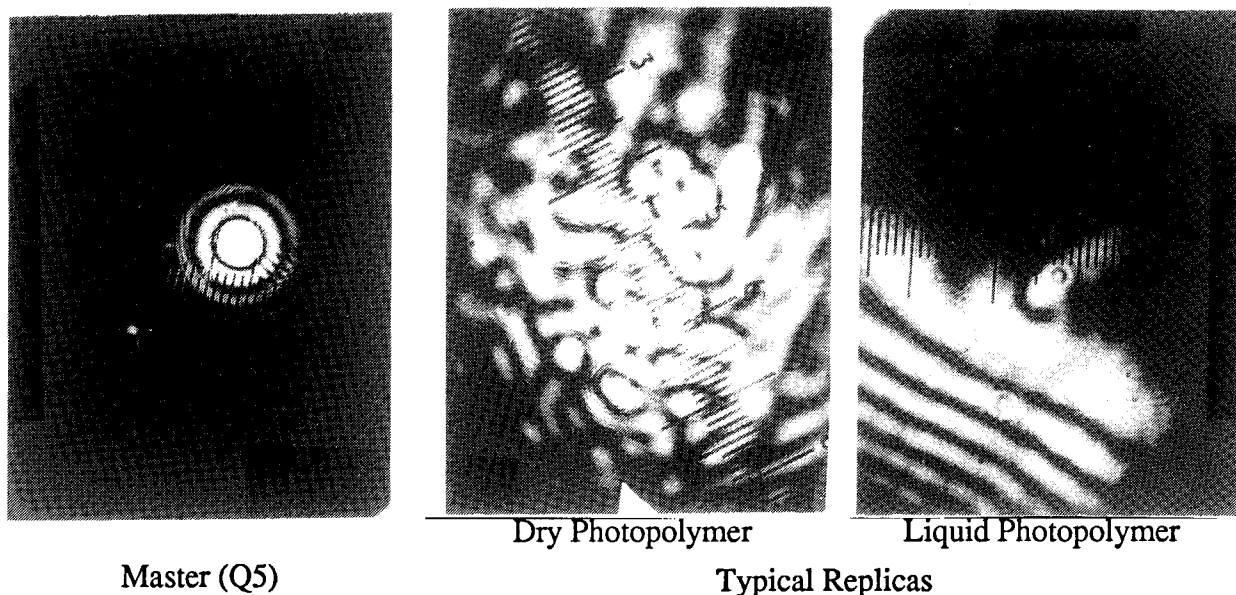


Figure 1. Point-source images formed by f/10 Fresnel phase lenses: master and two replicas.

One of the most promising candidates to satisfy the requirements for high fidelity and image quality is DuPont's SURPHEX™ family of dry photopolymers. DuPont initiated development of embossing procedures and SURPHEX™ films specifically for replication of diffractive elements in 1987. DuPont and Honeywell have collaborated since 1990 to achieve this goal, and recently DuPont¹ announced the replication of Honeywell's f/10 Fresnel phase lenses with diffraction-limited imagery in SURPHEX™ dry photopolymer film. The image quality assessment was performed by Honeywell, and our objective here is to summarize the results of the measurements.

2. Description of elements and measurements

The master elements in our experiments consisted of three prototype f/10 Fresnel phase elements of two, four, and eight phase levels fabricated using the standard "binary optics" procedure. Extensive characterization of processing errors, diffraction efficiency, and image quality of these elements has been reported previously^{3,4}. Three replicas of each diffractive element were done in SURPHEX™ on PMMA substrates using DuPont's dry photopolymer embossing (DPE) process, which is described in references 1 and 2. The substrates had a thickness of 2.8 mm and a diameter of 35 mm. Blank substrates were included in order to isolate the image degradation caused by the substrate itself. Surface quality of all substrates was measured with a Fizeau interferometer.

Image quality was characterized both qualitatively by photographs of the point-source image and quantitatively by measurements of the modulation transfer function (MTF). MTF was measured by means of a scanning knife-edge technique. Fidelity of the replicas was measured primarily by profilometry and SEM photos of the outermost Fresnel zones. Measurements of Fresnel zone widths and depths in the replicas equaled within 0.1 percent the values in the corresponding regions of the master elements. Thus, the fidelity of replication was extraordinarily good. The measured diffraction efficiency agreed with one percent, equal within the experimental error..

The photo of the point-source image formed by the four-level (Q5) master element is shown in Figure 1; it is representative of the photos for the two-level and eight-level elements. It illustrates the features of perfect, diffraction-limited imagery: a uniform, circular central disk surrounded by alternating dark and bright rings of uniform width. The modulation transfer functions (MTF) of the master elements are shown in Figure 2. The theoretically calculated MTF for a diffraction-limited element is displayed by the curve of unconnected small circles ("o"). The MTF curves for all elements are seen indeed to be diffraction-limited.

The point-source image formed by a four-level replica (28a-Q5) is shown in Figure 3. The MTF curves measured for a two-level, a four-level, and an eight-level replica are plotted in Figure 4. The image quality in these three replicas is clearly superior to that of the replicas in Figure 1. However, it is evident from both the photo and the MTF curves that a small, residual aberration remains; the image quality is very good, but not quite diffraction-limited. This slight aberration can be attributed to the surface quality of the PMMA substrates. For example, to show the magnitude of the aberration contributed solely by PMMA substrate, we inserted a blank substrate (35b)

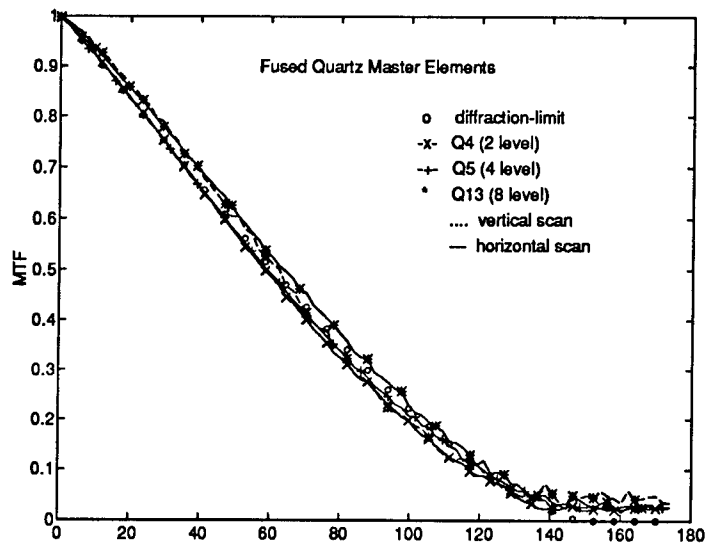


Figure 2. Measured MTF curves for the f/10 master elements.

in the beam incident on a fused quartz master and recorded the point-source image. The result is shown in Figure 5. The presence of the substrate clearly contributes astigmatism, and the magnitude is generally greater than observed in the replicas themselves.

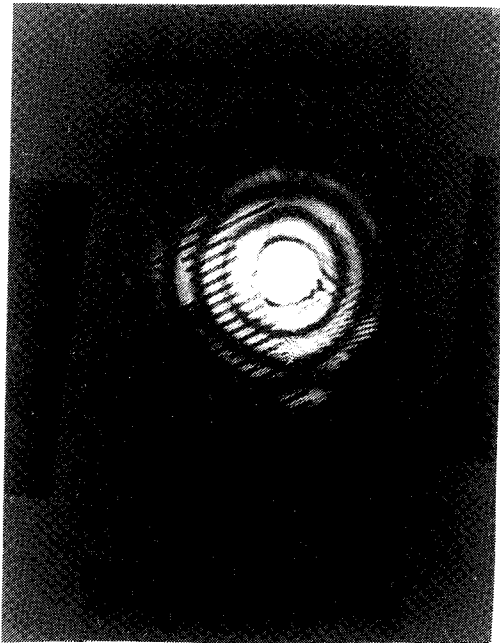


Figure 3. Point-source image of f/10 replica in SURPHEX™.



Figure 5. Aberration induced by PMMA substrate.

A direct measure of surface quality was also obtained by use of a Fizeau interferometer. Photographs of the resulting interference patterns are shown in Figure 6 for a blank fused quartz substrate and in Figure 7 for a blank PMMA substrate (35b). This amount of surface nonuniformity in the PMMA substrate is entirely consistent with the magnitude of aberrations observed in the replicated elements.

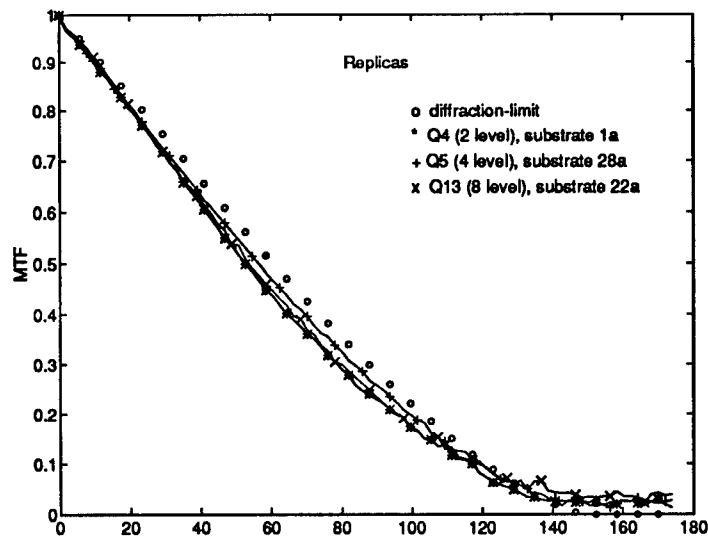


Figure 4. Measured MTF curves for the f/10 replicas.

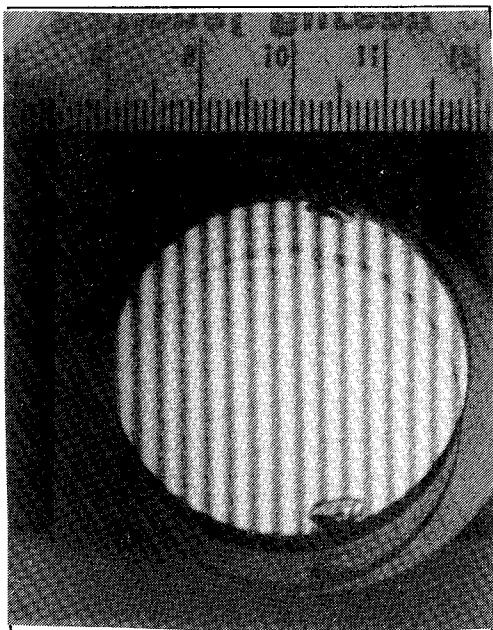


Figure 5. Surface quality of a fused quartz substrate.

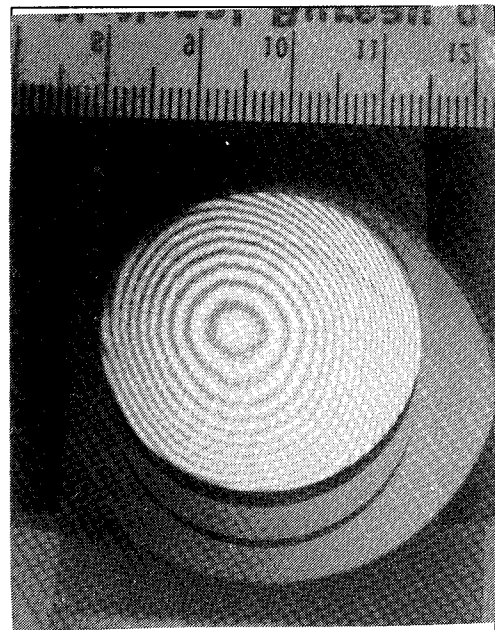


Figure 5. Surface quality of a PMMA substrate..

3. References

1. Felix P. Shvartsman, "Replication of Diffractive Optics," Critical Reviews on Diffractive and Miniaturized Optics, Sing Lee, ed., Volume CR49 (1993), in press.
2. Felix P. Shvartsman, "SURPHEX™: New Dry Photopolymers for Replication of Surface Relief Diffractive Optics," Proc. SPIE 1732 (Holographics International '92), 121-30 (1992).
3. J.A. Cox et al., "Diffraction efficiency of binary optical elements," Proc. SPIE 1211 (Computer and Optically Formed Holographic Optics), 116-24 (1990).
4. J.A. Cox, B. Fritz, T. Werner, "Process error limitations on binary optics performance," Proc. SPIE 1555 (Computer and Optically Generated Holographic Optics), 80-88 (1991).

CIM FOR FABRICATING HOE BY EMBOSSING AND INJECTION METHOD

Rong-Seng Chang, Chern Sheng Lin , Yun Long Lay

Institute of Optical Sciences, National Central University

Chung-Li, Taiwan 32054, TEL:886-2-8711684

Injection and embossing is an economical method of producing HOE (Holographic Optical Element) in large or small quantities and variable types. In this paper, we use CIM (computer integrated manufacturing) system to obtain the proper parameters of injection and embossing process. The automation measurement can assist in calculating the volume and shape of the metal model of the mold.

Since a surface-relief type hologram is an appropriate type for a HOE of mass production, , we previously developed a new method of analyzing the performance of a surface-relief type hologram fabricating system¹. A hologram embossing system can obtain a signing layer which is written upon to have the structure with an optical diffraction effect such as a hologram. The diffraction efficiency of the embossing master (with holographic fringes in photo resist) can be analyzed by

defining our new concepts for the fabricating process and grating profile characteristics. In order to reasonably resolve the problems of the diffraction efficiency we combine the optical and AI (artificial intelligence) sciences to find the key of HOE's fabricating process. Many uncertainties are unavoidable because we judge the process parameters using our experience . In this way , the stream of information reaching the brain via the visual process, is eventually reduced to a trickle that is needed to perform a specified task with a minimal degree of precision. In an ordinary HOE fabrication process, decision-making is made by the human mind. Furthermore , the ability to manipulate fuzzy sets and the consequent summarizing capability constitutes one of the most important assets of the human mind. Thus the availability of multipurpose fabricating of a more complex HOE with very simple and economical equipment will be reconfirmed in further research.

From the transfer function of embossing we correct the values of the embossing temperature and holding time. From our analysis, we improve the product quality and reduce waste. Some problems such as wrinkling, curling, and breakage in the plastic plate or the short life in the embossing master can be eliminated under the proper operation parameters. We believe this system will be valid in manufacturing the prototype of the holographic products.

From the experimental study of the HOE CIM system, the following conclusions are obtained.

1. A high diffraction efficiency of about 20 % is obtained by a holographic lens for image processing.
2. The system we adapt can provide the production of HOE more practically.

Agedal, Harald — DTuC3
 Anderson, Erik H. — DTuA2
 Andrés, P. — DTuD3
 Anthamatten, O. — DThA4
 Aoyama, Shigeru — DTuB17
 Armendariz, M. G. — DTuB18
 Athale, Ravindra A. — DWC1
 Atwood, David T. — DTuA2

Babin, Sergey — DWD2
 Bao, Gang — DMA3
 Barry, Stephen — DTuC2
 Bel'tyugov, V. N. — DWB5
 Bengtsson, Jorgen — DWC5
 Berger, D. — DThA5
 Beth, Thomas — DTuC3
 Blattner, P. — DTuA3
 Bona, G. L. — DWD4, DThA3
 Bostanjoglo, G. — DWC3
 Boyd, B. — DTuB19
 Brazas, John C. — DTuC2
 Britten, J. — DTuB19
 Brown, David R. — DTuB9
 Brundrett, David L. — DMA1
 Buczek, H. — DThA4
 Buralli, Dale A. — JMC1, DTuC
 Burge, Jim — DMB4
 Bussjager, R. — DWD3

Caber, Paul — DThB2
 Calvo, Maria L. — DTuB20
 Carson, R. F. — DTuB18
 Cerrina, Franco — DTuA1
 Chang, Ming-Pin — DTuB13
 Chang, Rong-Seng — DThB5
 Cheben, Pavel — DTuB20
 Chen, D. — DWC2
 Chen, F. T. — DWD3
 Chen, C. William — JMC3
 Cherkashin, V. A. — DWD5
 Clark, Matthew — DTuB15
 Climent, V. — DTuD3
 Clube, F. S. M. — DTuA3
 Cohen, Don — DThB2
 Coleman, Christopher — DWA3
 Conway, Patrick B. — DTuA4
 Cook, P. — DWD3
 Corless, R. F. — DTuB18
 Cox, Andrew C. — DTuA4
 Cox, J. Allen — DMA3, DWC, DThB4
 Craighead, H. G. — DWD3

Daiderich, Alfons — DTuC6
 Danilov, Victor — DWD2
 Daschner, Walter — DMD5
 Decker, D. — DTuB19
 Delisle, C. A. — DTuB12
 Deng, Ximing — DWC7
 Dixit, S. N. — DWC4
 Dobson, David C. — DMA3
 Dong, Bizhen — DTuB13
 Dopazo, Juan F. Román — DTuD5
 Duignan, Michael T. — DTuB7

Ehbets, P. — DTuA3
 Ehrhardt, R. — DMA4
 Ersoy, Okan K. — DTuB13

Fakiis, Dean — JMC4
 Fan, Dianyuan — DWC7
 Fan, Jiao — DWA4
 Fang, K. J. — DMB5
 Farn, Michael W. — JMC2
 Friberg, Ari T. — DTuD4

Gale, M. T. — DWD4
 Gallagher, Neal C. — DTuC4
 Gaylord, Thomas K. — DMA1, DWB
 Gilgen, H. — DThA4
 Glytsis, Elias N. — DMA1
 Gmitro, Arthur F. — DWA3
 Golub, M. A. — DTuC7
 Gramann, Wolfgang — DThA2
 Grann, Eric B. — DMA2, DTuA5, DWB3
 Gray, S. — DTuA3
 Grebel, H. — DMB5, DTuC5
 Gruetzner, J. K. — DMB3
 Gruhlke, Russell W. — DWC6
 Gu, Benyuan — DTuB13
 Guhr, J. — DWC3

Haas, F. — DWD3
 Hadley, G. R. — DTuB18
 Hammons, B. E. — DTuB18
 Han, Y. — DTuB12
 Haq, Tanveer Ul — DTuC4
 Hard, Sverker — DWC5
 Hazra, L. N. — DTuB12
 Heimbeck, Hans-Jörg — DTuB21
 Herzig, H. P. — DMB1, DTuA3, DThB
 Hies, T. — DThA5
 Hirsh, Jeffrey — DTuC2
 Hochmuth, Diane H. — DTuD2
 Holmér, Anna-Karin — DWC5
 Honey, D. A. — DWD3
 Hutley, Michael C. — DTuA, DThA1

Jahns, Jürgen — DMD, DWD
 Jaroszewicz, Z. — DTuD5
 Johnson, Eric G. — DTuB9, DTuD2

Kathman, Alan D. — DTuB9, DTuD2
 Keller, Paul E. — DWA3
 Kharissov, A. A. — DWD5
 Khonina, S. N. — JMC6
 Kim, Tae Wan — DMD3
 Kiryanov, V. P. — DWD5
 Kley, E.-Bernhard — DTuB6, DWD1
 Kolner, Brian H. — DTuD1
 Körner, T. O. — DMA4
 Korol'kov, V. P. — DWD5
 Koronkevich, V. P. — DTuB3, DWD5
 Kostuk, Raymond K. — DMD1
 Kotlyar, V. V. — JMC6
 Krackhardt, U. — DTuB10, DTuB16
 Krasnopernova, Azalia A. — DTuA1
 Kravitz, S. H. — DTuB18
 Kuhlowl, B. — DThA5
 Kung, Peter — DTuB8
 Kunz, R. E. — DWD4, DThA3

Lancis, J. — DTuD3
 Larsson, Michael — DMD5

Lay, Yun Long — DThB5
 Lee, Sing H. — DMD5, DWA4
 Lee, Seung Gol — DMD3
 Lefranc, Guy — DThA2
 Leger, J. R. — DMA, DWA, DWC2
 Leibenguth, R. E. — DTuB18
 Leis, A. V. — DWB5
 Li, Lifeng — DTuB19, DTuC2, DWB4
 Lin, Chern Sheng — DThB5
 Lin, Freddie — DMD2
 Loewen, Erwin G. — DTuB1
 Löfving, Björn — DWC5
 Lohmann, A. W. — DTuB16, DTuD, DWA1

Magnusson, R. — DWB2
 Mait, Joseph N. — DMB, DWC1
 Maker, Paul D. — DWA3
 Marchman, M. Herschel — DThB3
 Mayerhofer, Franz — DThA2
 Maystre, Daniel — DTuB1
 McDowell, Andrew J. — DTuA4
 McKee, P. — DWA2
 McKeon, Amanda L. — DTuC2
 McNeil, John R. — DThB3
 Merrill, R. — DWC4
 Minhas, B. K. — DThB3
 Missig, Michael D. — JMC5
 Mitreiter, A. — DWC3
 Moharam, M. G. — DMA2, DTuA5, DWB3
 Morris, G. Michael — JMC4, JMC5, DTuB, DWB1
 Morrison, Rick L. — DMD4

Naqvi, S. Sohail H. — DThB3
 Neal, D. R. — DMB3
 Nikolajeff, Fredrik — DWC5
 Nikolsky, I. V. — JMC6
 Noponen, Eero — DTuC1
 Nugent, K. A. — DWC4
 Nussbaum, P. — DTuA3

O'Shea, Donald C. — DTuB4, DTuB5
 Ojeda-Castañeda, J. — DWA1

Paige, E. G. S. — DWA5
 Pal'chikova, I. G. — DTuB3
 Parker, Richard A. — DTuA4
 Pavelyev, V. S. — DTuC7
 Pawlowski, E. — DThA5
 Perry, M. D. — DTuB19, DWC4
 Philippov, S. V. — JMC6
 Podlesny, John — DThB2
 Poleshchuk, A. G. — DWD5
 Pommet, Drew A. — DMA2, DTuA5, DWB3
 Popov, Evgeny K. — DTuB1
 Popov, Sergei Yu. — DTuD4
 Powell, H. T. — DWC4
 Prather, Dennis W. — DWC1
 Protsenko, S. G. — DWB5

Qian, Liejia — DWC7

Raguin, Daniel H. — DWB1
 Regnault, Ph. — DThA4
 Rockward, Willie S. — DTuB4
 Rossi, M. — DWD4, DThA3
 Rostalski, H.-J. — DWC3
 Rushford, M. — DWC4

Zaleta, David — DMD5, DWA4
 Zarschizky, Helmut — DTuC6, DThA2
 Zimmer, Ch. — DThA4

Saavedra, G. — DTuD3
 Scarbrough, R. H. — DWA5
 Schnabel, B. — DTuB6
 Shank, S. M. — DWD3
 Sheridan, J. T. — DMA4
 Shore, B. W. — DTuB19
 Shvartsman, Felix P. — DThB4
 Singer, W. — DTuB11
 Sinzinger, S. — DTuB11
 Skvarla, M. — DWD3
 Slinger, Chris W. — DTuA4
 Soifer, V. A. — JMC6, DTuC7
 Sommargren, Gary — DMB2
 Song, Li — DTuB8
 Song, Seok Ho — DMD3
 Southwell, William H. — DTuB2
 Stemmer, Albert — DTuC6, DThA2
 Stern, Margaret B. — DThA, DThB1
 Stuart, B. — DTuB19
 Suleski, Thomas J. — DTuB5
 Sweatt, William C. — JMC
 Sweeney, Donald W. — DMB2

Tajahuerce, E. — DTuD3
 Teiwes, Stephan — DTuC3
 Testorf, M. — DTuB11
 Thomas, I. — DWC4
 Thompson, Patrick L. — DTuB4
 Thurlow, A. — DWA2
 Tisserand, J. C. — DTuA3
 Towers, J. — DWA2
 Tsay, Su Chiou — DTuC5
 Tsonev, Lyubomir — DTuB1
 Turunen, Jari — DTuC1

Van der Gracht, Joseph — DWC1
 Vawter, G. A. — DTuB18
 Voirin, G. — DThA4

Wang, S.S. — DWB2
 Wang, Michael R. — DMA5, DMD2
 Warren, M. E. — DMB3, DTuB18
 Webb, Kevin J. — DTuC4
 Wei, Max — DTuA2
 Wendt, J. R. — DTuB18
 Wilson, Susan M. G. — DThB3
 Wojcik, Mike J. — DMD4
 Wood, Andrew P. — DTuA4
 Wood, D. — DWA2
 Word, J. C. — DTuB18
 Wyant, James C. — DThB2
 Wyrowski, Frank — DTuC1, DTuC3

Yamashita, Tsukasa — DTuB17
 Yang, Guozhen — DTuB13
 Yatagai, Toyohiko — DTuB14
 Yoshikawa, Nobukazu — DTuB14